

A PETROGRAPHIC AND GEOCHEMICAL CHARACTERIZATION  
AND THE EVALUATION OF THE EXPLORATION POTENTIAL FOR  
NICKEL SULFIDES IN SEVERAL MAFIC-ULTRAMAFIC  
INTRUSIVE COMPLEXES IN NEWFOUNDLAND

PATRICK G. COLLINS



**A petrographic and geochemical characterization and the evaluation of the exploration potential for nickel sulfides in several mafic-ultramafic intrusive complexes in Newfoundland**

by  
**Patrick G. Collins**

A thesis submitted to the School of Graduate Studies in partial fulfillment of the requirements for the degree of Master of Science

*Department of Earth Sciences, Memorial University of Newfoundland, St. John's, Newfoundland, Canada, A1C 5S7*

January, 2007

St. John's

Newfoundland



## **Abstract**

On the island of Newfoundland a number of mafic- to ultramafic intrusions are exposed; most commonly in the Dunnage Zone. These intrusive suites occur in a variety of tectonic environments, and have variable relationships with their host rocks. Nickel is extracted from intrusive rocks of similar compositions throughout the world. This thesis evaluates the potential of three intrusive complexes in Newfoundland to host economic Ni-Cu sulphide and/or platinum group element (PGE) mineralization.

The Red Cross Lake Intrusive Suite (RCLIS), located in central Newfoundland, is a ca. 431 Ma layered, mafic- to ultramafic intrusion. The Steel Mountain Anorthosite (SMA), located east of Stephenville, in the Southern Long Range Mountains, is a ca. 1275 Ma massive-type anorthosite that hosts abundant Fe-Ti oxides and variable mafic zones. The Taylor Brook Gabbro Suite (TBGS), located southeast of western White Bay, is a ca. 430 Ma gabbroic suite.

The RCLIS is divided into an Upper and Lower Series (US and LS respectively). The LS is comprised of predominantly gabbro and troctolite layers with minor dunite, olivine gabbro and serpentinite. The US had a gabbroic- to leucogabbroic protolith that is variably altered to pyroxene amphibole gabbro. Geochemical data indicate the RCLIS exhibits an intermediate to alkaline and sub-alkaline composition and is tholeiitic. The RCLIS evolved through fractional crystallization; it exhibits a progressive decrease in MgO and an increase in FeO+TiO<sub>2</sub> from the LS to the US. Sulfides comprise at most only a few weight percent; the maximum values are from country rock samples. Magmatic sulfides in the LS locally exhibit a high Ni tenor. Plagioclase composition averages An 69 in the LS and An 54 in the US, whereas paragneiss xenolith samples average An 47. Olivine composition averages Fo 83 in the LS and Fo 56 for the US; xenoliths average Fo 36. LS olivine is locally Ni-depleted with respect to its Fo content.  $\delta^{34}\text{S}$  ratios exhibit a range of 5.64‰, from -1.79‰ to +3.85‰. The heaviest ratio is from a country rock sample, whereas igneous samples are closer to 0.00‰, suggesting little country rock contamination.

The portion of the Steel Mountain Anorthosite (SMA) mapped is predominantly underlain by elongate, diffuse lenses of leuconorite, leucogabbro, norite and norite hosted by massive, recrystallized pink- to lilac coloured anorthosite. Massive Fe-Ti oxides occur locally in noritic units. Gabbroic units are relatively more altered, whereas noritic units more commonly preserve primary textures. Fe-Ti oxides exhibit complex exsolution textures. Lithochemistry was effective in separating the majority of samples along an evolutionary trend from Mg-rich melanorites to evolved anorthositic samples. Plagioclase becomes increasingly An-enriched as the rocks become more mafic. Clinopyroxene and orthopyroxene are consistently Mg-rich throughout the SMA. Locally, oxides display strong solid substitution and exsolution textures, which generally result from hematite exsolution in ilmenite or ulvöspinel exsolution in magnetite. In the Bishops quarries, hercynite is also common in magnetite. At Sheep Brook, pyrite contains up to 4.7 wt.% Ni in concentric bands. Sperrylite and several other unnamed Pt-Te and Pd-Sb phases were identified.  $\delta^{34}\text{S}$  ratios range from +7.33‰ to -2.41‰; the sulfides from Sheep Brook are near 1.00 ‰ whereas sulfides in the Bishop quarries massive oxides are negative at -2.41 ‰.

The Taylor Brook Gabbro Suite (TBGS) is heterogeneous at all scales. It comprises a concentrically layered pyroxene amphibole gabbro intrusion that is cut by multiple sets of mafic and felsic dikes. In the northern region of the intrusion a separate, more mafic and coarse-grained zone is recognized. Much of the TBGS has been altered to greenschist assemblages with variable degrees of recrystallization. TBGS samples display well-developed geochemical evolution and are locally Fe-Ti enriched. The TBGS exhibits a sub-alkaline composition and lithochemistry suggests that it was emplaced in a within-plate tectono-magmatic environment.  $\delta^{34}\text{S}$  ratios range from +2.22 ‰ to +4.81 ‰, suggesting a magmatic isotopic reservoir.

The RCLIS has the greatest Ni-Cu-PGE exploration potential because of the presence of olivine-rich ultramafic rocks, evidence for some country rock contamination, locally Ni-depleted olivine and high-Ni tenor sulfides cropping out in mafic and ultramafic rocks. The SMA has the potential for future discoveries of PGE mineralization in the Sheep Brook area; grassroots exploration based on structural analyses and geological mapping would be most effective at finding similar mineralization in the area. The TBGS has marginal exploration future, primarily because there are few rock types with characteristics to host orthomagmatic sulfide bodies. It is possible that the TBGS is only weakly eroded and that favourable stratigraphic horizons lie at depth.

## **Acknowledgments**

Many people and organizations are responsible for the production of this project. First, Dr. Derek Wilton, my supervisor, is greatly appreciated for his advice, timely reviews of my work, and most importantly, for allowing me as much freedom as I required during this research. His encouragement, especially towards the end of the project was great, and help to motivate me to finish before I left for a two month vacation to New Zealand, just prior to the completion of the final manuscript.

The Newfoundland and Labrador Department of Mines and Energy, Altius and Coast Under Stress provided financial support through some portion of this project and without their support this project would not have happened.

In October 2004 I broke my tibia and fibula quite badly. I was just beginning to process samples to be submitted for preparation for whole rock XRF analyses and PTS's. Without hesitation, Derek hired three assistants to help me get through this important phase of my research. I am grateful to him, and the students who he hired, John Foster, Megan Lake and Maggie Layman, for their dedicated work while I healed.

During my field work, I was aided by two great assistants, David Shinkle and John Scaplen, both who provided me with great rock hauling abilities, good conversation during long days, and most importantly, patience, while I scouted out some remote location in the most horrendous bush known to man, looking for outcrop. Furthermore, on a few days in the field, David and I were guided by west coast prospector Gerry Hull, while we investigated the Sheep Brook occurrence. Another west coast prospector, Len Musie, kindly offered me his cottage on Flat Bay Brook after he had known me for a mere 10 minutes. Len would later lead me to the Sheep Brook occurrence for further sampling in the spring of 2005. Both Len and Gerry's contributions to my sampling and understanding of the local geology of the SMA is greatly appreciated, and I admire these gentlemen for their dedication to prospecting. Newfoundland Hydro provided permission

and key access to the Flat Bay Brook hydro facility access road, for which I am greatly appreciative.

During the writing of this thesis, I shared many ideas and musings while I crunched through data with my fellow students, particularly my office mate, Michelle Huminiki, and other friends Ron Voordouw and Kate Souders. Their insight and ideas or help finding particular references or calculations for particular figures was beyond great – thanks guys!

Finally, my piles of data could not have been acquired as painlessly as they were without the able assistance by a few technicians in particular. Michael Shafer has helped me through more technical issues than I can count on both hands, from data collection methods, explaining and training me on the MLA-SEM lab at MAF-IIC, to helping me calibrate white balance on my photomicrographs. Also, Danny Mulrooney, the electron microprobe technician and friend was very helpful to me while I worked through my sample probing, especially, for example, when the microprobe computer crashed, or when my totals were off. Danny worked his best to help me through it all.

Finally, as all great acknowledgements do, I must thank my parents, Bill and Lori, for their constant encouragement (albeit remotely, in Dartmouth, Nova Scotia), and advice for how to deal with problems, scholastic or otherwise. Were it not for them, I may never have completed this project, or even started it, for they pushed me on through my undergraduate degree just to get to this point.

Thanks all, see you in the field!

## ***Table of Contents***

<b>Abstract</b>	ii
<b>Acknowledgements</b>	v
<b>List of Tables</b>	xi
<b>List of Figures</b>	xii
<b>List of Appendices</b>	xv
<b>Chapter 1: Introduction</b>	1
Chapter 1.1 Introduction and definition of objectives	1
Chapter 1.2 location and access	1
Chapter 1.3 Practical Implications	3
Chapter 1.4 Regional geology and historical exploration	4
Chapter 1.4.1 RCLIS Regional geology	4
Chapter 1.4.2 RCLIS Previous exploration	6
Chapter 1.4.3 SMA Regional geology	7
Chapter 1.4.4 SMA Previous exploration	9
Chapter 1.4.5 TBGS Regional geology	12
Chapter 1.4.6 TBGS Previous exploration	13
Chapter 1.5 Methodologies introduction	14
Chapter 1.5.1 Field mapping and sampling	14
Chapter 1.5.2 Petrography	15
Chapter 1.5.3 X-ray fluorescence analysis	15
Chapter 1.5.4 Platinum group element (PGE) analysis	15
Chapter 1.5.5 Electron microprobe analysis	16
Chapter 1.5.6 Sulfur isotope analysis	17
<b>Chapter 2: Red Cross Lake Intrusive Suite field geology</b>	19
Chapter 2.0 Introduction	19
Chapter 2.1 Field geology	19
Chapter 2.1.1 Lower Series	20
Chapter 2.1.2 Upper Series	25
Chapter 2.1.3 Xenoliths	27
Chapter 2.1.4 Sulfide mineralization	30
Chapter 2.1.5 Summary	30
<b>Chapter 3: Red Cross Lake Intrusive Suite Petrography</b>	32
Chapter 3.1 Introduction	32
Chapter 3.2 Lower Series mineralogy and petrography	34
Chapter 3.2.1 Lower Series plagioclase	35
Chapter 3.2.2 Lower Series olivine	39
Chapter 3.2.3 Lower Series pyroxene	41
Chapter 3.2.4 Lower Series sulfides	43
Chapter 3.2.5 Lower Series oxides	45
Chapter 3.3 Upper Series mineralogy and petrography	47
Chapter 3.3.1 Upper Series plagioclase	47
Chapter 3.3.2 Upper Series pyroxene	50
Chapter 3.3.3 Upper Series amphibole and biotite	52
Chapter 3.3.4 Upper Series accessory phases	55

Chapter 3.5	Petrological summary	57
<b>Chapter 4:</b>	<b>Red Cross Lake Intrusive Suite whole rock lithogeochemistry</b>	61
Chapter 4.1	Introduction	61
Chapter 4.2	Bivariate plots	61
Chapter 4.2.1	Harker diagrams	61
Chapter 4.3	General compositional nomenclature	68
Chapter 4.4	Igneous nomenclature	70
Chapter 4.5	Tectono-magmatic diagrams	73
Chapter 4.6	Sulfide calculations	75
Chapter 4.7	Base metal and sulfide diagrams	78
Chapter 4.8	Summary	84
<b>Chapter 5:</b>	<b>Red Cross Lake Intrusive Suite mineral geochemistry</b>	86
Chapter 5.0	Introduction	86
Chapter 5.1	Plagioclase	86
Chapter 5.2	Olivine	92
Chapter 5.3	Pyroxene	106
Chapter 5.4	Amphibole reaction rims	110
Chapter 5.5	Oxides	113
Chapter 5.5.1	Spinel series	113
Chapter 5.5.2	Rhombohedral series	121
Chapter 5.6	Sulfides	122
Chapter 5.6.1	Pentlandite	122
Chapter 5.6.2	Chalcopyrite	124
Chapter 5.6.3	Pyrrhotite	124
Chapter 5.7	Summary	130
<b>Chapter 6:</b>	<b>Red Cross lake Intrusive Suite sulfur isotopes</b>	134
Chapter 6.1	An overview of sulfur isotopes	134
Chapter 6.2	$\delta^{34}\text{S}$ isotope results	135
Chapter 6.3	Summary	139
<b>Chapter 7:</b>	<b>Discussion and conclusions</b>	140
Chapter 7.1	Overview	140
Chapter 7.2	Discussion	141
Chapter 7.2.1	Evidence for multistage emplacement history	141
Chapter 7.2.2	Evaluation of the economic potential of the RCLIS	144
Chapter 7.3	Conclusions	146
<b>Chapter 8:</b>	<b>Steel Mountain Anorthosite field geology</b>	147
Chapter 8.1	Introduction	147
Chapter 8.2	Mafic dikes	154
Chapter 8.3	Sheep Brook	156
Chapter 8.4	Summary	161
<b>Chapter 9:</b>	<b>Steel Mountain Anorthosite petrography</b>	162
Chapter 9.1	Introduction	162

Chapter 9.2	Mineralogy overview	163
Chapter 9.3	Plagioclase	166
Chapter 9.4	Pyroxene	170
Chapter 9.5	Garnet	173
Chapter 9.6	Oxides	178
Chapter 9.7	Sulfides	180
Chapter 9.8	Petrographical summary	186
<b>Chapter 10:</b>	<b>Steel Mountain Anorthosite whole rock litho-geochemistry</b>	<b>198</b>
Chapter 10.1	Introduction	198
Chapter 10.2	Bivariate diagrams	190
Chapter 10.2.1	Harker diagrams	190
Chapter 10.3	General composition	194
Chapter 10.4	igneous nomenclature	199
Chapter 10.5	Summary	199
<b>Chapter 11:</b>	<b>Steel Mountain Anorthosite mineral geochemistry</b>	<b>202</b>
Chapter 11.1	Plagioclase	202
Chapter 11.2	Pyroxene	212
Chapter 11.3	Garnet	217
Chapter 11.4	Amphibole and other secondary phases	222
Chapter 11.5	Sulfides and platinum group elements	226
Chapter 11.5.1	Sulfides	228
Chapter 11.5.2	Platinum group minerals	233
Chapter 11.6	Oxides	238
Chapter 11.6.1	Ilmenite Series	239
Chapter 11.6.2	Spinel Series	243
Chapter 11.6.3	Exsolution lamellae	247
Chapter 11.6.4	Oxide alteration	254
Chapter 11.7	Summary	254
<b>Chapter 12:</b>	<b>Steel Mountain Anorthosite sulfur isotopes</b>	<b>259</b>
Chapter 12.1	$\delta^{34}\text{S}$ isotope results	259
<b>Chapter 13:</b>	<b>Discussion and conclusions</b>	<b>263</b>
Chapter 13.1	Overview	263
Chapter 13.2	Orthomagmatic vs metasomatic oxides	263
Chapter 13.3	PGE occurrences	264
Chapter 13.4	Plagioclase colouration	265
Chapter 13.5	Conclusions	265
<b>Chapter 14:</b>	<b>Taylor Brook Gabbro Suite field geology</b>	<b>266</b>
Chapter 14.1	Introduction	266
Chapter 14.2	Field geology	266
Chapter 14.2.1	Igneous layering	266
Chapter 14.2.2	Contact relationships	270
Chapter 14.2.3	Xenoliths	274
Chapter 14.2.4	Mafic dikes	277
Chapter 14.2.5	Sulfide mineralization	282

Chapter 14.3	Taylor Brook Gabbro Pegmatite	282
Chapter 14.4	Late intrusive phases	285
Chapter 14.5	Summary	287
<b>Chapter 15: Taylor Brook Gabbro Suite petrography</b>		<b>289</b>
Chapter 15.1	Introduction	289
Chapter 15.2	Taylor Brook Gabbro Suite mineralogy and petrography	290
Chapter 15.2.1	Taylor Brook Gabbro Suite plagioclase	292
Chapter 15.2.2	Taylor Brook Gabbro Suite pyroxene	292
Chapter 15.2.3	Taylor Brook Gabbro Suite amphibole	294
Chapter 15.2.4	Taylor Brook Gabbro Suite accessory phases	297
Chapter 15.3	Taylor Brook Gabbro Pegmatite mineralogy and petrography	300
Chapter 15.3.1	Taylor Brook Gabbro Pegmatite plagioclase	301
Chapter 15.3.2	Taylor Brook Gabbro Pegmatite amphibole	301
Chapter 15.3.3	Taylor Brook Gabbro Pegmatite pyroxene	303
Chapter 15.3.4	Taylor Brook Gabbro Pegmatite accessory phases	303
Chapter 15.4	Taylor Brook Gabbro Suite petrographical summary	304
<b>Chapter 16: Taylor Brook Gabbro Suite litho-geochemistry</b>		<b>306</b>
Chapter 16.1	Introduction	306
Chapter 16.2	Bivariate diagrams	307
Chapter 16.2.1	Harker diagrams	307
Chapter 16.3	General compositional nomenclature	311
Chapter 16.4	igneous nomenclature	313
Chapter 16.5	Tectono-magmatic discrimination	315
Chapter 16.6	Summary	320
<b>Chapter 17: Taylor Brook Gabbro Suite sulfur isotopes</b>		<b>322</b>
Chapter 17.1	$\delta^{34}\text{S}$ isotope results	322
<b>Chapter 18: Discussion and conclusions</b>		<b>326</b>
Chapter 18.1	Overview	326
Chapter 18.2	Field relationships	326
Chapter 18.3	Geochemical considerations	327
Chapter 18.4	Conclusions	327
<b>References</b>		<b>328</b>

## List of Tables

Table 4.1	Calculated Ni-Cu-PGE contents	78
Table 5.1	Plagioclase core-rim An zonation	88
Table 5.2	RCLIS electron microprobe plagioclase summary	92
Table 5.3	Average CPX and OPX composition in the RCLIS	110
Table 5.4	A summary of RCLIS amphibole Mg#'s	111
Table 5.5	Cubic spinel cationic subdivisions	116
Table 5.6	A summary of Lower Series spinel analyses	118
Table 5.7	A summary of RCLIS ilmenite analyses	121
Table 5.8	A summary of Ni in pyrrhotite	128
Table 6.1	A summary of $\delta^{34}\text{S}$ isotopic ratios in the RCLIS	137
Table 11.1	Average and standard deviation of plagioclase composition	204
Table 11.2	A summary of crystal-type locations	204
Table 11.3	Average CPX and OPX compositions in the SMA	213
Table 11.4	Garnet composition in the SMA	218
Table 11.5	A summary of SMA pyrrhotite composition	227
Table 11.6	Platinum telluride mineral composition in the SMA	233
Table 11.7	Known Pt-Te mineral compositions	235
Table 11.8	Pd-Sb minerals in the SMA	237
Table 11.9	Pt-As minerals in the SMA	237
Table 11.10	A summary of SMA ilmenite analyses	239
Table 11.11	A summary of SMA spinel analyses	244
Table 12.1	A summary of $\delta^{34}\text{S}$ isotopic ratios in the SMA	260
Table 17.1	A summary of $\delta^{34}\text{S}$ isotopic ratios in the TBGS	325

## List of Figures

Figure 2.1	Geology of the RCLIS	21
Figure 2.2	RCLIS Lower Series layering textures	22
Figure 2.3	Gradational magmatic layering in the LS	24
Figure 2.4	Upper Series jointing textures	26
Figure 2.5	Examples of xenolith occurrences in the RCLIS	28
Figure 3.1	Lower Series and Upper Series ternary diagrams	33
Figure 3.2	Transmitted light photomicrographs of the LS	36
Figure 3.3	Transmitted light photomicrographs of the LS	40
Figure 3.4	Transmitted light photomicrographs of the LS	42
Figure 3.5	Reflected light photomicrographs of LS sulfides	44
Figure 3.6	Transmitted light photomicrographs of the US	49
Figure 3.7	Transmitted light photomicrographs of the US	49
Figure 3.8	Transmitted light photomicrograph of the Transition Zone	51
Figure 3.9	Transmitted light photomicrographs of the US	53
Figure 3.10	Transmitted light photomicrographs of the US	54
Figure 3.11	Transmitted light photomicrographs of the US	56
Figure 4.1	RCLIS Harker diagrams of wholerock lithogeochemistry	63-64
Figure 4.2	RCLIS total alkali silica (TAS) diagrams	69
Figure 4.3	RCLIS total alkali silica (TAS) diagrams	71-72
Figure 4.4	RCLIS Jensen plot for determining igneous nomenclature	74
Figure 4.5	Normative sulfide calculation flow chart	77
Figure 4.6	Pt-Pd whole rock geochemical trends	80-82
Figure 5.1	Plagioclase core and rim microprobe compositional data	89
Figure 5.2	RCLIS plagioclase ternary compositional diagram	90
Figure 5.3	Backscatter image of LS plagioclase compositional zoning	91
Figure 5.4	Backscatter images of olivine-plagioclase reaction rims	93
Figure 5.5	Backscatter images of US plagioclase compositional zoning	94
Figure 5.6	Backscatter images of US plagioclase compositional zoning	95
Figure 5.7	Map of the variation of plagioclase composition (An) in the LS	96
Figure 5.8	RCLIS Fo-Ni microprobe data from LS olivine	98
Figure 5.9	Ni distribution in individual LS olivines	99
Figure 5.10	Ni vs Fo compositional differences between RIC-02 and RIC-21	101
Figure 5.11	RCLIS and historical olivine data comparison	102
Figure 5.12	Backscatter image of seive-like olivine textures in RIC-51.1c	104
Figure 5.13	Strongly embayed olivine in RIC-23B	105
Figure 5.14	Olivine reaction rims in RIC-06	107
Figure 5.15	RCLIS pyroxene ranges in Wo-En-Fs compositional space	109
Figure 5.16	RCLIS Mg-Fe amphibole characterization	112
Figure 5.17	Amphibole reaction rims between plagioclase and pyroxene	114
Figure 5.18	Symplectically intergrown amphibole, olivine and plagioclase	115
Figure 5.19	Spinel nomenclature in a multicomponent compositional prism	117
Figure 5.20	RCLIS oxide ternary compositional diagram	119
Figure 5.21	Chromite exsolution in LS magnetite	120
Figure 5.22	Ilmenite analyses in TiO <sub>2</sub> -FeO-1/2 Fe <sub>2</sub> O <sub>3</sub> ternary space	123
Figure 5.23	Ni and Fe contents for RCLIS pentlandite	125

Figure 5.24	Co vs Ni and Co vs Fe in RCLIS pentlandite	126
Figure 5.25	Backscatter image of typical LS sulfide assemblage	127
Figure 5.26	Ni vs total metal/sulfur for RCLIS pyrrhotite polytypes & troilite	129
Figure 5.27	Backscatter image of hexagonal pyrrhotite exsolving from troilite	131
Figure 6.1	$\delta^{34}\text{S}$ ratios for RCLIS sulfides	136
Figure 6.2	RCLIS sulfur isotopes compared to different sulfur reservoirs	138
Figure 8.1	SMA geology map	148
Figure 8.2	Deformed SMA anorthosite- to leuconorite	149
Figure 8.3	Textural varieties of SMA norite	151
Figure 8.4	Anorthosite-norite pods at Lookout Pond in the SMA	152
Figure 8.5	Weakly layered megacrystic norite near Lookout Pond, SMA	153
Figure 8.6	Weakly foliated pink leuconorite and coarse-grained magnetite	155
Figure 8.7	Cliff-side exposure of a wide mafic dike in the SMA	157
Figure 8.8	Deformed lenses of massive sulfides at Sheep Brook	158
Figure 8.9	Strongly deformed anorthosite at Sheep Brook	159
Figure 8.10	Chloritized and amphibolitized mafic dikes at Sheep Brook	160
Figure 9.1	Ternary diagram of normative SMA mineralogy	164
Figure 9.2	Deformation microtextures in SMA plagioclase	168
Figure 9.3	Epidote alteration in transmitted, cross-polarized light	169
Figure 9.4	Scanned SMA thin section illustrating macroscopic textures	171
Figure 9.5	Mild, microscopic deformation in SMA orthopyroxene	172
Figure 9.6	Microscopic rutile inclusions in SMA orthopyroxene	174
Figure 9.7	Orthopyroxene replacement textures in the SMA	175
Figure 9.8	Examples of garnet reaction rims in the SMA	176
Figure 9.9	Double-shelled corona structures in SMA garnet reaction rims	177
Figure 9.10	Flame lamellae and pyrite cubes in deformed SMA pyrrhotite	182
Figure 9.11	Complex deformation lamellae in SMA pyrrhotite	183
Figure 9.12a	Breccia textures of pyrite and chalcopyrite from the Sheep Brook	185
Figure 9.12b	Growth banding and Ni enrichment in Sheep Brook pyrite	185
Figure 10.1	Harker diagrams for SMA whole rock geochemistry	191-192
Figure 10.2	Total alkali silica diagrams for SMA rocks	196
Figure 10.3	AFM diagram for SMA rocks	196
Figure 10.4	Trace element ratio diagrams for differentiating SMA lithologies	198
Figure 10.5	Igneous nomenclature for SMA rocks	200
Figure 11.1	Ternary diagram of An-Ab-Or feldspar compositional space	205
Figure 11.2	Distribution of feldspar compositions in the SMA	206
Figure 11.3	Backscatter image of lattice-controlled feldspar exsolution blebs	208
Figure 11.4	Plagioclase and pyroxene recrystallization microtextures	209
Figure 11.5	Plagioclase trace elements versus visible colouration	210
Figure 11.6	Ternary diagram of SMA En-Wo-Fs compositional space	212
Figure 11.7	Trace metal distribution in SMA orthopyroxene	214
Figure 11.8	Major element variation across SMA orthopyroxene	215
Figure 11.9	Compositional variation in traverses across SMA garnet	217
Figure 11.10	Compositional zoning in SMA-09 garnet	219
Figure 11.11	Backscatter images of garnet reaction rims	220
Figure 11.12	Amphibole composition in the SMA	222

Figure 11.13	Ternary diagram of SMA epidote	225
Figure 11.14	Texturally and compositionally complex reaction rim in the SMA	227
Figure 11.15	Ni vs Fe in pyrrhotite from the Sheep Brook massive sulfides	229
Figure 11.16	Ni vs Fe in pyrite from the Sheep Brook massive sulfides	229
Figure 11.17	False coloured backscatter images of Ni zoning in pyrite	231
Figure 11.18	Backscatter images of deformation textures from Sheep Brook	232
Figure 11.19	Backscatter images of a Pt-Te phase in Sheep Brook sulfides	235
Figure 11.20	Ultra-fine hematite exsolution lamellae in ilmenite in the SMA	240
Figure 11.21	Bivariate diagrams of compositional variation in SMA ilmenite	242
Figure 11.22	Spinel discrimination diagrams using microprobe data	245
Figure 11.23	SMA $\text{TiO}_2\text{-FeO-}1/2 \text{ Fe}_2\text{O}_3$ ternary diagram of SMA Fe-Ti oxides	248
Figure 11.24	Backscatter images of ilmenite-hematite exsolution lamellae	250
Figure 11.25	Backscatter images of magnetite-ulvospinel exsolution lamellae	252
Figure 11.26	Backscatter image of Fe-Ti oxide alteration in SMA-15	255
Figure 12.1	SMA $\delta^{34}\text{S}$ isotopic ratios	261
Figure 12.2	SMA sulfur isotopes compared to different sulfur reservoirs	262
Figure 14.1	A geological map of the TBGS and surrounding country rock	267-268
Figure 14.2	Magmatic layering textures in the TBGS	269
Figure 14.3	Oxide-rich cumulate layering textures in TBC-55	271
Figure 14.4	Chaotic, disrupted layering in the TBGS	272
Figure 14.5	Possible large stoped blocks of amphibolite or digested dikes	273
Figure 14.6	Strongly disaggregated mafic dike in TBGS country rock	275
Figure 14.7	Textural varieties of xenoliths in the TBGS	276
Figure 14.8	Xenolith-bearing pegmatite pipes in the interior of the TBGS	278
Figure 14.9	Textural varieties of mafic dikes in the TBGS	279
Figure 14.10	Magma mingling textures in the TBGS	281
Figure 14.11	Textural varieties of pegmatitic pipes in the TBGP	284
Figure 14.12	Large, atypical xenoliths along the TBGS-TBGP contact	286
Figure 15.1	Ternary diagrams of normalized TBGS mineralogy	291
Figure 15.2	Plagioclase recrystallization textures in the TBGS	293
Figure 15.3	Magmatic versus metamorphic textures of pyroxene in the TBGS	295
Figure 15.4	Partially pseudomorphed poikilitic pyroxene in the TBGS	296
Figure 15.5	Fe-Ti oxides and spinel with amphibole reaction rims	298
Figure 15.6	Biotite partially replaces secondary amphibole	299
Figure 15.7	Coarse-grained, prismatic epidote after medium-grained chlorite	302
Figure 16.1	Harker diagrams for TBGS whole rock geochemistry	308-309
Figure 16.2	Total alkali silica diagrams demonstrate geochemical trends	312
Figure 16.3	TAS diagrams are used to determine plutonic nomenclature	314
Figure 16.3	Fe+Ti - Al - Mg diagrams are used for plutonic nomenclature	314
Figure 16.4	Tectonomagmatic discrimination diagram for TBGS rocks	317
Figure 16.5	Tectonomagmatic discrimination diagram for TBGS rocks	318
Figure 16.6	Tectonomagmatic discrimination diagram for TBGS rocks	319
Figure 17.1	TBGS $\delta^{34}\text{S}$ isotopic ratios	324
Figure 17.2	TBGS sulfur isotopes compared to different sulfur reservoirs	325

## List of Appendices

Appendix 1.1	RCLIS sample locations	336
Appendix 1.2	SMA sample locations	337
Appendix 1.3	TBGS sample locations	338
Appendix 2.1	RCLIS mineralogy and nomenclature	340
Appendix 2.2	SMA mineralogy and nomenclature	342
Appendix 2.3	TBGS mineralogy and nomenclature	343
Appendix 3.1	RCLIS lithogeochemistry	346
Appendix 3.2	SMA lithogeochemistry	347
Appendix 3.3	TBGS lithogeochemistry	348
Appendix 3.4	Sulfide normalization example calculations	349
Appendix 4.1	RCLIS olivine mineral chemistry	351
Appendix 4.2	RCLIS pyroxene mineral chemistry	357
Appendix 4.3	RCLIS feldspar mineral chemistry	358
Appendix 4.4	RCLIS ilmenite mineral chemistry	362
Appendix 4.5	RCLIS spinel mineral chemistry	363
Appendix 4.6	RCLIS pyrrhotite mineral chemistry	364
Appendix 4.7	RCLIS pentlandite mineral chemistry	367
Appendix 4.8	RCLIS chalcopyrite mineral chemistry	369
Appendix 4.9	RCLIS other sulfide mineral chemistry	370
Appendix 4.10	SMA feldspar mineral chemistry	371
Appendix 4.11	SMA pyroxene mineral chemistry	373
Appendix 4.12	SMA garnet mineral chemistry	374
Appendix 4.13	SMA ilmenite mineral chemistry	375
Appendix 4.14	SMA spinel mineral chemistry	376
Appendix 4.15	SMA pyrrhotite mineral chemistry	377
Appendix 4.16	SMA pyrite mineral chemistry	378
Appendix 4.17	SMA chalcopyrite mineral chemistry	379
Appendix 4.18	SMA sphalerite mineral chemistry	380
Appendix 4.19	SMA unprocessed PGE mineral chemistry	381
Appendix 4.20	SMA normalized PGE mineral chemistry	382
Appendix 4.21	Electron microprobe accuracy and precision	383
Appendix 4.22	Electron microprobe elemental standards	384
Appendix 5	Sulfur isotopes for all intrusions	385

# **Chapter 1**

## **1.1 Introduction and definition of objectives**

Insular Newfoundland hosts abundant mafic to ultramafic intrusions that occur most commonly in the Dunnage Zone (Williams, 1979). These intrusive suites occur in many different tectonic environments, and have variable relationships with their host rocks. Historically, nickel has been extracted from intrusive rocks of similar compositions throughout the world (e.g. Naldrett, 2004), and these rock types continue to be of interest within the global nickel exploration community.

This thesis evaluates the potential of three intrusive complexes in Newfoundland to host economic or sub-economic Ni-Cu sulphide and/or platinum group element (PGE) mineralization. The techniques utilized in this thesis are of a general exploration program type and the work is intended to demonstrate how a variety of techniques may be utilized in the exploration for small Ni sulphide bodies.

The nature of this thesis requires that each intrusion be examined almost as a separate thesis so that all the data from each intrusion are presented, and conclusions stated before moving along to the next intrusion. The thesis presents data from the Red Cross Lake Intrusive Suite first, followed by the Steel Mountain Anorthosite and finally the Taylor Brook Gabbro Suite.

## **1.2 Location and access**

The Red Cross Lake Intrusive Suite (RCLIS) is located in central Newfoundland (NTS 12A/7 and 12A/7). The intrusion is centered on 0501035E and 5360428N in NAD 83, UTM Zone 21. Located approximately 50 km south of Buchans in the western Dunnage Zone, access to the RCLIS has historically been by a logging road, which originates in Millertown Junction. An attempt at access using this road with a 4x4 SUV in the summer

of 2004, however, was unsuccessful due to the overgrown and washed out condition of the final section of road. ATV access appears possible by these roads, although at least one key bridge no longer exists. Several hunting camps along the western shore of Red Cross Lake are evidence of recent access. The 2004 field work access was by helicopter from a major Abitibi Consolidated logging road that originates at a major turn on Highway 480 south of the Annieopsquotch Mountains.

The Steel Mountain Anorthosite (SMA) is located in western Newfoundland (NTS 12B/09 and 12B/08). The study area is centered on NAD 83, UTM Zone 21, 0406397E and 5359978N, approximately 20 km east of St. George's, at the end of Flat Bay Brook Road, a moderately well-maintained 15 km long gravel road. This road begins approximately 500 meters north of an Ultramar gas station located several kilometers south of the Stephenville Crossing exit ramp on the Trans Canada Highway. At the end of Flat Bay Brook Road is the Lookout Pond hydroelectric generating station, where Newfoundland Hydro controls access to the private road that services the hydro generating facilities. Permission to use this road and key-access for the gate across the road during field mapping was kindly granted by Newfoundland Hydro. At the top of this very steep access road, a 2 km walk is required to access the areas of interest; ATV access is possible from the top of the road.

The Taylor Brook Gabbro Suite (TBGS) area is located in northwestern Newfoundland (NTS 12H/11). The intrusion is centered over NAD 83, UTM Zone 21, 0489012E and 5498848N. The TBGS is southwest of White Bay, approximately 20 km west of the town of Hampden. It is accessible by well-maintained gravel logging roads that begin approximately 25 km south of Sop's Arm, along Highway 420. The access road heads west into the Northern Peninsula, parallel to the Upper Humber River, and branches several times to the north and west. Field areas mapped in the TBGS begin approximately 15 km along the main logging road at a fork to the northeast. Mapping in the southern TBGS was conducted largely along logging roads and to a lesser extent by foot traverses,

but outcrops are scarce away from logging roads. Herein the northern portion is termed the “Taylor Brook Gabbro Pegmatite” (TBGP) based on its distinctive composition and texture. In the TBGP, two logging roads were used to access the map areas for foot traversing and canoe work.

### **1.3 Practical Implications**

There are several implications for the research results contained herein. First, because of the number of intrusive bodies examined, there will be new data available to the geoscience community in general; geochemical and microprobe data specifically will be a boon to the exploration community. With the construction of a nickel hydro-smelter at Argentia to process ore from the Voisey’s Bay Ni-Cu-Co deposit, the discovery of smaller tonnage deposits on the island of Newfoundland will be of significance because of their potential use as feed for the smelter.

The Red Cross Lake Intrusive Suite has not been mapped in detail despite recommendations from previous exploration programs (Nuri, 1980; Barbour, 1998). The goals for research on the RCLIS are to develop a better understanding of the layering in the RCLIS and to determine the potential for this intrusion to host economic quantities of sulfide mineralization.

The goals for research on the noritic portions of the SMA were threefold. First, the SMA hosts several small to large magnetite deposits, and contains variable amounts of magnetite in association with pyroxene and bleached plagioclase. With regards to magnetite, the question arises as to whether it is orthomagmatic, or formed by metasomatic or metamorphic reactions, or some combination of both. Secondly, although rare, sulfides are locally present, and are associated with PGE anomalies in at least two locations in the SMA (Bradley, 1995; Pilgrim and Regular, 1998; Len Muise, 2004, pers. comm.). Characterizing the PGE distribution in sulfides will also be undertaken. Finally, plagioclase in the SMA varies from mauve or lilac colour, to dark purple. During field

mapping, the colour and distribution of purple to mauve plagioclase was noted; this unusual mineralogical characteristic will be subject to a petrographic and geochemical investigation.

The TBGS was chosen as a mapping target for much the same reasons as the Steel Mountain Anorthosite: there has been a lack of exploration in the area due to reconnaissance level mapping, combined with prospective Ni-Cu-PGE host rocks. As well, there are Ni-Cu-Co soil and lake sediment anomalies (Davenport, 1989; Rose, 1998; Harris and Rose, 1997). Lithochemical analysis has previously indicated a positive correlation between nickel and olivine (Rose, 1998 and references therein). Furthermore, mapping by Owen (1986, 1991) and Rose (1998) indicated that the gabbroic rocks of the TBGS have potential to host sulfide zones. The northern Taylor Brook Gabbro Suite was mapped by Owen (1986) as layered- to massive gabbro that is texturally and compositionally similar to the southern zone with the exception of a zone of pegmatitic gabbro that is compositionally distinct from the southern TBGS.

## **1.4 Regional Geology and Historical Exploration**

### **1.4.1 RCLIS Regional geology**

The Red Cross Lake Intrusive Suite is located in the western Dunnage Zone in central Newfoundland. The regional geology surrounding the RCLIS was mapped in several stages beginning with Riley (1957), who mapped the western Victoria Lake area.

Williams (1970) mapped the eastern half of the Victoria Lake area at a similar scale of 1:250000. Following this, Kean (1977) mapped the Victoria Lake (12A/06), and finally, Colman-Sadd (1987) mapped the Snowshoe Pond area (NTS 12A/07), at 1:50000. The Victoria Lake and nearby Valentine Lake regions have been the subjects of extensive mineral exploration-driven mapping projects, focused principally on the Ordovician-Silurian sedimentary and volcanic sequences that host Au and base metal occurrences (e.g. Thurlow 1987 and Nuri, 1980).

The region surrounding the RCLIS comprises two lithotectonic zones, based on age, structural relationships, and lithology. North and southwest of the RCLIS is a package of Ordovician, or older, metasedimentary and metavolcanic rocks, which are part of the Victoria Lake – Bay du Nord Groups (Riley, 1957; Williams, 1970; Colman-Sadd, 1987; Kean, 1977). The Victoria Lake Group comprises a linear belt of metasedimentary rocks located immediately north of the RCLIS, which contains variable lithologies including flattened siltstone, argillite, black shale, greywacke, sandstone, conglomerate and tuff (Kean, 1977). The spatially most abundant lithologies are rhythmically layered, alternating green, light gray, white and black siltstone, argillite, sandstone, and siliceous argillite. Black shale and argillite are locally abundant enough to form mappable units and are described as well cleaved, friable, and pyritiferous (Kean, 1977). Such lithologies would constitute an ideal sulphide contaminate for mafic magmas during emplacement. Immediately to the north of this Ordovician sequence is a thin, parallel unit of boulder conglomerate that is in unconformable contact with the metasedimentary rocks because, according to the maps by Kean (1977) and Williams (1970), the boulder conglomerates are of Devonian age. North of the boulder conglomerate is a thin unit of Devonian igneous rocks comprising granite, diorite, and gabbro. Northeast of the RCLIS are Ordovician volcanic and volcanogenic sedimentary rocks. The sedimentary rocks are rich in volcanic inclusions, and consist of thin beds of sandstone and shale, thick beds of sandstone, and unbedded conglomerate (Colman-Sadd, 1987). The volcanic rocks, where sampled during the field season of 2004, have a variable degree of deformation, from nearly massive (RIC-12) to strongly foliated (RIC-77). North of the volcanogenic sedimentary rocks are sequences of predominantly mafic volcanic rocks that are pillowed, massive, and may have volcanic breccias (Colman-Sadd, 1987). These volcanic rocks have not been formally assigned to a particular group, though based on similar ages, these rocks may be part of the Victoria Lake Group.

South of the RCLIS, the geology is dominated by significantly higher grade metamorphic rocks of variable protoliths and ages. The central to western portions of the lower RCLIS are in direct contact with moderate to strongly metamorphosed Ordovician sedimentary rocks that include middle to upper amphibolite facies quartzite, psammite, semipelite, and pelite that are locally migmatized (Colman-Sadd, 1987). Along the southeastern margin of the RCLIS is Silurian- to Devonian equigranular, locally megacrystic, strongly foliated, medium-grained, gray or pink biotite granite (Colman-Sadd, 1987). This variability in the degree of recrystallization or metamorphism in the country rocks was observed during mapping indirectly by a change in the composition of xenoliths along the basal contact of the RCLIS: the eastern contacts are dominated by massive to weakly foliated gray-pink granite, whereas the western contacts are dominated by amphibolite facies metasedimentary rocks.

#### **1.4.2 RCLIS Previous exploration**

There have been several exploration programs in the RCLIS. In 1979-1980, exploration and mapping of the A.N.D. Charter (Anglo Newfoundland Development Co.) was conducted by the Hudson's Bay Oil and Gas Company Ltd. (Nuri, 1980) and included the area of Red Cross Lake. Although the focus was VMS-style mineralization, they briefly explored and sampled the RCLIS, noting the layered nature of the southern portion and hence the favourable exploration potential for Ni-Cu-Co mineralization (Nuri, 1980). Further exploration was recommended, but there is no record of any more exploration by HBOGL. During 1998 exploration by a Mountain Lake Resources Inc. - Noranda Mining and Exploration Inc. joint venture project in the Valentine Lake area, a cursory investigation the RCLIS was conducted (Barbour, 1998). This exploration project was not focused on the RCLIS, thus only one day was spent collecting samples from the southern end of the intrusion (Barbour, 1998). Of the nine samples collected, seven were sent for detailed analysis by Dogan Paktunc at CANMET in Ottawa. Paktunc concluded, after assessing olivine compositions by electron microprobe analysis, that several

samples showed evidence for Ni depletion via an immiscible sulphide melt (Barbour, 1998).

Between 2003 and 2004, Falconbridge Ltd. mapstaked blocks of land that completely enclose the RCLIS. The nature of the exploration conducted by Falconbridge is unknown, because they are not required to make their data public until 2006.

### **1.4.3 SMA Regional geology**

Southwestern Newfoundland consists of two tectonostratigraphic zones, the Humber to the west and the Dunnage to the east (Williams, 1979; Williams et al. 1988). Subzones are divided on the basis of age, composition, and tectonic history and the boundaries are marked by prominent lineations or major faults (e.g. Currie and Piasecki, 1989; Williams et al., 1988; Currie and van Berkel, 1992; Currie et al., 1991; Currie, 1987). The Steel Mountain Anorthosite, dated at  $1274 \pm 18$  Ma (U-Pb zircon) by Currie and van Berkel (1992), is a major component of the eastern subzone of the Humber Zone, termed the Steel Mountain Subzone (Currie and Piasecki, 1989; Currie, 1987) and also referred to as the internal Humber Zone (Brem et al., 2002, 2003). The Steel Mountain subzone (SMS) is bounded to the east by the Long Range fault (LRF), which also marks the major boundary between the Humber and the Dunnage zones (Williams et al., 1988).

Brem et al. (2003) provide a summary of the Long Range Fault nomenclature. In the west, the SMS is bounded by the Grand Lake Fault (GLF), which is projected into St. George's Bay. Approximately 20 kilometers northeast of St. George's Bay, Carboniferous clastic allochthons obscure the Grand Lake Fault (Currie and van Berkel 1992 b). The LRF, also known as the Baie Vert-Brompton (BVB) line in the north, is a major structural feature that extends the length of western Newfoundland. East of the SMA it is expressed by a  $\leq 800$  m wide zone of anorthosite and gabbro gneisses that record multiple displacement events, both ductile and brittle or cataclastic (Brem et al. 2002). Brem et al. (2005) derived a U/Pb zircon age of  $456 \pm 12$  Ma for pink pegmatitic

dikes that intrude metasedimentary gneiss and are interpreted to be late syn-tectonic. Hence the age is interpreted to reflect the minimum age of deformation along the Long Range Fault. The Grand Lake Fault and the Long Range Fault are subvertical and, south of Grand Lake, bound low angle north to northwestward directed tectonic slices of variable age and lithology (Currie, 1987).

North of the SMA, Precambrian and Paleozoic basement rocks comprising gneisses with variable protoliths and ages are repeated in a multiply deformed and metamorphosed imbricate northwest to westward verging thrust stack (Cawood et al., 1994). The Disappointment Hill complex (DHC), a granulite facies, two-pyroxene gneiss (Owen and Currie, 1991) is the oldest unit in the Steel Mountain subzone and has been dated by U/Pb zircon at  $1498_{-8}^{+9}$  Ma (Currie et al., 1992). Brem et al. (2003) have questioned the DHC age relationships, suggesting that it may be an exotic block derived from the Dashwoods Subzone. However, in the absence of new geochronological data, coupled with the  $1498_{-8}^{+9}$  Ma age and previous mapping (Currie and van Berkel, 1992; Owen and Currie, 1991; Owen and Erdmer, 1989), this claim does not appear plausible. In particular, Currie et al. (1992) and Baird (1954) both document the presence of DHC inclusions within the SMA.

In addition to the DHC, other tectonic slices of various ages, and granitoid intrusions comprise the Steel Mountain subzone. The youngest unit within the SMS is the Hare Hill Granite, which is a massive, homogenous, coarse-grained pink- to pale red leucogranite that is only locally weakly recrystallized. The Hare Hill Granite was assigned an igneous U-Pb zircon age of  $608 \pm 4$  Ma Currie et al. (1992). Tectonically interleaved between the DHC and Hare Hill Granite, is a mixture of unnamed Proterozoic lithologies comprising leucocratic, granulite facies gneiss of trondhjemitic affinity, pale pink hornblende-biotite granite gneiss, and rare bands of garnetiferous biotite gneiss and layers up to 3 m thick of very coarse quartzite and marble (Currie and van Berkel, 1992). Biotite gneiss and feldspathic amphibolitic gneisses are strongly migmatized, exhibiting at least two distinct

phases of partial melting (Currie and van Berkel, 1992). The easternmost unit in the Steel Mountain subzone, tectonically overlying the unnamed orthogneiss is the younger Fleur de Lys Supergroup package of metamorphic rocks (Currie and van Berkel, 1992). These rocks have a sedimentary protolith, and consist of basal mica schist overlying mylonitic gneiss. Above the mylonite is an upward sequence of calc-schists with large lenses of marble mylonite, calc-schists, and locally thick layers of amphibolite, all overlain by a thick unit of micaceous flaggy quartzite and mica schist (Currie and van Berkel, 1992). The most distinctive unit of the Fleur de Lys package, located at the base of the imbricate thrust sheets, is a metaconglomerate that contains several different types of inclusions, including rare ones similar to the interleaved, unnamed orthogneiss described above (Currie and van Berkel, 1992). The Fleur de Lys Supergroup was emplaced by westward directed thrusting at amphibolite facies metamorphism.

According to Cawood et al. (1994, 1996) and Brem et al. (2002, 2003), emplacement of the internal Humber zone occurred over a prolonged period, beginning in the early to mid Ordovician, when the Dashwoods subzone, east of the LRF was thrust upwards, to the west, relative to the Notre Dame subzone (Brem et al., 2003). Between 465 Ma to 460 Ma, a complex period of westward directed thrusting resulted in major ductile deformation along the LRF, leading to the initial emplacement of the imbricate stack of units in the Steel Mountain subzone (internal Humber), and the westward transport of upper level allochthons of the external Humber zone (Brem et al., 2003). The latest movement, as documented by Cawood et al. (1994), includes further westward transport of Fleur de Lys allochthons and movement along the LRF accommodated by ductile deformation in the mid-Silurian (Currie and Piasecki, 1989; Cawood et al. 1994).

#### **1.4.4 SMA Previous exploration**

Exploration of the Steel Mountain Anorthosite has been limited, and generally restricted to Fe-Ti oxide deposits. In 1873, Alexander Murray (Baird, 1954) predicted, based on the discovery of massive oxide float in river beds in the St. George's Bay area, that a massive

oxide deposit was present in the highlands above St. Georges. In 1888, his predictions were substantiated when prospectors and trappers discovered massive magnetite lenses hosted in anorthosite. These were subsequently claimed by C.R. Bishop, and are now known as the Bishop North and Bishop South magnetite deposits (Baird, 1954). These deposits are located near the head waters of Sheep Brook. Analysis of the oxides indicated that they were rich in titanium, which was recognized in hand sample as exsolution lamellae, making the oxides less favourable for development as an iron resource (Baird, 1954).

In 1954, D.M. Baird completed a comprehensive study of these and other subsequently discovered oxide deposits. In this work much of the anorthosite intrusion was mapped, with particular attention paid to the textures and morphology of oxide concentrations. Baird also described in detail the different variations in anorthosite texture and composition. In addition to the Bishop North and South, another occurrence, called Bishop III was identified approximately 500 m west from Bishop South (Baird, 1954). Baird (1954) also describes several other oxide occurrences in the SMA that do not occur near the Bishop deposits. The Hayes Prospect is just outside the map area of this thesis, and crops out approximately half way between Hell's Gulch and Surveyor's Brook, both which drain into Flat Bay Brook, west of Lookout Brook. The smaller Hayes Prospect occurs as several discrete lenses or dike-like bodies that overall are quite similar to the Bishop Deposits.

The Hudson Prospect, which occurs on the south side of Flat Bay Brook, is accessed by foot up the Menduwagi Brook, by turning west part way up the brook, to a steep hill and outcrops that host the oxides. This occurrence is different from the others because it does not exhibit feldspar granulation or bleached halos surrounding the oxides. Also, there is up to 20% sulfide associated with the oxides in the form of pyrite and chalcopyrite (Baird, 1954).

No exploration was conducted on these occurrences, likely due to the high Ti content of the oxides, until 1994 when Loadstone Limited conducted field mapping and dip needle surveys to more accurately delineate the geometry of the known occurrences and to discover new oxide occurrences in the vicinity of the Bishop North and South deposits (Barrett, 1994). Their work did not contribute much more information than what Baird (1954) had already established. Loadstone proposed to exploit the deposits for industrial applications, which were less dependent on the impurities as they were on the physical properties of the oxides, namely their high specific gravity (Barrett, 1994, 1999). Three diamond drill holes were drilled, with a total length of ~410 m, to further define the geometry of Bishop North and South prior to excavation. Two bulk samples, the first of ~ seven tons, and the second of ~ ten tons were extracted by Loadstone for testing (Barrett, 1994). In 1997, Loadstone developed the deposit for use as ballast in the gravity-based Hibernia offshore platform. Barrett (1999) reported that as of 1999, approximately 60 000 tons remained, in two piles of crushed oxides at the Bishop site. Loadstone was unable to develop a use for the remaining ore and planned to reclaim the site. However, visits in 2004 and 2005 showed no evidence for reclamation.

Elsewhere in the SMA, exploration for precious metals and base metals had success in 1994 when Cabot Exploration, a partnership of prospectors, discovered high-grade Au-Ag mineralization hosted in quartz veins and associated with sulfides (Pilgrim and Regular, 1998). This mineralization is located at the top of Tim's Brook, a steep brook that flows into Flat Bay Brook about half way between Hell's Gulch in the west and Lookout Brook in the east. The best results from prospecting include a grab sample of 162.7g/t Au and 7.01 oz/t Ag ((Pilgrim and Regular, 1998). Mor-Bar Minerals conducted channel sampling in 1995 and drilled the Tim's Brook prospect in 1996 with little success in intersecting the surface mineralization at depth (Pilgrim and Regular, 1998; Bradley, 1995), hence the claims reverted back to Cabot Exploration.

From 1999 to present, grab samples from the Sheep Brook area, less than 2000 m downstream from the Bishop deposits, were collected by a group of local prospectors and have returned significant base metal and precious metal values from narrow, tectonized lenses of massive sulfides hosted in strongly deformed and silicified anorthosite and layered metagabbro. Maximum grades come from a sample of massive sulfide that contains 1.78 g/t Pt, 1.19 g/t Pd, 1.10% Ni, and 0.09% Co (Hull et al. 2003). Initial interest in this PGE mineralization for this study in 2003 was followed up during mapping in 2004 and a brief return visit in the spring of 2005 in cooperation with the prospectors. Documentation of PGM and base metal mineralization from their occurrence is documented for the first time in this thesis.

Near the eastern margin of the SMA, exploration along the LRF was conducted by Sixpoint (White and Green, 1995) and New Island Minerals (MacIntosh and French, 1995). Both ventures, which appear to have traversed across the LRF into Paleozoic rocks of the Dunnage Zone, were exploring for a combination of precious and base metals. Sixpoint delineated a zone of sheared mafic rocks and mafic dikes that host discordant quartz veins with chalcopyrite and pyrite that appear to be part of the Main Gut intrusion, a Silurian layered mafic intrusion (Cawood et al., 1994). New Island Minerals covered a broad area, and identified several zones of anomalous mineralization hosted in a variety of rock types. In particular, they identified anomalous Cu and Ni mineralization hosted in the Main Gut intrusion further north of the Sixpoint properties. New Island Minerals (1995) identified VMS-style mineralized float, hosting 19.7% Pb, 8.40% Zn, 0.42% Cu, and 12.9 oz/t Ag and elevated Sb (440 ppm), Au (85 ppb) and >110 ppm Cd (MacIntosh and French, 1995).

#### **1.4.5 TBGS Regional geology**

The Taylor Brook Gabbro Suite is located in the southeast corner of the Proterozoic Long Range Inlier (LRI), the largest exposure of basement rocks in the Appalachians (Owen, 1991; Heaman et al., 2002). The oldest rocks in the Inlier comprise leucocratic to

mesocratic polydeformed quartzofeldspathic gneisses, as well as thick lenses of granitic orthogneiss, which, according to Erdmer (1986), were largely derived from plutonic protoliths. Although previously thought to be Precambrian, the TBGS was recently dated by U-Pb zircon methods at  $430.5 \pm 2.5$  Ma, making it the first known example of Silurian magmatism in the Long Range Inlier (Heaman *et al.*, 2002).

The southeast edge of the TBGS is in fault contact with the Deer Lake basin, a Late Devonian to Early Carboniferous clastic basin that formed in an extensional tectonic regime (Hyde, *et al.*, 1988; Waldron *et al.*, 1998). The Deer Lake Basin was thrust westward over the TBGS, thus obscuring igneous contact relationships in that region.

At its southeastern margin, the TBGS intrudes massive to weakly foliated granite to granodiorite (Erdmer, 1986) that is part of a large suite of ca. 1020-1035 Ma plutonism in the Long Range Inlier (Owen and Erdmer, 1989; Heaman *et al.*, 2002). Further along the southeast margin (northwest), the TBGS intrudes metapelitic schists that locally comprise up to 90% sillimanite, and contain garnet and abundant biotite; calc-silicates overlie the metapelites and contain tremolite, diopside, and graphite (Erdmer, 1986). The northwest corner of the TBGS intrudes melanocratic quartz diorite that is locally gneissic (Erdmer, 1986). Much of the northern and western contacts are with granulite facies granodiorite-to granite gneiss that forms a large portion of the central LRI (Erdmer, 1986; Heaman *et al.*, 2002). In addition to the granulites, amphibolite and amphibolite gneiss of unknown age, and calc-silicates similar to the southeastern margin of the TBGS are intruded by the TBGS (Erdmer, 1986; Heaman *et al.*, 2002).

#### **1.4.6 TBGS Previous exploration**

Base metal exploration in the Taylor Brook area has been relatively limited, and overall the area has not been the subject of many exploration programs. Exploration has only exposed one mineral occurrence, that of semi-massive to massive Ni-Cu sulfides that are hosted by strongly biotite retrograded amphibolite in Grenville-aged rocks. The sulfides

and host are strongly sheared and appear to be strongly recrystallized and intimately intergrown with the biotite-rich retrograde assemblage.

The Newfoundland and Labrador Department of Mines and Energy conducted a soil and lake sediment survey in the Sandy Lake region, which includes the TBGS (Davenport, 1989). Follow-up reconnaissance sampling by Harris and Rose (1997), Rose (1998), Harris (1998; 1999) indicated there are anomalous levels of Ni-Cu-Co in the Twin Ponds area of the western Taylor Brook gabbro suite. Lithogeochemical analysis also indicated a positive correlation between nickel and olivine (Rose, 1998 and references therein).

In 1999 several small, but high-grade Ni-Cu-PGE occurrences (Layden Showing), were discovered in mafic Grenvillian rocks approximately 5 km from the western margin of the map area (Fitzpatrick et al., 2000). These, however, are unrelated to the TBGS.

## **1.5 Methodologies introduction**

Over the course of this research, many qualitative and quantitative analytical techniques were employed. What follows is a brief description of the specific techniques, and where applicable, specific operating conditions.

### **1.5.1 Field mapping and sampling**

Field mapping was conducted in the summer of 2004, from the beginning of July until the end of August. Where possible, logging roads were used to gain access, and often provided relatively fresh outcrop. The majority of outcrop was not accessible by vehicle, however, and mapping was conducted primarily by traversing on foot, and to a lesser degree, using a canoe to investigate islands or shorelines along lakes within the mapping areas. Sample locations were acquired using the Universal Trans Mercator projection (UTM) using a Garmin eTrex Legend with Map Source digital topographical maps (Appendix 1).

During sample collection, every attempt was made to derive representative rock samples and avoid alteration or weathering. Samples prepared for whole rock and PGE analysis were trimmed of all weathering rinds prior to crushing so that samples assayed represented fresh rock. Samples were first crushed using a jaw crusher, and then a swing mill to reduce the crushed fraction to a fine power at the processing facilities at the Newfoundland and Labrador Department of Mines and Energy.

### **1.5.2 Petrography**

Petrography was carried out on approximately 210 polished thin sections (PTS), which were made at Memorial University's in-house facilities; a small batch of massive sulfide and oxide samples were made by Gordon Brown at Dalhousie University. A Nikon LABOPHOT-POL polarizing microscope was used for all thin section observations. Petrographical observations are tabulated in Appendix 2.

### **1.5.3 X-ray fluorescence analysis**

Over 150 samples were prepared by the Newfoundland and Labrador Department of Mines and Energy for whole rock analysis at Memorial University. Samples were trimmed and crushed as described above before being prepared for XRF analysis. Methods employed in XRF analysis for this project are described in Longerich (1995). Samples were analysed on a Fisons/Applies Research Laboratories model 8420+ sequential wavelength-dispersive x-ray spectrometer. XRF geochemical data are presented in Appendix 3.

### **1.5.4 Platinum group element (PGE) analysis**

In addition to X-Ray fluorescence analysis at Memorial University, whole rock powders were submitted to Actlabs in Ontario for PGE analysis. A 30 g split is weighed, mixed

with fire assay fluxes and fused at 1050°C for 1 hour. This process creates a lead button, which, after cooling is separated from the slag and coupled at 1000°C to recover the Ag (doré bead) + Au, Pt, Pd. The Ag doré bead is digested in hot (95°C) HNO<sub>3</sub> + HCl. After cooling for 2 hours the sample solution is analyzed for Au, Pt, Pd by ICP/MS using a Perkin Elmer Sciex ELAN 6000 or 6100 ICP/MS (Hoffman and Dunn, 2002). Appendix 3 presents PGE geochemical data with the oxides described above.

In addition to ICP/MS methods for whole rock analysis, several other techniques were utilized for locating discrete platinum group minerals and then analyzing them. The Memorial University MicroAnalysis Facility- Inco Innovation Centre (MAF-IIC) facilities were used to locate PGM's and conduct qualitative (EDS) analyses. This technique utilized the *FEI Quanta 400* environmental SEM scanning electron microscope and mineral liberation analysis (MLA) software from JKTech at the University of Queensland Australia. Essentially, each polished thin section was scanned by the SEM, which generated several hundred to approximately 1500 backscatter "frames" or images. MLA software, using a user defined threshold, based on each grey scale image (255 grey tones) was set so that only grains of very high average atomic mass were measured by EDX methods. The MLA software output is a list of frames that contain grains that fall within the grey scale threshold. The user may then use other MLA software to analyse, amongst many parameters not discussed here, the composition and location within the sample. It is possible to navigate to a point of high average atomic mass and collect x-ray spectra to determine its composition and to image the point. Theoretically, a database of known phases is used to filter out phases not of interest. This technique was employed at the MAF-IIC labs so that only PGM grains were filtered. PGEs that were successfully identified by this technique were imaged and a 3-D coordinate for each grain recorded so that the points could be analysed at the Dalhousie University electron microprobe lab.

### **1.5.5 Electron Microprobe Analysis**

A large portion of data collected for this research was by electron microprobe analysis at the facilities at Memorial University, which feature a Cameca SX-50 electron microprobe. An accelerating voltage of 20 keV was used during all analysis, while beam current was dependent on the phase being analysed. For plagioclase, a beam current of 10 nA was employed whereas for all other phases (e.g. olivine, pyroxene, sulfide, oxides, garnet, amphibole, mica) a beam current of 20 nA was utilized. A defocused beam (~ 10 micron spot) was used for hydrous phases (e.g., amphibole and mica) and for feldspar whereas all other phases were analysed with a focused beam. Data were collected using SamX for Windows, which employs PAP correction algorithms. A program named F1, which is part of the SamX software bundle, facilitated offline computations.

All PGE analyses were conducted at Dalhousie University, using a JEOL 8200 electron microprobe. Beam conditions for PGE analyses are similar to oxide, silicate and sulfide analyses at MUN; an accelerating voltage of 20 keV and a beam current of 20 nA with a focused beam were employed. Data were collected on a Sun Ultra 10 UNIX computer and processed by ZAF matrix correction and Sun software.

Appendix 4 presents the data collected from the EMPA at both Memorial and Dalhousie University.

### **1.5.6 Sulfur isotope analysis**

Sulphur analysis were conducted at Memorial University using a Carlo-Erba NA1500 Series 2 Elemental Analyser/ConFloII Interface, coupled to a Finnigan MAT252 Isotope Ratio mass spectrometer. The isotopic standard IAEA-S-2 (NZ-2) and IAEA-S-3 were used as a calibration standard after the methods of Coplen et al., (2002).  $\delta^{34}\text{S}$  data are precise to 0.15‰ and 0.12‰ respectively. In total, 10 samples from the RCLIS, eight samples from the SMA, and six samples from the TBGS were analysed using this system.

Samples ranged from 0.098 mg to 0.408 mg, and were weighed at the Memorial University laboratories. These data are listed in Appendix 5.

The majority of samples used for sulphur isotope analysis did not contain abundant sulphide minerals and thus required secondary concentration. First, samples with the most abundant sulphides were crushed in a swing mill for 10- to fifteen seconds. Next, samples were filtered into a range of grain sizes using a shaker; four size fractions were collected:  $> 300\mu\text{m}$ ,  $300\text{-}180\mu\text{m}$ ,  $180\text{-}125\mu\text{m}$ , and  $<125\mu\text{m}$ . Only the  $300\text{-}180\mu\text{m}$  and  $180\text{-}125\mu\text{m}$  sizes were used for further concentration. Prior to hydroseparation, a magnet was used to remove magnetic particles. An HS-02 hydroseparator (Rudashevsky et al., 2002) was used to concentrate the sulphide minerals. In this procedure, the crushed and sieved fraction is mixed in  $\sim 5\text{-}10\text{g}$  portions in a small glass beaker into a slurry with water. This slurry is poured into a 1cm diameter vertical glass tube that is attached to the hydroseparator device. The HS-02 is attached to a water source that, when turned on, pulses water through the glass tube at preset volumes and rates. Initially, a slow rate of pulsing and a moderate volume of water are used and the pulsing action causes the sample to become suspended in the column of water in the glass tube; the lighter gangue minerals float to the top of the tube and eventually out of the top of the tube, into a collection beaker. Over varying times and with decreasing volumes of water and rates of pulsing, it is possible to winnow the majority of gangue minerals of the sample, leaving only heavy minerals, mainly non-magnetic oxides such as ilmenite, and some heavy silicates, such as olivine and pyroxene or amphibole, which are minimal. During separation, small samples of the overflowing particles are collected to determine what is being removed. If sulfide particles are present in the separates, the separation process is ceased. Following this concentration process, the sample is dried in a furnace until no water remains and is then hand picked under a low power binocular microscope, to ensure that only sulphide minerals are present. It is this final picked sample that was used for isotopic analysis.

## **Chapter 2: Red Cross Lake Intrusive Suite field geology**

### **2.0 Introduction**

Of key interest in prospecting and exploring for orthomagmatic base and precious metal sulfide deposits are the contact relationships between the intrusions and their host rocks, because the physical and geochemical processes that lead to sulfide mineral precipitation are typically focused there. As such, attempts were made to sample at higher frequencies proximal to the contacts, in the hope of defining textural, whole rock and mineral geochemical trends that might be characteristic of orthomagmatic Ni-Cu-PGE deposit types. As indicated below, this was not always possible, particularly in the RCLIS, where vegetation and overburden were both greater than expected. In this location, samples were taken wherever possible, because outcrop was scarce.

### **2.1 Field geology**

Field work conducted in 2004 had a variable resolution, depending on the abundance of outcrop. In general, outcrop was sparse, particularly in the south where large areas of bog and thick spruce trees blanket the land. To the north is extensive bog and scrub forest that was left to grow wild following logging in the early 1980's. Outcrop is best observed along the shoreline of the lake and on small islands at the southwest corner of Red Cross Lake. It is also prominent in the east, where a small river flows from highlands south of the intrusion, and permits river traversing with excellent exposure. At the southwest corner of Red Cross Lake, a river drains into the Lloyd River but was not accessible for mapping due to overly high water levels following hurricane rains. The low rolling hills in the area of the intrusion do not commonly exhibit cliff exposures, and even along former logging roads and ATV paths, outcrop is scarce. Locally, mapping resolution of 1:1000 was attained, but in general, resolution is limited to 1:20 000 or greater. Therefore, many contacts in the included maps generated from this field work are

assumed, and are based on a combination of supporting evidence from whole rock and microprobe geochemistry, both which identified similar trends as mapping.

One of the major accomplishments of this mapping is the subdivision of the RCLIS into three distinctive subzones, based on contrasting physical, textural and geochemical patterns. In general, the southern portion of the RCLIS has a mafic to ultramafic composition and exhibits well defined primary magmatic layering that is defined by a relative variation in mineralogical abundance and grain size. Herein, this portion of the intrusion is termed the Lower Series. The northern portion of the RCLIS exhibits a mafic-to intermediate composition and generally lacks layering, displaying a massive texture overall. There is evidence for extensive recrystallization in the northern portion of the intrusion that is not observed in the southern portion. Herein, the northern portion of the RCLIS is termed the Upper Series. A third zone, the Transition Zone is located between the Upper and Lower Series and shares characteristics of both the northern and southern portions of the RCLIS, but also exhibits unique field and petrographical characteristics. Figure 2.1 is a geological map of the RCLIS, which is described below; the bedrock in this map is derived from Colman-Sadd and Crisby-Whittle, 2004.

### **2.1.1 Lower Series**

The Lower Series comprises dunite, melatroctolite, troctolite, leucotroctolite, olivine gabbro, leucogabbro and pyroxene amphibole gabbro, with layering on a centimeter to decimeter scale (Figure 2.2). In general, the Lower Series becomes increasingly felsic towards the north, marked in particular by the loss of olivine part way up the Lower Series, which is replaced by pyroxene. Despite the large proportion of mafic minerals in the Lower Series, these rocks have a fresh appearance, with little weathering (bleaching), or serpentinization. Sulfides are visible in hand sample where they exceed 1-2 percent, and it is even possible to discern rare pentlandite in hand sample. The fresh nature of the rocks makes it possible to observe mineralogy and textures at an outcrop scale quite

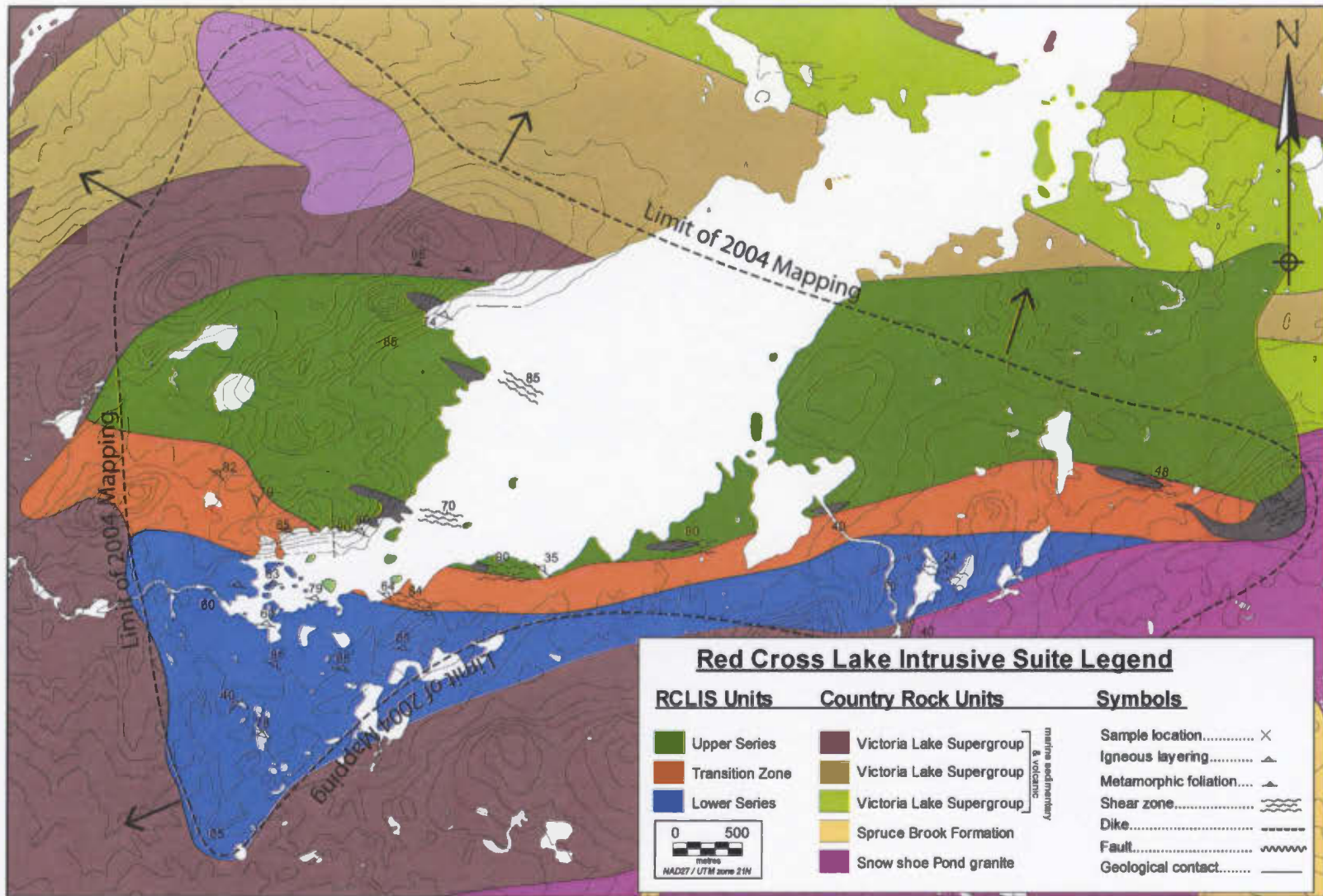


Figure 2.1. A geological map of the RCLIS and surrounding country rock. A detailed description of each unit is provided in Chapter 2. Note the scale bar in bottom left corner of the legend. North is towards the top of the map. Country rock geology is modified after Colman-Sadd and Crisby-Whittle (2004).



Figure 2.2. Examples of magmatic layering in the Lower Series. (a) melatroctolite to dunite layers (melacratic) alternate with troctolite layers (leucocratic). Layering is not traceable for long distances because of the lack of outcrop, but layers exhibit relatively consistent orientations within outcrops. This image is from near RIC-01; (b) in the upper Lower Series, layers are less frequent and exhibit more gradational layers. This image is of an olivine-rich layer leucogabbro. A second, diffuse layer is visible where the sledgehammer handle turns blue. This image is from RIC-20. Note hammer for scale in (a).

easily. In general, further to the north, there is an increase in recrystallization, which is probably a function of the proximity to the transitional zone that separates of the Lower and Upper Series. One unusual characteristic of the Lower Series is the distribution of dunite and melatroctolite. Although found in some basal rocks, the largest occurrence of these rocks is approximately 2/3 of the way up in Lower Series, which is uncharacteristic of normal layering processes.

Layering in the Lower Series consistently strikes between  $\sim 250^\circ$  and  $300^\circ$ , averaging  $265^\circ\text{W}$ , and dips predominantly subvertical to steeply north. Layering is defined primarily by the relative abundance of olivine and pyroxene to plagioclase, and by the ratio of pyroxene to amphibole in the pyroxene amphibole gabbro. Layering in the Lower Series rocks has adcumulate and poikilitic (heteradcumulate) textures. Individually, layers have well-developed adcumulate textures at their base, whereas further up, layers become progressively orthocumulate. Plagioclase and clinopyroxene typically form oikocrysts and enclose olivine chadacrysts, which are relatively fresh in outcrop. In other places within the layered rocks, pyroxene crystals up to a few centimeters in diameter exhibit weakly deformed or elongated sub-poikilitic textures. It is common to observe well-developed gradational olivine layering in the troctolitic and olivine gabbro units, indicating top to the north (Figure 2.3). At outcrop scale, layers are generally continuous, although they may undulate slightly and thickness is somewhat variable along strike. In the northern portion of the Lower Series, rocks comprise pyroxene amphibole gabbro, leucogabbro, and amphibole gabbro, and layering is all but absent. The lack of layering is one of the criteria that distinguish the Lower and Upper Series, hence a transition zone of mixed textures marks the boundary between the Upper and Lower Series. In other locations within the Lower Series, varitextured melagabbro has been observed, although, due to the poor outcrop exposure in the map area, the lateral extent is indeterminable.



Figure 2.3. An image of magmatic layering from the area near RIC-30. Layering in the Lower Series is sharp (Figure 2.1a), but more commonly exhibits a gradational texture. In this image, layers exhibit relatively sharper melacratic bases that grade into more diffuse, leucocratic tops. Layering in this image, as in all outcrops, grades to the north (see arrow, top right corner). The aggregate of plagioclase crystals near the top centre of the image is unexplained, but appears to have formed syn- to post-layering, because it cuts layers, but appears to have caused the layer it rests on to warp downwards, suggesting the layers were not fully crystallized when it formed. Note the pen for scale.

In the southeastern portion of the RCLIS, massive- to weakly layered green-grey mafic-ultramafic rocks were identified during a river traverse. These rocks, which occur within one kilometer of the basal contact, contain abundant biotite schist and quartzofeldspathic gneiss xenoliths of variable size. Reaction rims suggest the xenoliths have been partially resorbed. In these rocks, the crystals appear massive to interlocking, varying from medium to coarse-grained. Some of the more mafic samples are host to several percent sulfides, but mineralogy was not determinable in hand sample. This unit is relatively homogeneous on an outcrop scale, but does exhibit vertically dipping compositional layering over several dozens of meters. It is possible that this area is a more strongly altered correlative of the Lower Series in the southeast. These relationships are discussed in more detail below.

### **2.1.2 Upper Series**

Within the Upper Series, textures are relatively less variable compared to the LS, because the rocks are generally massive, and cut by late fractures or joints (Figure 2.4). In some places a weak tectonic fabric is developed, causing weak mineral lineation. The Upper Series is characterized by a relative abundance of biotite and granular pyroxene, which occur as glomeroporphyrocrysts and as discrete, irregular individual grains. Biotite varies from 1% up to 10% and appears to be controlled, at least partially, by proximity to biotite-bearing xenoliths, which are discussed below. There is a lack of sulfide mineralization in the Upper Series, such that when rusty patches of outcrop are observed, it can be attributed to the oxidation of biotite and/or possibly pyroxene. Oxides were observed in several outcrops, but they were not large enough to be identified; petrography indicates that they are largely ilmenite and lesser magnetite.

North of the main mass of the RCLIS is massive biotite and pyroxene-bearing granite. Previous workers have suggested that this intrusion is related to the RCLIS (Kean, 1977). However, 2004 field mapping demonstrated that there is no direct contact with the



**Figure 2.4.** The Upper Series is relatively massive and is locally cut by joint-sets. There does not appear to be a preferred orientation of jointing from one outcrop to the next. These rocks have an amphibolitized leucogabbro mineralogy. Note compass for scale.

RCLIS body, and hence there is no field evidence to relate the RCLIS and this northern granitoid intrusion.

### **2.1.3 Xenoliths**

One of the main features of the RLCIS that is not addressed in any detail by previous authors (e.g. Kean, 1977; Nuri et al., 1980; Barbour, 1998) is the abundance of heterolithic xenoliths and their distribution throughout the intrusion. Xenoliths are widespread in the RCLIS, but their distribution is restricted, for the most part, to the Upper Series, proximal to the Upper Series – Lower Series boundary (transition zone). In the Lower Series, xenoliths are uncommon and occur proximal to the basal contact with country rocks.

Xenoliths in the RCLIS occur in three main groups. The most common mode of occurrence is in the Upper Series in narrow, layer-parallel belts that range in thickness from one up to nearly 10 meters (Figure 2.5a). These xenolith belts are approximately parallel to the local layering in the Upper Series and to the overall orientation of layering within the Lower Series and locally they are weakly- to strongly sheared (Figure 2.5b, c). Locally, sheared rocks grade from strongly to weakly deformed in the margins to the centers of the xenolith belts, respectively. The xenoliths in these belts have their long axis aligned parallel to the belts but do not appear to have been deformed in the host belts. Locally, the belts comprise approximately 90% heterolithic xenoliths, although the average xenolith belt contains approximately 25% xenoliths. The matrix to the xenoliths is quite variable and ranges from biotite-rich leucogabbro to gabbro to pyroxene amphibole gabbro, to granitic pegmatite; leucocratic rocks are the dominant host to the xenoliths. Xenolith composition is dominated by biotite paragneiss or schist, and to a lesser extent, quartzofeldspathic gneiss. Xenoliths range from a few centimeters up to 50 cm long. Many of the paragneiss xenoliths exhibit a dark coloured, fine-grained biotite-rich reaction rim of variable thickness, suggesting that they were in contact with the magma for a long duration, but that the magma was not hot enough to completely digest

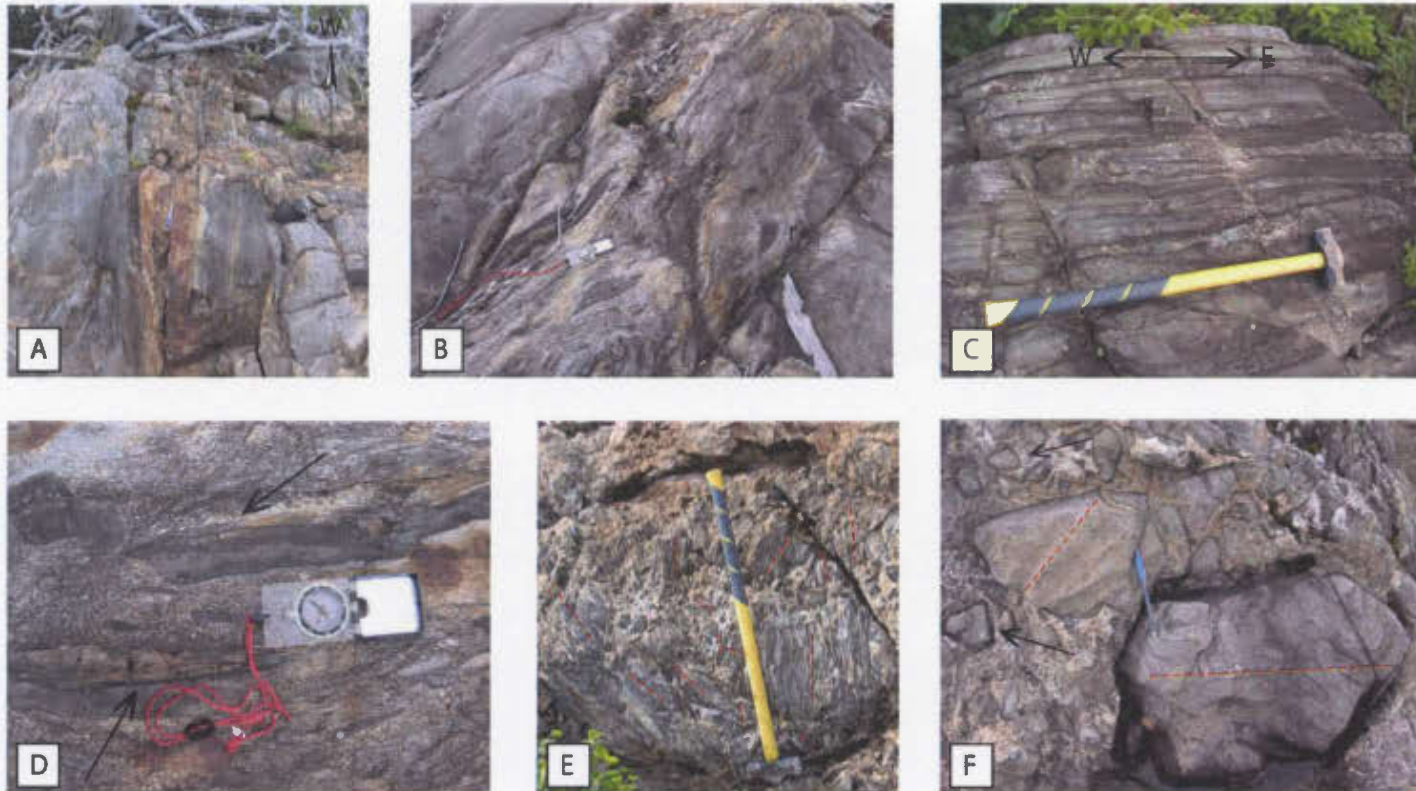


Figure 2.5. Examples of xenolith occurrences in the RCLIS. (a) xenoliths are hosted by variably sheared belts that range from 1-10 m. Pictured here, in RIC-23, is an ~2 m wide section of a 5 metre wide belt. Xenoliths are visible throughout this image; image is looking west, parallel to the strike of the belt; (b) xenolith belts exhibit variable degrees of shearing. Pictured here, in RIC-32, is a relatively weakly sheared zone. Note the alignment of xenoliths' long axes to the direction of shearing. Note the 'r' in center right, denoting a xenolith with a prominent reaction rim; (c) strongly deformed igneous rocks at the periphery of a large xenolith belt near RIC-51. These textures suggest that the host rocks were not completely crystallized when they were sheared; arrows indicate the orientation of sheared layers; (d) arrows in this image from RIC-32 indicate reaction rims surrounding metasedimentary xenoliths. Note the granular texture of the host rocks; (e) brecciated xenoliths from RIC-51 in this image are randomly oriented, as denoted by dashed red lines, which mark the orientation of the metamorphic fabric in the xenoliths. This photograph was taken ~20 m from the image in C; (f) this image is of large, randomly oriented layered ultramafic xenoliths. Dashed lines indicate magmatic layering and arrows denote reaction rims. This image is from RIC-51 and was taken ~10 m from the image in E.

the xenoliths (Figure 2.5d). Country rock composition and distribution seems to exert a weak control on the composition and distribution of xenoliths. For example, where RCLIS country rock is quartzofeldspathic gneiss, xenolith composition is dominated by quartzofeldspathic gneiss. Every xenolith belt has an association of dendritic to wispy veins or pegmatites, which are likely the result of fluids released during melting of the xenoliths, which often appear to have been partially melted or assimilated. Locally, these pipes and associated fluids resemble hydrothermal breccias (Figure 2.5e). In some cases pegmatite pipes are present that do not always have a direct spatial association with xenoliths, but are generally proximal to the xenolith zones. Some of these belts contain rare, mafic to ultramafic cumulate xenoliths (Figure 2.5 f) that have textures not identified elsewhere in the intrusion and thus may represent a facies from greater depth, or closer to the basal contact, which is obscured everywhere by overburden and vegetation.

The second most common xenolith mode is as large rafts that measure at least 50 m<sup>2</sup> in outcrop. These are only observed in the southeast portion of the intrusion, where there is good exposure along a small river. These rafts are usually composed of quartzofeldspathic gneiss, which might explain their larger size, as perhaps they were more difficult for a small pluton to digest.

The final xenolith type consists of small zones with small, heterolithic xenoliths composed mainly of quartzofeldspathic gneiss and subordinate amounts of biotite schist. The xenoliths are uncommonly sheared. Individual xenoliths are subrounded to subangular and smaller than in other xenolith zones, averaging <5 cm and comprising < 5% of the total rock volume. These zones are not spatially extensive, have variable orientations relative to magmatic layering and appear to form xenolith belts of sorts. Due to poor outcrop exposure, however, it is difficult to estimate their lateral continuity or overall distribution, although several outcrops along the basal contact exhibited similar

xenolith characteristics. They are most common near the basal contact of the RCLIS in the southeast.

#### **2.1.4 Sulfide mineralization**

The RCLIS hosts minor amounts of sulfide mineralization, which occur only in the Lower Series ultramafic rocks, particularly in troctolite and olivine gabbro of the southwestern region and in a strongly altered zone of ultramafic rocks to the southeast. Sulfide textures include fine to medium-grained irregular blebs, which are interstitial to silicate grains and constitute up to 2% of the rock. These textures indicate the presence of an immiscible sulfide liquid that crystallized as blebs, a characteristic of primary magmatic sulfides. Typically, it was not possible to directly observe sulfides in the outcrop, because surfaces are weathered, although where fresh bedrock was exposed, the presence of sulfides is apparent and discernable by discrete rusty patches on an otherwise clean looking outcrop. Where coarse enough to identify, the sulfide mineral assemblage includes pyrite, pyrrhotite, and chalcopyrite. Rocks in the Upper Series are essentially devoid of sulfides, although rare sulfides occur in the xenolith belts in association with rusty xenoliths, where it is likely that there are remobilized sedimentary sulfides. In some weakly layered, varitextured olivine gabbro located in the upper Lower Series, sulfides are more concentrated at the base of layers.

#### **2.1.5 Summary**

The Red Cross Lake Intrusive Suite is far more heterogeneous than previous work has indicated. The 2004 field season permitted subdivision of the RCLIS into internal units that share similar compositional and textural affinities. Heterogeneities are mainly reflected by the widely distributed xenolith belts that occupy shear zones that are oriented parallel to Lower Series layering. Layering in the RCLIS has a consistent east-west orientation, which is consistent with that defined in previous work (Kean, 1977). A distinct compositional and lithological change occurs from the southwest corner of the

RCLIS, which exhibits the most mafic composition, towards the north, where the intrusion has a pyroxene amphibole gabbro composition. This change occurs over a relatively short distance, less than 200 meters in some locations. Due to the lack of outcrop, and the presence of Red Cross Lake itself, it is not possible to fully understand the role of the xenolith belts, and to determine if they separate internal units of variable composition.

The presence of nickel and copper sulfides within the Lower Series of the RCLIS is significant, especially given the presence of xenolith contamination; however, the abundance of sulfides is unimpressive, rarely exceeding a few percent.

## Chapter 3: Red Cross Lake Intrusive Suite Petrography

### 3.1 Introduction

The Red Cross Lake Intrusive Suite is divided into two series, based on a combination of field observations, geochemistry, and petrography. This section describes the mineralogy and petrography in each series separately, noting where textures are unique to a particular rock type.

Rock names are based on visual estimations of modal abundances and then the three most abundant silicate phases were normalized to 100%, and plotted on ternary diagrams developed by Streckeisen (1976) (Figure 3.1). Where there are contradictions between calculated and observed rock nomenclature, petrographical observations are favoured because of the assumptions associated with normalized plotting. However, in altered samples, more weight is placed on calculated rock names, and the names applied do not necessarily reflect a protolith name, but the actual mineralogy. For example, an altered gabbroic rock (i.e. Upper Series gabbro) is typically classified as a pyroxene amphibole gabbro, which reflects the presence of secondary amphibole, as well as primary pyroxene.

In total, 55 polished thin sections were examined from the RCLIS area, although two of these PTS's are actually from a separate, unnamed intrusion, which crops out along the southern shores of Victoria Lake, approximately 30 km SW from Red Cross Lake. Twenty-one sections are from the Lower Series, 19 from the Upper Series, three of country rock and 10 of xenoliths comprising both country rock xenoliths and suspected autoliths. Appendix 2 summarizes modal mineralogy and assigned lithologies for the samples described below.

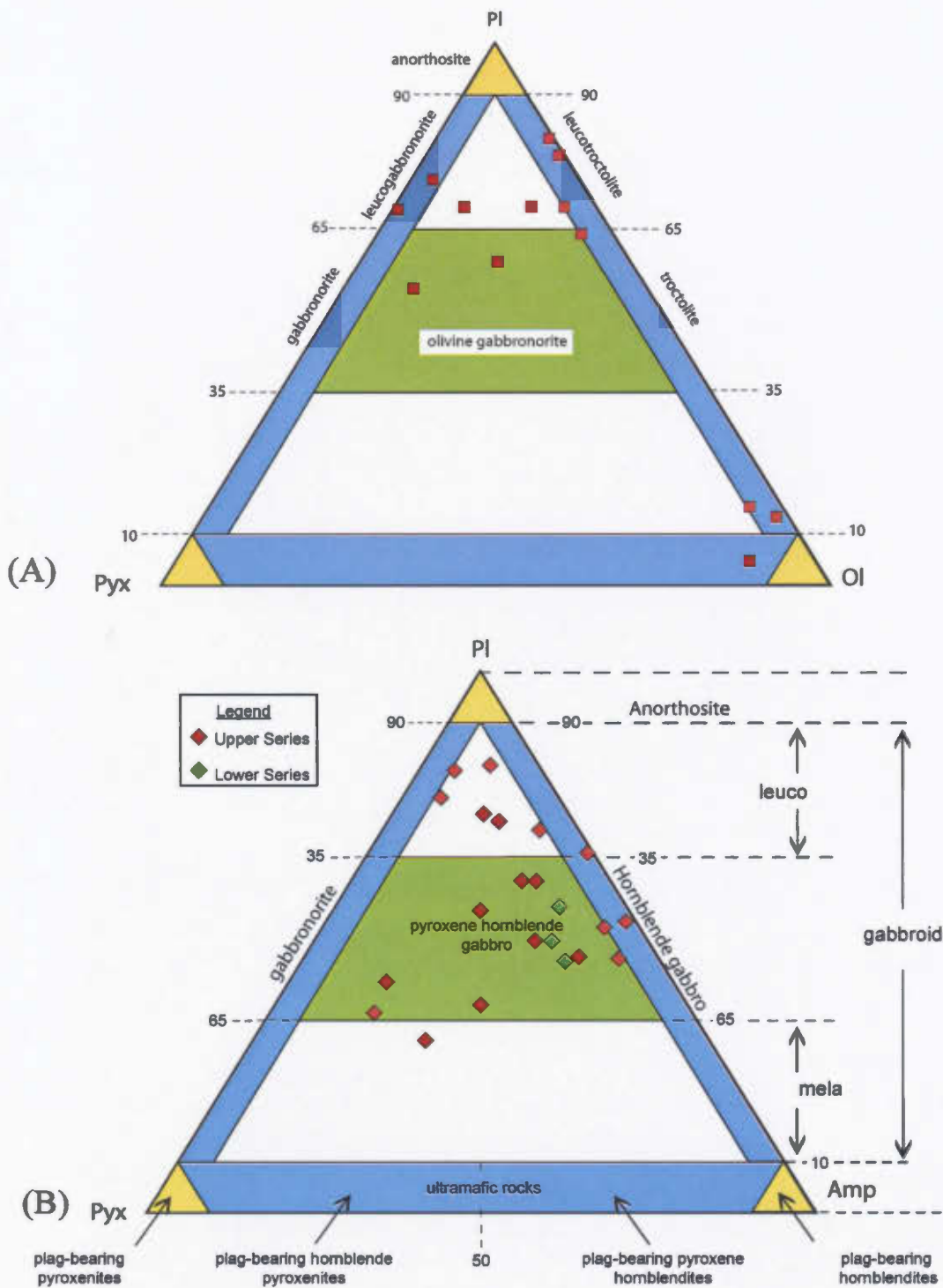


Figure 3.1 Mineralogy from the Lower Series (A) and the Upper Series (B) are presented as normalized data on these ternary diagrams after Streckeisen (1976). Normalization procedures are explained in the text. Lower Series samples lie mainly in the leucotroctolite, leucogabbro and olivine gabbro fields. A small group fall in the melatroctolite- to ultramafic field. Upper Series samples are more variable, but fall mainly in the pyroxene hornblende gabbro field with lesser samples in the leucopyroxene hornblende gabbro field and pyroxene hornblende field.

### **3.2 Lower Series mineralogy and petrography**

The Lower Series comprises two main rock types: troctolite and gabbro. Other rock types are present in lesser abundances, including serpentinite, dunite and one occurrence of a mafic dike, located in the southeast portion of the Lower Series. Overall, the Lower Series has a progressive variation in textures and composition from primitive, cumulate, melanocratic mafic rocks at the base (south), into more evolved leucocratic mafic rocks stratigraphically up (north).

Troctolite is the most abundant rock type in the Lower Series. It varies in modal mineralogy between locations, but textures appear to be independent of location. Olivine contents vary from 85 to 80% in melatroctolite to 25 to 20% in leucotroctolite; the average olivine abundance is approximately 30%. Plagioclase comprises the majority of the remaining minerals, although minor amounts, not exceeding 10%, of clinopyroxene, orthopyroxene, serpentine, sulfides and oxides are present.

Leucogabbro and pyroxene amphibole gabbro comprise the remainder of the Lower Series, and have variable relationships with the surrounding troctolite. Leucogabbro includes lesser amounts of olivine gabbro, olivine gabbro, and leucogabbro, which, herein, are grouped together and called leucogabbro. Leucogabbro constitutes the second most abundant rock type in the Lower Series and is associated typically with troctolites, especially olivine gabbros, thus comprising the leucocratic portions of igneous layers.

Leucogabbro modal mineralogy is quite variable, due in part to its wide spatial distribution, but particularly because it is locally spatially associated with the transition zone, which, as the name suggests, marks the transition from Lower Series to the Upper Series. On average, leucogabbro and associated gabbroic rocks comprise approximately 63% plagioclase, 14% clinopyroxene, 2% orthopyroxene, 7% amphibole (hornblende, actinolite, tremolite), 5% biotite, 7% olivine, and trace quartz.

Transition zone rocks have undergone modification of primary mineralogy, but commonly original igneous textures appear to be preserved. Therefore, textural variation is the key means for distinguishing pyroxene amphibole gabbros from the Upper and those of the Lower Series. Although some pyroxene amphibole gabbros are undoubtedly primary in origin, most show textural evidence that suggests that they formed mainly by the (metasomatic?) replacement of gabbroic, and to a lesser extent, troctolitic rocks, commonly as amphibole pseudomorphs of pyroxene.

Pyroxene amphibole gabbros from the Lower Series are limited to three samples, thus averages are not particularly meaningful, but are presented here so that the Lower and Upper Series rocks may be compared. Plagioclase averages 47%, clinopyroxene 10%, orthopyroxene 3%, amphibole (hornblende, actinolite, tremolite) 30%, biotite 4%, and trace quartz. Although the norite suffix is used to name these rocks, it is based on the normalized pyroxene composition, and might not reflect true mineralogy. This approach was used to standardize nomenclature for more altered rocks, as mentioned above.

### **3.2.1 Lower Series plagioclase**

In the most mafic samples, such as dunite or melatroctolite, plagioclase textures are markedly different from elsewhere in the Lower Series. In these samples, plagioclase is poikilitic and predominantly contains olivine chadacrysts. The plagioclase oikocrysts may be quite coarse-grained, as demonstrated by the optical continuity in some plagioclase crystals that may span a large proportion of a PTS (Figure 3.2a). Although less common, plagioclase oikocrysts may contain oxide (magnetite, chromite), and sulfide (pyrrhotite, pentlandite, chalcopyrite) chadacrysts. Poikilitic plagioclase is more altered than layered plagioclase. Fractures that radiate from olivine and contain serpentine, commonly continue into plagioclase, resulting in sericitization. It is possible that the fluid responsible for the hydration of olivine also sericitized the plagioclase.

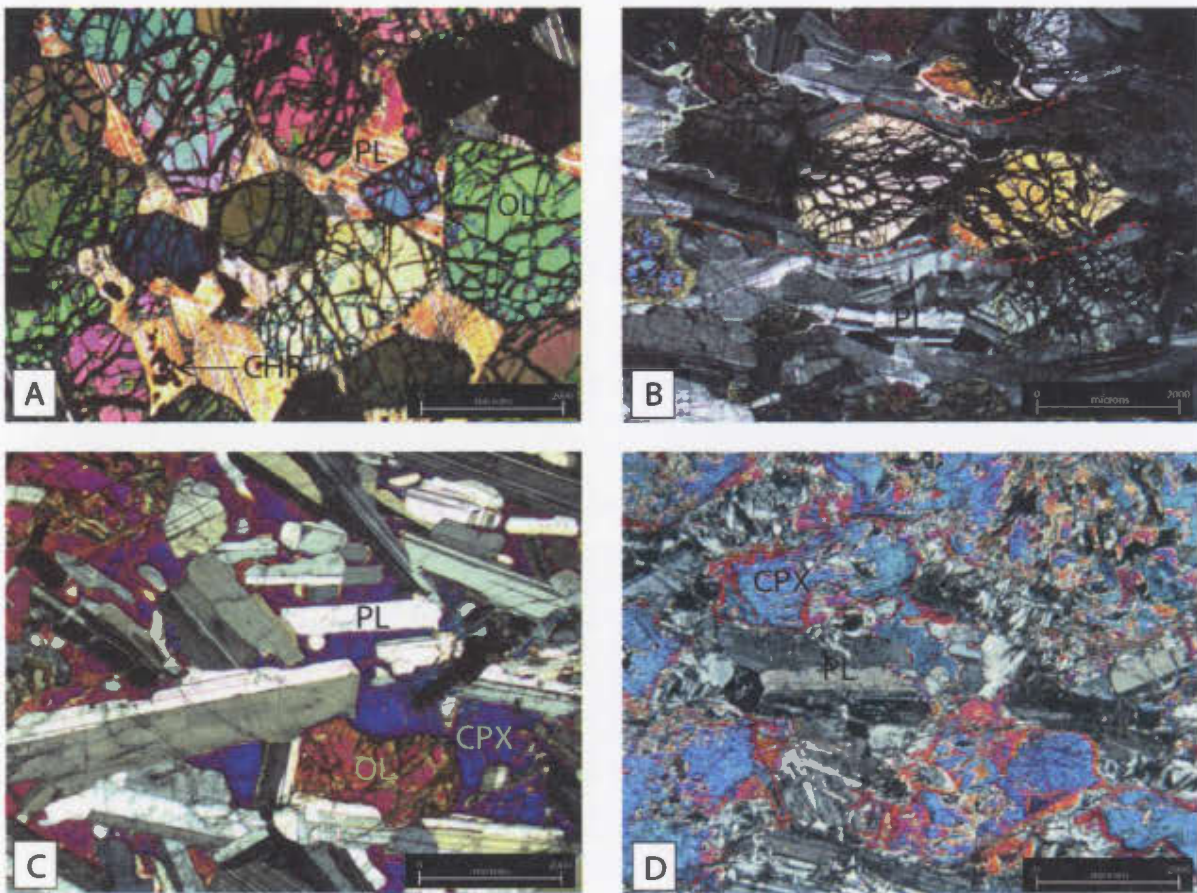


Figure 3.2 Transmitted light photomicrographs from the Lower Series in the RCLIS. (a) subhedral, rounded, coarse-grained olivine in RIC-21 is suspended in coarse-grained plagioclase oikocrysts (plagioclase is orange); (b) locally, elongate laths of plagioclase are warped or bent around rounded olivine crystals (trace of plagioclase orientation in red dashed lines); (c) very coarse-grained clinopyroxene oikocrysts host olivine and plagioclase chadacrysts. Note that plagioclase chadacrysts are substantially smaller than matrix plagioclase; (d) near the upper Lower Series, clinopyroxene is commonly rimmed by amphibole (orange) and locally completely pseudomorphed (some blue-pink crystals are amphibole). Note scales in lower right corner. Abbreviations are olivine (OL); plagioclase (PL); clinopyroxene (CPX) and chromite (CHR)

The texture of plagioclase in most troctolites and gabbroic rocks, where plagioclase is the predominant phase compared to melatroctolite and dunite, is relatively uniform.

Plagioclase is coarse- to medium-grained, elongate to stubby, subhedral to anhedral with a lath- to tabular morphology. Laths may exhibit a parallel to subparallel orientation, or a random orientation regardless of whether they are in a troctolitic or gabbroic rock.

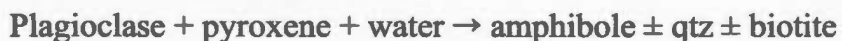
Parallel plagioclase crystals are one of the main parameters that define igneous layering.

Most grain boundary contacts between parallel crystals are straight, with smoothly curved to subangular grain boundaries where crystals terminate. However, some plagioclase crystals approach a granoblastic texture, with well-developed 60-120° triple point boundaries. Samples that exhibit local granoblastic plagioclase textures commonly preserve strained, partially recrystallized plagioclase, suggesting that the granoblastic texture is secondary. In layered samples that contain olivine, elongated, parallel plagioclase may down-warp underneath olivine and above may appear to be draped over the olivine crystals (Figure 3.2b). These plagioclase crystals can exhibit minor internal strain expressed as undulose extinction, suggesting that this texture developed after initial crystallization, and may therefore be evidence for compaction of the crystal pile during crystallization.

In samples with a gabbroic composition, where olivine is less abundant and clinopyroxene is the predominant mafic phase, plagioclase typically exhibits different textures. Layering, defined above by parallel oriented plagioclase laths, is less common in gabbroic samples. Plagioclase is more commonly randomly oriented, and shows more evidence for recrystallization. The transition from rocks with parallel oriented plagioclase to randomly oriented plagioclase generally occurs further away from the base of the Lower Series, approaching the transition zone. When CPX is abundant, plagioclase is commonly interstitial and forms distinctly smaller chadacrysts within the poikilitic pyroxene (Figure 3.2c). Plagioclase chadacrysts within clinopyroxene and orthopyroxene have a fresher appearance than nearby matrix plagioclase.

Samples in the uppermost Lower Series, that are closest to the transition zone, exhibit the greatest textural variation and share characteristics of both the Upper and Lower Series. In particular, plagioclase in pyroxene amphibole gabbro is relatively variable compared to dunite, troctolite and leucogabbro. Plagioclase crystals are randomly oriented, inequigranular and anhedral, with lesser amounts of subparallel, subhedral elongate to stubby laths. Grain boundaries are curved and irregular in randomly oriented crystals and somewhat straighter in subparallel oriented crystals. Where crystals are subhedral and have a subparallel orientation, they resemble leucogabbro and olivine gabbro in the Lower Series. Plagioclase occurs as chadacrysts in pyroxene, and similar to gabbroic samples, chadacrysts are fresher than matrix plagioclase, which often exhibit undulose extinction and weak sericite alteration. It appears that enclosure in pyroxene shielded these inclusions from outside alteration. Locally, plagioclase has weak oscillatory zoning that is interpreted as a primary feature.

A texture not noted in other Lower Series rocks involves the widespread pseudomorphing of pyroxene oikocrysts by amphibole. These reactions consume plagioclase by the general reaction:



The result of this reaction is that plagioclase in contact with secondary amphibole is corroded or embayed (Figure 3.2d). Potassium to form biotite is not included in the reaction, but may be derived in part from digested paragneiss xenoliths and small amounts of orthoclase. Biotite pseudomorphing amphibole textures are more common in the US, where xenoliths are more common. Sericite alteration in these crystals is weak and locally most intense along late fractures.

Recrystallization textures in the Lower Series are uncommon but are more typical in pyroxene amphibole gabbros than in troctolites or gabbroic rocks. Those textures include

weak localized undulose extinction and diffuse albite twinning and grain boundaries, subgrain formation, weakly warped or bent albite twinning, and local brittle fracturing of crystals.

### **3.2.2 Lower Series olivine**

In melatroctolite and dunite, olivine is the most abundant phase. Olivine in these lithologies is the most coarse-grained compared to other olivine-bearing lithologies. Alteration to serpentine, magnetite and iddingsite is common in these ultramafic rocks, compared to the mafic olivine-bearing rocks.

In troctolite and olivine-bearing gabbro, olivine is relatively consistent. Average grain size is medium, though in melanocratic samples olivine tends to be coarser-grained. Generally, the smallest olivine crystals occur as inclusions in pyroxene. Olivine is equigranular, subrounded, and may be slightly elongated or form elongated interconnected chains parallel to the plagioclase laths (*i.e.* layer parallel) (Figure 3.3a). In olivine gabbros, olivine may have an irregular shape when in contact with poikilitic pyroxene. Less commonly, olivine is interstitial to plagioclase. Grain boundaries with surrounding phases are normally smooth

Olivine in some troctolite and olivine gabbro samples has a smooth rim of clinopyroxene and/or amphibole and/or serpentine separating it from direct contact with surrounding plagioclase (Figure 3.3b). The clinopyroxene rims are thin and unaltered, and have a smooth contact relationship, suggesting that this is a magmatic texture, possibly related to trapped liquid evolution. However, amphibole rims typically exhibit subtle symplectic textures that are commonly only visible in backscattered electron images. These rims are discussed in Chapter 5.

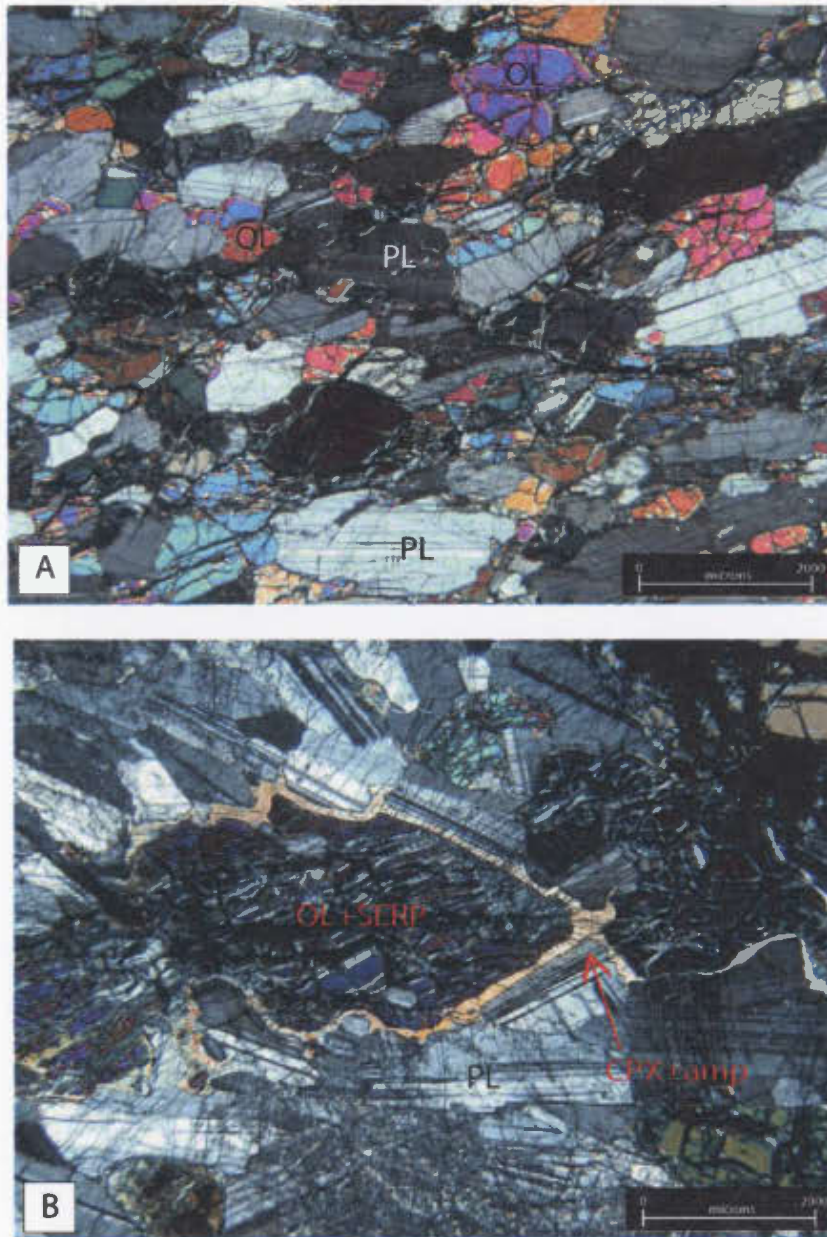


Figure 3.3 Transmitted, crossed-polarized light photomicrographs of the Lower Series in the RCLIS. (a) Relatively fine-grained olivine occurs as weakly elongated crystals in discontinuous chains that, along with elongated plagioclase, define the orientation of magmatic layering (RIC-03); (b) locally, altered olivine  $\pm$  serpentine is enclosed in thin, smooth rims of clinopyroxene and/or orthopyroxene  $\pm$  hornblende. The smooth, even texture and infilling of interstices between plag and olivine suggests this texture is magmatic, rather than a secondary alteration product. Abbreviations are as per Figure 3.2. Note scale bars in the lower right corner.

Olivine may contain small rare plagioclase and sulfide inclusions, or more commonly chromite or magnetite. Plagioclase inclusions are round to tabular, whereas sulfide inclusions are round and blebby.

Olivine typically alters to serpentine and iddingsite, which commonly occupy fractures. Alteration is weakest in troctolites and layered gabbroic rocks. Alteration increases to the north, towards the transition zone, and, aside from fracture-filled alteration, is expressed as rims of fibrous serpentine, actinolite and chlorite.

### **3.2.3 Lower Series pyroxene**

Pyroxene is uncommon in ultramafic rocks, but in several samples in the southeast, coarse-grained poikilitic orthopyroxene, up to 10 mm in diameter encloses olivine and is pseudomorphed by amphibole and serpentine. Melatroctolite in the southwest may contain a low abundance (<3%) of clinopyroxene or orthopyroxene oikocrysts that enclose olivine or plagioclase.

In troctolites, pyroxene is <5% and forms thin films or rims surrounding olivine, separating it from plagioclase. A progressive change in pyroxene texture occurs with increasing abundance. The progression from films and rims around olivine to interstitial and amoeboid crystals occurs first in some troctolites and olivine gabbro. With increasing abundance, such as in olivine gabbro and other gabbroic lithologies, clinopyroxene becomes the dominant mafic phase. It occurs as coarse- to megacrystic oikocrysts, and less commonly sub-poikilitic crystals (Figure 3.4a).

Clinopyroxene and lesser orthopyroxene oikocrysts have sharp contacts with surrounding phases, which comprise plagioclase and minor quantities of olivine. Pyroxene oikocrysts contain chadacrysts of olivine and plagioclase; both are finer-grained and fresher than their matrix equivalent. Coarser-grained clinopyroxene oikocrysts may be elongate approximately parallel to layering.

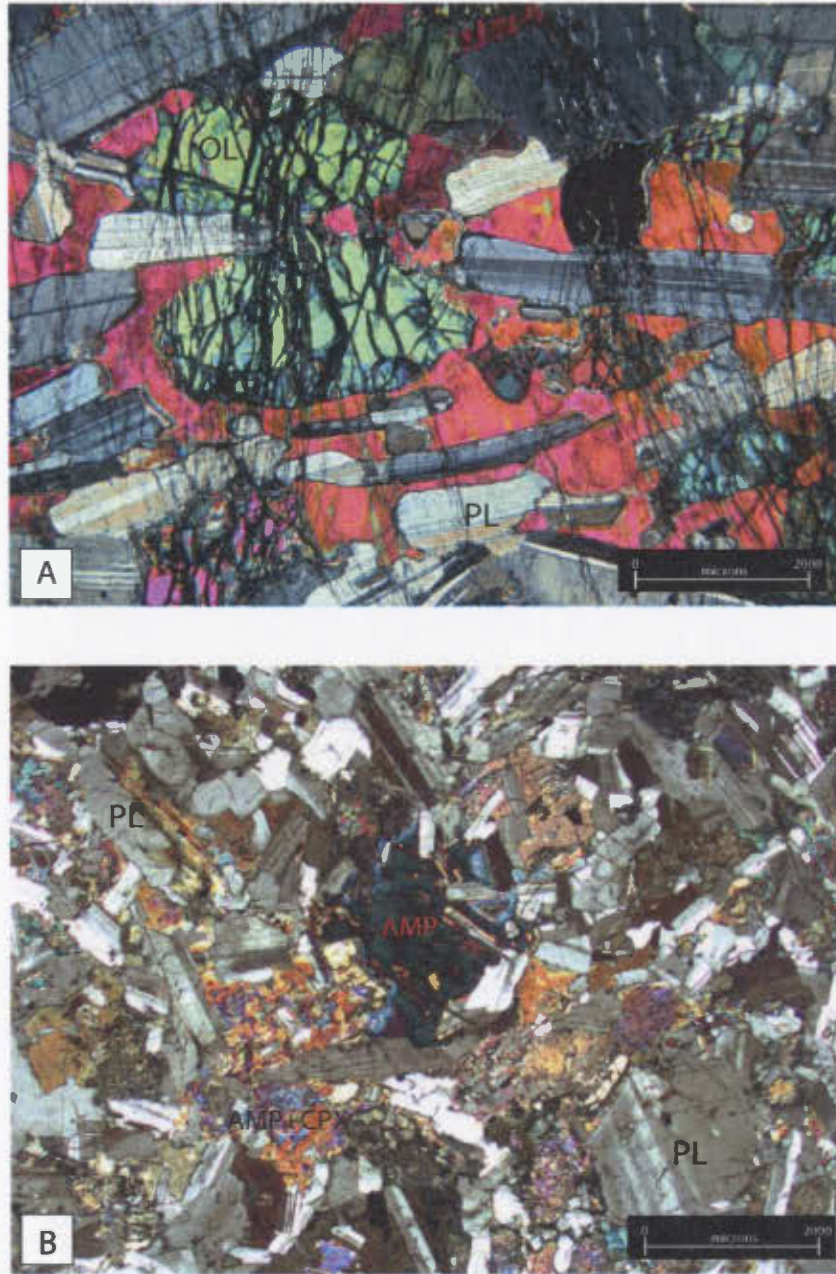


Figure 3.4 Transmitted, crossed-polarized light photomicrographs of the Lower Series in the RCLIS. (a) Clinopyroxene progresses from thin films as in Figure 3.3b to interstitial, sub-poikilitic crystals, to small oikocrysts, as illustrated in this image of RIC-30B; (b) towards the top of the Lower Series, near the transition zone, pyroxene may be partially- to completely pseudomorphed by amphibole. In this image, from RIC-48, near the lower left corner CPX is partially replaced and in the center of the image, a partially extinct crystal of hornblende pseudomorphs a sub-poikilitic CPX crystal. Note that this replacement texture preserves the optical continuity of CPX. Plagioclase in this and similar samples is randomly oriented compared to previous figures where it is subparallel. Note that in 'b', plagioclase exhibits a feathery or diffuse extinction texture and commonly exhibits undulose extinction. Note scale bars in lower right corners.

Closer to the transition zone in pyroxene amphibole gabbros, clinopyroxene textures are very similar to those described above, although grain size decreases slightly. However, pyroxene is commonly rimmed or partially pseudomorphed by hornblende, which may be subsequently replaced by biotite and/or actinolite. Uncommonly, the contact between plagioclase and amphibole is symplectic. It is not clear if the initial hornblende rim is primary, or if it represents the initial stage of pyroxene alteration, but based on the symplectic textures, it seems more likely that it is secondary. Wholesale amphibole pseudomorphing of pyroxene is found throughout pyroxene amphibole gabbros (Figure 3.4b). Textures unambiguously indicate that this replacement is secondary because of the preservation of the primary pyroxene textures, the presence of inclusions of grungy, altered looking pyroxene within amphibole, and throughout different samples, the progression of replacement is observed in incremental steps. Uralitization occurs in the cores and rims of some pyroxene crystals, and is distinct from amphibole replacement.

In some samples, clinopyroxene contains fine inclusions of rutile, which average 3-5% by volume, but may be 10-15%. The inclusions are subhedral to euhedral, and parallel to pyroxene cleavage planes.

#### **3.2.4 Lower Series sulfides**

Sulfides in troctolites are uncommon, not exceeding 2 to 3% by volume and generally average  $\leq 1\%$ . In decreasing order of abundance, sulfides comprise pyrrhotite, pentlandite, chalcopyrite, pyrite, bornite, cubanite and millerite; the latter two phases were detected only by EMPA. In gabbroic samples, sulfides rarely exceed 1%, and in pyroxene amphibole gabbro sulfides are  $< 1\%$ . Bornite and millerite were not observed in gabbroic samples. Troctolites and gabbros share similar textures, but textures change in pyroxene amphibole gabbro.

Sulfides are commonly subrounded to irregular blebs or polymineralic aggregates of blebs interstitial to silicates (Figure 3.5). In pyroxene amphibole gabbro, sulfides are disseminated or fine-grained, irregular, corroded and ragged blebs. Although uncommon, some layered samples show a minor increase in sulfide concentration at the transition between layers, such as between dunite and troctolite.

Pentlandite occurs in two main textures. First, it is coarse-grained, granular to massive aggregates and secondly, as flame exsolution lamellae. Granular pentlandite is relatively more abundant in troctolite samples and is concentrated along, but not limited to, the margins of pyrrhotite; in troctolites this may constitute >30% (not exceeding 50%) of a sulfide bleb. Flame exsolution lamellae are localized along fractures in pyrrhotite and along grain boundaries between pyrrhotite and silicates. In gabbros, flame exsolution pentlandite is more common and is the only pentlandite texture observed in pyroxene amphibole gabbro. EMPA analysis detected millerite in one altered troctolite sample.

Chalcopyrite, which is less abundant than pentlandite in most troctolite and gabbro samples, occurs as discrete blebs or with pyrrhotite blebs. Bornite occurs in several samples as fine exsolution lamellae in chalcopyrite. Although rare, cubanite exsolution lamellae were noted in RIC-01.

Alteration of primary sulfides in ultramafic lithologies is uncommon, but occurs as veinlets or fractures that host outward radiating masses of marcasite, fine black grunge, and veinlets of magnetite. Alteration appears to increase where sulfides are in contact with olivine. In gabbroic samples, alteration is similar, but affects a smaller proportion of sulfides. In these samples, secondary pyrite and marcasite locally exhibit a colloform texture. Sulfides in pyroxene amphibole gabbro exhibit the greatest degree of alteration, which is consistent with the higher degree of silicate alteration. Up to >90% of sulfides have a smooth, rim of hematite that embays surrounding sulfides. This indicates that a change in oxygen and/or sulfur fugacity occurred. Secondary silicates (e.g. actinolite,

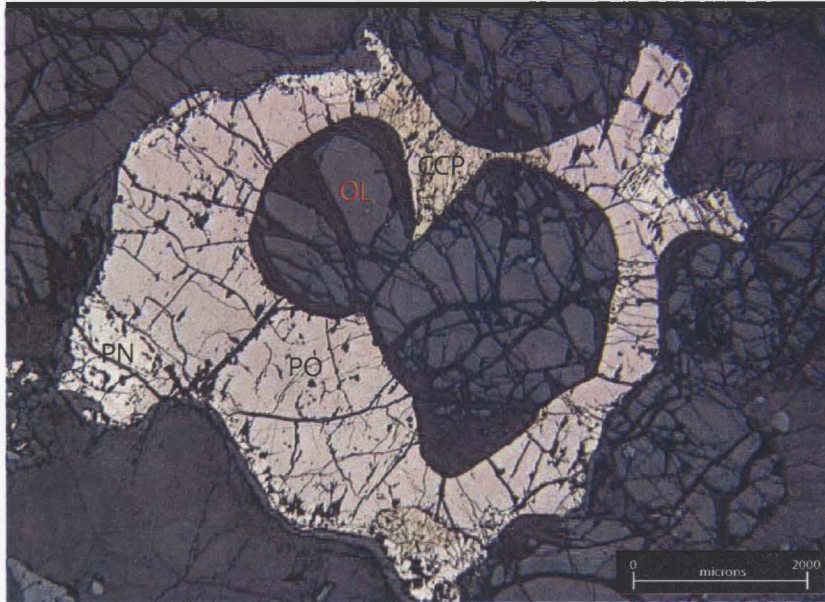


**Figure 3.5** Reflected light photomicrograph from the Lower Series in the RCLIS. Sulfides commonly occur as polymineralic interstitial blebs in the LS. This bleb, in RIC-01 comprises mainly pyrrhotite (PO) and lesser pentlandite (PN) and chalcopyrite (CCP). Pentlandite exhibits a relatively coarse-grained granular texture in this and most other troctolite samples, whereas in Upper Series samples and more gabbroic samples, pentlandite occurs as flame exsolution. Note scale bar in lower right corner.

biotite) cross-cut the hematite alteration rims, indicating silicate alteration post-dates sulfide alteration.

### **3.2.5 Lower Series oxides**

Lower Series oxides comprise magnetite, ilmenite and chromite. In ultramafic rocks, ilmenite is absent, whereas in leucocratic mafic rocks, chromite is absent.

Primary textures in troctolites include euhedral to subhedral chromite, and magnetite and rounded blebs of magnetite that are interstitial to olivine and plagioclase and as inclusions in both phases. In gabbroic samples, oxides are smaller, rounded to amoeboid blebs intercumulus to silicates. Magnetite also occurs in what appear to be exsolution lamellae in pyrrhotite and pentlandite. Some magnetite exhibits cleavage-controlled ilmenite exsolution lamellae, particularly in leucotroctolite. To the north, closer to the transition zone, where pyroxene amphibole gabbro is present, oxides become coarser-grained and exhibit interstitial to amoeboid or weakly poikilitic textures, enclosing small laths of plagioclase and biotite.

Ilmenite is uncommon in troctolitic rocks, but occurs as discrete subhedral crystals, massive accumulations associated with sulfides and exsolution lamellae within magnetite. Gabbroic rocks contain more magnetite and ilmenite and less chromite, but textures are similar to troctolites.

Oxides in the pyroxene amphibole gabbros appear to be slightly more concentrated at contacts between biotite and clinopyroxene, or biotite and plagioclase, or in other locations, oxides are surrounded by biotite. In both cases it is unknown whether this is a primary or secondary texture. There is a variable contact relationship between magnetite and/or ilmenite and pyroxene and biotite: in some locations oxides appear to grow at the expense of the silicates, whereas in other locations the reverse is true. The significance of this relationship is unknown.

Secondary textures in troctolites include fracture infillings and late injections of magnetite into sulfide blebs. Oxidation and hydration of olivine forms serpentine, iddingsite, and magnetite, the latter occurring as ragged veinlets and symplectic rims in contact with pyroxene or plagioclase.

### **3.3 Upper Series mineralogy and petrography**

The Upper Series is distinct from the Lower Series based on mineralogy, texture, degree of alteration and recrystallization. All rocks in the Upper Series have a gabbroic protolith, but recrystallization is widespread. The Upper Series comprises leucogabbro and pyroxene amphibole gabbro. These rock names were derived by normalizing the four most abundant minerals – plagioclase, clinopyroxene, orthopyroxene and amphibole (hornblende + actinolite + tremolite) to 100% and then plotting them on ternary diagrams after Streckeisen (1976).

Pyroxene amphibole gabbro is the most abundant rock type in the Upper Series and Variation in composition does not appear to have a regular spatial distribution. Plagioclase averages approximately 45%, and ranges from 60% to 35%. Pyroxene is mainly CPX, but combined with OPX averages approximately 14%, to a maximum abundance of 45% and a minimum of 0%, in a sample dominated by amphibole instead of pyroxene. Amphibole, which includes hornblende, actinolite, and possibly tremolite, averages approximately 23%, with a maximum of 40% and a minimum of 12%. Biotite occurs in all pyroxene amphibole gabbro samples, and averages 8%, ranging from 10% to 2%.

Leucogabbro is concentrated within the transition zone and proximal to xenolith belts in the Upper Series. Plagioclase averages 70% (80% to 60%). Clinopyroxene averages 8% (13% to 5%) and orthopyroxene averages 2% (0% to 5%). Amphibole is more abundant,

averaging 12% (20% to 5%). Biotite, present in all leucogabbro samples, averages 7%, (15% to 1%). Accessory phases include olivine and quartz, both of which average 1%.

### 3.3.1 Upper Series plagioclase

Plagioclase occurs as granular to elongate, equigranular to inequigranular, subhedral to anhedral crystals. Plagioclase may be irregularly shaped, particularly when it is interstitial to pyroxene. Plagioclase orientation is commonly random, but subparallel, elongated laths locally define weak igneous layering. Grain boundaries vary from smooth to angular. Smoothly embayed grain boundaries occur between amphibole, which commonly grows by consuming plagioclase via the general reaction:  $pl + pyx + H_2O \rightarrow amp + qtz$

Plagioclase commonly contains inclusions of amphibole and less often, oxides and rare sulfides. Rarely, amphibole inclusions form chains that appear to mark a former irregular grain boundary (Figure 3.6). This suggests plagioclase was corroded, amphibole formed, and then plagioclase continued to grow a second time. EMPA analyses confirm large differences in An composition in rim and cores of plagioclase in these examples.

Recrystallization textures are more common in the Upper Series, particularly near the transition zone and proximal to xenolith belts, particularly in leucogabbro. Deformation textures are uncommon and other phases show no evidence for deformation-induced recrystallization. Therefore, these textures might result from metasomatic recrystallization and minor stress. Textures include common irregular concentric zoned extinction, weak undulose extinction, uncommon subgrains and bent or fuzzy albite twins (Figure 3.7). Some samples have two distinct populations of plagioclase. The majority of plagioclase is as described above, but 1-2% are large, strongly embayed, recrystallized crystals. These crystals are strongly zoned and appear to have been corroded and then experienced a second stage of growth. Because of the markedly different textures, it is possible they may not have crystallized *in situ*, thus they may be autocrysts. Oscillatory

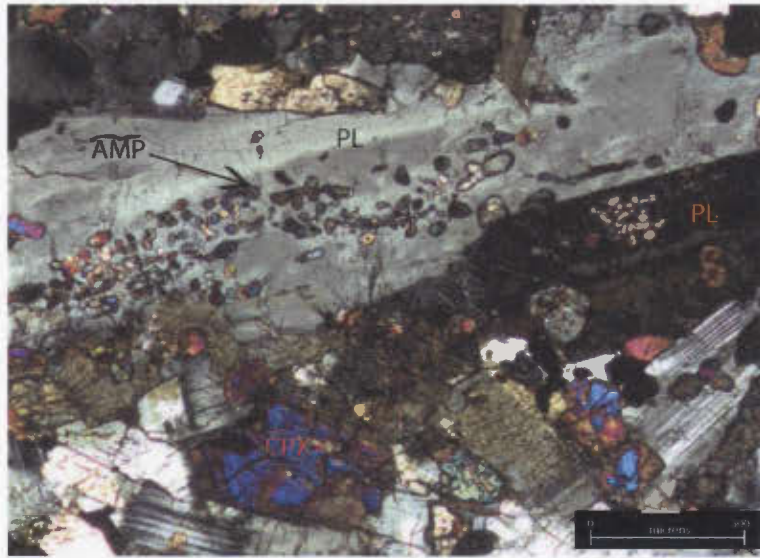


Figure 3.6 Transmitted, crossed-polarized light photomicrograph from the Upper Series of the RCLIS. In this image, from RIC-50, the central plagioclase crystal is several times larger than the surrounding plagioclase, exhibits relatively greater undulose extinction and contains clusters of granular amphibole. These textures suggest that this crystal, and other similar ones in different samples may have been entrained by the magma during emplacement and transported from the Lower Series. Extinction patterns suggest that the granular amphibole inclusions mark a boundary within the plagioclase crystal, suggesting it may have been partially resorbed and then crystallized further.

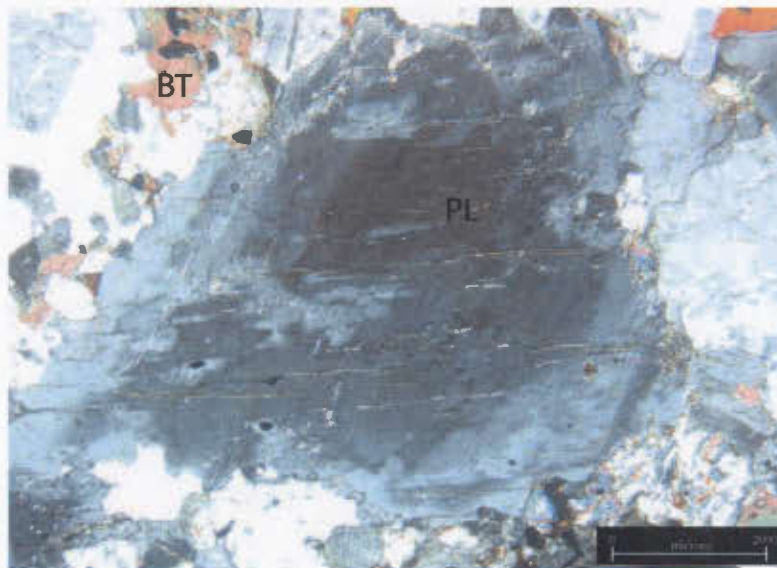


Figure 3.7 Transmitted, crossed-polarized light from the Upper Series of the RCLIS. This image, from RIC-51A, shows plagioclase textures similar to Figure 3.6, but without granular amphibole. This crystal is very coarse-grained compared to the surrounding “matrix” plagioclase and exhibits a complex zoning pattern, highlighted by the extinction pattern. This pattern is also indicative of resorption or metasomatism of the crystal and subsequent growth at a distinctly different composition. Note scale bar in lower right corner for scale.

zoning is common in these crystals and zone boundaries are usually irregular, which is best observed under cross-polarized light.

Alteration comprises sericite alteration along fractures and sometimes along contacts with amphibole. Alteration cross-cuts all textures and is therefore the latest event.

### **3.3.2 Upper Series pyroxene**

Pyroxene exhibits two distinct textures in the Upper Series and both are variably preserved. First, poikilitic pyroxene is rare inside the transition zone, but more common near the top of the Lower Series and near the base of the Upper Series. Oikocrysts comprise clinopyroxene and lesser orthopyroxene and commonly contain small subrounded, elongated inclusions of plagioclase and rounded inclusions of olivine; olivine inclusions are relatively fresh compared to olivine in the matrix. Oikocrysts contains less abundant inclusions of magnetite, ilmenite and pyrrhotite. Poikilitic pyroxene also contains distinctive rutile inclusions that are apparently crystallographically controlled, because they are elongated parallel to cleavage. Their mechanism of formation is unknown.

Entering the transition zone, poikilitic pyroxene grades into subpoikilitic to granular textures (Figure 3.8). Granular to interstitial pyroxene is relatively more abundant in the upper portion of the Upper Series. Granular to subpoikilitic pyroxene contains quartz, biotite and amphibole inclusions. It is possible that some granular or interstitial pyroxene is actually recrystallized or metasomatized poikilitic pyroxene, but secondary overprinting makes this relationship ambiguous.

Pyroxene alteration is most commonly uralitization. This occurs from the core outwards and is usually cleavage controlled, so that the pyroxene cores have a brown-black grungy appearance, whereas rims are relatively fresher. Biotite and actinolite pseudomorphs after poikilitic and granular pyroxene are widespread. Aside from biotite and actinolite

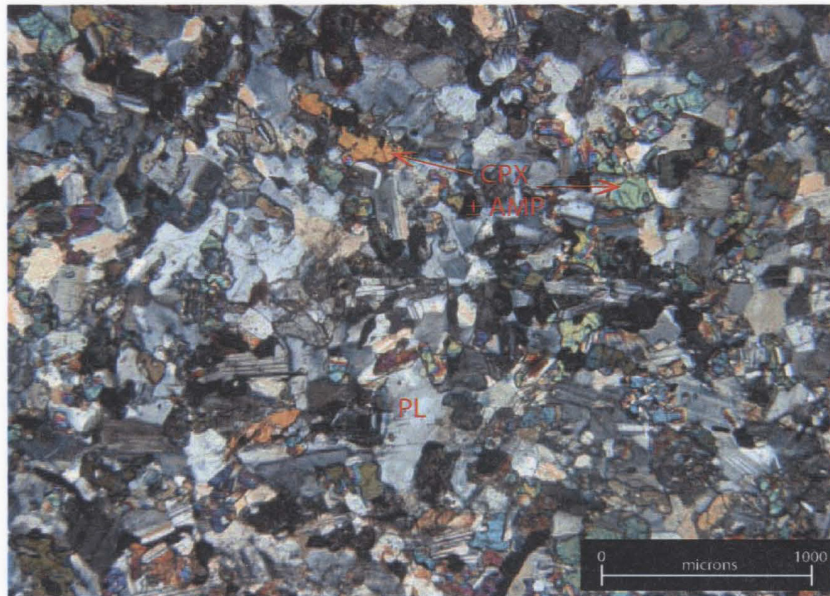


Figure 3.8 Transmitted, crossed-polarized light image from the transition zone of the RCLIS. In this image, from RIC-23, pyroxene has become granular and plagioclase is randomly oriented and irregular. Plagioclase also exhibits diffuse extinction patterns. Amphibole locally replaces pyroxene, mainly CPX. Note scale bar in lower right corner.

replacement, hornblende can form a rim surrounding only poikilitic pyroxene, as described in previous sections. Locally, actinolite and biotite replace this rim, suggesting that it may be a primary, or early alteration feature. Locally, symplectic reaction rims between amphibole rims and plagioclase are developed that comprise wormy amphibole intergrown with plagioclase and quartz.

### **3.3.3 Upper Series amphibole and biotite**

Amphibole textures suggest it is a secondary phase resulting from pyroxene alteration; exceptions are the thin rims around poikilitic pyroxene and olivine described above. Amphibole occurs as fine-grained uralite that commonly originates in the core and radiates outwards along cleavage planes. Fibrous, acicular to bladed masses of actinolite and possible tremolite are medium- to coarse-grained and replace pyroxene in a manner similar to that of uralite. It is common for amphibole to pseudomorph entire pyroxene oikocrysts and less commonly subpoikilitic and granular pyroxene (Figure 3.9a). Evidence for pseudomorphic amphibole is optical continuity and small relict islands of pyroxene. A range of textures demonstrates the progressive nature of this reaction.

Hornblende also occurs at the contact between plagioclase and pyroxene, embaying plagioclase; textures suggest amphibole grows at the expense of plagioclase (Figure 3.9b). These reaction-controlled grain boundaries may be marked by symplectic intergrowths of amphibole, quartz and plagioclase.

Biotite is ubiquitous in the Upper Series and exhibits variable textures and abundances. It is present as anhedral, elongate and ragged crystals, often intergrown with actinolite where pyroxene alteration occurs. Biotite interstitial to plagioclase in some samples appears to be a primary texture compared to other occurrences, because there is no evidence for it having replaced a previous phase. Biotite regularly pseudomorphs pyroxene oikocrysts, similar to amphibole described above (Figure 3.10). Locally, biotite may replace hornblende and actinolite that previously pseudomorphed pyroxene.

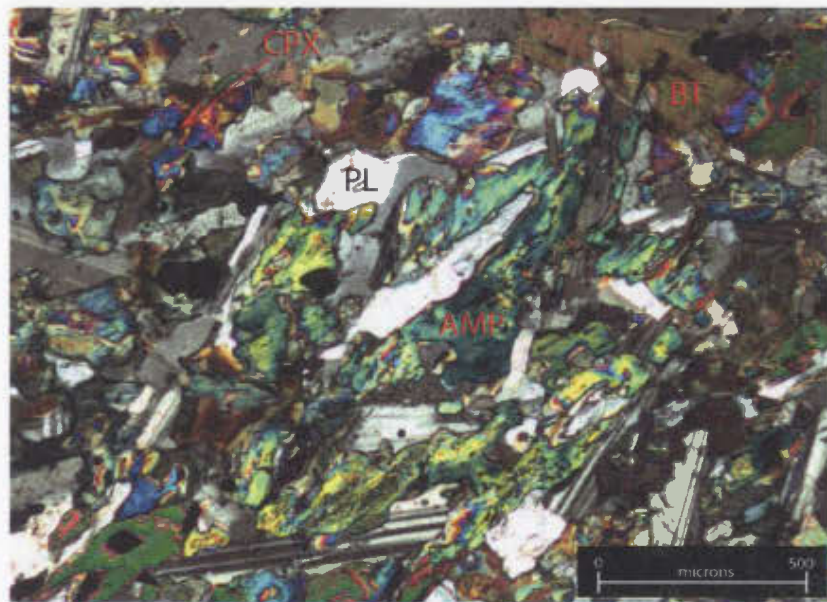
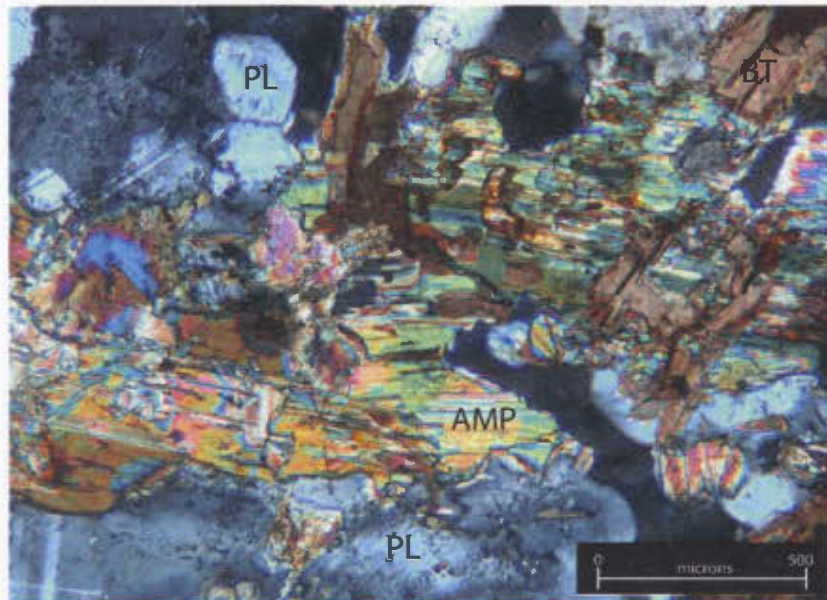


Figure 3.9 Transmitted, crossed-polarized light image from the Upper Series of the RCLIS. (a) in this image, from RIC-56, clinopyroxene is completely replaced by a combination of hornblende (HB) and uraltite (UR), which is subsequently consumed by biotite. Plagioclase in these samples is clouded by fine amphibole inclusions; (b) plagioclase is embayed by amphibole and biotite, which are replacing interstitial clinopyroxene. The textures in this image, from RIC-76 indicate that plagioclase is consumed in these reactions. Note scale bars in lower right corner.

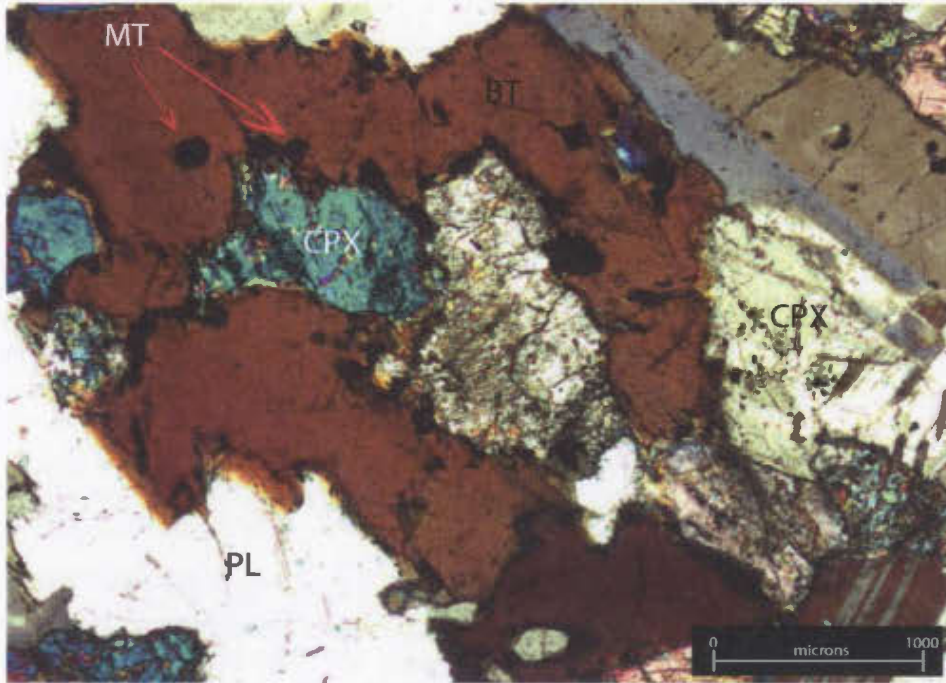


Figure 3.10 Transmitted, crossed-polarized light in the Upper Series of the RCLIS. In this image, from RIC-67, secondary biotite is consuming clinopyroxene and plagioclase. CPX contains numerous granular inclusions of amphibole, similar to previous figures. The reaction between biotite and clinopyroxene appears to form magnetite ( $\pm$  ilmenite). Note scalebar in lower right corner.

Although it locally contains oxide inclusions, biotite has a fresh, “clean” appearance relative to surrounding phases, especially pyroxene and even compared to amphibole, which supports a late origin.

### **3.3.4 Upper Series accessory phases**

Oxides and sulfides occur most commonly as disseminated to fine rounded to subrounded blebs, usually interstitial to silicates or as inclusions within silicates. Locally, magnetite contains pyrite or pyrrhotite inclusions. Ilmenite and less commonly magnetite occur as coarse-grained poikilitic to interstitial crystals or aggregates interstitial to poikilitic pyroxene (Figure 3.11). Smaller, irregular amoeboid crystals of ilmenite occur in the cores of secondary biotite, but the exact reaction or process to form these textures is unknown and it is unknown if these oxides are primary or secondary. Some sulfides exhibit a rim of hematite that embays the sulfide grain, suggesting that it grew at the expense of sulfide, probably as the fluid composition became more oxidizing.

Quartz is interstitial to plagioclase and pyroxene and appears fresh. It is symplectically intergrown with amphibole and plagioclase. Olivine in Upper Series samples is uncommon and only occurs as inclusions within pyroxene or amphibole that pseudomorphed pyroxene. The inclusions are small, rounded to subrounded and commonly altered and fractured. Olivine occurs within the matrix of some samples, but it is more strongly altered than when it is an inclusion, indicating that the inclusions were shielded from alteration. Epidote is uncommon and where present, occurs as small prismatic or diamond shaped crystals, or irregular, fine-grained masses associated with altered plagioclase and pyroxene. RIC-17 contains abundant fine-grained masses and aggregates of subhedral epidote.

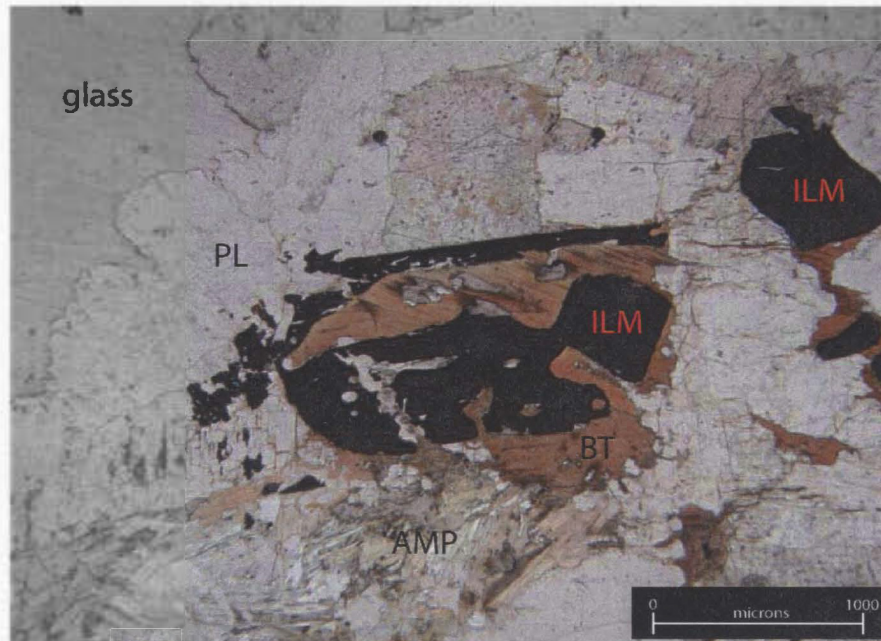


**Figure 3.11** Transmitted, plane-polarized light image from the Upper Series of the RCLIS. In this image, skeletal ilmenite is intergrown with coarse-grained sheaves of biotite. It appears that fibrous amphibole is cutting ilmenite and biotite. The relative timing relationship in this image is ambiguous whether ilmenite is consuming biotite or biotite is reacting with ilmenite.

### **3.5 Petrographical Summary**

In the Lower Series, olivine cumulates (dunite, melatroctolite) were the first lithologies to crystallize. Spinel crystallized first, based on its presence as subhedral to euhedral inclusions within olivine, which crystallized slightly later. Rare sulfide inclusions in olivine, but not in spinel, suggest that sulfides evolved as an immiscible phase slightly later than spinel crystallized. The interstitial phase varies from sample to sample or within different layers, but is either orthopyroxene or plagioclase, which either way, was the last phase to crystallize. Why these lithologies are not located at the base of the intrusion, but approximately 1/3 up the Lower Series, is unknown, but microprobe analysis of olivine and plagioclase indicate that they have the most primitive mineral compositions (e.g. Fo 85-87, An 77-76). These samples originate from layers that appear to be conformable with the layers above and below it, thus the geometry does not support these rocks being a feeder outlet.

Troctolites and primitive gabbros, which occur stratigraphically above and below the ultramafic rocks crystallized next. In these lithologies, sulfide and oxide liquids were still present, and were incorporated into both plagioclase, olivine and poikilitic pyroxene, though the latter contains few opaque inclusions. Plagioclase and olivine crystallized coevally. Olivine contains plagioclase inclusions and some olivine is interstitial to plagioclase, suggesting some plagioclase crystallized prior to olivine. The thin rims of amphibole and pyroxene surrounding olivine suggest either that a small volume of trapped liquid reacted with surrounding plagioclase and olivine to form the rims, or that during cooling and solidification of the cumulate pile, olivine reacted with plagioclase to form these reaction rims.

Evidence for late, subsolidus changes in sulfides and oxides includes exsolution textures in chalcopyrite, pyrrhotite and spinel. Bornite exsolving from chalcopyrite, flame exsolution of pentlandite from pyrrhotite, magnetite exsolution from chromite and ilmenite exsolution from magnetite are all late reactions.

Farther north, pyroxene gabbros crystallized late. Olivine is present mainly as inclusions in some of these samples, suggesting that though some olivine crystallized, it is not apparent how much was present before alteration. Plagioclase, oxides and sulfides crystallized together, early, similar to other gabbroic rocks. Pyroxene crystallized later based on its poikilitic texture. Pyroxene rarely contains oxides or sulfide inclusions, suggesting by the time it crystallized, the oxides and sulfides had already crystallized. The presence of larger interstitial oxide grains suggests that concentration and crystallization of oxides continued during silicate crystallization.

Following the crystallization of pyroxene, hornblende rims formed along their margins. It is not apparent if this reaction occurred during crystallization of the magma, or if it is a secondary reaction. Regardless, these rims generally predate wholesale actinolite and biotite replacement of pyroxene by amphibole. Uralitization occurred after the formation of hornblende rims, because locally it cuts these rims. Actinolite and biotite alteration occurred after hornblende rims, and always cross-cut the rims. Biotite locally cuts actinolite, indicating it continued to crystallize after actinolite.

Most pyroxene amphibole gabbro sulfides have a rim of hematite that is locally truncated by silicate alteration minerals. This indicates that the sulfide oxidation occurred prior to alteration of silicates. Some oxides, both magnetite and ilmenite locally truncate actinolite, plagioclase, biotite and hornblende, suggesting that there may be secondary growth of oxides.

The transition zone between the Upper and Lower Series is suspected to have developed after initial crystallization or emplacement of magma and that initial crystallization of the RCLIS was relatively continuous. This assumption is based on textures in the transition zone, which appear to overprint primary textures that show a continuous change from the Lower Series to the Upper Series. However, the cause of the abundant xenoliths and

associated alteration that defines the transition zone is still enigmatic. Because of the gradational nature of the contacts between the transition zone and the Upper and Lower Series, the contacts defined on the map are somewhat arbitrary.

In the Upper Series, plagioclase crystallized first, followed shortly by pyroxene, as indicated by the poikilitic textures of pyroxene and the presence of plagioclase chadacrysts in primary pyroxene. Oxide inclusions within plagioclase and pyroxene, but sulfide inclusions only in pyroxene indicate that oxides crystallized early in the petrogenesis, while sulfides began to crystallize slightly thereafter. The interstitial and subpoikilitic texture of ilmenite, and less commonly magnetite indicate that the majority of oxides crystallized after plagioclase and pyroxene. If the thin hornblende rims associated with some pyroxene oikocrysts are primary, they would be the final primary phase to crystallize, and likely formed as a reaction between trapped liquid that formed poikilitic pyroxene, and already crystallized plagioclase. The presence of olivine chadacrysts ( $FO_{68}$ ) with plagioclase ( $AN_{54}$ ) and pyroxene textures similar to Lower Series rocks in RIC-63, close to the top of the intrusion not well understood. It is possible this is a large block of rock that was transported from below during a later pulse of magma, but this does not seem plausible. It is more likely that a late injection of magma into the Upper Series is responsible these rocks. The alteration is consistent with Upper Series rocks, suggesting that this injection predates alteration and recrystallization.

Secondary minerals include amphibole and biotite, and possibly some oxides. If the hornblende rims are not primary, cross-cutting relationships suggest that they are the initial alteration phase, because they are cut by all subsequent alteration phases. Uralite, which is concentrated in the cores of many pyroxene crystals is also probably early to form. Medium- to coarse grained actinolite formed next, cross-cutting uralite and rims of hornblende. In some samples, a late phase of hornblende forms in reaction with actinolite and plagioclase. Biotite is intergrown with actinolite, suggesting it is coeval with actinolite, but in many locations, it appears that biotite is in fact consuming actinolite,

making it the final major alteration phase. There is a strong spatial association between biotite and ilmenite, and locally amphibole, but it is not possible to determine the paragenetic relationship between these phases.

Paragenetic relationships in leucogabbro samples are quite similar to those in pyroxene amphibole metagabbro samples, but there are a few differences, reflecting the relatively greater degree of recrystallization textures in these samples. Poikilitic and interstitial pyroxene is unambiguously primary, indicating they crystallized during and after plagioclase crystallization. However, granular and granoblastic pyroxene occur in samples that have been recrystallized, complicating paragenetic relationships. The lack of, or minimal amount of amphibole spatially associated with granular pyroxene indicates that either recrystallization occurred before major amphibole alteration, and the granular texture was more resistant to alteration, or that recrystallization destroyed initial amphibole alteration; the later seems less likely, because in other samples, there is usually good preservation of relict phases. Biotite, as in PAG samples, is a late phase, usually cross-cutting actinolite and hornblende alteration. Oxides are often located in the cores of biotite, and have an amoeboid texture, suggesting that the oxides crystallized first; secondary oxides associated with biotite or pyroxene are usually cleavage controlled thin rods or lamellae. The relatively strong spatial association between biotite and ilmenite or magnetite is not understood.

## **Chapter 4: Red Cross Lake Intrusive Suite Whole rock lithochemistry**

### **4.1 Introduction**

Fifty-nine samples from the RCLIS were analysed by the XRF methods outlined above and two duplicate samples were used to calculate precision (Appendix 3). All major oxides were analysed ( $\text{SiO}_2$ ,  $\text{Al}_2\text{O}_3$ ,  $\text{MgO}$ ,  $\text{CaO}$ ,  $\text{Fe}_2\text{O}_3$  (Fe total),  $\text{Na}_2\text{O}$ ,  $\text{K}_2\text{O}$ ,  $\text{TiO}_2$ ,  $\text{P}_2\text{O}_5$ ,  $\text{MnO}$ ). Additionally, the trace elements S, Cl, Sc, V, Cr, Ni, Cu, Zn, Ga, As, Rb, Sr, Zr, Y, Nb, Ba, Ce, Pb, Th and U (<1%,) were also analysed. Precious metals (Pt, Pd and Au) were analysed by fire assay ICP-MS methods. LOI is not reported in these analyses, but major oxides are normalized to 100% anhydrous for all diagrams.

This chapter presents data in several sections. First, major element data are presented followed by trace element data. In general, Upper and Lower Series data and all xenolith samples and country rock samples are categorized in this fashion throughout the rest of the geochemical chapters. Most plots illustrate a distinction between Upper and Lower Series samples, justifying this separation. Although the data show overall trends, caution must be used when drawing conclusions reliant on only lithochemical results, because the samples, particularly from the Lower Series, were obtained from cumulate rocks, and generally, from small outcrops, thus they may misrepresent some geochemical trends. However, the data, for the most part, are supported by field and electron microprobe data as being generally representative.

### **4.2 Bivariate plots**

#### **4.2.1 Harker Diagrams**

Harker diagrams are used to plot the major oxides ( $\text{TiO}_2$ ,  $\text{Al}_2\text{O}_3$ ,  $\text{Fe}_2\text{O}_3$ ,  $\text{Na}_2\text{O}$ ,  $\text{CaO}$ ,  $\text{MgO}$ ,  $\text{K}_2\text{O}$ ,  $\text{P}_2\text{O}_5$ ) and identify large-scale geochemical trends. In these plots, oxides are

normalized to 100%, ignoring trace elements, which generally total less than 1% combined.

SiO<sub>2</sub> vs TiO<sub>2</sub> (Figure 4.1a) defines a subvertical, positive slope with a broadly linear trend towards TiO<sub>2</sub> enrichment in Upper Series samples. The behaviour of TiO<sub>2</sub> in the Lower Series is different from the Upper Series. In the Lower Series, there is a clear positive correlation between SiO<sub>2</sub> and TiO<sub>2</sub> such that when SiO<sub>2</sub> increases, so does TiO<sub>2</sub>. Aside from a few samples, the Lower Series does not have much overlap with the Upper Series. The Upper Series pattern is somewhat different from the Lower Series because there is less variability between SiO<sub>2</sub> and TiO<sub>2</sub> such that much of the data plot in a broad cluster with some samples exhibiting elevated TiO<sub>2</sub> concentrations. This suggests that there was more overall differentiation in the Lower Series than in the Upper Series. Field and petrographic evidence indicates that the Upper Series is more homogenous, supporting this conclusion.

SiO<sub>2</sub> vs Al<sub>2</sub>O<sub>3</sub> (Figure 4.1b) plots as a broad circular cluster where the Lower Series is slightly more enriched in Al<sub>2</sub>O<sub>3</sub> and at the same time has relatively lower SiO<sub>2</sub> concentrations. One major difference in these data compared to the SiO<sub>2</sub> - TiO<sub>2</sub> plot is that there is a subpopulation within the Lower Series; this subgroup, which appears in several other Harker diagrams, exhibits distinctly lower Al<sub>2</sub>O<sub>3</sub> and slightly lower SiO<sub>2</sub> concentrations. The six samples in this group are RIC-01, 02, 21, 65, 69 and 68A, which are all ultramafic and include serpentinite, melatroctolite and dunite. A reasonable explanation for the considerably lower Al<sub>2</sub>O<sub>3</sub> concentrations compared to the rest of the population is that these samples contain a minimal amount of plagioclase and otherwise contain mainly pyroxene and olivine, both Al<sub>2</sub>O<sub>3</sub>-free phases.

In the SiO<sub>2</sub> vs Fe<sub>2</sub>O<sub>3</sub> diagram (Figure 4.1c) both the Upper and Lower Series samples exhibit weak, subvertical negative slopes. The Lower Series and Upper Series exhibit similar ranges in Fe<sub>2</sub>O<sub>3</sub> values, although the Lower Series is relatively poorer in SiO<sub>2</sub> and

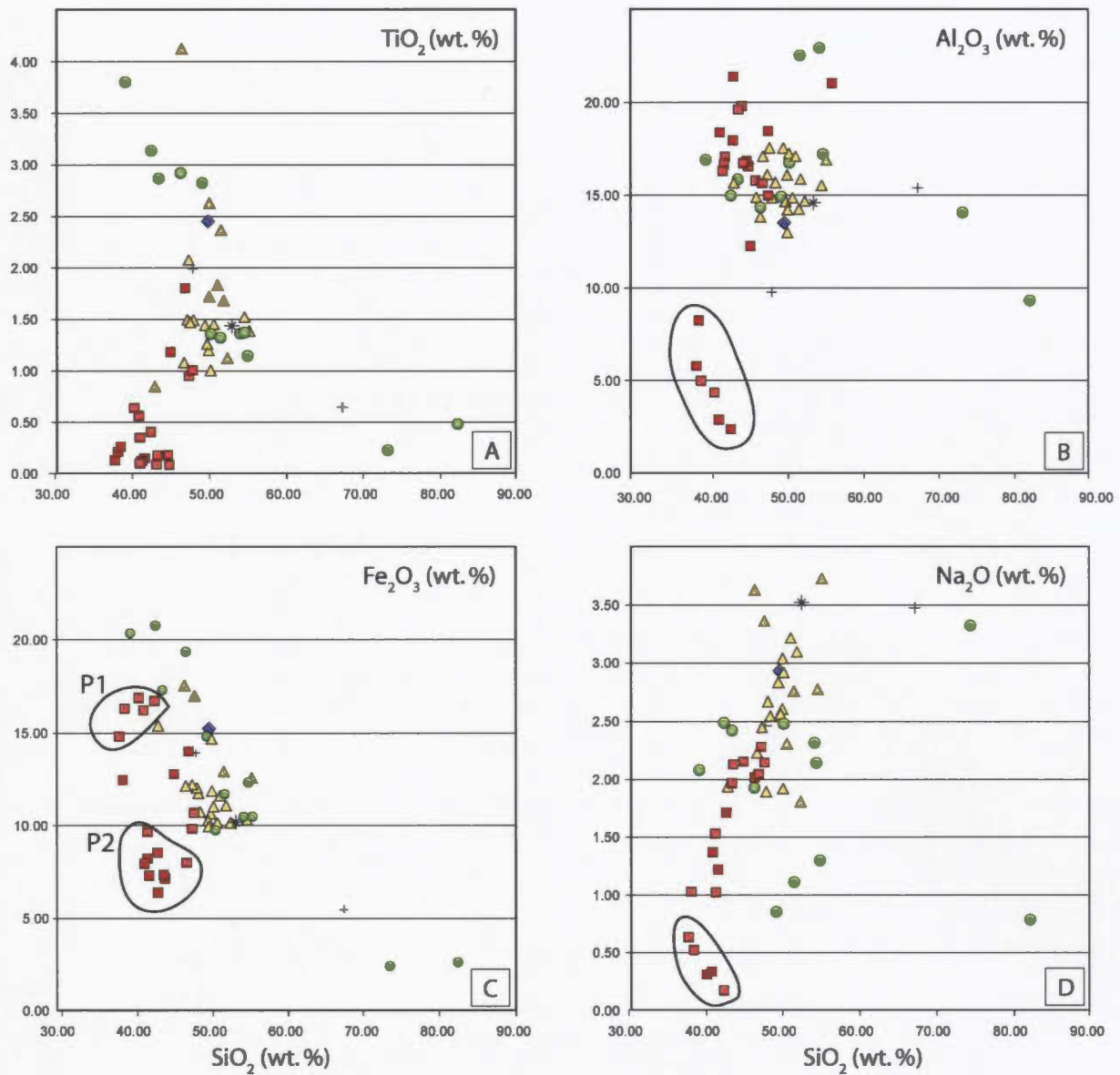
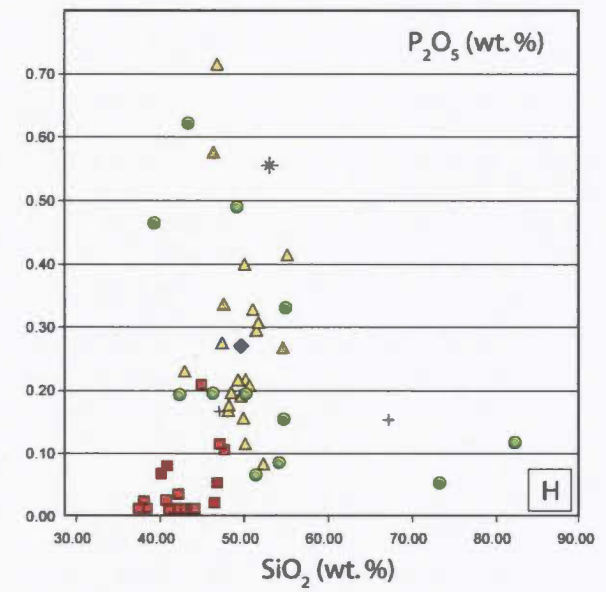
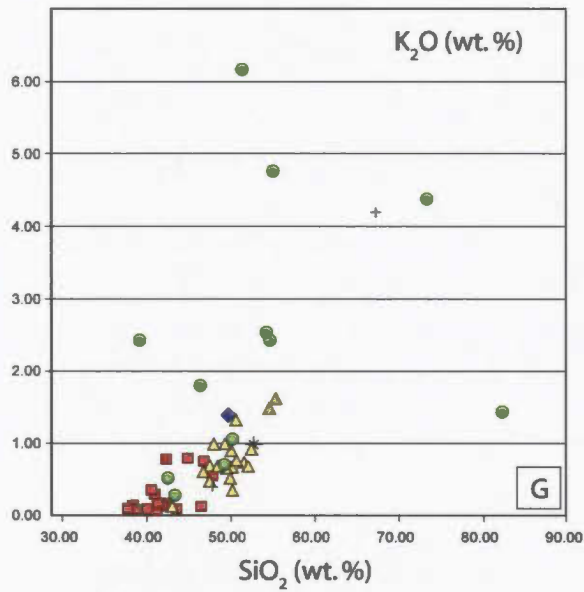
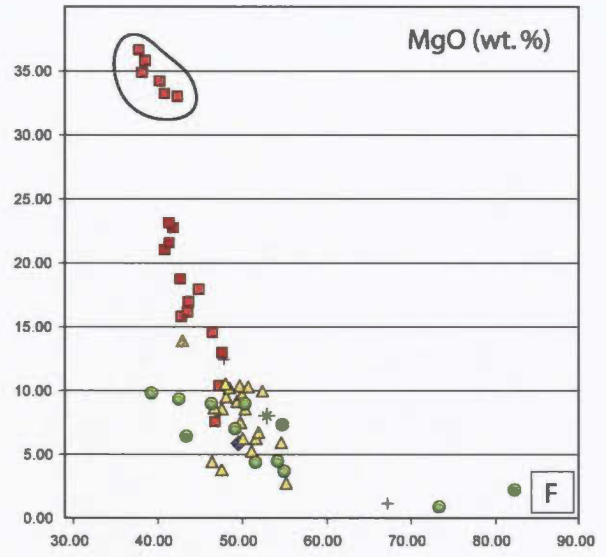
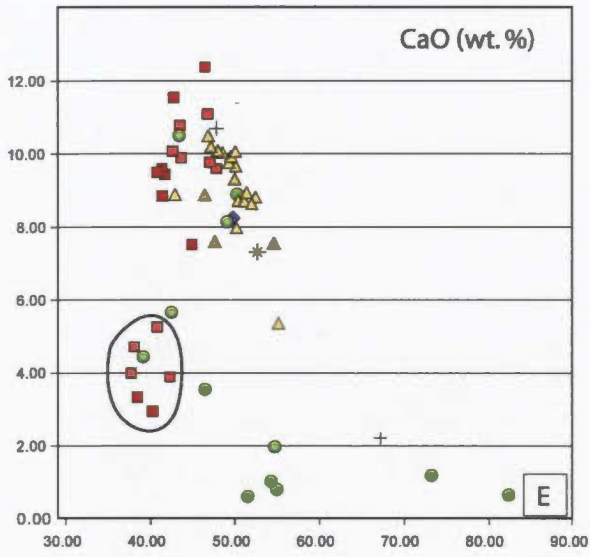


Figure 4.1. Harker diagrams for RCLIS whole rock data. Descriptions for each diagram are given in the text. A global legend for all eight diagrams is given at the bottom of the following page. All diagrams have SiO<sub>2</sub> on the x-axis and the y-axis oxide is noted in the upper right corner of each diagram. Circled groups of data are described in the text. All data is in weight percent and Fe<sub>2</sub>O<sub>3</sub> is total Fe.



Fe<sub>2</sub>O<sub>3</sub>. The Lower Series defines two distinctive clusters of data: one smaller group of high Fe<sub>2</sub>O<sub>3</sub> and low SiO<sub>2</sub> (P1 on Figure 4.1c), which corresponds to the same group identified on the Al<sub>2</sub>O<sub>3</sub> plot (minus RIC-01) and a second group that contains most other samples in the Lower Series, which have a relatively higher SiO<sub>2</sub> vs Fe<sub>2</sub>O<sub>3</sub>. The Upper Series plots in a relatively tight cluster, with several samples plotting higher in Fe<sub>2</sub>O<sub>3</sub>. An explanation for the high Fe<sub>2</sub>O<sub>3</sub> group is not simple, because several phases contain Fe. In this case, however, one variable that can be ruled out is an above average sulfide abundance, because the samples in this group rank 3, 7, 8, 12 and 16 for RIC-21, 02, 65, 69 and 68A respectively for all samples in terms of calculated sulfide abundance (presented below). If sulfides were the main control on Fe<sub>2</sub>O<sub>3</sub> abundances, then the samples with the highest sulfide concentrations would be expected to plot at the top of the Fe<sub>2</sub>O<sub>3</sub> field, but they don't. Another factor that can probably be eliminated is a strong control by silicates, because these samples are all ultramafic and are generally enriched in magnesium rather than iron, which is demonstrated in the SiO<sub>2</sub> vs MgO plot (Figure 4.1f). One commonality that these samples share however is relatively abundant Fe-Ti-Cr oxides (magnetite, Fe<sub>3</sub>O<sub>4</sub>; ilmenite, FeTiO<sub>3</sub>; chromite, FeCr<sub>2</sub>O<sub>4</sub>); the mole percentage of Fe in these three phases is approximately 73%, 37% and 25%, respectively. This seems to be the reason for the elevated Fe<sub>2</sub>O<sub>3</sub>, especially in combination with relatively high to moderate sulfide contents.

SiO<sub>2</sub> vs Na<sub>2</sub>O (Figure 4.1d) illustrates a strong linear trend with a positive slope. In particular, the Lower Series samples fall on a tight line that fades into a slightly less defined, trend in the Upper Series. There is one subpopulation of note in the Lower Series, which exhibits notably lower Na<sub>2</sub>O concentrations. This subpopulation includes the same samples as the Fe<sub>2</sub>O<sub>3</sub> subpopulation (RIC-02, 21, 65, 68A and 69). The most logical explanation for this trend is an increase in the abundance of albitic plagioclase in the Upper Series, which is supported by microprobe data presented below. For the low-Na<sub>2</sub>O group, a similar argument of a small volume of plagioclase (albite) is supported by petrographic evidence and Al<sub>2</sub>O<sub>3</sub> data.

The SiO<sub>2</sub> vs CaO plot (Figure 4.1e) has a pattern similar to that of Fe<sub>2</sub>O<sub>3</sub> and Al<sub>2</sub>O<sub>3</sub>, which is a cluster of all samples together rather than a strongly defined linear trend. However, Lower Series samples show generally lower SiO<sub>2</sub> values for the same CaO contents as the Upper Series samples. Overall, Lower Series samples have higher CaO concentrations relative to the Upper Series. Also distinctive on this plot are the xenolith samples, which have quite low CaO concentrations, regardless of SiO<sub>2</sub> concentrations. The xenoliths are dominated by quartz-biotite-garnet rich samples, and are notably plagioclase-poor. Similar to previous plots, the Lower Series exhibits a subpopulation with distinctly lower CaO concentrations for similar SiO<sub>2</sub> values. These samples comprise RIC-01, 02, 21, 65, 68A and 69, which is the same set of samples that exhibit similarly distinct values of Al<sub>2</sub>O<sub>3</sub>, Fe<sub>2</sub>O<sub>3</sub>, and Na<sub>2</sub>O, as well as MgO, discussed below. Consistent with these samples, the most logical explanation for the lower CaO is a lack of anorthitic plagioclase. Furthermore, olivine-rich rocks are depleted in CaO compared to the clinopyroxene + plagioclase rich rocks.

The SiO<sub>2</sub> vs MgO plot (Figure 4.1f) displays a tightly defined, negatively sloping linear trend. Upper Series samples have the lowest MgO concentrations and the highest SiO<sub>2</sub> concentrations and their pattern is not as tightly defined as the Lower Series. Lower Series samples define a tight line with increasing MgO with decreasing SiO<sub>2</sub> – a trend common in layered mafic to ultramafic rocks. Lower Series samples RIC-01, 02, 21, 65, 68A and 69 plot as a subpopulation, with the highest MgO and lowest SiO<sub>2</sub> concentrations in the sample suite. The principal control on MgO concentration is the abundance and composition of olivine, although clinopyroxene may contain MgO and influence the shape of the curve. In the Lower Series, both CPX and olivine are present, but there is a greater variation in the abundance in olivine than in CPX, suggesting, particularly in the subpopulation, which is CPX-free, that olivine abundance controls the trend of this line. Microprobe data indicate that from the base of the Lower Series towards the transition zone between the Upper and Lower Series, olivine compositions

become more fayalitic, thus MgO concentrations in Lower Series samples decrease. In the Upper Series, aside from a few samples that contain olivine chadacrysts, pyroxene and amphibole are the primary controls on MgO concentration in a sample. The less defined trend in the Upper Series is evidence of multiple controls that may not all operate together, compared to olivine as the main control in the Lower Series. Xenolith samples in this plot define a relatively shallow negatively sloping trend.

The SiO<sub>2</sub> vs K<sub>2</sub>O plot (Figure 4.1g) does not have a strong pattern, except that it exhibits a broad positive slope. The majority of Lower Series samples plot near 0% K<sub>2</sub>O, whereas the Upper Series samples show a positive correlation between increasing SiO<sub>2</sub> and K<sub>2</sub>O. It appears that the xenolith and country rock samples, which contain abundant biotite, and some which contain significant amounts of orthoclase (e.g. RIC-61, 38A), pull the overall maximum value of K<sub>2</sub>O plotted up, resulting in a relative compression of the actual RCLIS samples. A plot that excludes these samples and country rock samples is more informative. A small group of samples from the Lower Series plot much higher than the average Lower Series, which average < 0.30% K<sub>2</sub>O. These samples comprise RIC-68A, 63, 46, 24 and 18, and do not exhibit any spatial or mineralogical correlation and, therefore may not reflect a particular trend or process. In addition, the Lower Series also has three outliers, RIC-67, 56 and 49. RIC-67 and 49 are quite close to each other and although RIC-56 is not nearby, all samples are leucogabbros. However, there does not appear to be any correlation in K<sub>2</sub>O between these leucogabbro samples and other leucogabbro samples. It is interesting to note that the only mafic dike in the sample suite plots very enriched in K<sub>2</sub>O, which might reflect the intense alteration of this sample, assuming there was a net gain in K<sub>2</sub>O.

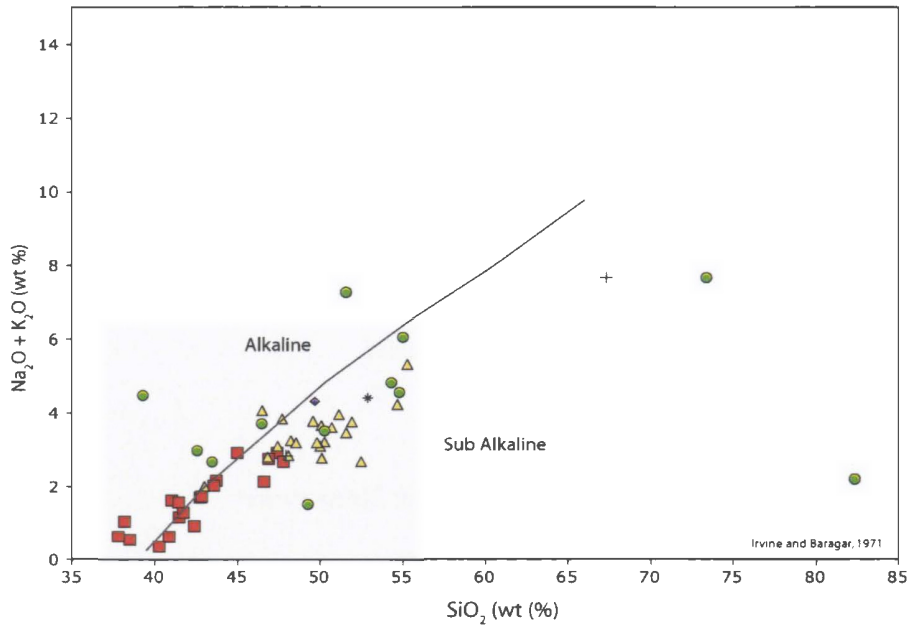
The SiO<sub>2</sub> vs P<sub>2</sub>O<sub>5</sub> plot (Figure 4.1h) does not exhibit any particularly strong trends. The only notable pattern is that nearly all Lower Series samples contain less P<sub>2</sub>O<sub>5</sub> than the Upper Series. There is little variation in P<sub>2</sub>O<sub>5</sub> with changing concentration of SiO<sub>2</sub>.

Although not specifically addressed, in all of these diagrams the mafic dike that is located in the southeast portion of the Lower Series plots within the Upper Series field. In fact, it often shows a more evolved geochemical signature than Upper Series samples.

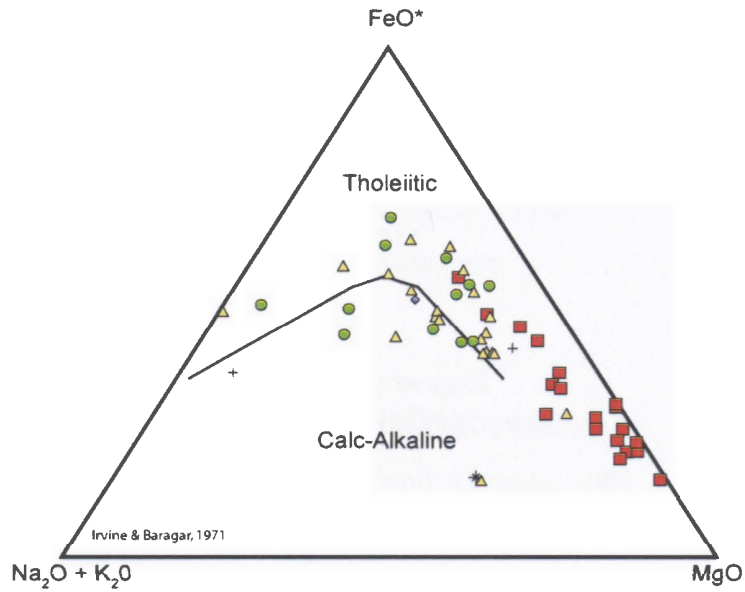
### 4.3 General compositional nomenclature

Total alkali ( $\text{Na}_2\text{O}+\text{K}_2\text{O}$ ) silica diagrams (TAS) indicate that majority of samples fall near the line that divides alkaline from sub-alkaline rocks (Figure 4.2a). This particular diagram does not adequately differentiate the samples. However, in all TAS diagrams the Lower and Upper Series samples separate quite well along a line of increasing  $\text{Na}_2\text{O}+\text{K}_2\text{O}$  and  $\text{SiO}_2$  in a smooth, relatively continuous pattern, suggesting that they might be related through fractional crystallization or some other crystallization process.

AFM diagrams plot calculated FeO vs  $\text{Na}_2\text{O}+\text{K}_2\text{O}$  vs MgO and are useful for determining the relative tholeiitic nature of volcanic rocks compared to their calc-alkalinity. Figure 4.2b distinguishes between the Lower and Upper Series samples, which clearly separate out along a line that begins near the MgO corner, with the most mafic samples in the Lower Series. There is a small group of samples that is distinctly more magnesian than others are; these more Mg-rich samples are the same group that consistently separated out on the Harker diagrams in figure 4.1. The trend of the samples evolves towards the FeO corner of the diagram, indicating that samples gradually become more FeO rich at the expense of MgO. This is likely the result of a gradual loss of Mg-rich olivine, which results in a relative enrichment of FeO in the crystallizing magma. Most Upper Series samples cluster just below the FeO apex, where the tholeiite - calc-alkaline trend line begins to slope towards the  $\text{Na}_2\text{O}+\text{K}_2\text{O}$  corner. Several samples from the Upper Series and some xenoliths fall along this negatively sloping line, reflecting an abundance of Na and K-rich phases such as albite, orthoclase and perhaps biotite.



(a)



(b)

Figure 4.2. A. This TAS diagram does not separate the RCLIS samples from alkaline or sub-alkaline very well, but it does show the smooth evolutionary trend of the magma, and differentiates Lower and Upper Series samples. B. Samples in this AFM diagram exhibit a typical fractional crystallization trend with the most mafic ( $\text{MgO}$ -rich) samples in the lower right corner. Upper Series samples are less tightly clustered. Samples are: Lower Series (■); Upper Series (▲); mafic dike (●); xenoliths (●); country rocks (+); Victoria Lake (\*).

## 4.4 Igneous nomenclature

Total alkali silica diagrams can be useful for classifying igneous volcanic (e.g. Irvine and Baragar, 1971; LeMaitre, 1989) and plutonic (Wilson, 1989) rocks, although the Wilson (1989) diagram is a simple modification of the Cox (1979) Figure 2.2. These diagrams require that samples are not altered, a criterion that is met by most RCLIS samples.

Figure 4.3a, after LeMaitre (1989), indicates which volcanic rock names should be applied to the samples. Under this nomenclature, most Lower Series samples are picro-basalts, or even more magnesium-rich, whereas the Upper Series has a basaltic composition. Using the same data set, but applying the plot of Wilson (1989) (Figure 4.3b), which uses plutonic nomenclature, the Lower Series plots outside the gabbro field, along a trend towards lower  $\text{SiO}_2$  and  $\text{Na}_2\text{O}+\text{K}_2\text{O}$ . There are two distinct country rock samples; one is a volcanic rock, which on the volcanic classification diagram plots as a basalt, whereas the other is a felsic plutonic rock that on plutonic diagram (Wilson, 1989) plots along the boundary between an alkali granite and a quartz diorite. Although quite far along the projected trend of the Upper and Lower Series, this rock does lie on approximately the evolutionary trend of the main mass of the RCLIS.

An additional diagram for classifying igneous rocks is a ternary diagram that plots the cations ( $\text{Fe}^{2+} + \text{Ti}^{4+}$ ) vs  $\text{Al}^{3+}$  vs  $\text{Mg}^{2+}$ . This diagram, (so-called Jensen diagram after Jensen and Pyke (1982) (Figure 4.3c), is particularly useful for the RCLIS. In this study, it is modified using plutonic names in a manner similar to Wilson (1989). Similar to previous diagrams, there are two distinct populations in the Lower Series. A group of six samples (RIC-01, -02, -21, -65, -69A and -69) falls in the dunite/peridotite field. These six samples are the same as in previous diagrams. The majority of the remaining Lower Series samples plot between the olivine gabbro and the high-Fe and Mg gabbro fields. Nearly all Upper Series samples plot in the “high-Fe gabbro” field, reflecting their trend towards relatively higher Fe ( $\pm\text{Ti}$ ) contents. The granitoid country rock, RIC-61 falls in the granodiorite field, which is consistent with the TAS diagram of Wilson (1989).

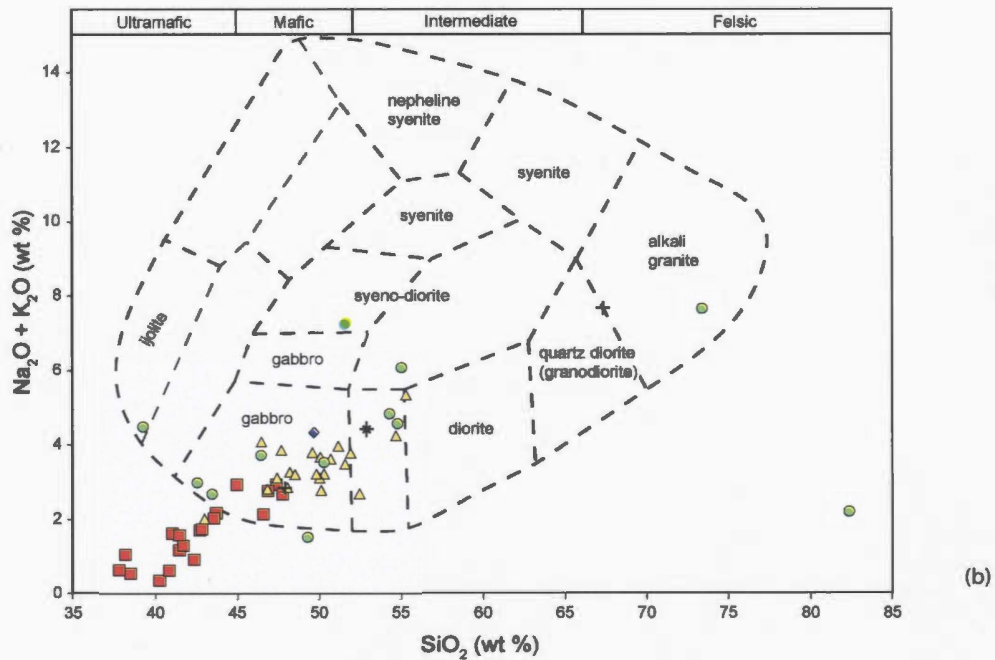
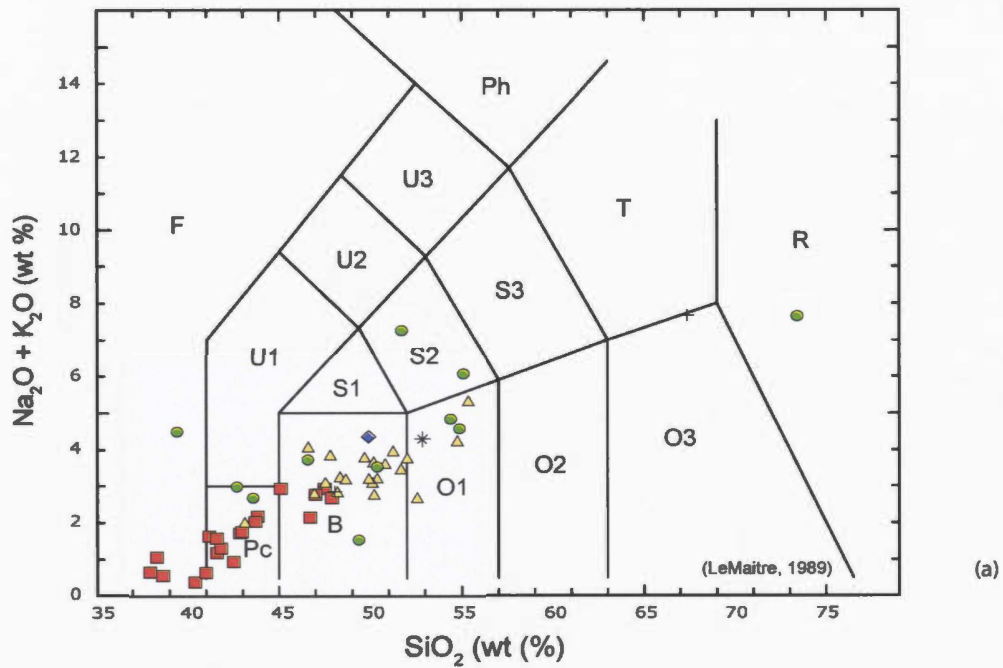


Figure 4.3. Total alkali silica (TAS) diagrams of RCLIS whole rock data. (a) This diagram indicates that much of the Lower Series has a microbasalt composition, while much of the Upper Series is basaltic. (b) This diagram uses plutonic names, indicating the Lower Series is more mafic than gabbros, while the Upper Series has a gabbroic composition (modified from Wilson, 1998). Samples are: Lower Series (■); Upper Series (△); mafic dike (◆); xenoliths (●); country rocks (+); Victoria Lake (\*).

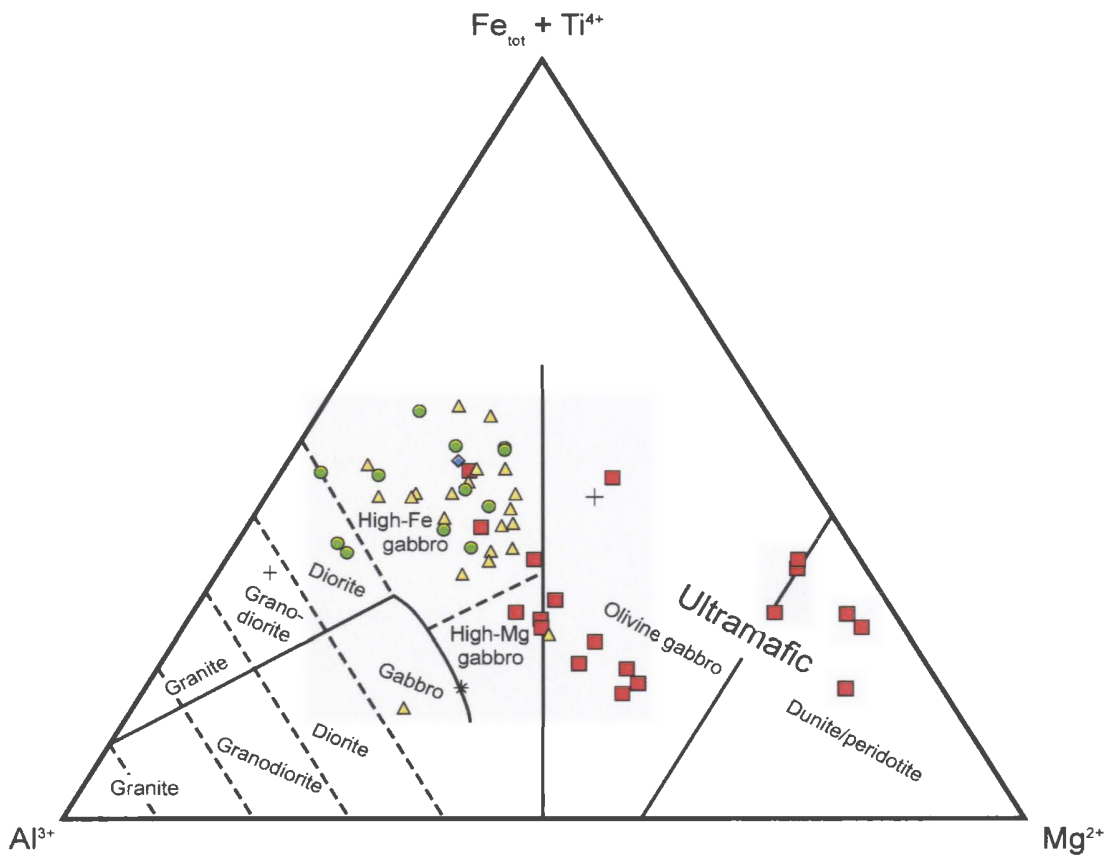


Figure 4.3 (c) This Jensen plot illustrates the ultramafic nature of the Lower Series and emphasises the separation between it and the Upper Series, which has an Fe-(Ti) rich composition. Samples are: Lower Series (■); Upper Series (△); mafic dike (◆) xenoliths (●); country rocks (+); Victoria Lake (\*). An explanation of the data is given in the text. Modified from Jensen and Pyke, (1986).

## 4.5 Tectono-magmatic diagrams

Immobile elements are useful in the study of volcanic and plutonic rocks because they are generally immune to metamorphism and alteration. There are several reasons, however, that these types of diagrams should be used with caution. In particular, because immobile elements behave incompatibly (to a variable degree depending on the composition of the magma) and are partitioned into particular phases preferentially, their use for cumulate rocks is generally avoided, because they do not represent the true bulk composition of a particular magma. However, because the RCLIS is a layered intrusion and exhibits cumulate layering in the Lower Series, it is difficult to avoid. Therefore, some of these diagrams might not be completely representative, and there are in fact several problems, which are discussed below.

To determine the tectono-magmatic setting, two diagrams were created. First, a ternary diagram of  $(\text{Ti}/100) - \text{Zr} - (\text{Y} \times 3)$  (Figure 4.4a), is used to sub classify rocks with a basaltic composition. In this diagram, most of the Upper Series and approximately half of the Lower Series samples plot in the “D” field, which corresponds to within-plate basalts. The remaining Lower Series that do not fall in field D tend to plot towards the Ti/100 corner, indicating that these samples are relatively Ti enriched, which is consistent with petrographical results, which demonstrate abundant ilmenite in some of these samples.

A diagram of Zr vs Zr/Y (Pearce and Norry, 1979) (Figure 4.4b) was also used to classify basaltic rocks. This diagram indicates that most Upper Series samples and slightly less than half of the Lower Series samples fall within the within-plate basalt field. The consistency of these two diagrams suggests that the magmas that formed the RCLIS were generated in a within-plate tectonic environment. The samples that plot in the volcanic-arc basalt fields may have assimilated volcanic-arc basalt country rock, such as the Victoria Lake Group.

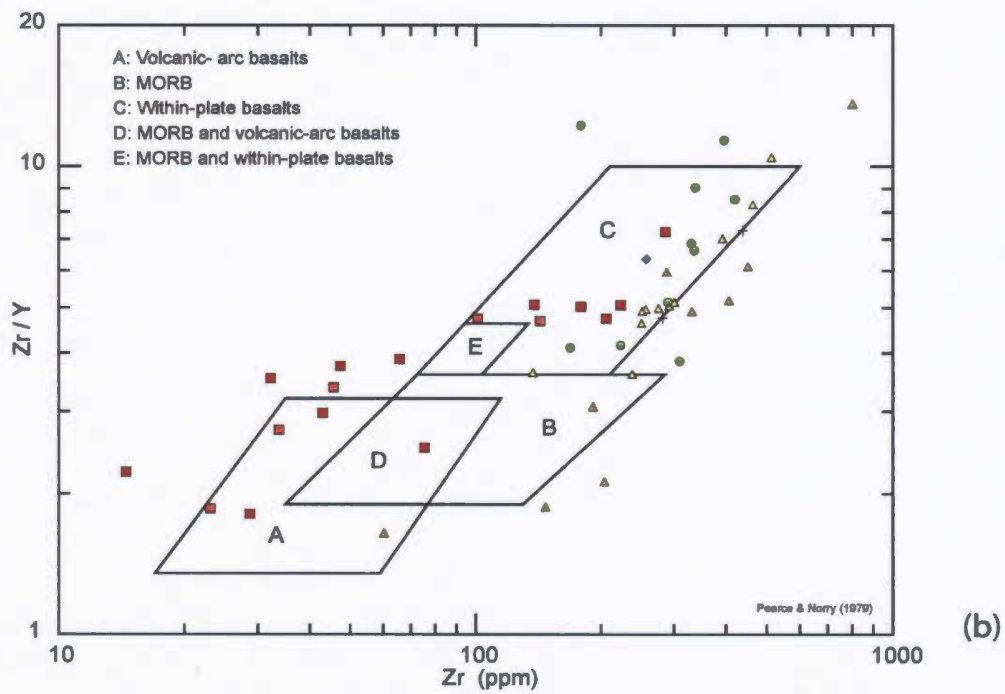
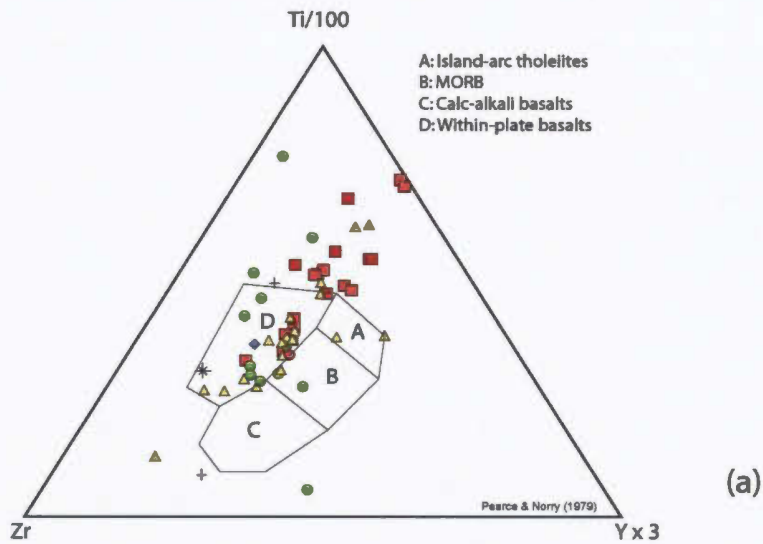


Figure 4.4. Tectono-magmatic environment diagrams from RCLIS whole rock data. These diagrams indicate the tectonic environment the RCLIS magmas were emplaced in. Both diagrams generally support a within-plate environment. Lower Series (■); Upper Series (▲); mafic dike (◆) xenoliths (●); country rocks (+); Victoria Lake (\*).

Many other plots can be used to discriminate between different tectonic environments of basalts, but a shortfall of the data for the RCLIS is that for many of the samples, the abundance of the immobile elements are very low or non-existent, because these elements are commonly enriched in more evolved rock types. Thus, the number of plots of this type that can be used without too much error is minimal. In addition, many of these plots are designed for basaltic rocks (or gabbro), but much of the Lower Series has too little SiO<sub>2</sub> to plot properly. However, to a first approximation, the RCLIS formed in a within-plate tectonic environment.

#### **4.6 Sulfide calculations**

The sulfur concentrations in the RCLIS are relatively low, but it is useful to re-calculate sulfur content as 100% sulfide to investigate the metallogenic potential. A major error in these calculations is assuming that all Ni analysed is present as Ni sulfide. As demonstrated by the microprobe data, RLICS olivine contains up to 2400 ppm Ni and samples may be enriched in Ni but not necessarily S. This section presents calculated modal sulfide abundances for pyrrhotite, pentlandite and chalcopyrite. To reduce the major uncertainty of the host for nickel, microprobe data for Ni in olivine are also presented.

The method for calculating modal Ni sulfide abundances is relatively simple, but several assumptions must be made. First, it is assumed that all sulfur occurs in sulfide minerals. This assumption is supported by petrography, which did not identify any sulfates such as gypsum or barite. Next, sulfide mineralogy is assumed to comprise only pyrrhotite, pentlandite and chalcopyrite to simplify the calculations. Petrography also supports this assumption, although in the Upper Series there is less pyrrhotite and more pyrite, but this assumption does not affect the economically significant sulfides. It is assumed that all Cu resides in chalcopyrite – an assumption validated by the data presented below.

Modal Ni-Cu sulfide mineralogy calculations are shown in detail in Appendix 3, but are outlined here. First, the weight percent of each element in a sulfide mineral is calculated by dividing the molecular weight of the element by the atomic mass of the mineral. Second, the mineral chalcopyrite is “made” by dividing the total weight percent of Cu in the whole rock assay by the weight percent Cu in chalcopyrite. Next, pentlandite is made, but first an olivine correction factor must be calculated. To do this, microprobe data are utilized to estimate the Ni content in olivine in each olivine-bearing sample. For Lower Series samples an average of 21 analyses per sample were used to calculate the average Ni in olivine concentration. As demonstrated below, core to rim zoning was not strong, so it is valid to average analysis from all points within an olivine crystal. To calculate the true weight percent Ni in sulfide, the product of the average weight percent Ni in olivine per sample multiplied by the percent olivine in each sample was subtracted from the weight percent Ni from the whole rock assay. Where a sample did not contain olivine, all Ni was attributed to pentlandite, and where a sample was known to contain olivine but was not analysed by microprobe, which only occurs in the Lower Series, the average Ni in olivine was used for the calculations. The same process to “make” chalcopyrite is used to make pentlandite, but the Ni used in the calculation is the corrected percentage. To make pyrrhotite the process is somewhat more complicated. The weight percent sulfur from the whole rock assay is subtracted from the weight percent of sulfur in chalcopyrite multiplied by the calculated percent chalcopyrite in the sample and the weight percent sulfur in pentlandite multiplied by the percent pentlandite calculated, which is all then divided by the calculated weight percent of sulfur in pyrrhotite. This process is illustrated in the flow chart below (Figure 4.5).

The result of these calculations (Table 4.1) indicates that the two highest percentages of sulfide mineralization are in two different xenolith samples (RIC-53 and 78B) rather than Lower Series samples. However, the calculated maximum pentlandite and chalcopyrite data indicate that all samples with elevated base metal concentrations are located in the Lower Series, although the sample with the maximum percentage of pentlandite does not

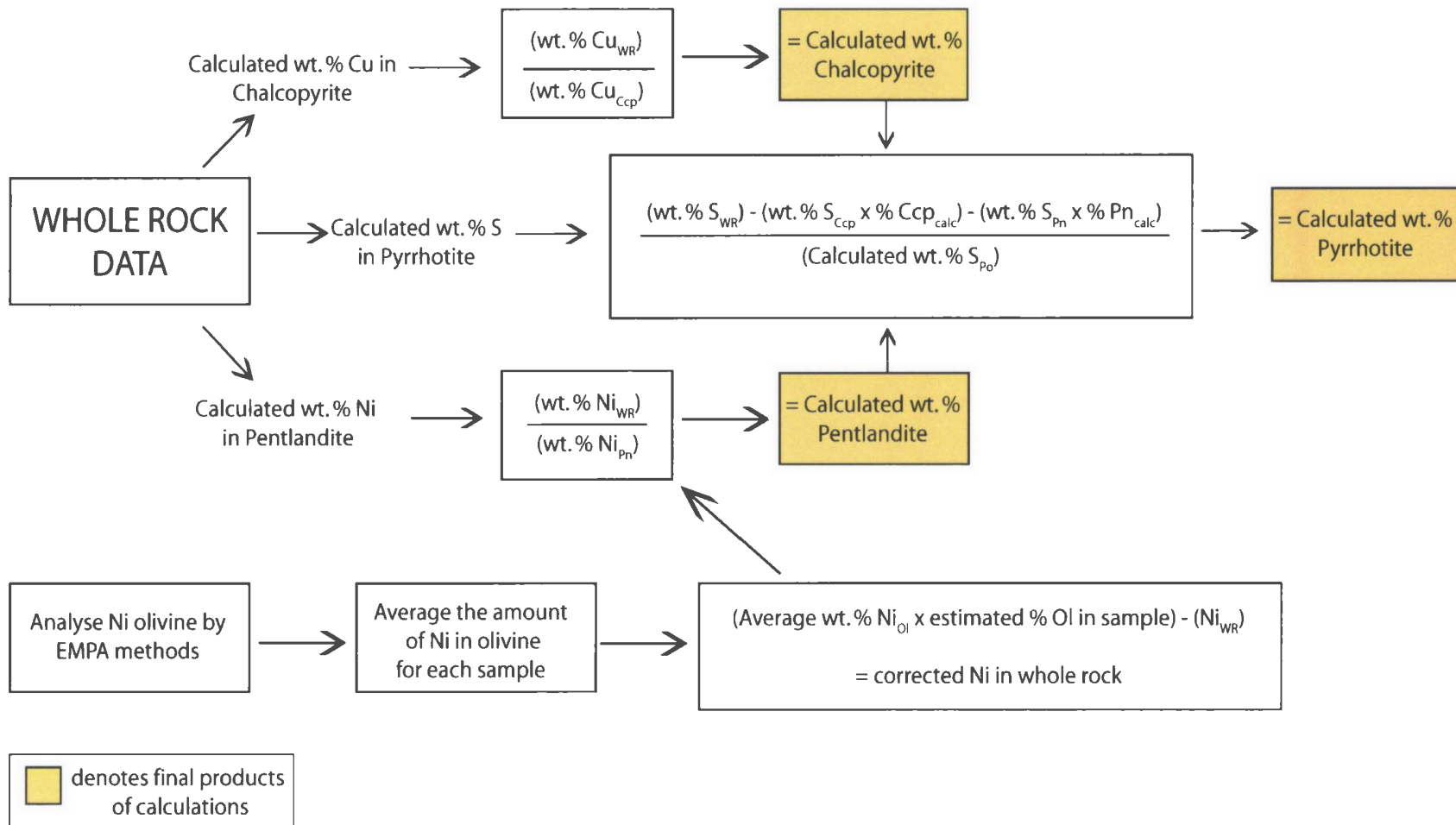


Figure 4.5. This flowchart demonstrates the workflow for the calculation of normative sulfides. During these calculations, chalcopyrite must be “produced” first, then pentlandite and finally pyrrhotite because pyrrhotite requires information from Ccp and Pn before it can be calculated. A detailed description of calculations is provided in the text.

correspond with the maximum chalcopyrite samples. The results of the calculated modal abundances are generally consistent with petrographical results. These calculations highlight the low sulfide abundances noted in the field and during petrographical study of the samples.

<b>(a)</b>				
<b>Sample</b>	<b>% ccp</b>	<b>% Pn</b>	<b>% Po</b>	<b>% Sulfide</b>
RIC-53	0.0368	0.0350	3.2502	3.3220
RIC-78B	0.0223	0.0138	2.9093	2.9454
RIC-21	0.1328	0.1087	2.2943	2.5358
RIC-06	0.0921	0.2094	1.6808	1.9823
RIC-25	0.0336	0.0142	1.6965	1.7442
<b>(b)</b>				
<b>Sample</b>	<b>% ccp</b>	<b>% Pn</b>	<b>% Po</b>	<b>% Sulfide</b>
RIC-65	0.0993	0.3847	0.9261	1.4101
RIC-68A	0.0710	0.3460	0.1736	0.5906
RIC-69	0.0379	0.3263	0.3421	0.7063
RIC-06	0.0921	0.2094	1.6808	1.9823
RIC-27	0.0175	0.1578	-0.0978	0.0776
<b>(c)</b>				
<b>Sample</b>	<b>% ccp</b>	<b>% Pn</b>	<b>% Po</b>	<b>% Sulfide</b>
RIC-21	0.1328	0.1087	2.2943	2.5358
RIC-01	0.1009	0.0357	1.2693	1.4059
RIC-65	0.0993	0.3847	0.9261	1.4101
RIC-02	0.0928	0.1495	1.1427	1.3850
RIC-06	0.0921	0.2094	1.6808	1.9823
<b>(d)</b>				
<b>Sample</b>	<b>% ccp</b>	<b>% Pn</b>	<b>% Po</b>	<b>% Sulfide</b>
RIC-53	0.0368	0.0350	3.2502	3.3220
RIC-78B	0.0223	0.0138	2.9093	2.9454
RIC-21	0.1328	0.1087	2.2943	2.5358
RIC-25	0.0336	0.0142	1.6965	1.7442
RIC-06	0.0921	0.2094	1.6808	1.9823

**Table 4.1.** This table presents the results of calculated Ni-Cu-Fe sulfide contents. (a) top 5 maximum calculated sulfides. Note the low calculated chalcopyrite and pentlandite abundance in the top two samples, both of which are xenoliths; (b) top 5 calculated pentlandite samples after Ni in olivine corrections; (c) top 5 calculated chalcopyrite samples; (d) top 5 calculated pyrrhotite. This is similar to the top overall sulfide except that RIC-06 has less pyrrhotite and more pentlandite than RIC-25.

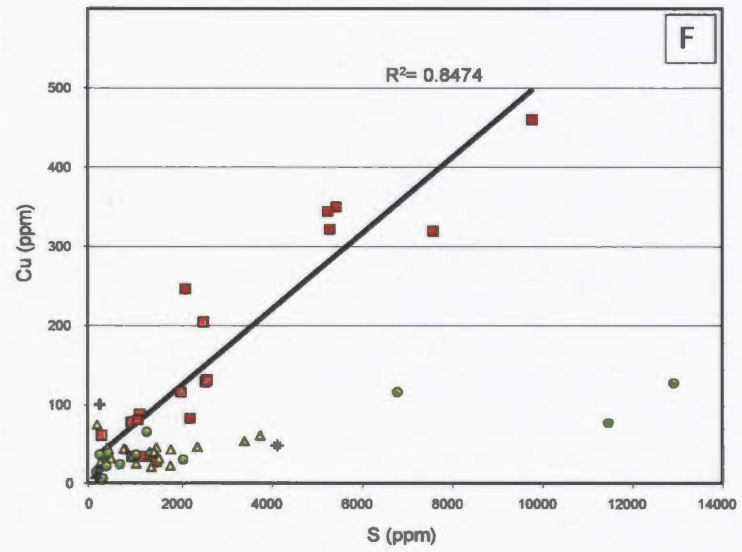
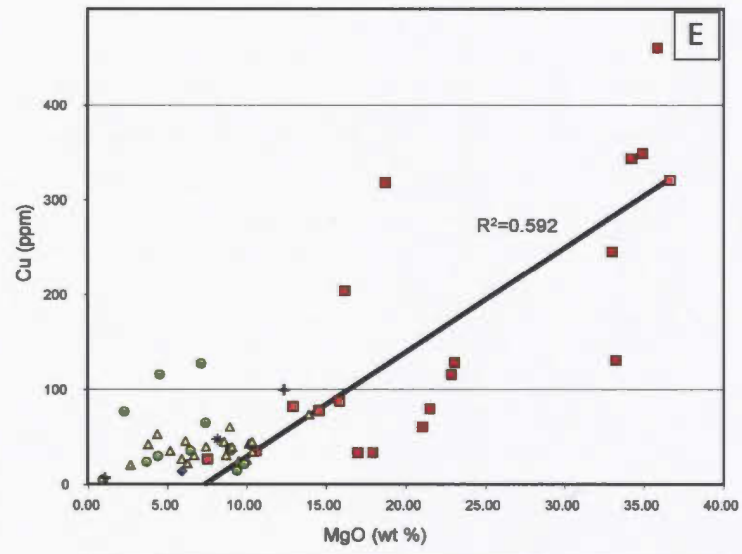
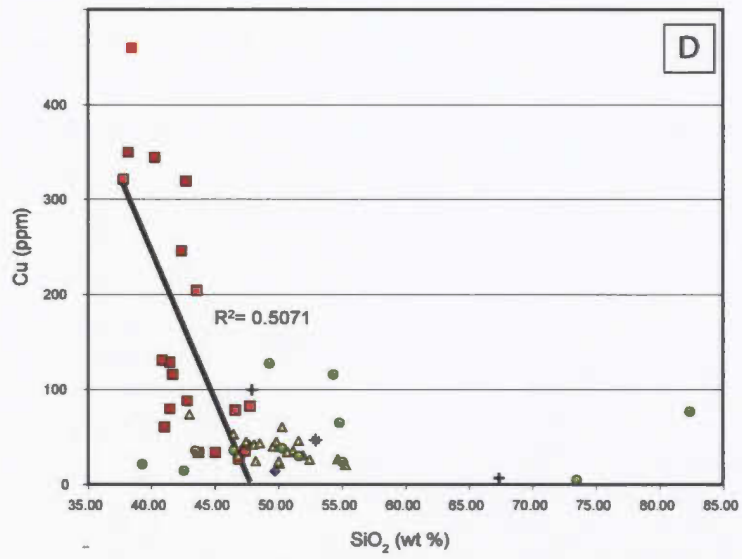
#### 4.7 Base metal and sulfide calculations

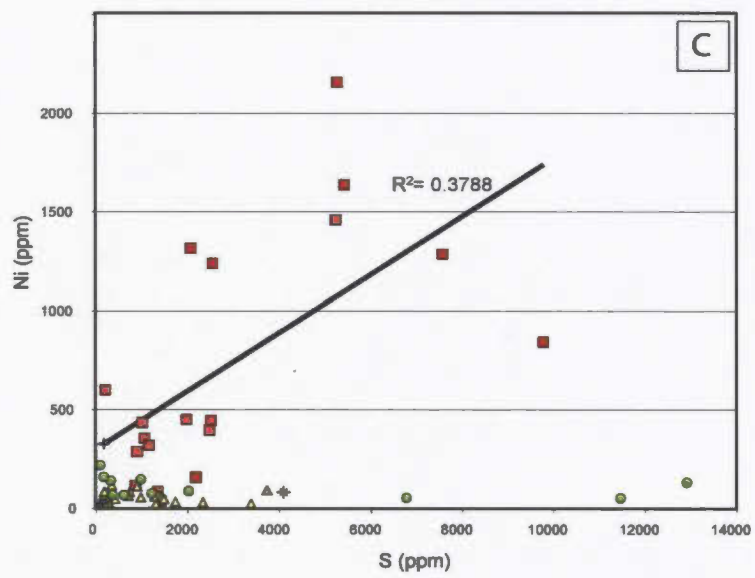
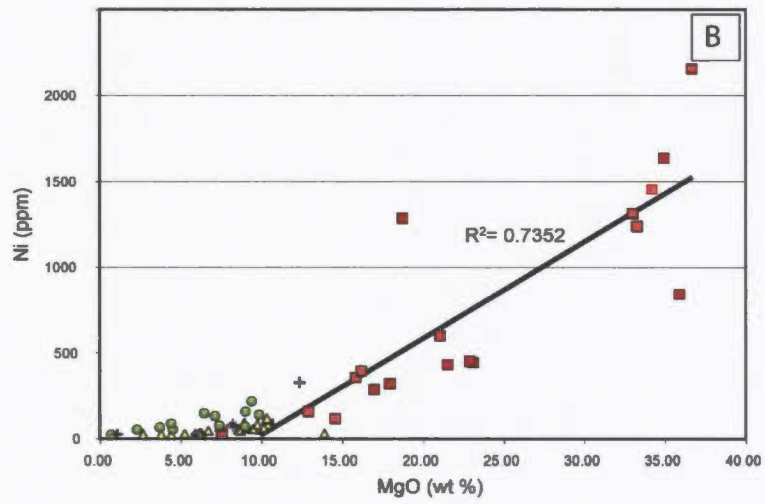
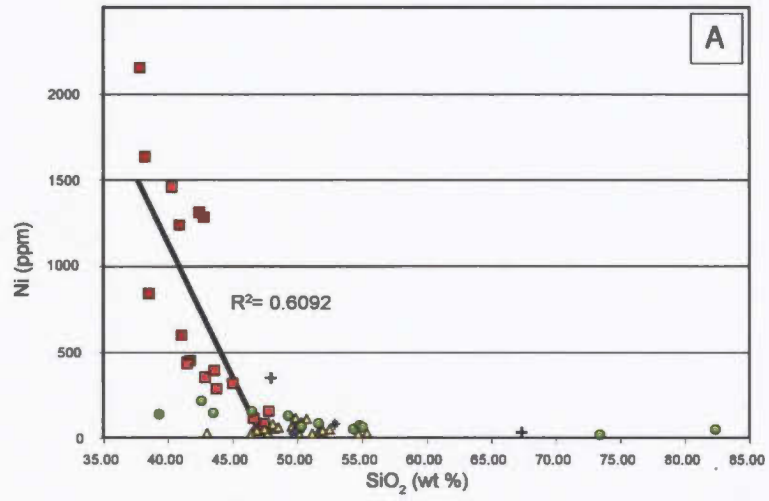
A key objective of this study was to determine the potential for the RCLIS lithologies to host sulfide mineralization and to determine the geochemical behaviours of the

economically significant metals (Ni, Cu, Pt, Pd). A first step in this process is to create diagrams that demonstrate the relationships between these metals and several oxides and sulfur, which represent to the two major chemical reservoirs for the metals (silicates and sulfides). First, by plotting Cu, Ni and Pt+Pd vs SiO<sub>2</sub> it is possible to determine if the metals have a positive correlation with SiO<sub>2</sub>, which would suggest that the metals reside in silicate phases rather than sulfides. Secondly, by plotting the metals versus MgO, the correlation between the metals and a mafic host rock can be established, because MgO can be used as a proxy for relative olivine content. Finally, plotting these metals versus sulfur can establish if there is a positive correlation between a sulfide phase and the metals, which is the ideal result.

The diagram of SiO<sub>2</sub> versus Ni (Figure 4.6a) indicates that Ni concentrations are quite low in all rocks except the Lower Series. In this diagram, Ni has a negative sloping trend with SiO<sub>2</sub> with a relatively strong correlation ( $R^2 = 0.609$ ). These data cannot be interpreted without first examining other plots that illustrate how Ni behaves with MgO and S. MgO vs Ni (Figure 4.6b) has a positive slope with a strong correlation ( $R^2 = 0.735$ ). In the Lower Series, the main control on MgO concentration is olivine. Nickel in olivine has a relatively high partition coefficient (e.g. ~6 to 30), (e.g. Arth, 1976; Naldrett, 2004) and although not as great as Ni in sulfide ( $D = \sim 100-500$ ) (Naldrett, 2004), it is significantly greater than other silicates. This positive correlation between MgO and Ni suggests that much of the Ni resides in olivine rather than in a sulfide phase. This is supported by the S vs Ni diagram (Figure 4.6c), which shows a more dispersed pattern where Ni does not show as strong a correlation with S; the  $R^2$  value is only 0.380, which is nearly half the correlation between MgO and Ni. These diagrams suggest therefore that most Ni resides in olivine rather than sulfides.

To determine how copper behaves in the magma during crystallization, the same three plots are used. SiO<sub>2</sub> vs Cu (Figure 4.6d) defines a negative slope with an  $R^2$  value of 0.509, which is somewhat less than the correlation between Ni and SiO<sub>2</sub>. MgO vs Cu





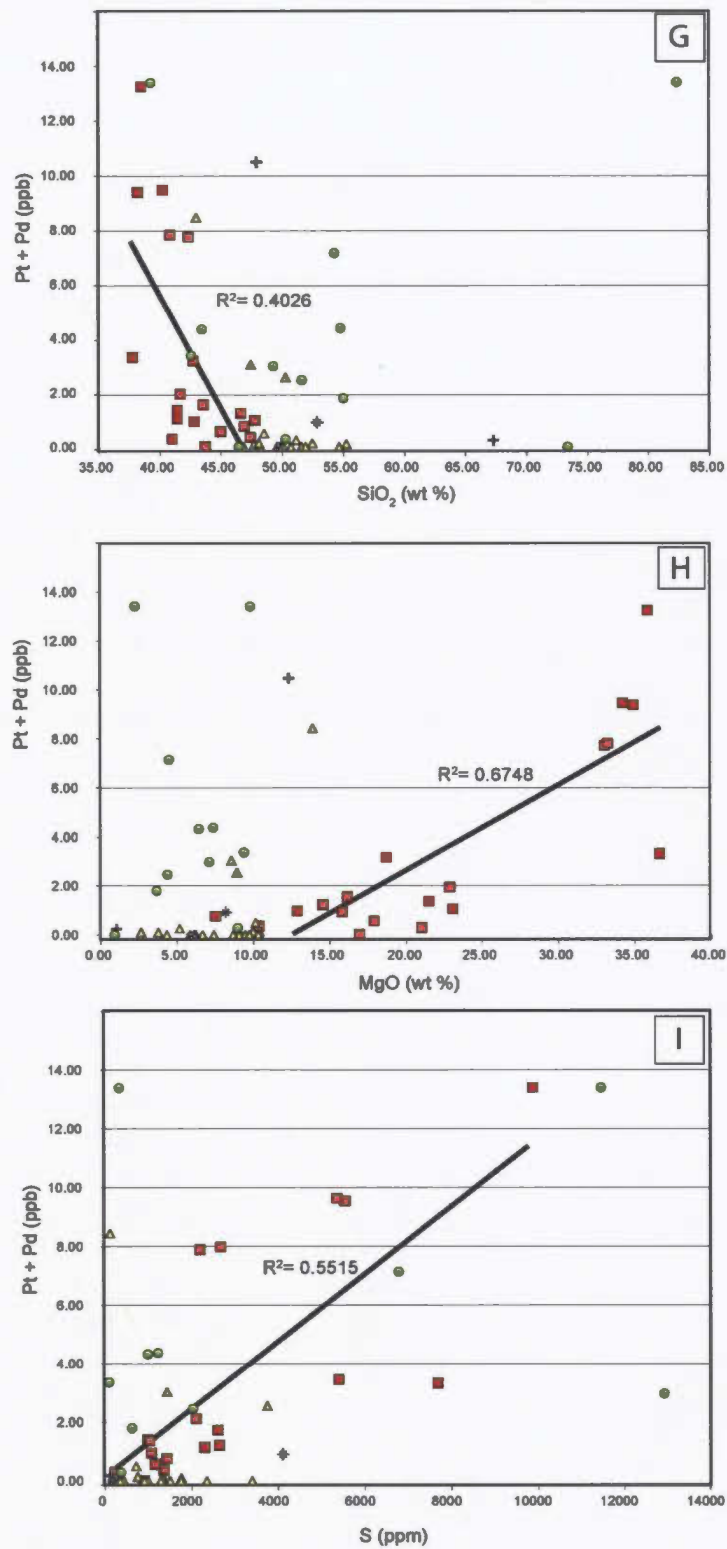


Figure 4.6. Pt-Pd whole rock geochemical data from the RCLIS. Pt+Pd are plotted against SiO<sub>2</sub> (a-c), MgO (d-f) and S (g-i). R<sup>2</sup> values were calculated in Microsoft Excel. Refer to the text for a complete explanation of the diagrams.

(Figure 4.6e) has a positive trend and an  $R^2$  value of 0.592 – although positive, not much greater than the correlation between  $\text{SiO}_2$ . Compared to Ni, Cu does not correlate as well with MgO. S vs Cu (Figure 4.6f) illustrates a strong positive slope with an  $R^2$  value of 0.874 – the greatest correlation factor amongst the metals plotted in this comparison. This indicates that Cu is present in sulfide phases rather than silicate phases, including olivine. Cu has a partition coefficient of  $D= 700$  compared to  $\sim 150$  for Ni into a sulfide melt over a silicate melt, and results are consistent with this.

The RCLIS exhibits very low concentrations of platinum and palladium, even in the most mafic portions of the intrusion, where they should have the greatest abundances (i.e., the Lower Series). It is interesting to note, however that several xenoliths have relatively high concentrations of Pt and Pd – a sulfide-rich quartz schist and a biotite amphibole metagabbro (RIC-78B and RIC-23A respectively) both exceed the maximum concentration of any sample from the Lower Series for reasons unknown. Pt+Pd vs  $\text{SiO}_2$  (Figure 4.6g) has a negative slope with a correlation coefficient of  $R^2= 0.403$ . Pt+Pd vs MgO (Figure 4.6h) has a positive slope with a relatively strong correlation of  $R^2= 0.675$ . This is greater than Cu, but less than Ni. Finally, S vs Pt+Pd (Figure 4.6i) defines a positive slope with a correlation of  $R^2= 0.552$ , surprisingly, which is lower than the correlation with MgO. MgO vs S does not show a strong correlation ( $R^2= 0.353$ ), thus one cannot assume that with increasing MgO, there are increasing sulfide contents. In addition, this diagram and most others show two distinct populations in the Lower Series, which were described above.

These data indicate that Ni correlates most strongly with MgO, which is a proxy for olivine. Cu correlates best with sulfide, and Pt-Pd correlates most strongly with MgO. In the case of Pt+Pd, it is possible that the very low concentration levels introduce errors and uncertainty into the data, because one would expect that Pt+Pd would have the strongest correlation with sulfur. Plots of Cu versus Pt+Pd (not shown) have a relatively low  $R^2$  (0.315) value, but are higher than Ni versus Pt+Pd (not shown) ( $R^2= 0.1801$ ),

which suggests that Pt and Pd favour those samples that have relatively higher Cu than Ni.

#### **4.8 Summary**

The RCLIS major oxide geochemistry defines several strong, well-defined trends that are characteristic of fractional crystallization. In particular, the Lower Series shows narrowly constrained trends from ultramafic, MgO- and Fe<sub>2</sub>O<sub>3</sub>-rich compositions to mafic, moderate MgO compositions. This is explained through the crystallization of Mg-rich olivine in the Lower Series, which became progressively more Fe-rich towards the Upper Series. The Upper Series has a more evolved composition than the Lower Series and generally plots in a continuous trend from the Lower Series. It does not show the same narrowly constrained pattern, however, but plots as a broad cluster of samples, indicating less internal evolution or differentiation. The major oxide trends are supported by petrography, which indicates that most patterns in the oxide diagrams are related to changes in the modal abundance of major silicate phases.

The RCLIS has a composition intermediate to alkaline and sub-alkaline rocks and on an AFM diagram shows a well-defined evolutionary trend from Mg-rich rocks in the Lower Series to Fe ( $\pm$  Ti)-rich rocks in the Upper Series. Overall, the rocks have a tholeiitic composition as defined on this diagram.

Total alkali silica diagrams were used to elucidate the proper nomenclature of the RCLIS rocks. First, on a diagram designed for volcanic rocks, the Lower Series plots in the picobasalt field and outside the formally defined fields towards the lowest Na<sub>2</sub>O+K<sub>2</sub>O and SiO<sub>2</sub> values. Plutonic names for the RCLIS are peridotite to dunite for the most ultramafic samples and olivine gabbro to Mg-rich gabbro for the Lower Series, whereas the Upper Series has an Fe-rich gabbroic composition.

Sulfide calculations indicate that the most sulfide-rich samples are several metasedimentary xenoliths, followed by Lower Series samples. Samples containing the most calculated pentlandite and chalcopyrite are from basal to mid-Lower Series, while the Upper Series is relatively Ni barren. The total calculated sulfide contents for the Lower Series are unexpectedly low for rocks with an ultramafic composition like these. Olivine (MgO) has the greatest control over the relative content of Ni in Lower Series samples, while sulfur abundance controls the relative concentration of Cu, because Cu does not commonly reside in silicate host phases and MgO appears to control platinum and palladium abundances more than SiO<sub>2</sub> and S.

Many diagrams defined a small sub-population of samples in the Lower Series. Half of these samples are from the southwestern corner of the intrusion (RIC-01, 02, 21) whereas the other half are from the southeastern corner (RIC-65, 68A, 69). The similar composition despite different locations and appearance suggests that prior to recrystallization and hydration of the southeastern samples both might have been quite similar, possibly defining a basal horizon of the intrusion.

## Chapter 5: Red Cross Lake Intrusive Suite Mineral Geochemistry

### 5.0 Introduction

Twenty-five samples from the RCLIS were analysed by electron microprobe. Major phases investigated were plagioclase, olivine, pyroxene, amphibole, several sulfides and several oxides. The main objectives of these analyses were to determine the composition of specific phases and to determine if there was zoning present, and if so, on what scale (i.e. mineral, sample, unit, series). Probe analyses were also used to detect trace elements that might be in solid solution with certain phases such as pyrrhotite and olivine.

Data are presented on a mineral-by-mineral basis in the framework of previously established rock units (i.e. Upper and Lower Series). All electron microprobe data are listed in Appendix 4, including probe detection levels, accuracy and precision calculations. Only data with >97.5% and <102.5% weight percent oxide are presented. Data outside this range may be observed for a number of reasons, the main ones being analysis of uneven surfaces, heterogeneous point analysis such as minute inclusions that include or do not include elements in the analysis file, analysis too close to the edge of another phase, and hydrous phases. As well, analytical uncertainty related to hardware is also a possible factor for non-100% analysis.

### 5.1 Plagioclase

Nineteen plagioclase-bearing samples were analysed, comprising eight Lower Series samples, nine samples from the Upper Series and two xenolith samples. Plagioclase was analysed for SiO<sub>2</sub>, Al<sub>2</sub>O<sub>3</sub>, CaO, Na<sub>2</sub>O, K<sub>2</sub>O, and FeO; Ba, Rb and Sr were not measured. The purpose for analyzing plagioclase-bearing samples was mainly to characterize their overall composition, and secondly, to determine the degree of zonation within individual crystals, particularly in samples that exhibited optical evidence for zoning. Normally, at

least one core and one rim were measured for any crystal analysed, but in some instances, this was not possible due to crystal morphology, or because back scatter images did not reveal any obvious zonation. When only one analysis was measured for a given sample, it was always in the core of the crystal.

Lower Series plagioclase averages An 69 with a standard deviation of 9.3 for 65 analyses, including all types of analyses (i.e. core, rim and interstitial). Lower Series core and rim analysis indicate measurable compositional differences. Cores average An 73 with a standard deviation of 8.4, whereas rims average 66 with a standard deviation of 8.7 and sample populations of 30 and 25, respectively. The remaining 11 analyses did not fall into core and rim morphologies. Lath shaped crystals were the main crystal morphology analysed in the LS; optically, these crystals do not exhibit obvious internal zonation.

Upper Series samples average An 54 with a standard deviation of 10.5 for all 73 analyses. Upper Series core measurements average An 55 with a standard deviation of 11.2 and rim analyses are An 51, with a standard deviation of 6.4 for 57 and 11 core and rim analyses, respectively. The crystal morphologies measured in the US were more variable than in the LS, which is partly a reflection of the greater variation in overall crystal morphology and partly because previously identified obviously zoned crystals were focused on during probe analysis.

The two xenolith samples are from a deformed belt that contained multiple types of xenoliths. These two samples preserve a texture not noted elsewhere in the field and are dissimilar to country rocks, thus they may be autoliths. The compositions in these samples may represent those of an unexposed portion of the intrusion, or from somewhere lower in the plumbing system of the intrusion. Xenolith samples average An 47 with a standard deviation of 10.6 for a sample size of 28. Cores average An 49 with a standard deviation of 14.1 for 13 analyses. Rims show less variation, averaging An 44

with a standard deviation of 5.9 for 13 analyses. Most crystals analysed in these samples exhibit a granoblastic, recrystallized texture, which is atypical for the intrusion in general.

Figure 5.1 graphically illustrates the compositional differences between rim and core of the Lower and Upper Series and the xenolith samples, and Table 5.1 presents a summary of core and rim data, sorted by series.

<b>Series</b>	<b>Core Avg.</b>	<b>Rim Avg.</b>	<b>Std. Dev.</b>	<b>n</b>
Lower	72.0	-	8.4	30
Upper	54.6	-	11.2	57
Xenoliths	48.7	-	14.4	13
Lower	-	66.1	8.3	25
Upper	-	50.6	6.4	11
Xenoliths	-	44.5	5.9	13

**Table 5.1.** Data for core and rim zonation in An content is presented first by core and then by rim data. The standard deviation corresponds to the type of data listed (i.e. only for core or only for rim).

Figure 5.2 shows the distribution of all RCLIS plagioclase samples in An-Ab-Or compositional space. As indicated above, Lower Series samples average An 69, which is essentially on the boundary that separates bytownite from labradorite. However, the diagram appears to show more samples clustered in the bytownite field and a smaller group that falls in the lower bytownite to upper andesine fields. These latter data are mainly from RIC-18, which has lower An contents than other LS samples, and likely drags the average down to An 69. RIC-18 compositions are typical of US samples, suggesting that based on microprobe data, this sample may belong to the Upper Series. Furthermore, RIC-18 exhibits zoning patterns typical of the US (Figure 5.3). Upper Series analyses are most concentrated in the mid-andesine compositions and gradually taper off into the more Ca-rich labradorite field. There are no obvious outliers amongst these data. Xenolith analyses cluster near the upper boundary between andesine and labradorite, although there are several outliers greater and less than the average composition.

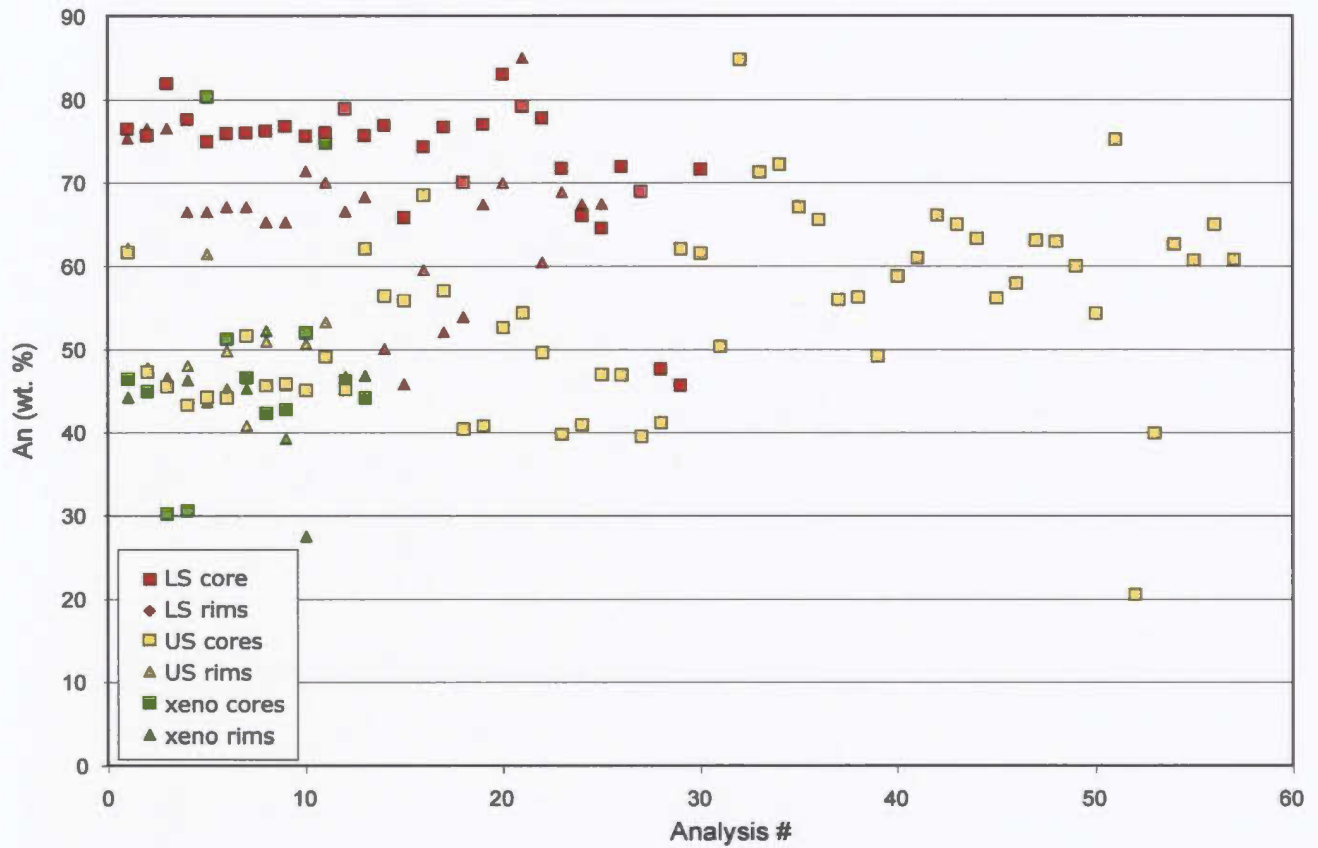


Figure 5.1 Plagioclase cores and rims exhibit distinctive compositions. In general, rims display a relatively more albitic composition. This is most evident in Lower Series samples compared to Upper Series and xenolith analyses. This is a reflection of the wider range of plagioclase morphologies in the Upper Series. Despite the less pronounced core-rim variation in Upper Series plagioclase, these analyses display the widest compositional range overall.

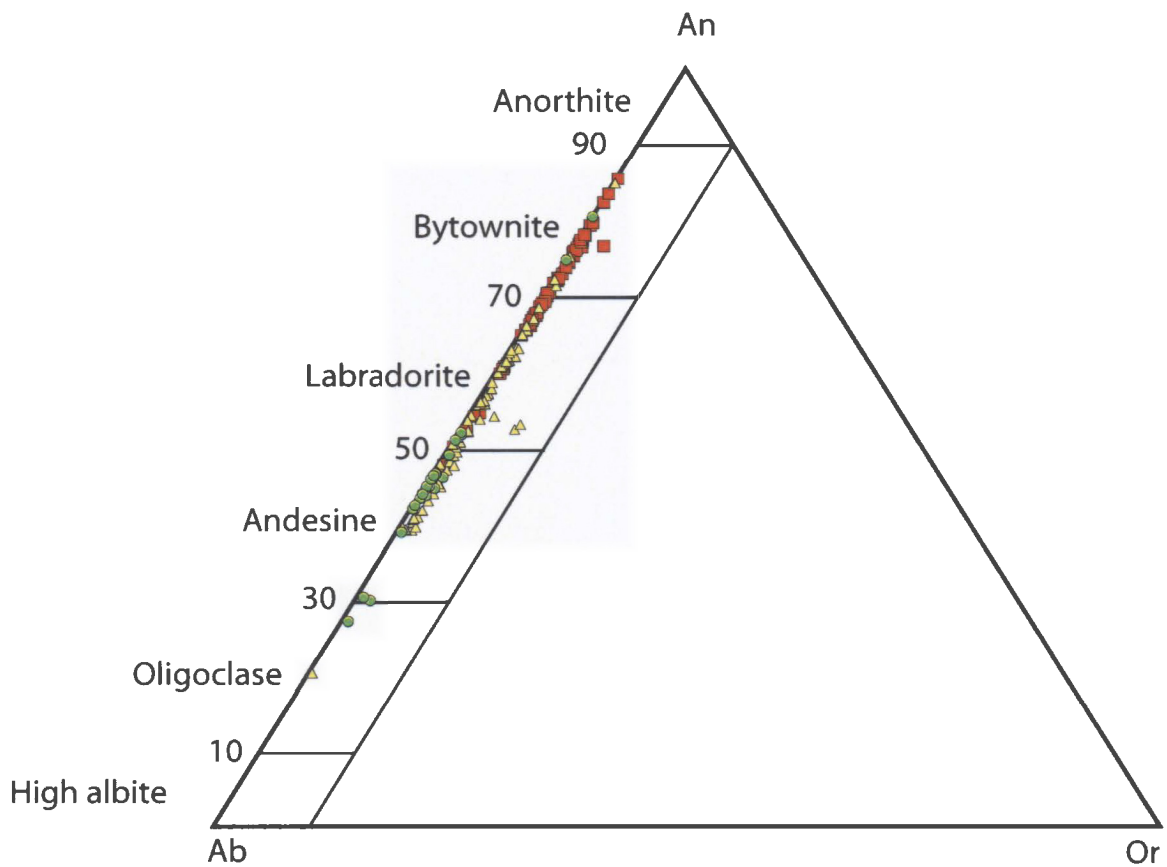
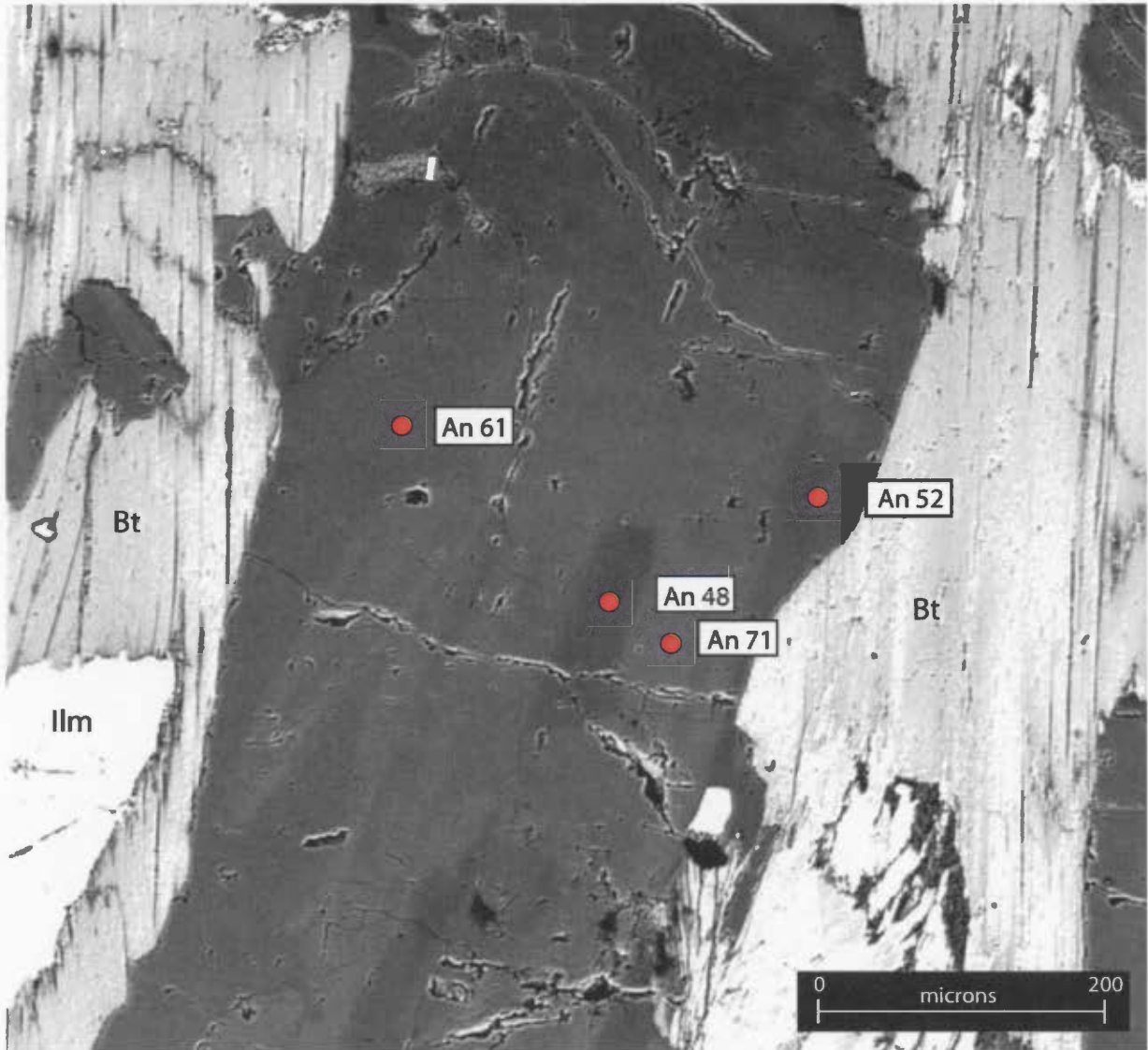


Figure 5.2 An-An-Or diagram of microprobe data for RCLIS samples. Plagioclase from the Lower Series is distinctly more calcic, averaging near the bytownite-labradorite compositional boundary. Upper Series samples are somewhat less calcic, averaging near the andesine-labradorite compositional boundary. Xenolith samples are the least calcic, with an average composition within the andesine field.



**Figure 5.3** Backscatter microprobe image illustrating compositional zoning in plagioclase in RIC-18. This zoning is irregular and exhibits local zones that strongly contrast with surrounding compositions. Biotite on either side of the zoned plagioclase is locally embayed by the more albitic plagioclase, but the reverse texture is also notable.

Lower Series plagioclase zonation is uncommon, and usually only occurs in isolated locations, generally not as rim-core zonation within a crystal, but as late interstitial concentrations of more albitic plagioclase, which is expected in evolving fractionally crystallized rocks. Where reaction rims between olivine and plagioclase occur (Figure 5.4), amphibole and pyroxene are often present as thin rims that separate olivine and plagioclase. However, there was no obvious zonation of plagioclase adjacent to the reaction rim. Upper Series plagioclase is more commonly zoned and zonation is commonly irregular or patchy (Figure 5.5), but also exhibits textures suggestive of corrosion and secondary growth. For example, Figure 5.6 illustrates a core of relatively homogenous plagioclase (An 63-65) and a sharp boundary between darker, more albitic plagioclase (An 46-48). This texture, with sharp embayed boundaries suggests that this plagioclase crystal was corroded (and many similar ones in the US) and had a second phase of growth form the albitic rim.

Overall, the Lower Series plagioclase appears to be distinct from the Upper Series plagioclase, despite the zonation patterns (Figure 5.7).

<b>Series</b>	<b>An (wt. %)</b>	<b>Std. Dev.</b>	<b>n</b>
Lower	69.1	9.3	65
Upper	53.6	10.5	73
Xenoliths	46.6	10.6	28

**Table 5.2** A summary of RCLIS plagioclase electron microprobe data for each series. This table indicates that LS samples, on average, the more An-rich in the RCLIS, followed by US and xenolith analyses.

## 5.2 Olivine

Fifteen olivine-bearing samples were analysed, which comprise ten samples from the Lower Series, three from the Upper Series and two xenoliths. Olivine analyses measured SiO<sub>2</sub>, Cr<sub>2</sub>O<sub>3</sub>, FeO, MnO, MgO and NiO; microprobe software, described above, calculated the weight percent forsterite and fayalite. The goals of the olivine analysis were to determine olivine composition from intrusion scale to sample scale and in

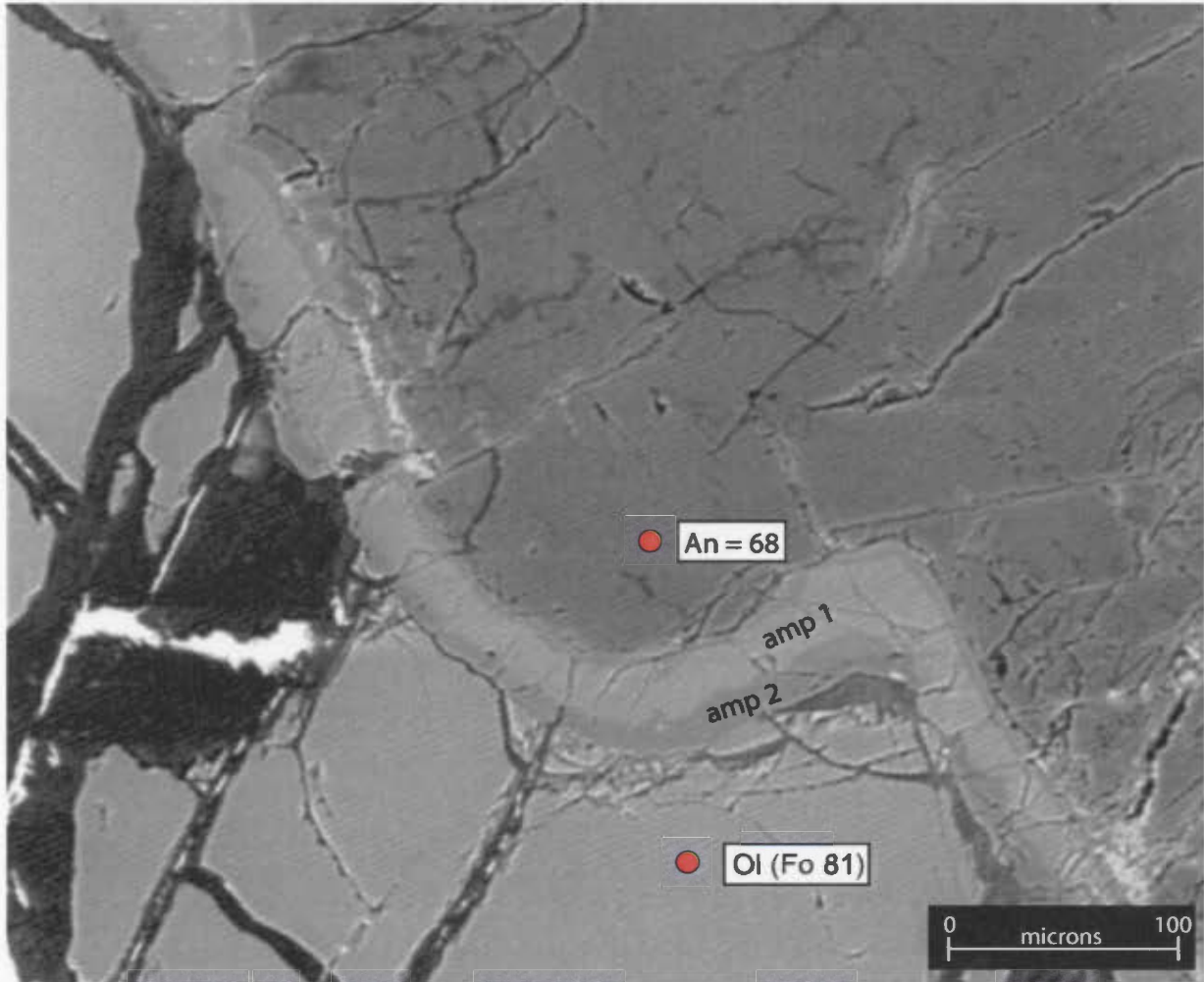


Figure 5.4 At the contact between olivine and plagioclase it is common to observe rims of amphibole and/or pyroxene. In many instances, more than one generation of amphibole is present. When this occurs the amphiboles reflect the composition of the adjacent phase. Amphibole adjacent to Mg-rich olivine is Mg-rich whereas amphibole adjacent to calcic plagioclase is Ca-rich. This example is from RIC-22.

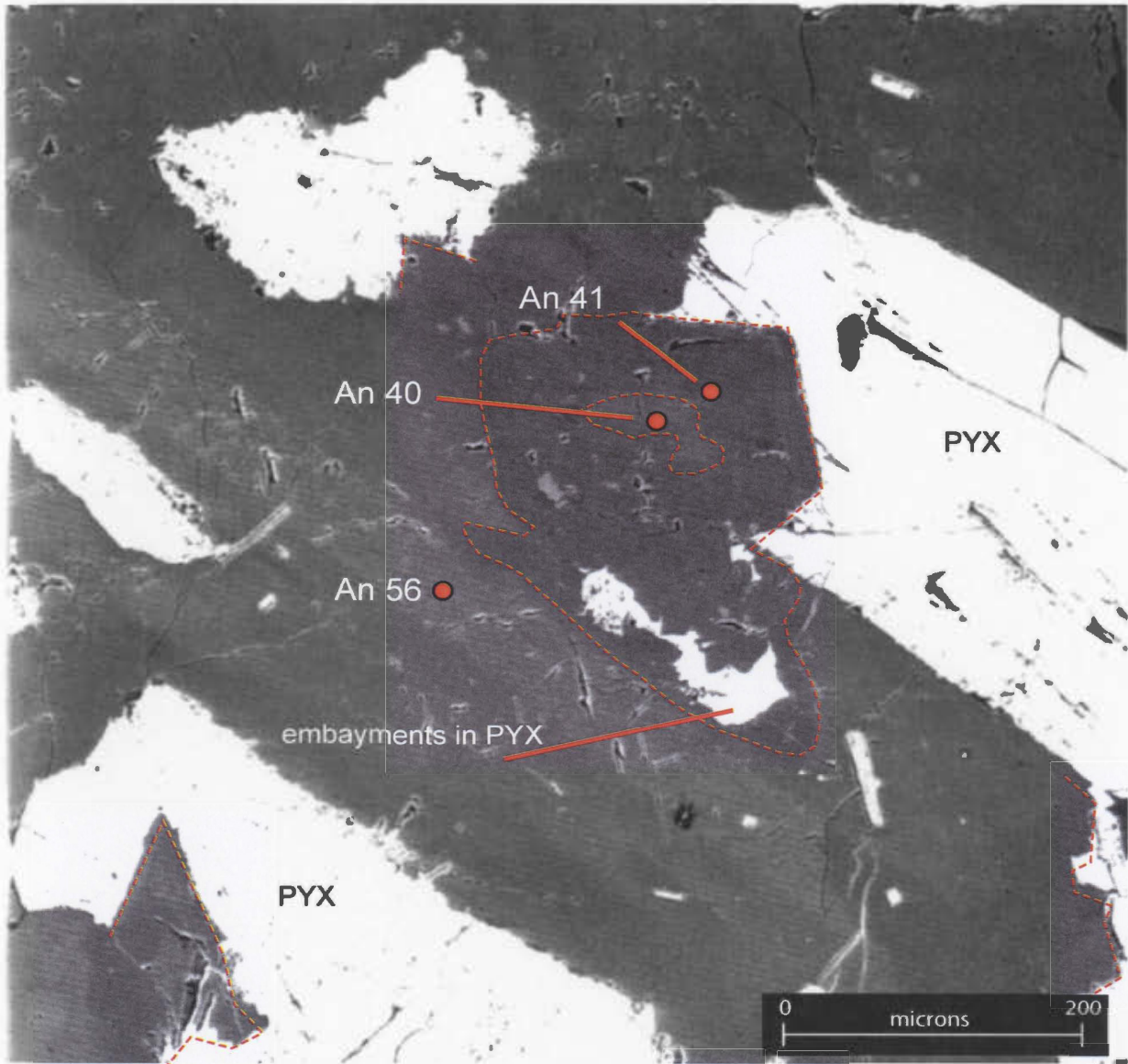


Figure 5.5 Upper Series plagioclase zoning is commonly irregular and commonly appears to truncate other zoning textures. In this example from RIC-56, dotted lines highlight where more albitic plagioclase (darker) truncates both compositional zoning, which trends SE-NW, outlining the edges of plagioclase laths, and pyroxene (PYX). This suggests that albitic fluids crystallized relatively late.

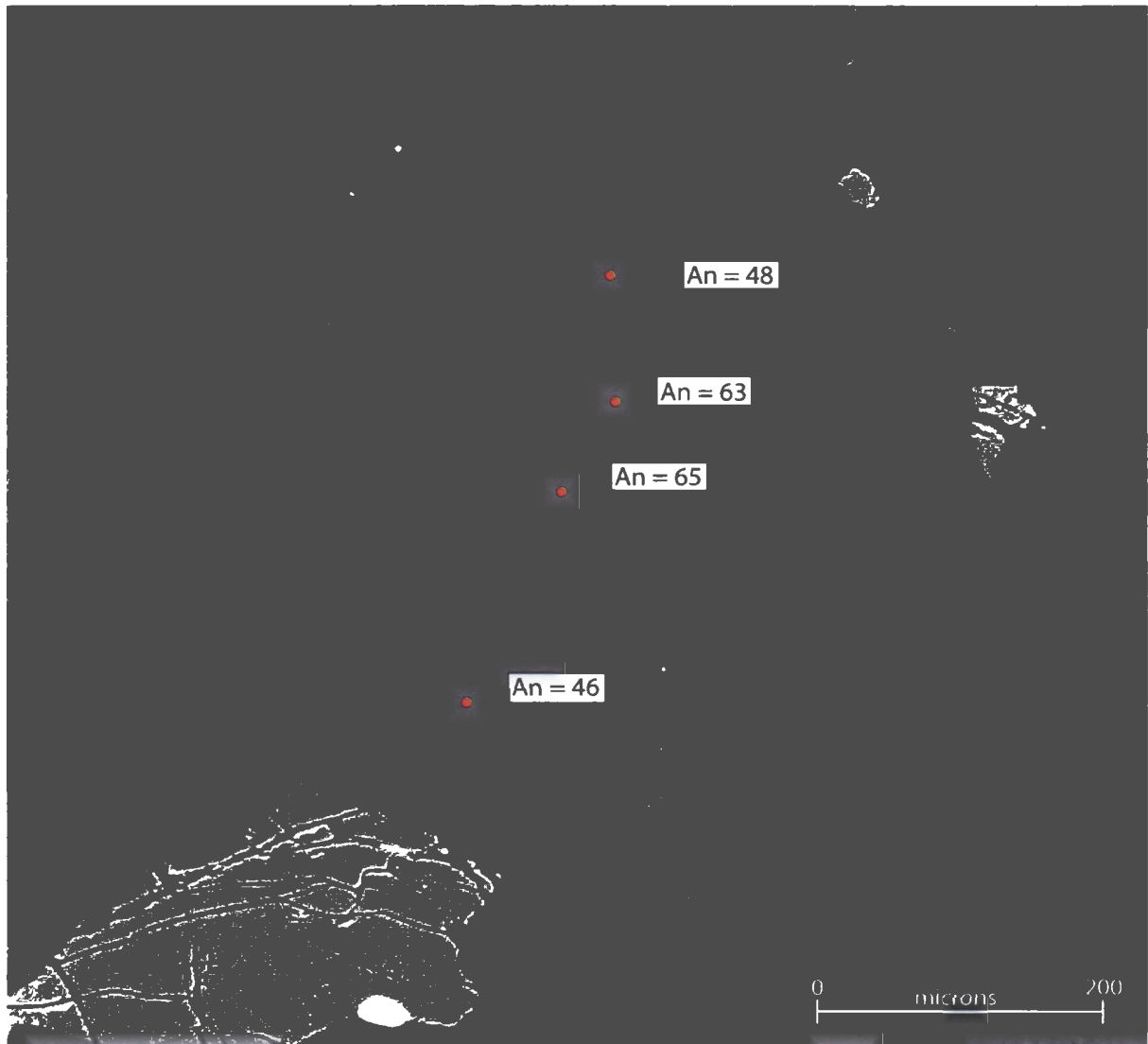


Figure 5.6 Compositional zoning in the Upper Series is typically quite pronounced and marked by a homogenous core truncated and/or corroded by relatively more albitic plagioclase around the rims. This example is from RIC-63, but many other samples demonstrate similar textures that are not apparent in optical observations.

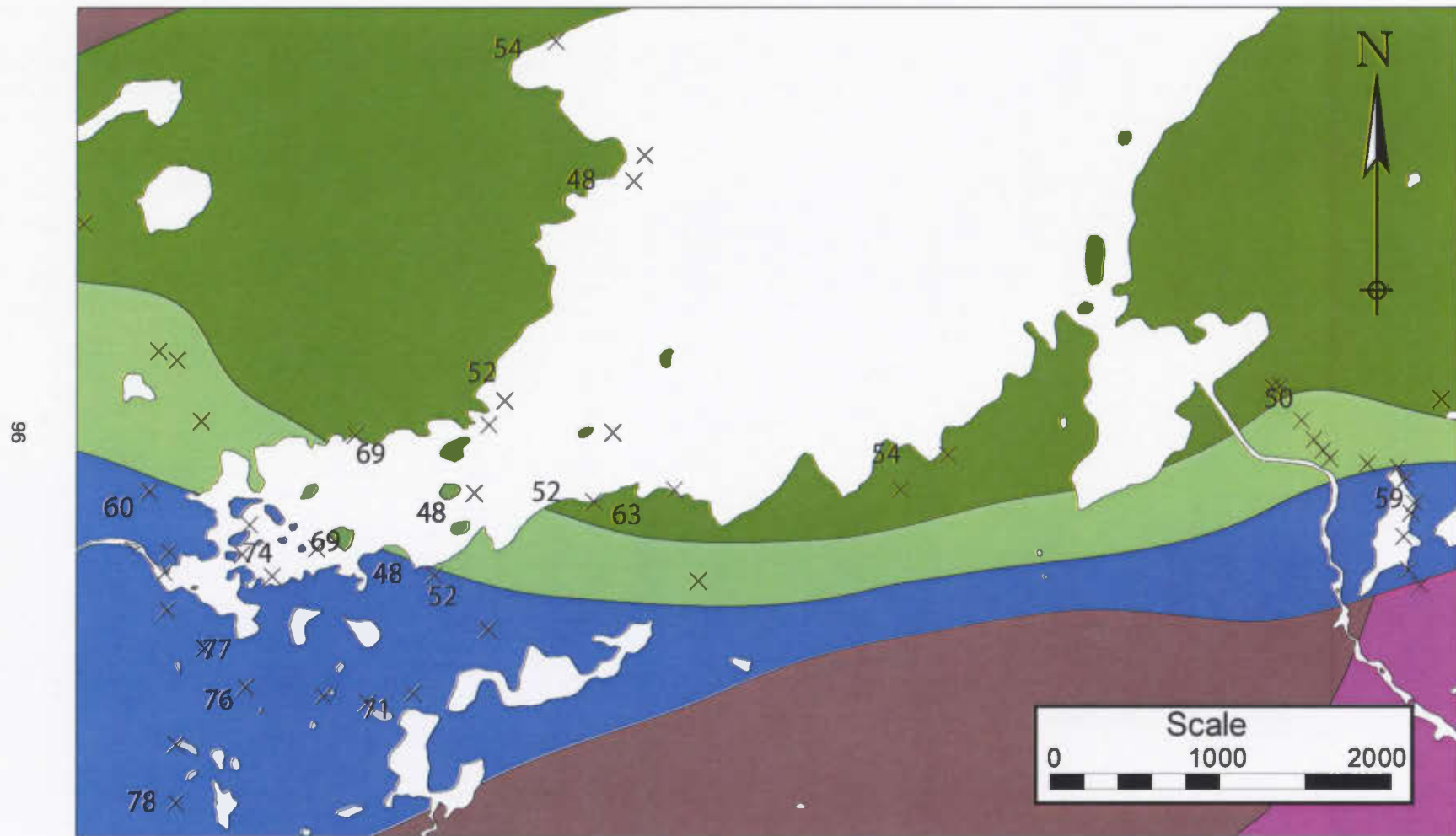


Figure 5.7 This map of the southwest portion of the RCLIS illustrates the variation in An compositions of plagioclase (numbers). The blue unit is the Lower Series, the bright green is the transition zone and the dark green is the Upper Series. Despite the difference in plagioclase compositions in the Upper and Lower Series, there is no sharp boundary where composition changes, but a gradational boundary is present instead.

particular, to characterize Ni zonation and Fo zonation within individual crystals. Overall, Upper Series samples lack olivine, thus most samples are from the Lower Series, although xenolith samples and some Upper Series samples contained olivine and were analysed.

Based on the olivine data presented below, RIC-18 and RIC-24 were not included in the Lower Series, because they had compositions characteristic of Upper Series samples. This pattern is consistent with plagioclase data, which also indicates that these samples are part of the Upper Series. Furthermore, RIC-23B is not included in Upper Series, but is discussed in the xenolith section below because it does not share the characteristics of any part of the intrusion, thus it is treated separately.

Lower Series samples average Fo 83 with a standard deviation of 2.3 for 176 analyses. The same analyses contain an average of 1277 ppm Ni with a standard deviation of 485. Zoning within individual olivine crystals is minor, but there exists considerable variation within the Lower Series as a whole (Figure 5.8). In LS olivine, the average standard deviation of forsterite for most samples is less than 0.5, but Ni is more variable, with standard deviations ranging from <0.02 to ~ 250 within a single sample. However, the variable Ni contents in individual samples do not reflect systematic zoning from high Ni concentrations in the core to low Ni concentrations in the rim, for example, which would be expected if Ni was removed from olivine late in crystallization. Instead, zoning is reversed in a few samples (i.e. low Ni in core, high Ni in rim), or random (Figure 5.9).

Most chemical variability relates to the location of the sample, such that similar regions exhibit similar average Fo compositions with some variation in Ni. Overall, Ni decreases with decreasing Fo, but several samples do not follow this trend. In addition, the systematic decrease in Ni and Fo does not occur in a spatially consistent pattern, such as high Fo and Ni at the base of the LS, progressing to lower Fo and Ni further towards the top of the LS. This would be expected for normal fractional crystallization in which there

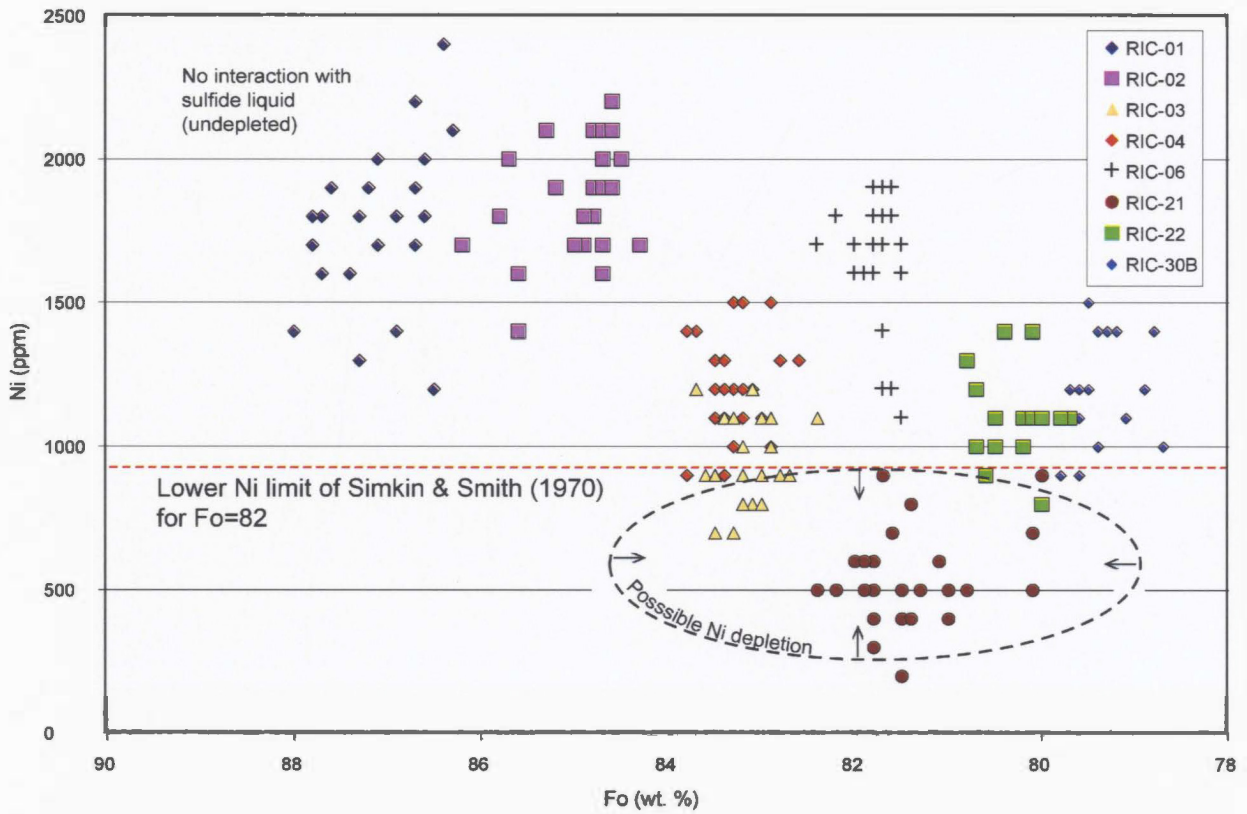


Figure 5.8 Fo-Ni microprobe data for olivine from the RCLIS. Within the Lower Series, each sample exhibits a distinguishable composition. The compositional range of most samples does not overlap with other samples. RIC-21 exhibits notable Ni depletion relative its Fo content. The dotted line represents the lower limit of Ni content for a sample of Fo 82 (the average composition of RIC-21) according to Simkin & Smith, 1970; (see also Figure 5.11).

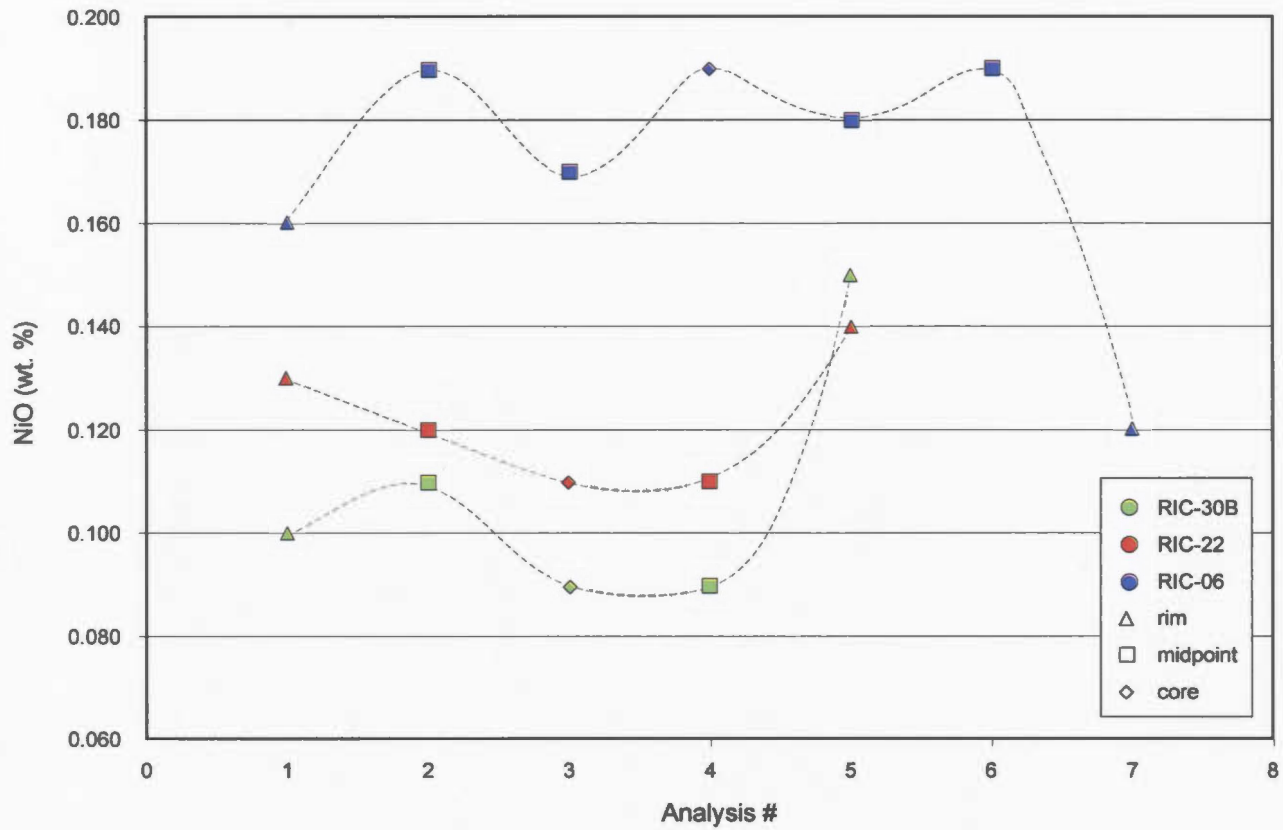


Figure 5.9 Diagram of Ni vs location in crystal for LS samples. Many olivine crystals in the LS do not exhibit any systematic zonation patterns from core to rim. These analyses are single crystal traverses from RIC-30B, 22 and 06. RIC-06 and 22 exhibit relatively low Ni in the core and elevated contents towards the rim, whereas RIC-06 has a random Ni distribution pattern. Symbols are used to distinguish the different spatial locations of the analyses and colours are constant for each sample.

was no interaction with a sulfide melt, particularly if there was just one main pulse of magma that differentiated with little outside influence or later magma pulses. Instead, the basal part of the LS has below average Fo and Ni, which then increase slightly towards the north. One area, near the river that drains Red Cross Lake, has anomalous Ni in olivine, exhibiting quite high Fo and Ni values (e.g. samples RIC-01, 02). Proximal to this area, in the islands of the west side of the lake, several samples have average to weakly elevated Fo values (Fo 81-83), but significantly lower Ni concentrations (samples RIC-03, 04 and particularly RIC-21). Figure 5.10 shows the contrasting compositions in two samples that are < 500 m apart. RIC-21 is depleted in Ni relative to RIC-02. This marked depletion in Ni compared to other samples with similar Fo values, suggests that these samples may have had Ni stripped through interaction with an immiscible sulfide melt, causing Ni to partition preferentially into the sulfide liquid over the olivine.

Figure 5.11 is a combination of compiled data from Simpkin and Smith (1970) and RCLIS data. The main trend of the Simpkin and Smith data defines the typical pattern of fractionally crystallized plutonic olivine. RCLIS samples are subdivided into LS, US and xenoliths. This diagram clearly indicates that a portion of LS samples fall below the normal curve such that for a given Fo composition, they have considerably less Ni than would be expected. A logical explanation is that these samples interacted with a sulfide melt.

Upper Series samples average Fo 56 with a standard deviation of 8.8 for 47 analyses. These samples contain an average of 471 ppm Ni with a standard deviation of 419. Systematic core-rim zoning in olivine crystals in the US does not occur. Within individual crystals, there is little variation in Fo and some degree of Ni variation, but Ni variation does not follow any pattern. Only four samples in the US contained olivine and they are widely distributed, so it is not possible to determine if there is any overall pattern in olivine variation within the US. In addition, most olivine crystals analysed were chadacrysts and not matrix olivine, so it is difficult to ascertain if variations in olivine

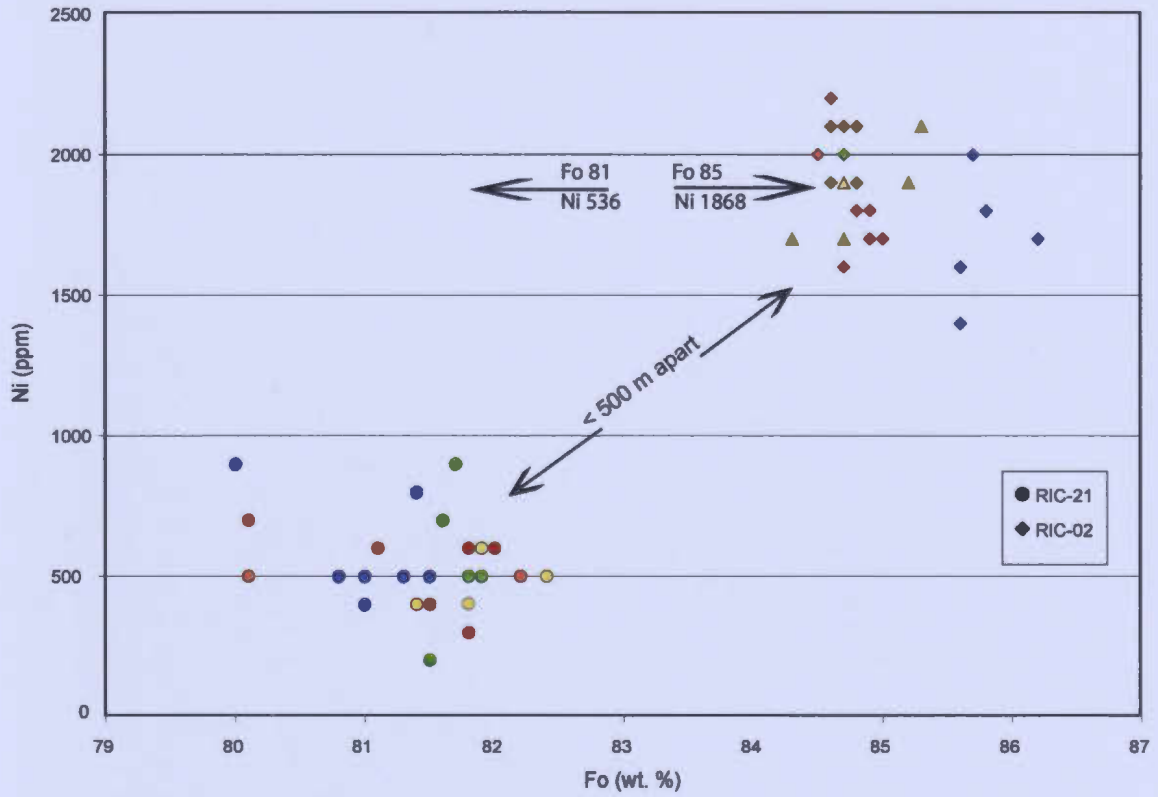


Figure 5.10 Ni vs Fo diagram for samples RIC-02 and RIC-21. These samples are less than 500 metres apart, but exhibit strongly contrasting Ni contents. They exhibit similar Fo contents, but Ni is markedly low in RIC-21. This suggests that the area surrounding RIC-21 may have had Ni stripped from olivine during crystallization. Different colours for each sample represent individual crystals, which were analysed as traverses.

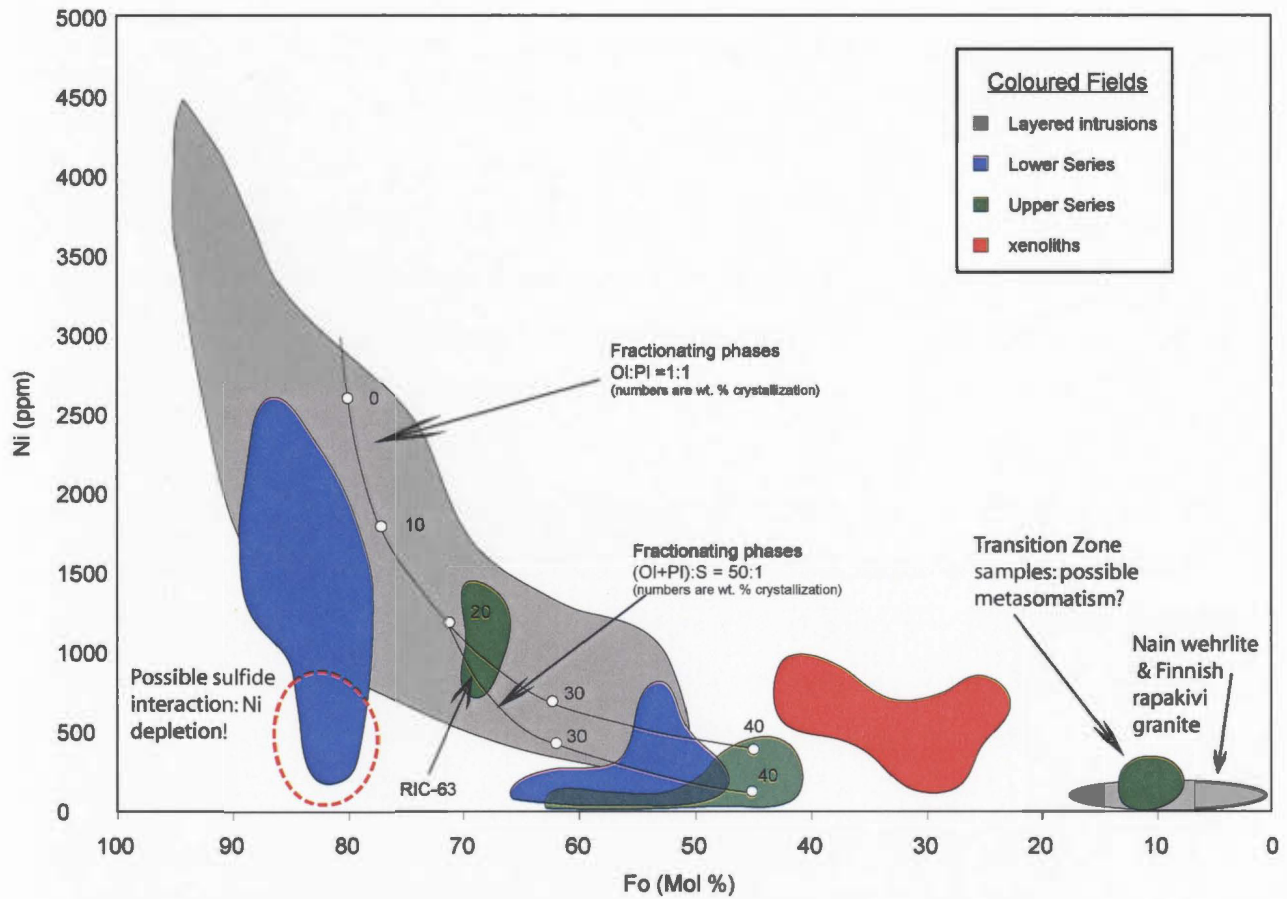


Figure 5.11 A compilation of plutonic olivine analyses from Simkin and Smith, (1970) compared with RCLIS olivine analyses. Lower Series analyses generally lie within the Simkin and Smith's range, although their overall trend is slightly steeper. Of interest is the lobe of samples that fall significantly below this trend, exhibiting relatively low Ni for a given Fo composition. Xenolith samples have unique compositions compared to Simpkin and Smith and RCLIS data. Upper Series samples also generally lie within the main trend. An exception to this is RIC-23B, from near the transition zone. This sample exhibits extremely low Fo and Ni contents. Fractional crystallization trends are modified after Li and Naldrett, (1999) (see that text for a detailed explanation).

composition result from interaction with their host oikocryst, or if the variation occurred before they became enclosed. It is possible that olivine was trapped early during crystallization of the US, preserving an original composition, having been shielded from interaction with the surrounding magma. RIC-63 has a notably Fo-rich composition for its location near the northern most edge of the US, near the contact with country rock. RIC-63 olivine has an average of Fo 68, which is typical of middle LS samples (Figure 5.11). These olivine crystals are small chadacrysts enclosed in clinopyroxene and the sample exhibits some (pre-recrystallization) textures similar to LS samples. Implications for this sample are discussed below.

Xenolith samples average Fo 36 with a standard deviation of 3.6 for 22 analyses. These samples contain an average of 705 ppm Ni with a standard deviation of 181. Xenolith samples fall into two categories. First, sample RIC-51 originates from a breccia-rich belt proximal to the upper portion of the LS near the transition zone. These samples exhibit textures unrecognized elsewhere in the RCLIS (Figure 5.12). These textures are magmatic in origin and thus likely represent autoliths, since there are no known plutonic country rocks nearby to the RCLIS that these samples could represent, thus they must be a component of the RCLIS. The composition of both RIC-51 samples are relatively consistent and do not exhibit any major core-rim zonation in Fo or Ni. However, the composition of these samples, like their textures, is atypical of RCLIS samples and they do not fall in the main field of data defined by Simpkin and Smith (1970) (Figure 5.11). A population of data from RIC-23B, previously thought to be a xenolith is contentious because it is possible that it is not a xenolith or an autolith, but represents an extremely evolved magma that was injected late, along a shear zone, proximal to the LS-transition zone contact. This sample also exhibits atypical textures that are perhaps intermediate between RIC-51 xenoliths and typical LS olivine textures (Figure 5.13). It is also possible that this sample, due to its proximity to increased late magmatic fluid flow, was affected by metasomatic fluids, which removed Mg, and replaced it with Fe. However, the very

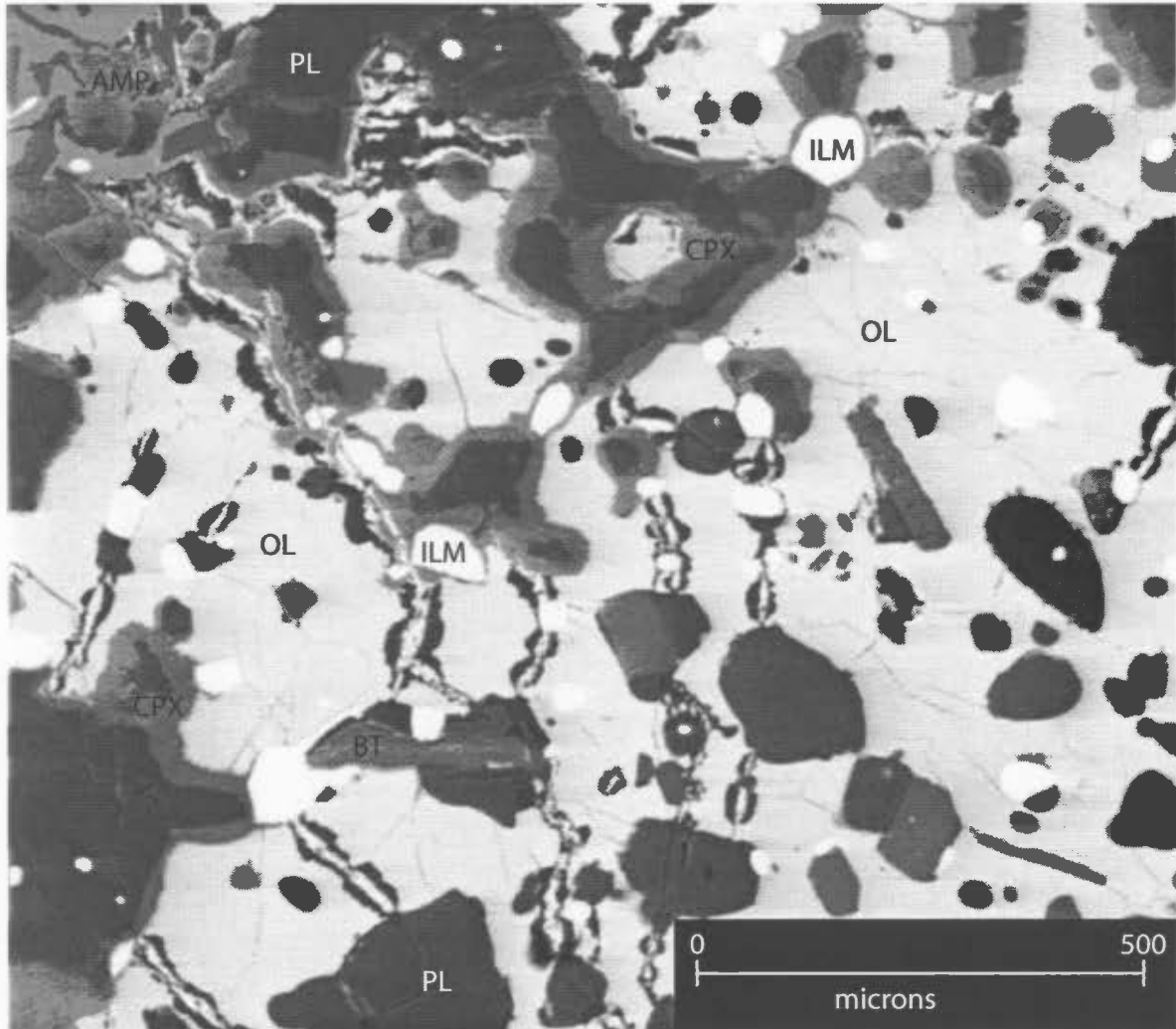


Figure 5.12 Backscatter electron image of sample RIC-51.1c. This sample exhibits seive-like textures unrecognized elsewhere in the RCLIS. These olivine (OL) oikocrysts contain inclusions of granoblastic plagioclase (PL), ilmenite (ILM), chromite (not shown in this image), biotite (BT) and amphibole (AMP). Plagioclase embays olivine and is locally associated with reaction rims of clinopyroxene (CPX). Note scale bar in lower right corner.

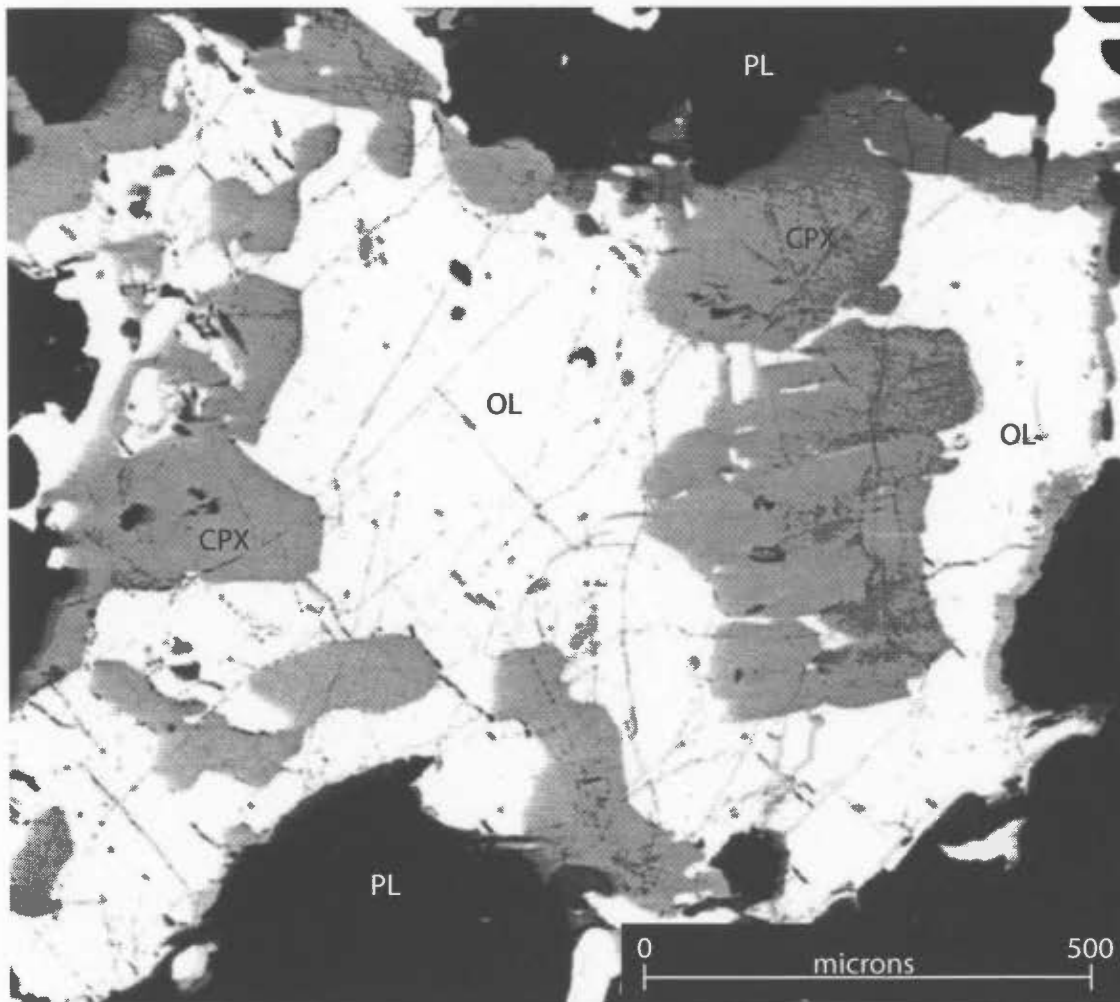


Figure 5.13 Backscatter electron image of sample RIC-23B. Olivine is strongly embayed by clinopyroxene and plagioclase. Plagioclase is also embayed into clinopyroxene and exhibits a relatively albitic composition, suggesting it is a late replacement feature. Note scale bar in lower right corner.

low Ni and Fo values more likely result from extreme differentiation. There is not enough evidence to positively state the nature of this sample.

As discussed in Chapter 3, many olivine crystals exhibit thin rims of clinopyroxene and locally amphibole and serpentine. In backscatter images, clinopyroxene is homogenous and exhibits smooth grain boundaries, suggesting that is probably a primary magmatic feature, because it lacks textures typical of metamorphic reactions such as symplectic intergrowths or remnant reacted minerals. However, the serpentine reaction rims are secondary. No analyses of serpentine were completed. Using petrography alone, the origin of the amphibole rims was contentious, because the rims are microscopic textures that approach the limits of the microscope. However, imaging by the microprobe confirms that these rims are a secondary feature, forming at the expense of pyroxene and plagioclase, which is the most common association in LS samples. In BSE images, subtle symplectic intergrowths of pyroxene and amphibole were observed, a texture commonly associated with metamorphic reactions. Amphibole rims are also locally embayed into plagioclase suggesting a general reaction of: pyroxene + plagioclase  $\rightarrow$  Mg-amphibole. Figure 5.14 is an example of these rims, with compositions noted where measured quantitatively.

### 5.3 Pyroxene

Fourteen pyroxene-bearing samples were analysed, comprising five Lower Series, eight Upper Series and two xenolith samples. Pyroxene analyses measured SiO<sub>2</sub>, TiO<sub>2</sub>, Al<sub>2</sub>O<sub>3</sub>, Cr<sub>2</sub>O<sub>3</sub>, FeO, MnO, MgO and CaO. Fe<sub>2</sub>O<sub>3</sub>(calc) and FeO(calc); end-members were calculated off-line by the microprobe software described above. The primary goal of the pyroxene analysis was to characterize the overall composition of the Lower and Upper Series and to determine the composition of exsolution lamellae present in some clinopyroxene crystals. Furthermore, microprobe analyses were used to determine if there are distinct compositional differences between different pyroxene textures (e.g. poikilitic vs granular).

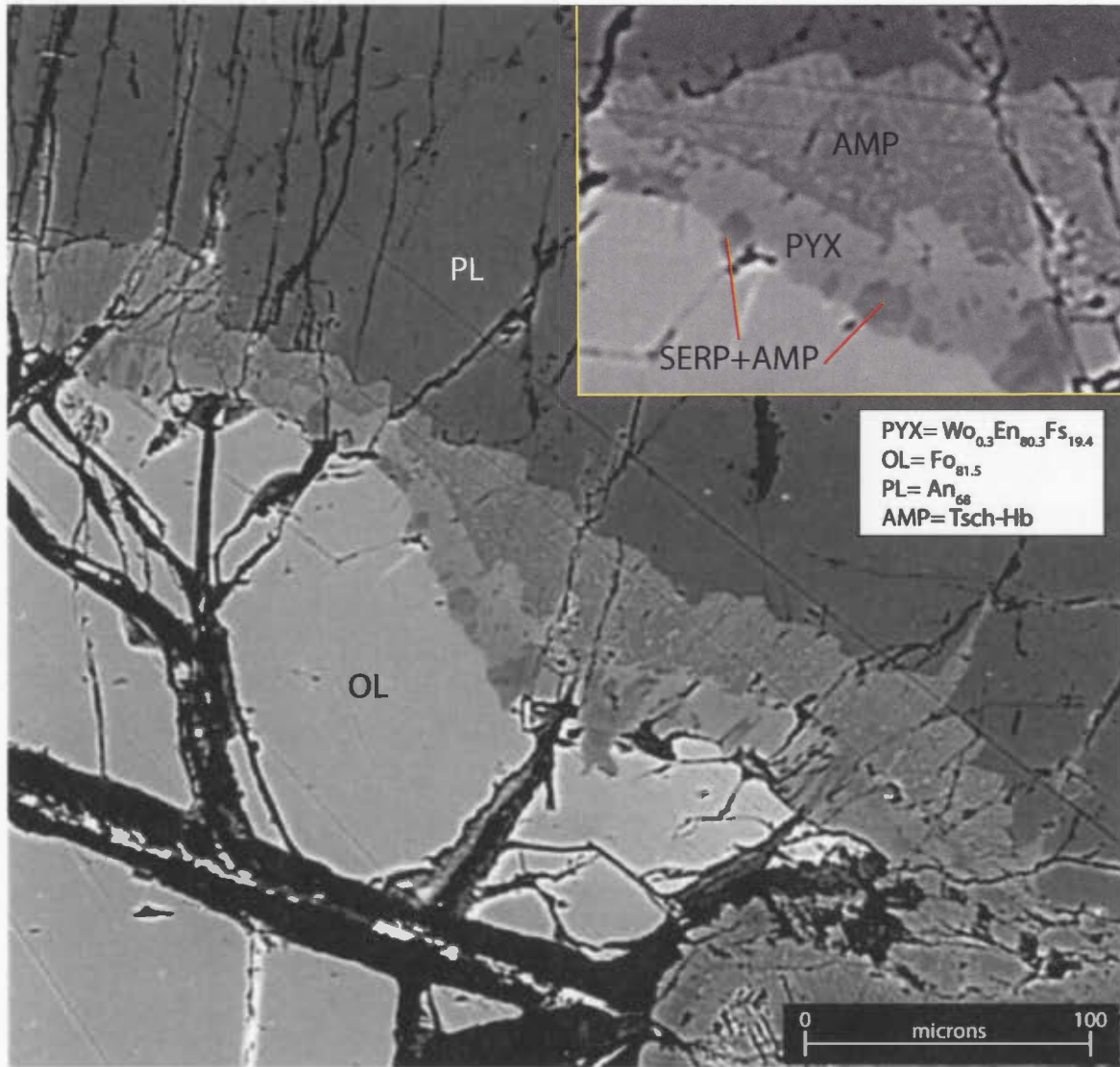


Figure 5.14. Backscatter electron image of sample RIC-06. Olivine exhibits several different types of rims, of which this is the most common. A pyroxene rim (cpx or opx) adjacent to olivine reacts with plagioclase (PL) to form a symplectic intergrowth of amphibole and pyroxene. Note that locally, pyroxene is altered to serpentine or amphibole. Note the scale bar in the lower right corner.

Although Lower Series pyroxene comprises mainly clinopyroxene, microprobe analyses for both orthopyroxene and clinopyroxene are presented below. Eight orthopyroxenes and seven clinopyroxenes were analysed in the Lower Series. Of the seven clinopyroxene analyses, all but one fall in the diopside field, or very near to the boundary between diopside and augite. One analysis, from RIC-27, lies in the pigeonite field. Diopside samples have an intermediate composition and the pigeonite analysis is relatively Mg-rich (Figure 5.15). There is no internal zoning in LS clinopyroxene, although some variation within individual crystals is present, but likely a result of fine-scale orthopyroxene exsolution lamellae that result in impure analyses.

There are eight Lower Series orthopyroxene analyses, which all exhibit an enstatite composition, although the compositional range is not as tightly confined as clinopyroxene analyses. These analyses demonstrate a trend towards more elevated Fe orthopyroxene in some samples. Overall, LS orthopyroxene analyses are of intermediate enstatite composition. Table 5.3 summarizes OPX and CPX compositions for the Lower and Upper Series and xenolith analyses. Figure 5.15 illustrates the distribution of Lower, Upper and xenolith analyses in Wo-En-Fs compositional space.

Upper Series analyses comprise both clinopyroxene and orthopyroxene. There is a notable chemical distinction between Upper and Lower Series compositions (Figure 5.15). US samples are more Fe-rich relative to LS samples. US clinopyroxene is also restricted to diopside compositions aside from two outliers, one in the augite field and the other in the wollastonite field. The augite analysis comes from a partially replaced clinopyroxene oikocryst, but other analyses from this crystal are consistently diopsidic. The wollastonite analysis is from the edge of a replaced diopside crystal adjacent to Ca-rich plagioclase, suggesting Ca from plagioclase was consumed to form the reaction rim.

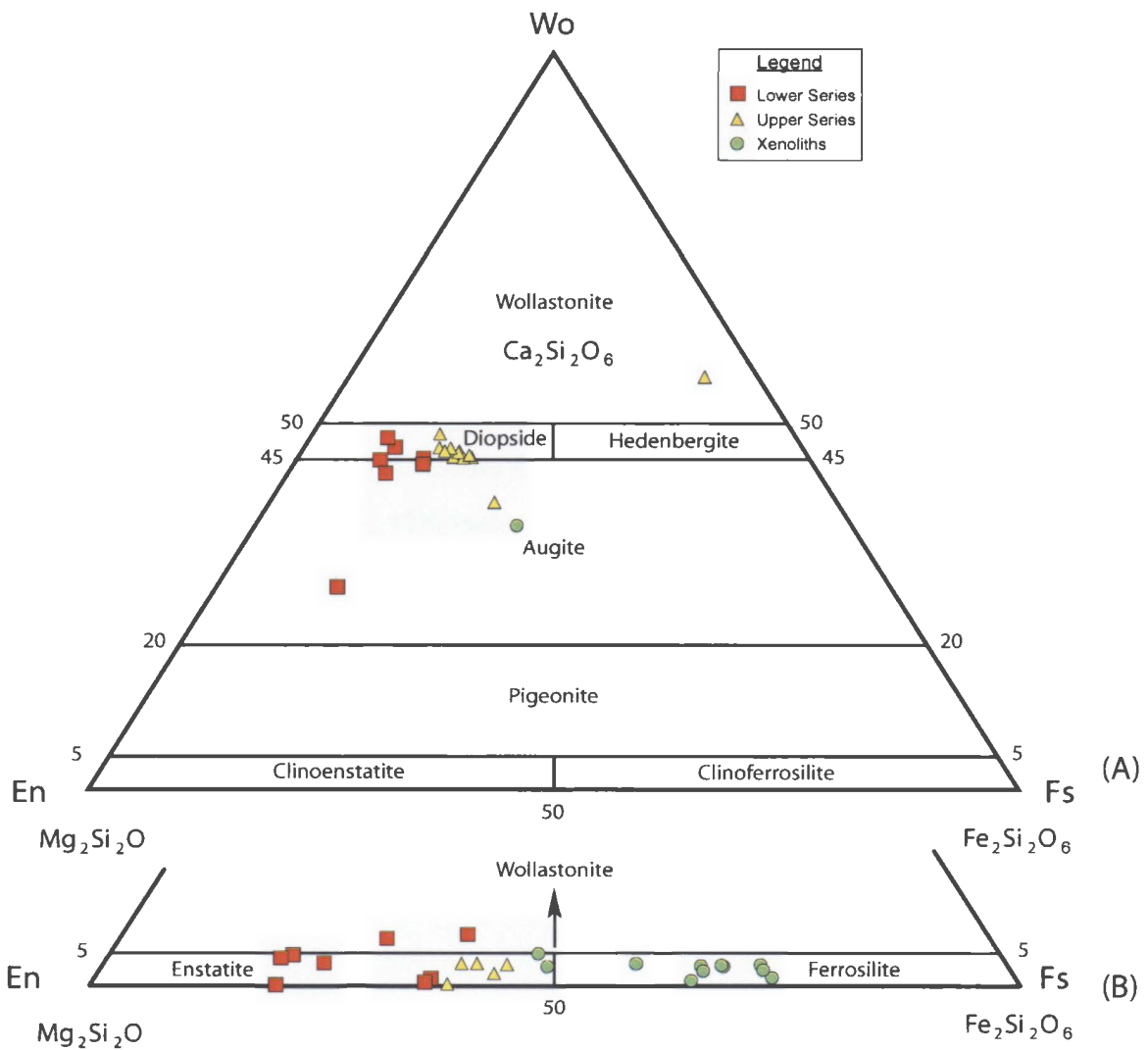


Figure 5.15 Compositional ranges and nomenclatures of clinopyroxene (a) and orthopyroxene (b) in the RCLIS. (a) Lower Series CPX analyses exhibit a more Ca-Mg rich composition than the Upper Series and xenolith analyses. (b) Lower Series OPX analyses are also distinctly more Mg-rich. Xenoliths are predominantly Fe-rich OPX (modified after Morimoto, 1988)

There are five US orthopyroxene analyses, all which exhibit an enstatite composition. Compared to the LS, US enstatite compositions are more tightly constrained and Fe-rich. These samples fall just to the left of the enstatite-ferrosilite boundary.

There are 12 xenolith analyses from two samples. Xenolith samples include RIC-23B, which is described here because it originates in a xenolith-rich area. Aside from an analysis of an augite reaction rim between olivine and plagioclase in sample RIC-51.1c, nearly all analyses have a distinctive Fe-rich composition, falling into the ferrosilite field. This is especially true for RIC-23B, which contains Fe-rich pyroxenes. Fe-rich pyroxene compositions are consistent with Fe-rich olivine analyses described above, suggesting that this sample may be a product of extreme differentiation resulting in Fe enrichment in the magma. It is interesting to note that although pyroxenes and plagioclases in samples RIC-23B and RIC-51.1c exhibit similar compositions, olivine from these two samples is quite different.

<b>Series CPX</b>	<b>Wo (Ca)</b>	<b>En (Mg)</b>	<b>Fs (Fe<sup>2+</sup>)</b>
Lower	42.75	46.54	10.70
Upper	46.30	35.23	18.47
Xenoliths	36.03	36.35	27.62

<b>Series OPX</b>	<b>Wo (Ca)</b>	<b>En (Mg)</b>	<b>Fs (Fe<sup>2+</sup>)</b>
Lower	3.43	69.60	26.97
Upper	2.37	57.55	40.078
Xenoliths	2.63	34.79	62.58

Table 5.3. These tables summarize the average composition of clinopyroxene (CPX) and orthopyroxene (OPX) for the Lower and Upper Series and xenoliths. Lower Series analyses of CPX and OPX are more Mg-rich than Upper Series and xenolith analyses. Furthermore, xenolith analyses are the most Fe-rich of the three populations in both CPX and OPX.

Exsolution lamellae in pyroxene were too fine to derive accurate analyses, but suggest that OPX exsolves from CPX.

## 5.4 Amphibole and reaction rims

Thirteen samples exhibiting amphibole reaction rims were analysed, including six LS, six US and one xenolith sample. Amphibole analyses measured SiO<sub>2</sub>, TiO<sub>2</sub>, Al<sub>2</sub>O<sub>3</sub>, Cr<sub>2</sub>O<sub>3</sub>, FeO, MnO, MgO, CaO, Na<sub>2</sub>O, K<sub>2</sub>O and NiO; Cl, F and H<sub>2</sub>O were calculated off-line assuming 2 OH to account for elements not analysed for by the probe. The primary goal of amphibole analysis was to characterize the composition of amphibole reaction rims.

These data were used in all diagrams and calculations. Figure 5.16 is a plot of Si cations vs Mg# after Hawthorne, (1981) and was employed to classify the amphibole analyses. LS samples are more Mg-rich than US samples, and xenolith samples have approximately equal Mg-numbers compared to Upper Series samples. Table 5.4 summarizes Mg# data from the analyses.

Series	Avg Mg#	StDev	n
Lower Series	0.7	0.1	10
Upper Series	0.4	0.07	15
Xenoliths	0.4	0.05	9

Table 5.4 A summary of amphibole magnesium numbers. Composition of pyroxene is distinctive for Lower and Upper Series samples, but xenoliths are similar to Upper Series samples.

Based on the Hawthorne (1981) subdivisions, LS samples range from tschermakite to magnesio-hornblende, whereas US samples span a wider compositional range, from ferro-actinolite to Fe-actino-hornblende. Xenolith samples are also relatively Fe-rich, and span the same compositional range as the US samples. There is no distinct cluster of any particular composition in this diagram, suggesting that perhaps the composition of the amphibole depends on relatively local constraints. The overall magnesian LS amphibole and iron-rich US amphibole may be a reflection of the overall bulk composition of each sample (*i.e.* a magnesium-rich area contains Mg-rich secondary amphibole and an Fe-rich area contains Fe-rich secondary amphibole). This is consistent with reaction textures, which indicate that amphibole forms directly from the

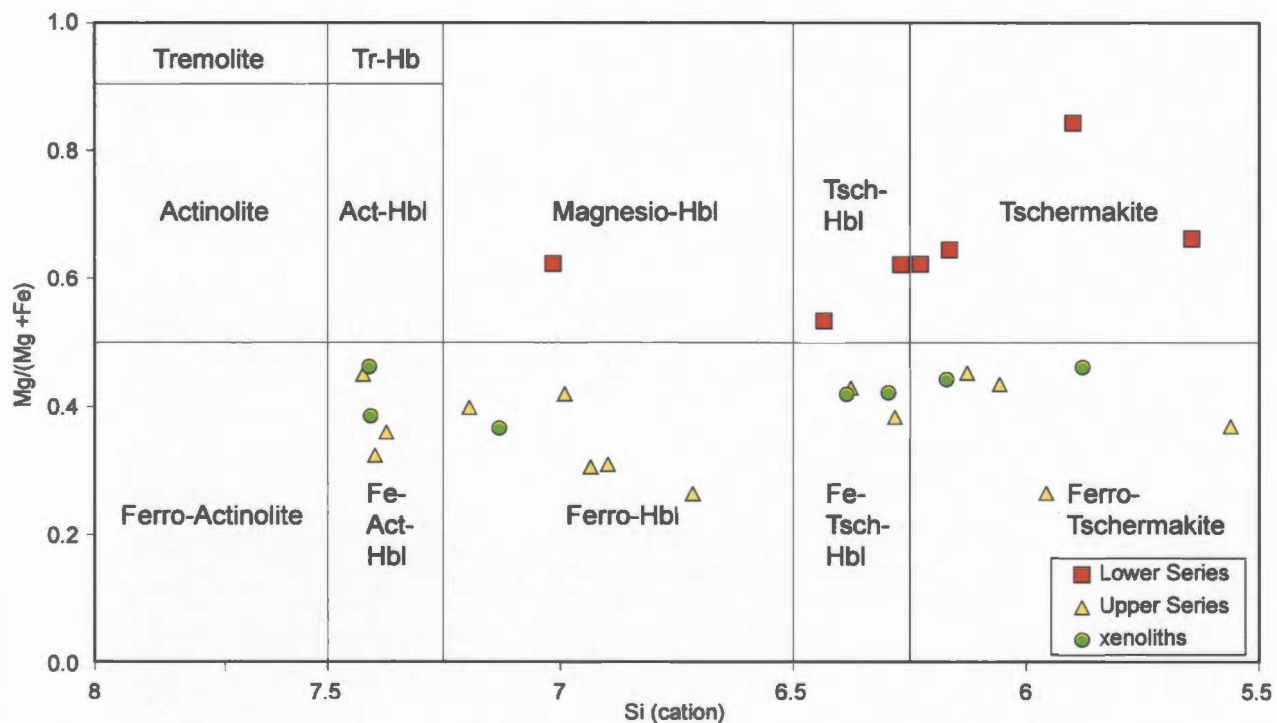


Figure 5.16 This diagram is used to classify Fe-Mg amphibole by plotting Si cations vs Mg#. LS analyses are Mg-rich, and fall mainly in the tschermakite-Hbl to tschermakite compositional range, while US and xenolith samples are distinctly more Fe-rich, mirroring the pattern of most other phases (modified after Hawthorne, 1981).

consumption of adjacent phases. Therefore, amphibole consuming fayalitic olivine or enstatitic pyroxene would be more Mg-rich than amphibole formed adjacent to more Fe-rich phases.

As described in Chapter 3, reaction rims are relatively common in samples throughout the RCLIS. In general, amphibole reaction rims exhibit a variable composition. Figure 5.17 is an example of typical reaction rim textures between pyroxene and plagioclase, which is observed in both Lower and Upper Series samples. Similar textures are observed in Figure 5.15, except that olivine is present there. The similarity of these reaction rim textures suggests that olivine is not a prerequisite phase, because the reaction occurs between just the pyroxene and plagioclase, hence the widespread distribution of this texture in the RCLIS despite the limited extent of olivine. Locally, pyroxene forms spectacular symplectic textures intergrown with plagioclase adjacent to clinopyroxene and olivine (Figure 5.18). These textures generally occur in more strongly altered samples where amphibole replacement of pyroxene and/or olivine is relatively advanced.

## 5.5 Oxides

Eighteen oxide-bearing samples were analysed, which comprise nine LS, eight US and one xenolith sample. Analyses measured  $\text{SiO}_2$ ,  $\text{TiO}_2$ ,  $\text{Al}_2\text{O}_3$ ,  $\text{Cr}_2\text{O}_3$ ,  $\text{FeO}$ ,  $\text{MnO}$ ,  $\text{MgO}$  and  $\text{NiO}$ ;  $\text{FeO}_{\text{calc}}$  and  $\text{Fe}_2\text{O}_{3\text{calc}}$  were computed off-line. The primary objective of the oxide analysis was to determine the composition of oxides, particularly because of possible extensive solid solution. Some RCLIS oxides were noted to exhibit exsolution textures in reflected light, thus microprobe analyses were also used to investigate the composition of the different exsolution species. In the RCLIS, two main groups of oxides were identified by reflected light and confirmed by microanalyses. The phases are from the cubic and rhombohedral series of spinel (Lindsley, 1991).

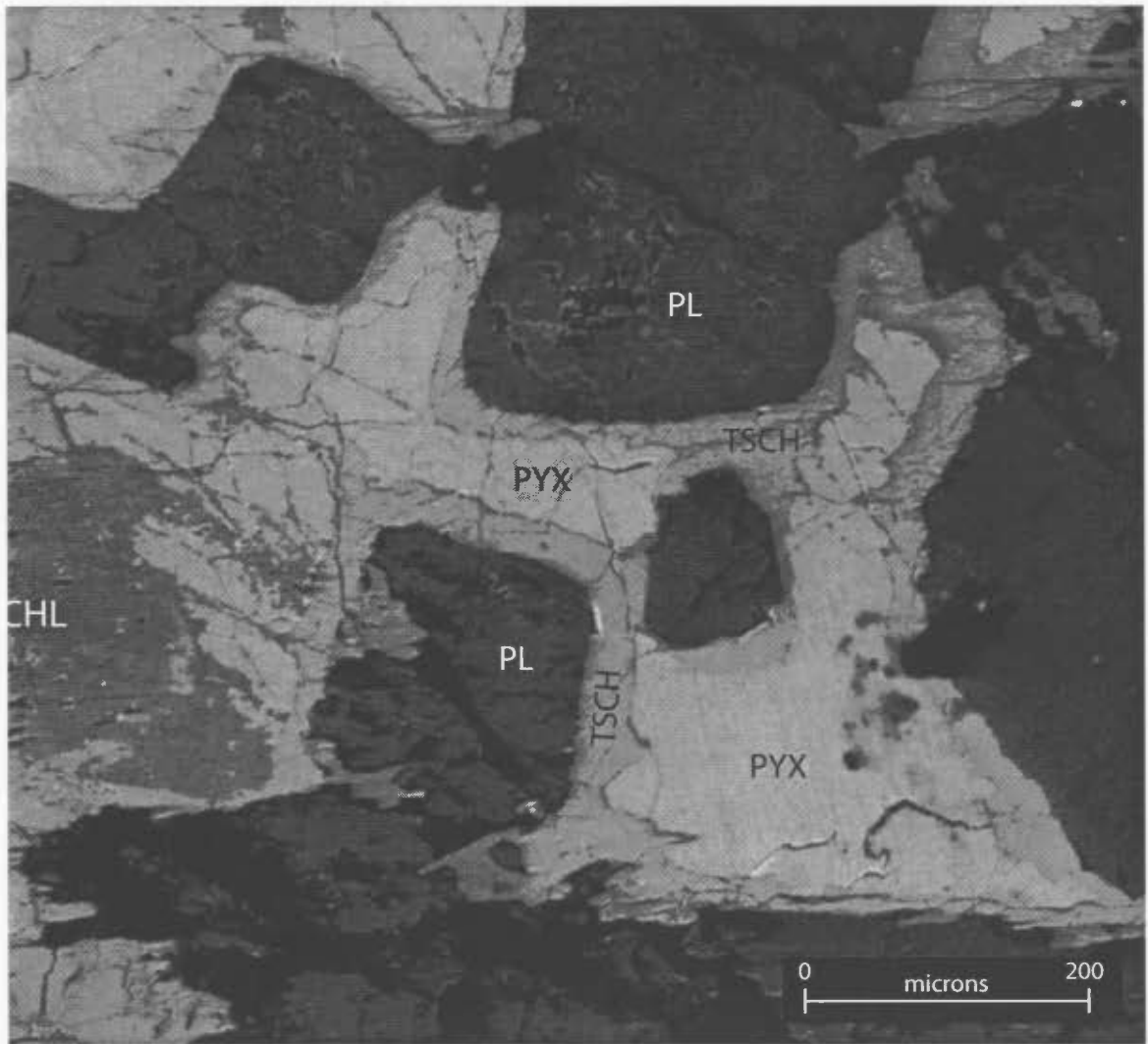


Figure 5.17 Backscatter electron image of sample RIC-27 exhibits secondary amphibole rims. Here, poikilitic- to sub-poikilitic clinopyroxene is consumed by amphibole in the general reaction  $pyx + plag \rightarrow amp$ . In this sample amphibole is Mg-rich with a tschermakite composition.

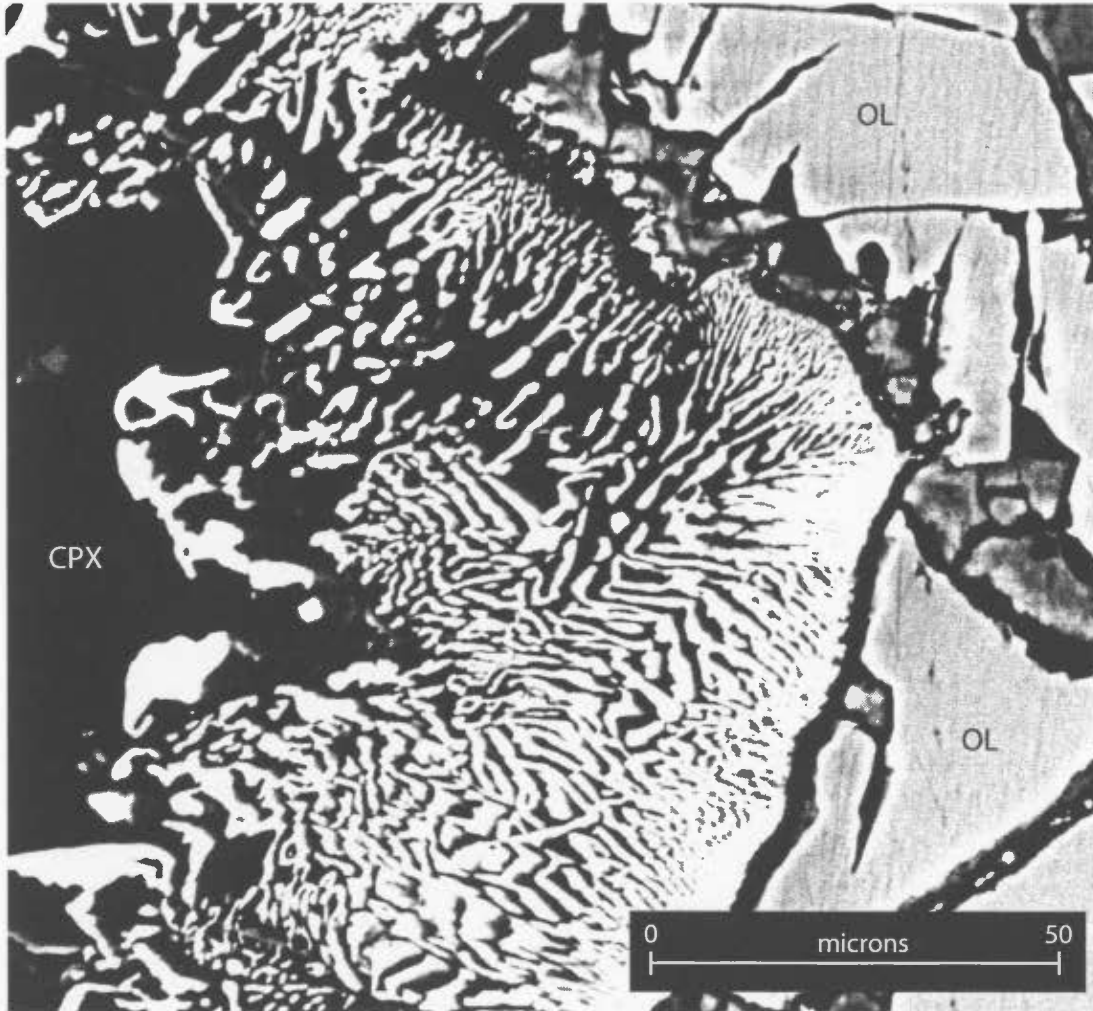
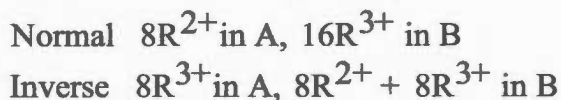


Figure 5.18 Backscatter electron image of RIC-24. Amphibole locally forms spectacular symplectic textures where clinopyroxene (CPX) and olivine (OL) react. These textures are most common in more strongly altered samples. Amphibole is not labeled, but it is the vermicular textured symplectite.

### 5.5.1 Spinel Series

Minerals from the spinel series *sensu stricto* are cubic and exhibit either a normal or inverse structure, which is based on the orientation of the A and B structural sites.

According to Waychunas, (1991) and Deer et al. (1992) the general formula for spinel is  $R_8^{2+}R_{16}^{3+}O_{32}$  and the two distributions are:



The spinel group is further subdivided based on the trivalent ion in the B-site. Table 5.5 lists the spinel series minerals defined by these subdivisions.

2+ Cation	Spinel Series (Al)	Magnetite Series (Fe)	Chromite Series (Cr)
Mg	Spinel	Magnesioferrite	Magnesiochromite
Fe <sup>2+</sup>	Hercynite	Magnetite	Chromite
Zn	Gahnite	Franklinite	-
Mn	Galaxite	Jacobsite	-
Ni		Trevorite	-

Table 5.5. Cubic spinel is further subdivided by the trivalent cation, which is located in the B site. For most analyses of cubic spinel in the RCLIS the 2+ cation was Fe, thus hercynite, magnetite and chromite are the main species observed.

Interpretation of the analytical data for these phases is complicated for several reasons. First, the instrument cannot differentiate between Fe<sup>2+</sup> and Fe<sup>3+</sup>, which can affect how one classifies the analysed phase. Secondly, extensive solid solution occurs throughout cubic spinel, as illustrated by Figure 5.19. In this diagram, all cubic spinel species are shown in a compositional prism. In this prism, solid solution is possible between any phase, thus pure end-members are uncommon and instead analyses comprise a mixture of divalent and trivalent elements encompassing the range of solid solution. Figure 5.20 illustrates where RCLIS samples fall in magnetite-hercynite-chromite compositional space.

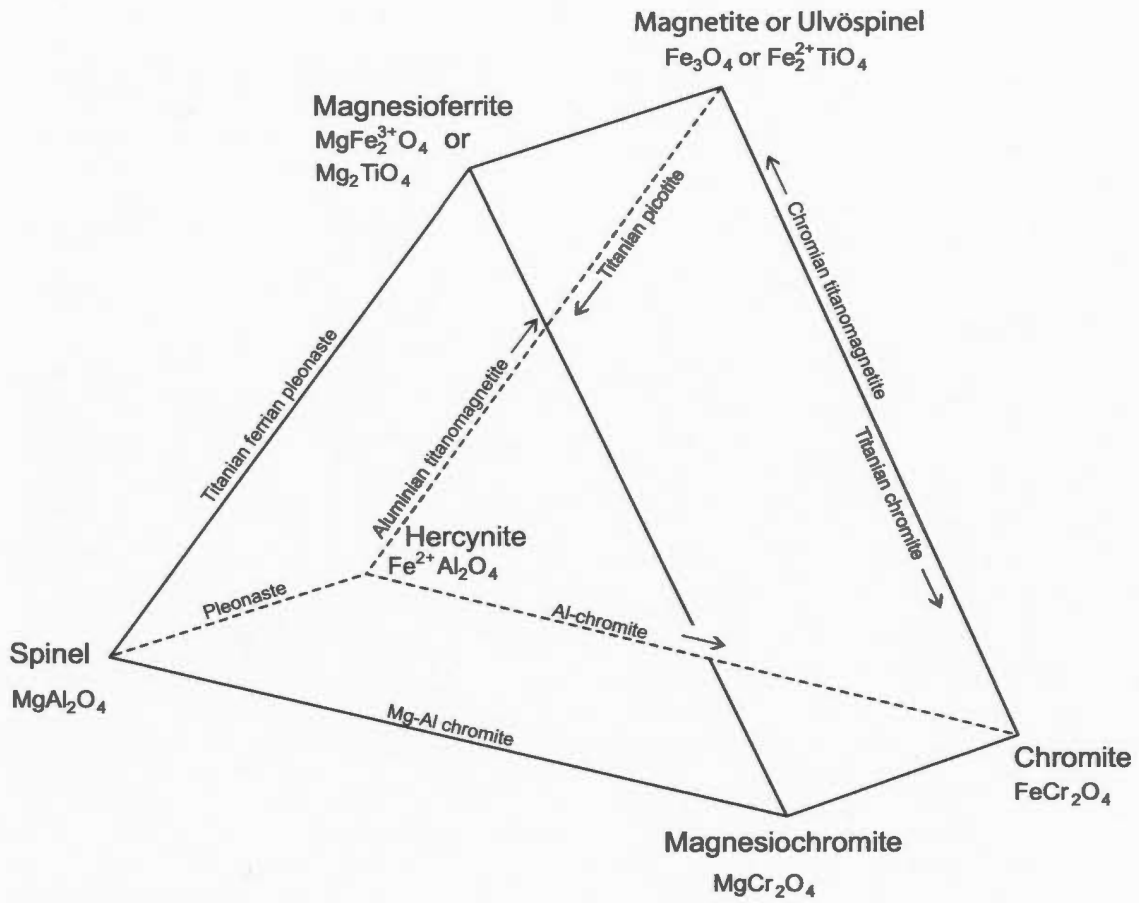


Figure 5.19 Nomenclature for compositions in the multicomponent spinel prism. The bases of the triangles are defined by normal spinels and the vertices by inverse spinels; the latter may be divided into  $\text{Fe}^{2+}$  and  $\text{Ti}^{4+}$  and  $\text{Fe}^{3+}$  (modified after Deer et al., 1992).

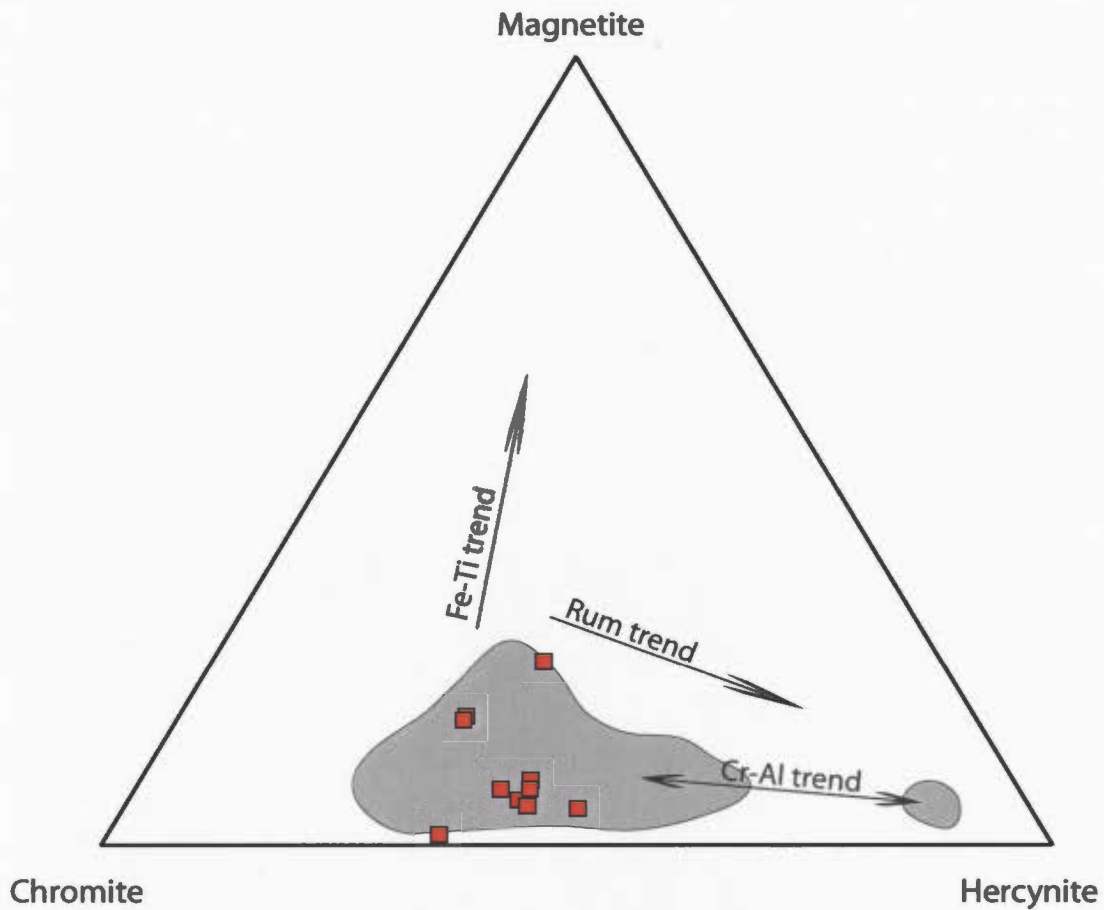


Figure 5.20 A ternary diagram summarizing spinel end-member compositions in the LS of the RCLIS. The Fe-Ti, Cr-Al and Rum trends are defined by Barnes and Roeder (2001) based on many thousands of samples and readers are referred to this paper for the full details. LS spinel plots in the central Cr-trend, which, according to Barnes and Roeder (and references therein), implies that spinel equilibrated with olivine of composition and constant temperature. The slope of this trend is the basis for the olivine-spinel termobarometer (Sack and Ghiorso, 1991).

Ten analyses of spinel from five LS samples are presented below. Analyses reveal that spinel composition is variable, although in general it exhibits an aluminous chromite composition, with a minor amount of spinel ( $\text{MgAl}_2\text{O}_4$ ). Spinel analyses were plotted on a ternary diagram (Figure 5.20) using the three most abundant trivalent ions from the analyses, Cr, Al and Fe. These three elements account for the phases chromite, hercynite and magnetite, respectively, and all have  $\text{Fe}^{2+}$  as the divalent ion. Magnetite with Ti present is called ulvöspinel, but these analyses indicate that ulvöspinel does not exceed 6 wt. % solid solution in magnetite. To plot these analyses, each trivalent ion was normalized with respect to the other ions and then plotted in Microsoft Excel using macros within a spreadsheet. Using this method, the percentage of the chromite end-member was calculated by:  $(100 \times \text{Cr}_2\text{O}_3)/(\text{Cr}_2\text{O}_3 + \text{Al}_2\text{O}_3 + \text{Fe}_2\text{O}_3)$ . The composition of these three end-members is relatively consistent and is listed in Table 5.6

	<b>Chromite</b>	<b>Hercynite</b>	<b>Magnetite</b>
Average	52.18	38.43	9.39
StDev	5.55	5.61	6.85

Table 5.6. Summary of Lower Series spinel analyses. All three end members have a relatively consistent composition, although some samples contain relatively more MgO, this data is not presented.

Analyses from RIC-01 and 02 contained an average of ~11 weight percent MgO, indicating that solid solution of the minerals spinel, magnesioferrite and magnesiochromite are also present to some degree in these samples, but tetrahedral plots including MgO were not calculated.

Although the majority of spinel crystals were homogenous, very fine exsolution lamellae were detected in several euhedral spinel crystals (Figure 5.21) and analysis indicates they are relatively more Cr-rich compared to the host. It is possible that these are examples of chromite exsolving from magnetite or hercynite, but there are not enough examples coarse enough to determine this accurately.

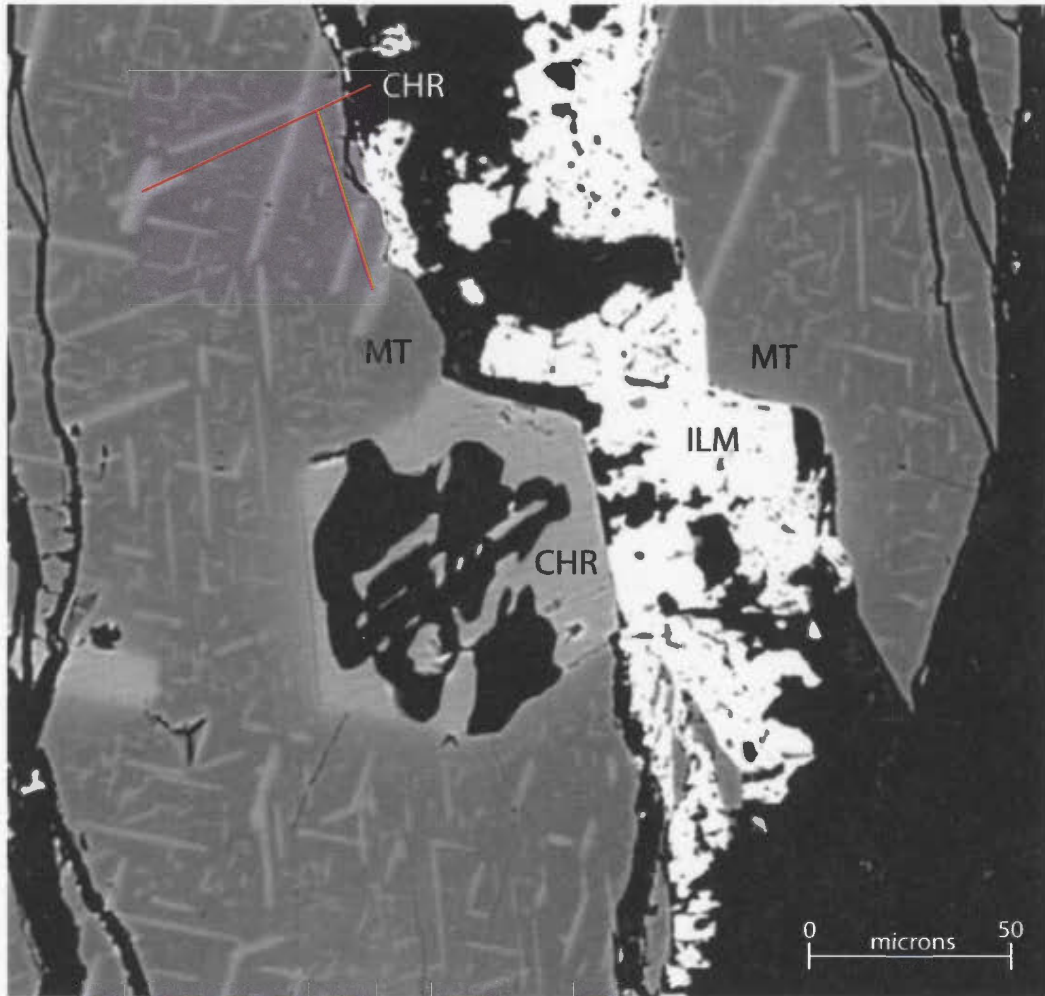


Figure 5.20 Backscatter electron image of sample RIC-21. The oxides pictured here, exhibit well-developed exsolution. The main phase, dark grey, is magnetite (MT), which is exsolving chromite (CHR). The larger chromite crystal in the centre of the image is an inclusion in magnetite, indicating that chromite crystallized before magnetite. The white phase cross-cutting magnetite is ilmenite (ILM), which is the final primary phase to crystallize. All phases are truncated by secondary alteration minerals (black).

### 5.5.2 Rhombohedral Series

Rhombohedral spinel, as the name suggests, has a rhombohedrally centered crystal structure rather than a cubic structure. Similar to the cubic spinel series, considerable solid solution occurs between the different end members. The most common rhombohedral series spinel is ilmenite,  $\text{FeTiO}_3$ , which is most accurately written  $(\text{Fe, Mg, Mn})\text{TiO}_3$  because there is extensive solid solution between Mg and Fe end-members. Experiments have demonstrated that at high temperatures, ilmenite and hematite exhibit complete solid solution. However, upon cooling, a miscibility gap develops and hematite solubility in ilmenite decreases and it exsolves (e.g. Lindsley, 1991; Deer et al., 1992).

Ilmenite from the RCLIS is relatively homogenous in backscatter images, indicating that reflected light observations were representative. Eighteen LS, 19 US and 12 xenolith analyses were collected from ilmenite. The results of these analyses are tabulated below, indicating that solid solution in ilmenite occurs, but it is not particularly pronounced. Ilmenite is presented in terms of the four end members, Fe, Ti, Mn and Mg. These data indicate that solid solution is most common in the Lower Series, where an average of ~8 wt. percent geikielite, the Mg end member is present. Lower Series and xenolith analyses do not exhibit this level of solid solution. Given the trend above, whereby minerals reflect the bulk composition of the area they were sampled from, this is an expected result – most Lower Series phases are somewhat enriched in Mg, while the compositional ranges for Upper Series and xenolith samples is more tightly constrained.

Series	Ilmenite (Ti)	Geikielite (Mg)	Pyrophanite (Mn)	Hematite (Fe)
LS Avg.	89.24	8.15	2.38	0.23
LS StDev.	9.54	9.44	0.73	0.62
US Avg.	95.32	1.94	2.38	0.36
US StDev.	1.93	2.40	0.71	0.87
Xeno Avg.	94.84	2.07	2.17	0.92
Xeno StDev.	1.91	1.21	0.61	0.93

Table 5.7. Summary of RCLIS ilmenite mineral chemistry. Lower Series samples are, on average, more Ti-poor than the Upper Series and xenoliths. Mn and Fe end members are negligible.

Figure 5.22 illustrates the distribution of ilmenite samples in  $\text{TiO}_2\text{-FeO-(1/2 Fe}_2\text{O}_3)$  compositional space. In this diagram the trends noted in the table above are not as apparent, because geikielite, the Mg end member was not plotted, thus LS samples plot closer towards the  $\text{TiO}_2$  corner due to normalizing effects. As in cubic spinel analysis, a tetrahedral diagram was not created to illustrate the solid solution between the four end-members, because the  $\text{TiO}_2\text{-FeO-(1/2 Fe}_2\text{O}_3)$  diagram is the standard method for presenting ilmenite data.

## 5.6 Sulfides

Seventeen sulfide-bearing samples were analysed, which comprise ten LS samples, six US samples and one xenolith sample. Sulfide analyses measured S, Fe, Co, Ni, Cu and Zn. The primary goal of the sulfide analysis was to characterize the composition of the main sulfide minerals, pyrrhotite, pentlandite and chalcopyrite, which were identified during petrographical study. Secondly, to quantify the trace element contents in these minerals, Ni in pyrrhotite and Co in pentlandite, for example. Finally, analysis was conducted to determine if chemical zoning not visible under microscopic observation was present.

There are a total of 120 LS analyses, comprising pyrrhotite, pentlandite, chalcopyrite and one analysis of both pyrite and millerite. There are 20 sulfide analyses from the US, comprising chalcopyrite, pyrrhotite and pyrite. Xenoliths comprise seven analyses that include just pyrrhotite and pentlandite. This section will address each phase within Upper and Lower Series individually.

### 5.6.1 Pentlandite

There are 39 pentlandite analyses from eight LS samples and one xenolith sample, RIC-51.1c. Pentlandite composition is somewhat variable, exhibiting low Ni contents and relatively high Fe contents compared to the accepted pentlandite composition of ~33%



Fe, 34% Ni and 33% S. Figure 5.23 is a plot of Ni vs Fe in pentlandite. There is no correlation between these elements. If high Fe contents were responsible for low Ni contents, then a negative correlation would be expected. This suggests that a different element is substituting for Ni. A reasonable explanation for the variation of pentlandite composition is unknown. Many pentlandite analyses indicate the presence of Co in trace to several weight percent. Figure 5.24a demonstrates the quantity of Co in pentlandite. There is no pattern of variation between Ni and Co or Fe and Co (Figure 5.24b), suggesting that the process for Co substitution in pentlandite is not predictable and does not occur in a systematic way. In addition, the spatial distribution of Co in pentlandite is irregular, as illustrated by Figure 5.25. Pentlandite does not show any degree of systematic core-rim zoning in any major constituent.

### **5.6.2 Chalcopyrite**

There are 14 chalcopyrite and one cubanite analyses, of which 11 are from the LS and the rest are from the US. The composition of chalcopyrite is quite consistent and does not contain more than 0.2 weight percent of any trace element. The most abundant trace element in chalcopyrite is Zn followed by Ni.

### **5.6.3 Pyrrhotite**

There are 89 pyrrhotite analyses from nine LS, five US and one xenolith samples. Pyrrhotite composition is somewhat variable, mainly in the ratio of Fe to S. Pyrrhotite has the general formula  $Fe_{(1-x)}S$  ( $0 < x < 0.125$ ) (Carpenter and Desborough, 1964), which includes both monoclinic and hexagonal pyrrhotite. Using the ratio of atomic metal to sulfur (M/S) it is possible to distinguish between the different pyrrhotite types as well as troilite (FeS) (Czamanske et al. (1992). In their study, they calculated that monoclinic pyrrhotite has  $M/S = 0.858-0.883$ , hexagonal pyrrhotite has  $M/S = 0.909-0.923$  and troilite  $M/S = 0.980-1.003$ . Similar to the methods of Kissin (1974) and Arnold (1971), a slightly broader range is employed in this thesis as follows:

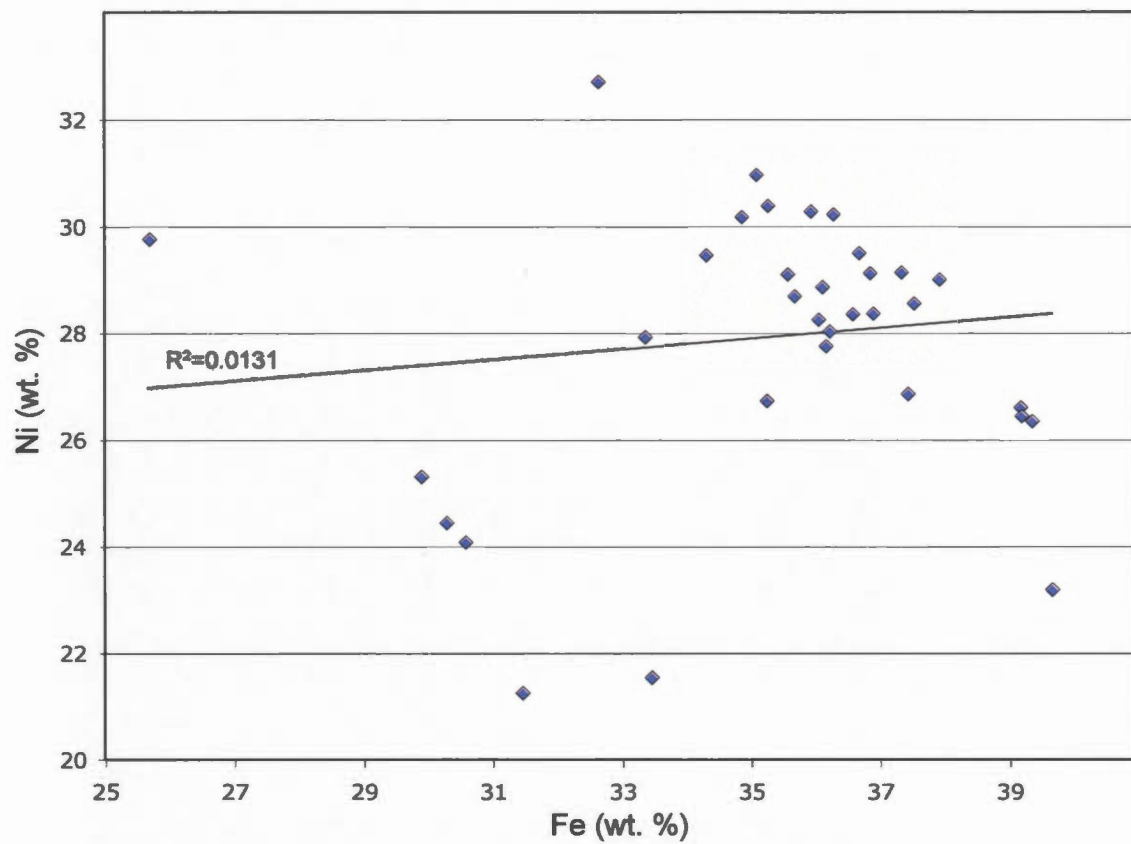


Figure 5.23 A diagram of Ni vs Fe contents in pentlandite for LS samples. The data plot as a broad cluster with several outliers. There is little correlation between Ni and Fe weight percents, suggesting that in samples with low Ni concentrations, an increase in Fe is not the reason.

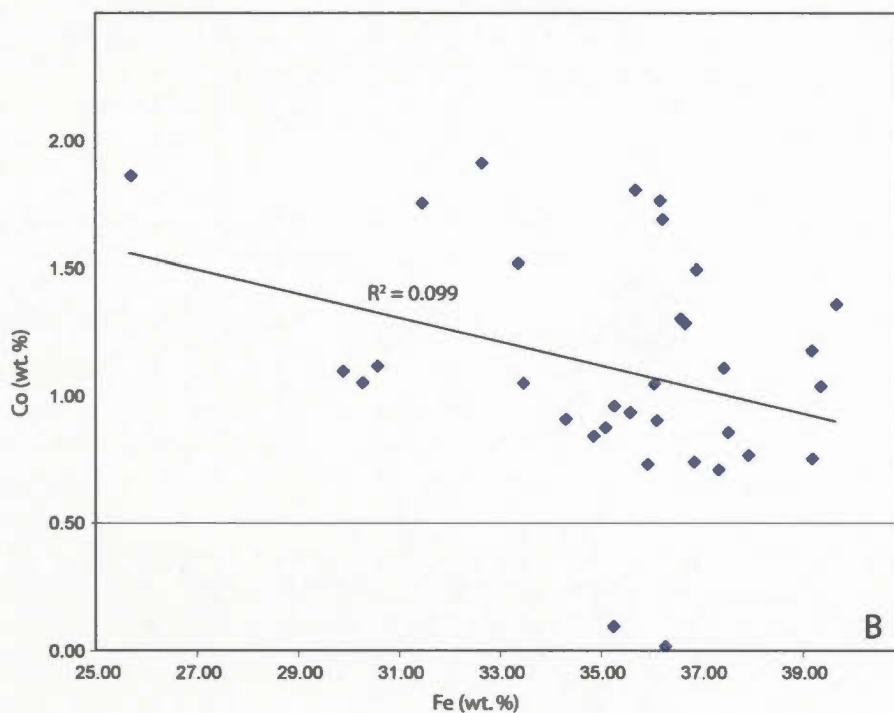
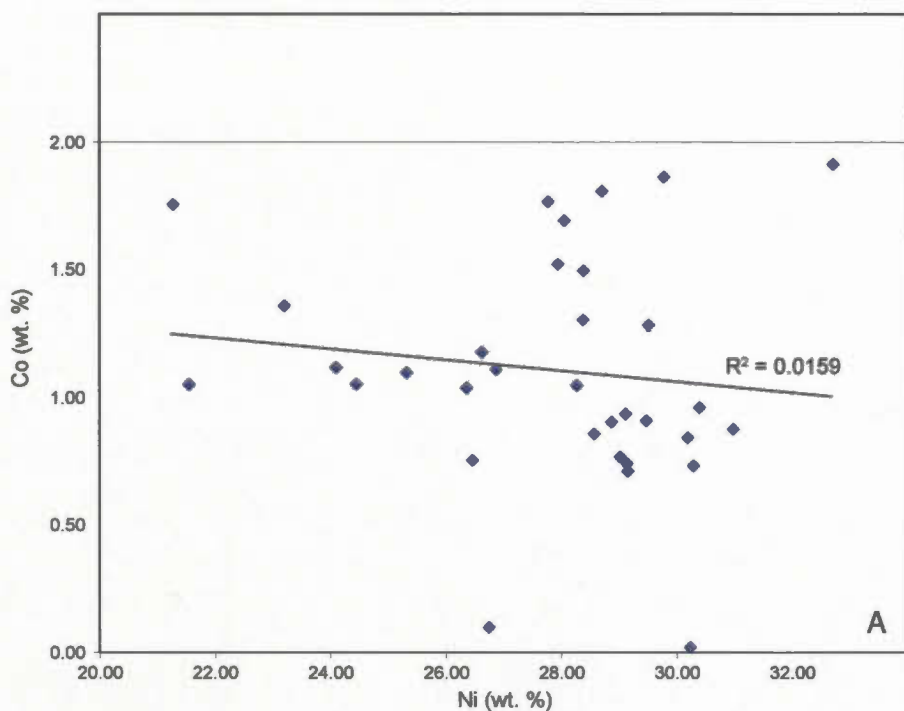


Figure 5.24 Diagrams of Co vs Ni (a) and Co vs Fe (b) in pentlandite for LS samples. Cobalt vs nickel in pentlandite does not exhibit a predictable trend (a). Cobalt vs iron in pentlandite shows an even weaker trend (b). The lack of pattern makes prediction about what causes high Co in pentlandite speculative.

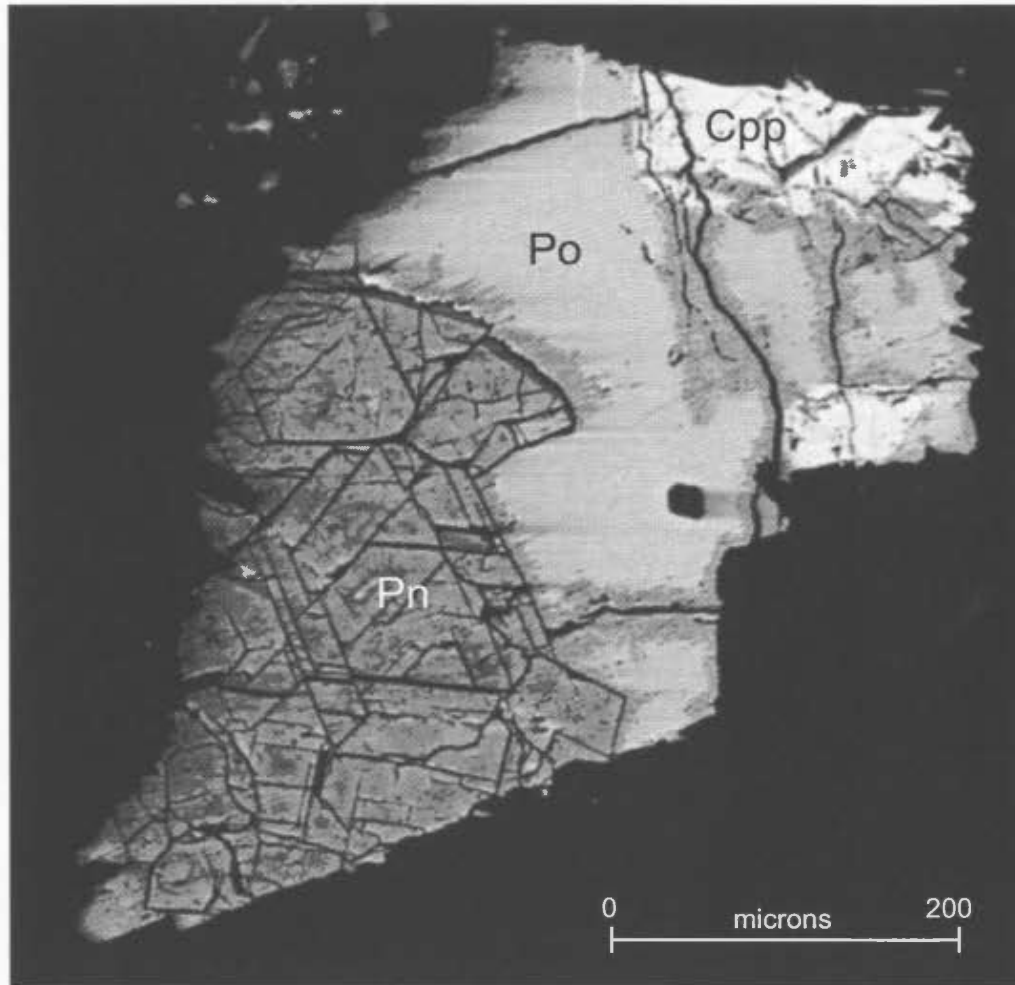


Figure 5.25. Backscatter electron image of a sulfide bleb in sample RIC-30. Pyrrhotite (Po) shows weak alteration along grain edges and pentlandite (Pn) reveals well-developed cleavage. The mottled appearance of pentlandite is due to the variable quantities of randomly distributed cobalt (the brighter the pentlandite, the more Co is present).

Monoclinic pyrrhotite: M/S = 0.858-0.883

Hexagonal pyrrhotite M/S = 0.909-0.923

Troilite M/S = 0.980-1.003

Based on the above compositional ranges, the LS samples contain 28 analyses with M/S greater than the limits of troilite, 13 analyses within the troilite range, 23 analyses within the hexagonal pyrrhotite range and 2 analyses in the monoclinic range. No troilite was detected in the Upper Series, but there are seven hexagonal and eight monoclinic pyrrhotite analyses. Of the six xenolith analyses, two are hexagonal pyrrhotite and three are monoclinic pyrrhotite and one analysis has a M/S ratio below the limits of monoclinic pyrrhotite. Figure 5.26 illustrates these patterns graphically.

Nickel does not substitute into troilite and the different pyrrhotite types in the same concentrations. The following trends, summarized in Table 5.8 are apparent from Figure 5.26. First, analyses with M/S >troilite contain the second least amount of Ni in solid solution, followed by troilite. Hexagonal pyrrhotite contains less Ni in solid solution than monoclinic pyrrhotite, although both polytypes have high standard deviations. Metal to sulfur ratios are somewhat different, because they account for all metals analysed (Fe, Ni, Cu, Co, Zn), thus an increase in Ni is generally off-set by a decrease in other metals, particularly Fe. Such is the case in RIC-02, where one analysis contains ~3.5 At. % Ni, but is also ~ 3.5 At. % lower in Fe, thus the M/S ratio is average, despite the high Ni. This analysis is not included in the table below because it is so far outside the normal range.

Phase	Ni Avg	Ni StDev	M Avg	M StDev
> troilite	0.034	0.040	1.009	0.006
troilite	0.013	0.011	1.001	0.002
hexagonal	0.098	0.118	0.944	0.038
monoclinic	0.357	0.141	0.877	0.010

Table 5.8. A summary of Ni in pyrrhotite and total M/S ratios in pyrrhotite for troilite and hexagonal and monoclinic pyrrhotite.

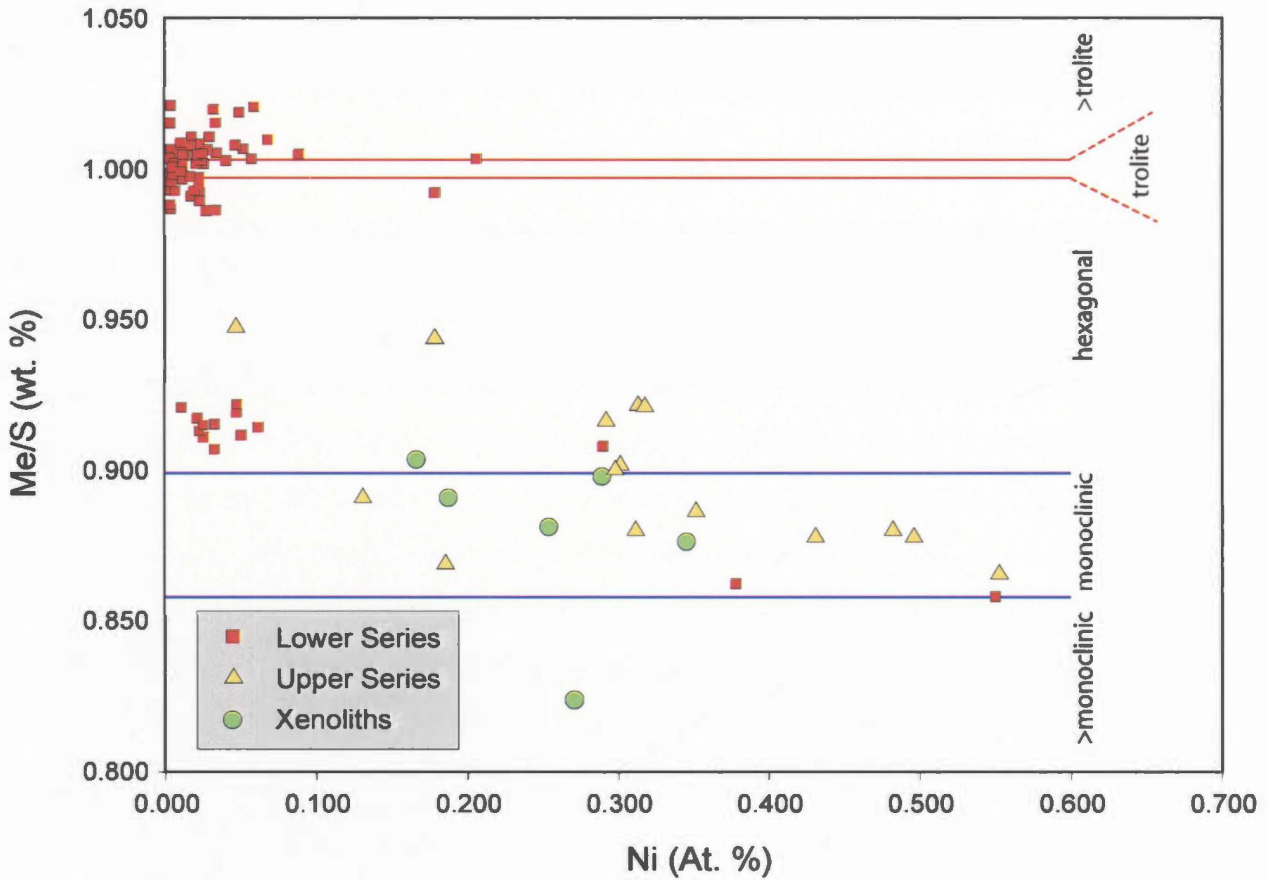


Figure 5.26 A diagram of Ni vs total metal/sulfur (Me/S) for sulfides in the RCLIS. Pyrrhotite polytypes and troilite (FeS) are a function of total metal to sulfur ratios (M/S). From these data, it is apparent that the greater the M/S ratio, the less capacity the phase has to host Ni in solid solution. Lower Series analyses were predominantly of high M/S Fe sulfides while Upper Series analyses comprise predominantly lower M/S Fe sulfides.

Troilite is easily detected in backscatter electron images because it has a higher average atomic mass relative to hexagonal and monoclinic pyrrhotite because of the higher relative metal content, but in RCLIS samples, it is not discernable in reflected light. The typical texture of troilite in Lower Series samples is as lens-like exsolution lamellae or, more commonly as the host to hexagonal pyrrhotite exsolution lamellae (Figure 5.27).

## 5.7 Summary

Plagioclase composition varies from an average of An 69 in the Lower Series to ~ An 54 in the Upper Series and ~ An 47 in xenolith samples. This compositional difference changes gradationally from Lower to Upper Series with no areas documenting sharp boundaries of different plagioclase composition. Zoning is also present at a crystal scale, with the most zoning occurring between core and rims in US samples. In many examples in the US, more albitic compositions appear to truncate relict cores with relatively more Ca-rich compositions.

Olivine composition in the Lower Series averages Fo 83 and Fo 56 for the Upper Series whereas xenolith samples average Fo 36. Olivine exhibits an overall systematic change from Mg-rich in the Lower Series to intermediate values in the Upper Series. Xenolith samples are more variable, but generally more evolved than Upper Series samples. Despite the overall evolution to Fe-rich olivine in the RCLIS, there is no systematic, predictable change in the Lower Series, from primitive basal rocks to more evolved in the upper portion of the Lower Series. Instead, a zone closer to the top of the Lower Series exhibits the highest Fo values. Fo content in olivine is quite consistent within individual olivine crystals and samples, but Ni in olivine displays no systematic zonation patterns. Instead, it is randomly distributed, or in some cases, reverse-zoned, with low Ni in the core and high Ni in the rims. Several Lower Series samples display relatively low Ni values for their Fo contents. This suggests that Ni has been stripped from these samples. Upper Series samples do not show internal zonation in Fo, and Ni is again, randomly

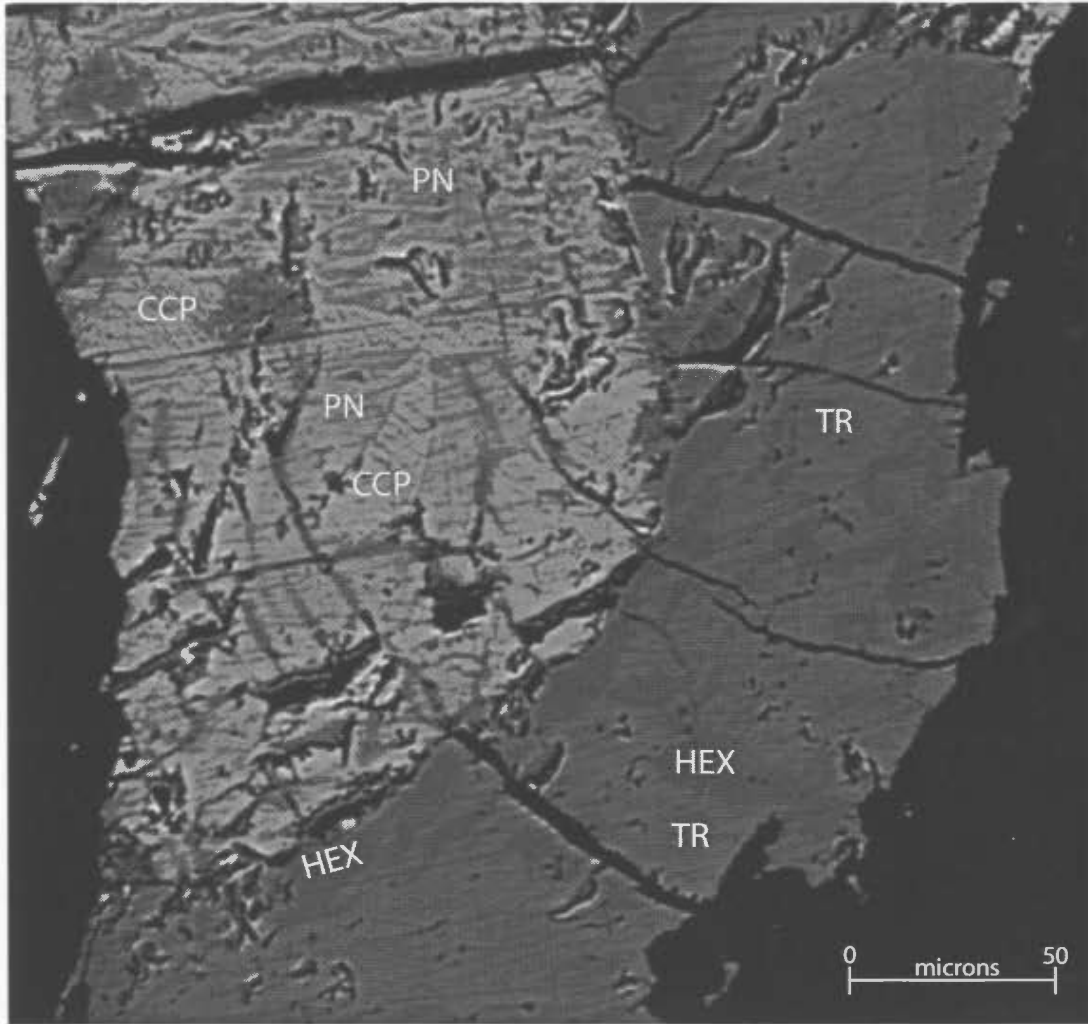


**Figure 5.27** Backscatter electron image of RIC-21 sulfides. This sample contains hexagonal pyrrhotite (HEX) exsolving from troilite (TR). In BSE images such as this, troilite appears relatively brighter than hexagonal pyrrhotite because it has a higher average atomic mass because of the higher metal/sulfur ratio compared to pyrrhotite. Also in this image is chalcopyrite (CCP) exsolving from pentlandite (PN). Note the scale bar in the lower right corner.

distributed. The samples are too widely spaced to indicate whether or not large-scale zonation of the Upper Series is present. Olivine in xenoliths is not zoned in Mg content and Ni is randomly distributed at a crystal scale.

Analyses of clinopyroxene and orthopyroxene from the Lower Series exhibit diopside and enstatite compositions, respectively. Upper Series samples are similar, but notably more Fe-rich. Xenolith samples are mainly orthopyroxene, and have a distinctly more Fe-rich composition. This trend echoes that of olivine, particularly the strongly Fe-enriched composition. Internal compositional zonation was not noted in RCLIS samples.

Amphibole is not a primary phase, occurring as reaction products mainly between pyroxene and plagioclase, but also olivine and plagioclase or olivine and pyroxene. The composition of amphibole reaction rims appears to be strongly influenced by the reactants, such that an Mg-rich olivine reacting with a Ca-rich plagioclase will produce Mg-Ca rich amphiboles.

Oxides in the RCLIS fall into two main spinel series, based on crystal structure. Analyses of cubic spinel was mostly of the normal (as opposed to inverse) spinel type, comprising Al-rich chromite. Most spinel of this type is homogenous, exhibiting little exsolution of other spinel. Locally, chromite exsolution lamellae are present in magnetite. Spinel analyses from the most Mg-rich rocks also contain an average of 11 weight percent MgO. Rhombohedral spinel comprise the second major oxide group. Ilmenite is the primary phase in this spinel series. Lower Series samples are more MgO rich, which is expressed as an average of 8 weight percent geikielite, the MgO end-member of ilmenite. Upper Series samples contain less MgO, averaging ~2 weight percent. Most rhombohedral oxides are homogenous, but locally exhibit exsolution of hematite.

Pyrrhotite, pentlandite and chalcopyrite were the primary sulfide phases analysed in the RCLIS. Pentlandite analyses are relatively Ni poor compared to the accepted

stoichiometry. A simple substitution of Fe for Ni does not adequately explain this trend. RCLIS pentlandite contains variable Co contents, but there does not appear to be any systematic zoning within pentlandite crystals or aggregates, or within samples.

Chalcopyrite analyses did not reveal any major trace element concentrations or zoning of any type. Chalcopyrite composition is normal in all respects.

Pyrrhotite is primarily hexagonal, with minor monoclinic amounts, mainly in Upper Series samples. The iron sulfide troilite was detected in several Lower Series samples by calculating the metal to sulfur ratios. Troilite contains the least amount of Ni in solid solution compared with hexagonal pyrrhotite, which contains relatively more, and monoclinic pyrrhotite, which hosts the greatest Ni concentrations. Troilite is locally massive with irregular- to lens-like exsolution lamellae of hexagonal pyrrhotite.

## Chapter 6: Red Cross Lake Intrusive Suite Sulfur Isotopes

Ten sulfide separates were prepared for sulfur isotope analysis from six Lower Series, one Upper Series and one country rock sample. All of the sulfides occurred as disseminated to blebby sulfides, as described in Chapter 3. The procedures for preparing and processing these samples are described in detail in Chapter 1 and the data are presented in Appendix 5.

The goal of sulfur isotope analyses was to characterize the isotopic composition of sulfides in the RCLIS and surrounding country rocks so that the degree of potential contamination by country rock sulfur could be assessed. A brief overview of sulfur systematics is provided below to establish a framework for the description of results.

### 6.1 An overview of sulfur isotopes

Sulphur has four naturally occurring isotopes:  $^{32}\text{S}$ ,  $^{33}\text{S}$ ,  $^{34}\text{S}$ , and  $^{36}\text{S}$ , which have relative abundances of 0.9503957, 0.0074865, 0.0419719, and 0.0001459 respectively (Coplen et al. 2002 and references therein). Sulphur isotope composition data are reported as a ratio between two isotopes, usually as a ratio of  $^{34}\text{S}/^{32}\text{S}$ , which is then compared to a standard, usually CDT (Attendorn and Bowen 1997; Nielson 1979) and is called  $\delta$ -notation (Nielson 1979), and follows the form:

$$\delta^{34}\text{S}(\text{‰}) = \left[ \frac{R_{sa} - R_{std}}{R_{std}} \right] \times 1000 \quad \text{where } R = \frac{^{34}\text{S}}{^{32}\text{S}} \text{ (Nielson, 1979)}$$

sa= sample; std= standard

based on these calculations, a positive  $\delta^{34}\text{S}$  value, expressed in per mil (‰), is enriched in  $^{34}\text{S}$ , and depleted in  $^{32}\text{S}$ . It is termed “heavy”. Conversely, a negative  $\delta^{34}\text{S}$  per mil is said to be  $^{34}\text{S}$  depleted ( $^{32}\text{S}$  enriched) and is termed “light”.

Terrestrial sulfur reservoirs occur in a multitude of geological settings with vastly different isotopic compositions. Isotopic variations of sulfur occur because sulfur isotopes are easily fractionated. Mass-dependent isotopic fractionation is the most widespread means of sulfur fractionation, partly because of the many valence states (-2, 0, +4, +6) (Brownlow, 1996; Attendorn and Bowen, 1997). Geologically speaking, the two principal processes that fractionate sulphur isotopes are: 1) the inorganic precipitation of sulfates from seawater as evaporites, and 2) bacterial sulphate reduction (BSR) and its subsequent incorporation into sedimentary pyrite e.g. framboidal pyrite (Strauss 1997; Nielsen 1979). Sedimentary pyrite, which is often cited as a source of sulfur in orthomagmatic sulfide deposits, exhibits a  $\delta^{34}\text{S}$  range from approximately -50‰ to +25‰ (Rollinson, 1993). Typical reduced sulfides in an open reservoir exhibit negative  $\delta^{34}\text{S}$  isotope ratios (Strauss, 1997). MORB and other magmatic rocks exhibit a far more reserved range, from  $\sim \pm 2$  ‰ for the former to  $\sim \pm 10$  ‰ for the latter.

## 6.2 $\delta^{34}\text{S}$ isotope results

$\delta^{34}\text{S}$  ratios in the Lower Series range from -1.8 ‰ in RIC-21, to +2.6 ‰ in RIC-65. Two Upper Series sulfides from RIC-15 and 51A have  $\delta^{34}\text{S}$  ratios of +1.5 ‰ and 1.5 ‰, respectively. One xenolith sample was used as a proxy for country rock, RIC-53, (a biotite-garnet schist), exhibits a  $\delta^{34}\text{S}$  value of +3.8 ‰, which is the most positive  $\delta^{34}\text{S}$  value from the suite (Figure 6.1). Although RIC-53 is a xenolith, its mineralogy and overall appearance is consistent with descriptions of country rock (e.g. Kean, 1977). This assumption is further supported by an abundance of this lithology as xenoliths throughout the RCLIS. Table 6.1 presents the RCLIS  $\delta^{34}\text{S}$  ratios and the sulfide mineral that was analysed. In most samples, sulfides were fine-grained and in low concentrations such that it was not possible to separate the different phases. Most LS sulfide separates comprise a mixture of pyrrhotite and pentlandite. The US sample is only pyrrhotite, and RIC-53 comprises pyrrhotite and pyrite.

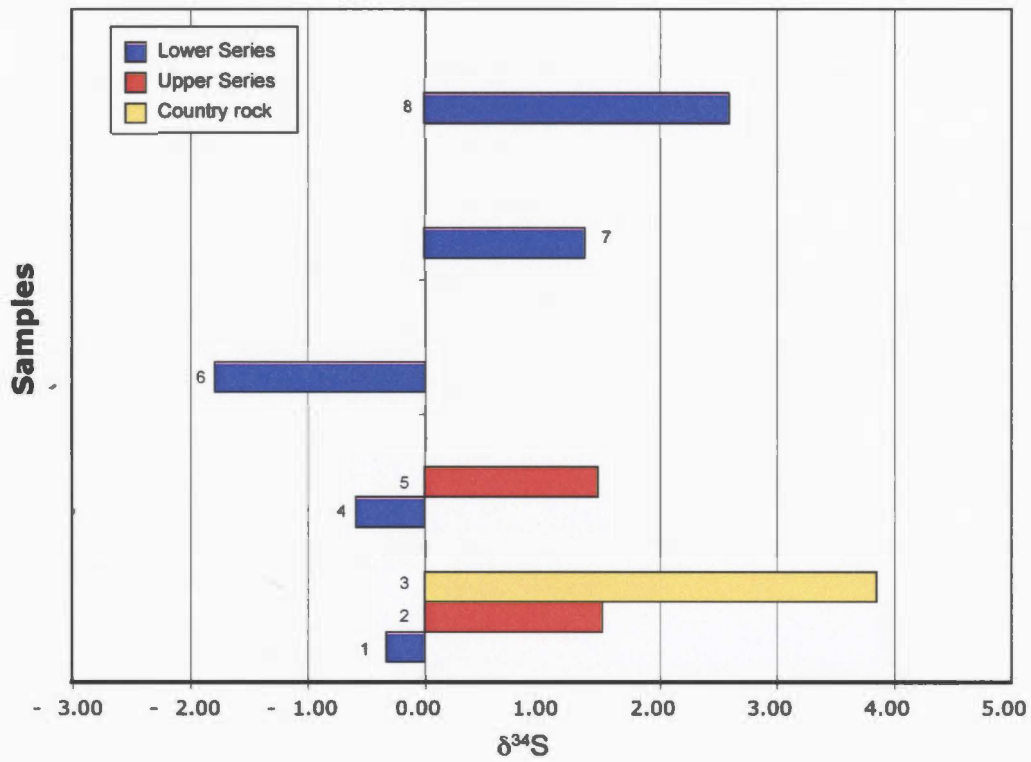


Figure 6.1 A diagram of  $\delta^{34}\text{S}$  ratios for the RCLIS. Lower Series samples exhibit the widest isotopic range amongst igneous RCLIS samples. One xenolith sample, RIC-53, is used as a proxy for country rock so that potential sulfur contamination from country rock can be evaluated. As discussed in the text, it appears that only local S assimilation has occurred in the RCLIS.

Sample ID	Series	$\delta^{34}\text{S}$ VCDT (‰)	Rock type	Phase
RIC-02	Lower	- 0.3	dunite	Po + Pn
RIC-06	Lower	- 0.6	troctolite	Po + Pn
RIC-21	Lower	- 1.8	melatroctolite	Po + Pn
RIC-22	Lower	1.4	leucogabbro	Po + Pn
RIC-65	Lower	2.6	serpentine	Po + Py
RIC-15	Lower	1.5	leucogabbro	Po
RIC-51A	Upper	1.5	leucogabbro	Po
RIC-53	Xenolith	3.8	Bt-Grt schist	Po + Py

Table 6.1. A summary of  $\delta^{34}\text{S}$  ratios from the RCLIS. Most LS samples comprise pyrrhotite and pentlandite, while the rest are pyrrhotite and/or pyrite. No chalcopyrite separates were analysed because its low abundance made concentration of a suitable size difficult.

Figure 6.1 is a diagram of all RCLIS  $\delta^{34}\text{S}$  ratios. Each sample is plotted as a point along a scale of positive and negative  $\delta^{34}\text{S}$  ratios in per mil units.

Figure 6.2 illustrates the  $\delta^{34}\text{S}$  values for a range of igneous rocks and volcanic gases (e.g.  $\text{H}_2\text{S}$ ,  $\text{SO}_4$ ) (Rollinson, 1993). This diagram is useful for comparing  $\delta^{34}\text{S}$  samples against known S reservoirs. The narrow range for all of the RCLIS samples is indicative of a relatively primitive sulfur source. Aside from the supracrustal country rock sample, RCLIS samples fall within the range of unfractionated MORB  $\delta^{34}\text{S}$  values. The xenolith sample is somewhat more positive than the RCLIS igneous samples. A value of +4 ‰ lies within the range of marine shale and pyrite (Rollinson, 1993), which is compatible with the host rock, which is presumed to have been deposited in a marine environment (Kean, 1977).

The limited amount of data and limited compositional range between the country rock sample and igneous RCLIS samples does not permit the modeling of sulfur mixing. However, given the range of  $\delta^{34}\text{S}$  compositions within the Lower Series in particular, especially in light of the lithological and geochemical similarities, it is possible that if assimilation of sulfur from country rock xenoliths occurred, it was at a local scale rather

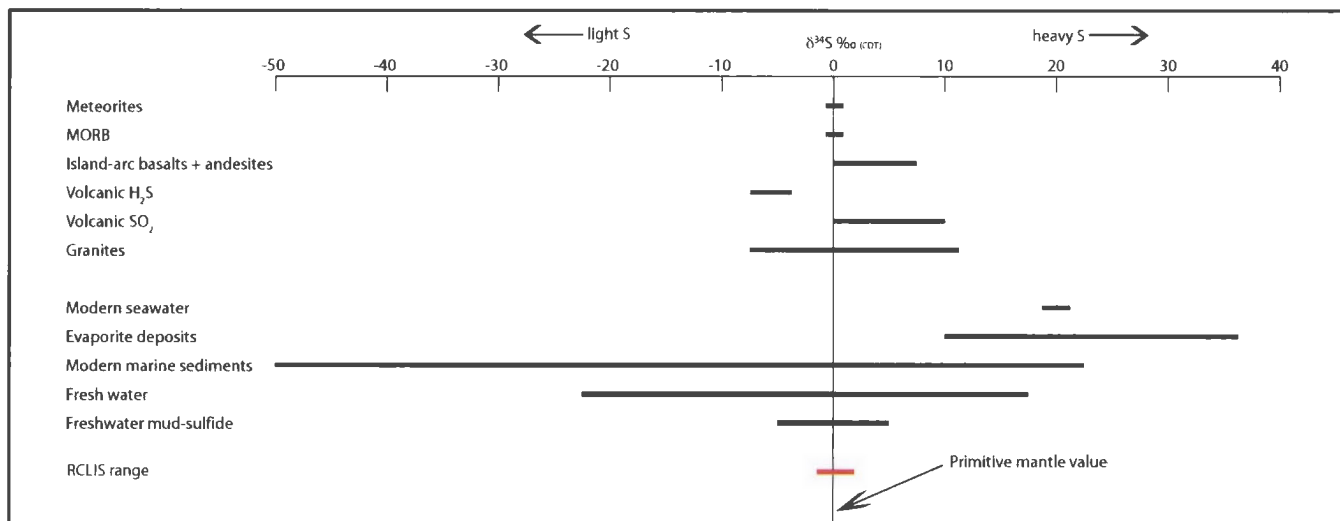


Figure 6.2 A compilation diagram of  $\delta^{34}\text{S}$  sulfur ranges from various igneous sources (top) and sedimentary or water reservoirs (bottom). The various ranges are compiled in Rollinson (1993). RCLIS igneous samples are presented at the bottom of the diagram for comparative purposes. It appears that RCLIS samples are most similar to MORB and island-arc + andesites, which is compatible with other data presented above.

than widespread assimilation and subsequent homogenization. For example, the most positive  $\delta^{34}\text{S}$  values (*i.e.* closest to RIC-53) are located relatively close to potential zones of contamination. RIC-65 for example, is < 1 km from the basal contact of the RCLIS, and mapping in this area noted locally abundant partially digested biotite-garnet schist xenoliths. Likewise, in the Upper Series, RIC-15 is located near the assumed western contact between metasedimentary and metavolcanic rocks and the RCLIS. It is possible that the RCLIS consumed volcanic (island-arc ?) country rock in the vicinity of RIC-15, giving it a positive  $\delta^{34}\text{S}$  value. Conversely, RIC-21, which exhibits the lowest  $\delta^{34}\text{S}$  value of RCLIS samples, is located relatively distant from observed sites of contamination, such as xenolith-hosting shear zones, as is the case for RIC-51A.

### **6.3 Summary**

Ten sulfide concentrates were analysed for  $\delta^{34}\text{S}$  in the RCLIS. These samples range from -1.79 ‰ to 2.6 ‰ for igneous samples and one xenolith sample assumed to represent the country rock exhibited a value of +3.85 ‰. The most likely explanation for these results is that igneous samples had an initial  $\delta^{34}\text{S}$  composition close to 0 ‰, which is equivalent to MORB  $\delta^{34}\text{S}$  compositions. There is ample field evidence for contamination of the magmas by country rock xenoliths, such that during emplacement of the RCLIS, country rock sulfur was likely assimilated. Assimilation however, may have occurred only at a relatively local scale. This process would explain why samples that are located closest to zones of potential contamination exhibit  $\delta^{34}\text{S}$  values closest to that of the country rock.

## Chapter 7: Discussion and conclusions

### 7.1 Overview

Mapping and a detailed, multifaceted geochemical evaluation of the Red Cross Lake Intrusive Suite was conducted to evaluate its Ni-Cu-PGE potential and define its emplacement history. The results from this study indicate that:

1. The RCLIS is far more heterogeneous than previous mapping indicated. Mapping, petrography and geochemistry established three main lithogeochemical subdivisions: the Lower Series, Upper Series and Transition Zone.
2. Lower Series rocks exhibit ultramafic to mafic compositions, cumulate olivine and plagioclase, poikilitic plagioclase, CPX and subordinate OPX.
3. LS geochemical trends indicate that fractional crystallization has resulted in progressively more evolved compositions. The most mafic samples are not located at the base of the intrusion, but part way up the stratigraphy of the LS.
4. Olivine is rare in the US and samples are dominated by laths or irregular anhedral plagioclase, partially replaced poikilitic to subpoikilitic CPX and subordinate OPX and Fe-Ti oxides.
5. US rocks exhibit mafic compositions with an Fe-Ti enriched signature, and are more fractionated than LS rocks. Geochemical signatures are more homogenous, suggesting that most fractionation occurred prior to emplacement, possibly in a parental magma chamber.
6. Transition Zone rocks exhibit a composition that overlaps both LS and US rocks, and the zone is defined mainly by petrography. The TZ separates the LS and US stratigraphically and exhibits irregular, gradational contacts. Locally, TZ boundaries are defined by elongate belts of sheared, xenolith-bearing zones. Xenoliths comprise country rocks and autoliths and are cemented by pegmatitic, metasomatised ultra-evolved magmas (e.g. Fo=10).

7. Microprobe data indicate most LS olivines contains normal Ni contents relative to their Fo contents. Ni-depleted magmas occur in the SW corner of the LS, at the west end of the Red Cross Lake. Some US plagioclase with strongly embayed internal zones exhibit core compositions similar to those of LS plagioclase and rims with typical US compositions, suggesting that US magmas entrained LS plagioclase during emplacement.
8. Most RCLIS igneous sulfide separates exhibit mantle-like  $\delta^{34}\text{S}$  signatures, but some results suggest that localized crustal S contamination occurred. Normative calculations suggest that the country rock contains several wt. % sulfides, thus if widespread contamination had occurred, sulfides would be more abundant in the RCLIS.

## **7.2 Discussion**

### **7.2.1 Evidence for multistage emplacement history**

Whole rock geochemical data demonstrate that the Upper and Lower Series are geochemically distinct, but that they most likely originated from the same parental magma. The data define the primitive composition of Lower Series samples, and a relatively fractionated Upper Series composition. The spatial distribution of mafic samples, however, provides evidence that emplacement of the LS did not occur as one large pulse of ultramafic magma that subsequently differentiated, forming the layered LS rocks. Some of the most mafic compositions in the LS occur relatively far north of the assumed basal contact, whereas less mafic samples lie stratigraphically below them. This pattern may be indicative of a series of pulses of magma with slightly different compositions being emplaced as sills or sheets. In this model, the Upper Series would represent the latest major pulse of magma, which originated from the same parental magma chamber as the LS magma. The distinct gap between the average LS and US compositions in most bivariate and ternary diagrams would be produced if a short delay in an otherwise relatively continuous series of magma injections occurred between the emplacement of LS and US magmas. If the parental magma continued to fractionate it

may be possible that when emplaced, US magmas would exhibit a distinctly more evolved composition, compared to LS rocks. Other bivariate diagrams from Chapter 4, such as  $\text{TiO}_2$  vs  $\text{SiO}_2$  support the strongly evolved nature of US samples, but also highlight the relatively evolved composition of several LS samples. It may be possible that the large pulse of magma responsible for the US was also injected laterally into some regions of the LS.

Mineral geochemistry provides further support to this model. In particular, olivine compositions are distributed in a reverse pattern compared to many intrusions, in which the most primitive olivine compositions occur at the basal contact and become more evolved upwards. If the LS formed by a single pulse of mafic to ultramafic magma, the most primitive compositions would be expected to occur at the base of the intrusion and evolve to more Fe-rich compositions towards the top of the LS. If the LS was emplaced through a series of pulses, it would be possible to attain the present compositional signature. A late pulse of primitive magma into the upper part of the LS could explain these compositions.

Olivine in several samples near the upper portion of the US (e.g. RIC-63) exhibits olivine compositions and plagioclase compositions that are typical of the upper Lower Series to lowest Upper Series. A breccia belt is present near the olivine-bearing sample (2-300 m), but is not directly related to the sample location. However, a breccia belt this far north suggests that the area is dynamic, despite the surrounding homogenous rocks. It is possible then that the area surrounding RIC-63 represents a separate pulse of relatively primitive magma, or that the sample is from a large block that was transported from lower in the system. Given the difficulty of entraining a large, relatively dense block of crystallized rock and transporting it upwards several kilometers through viscous magma, the former explanation is more reasonable.

Petrography and mineral chemistry exhibit evidence that during the emplacement of the US, LS plagioclase crystals were entrained and are preserved in the US. Uncommon megacrystic (relative to the average US plagioclase grain size) plagioclase crystals in the US exhibit embayed, corroded internal textures. The core composition of some of these crystals is similar to the upper portion of the LS and rim compositions similar to the US. This suggests that US magma interacted with, and entrained material from the LS, suggesting that it was emplaced in a later pulse relative to LS rocks.

Field geology provides compelling evidence for a multistage process of emplacement. The presence of xenolith belts that are parallel to layering in the LS and the US may indicate the preservation of roof rocks or basal country rocks that have not been completely digested during emplacement of the RCLIS into country rocks. Emplacement of sheet-like intrusive rocks commonly exploits weaknesses or fabrics in the host rock (e.g. Pollard et al., 1975). The orientation of layering in the RCLIS appears to mimic the orientation of the country rock fabric as mapped by Kean (1977), suggesting that regardless of whether or not the RCLIS was emplaced as sheets, it appears to have exploited the metamorphic fabric of the Victoria Lake group. It is possible the xenolith belts represent preserved remnants of steeper roof rocks that were not completely assimilated during emplacement. Pollard et al. (1975) indicate that host rocks are commonly entrained and deformed in sheeted intrusions; a common feature of the RCLIS xenolith belts. The lack of xenolith belts in the LS, where sheeted pulses of magma are invoked to explain the reversed olivine composition may be because they are covered by the lake and glacial overburden, but given it seems more probable that the magmas were hotter thus assimilation was more effective and xenolith belts in the LS are not preserved as commonly.

The north-dipping orientation of magmatic layering is evidence that the reverse compositional trend in olivine does not occur because the LS is “upside down” (i.e. crystallized as a large body of ultramafic magma from the north to the south). It would be

expected that layering and cumulate textures would indicate top to the south if the LS was in fact upside down.

### **7.2.2 Evaluation of the economic potential of the RCLIS**

The key criteria for a mafic or ultramafic intrusion to host economic quantities of Ni-Cu-PGE sulfide mineralization are summarized by Naldrett, (2004).

1. That a magma contains sufficient concentrations of Ni, Cu and PGE such that, if immiscible sulfides develop within it, these sulfides will become enriched in these metals.
2. That the magma becomes saturated in sulfide and segregates an immiscible sulfide phase.
3. That these sulfides react with a sufficient quantity of magma to concentrate chalcophile elements to an economic level.
4. That the sulfides are themselves concentrated in a restricted locality where their abundance is sufficient to constitute ore.

The RCLIS appears to satisfy criteria one and two locally, but it is difficult to ascertain whether or not criteria three and four are met.

Criterion 1 is met for Ni and Cu by most olivine-bearing LS magmas on the basis of olivine and whole rock geochemistry, but it appears that PGEs occur in considerably lower concentrations than would be expected for a magma with these Ni concentrations McDonough & Sun, (1995). Many samples in the LS contain over 1500 ppm Ni in whole rock geochemical data and olivine microprobe data indicate that many olivine crystals contain abundant Ni. For example, RIC-02 contains > 2100 ppm Ni in whole rock and olivines average nearly 1900 ppm, suggesting that sulfides may contain the remaining Ni. Compared to other economic Ni-Cu deposits, the Ni compositions of olivine and whole rock appear to be sufficient, but there is no set “limit” as to how much Ni should be

present in a magma to form Ni sulfides. For example, a study by Li et al. (2000), indicates that the average Ni composition of unmineralized to disseminated ( $S \leq 0.5$  wt. %) rocks at Voisey's Bay such as normal troctolite, varitextured troctolite and feeder olivine gabbro vary from 308, 939 to 74 ppm, respectively.

R-factor is the ratio of the mass of silicate magma to sulfide liquid in a crystallizing intrusion (e.g. Campbell and Naldrett, 1979 and Kerr and Leitch, 2005). This relationship is critical in determining the potential for silicate magma to evolve sulfides with an economic tenor. A detailed discussion of R-factor geochemistry is beyond the scope of this thesis, but essentially, R-factor suggests that the greater the mass of silicate liquid that interacts with a given mass of sulfide liquid, the greater the R-factor. Therefore, if a silicate magma exhibited a low Ni concentration, but a large volume of that low-Ni magma interacted with a small volume of sulfide liquid during emplacement, the sulfides could potentially scavenge Ni from the magma and attain a high Ni tenor, similar to a smaller volume of magma with a higher Ni content. If the RCLIS was emplaced as a series of pulses, undepleted magma pulses would be able to interact with a sulfide liquid, raising the Ni-tenor of the liquid. Locally, the presence of high-Mg, low-Ni olivines suggests that this process may have occurred in the LS.

The presence of primary sulfide blebs in virtually every LS sample indicates that Criteria 2 is met by the RCLIS. However, calculations in Chapter 4 suggest that the volume of sulfide that evolved from the LS is quite low.  $\delta^{34}\text{S}$  values indicate that there was only local sulfur assimilation by the magma, which might be a reason for the relatively low volume of sulfides in the LS. It is possible that a larger volume of sulfides formed, but it may be undiscovered, or the sulfides evolved in the parental chamber and were not emplaced along with silicates. Without further mapping, mineral chemistry data and geophysical investigations, the postulated existence of a significant volume of sulfides remains pure speculation. Li et al. (2000) indicate that at Voisey's Bay the barren Mushaua intrusion did not experience the assimilation and subsequent sulfide saturation

that the magma that became Voisey's Bay did. Therefore, it appears that in many intrusions where adequate Ni is present, the availability of S is the make or break factor as to whether or not Ni-sulfides form.

It is difficult to evaluate Naldrett's 3<sup>rd</sup> and 4<sup>th</sup> criteria because as of yet, no large sulfide occurrences are known in the RCLIS. It is possible that large volumes of sulfides formed, and were concentrated (economic or sub-economic levels), but the general lack of exploration in this intrusion and the lack of outcrop (from till or lake cover) experienced during mapping has hidden these sulfide bodies. On the other hand, it is also possible that the sulfides observed during mapping are representative of the sulfides in the RCLIS. If the model advanced above is correct and the RCLIS was emplaced by several pulses of magma, the RCLIS has the potential to have a high R-factor and produce high-grade Ni-sulfides, because petrography indicates that sulfides were present for the duration of olivine crystallization. A pulse of undepleted olivine-bearing magma interacting with sulfides during emplacement is a potential mechanism for upgrading a small volume of low-grade sulfides. The presence of the Ni-depleted magma near the SW corner of Red Cross Lake may be a sign that during emplacement, this pulse of magma interacted with a sulfide liquid stratigraphically lower, which stripped Ni.

### **7.3 Conclusions**

The potential for the RCLIS to host economic accumulations of Ni-Cu-PGE mineralization is weak- to moderate, but could be more completely investigated with geophysical or other subsurface exploration techniques. Textures and mineralogy in the Lower Series are encouraging from an exploration perspective, but more work is required.

In the end, however, combined evidence from olivine probe analyses, sulfide petrography and normative sulfide calculations suggest that only small, isolated volumes of sulfide liquid evolved and interacted efficiently with nearby olivine in the RCLIS.

## Chapter 8: Steel Mountain Anorthosite field geology

### 8.1 Introduction

Mapping during the summer of 2004 identified several interesting textural features in the SMA and was successful in further delineating the extent of norite bodies. First, mapping was able to delineate between a lilac- to purple-coloured anorthosite and normal white- to grey anorthosite, as described by Baird (1954) and van Berkel *et al.* (1987). The pink- to purple coloured anorthosite is commonly associated with orthopyroxene and clinopyroxene in irregular lens-shaped bodies within normal, white-grey anorthosite. Although the contacts between all units in the map area are gradational and recrystallized, it is possible to locally define a boundary between white, megacrystic to granular plagioclase anorthosite (normal anorthosite), and lilac- to purple medium-grained, granular, recrystallized anorthosite. Figure 8.1 is a geological map of the study area in the SMA; units and textures are described in detail below; the bedrock in this map is derived from Colman-Sadd and Crisby-Whittle, 2004.

Within the study area, orthopyroxene and clinopyroxene, which commonly occur together in a ratio of ~ 5:1, exhibit three, locally four, distinctive textures. First, along the margins between normal and pink anorthosite, there is an increased amount of leucogabbro compared to leuconorite, although they are texturally identical. Pyroxene ranges from 10 to 15%, occurs as deformed sheets, lenses, and discontinuous stringers, and is surrounded by granular, recrystallized, penetratively deformed fine- to medium-grained white anorthosite. The above pyroxene locally cross-cuts the main fabric of the anorthosite or leucogabbro or leuconorite, and there is an advanced degree of chloritization and/or uralitization in these rocks (Figure 8.2).

Secondly, when approaching units mapped as norite by van Berkel *et al.* (1987), plagioclase becomes pink coloured, has a granular texture, and shearing diminishes slightly, although initially pyroxene grains are still relatively altered to amphibole and

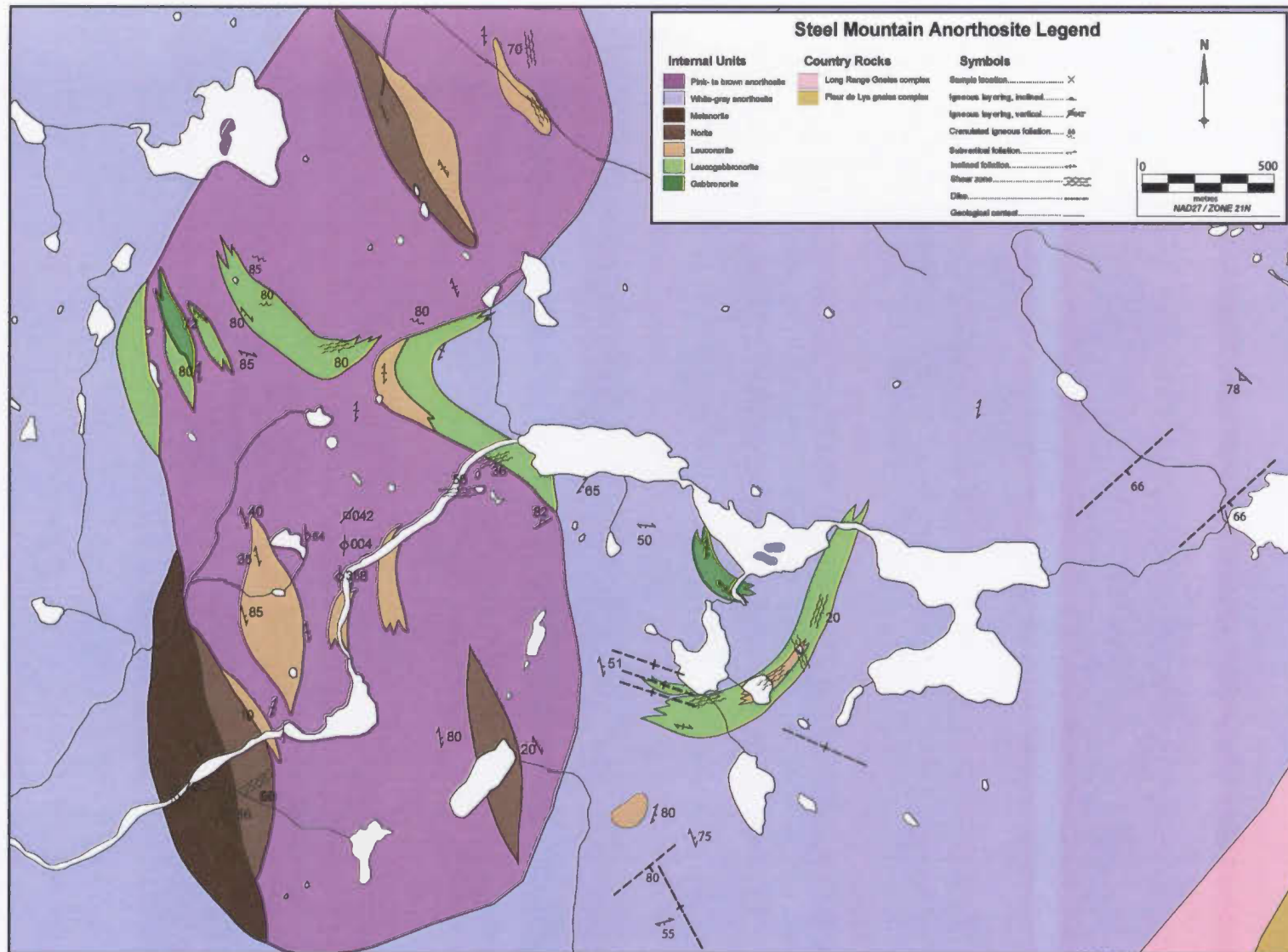


Figure 8.1 A geological map of the SMA. A detailed description of each unit is provided in Chapter 8. Note legend in top right corner of the map. North is towards the top of the map. The geology outside of the mapped area was modified after Colman-SAdd and Crisby-Whittle, 2004.

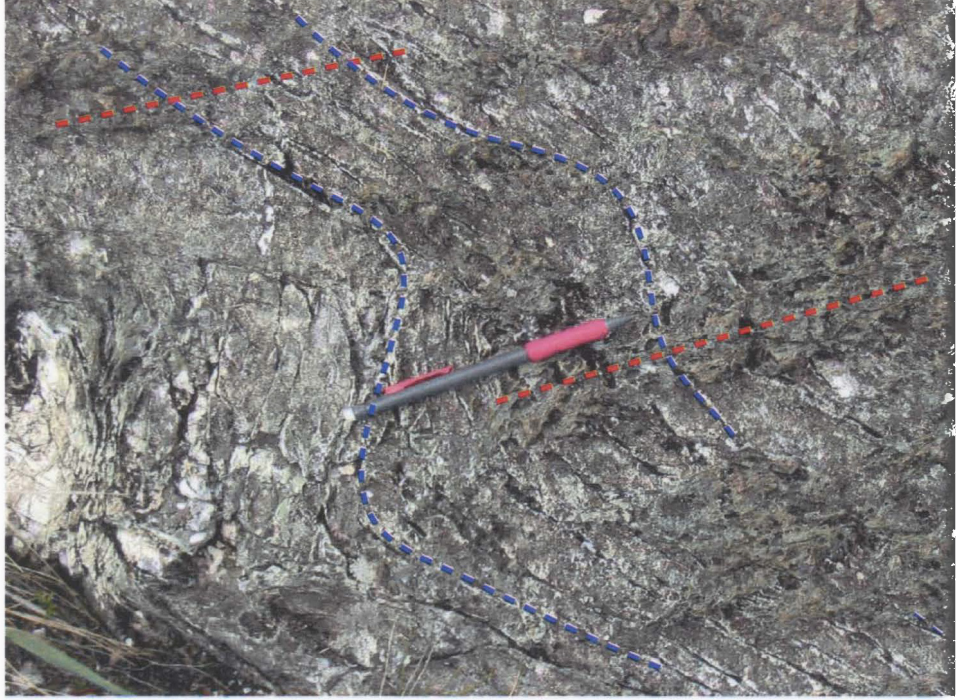


Figure 8.2 This image is from SMA-04. In the vicinity of this location, at the margins of pink plagioclase/leuconorite areas, white anorthosite is cut by pyroxene, which occurs as chloritized and amphibolitized sheets (red dashed lines) that cut the main fabric of anorthosite (blue dashed lines).

chlorite. Orthopyroxene is the dominant pyroxene in the interiors of the leuconorite bodies, occurring as sheared, weakly porphyroclastic, and locally approximately equigranular crystals or aggregates of crystals that constitute up to 20 % of the rock. In many instances, orthopyroxene appears to be metastable and it is partially altered to lower grade assemblages as indicated above.

Finally, the two other predominant textures of pyroxene commonly occur together, although it is not apparent if there is interdependence between them. Here, orthopyroxene occurs as mega-oikocrysts or glomeroporphyrocrysts, sometimes up to 30 cm in diameter, in association with very coarse-grained subhedral to granular pink to dark pink-purple plagioclase (Figure 8.3a). This texture is found only in the most mafic regions of the map area, and is spatially associated with intercumulus, megacrystic pyroxene (Figure 8.3b). Texturally, the intercumulus pyroxene appears to be later than the poikilitic pyroxene. Where the intercumulus pyroxene occurs, a large pyroxene-free halo commonly surrounds the mafic clusters, and is essentially pure plagioclase (i.e. pyroxene accumulations are surrounded by a depletion halo) (Figure 8.4). The pyroxene-rich and anorthosite-rich zones define a zone of weakly layered rocks that might preserve primary igneous textures, or only weakly deformed primary textures (Figure 8.5). The process that would lead to this texture is unknown, but it is quite possible that it results from remobilization of interstitial (mafic) melt during high temperature emplacement and recrystallization within a partially solidified crystal framework. (Lafrance et al., 1996; Hunter, 1996; Ron Voordouw, pers. comm., 2004).

Recrystallization in plagioclase is ubiquitous in the map area, but variable degrees of recrystallization do occur. Along the margins between “normal” plagioclase and “coloured” plagioclase, small angular, fragmental porphyroclasts of pale pink plagioclase are suspended in a granular white plagioclase matrix, implying mixing between the two, probably during deformation related to emplacement. Aside from the most mafic regions mentioned above, where plagioclase is still preserved as euhedral to subhedral cumulate

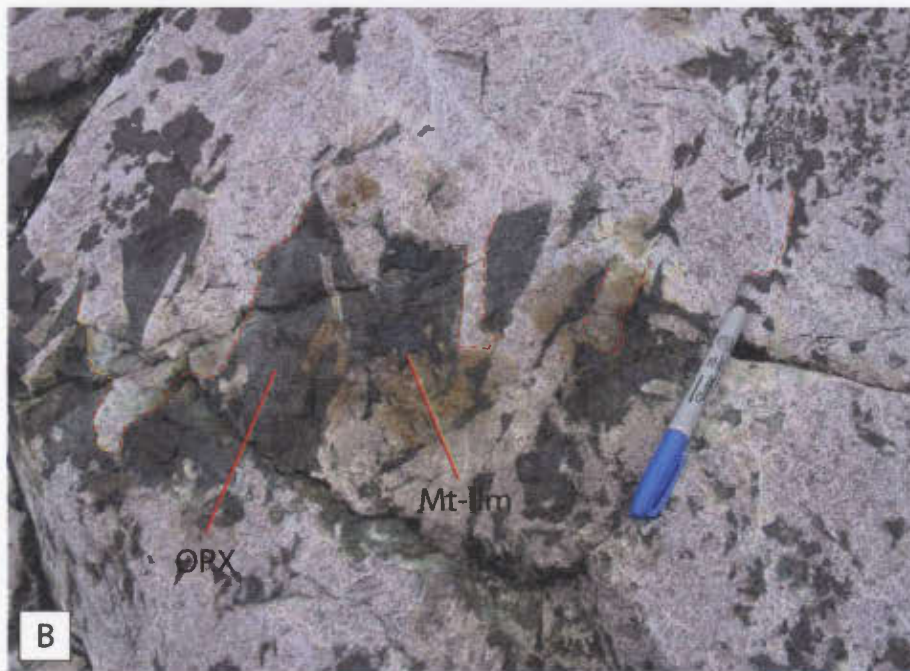


Figure 8.3 Examples of pink plagioclase in norite from below Lookout Pond hydro dam (SMA-32 to 44). (a) mega-oikocrysts or glomeroporphyrocrysts of OPX are separated by granulated megacrystic pink plagioclase. These OPX crystals or aggregates are somewhat elongated and define a weak layering trend; (b) the above OPX texture is locally associated with very coarse-grained intercumulus OPX. Although granulated or altered, the outlines of plagioclase in this image are denoted by the angular contacts with OPX and some contacts are outlined in red dashed lines locally. Coarse-grained interstitial magnetite and ilmenite are spatially associated with OPX. Note the markers for scale in both images.



Figure 8.4 In the area below Lookout Pond reservoir (SMA-32-44), mega-oikocrysts, or glomeroporphyrocrysts of OPX are spatially associated with large areas that are nearly completely devoid of pyroxene and Fe-Ti oxides. In some cases, the coarse-grained, interstitial OPX appears to protrude into these “pyroxene depletion halos” (blue arrows). It is possible that during emplacement, minor readjustments or relaxations of the crystal mush promoted interstitial exchange and aggregation of oikocrystic OPX into the coarse-grained interstitial texture of OPX.



Figure 8.5 On an outcrop scale, the textures described in Figures 9.2 and 9.3 are weakly layered (dashed red line). This layering, photographed here at SMA-44, is consistent for several hundred meters down the river bed below the Lookout Pond reservoir. It is possible to observe the “pyroxene depletion halos” and both OPX textures in this image. Note compass for scale.

megacrysts, plagioclase in the pink anorthosite or norite rarely occurs as megacrysts and instead is generally equigranular on an outcrop scale, although medium to coarse-grained purple porphyroclasts in the pink matrix plagioclase are locally common. This type of texture is quite typical of massif-type anorthosites, and is indicative of widespread recrystallization during emplacement (*e.g.* Hunter, 1996).

Magnetite commonly occurs in association with large very coarse-grained lenses or clusters of orthopyroxene, where it forms irregular clots, cubes, rims, lenses or dike-like linear concentrations, or replaces pyroxene (Figure 8.6). Smaller clusters of orthopyroxene with or without oxides locally display a thin corona of rounded red garnets. These textures are common in other massif-type anorthosites, such as the Adirondacks (*e.g.* McLelland and Whitney, 1977). Garnet forming reactions are discussed in more detail in a later chapter.

In one area, an irregularly-shaped pod approximately 10 m<sup>2</sup> of altered norite with a distinctive rim of magnetite was observed in contact with granular white fine-grained anorthosite.

Sulfides, aside from those occurring at Sheep Brook and other places described by Baird (1954), but not visited during field work, are rare, comprising pyrite and less commonly chalcopyrite and are spatially associated with orthopyroxene and magnetite, or are present as inclusions within massive oxides in some cut slabs.

## **8.2 Mafic dikes**

A diabase dike swarm was noted on the eastern margin of the map area in a location previously mapped by van Berkel *et al.* (1987) as two smaller norite pods; there is no evidence for norite bodies here – only white, sugary textured anorthosite. The dikes are parallel over a width of approximately one kilometer and have variable thicknesses, from

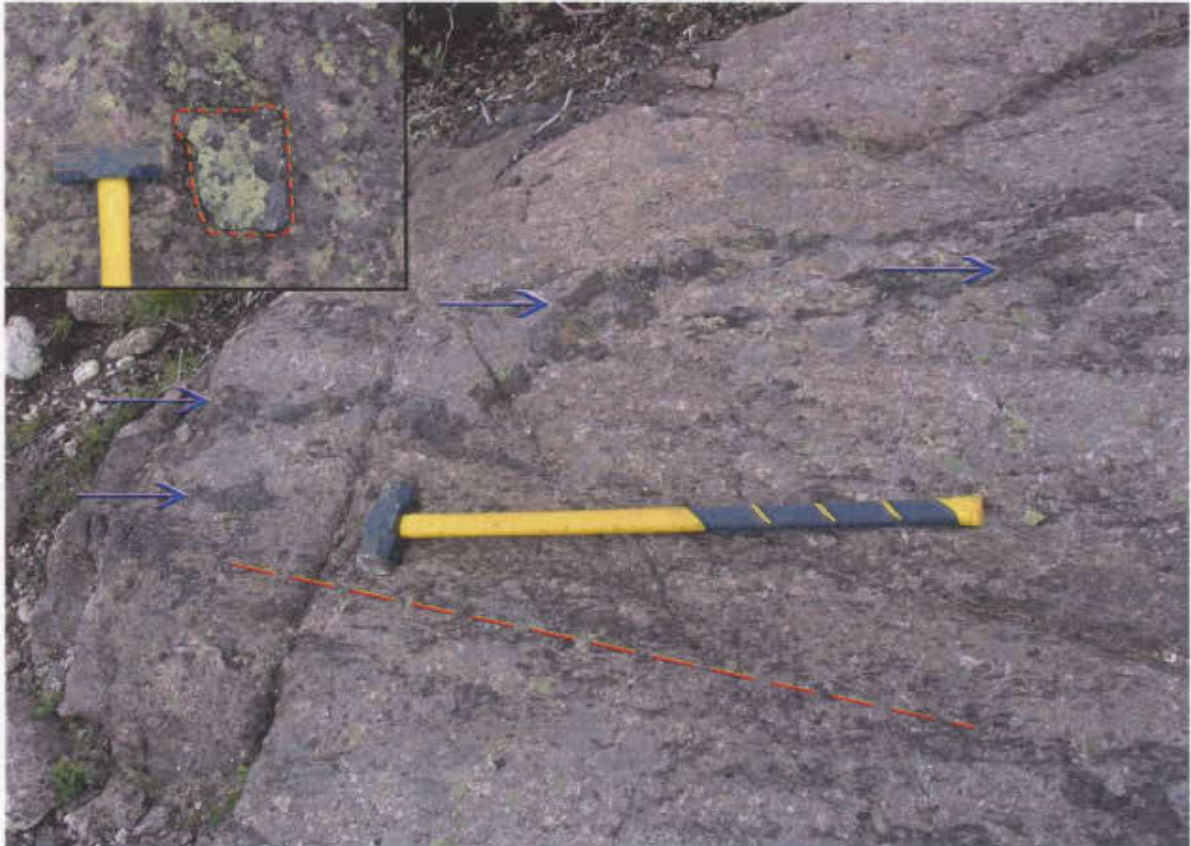


**Figure 8.6** This image, from SMA-51, illustrates a common texture of weakly foliated pink leuconorite and coarse-grained, discontinuous lenses and elongate aggregates of magnetite and ilmenite. This outcrop exhibits an above average abundance of oxides, but the texture is similar in many outcrops with lesser oxide content. The oxides in this outcrop appear completely undeformed in reflected light microscopy, suggesting they had not fully cooled during the formation of the foliation. If this is the case, foliation occurred at relatively high temperatures. Foliation is indicated by the dashed red line and aggregates of Fe-Ti oxides by blue arrows. The inset is an example of a large cube of magnetite in a nearby outcrop. These cubes are common on some outcrops, and vary significantly in size.

one meter to approximately four meters wide; dike spacing is irregular. The largest dike marked the edge of an ~50 meter high cliff at the top of the north side of Flat Bay Brook valley and its thickness was variable along strike, from two to four meters (Figure 8.7). The margins of the dikes were commonly sheared subparallel to their strike angle, and chilled margins were absent. No dikes were observed cutting the coloured plagioclase anorthosite or noritic bodies; hence, they are restricted therefore to the normal anorthosite. The areas where the dikes are most abundant are characterized by white to cream coloured plagioclase with a distinctly sugary, recrystallized texture, suggesting that they provided heat to drive local recrystallization, and in thin section it appears to have resulted in textural equilibrium (*i.e.*, granoblastic/mosaic textures, and recovery recrystallization). It is possible however, that the host rocks have had a different history of recrystallization relative to the coloured plagioclase anorthosite prior to dike emplacement. The dikes contain magnetite, ilmenite, pyrite, and rare chalcopyrite.

### **8.3 Sheep Brook**

The Sheep Brook area is host to a notable sulfide occurrence and was examined briefly during the 2004 field season and in more detail in the spring of 2005. At this site, several thin (2 to 5 cm) tectonically dismembered massive sulfide lenses (Figure 8.8) approximately 20 to 75 cm long are hosted in strongly folded and sheared silicified anorthosite to gabbro-norite (Figure 8.9). Sulfides comprise pyrrhotite, pyrite, chalcopyrite and possible bornite. Samples from this location vary from 1.6 g/t to 2.56 g/t Pt+Pd, and 1.17 to 1.53% Ni. At least one strongly chloritized and amphibolitized mafic dike cuts the outcrop that hosts the sulfides (Figure 8.10), but is not in direct contact with sulfides and cannot be directly correlated with the sulfides; however, the sulfide lenses are enclosed in thin (<2 cm) sheets of schistose mafic material (e.g. Figure 8.8). One cliff-side outcrop exhibits three thin mafic dikes, but given the strongly deformed nature of this site, it is highly possible this is all the same dike, but tectonically disrupted.



Figure 8.7 The image is taken from SMA-65, looking east up the Flat Bay Brook valley. The image indicates the proposed trace of a mafic dike (dashed red lines) observed in several locations along strike at the edge of a cliff. This dike was sampled at SMA-65. The contact of the dike (inset) at SMA-65 is irregular and embayed into sugary- to granular, white anorthosite. This dike is morphologically similar to several other mafic dikes observed in more accessible areas in the vicinity of this dike.

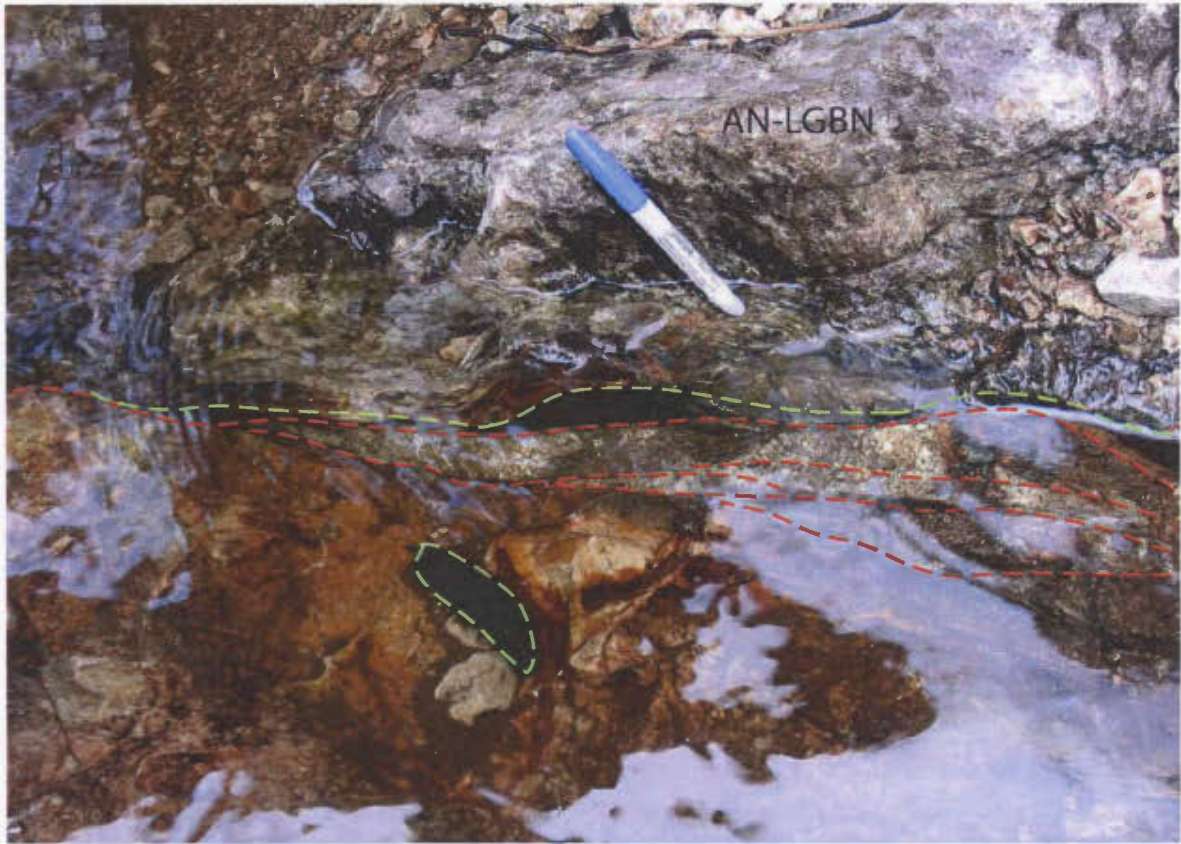


Figure 8.8 This image is of one of several thin, tectonically dismembered lenses of massive sulfides in Sheep Brook. The sulfides are only present underwater, making sampling difficult. Red dashed lines mark the outline of the sulfides and imbricated “tectonic stacks” of sulfides. Mineralogy in some stacks is different, but in this image most sulfides comprise pyrite with minor pyrrhotite. The stacked lenses of sulfides are separated by thin selvages of strongly deformed mafic dike material, which is outlined in green at the top (east) side of this lens, as well as a fragment broken off during sampling. Note marker for scale.

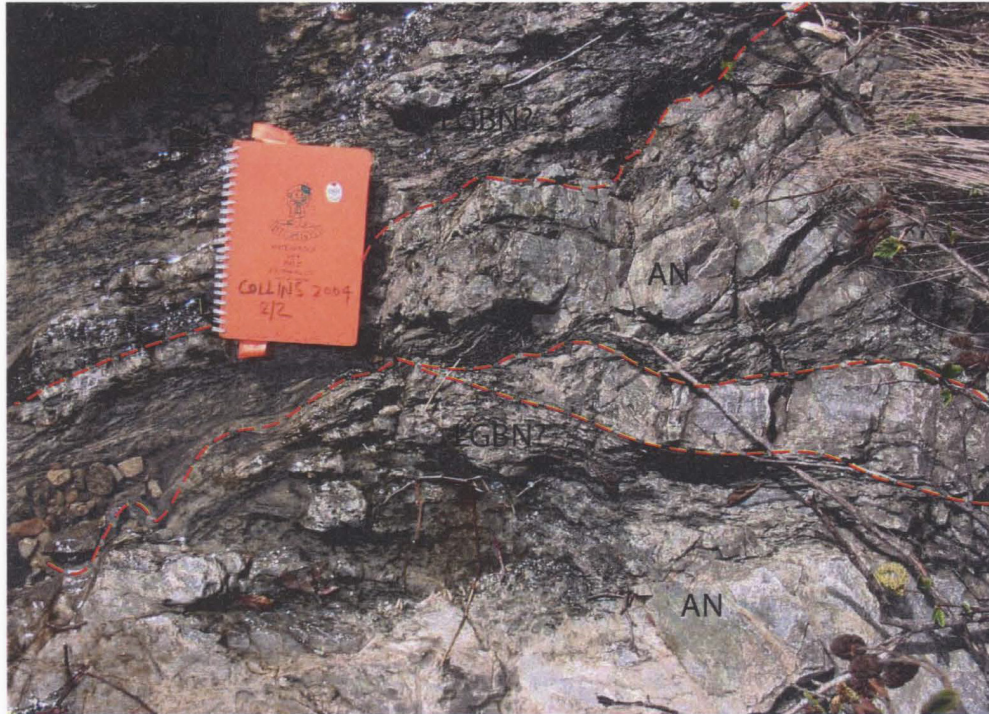


Figure 8.9 Rocks in the Sheep Brook valley comprise strongly deformed anorthosite and leucocratic mafic rocks, possibly leucogabbro. Anorthosite in particular appears to have been strongly silicified and resembles quartzite in outcrop. It is bound on both sides in this image by strongly sheared mafic rocks (LGBN?). The anorthosite itself is also folded, the outline of which is traced by red dashed lines. The field book for scale is ~ 10 x 20 cm.



Figure 8.10 This image is of the base of the cliff that marks Sheep Brook valley. Strongly chloritized and amphibolitized mafic dikes are present in this location only. It is highly possible, especially given the strong tectonic fabric in this area, that there is only one dike that has been disrupted. Red dashed lines outline the dike contact with silicified anorthosite, which resembles the anorthosite in Figure 9.7. Note the GPS unit in the bottom right corner for scale.

## 8.4 Summary

Mapping in the Steel Mountain Anorthosite delineated several noritic bodies. The pink-to lilac plagioclase zones appear to be associated with more mafic rocks, and are weakly bounded by shear zones in the center of the map area. Mapping has reduced the size the norite map units of van Berkel *et al.* (1987), and allowed further subdivision of mafic rocks. Identification and characterization of small deformed lenses of massive sulfide that host relatively significant PGE mineralization was identified outside the main map area, nearby to the Bishop magnetite quarries. Identification of new diabase dike swarms was also accomplished during this mapping project.

## Chapter 9: Steel Mountain Anorthosite Petrography

### 9.1 Introduction

The Steel Mountain Anorthosite contains many small lenses of norite, leuconorite, leucogabbronorite and gabbronorite, as well as a zone of distinctive pink- to lilac coloured matrix plagioclase. This chapter describes the mineralogical and microtextural relationships in this map area.

Rock names are based on a combination of field geology, petrography and calculated rock names, which are summarized in Appendix 2. Although maps indicate finite contacts and boundaries between different units, it should be emphasized that all contacts in reality are gradational and are either preserved or weakly recrystallized magmatic contacts, or more commonly, variably recrystallized and deformed contacts. Therefore, mineralogical relationships are not discussed within a framework of rock names; instead, each mineral is described individually, because textures for each phase do not vary significantly. Where unique or distinguishing textures occur in only one rock type, these are specifically described.

Several regions in this map area exhibit a strong greenschist overprint that obscures primary mineralogy and sometimes textures. To reflect primary magmatic assemblages, which are of more interest with respect to iron oxide and sulfide mineralization, rather than alteration, petrographical observations were used to calculate a normative mineralogy. A visual estimate of the relative abundance of all phases was made in which it was assumed that all epidote in a thin section was derived from plagioclase and all mafic alteration phases originated from primary mafic phases; mafic alteration phases (e.g. chlorite, actinolite) were summed together. In order to allocate the sum of alteration minerals to a primary assemblage, an average ratio of OPX to CPX from fresh rocks was calculated. This ratio was applied to the alteration assemblage so that some was allocated to OPX and some to CPX. Finally, the ratios between plagioclase, orthopyroxene and

clinopyroxene were plotted on ternary diagrams of Streckeisen (1976) (Figure 9.1). These assumptions are generally supported by petrography and field work. Where they are not reasonable, field data and petrography are favoured. This is often the case where normalized names fall close to a tie-line between different lithologies on ternary plots, or where alteration is not amenable to normalizing calculations.

Although close to 100 waypoint observations and dozens of samples were collected in the SMA, due to time and budgetary constraints only thirty polished thin sections were studied from the anorthosite, of which four are massive sulfides from the Sheep Brook area and three are massive oxides from the Bishop South quarry.

Oxide textures from small massive lenses in the main map area are texturally and mineralogically similar to those from the Bishop South quarry, therefore, all oxides are discussed in one section. Sulfides are very rare in the main map area and are only briefly mentioned in the description of massive sulfides from the Sheep Brook area – the only location with significant sulfide accumulations.

## **9.2 SMA mineralogy overview**

This section summarizes the mineralogical abundances in thin section only and as such, is not entirely representative of the field area for some specific thin sections, particularly those from areas with very coarse grain size.

Anorthosite is the most abundant lithology in the map area and averages 97% plagioclase, 1% orthopyroxene 1% clinopyroxene and 1% oxides (ilmenite and magnetite) based on visual estimations combined with calculated mineralogy. The only major variation in anorthosite is grain size, degree of recrystallization and the colour of plagioclase – either pink or white. Normalizing calculations did not significantly affect the relative mineral abundances in these samples.

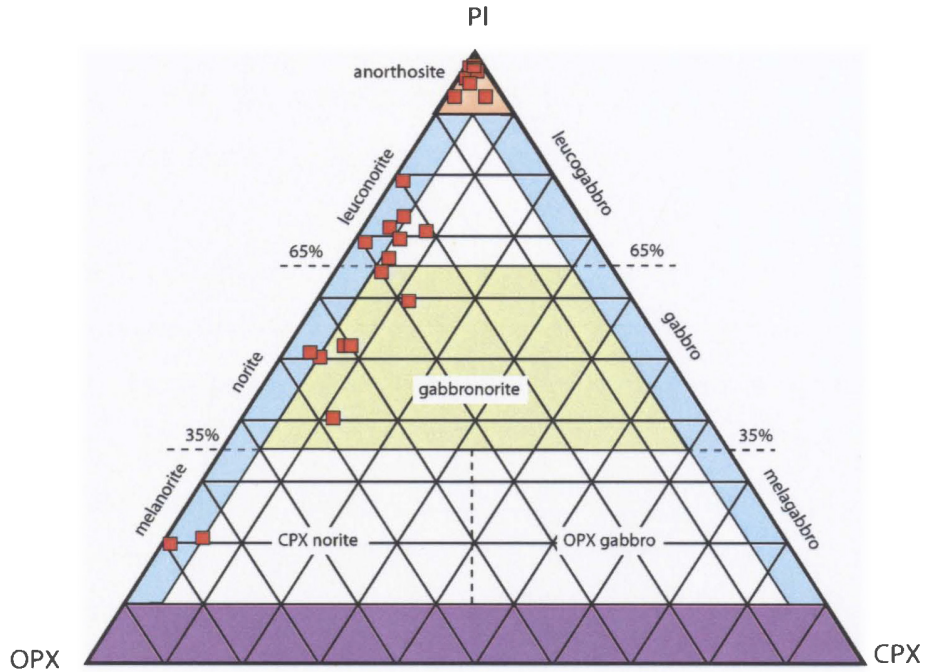


Figure 9.1 Normative mineralogy for the SMA, after Streckeisen (1976). A description of plotting procedures is described in the text. Most samples lie within the anorthosite and leuconorite fields, as well as gabbronorite and leucogabbro. From this diagram the abundance of OPX dominated rocks is obvious.

Leuconorite is the second most abundant lithology studied in thin section and averages 69% plagioclase, 13% orthopyroxene, 1% clinopyroxene, 4% amphibole, 5% biotite plus chlorite, 2% quartz, 3% epidote and 2% magnetite plus ilmenite. Only plagioclase, OPX, CPX, and oxides are primary in these samples. Normalization calculations result in a change to 74% plagioclase, 24% OPX and 3% CPX – a notable increase in only orthopyroxene, which is supported by textural evidence.

Gabbronorite is the third most abundant lithology studied in thin section and averages 54% plagioclase, 6% orthopyroxene, 3% clinopyroxene, 24% amphibole, 9% biotite plus chlorite, 2% quartz, 3% epidote and 2% magnetite plus ilmenite; some samples contain minor amounts of garnet. Gabbronorite samples have experienced a greater amount of greenschist alteration than most other rock types and normalization calculations were used to generate a theoretical primary mineralogy. The normalized assemblage averages 58% plagioclase, 34% OPX and 8% CPX. Again, textural evidence supports this assumption.

Leucogabbronorite is the next most abundant lithology studied in thin section and averages 68% plagioclase, 7% orthopyroxene, 3% clinopyroxene, 15% amphibole, 5% biotite plus chlorite, and 2% magnetite plus ilmenite. These samples are relatively altered to greenschist assemblages compared to noritic samples and like the gabbronorite samples, normalizing calculations were applied to estimate the primary mineral assemblage. The normalized assemblage averages 70% plagioclase, 24% OPX and 6% CPX.

The most mafic rocks in the map area are norite and melanorite. Only two thin sections were cut for each lithology, because of their consistent textures and narrow spatial distribution. Despite the small number of samples for these lithologies, thin sections were derived from representative locations and mineral assemblages can be extrapolated for similarly mapped locations based on field observations. In norite, plagioclase averages

50%, orthopyroxene 40%, clinopyroxene 4%, amphibole 5% and magnetite plus ilmenite 1% and some samples contain minor secondary garnet. Normalized compositions comprise 51% plagioclase, 45% OPX and 5% CPX. The small change from actual mineralogy reflects the low degree of alteration in this lithology. Melanorite, which is always spatially associated with norite comprises 20% plagioclase, 74% orthopyroxene, 3% clinopyroxene, 1% amphibole and 2% magnetite plus ilmenite and minor garnet. The normalized assemblage varies little, comprising 20% plagioclase, 77% OPX and 3% CPX.

### **9.3 SMA plagioclase**

Plagioclase is the most abundant phase in nearly every thin section examined. Despite its association with several different rock types, plagioclase textures are relatively similar throughout the map area. Plagioclase is most commonly present as anhedral, irregular to granular crystals that vary from medium- to coarse grained. Where local granoblastic plagioclase occurs, there is a bimodal equigranular distribution between relict porphyroclasts and recrystallized grains. Grain boundaries between plagioclase and other phases are variable, most commonly smoothly irregular and lobate or cusped and less often, seriate and subangular. Smooth embayments of one grain of plagioclase into another are common and likely result from pressure dissolution recrystallization. In many places, plagioclase in the map area exhibits a distinct pink pleochroism that is recognizable from outcrop down to thin section, but there is no apparent petrographical evidence for the cause of this pleochroism. Recrystallization and/or hydrous (sericite, epidote) alteration appear to remove pink colouration.

Plagioclase recrystallization is ubiquitous, and textures are quite variable. In general, the least amount of recrystallization occurs in the most mafic samples, whereas anorthositic samples have relatively higher recrystallization. Core and mantle, grain boundary migration, and deformation lamellae are the most common recrystallization textures, whereas pressure dissolution, warped exsolution lamellae and granoblastic textures are

less common (Figure 9.2a). Granoblastic textures are nearly exclusive to samples with white plagioclase and are located in the eastern portion of the map area. If these samples once contained pink plagioclase, the pervasive recrystallization has removed such colouring. Recovery recrystallization textures comprise subgrain formation, which is associated with deformation bands and undulose extinction. Subgrains and undulose extinction are ubiquitous in every sample. Granoblastic samples typically contain relict megacrysts, suggesting true equilibrium textures have not been attained (Figure 9.2b). These textures are frequently close to nearby mafic dikes, suggesting that dikes may have provided a heat source to drive static recrystallization because there are no kinematic indicators that suggest recrystallization occurred in response to deviatoric stress.

Plagioclase is relatively free of inclusions, but some crystals contain a fine dusting, or rare blebs, of oxides; even rarer are fine rutile needles. In SMA-09, some plagioclase contains CPX inclusions.

Plagioclase is altered to sericite along some grain boundaries and late fractures, particularly those where mafic minerals are also altered, suggesting pervasive fluid migration throughout the sample. More intense alteration results in saussuritization, also common in pervasively altered samples (Figure 9.3). In general, altered samples are usually closer to shear zones. Sericitization and saussuritization overprint all other modes of recrystallization, thus they are the latest event to affect these rocks.

In general, textures in plagioclase suggest medium to high temperature recrystallization with local late low to medium temperature recrystallization, all overprinted by low temperature alteration.

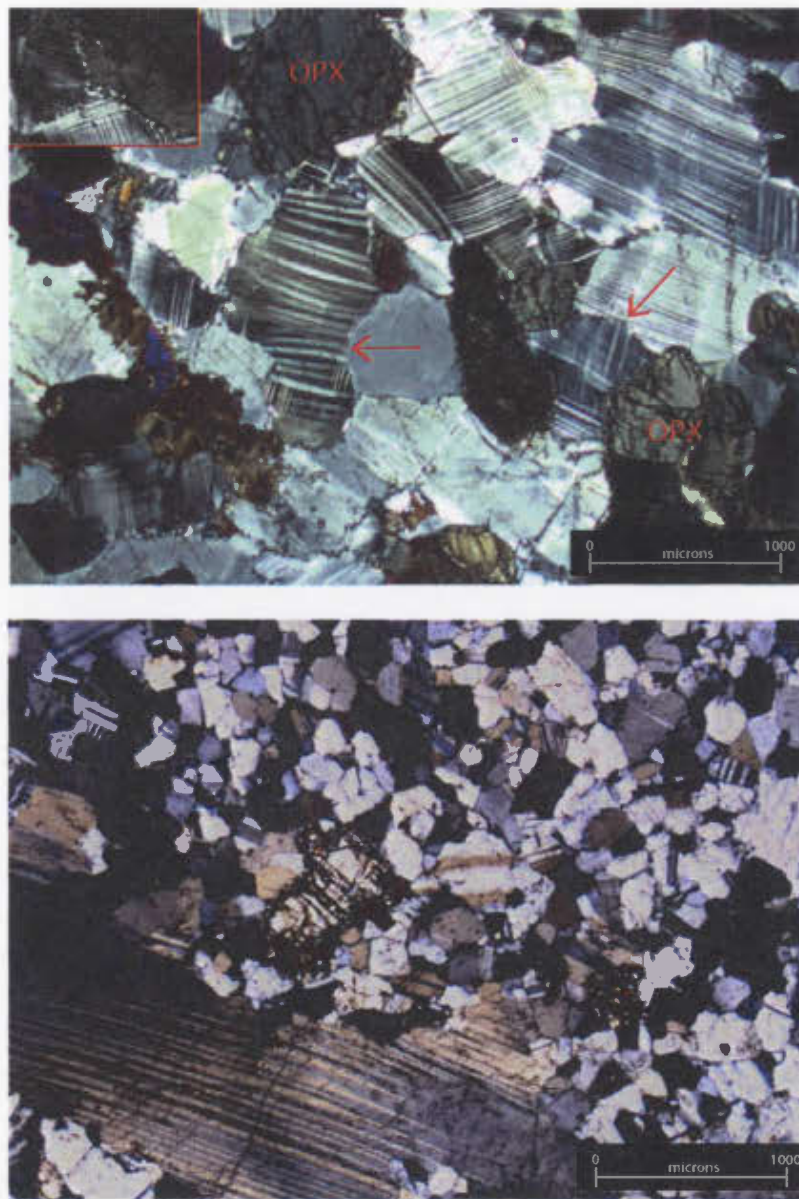


Figure 9.2 Transmitted, crossed-polarized light images from the SMA. (a) This image presents several examples of recrystallization of plagioclase. Undulose extinction and warped exsolution lamellae are common, particularly near the center of the image. Pressure solution is indicated by red arrows. Rims of recrystallized plagioclase (core and mantle) are present in the inset. The field of view in the inset is  $\sim 200\mu\text{m}$ ; (b) in this image, from SMA-73, plagioclase exhibits a granoblastic texture. Relict grains of plagioclase are common, suggesting that textural equilibrium has not been attained. The mechanism for this recrystallization texture is unknown, but it is possible that recovery recrystallization was in response to heat provided by nearby mafic dikes. Note scale bar in lower right corner.

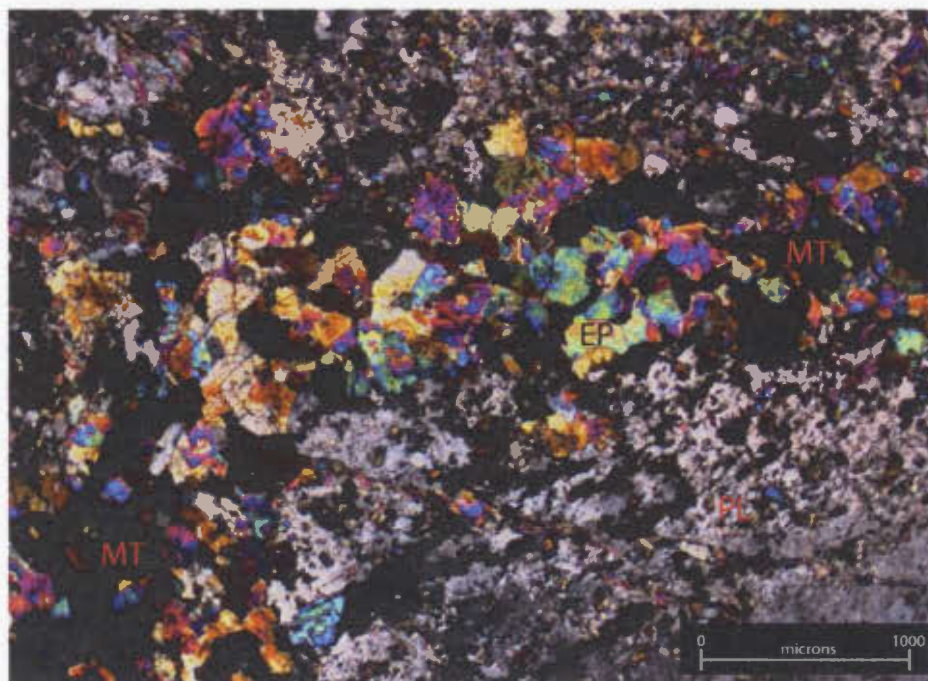


Figure 9.3 Transmitted, crossed-polarized light photomicrograph from the SMA. This image, from SMA-61A, illustrates coarse-grained and fine-grained sausseritization. There are two epidote textures in this image. First, coarse-grained epidote cutting from the lower left corner to the upper right corner of the image is associated with Fe-Ti oxides and several small quartz-carbonate veinlets. This epidote is strongly zoned. The second texture is the fine-grained sheaves or plates of epidote that are replacing plagioclase, in the lower right corner, for example, where megacrystic plagioclase is speckled with epidote. Note scale bar in the lower right corner.

## 9.4 SMA orthopyroxene and clinopyroxene

Orthopyroxene and clinopyroxene textures are very similar and are discussed together. Preservation of pyroxene is greatest in noritic rocks, whereas in gabbronoritic rocks it is more altered.

Most commonly, pyroxene occurs as coarse- to medium-grained, anhedral, irregular aggregates. Less commonly, pyroxene has a bimodal grain size where both coarse-grained aggregates and medium-grained individual granular crystals are present (Figure 9.4a). Sample SMA-37 contains alternating layers of subrounded, equigranular orthopyroxene and clinopyroxene (Figure 9.4b). Grain boundaries are usually smooth to subangular and in aggregates, these boundaries locally approach  $120^\circ$  triple point junctions. Locally, grain boundaries in contact with plagioclase or garnet are smoothly embayed.

The degree of pyroxene recrystallization is relatively less than in the surrounding plagioclase, which could be a function of the timing of deformation with respect to the relative crystallization of plagioclase and pyroxene, or it may be related to the temperature that pyroxene recrystallizes compared to plagioclase. The most common recrystallization texture is warped cleavage and development of weak deformation bands that locally grade into subgrains (Figure 9.5). More strongly deformed samples exhibit the same textures, but with greater progression. In some coarse-grained aggregates, the orientation of deformation bands or crenulation axes are not always parallel in adjacent crystals, suggesting that rotation of individual crystals occurred subsequent to crenulation. Recovery recrystallization comprises weak undulose extinction and local subgrain formation.

Pyroxene contains inclusions of oxides, which occur as small rounded blebs, and small rounded crystals of plagioclase. Orthopyroxene contains clinopyroxene inclusions, but the reverse relationship is not noted. Orthopyroxene in particular contains abundant fine-

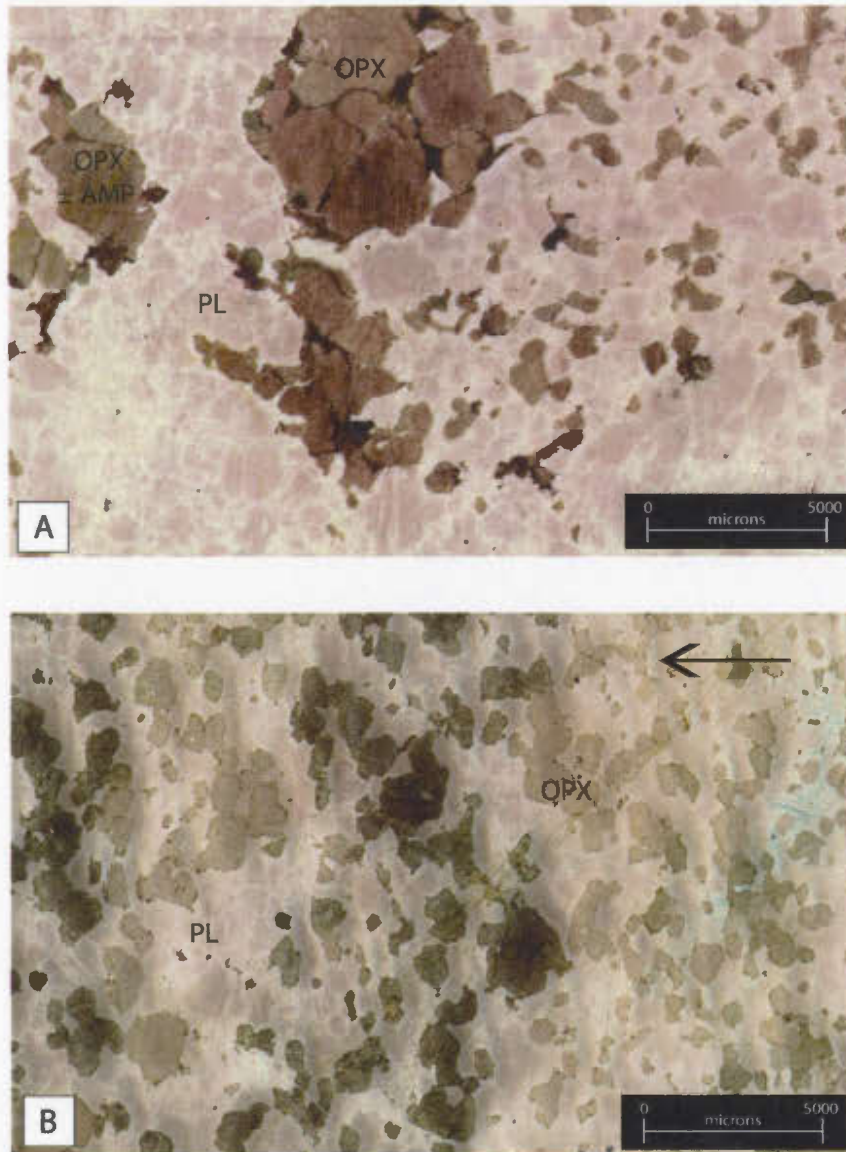


Figure 9.4 Scanned polished thin sections from the SMA in normal light. (a) This sample, from SMA-48, illustrates the two main pyroxene morphologies, which occur at a thin section scale, but resemble the patterns of some outcrops (e.g. Figure 8.3a). Orthopyroxene occurs as coarse-grained aggregates and individual, interstitial grains. The pink colour of plagioclase is obvious in this image. Large, OPX-free areas occur where coarse-grained plagioclase was present, prior to granulation; (b) in SMA-37, magmatic layering is preserved (arrow indicates way up). In this image, layers of OPX and CPX alternate with white plagioclase. CPX is dark green because it is nearly completely replaced by granular amphibole and urallite, whereas OPX is hardly replaced at all. Note scale bars in lower right corner.

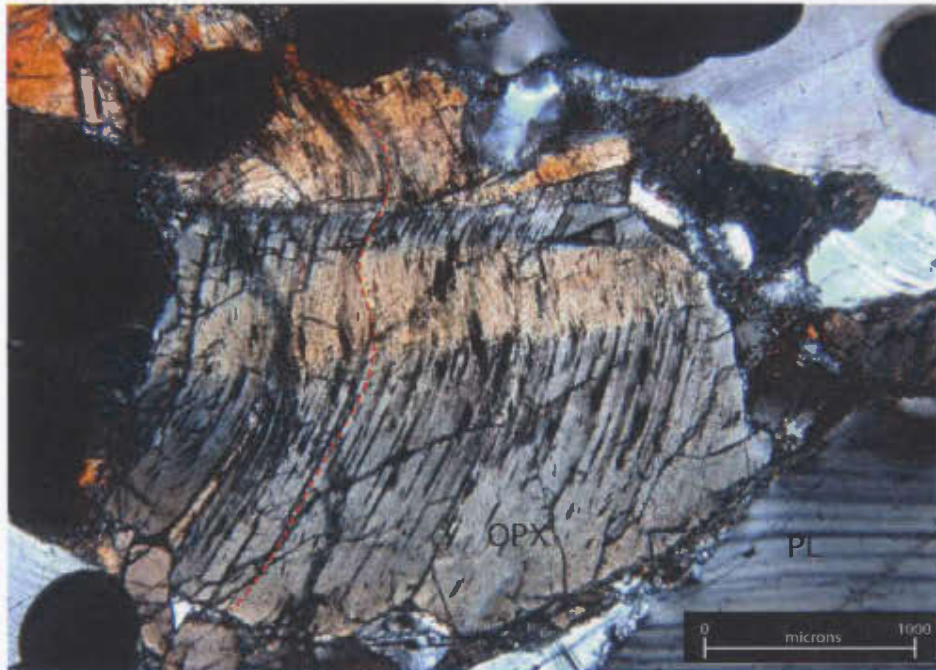


Figure 9.5 Transmitted, partially crossed-polarized light photomicrograph from the SMA. In this image, from SMA-57, orthopyroxene exhibits mild deformation textures, which causes undulose extinction, noted by the light orange band running L-R in the main OPX crystal. Cleavage in OPX is crenulated, and the trace of the crenulation fabric tracks continuously into an adjacent crystal at the top of the image. The dark black dots in this image are marker. Note the scale bar in the lower right corner.

grained inclusions of rutile, up to a few weight percent, which are oriented parallel to the main {210} cleavage plane (Figure 9.6). These inclusions are elongate diamond shaped or may be skeletal. Recrystallization in pyroxene eliminates these inclusions.

Alteration in pyroxene is quite variable. Many gabbro-noritic samples have little primary pyroxene remaining because it is pseudomorphed by fibrous amphibole, likely actinolite, chlorite and biotite. There is little gradation between strongly altered samples and relatively fresh samples. The freshest samples exhibit thin rims of intergrown actinolite and biotite sheaves. In more altered examples, biotite and amphibole penetrate the pyroxene grains along cleavage or fractures (Figure 9.7). Uralitization is the most common type of alteration in fresher samples and occurs as localized grungy zones, often in the core. Fractures may be filled with fine, granular oxides and plagioclase or quartz. Clinopyroxene alters more readily than orthopyroxene in all samples. Another type of pyroxene reaction involves the growth of garnet at the expense of pyroxene.

### **9.5 SMA garnets**

Garnet is present in small quantities in some norite and leuconorite samples. Four thin sections contain garnet, while an additional location not sampled was noted to contain garnets. Garnets occur in two mineralogical associations but are texturally similar. Subrounded, homogenous, inclusion-free, pale pink- to red garnet forms discontinuous, granular rims either at the contact between plagioclase and orthopyroxene (Figure 9.8a), or pyroxene and Fe-Ti oxides (Figure 9.8b), the latter being less common. Grain size varies from 600  $\mu\text{m}$  to 1200  $\mu\text{m}$ . Garnets formed between plagioclase and pyroxene always exhibit a reaction rim of variable thickness. Reaction rims vary from single to double symplectic coronas, but whether single or double, the rim products are the same (Figure 9.9). Symplectic rims are very fine-grained and optical identification was not possible. Microprobe analysis indicates the symplectites are an epidote-plagioclase intergrowth, which is an unusual assemblage and may not be primary. It is more likely to have been an initial amphibole-quartz intergrowth that altered to plagioclase and epidote.



Figure 9.6 Transmitted, normal light photomicrograph of the SMA. Orthopyroxene and clinopyroxene in the SMA commonly contain rutile inclusions. In this image, from SMA-48, OPX exhibits abundant inclusions of skeletal rutile. The distribution of rutile appears to be controlled by a crystallographic plane in OPX. The dusty appearance in the grain of OPX is caused by even finer rutile inclusions. Note scale bar in the lower right corner.

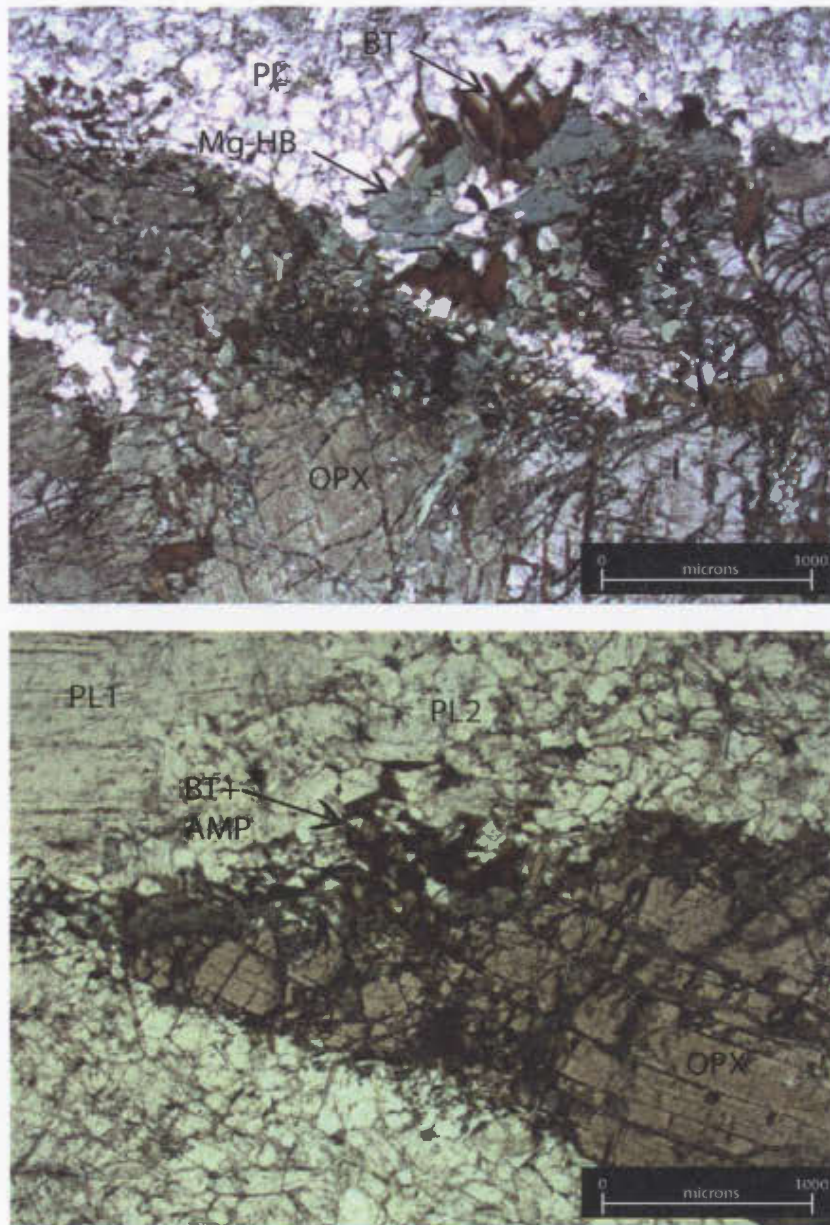
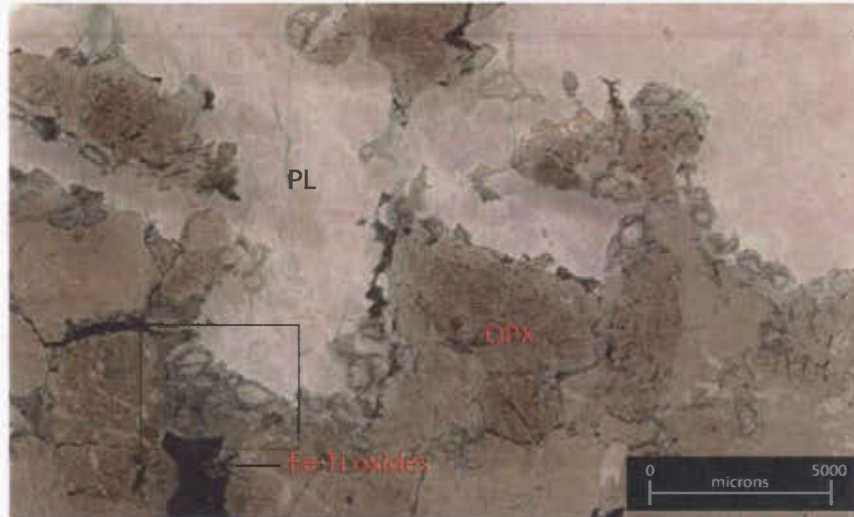


Figure 9.7 Transmitted, normal light photomicrograph of the SMA. Orthopyroxene in these two images, both from SMA-73, is partially replaced by a combination of coarse sheaves of biotite and intergrown green amphibole, which microprobe analysis indicates to be Mg hornblende or Mg hornblende-tschermakite. Alteration begins on the rims and progresses to the core of the crystals along deformation induced cracks, gradually replacing the entire crystal. Note in both figures that the plagioclase directly surrounding OPX is granoblastic in this sample, but this is not always the case. Note scale bars in the lower right corners.



**Figure 9.8** Scanned polished thin sections from the SMA in normal light. (a) The primary association of garnet is at the contact between plagioclase and OPX, where it occurs as discontinuous chains. The box indicates where the photo in Figure 9.9 is taken. Note the pink colour of plagioclase in this image. The angular contacts between plagioclase and OPX occur because plagioclase was formerly coarse-grained crystals that are now granulated; (b) garnets occur at the contact between OPX and Fe-Ti oxides as well, although this association in the main map area is less common. Some massive oxide ore bodies of the Bishop South quarry are locally surrounded by a halo over one meter wide of garnets. Note that garnets in this association are not altered as they are in 'a', above. Note scale bars in the lower right corner.

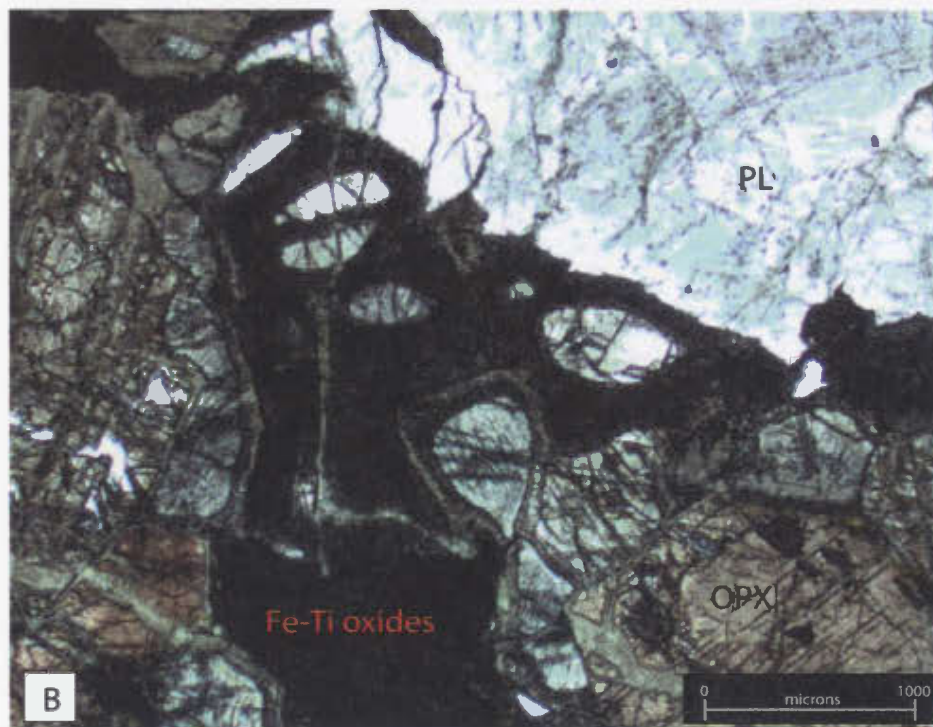
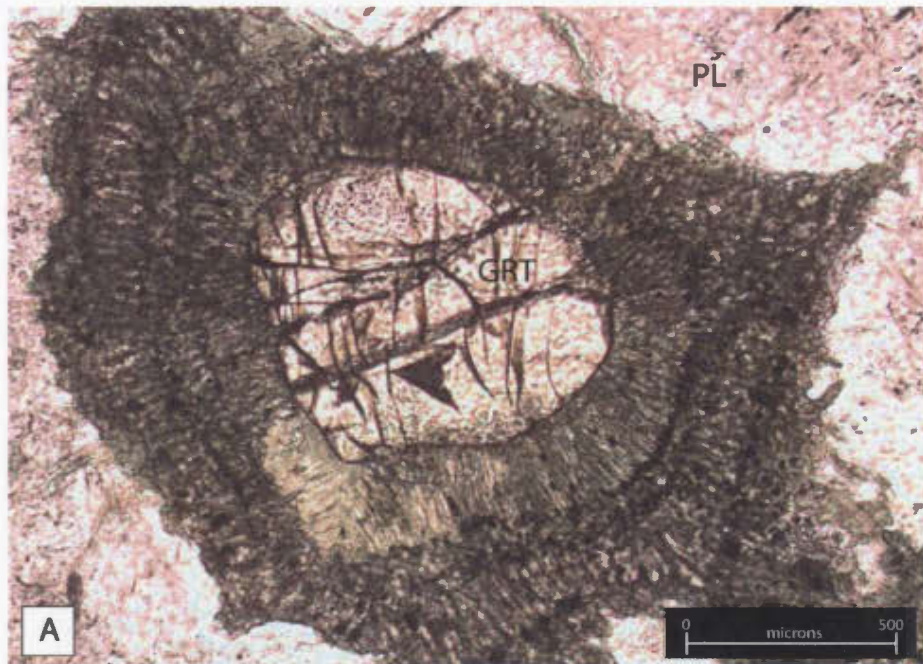


Figure 9.9 Transmitted, normal light photomicrograph from the SMA. (a) garnet exhibits complex, double-shelled corona structures comprising plagioclase + amphibole + epidote. Each shell is separated from the next by a discontinuous shell of nearly pure magnetite; (b) an overview of a garnet cluster, all exhibiting the same double-shelled coronas. Note that OPX has also been affected by greenschist retrograde metamorphism. Note scale bars in the lower right corner.

Discontinuous rims of fine magnetite grains are present at the contact between first and second generation coronas and are disseminated throughout the symplectites in lower abundances. Where garnet forms between orthopyroxene and Fe-Ti oxide, reaction rims are not present.

It seems likely that garnet rims formed during cooling of the host rock under dry metamorphic or igneous conditions. Later, during decompression, when fluids were introduced to the rock, an assemblage of hydrous minerals formed symplectic coronas around garnet, likely consuming them during the reactions. Symplectite assemblages are similar to other greenschist alteration products observed in the map area and may have formed around the same time.

## **9.6 SMA oxides**

Most textures described below are very complex and involve extensive solid solution reactions that require introduction of microprobe mineral chemistry, thus a cursory description is provided in this section and complete description and discussion is outlined in the electron microprobe chapter. All figures in this section are located in Chapter 11 because the oxide species described in this chapter are most easily represented by backscatter electron images.

Oxides are present throughout the map area, typically spatially associated with pyroxene, but are notably absent or minor in altered samples. Oxides comprise magnetite, ulvöspinel, ilmenite, hematite, hercynite and rutile. Oxides occur in four different morphologies: (1) at the Bishop quarry oxides are massive; (2) in the map area small (up to 2-3 m by 0.5 m) discrete lenses of massive oxides are present (e.g. Figure 8.6); (3) pyroxene crystals contain fracture-hosted oxides; (4) in all areas, aside from the quarry, oxides blebs of variable size and shape are randomly distributed interstitially within silicates.

Massive oxides and many medium or fine-grained oxides exhibit a consistent exsolution texture that is independent of oxide location and/or quantity. This texture consists of ilmenite trellis- and sandwich-type exsolution lamellae in a magnetite host (Figure 11.24, 11.25). Probe data indicate that ilmenite varies from nearly pure end member ilmenite to ilmenite-hematite solid solution (Ilm-Hem)<sub>ss</sub> and that magnetite varies from nearly pure end member magnetite to ulvöspinel-magnetite solid solution (Usp-Mt)<sub>ss</sub>. Trellis lamellae form by the oxidation of (cubic) magnetite-ulvöspinel solid solution, which results in exsolution of (rhombohedral) ilmenite-hematite solid solution along spinel {111} planes (Haggerty, 1991). Trellis lamellae have sharp, straight contacts with host magnetite, but may pinch and swell in the plane of a thin section. These lamellae commonly originate at grain boundaries and taper to a point into the core of a magnetite grain, often with a flame-like morphology, which is characteristic of diffusion-controlled crystal growth (Haggerty, 1991). Trellis lamellae have two size populations. First, relatively coarse Ilm-Hem<sub>ss</sub> lamellae range in thickness from ~150 µm to ~10 µm. Coarse lamellae are surrounded by depletion halos within the host Mt-Usp<sub>ss</sub> that are free of the second, smaller population of lamellae. The second, smaller population occurs in the zones between depletion halos in magnetite. These lamellae range between 2-3 µm to sub-micron and are still visible in ~ 10 000x magnification backscatter electron images. These lamellae are discontinuous and have a smaller aspect ratio but are still distinctly elongate. Coarse ilmenite lamellae host very fine trellis-like lamellae that resemble the fine lamellae described above. In reflected light they are the same colour as the host magnetite, but they are too fine to analyse with the electron microprobe. Based on the texture and progressive oxidation exsolution reactions, it is possible these lamellae form from progressive oxidation of ilmenite, or perhaps a second event of reduction of Ilm-Hem<sub>ss</sub> back to magnetite or ulvöspinel.

Massive oxides from the Bishop deposit contain other exsolution textures not commonly observed in small lenses of massive oxides outside of the deposit. First, magnetite hosts sandwich lamellae of ilmenite (Figure 11.25). These lamellae are not cut by trellis

lamellae but are cut by other lamellae types, indicating they were the last to crystallize. Some magnetite hosts exsolution lamellae of hercynite-spinel solid solution (i.e. pleonaste) along the {111} plane. Hercynite locally forms discrete crystals, aggregates or anhedral masses within magnetite (Figure 11.25).

Oxide blebs from outside the Bishop quarries, particularly in more altered samples, show a progression of oxidation not noted in massive oxides. This consists of patchy zones of ilmenite that are further oxidized to rutile and nearly pure hematite. These textures often truncate primary oxidation exsolution lamellae and are locally intergrown with silicates such as actinolite and biotite, suggesting that silicate oxidation post-dates initial oxide exsolution and that alteration fluids were oxidizing.

Oxides are common as small, interstitial blebs and fine, rounded to subrounded inclusions in plagioclase, and less commonly in pyroxene. These blebs commonly exhibit fine oxidation exsolution lamellae of hematite within ilmenite. In larger blebs (20-100  $\mu\text{m}$ ), ultra-fine secondary magnetite exsolution lamellae occur within relatively coarse-grained hematite exsolution lamellae.

Fracture-hosted oxides consist of fine rounded to subrounded blebs of magnetite and minor ilmenite. Infrequently, larger blebs exhibit oxidation exsolution lamellae of ilmenite from magnetite. It is possible that the latter are relict inclusions because they are similar in size, composition and textures to blebs in fresher pyroxene and plagioclase.

## **9.7 SMA sulfides**

Sulfides are rare in the map area and never exceed 1%. Sulfides comprise pyrite and chalcopyrite and rare pyrrhotite. Where present, sulfides are commonly fine round blebs interstitial to plagioclase or pyroxene, and rarely as inclusions within oxide blebs. Some pyrite blebs are corroded or skeletal as a result of alteration and overgrowth by silicates

such as actinolite and biotite. In places hematite forms rims around pyrite and exhibits embayed contacts, indicating it is consuming pyrite.

The Sheep Brook area contains several, thin, sheared lenses of massive sulfide. Lenses are compositionally layered, but textures are ambiguous as to whether or not layering is primary or the result of recrystallization. Sulfides comprise pyrrhotite, pyrite and chalcopyrite with minor covellite, sphalerite, galena and platinum group metals (identified by microprobe analysis).

At Sheep Brook, pyrrhotite is the most abundant sulfide phase followed by pyrite and chalcopyrite. Pyrrhotite is massive and relatively fresh but contains irregular lenses or layers of pyrite and discrete pyrite cubes, veinlets of chalcopyrite and minor discontinuous, folded lenses of oxides (Figure 9.10). Pyrrhotite exhibits textures characteristic of intense deformation-induced recrystallization. In crossed polarized reflected light, deformation lamellae are ubiquitous, and multiple generations are apparent based on cross-cutting relationships (Figure 9.11). First, some grains exhibit only faint, feathery or diffuse, parallel bands of pressure lamellae that end abruptly at the end of the grain. These twins are not recognizable in plain reflected light. More commonly, in massive pyrrhotite, grains are cross-cut by parallel to sub-parallel, curved, warped and locally kinked flame or lenticular shaped pressure lamellae that locally exhibits an inconsistent orientation between individual grains (i.e. the lamellae are off-set). Lamellae textures are complex and commonly more than one generation of lamellae cut or truncate another, and locally lamellae themselves host finer, more diffuse pressure lamellae. Lamellae commonly end abruptly at grain boundaries. Overall, textures indicate that the orientation of lamellae is crystallographically controlled. Lamellae often converge or bend into subgrain boundaries or deformation bands. High strain zones such as subgrain boundaries host pyrite flame exsolution lamellae; flame exsolution lamellae also develop along grain boundaries or fractures in pyrrhotite.

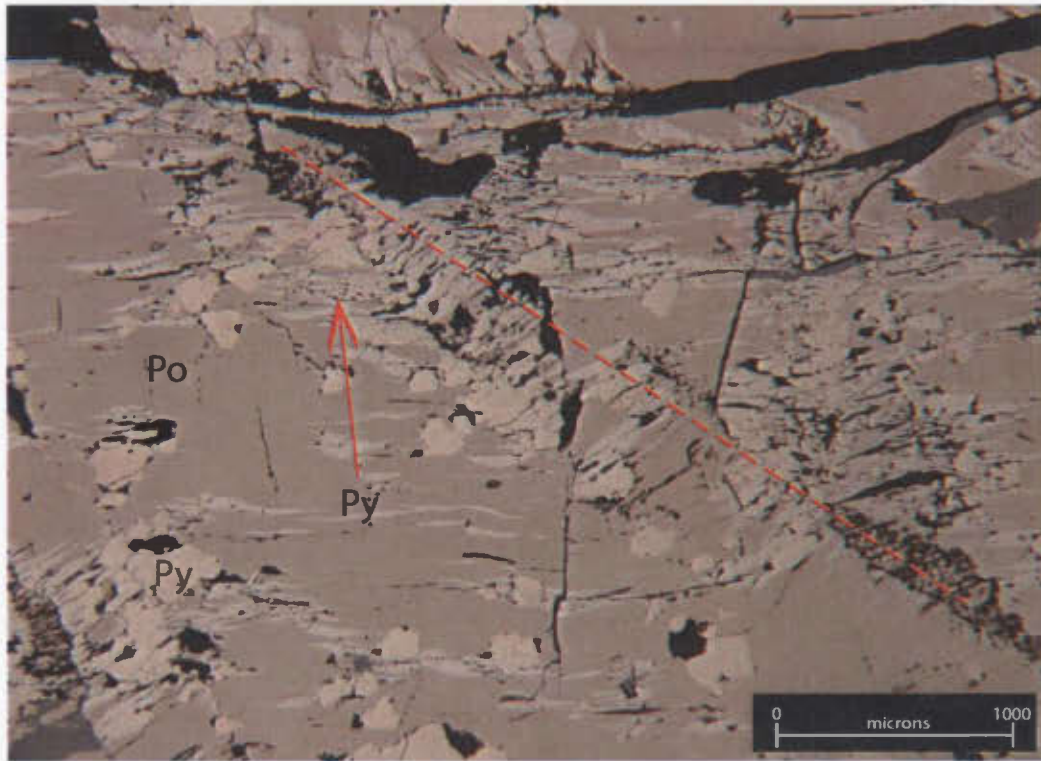


Figure 9.10 Reflected, normal light photomicrograph from the SMA. This image is typical of Sheep Brook pyrrhotite (SMA-40), which exhibits abundant pyrite cubes and pyrite flame lamellae. Pyrite lamellae appear to form in response to deformation, because they are most commonly located at the inflection point of crenulated cleavage or intersecting deformation lamellae in pyrrhotite. The axis of a major crenulation fabric in this sample is defined by the dashed red line in this image. Note scale bar in the lower right corner.

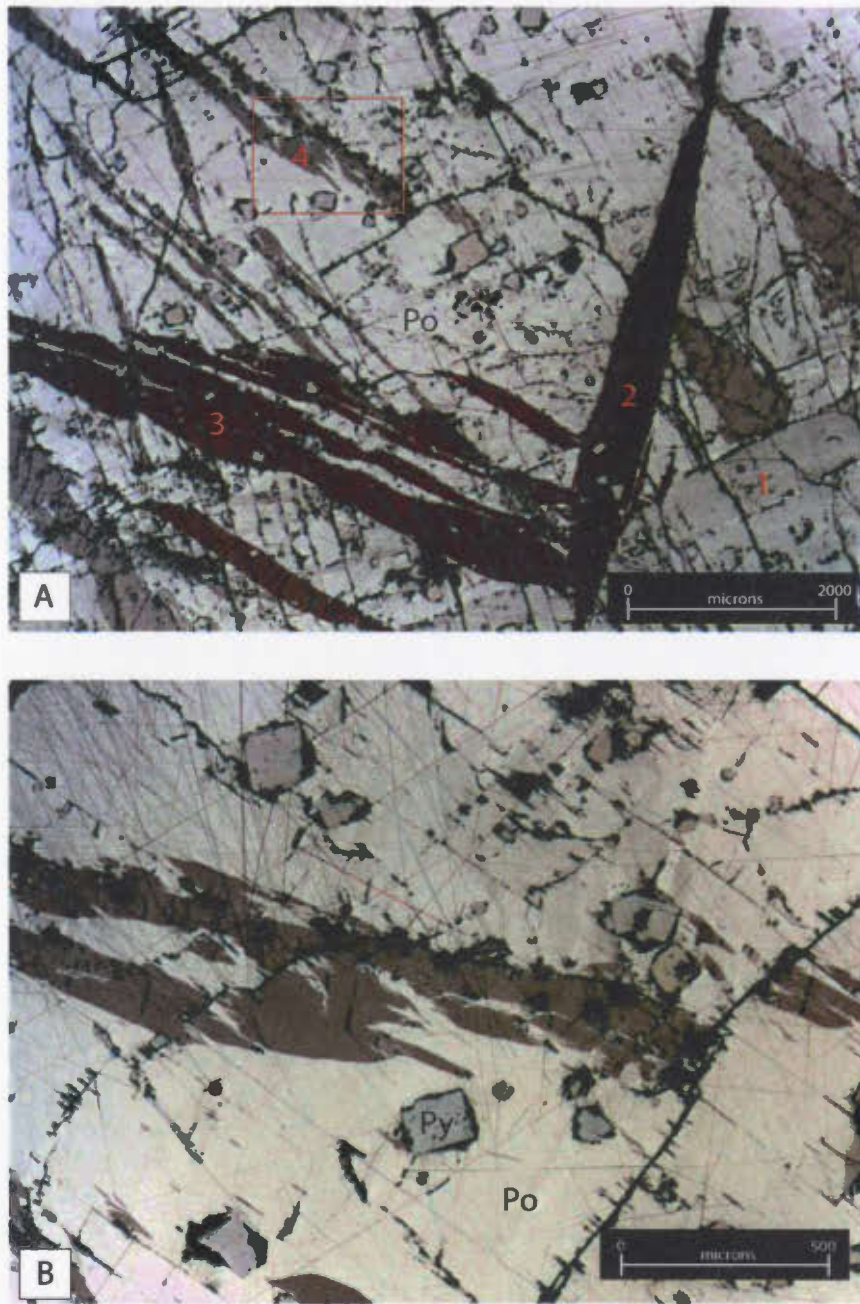


Figure 9.11 Reflected, partially crossed polarized light photomicrograph from the SMA. (a) Deformation lamellae are complex in most pyrrhotite in the Sheep Brook area, such as in SMA-40-1C. At least four generations appear to be present, based on cross-cutting relationships. It is possible however, that some of these lamellae are just orthogonal lamellae of the same set, despite that they do not go extinct at the same time; (b) This image is from the box in 'a' and is a detailed image of the finer lamellae. The tapered points on these lamellae is characteristic of deformation. Note that pyrite cubes in both images are surrounded by gangue and appear to overprint the lamellae. These lamellae are not present in BSE images, suggesting there is no compositional differences between lamellae. Note the scale bars in the lower right corners.

Pyrite varies from massive layers to small aggregates to discrete grains. Massive pyrite is commonly brittle fractured or brecciated and subsequently in-filled by chalcopyrite veinlets (Figure 9.12a). This texture is typical of low-temperature brecciation and it is likely that chalcopyrite was remobilized into the secondary porosity that was created during brecciation.

Discrete pyrite cubes surrounded by thin rims of gangue are common in the above massive, deformed pyrrhotite. The timing of these cubes is ambiguous. Many larger pyrite cubes exhibit weak concentric compositional zoning, visible in reflected light (Figure 9.12b), and indicated by microprobe analysis to be Ni-Co enriched bands (refer to Chapter 11 for data and back scatter images); these cubes locally contain small, irregular cores of pentlandite. There is no evidence for strain shadows or recrystallization surrounding these cubes, which appear to cut deformation textures in pyrrhotite, suggesting that they post-date deformation. One polished thin section contains a zone of fine pyrite layers hosted in gangue that have been kinked and crenulated reflecting the penetrative deformation that has affected these sulfides.

Massive chalcopyrite is relatively homogenous and does not exhibit the deformation textures of pyrrhotite, suggesting that it is more easily recrystallized. Massive chalcopyrite contains randomly distributed cubes of pyrite, some which have thin rims of pyrrhotite or hematite, either way, pyrite in this morphology is not in direct contact with chalcopyrite. That both massive pyrrhotite and chalcopyrite contain pyrite cubes with gangue rims suggests that the pyrite formed at the same time and that recovery recrystallization in massive chalcopyrite occurred, followed by development of pyrite cubes.

One sample contains ductilely deformed veinlets of oxides that exhibit similar exsolution textures as described above. These veinlets are folded and boudinaged on a microscopic scale. Other minor phases include galena and sphalerite. Galena occurs as irregular, fine

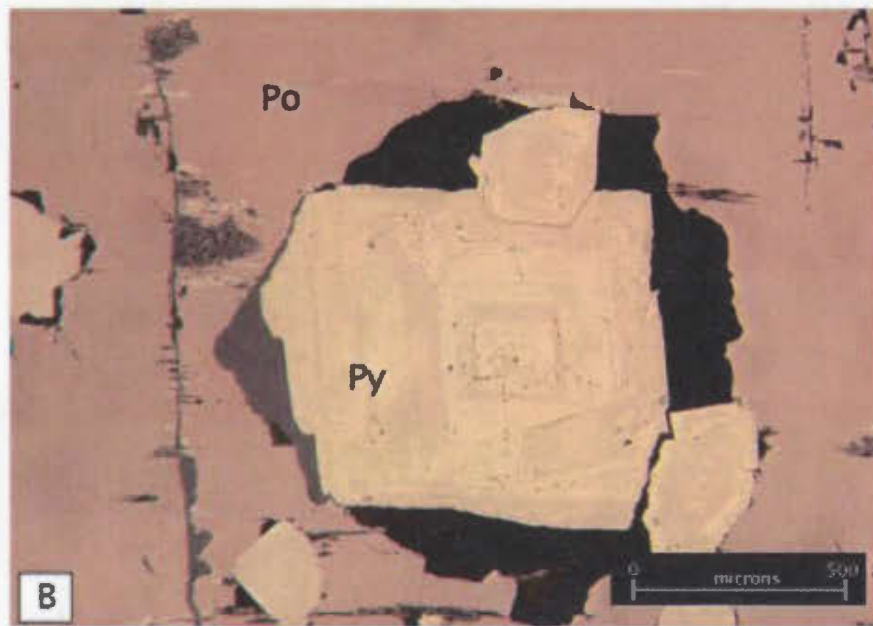
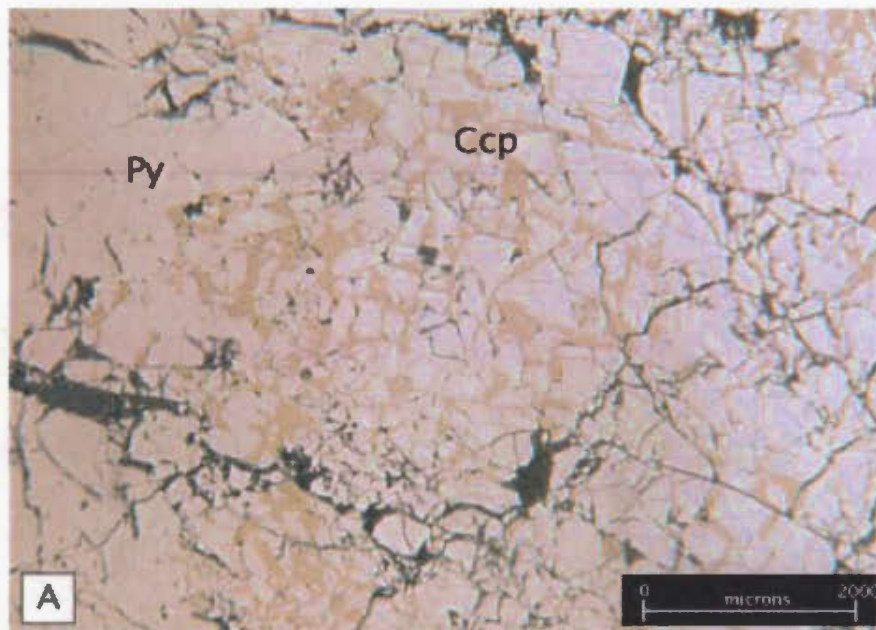


Figure 9.12 Reflected light photomicrograph from the SMA Sheep Brook location. (a) Brittle fractured and brecciated pyrite containing chalcopyrite. These textures suggest that low-T brecciation and subsequent remobilization of ccp into secondary porosity occurred; (b) This image is an example of Ni-och growth banding in pyrite. The image has been processed to accentuate the colour contrast between Ni-poor (darker) and Ni-rich (whiter) bands. Note the scale bars in the lower right corners.

to medium-grained crystals or aggregates, typically proximal to fractures or adjacent to pyrite cubes. Sphalerite occurs as irregular blebs and ragged veinlets within pyrrhotite and is locally spatially associated with galena and/or pyrite. Discrete platinum group minerals (PGM) have been identified in several samples from the Sheep Brook area by SEM-MLA techniques described in Chapter 1 and are discussed in the electron microprobe chapter.

## **9.8 Petrographical summary**

Textures observed throughout the Steel Mountain Anorthosite are relatively consistent, permitting a generalized petrogenetic sequence to be described for the map area.

Plagioclase textures in particular are consistent and show local variations in the degree of recrystallization indicative of medium to high temperature recrystallization. Plagioclase was the first major phase to crystallize in the SMA. During plagioclase crystallization, oxides formed immiscible droplets and were trapped as inclusions within some plagioclase crystals. Pervasive granulated plagioclase microtextures indicate granulation and recrystallization developed at a relatively high temperature, suggesting that perhaps granulation and recrystallization occurred syn-emplacment.

An immiscible oxide phase must have been present for most of the crystallizing period, because oxides are observed in all primary silicate phases, which petrography indicates crystallized over a range of time. In particular, at the Bishop deposits, a very large volume of oxides was present as an immiscible phase until late in the crystallization sequence, because the oxides form late lens- or dike-like bodies that cross-cut all other phases.

Pyroxene began to crystallize while plagioclase was still crystallizing, which is indicated by the presence of round pyroxene blebs in some plagioclase megacrysts. In the field and in thin sections, pyroxene textures suggest it crystallized later than plagioclase. Pyroxene

is interstitial to plagioclase nearly everywhere, and particularly where it is interstitial to granulated plagioclase, it is notably less deformed, suggesting that it was present as a liquid phase during the onset of plagioclase granulation. Grain boundaries where pyroxene is embayed into, or shows cusped contacts with plagioclase, suggest that pyroxene crystallized after plagioclase. Some of the larger pyroxene aggregates are weakly to moderately deformed, which could be because they crystallized during emplacement-related deformation, or it could be that deformation in the Paleozoic caused this deformation. A less likely scenario is that pyroxene crystallization was contemporaneous with plagioclase crystallization, because at high temperatures plagioclase deforms more easily than pyroxene, therefore plagioclase would deform but pyroxene would show less evidence for deformation (Passchier and Trouw, 1996). However, the former hypothesis, which suggests most pyroxene crystallized syn- to late relative to plagioclase, is supported by field and petrographic evidence

Garnet formed after all primary silicate phases crystallized, but before greenschist alteration phases formed. The spatial distribution and textures of garnet indicate that it grew at the expense of the phases it is in contact with, such as plagioclase, pyroxene and Fe-Ti oxides. The clean, homogenous, inclusion-free, unzoned (EMPA analysis) texture of garnet is typical of slow, diffusion-controlled growth, and several authors have attributed this growth to a post-magmatic setting (McLelland and Whitney, 1977; Whitney and McLelland, 1972). Symplectic rims around garnet appear to have formed in multiple stages, because there is generally more than one rim. Due to a lack of cross-cutting textures it is difficult to constrain the relative timing of these rims. However, it is commonly accepted that these types of symplectic overgrowths form during uplift and the resultant decompression, when water is introduced and the lower temperatures assemblages that comprise the coronas are stable (Winter, 2001).

Alteration of mafic minerals (uralitization, amphibolitization) and felsic phases (sericitization, saussuritization) all involve hydration reactions. Pyroxene rims of

actinolite and biotite are late products and cross-cut deformation textures but are not themselves deformed. Chlorite locally consumes actinolite and biotite and is the latest alteration phase. The formation of these phases is coeval with the formation of sericite and epidote in plagioclase, and throughout the samples there are mutually cross-cutting relationships between late felsic and mafic alteration phases.

## **Chapter 10: Steel Mountain Anorthosite Whole Rock Lithochemisrtry**

### **10.1 Introduction**

Twenty-six samples from the SMA were analysed by XRF and ICP-MS methods outlined above. Appendix 3 lists the geochemistry for all SMA samples. All major oxides were analysed ( $\text{SiO}_2$ ,  $\text{Al}_2\text{O}_3$ ,  $\text{MgO}$ ,  $\text{CaO}$ ,  $\text{Fe}_2\text{O}_3$  (Fe total),  $\text{Na}_2\text{O}$ ,  $\text{K}_2\text{O}$ ,  $\text{TiO}_2$ ,  $\text{P}_2\text{O}_5$ ,  $\text{MnO}$ ). Additionally, the trace elements S, Cl, Sc, V, Cr, Ni, Cu, Zn, Ga, As, Rb, Sr, Zr, Y, Nb, Ba, Ce, Pb, Th and U (<1%,) were also analysed. Precious metals (Pt, Pd and Au) were analysed by fire assay ICP-MS. LOI is not reported in these analyses, but major oxides are normalized to 100% anhydrous for all diagrams.

This chapter presents data in several sections. First, major element data and some minor element data are presented followed by minor element and trace element data. Samples are organized by rock type, which is based on petrography. The nomenclature used for samples is consistent with the maps. Most plots show a distinction between different rock types, as would be expected, but there are a few exceptions, where particular samples consistently plot with different rocks types, suggesting that the polished thin section was not representative of the bulk samples used for XRF analysis. Alteration in these rocks is minimal, and microprobe analysis confirms that there is little mobility of K, Na and Ca during recrystallization; therefore, diagrams involving mobile elements such as K, Na and Sr are valid as primary magmatic compositions. Many plots used for the RCLIS and TBGS are designed for rocks with a basaltic/gabbroic composition with specific ranges of  $\text{SiO}_2$  but many samples in the SMA do not fall within this compositional range. In fact, many other elements are below detection limits in these samples, thus only a limited amount of these standard plots are presented for these samples. One population of samples is not included in the diagrams presented below: massive sulfide and massive oxides, which do not contain sufficient major oxides to plot on these types of diagrams.

## 10.2 Bivariate diagrams

### 10.2.1 Harker diagrams

Harker diagrams were used to plot the major oxides ( $\text{TiO}_2$ ,  $\text{Al}_2\text{O}_3$ ,  $\text{Fe}_2\text{O}_3$ ,  $\text{Na}_2\text{O}$ ,  $\text{CaO}$ ,  $\text{MgO}$ ,  $\text{K}_2\text{O}$ ,  $\text{P}_2\text{O}_5$ ) and identify large-scale geochemical trends. In these plots, oxides are normalized to 100%, ignoring trace elements, which generally total less than 1% and are thus insignificant.

$\text{SiO}_2$  vs  $\text{TiO}_2$  (Figure 10.1a) defines a weak negative correlation between  $\text{SiO}_2$  and  $\text{TiO}_2$ ; the trend is relatively weak for leucogabbro samples ( $R^2 = 0.32$ ) whereas anorthosite samples have  $R^2 = 0.93$ . This diagram is able to distinguish the different rock types on a large scale, indicating that the anorthosite samples contain the least amount of  $\text{TiO}_2$  and the more mafic noritic samples contain the most. The single mafic dike sample, SMA-65, has a distinctive signature, with low  $\text{SiO}_2$  and the most abundant  $\text{TiO}_2$  concentration. This dike is texturally and morphologically similar to several other dikes in the mapped area, thus it is assumed that this composition is representative of the mafic dikes in the SMA region. One leuconorite sample, SMA-71, plots within the anorthosite samples, suggesting that the thin section was not representative of the sample used for XRF analysis. Similarly, SMA-61B, termed anorthosite, plots within the more mafic samples. This name is based on field geology, because a large region surrounding this sample location had an anorthositic composition.

$\text{SiO}_2$  vs  $\text{Al}_2\text{O}_3$  (Figure 10.1b) exhibits a positive sloping trend, where  $\text{Al}_2\text{O}_3$  increases with increasing  $\text{SiO}_2$ . Anorthositic samples have the greatest  $R^2$  value (0.97) and leucogabbro the lowest ( $R^2 = 0.60$ ). This suggests that the primary control on  $\text{Al}_2\text{O}_3$  is plagioclase, because there are no other major minerals except amphibole that contain aluminum in these samples and amphibole is less voluminous and generally related to mafic mineral alteration. However, samples with abundant pyroxene will also control the  $\text{Al}_2\text{O}_3$  trend. As with other diagrams, the different rock types fall along a smooth line, and are generally separate from each other. However, samples SMA-71 and SMA-61B both

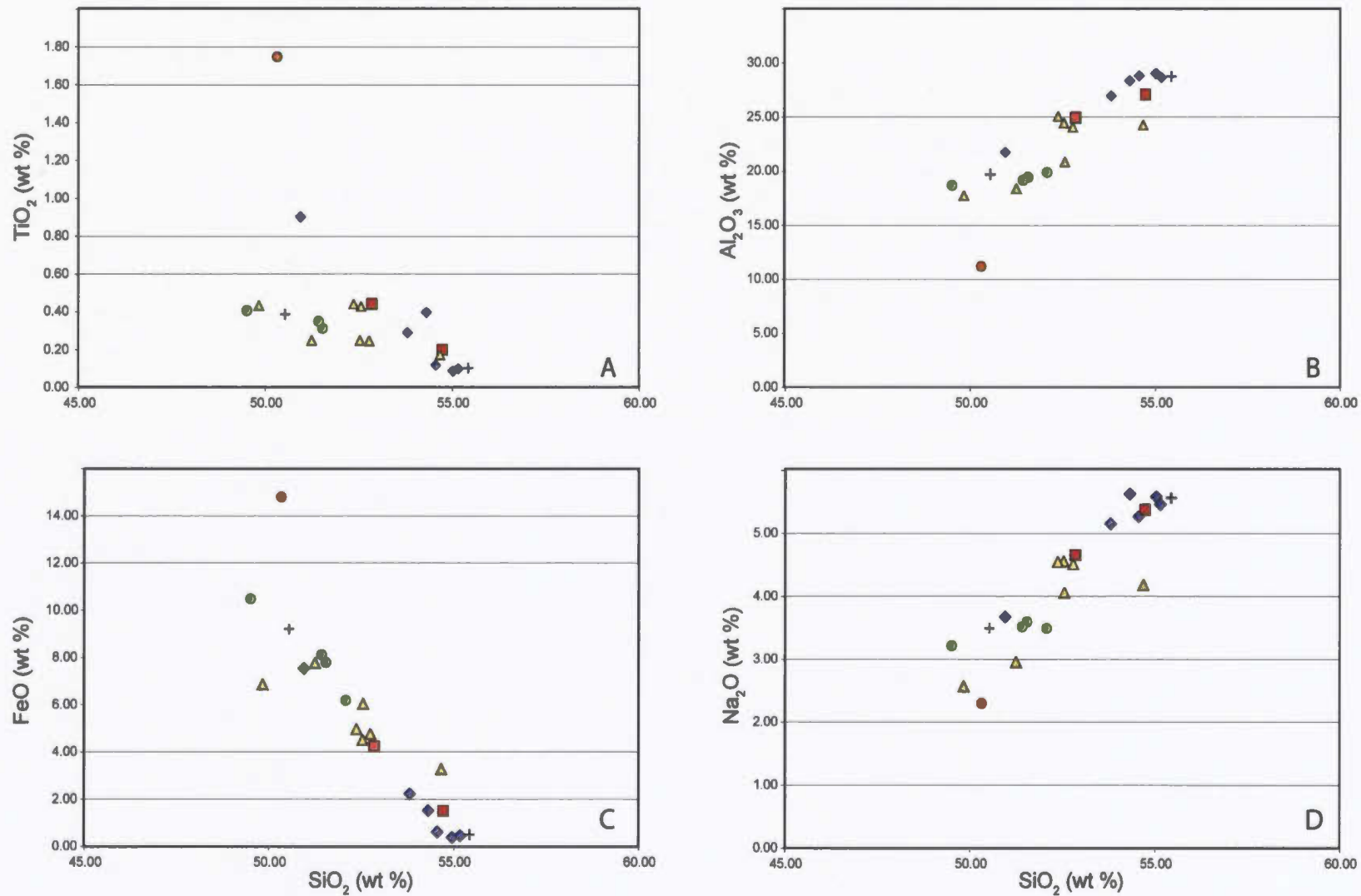
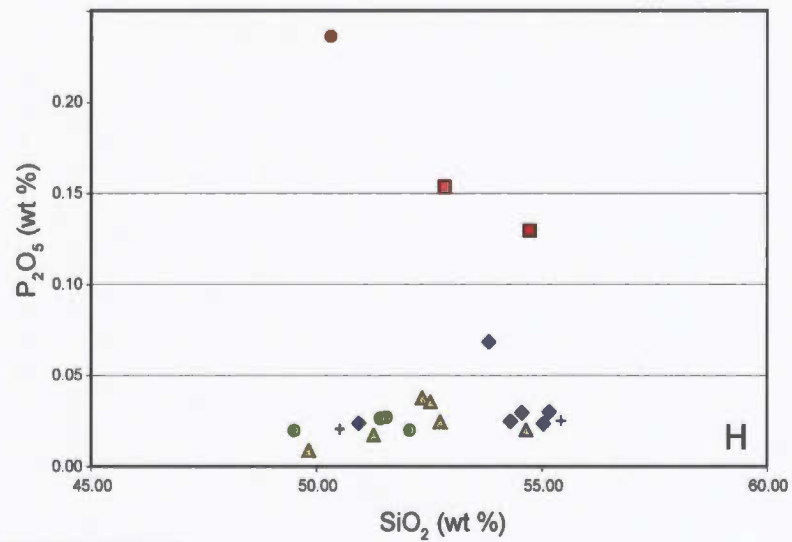
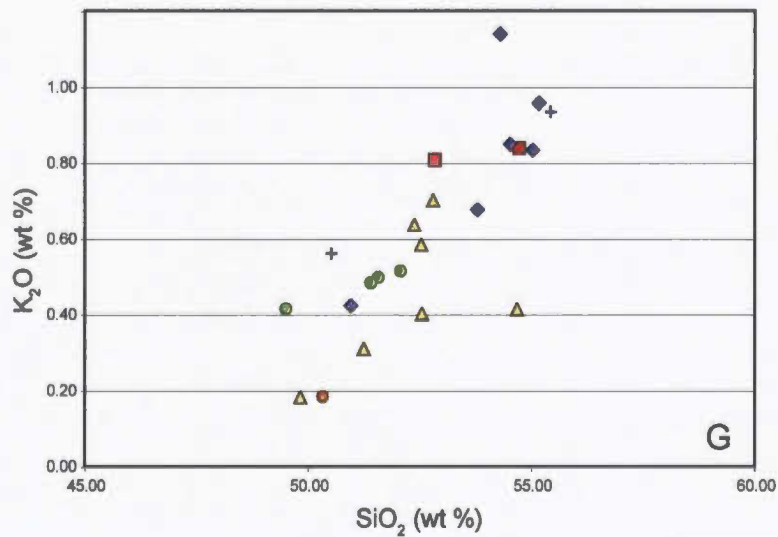
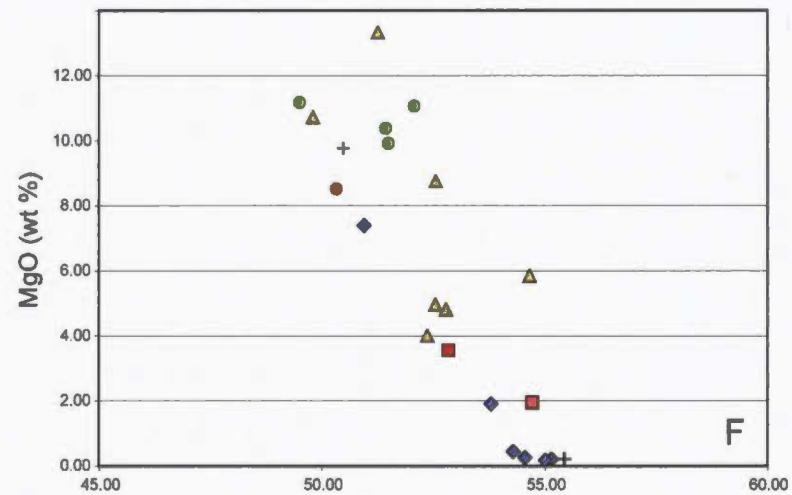
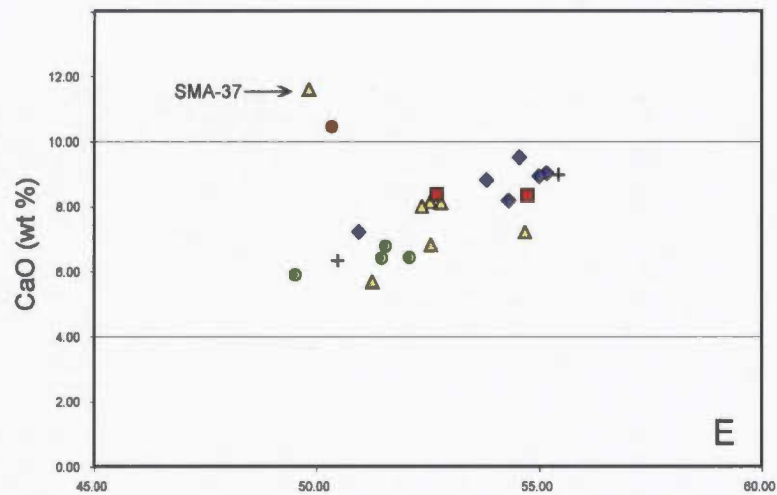


Figure 10.1 Harker diagrams for SMA whole rock data. Descriptions for each diagram are given in the text. A global legend for all eight diagrams is given at the bottom of the preceding page. All diagrams have  $\text{SiO}_2$  on the x-axis and the y-axis oxide is noted.  $\text{FeO}$  is  $\text{FeO} + \text{Fe}_2\text{O}_3$ .



abundance of orthopyroxene and clinopyroxene. Since OPX is relatively more abundant and microprobe data indicates that all OPX has an enstatite composition, OPX abundance is most likely the main control on the shape of this data trend. The most MgO-rich samples are leuconorite and norite, supporting this conclusion.

SiO<sub>2</sub> vs K<sub>2</sub>O (Figure 10.1g) defines a strong positive correlation with a shape quite similar to those of Al<sub>2</sub>O<sub>3</sub> and Na<sub>2</sub>O. K occurs mainly in orthoclase and biotite.

Petrography and microprobe analysis did not establish the presence of significant orthoclase, but, nevertheless, the most K-rich samples are anorthosite. This suggests that there is more orthoclase present than originally suspected, or that there are other hosts for K, because the anorthositic samples do not contain very much biotite.

SiO<sub>2</sub> vs P<sub>2</sub>O<sub>5</sub> (Figure 10.1h) has a flat shape, aside from several outliers. This trend indicates that all samples have relatively low P<sub>2</sub>O<sub>5</sub>, and that there is little variation with P<sub>2</sub>O<sub>5</sub> concentration with SiO<sub>2</sub>. The mafic dike is the most P-rich sample, followed by the only two gabbro-norite samples in this selection. A plot of P<sub>2</sub>O<sub>5</sub> versus Cl (not shown) shows little correlation, suggesting that some P might not be related to apatite. This plot highlights the overall lack of phosphate, even in massive oxide samples. Several large Fe-Ti oxide deposits associated with mafic rocks within similar aged anorthosites in Quebec (e.g. Labrivillé) contain significant P concentrations and the rocks are called nelsonites. It is possible that these rock types may have been part of the oxide deposits in the SMA but were mined out before they were identified.

### **10.3 General composition**

TAS diagrams are useful for classifying igneous volcanic (e.g. Irvine and Baragar, 1971; LeMaitre et al., 1989) and plutonic (Wilson, 1989) rocks, although Wilson (1989) is a simple modification of Figure 2.2 of Cox (1979). These diagrams require that samples are not altered, a criterion that is met by most, but not all samples. Many samples are recrystallized, but microprobe analysis of recrystallized and non-recrystallized

plot outside the expected locations for their respective rock type. The mafic dike has a distinctively lower  $\text{Al}_2\text{O}_3$  concentration relative to  $\text{SiO}_2$ , suggesting it has less plagioclase, an observation supported by petrography.

$\text{SiO}_2$  vs  $\text{FeO}$  (Figure 10.1c) defines a strong negative correlation. In most samples, petrography indicates the major hosts for Fe are orthopyroxene and Fe-Ti oxides. Therefore, this trend is reflective of increasing OPX, and partly increasing Fe-Ti oxide contents.

$\text{SiO}_2$  vs  $\text{Na}_2\text{O}$  (Figure 10.1d) exhibits a good positive correlation. Similar to  $\text{Al}_2\text{O}_3$ , the major host of Na is plagioclase. Microprobe data indicate that plagioclase contents have a relatively restricted An range, from approximately  $\text{An}_{50}$  to  $\text{An}_{55}$ . Anorthosite samples have a relatively restricted compositional range, aside from SMA-61B, which plots with gabbro samples, conversely gabbro and other mafic rocks have a wider Si:Na range. Again, the mafic dike, SMA-65 has a distinctively lower Na concentration, reflecting its relatively lower plagioclase content.

$\text{SiO}_2$  vs  $\text{CaO}$  (Figure 10.1e) has only a weak positive correlation. There are two major outliers – SMA-65, the mafic dike, and SMA-37. Unlike Al and Na, there are multiple hosts for Ca in these samples. Plagioclase is still volumetrically the main host, but some samples also contain clinopyroxene. The anorthosite samples are distinguished from those samples bearing clinopyroxene because of higher amounts of  $\text{SiO}_2$ . In the case of SMA-37, not only does it have the highest average An content ( $\text{An}_{56}$ ), but it also has relatively abundant CPX compared to other mafic samples. SMA-65 doesn't contain as much plagioclase, but the elevated CaO contents could be explained by relatively abundant CPX and calcic amphibole (e.g. hornblende and tremolite).

In  $\text{SiO}_2$  vs  $\text{MgO}$  (Figure 10.1f) there is a strong negative correlation. The different rock types are relatively distinct on this diagram, controlled most likely by the relative

plagioclase and orthopyroxene indicates that major element mobility was minimal, suggesting that these data represent the true bulk composition of these rocks.

Figure 10.2 indicates that the SMA rocks in the map area have a sub-alkaline composition.

AFM diagrams (Figure 10.3) graphically determine the overall composition of the samples and to identify major geochemical trends that may be related to evolution and fractional crystallization of the magma. This diagram is intended for mafic volcanic rocks, but it is used here for mafic to intermediate plutonic rocks, therefore care is required in the use of nomenclature.

Most samples have a calc-alkaline composition, although anorthositic samples fall in the tholeiitic field. The data define a vertical trend from the FeO corner down towards an intermediate value between the alkali and MgO corners. This trend is atypical of samples that have evolved through normal fractional crystallization. However, the trend of the data is consistent with the mineralogy in that most samples in the calc-alkaline field contain some orthopyroxene, (i.e. pulls the data towards the MgO corner), which is balanced by plagioclase, which pulls data towards the alkali corner. That anorthosite samples plot near the FeO corner is not likely a reflection of Fe enrichment. Petrography did not identify significant Fe-Ti oxides in anorthosite samples. Furthermore, in the FeO vs SiO<sub>2</sub> Harker diagram in Figure 4.1c, anorthosite samples are clearly FeO-poor. Therefore, this might just reflect the fact that this diagram only represents an average of 15% of the oxides in any sample. SiO<sub>2</sub>, Al<sub>2</sub>O<sub>3</sub> and CaO are all absent from this diagram and all have a greater control over anorthosite composition than alkalis, MgO and FeO.

The Steel Mountain anorthosite is depleted in many trace elements that are normally used to construct trace element discrimination diagrams, so it is not possible to present the same diagrams as for the RCLIS or the TBGS. The abundance of plagioclase in many of these samples permits the use of several diagrams with Sr and Ba. Sr substitutes readily

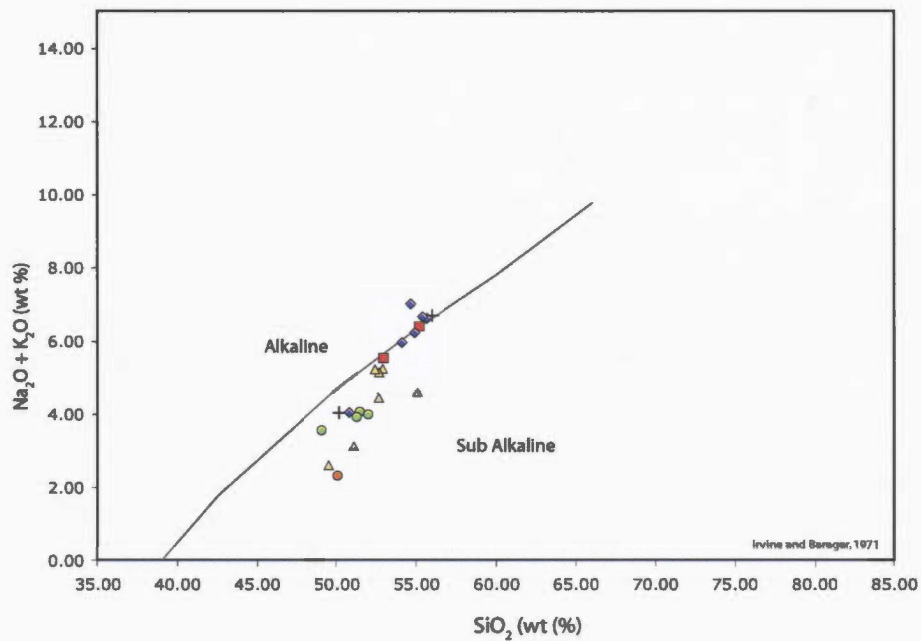


Figure 10.2 This total alkali silica diagram (TAS) indicates that SMA samples exhibit an overall subalkaline composition. Anorthosite samples demonstrate a weak affinity to alkaline compositions. The legend is located in the top right corner of Figure 10.3.

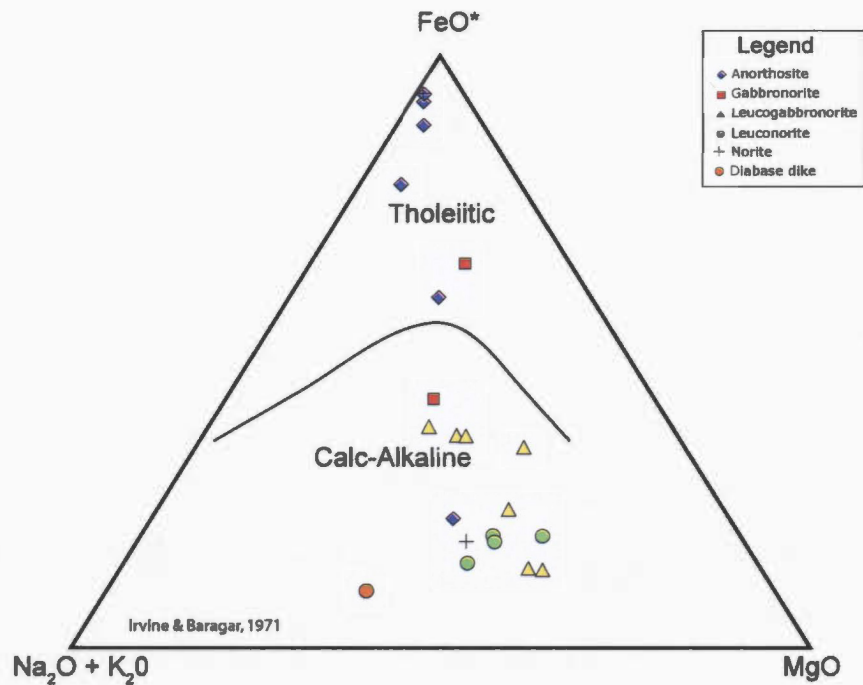


Figure 10.3 This AFM diagram indicates that aside from anorthosite samples, the SMA has a calc-alkaline composition. The samples do not show strong evidence for compositional evolution. For a discussion of the apparent Fe enrichment in anorthosite samples, refer to text. the legend for both Figure 10.2 and 10.3 is in the upper right corner.

into plagioclase in place of Ca ( $D= 2.8$  to  $15.6$ ) and can be used to monitor relative differentiation in samples.

$Al_2O_3$  vs Sr (Figure 10.4a) exhibits a well-defined trend with a positive slope. Plagioclase is the only major host for Al in most of these rocks, aside from amphibole and biotite, which are secondary in most samples, and because Sr substitutes into plagioclase for Ca, this diagram is useful for illustrating the relative differentiation. Anorthosite samples plot at the upper end of the curve, the mafic dike plots in the bottom corner with the lowest amount of Sr and  $Al_2O_3$ , and the intermediate mafic samples fall along the main trend.

CaO vs Sr (Figure 10.4b) is similar to  $Al_2O_3$  vs Sr, except that SMA-65 (mafic dike) and SMA-37 plot significantly off-trend relative to the rest of the samples. Similar to previous plots involving CaO, SMA-37 shows a relative CaO enrichment, likely reflecting the greater abundance of CPX and relatively Ca-enriched plagioclase compositions. The mafic dike, SMA-65 contains more CaO relative to  $Al_2O_3$ , suggesting that in this sample other Ca-bearing minerals have a strong influence on the overall composition. Notably, this sample has considerable fracture-hosted late calcite, which may have derived some of its Ca from plagioclase and some from the alteration of pyroxene, although the calcite-bearing fluids probably did not originate completely locally.

Ba vs  $K_2O$  (Figure 10.4c) exhibits a positive linear slope and illustrates the general trend of differentiation in the map area. The different lithologies break out into separate groups relatively well, particularly norite and melanorite samples. Anorthosite samples have the highest values and the more mafic samples plot lower on the data trend. The mafic dike has the lowest  $K_2O$  to Ba ratio of all the samples, probably because there is very little orthoclase or biotite as  $K_2O$  hosts and little Ba as well.

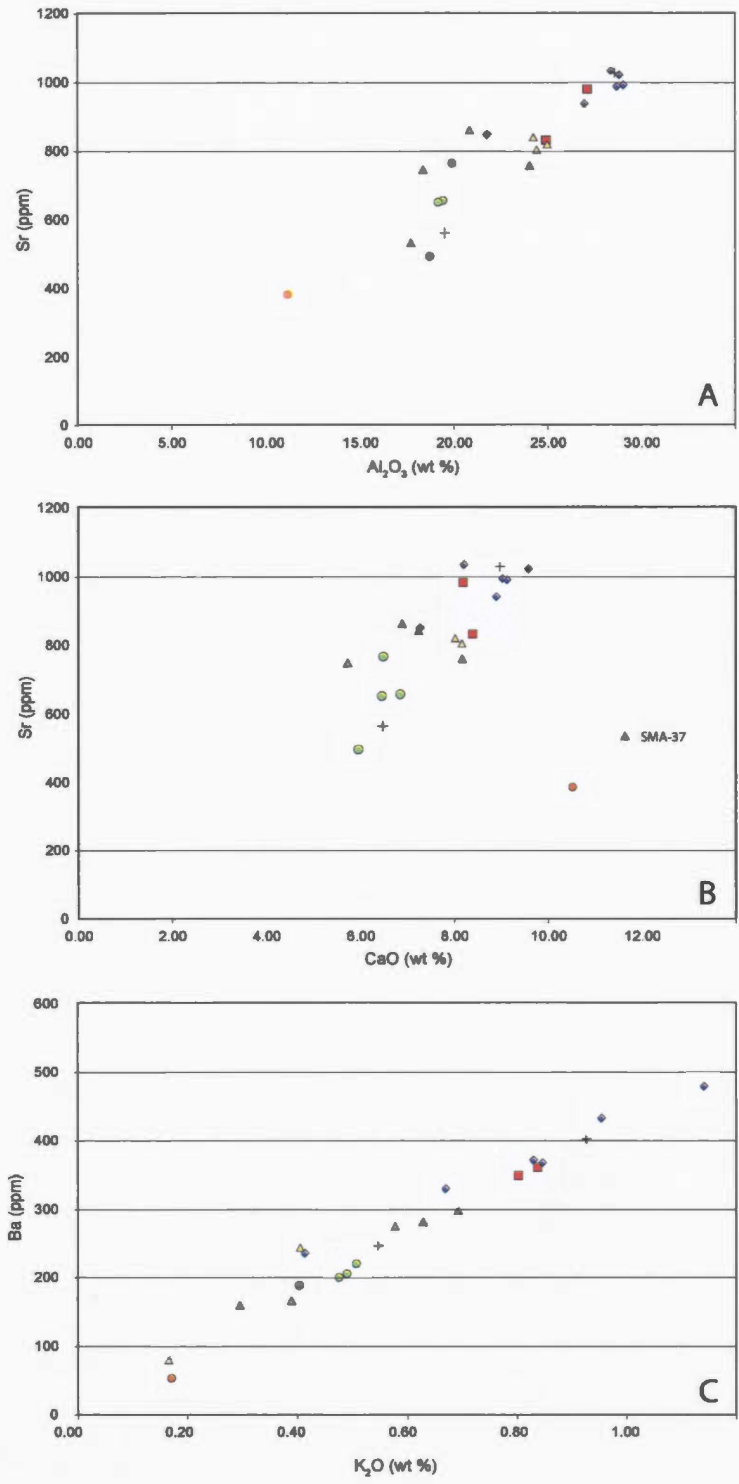


Figure 10.4 The trace elements Ba and Sr are plotted against major oxides to illustrate the relative differentiation between different lithologies in the SMA. All three diagrams consistently differentiate between lithologies, indicating that the SMA nomenclature is accurate. Refer to the text for a complete discussion of the diagrams.

## 10.4 Igneous nomenclature

Figure 10.5a, after Wilson (1989) is used to classify plutonic igneous rocks, but does not specifically classify anorthositic rocks, and does not differentiate between norite and gabbro compositions (these rocks differ in the modal abundance of mafic minerals). Anorthosite samples plot in the syeno-diorite field, whereas most other samples plot in the lower right corner of the main gabbro field and in the adjacent unnamed field that separates the gabbro field from diorite (i.e. illustrates the mafic to intermediate composition of the SMA samples.)

The Jensen plot (Figure 10.5b) after (Jensen and Pyke, 1982) plots ionic  $\text{Fe}^{2+} + \text{Ti}^{4+}$  versus  $\text{Al}^{3+}$  versus  $\text{Mg}^{2+}$  and Figure 4.5b is adapted from volcanic to plutonic nomenclature in a manner similar to Wilson (1989). On this diagram, most anorthosite samples plot in the granitic corner, reflecting Al abundance compared to Fe+Ti and Mg. Leucogabbro-norite samples fall mostly within the diorite field and trend into the high-Mg gabbro field, whereas leuconorite and norite samples fall within the high-Mg gabbro field. The mafic dike has a distinct composition and plots near the upper boundary line between olivine gabbro and high-Fe gabbro.

## 10.5 Summary

Major oxide geochemical data for the mapped area of the Steel Mountain Anorthosite defines several relatively well-constrained trends that are indicative of fractional crystallization and clearly demonstrate the control major minerals had on the bulk geochemistry. In particular, plagioclase controls  $\text{Al}_2\text{O}_3$ , CaO,  $\text{Na}_2\text{O}$ ,  $\text{K}_2\text{O}$  and the overall  $\text{SiO}_2$  concentration. Anorthosite samples consistently plot at the high end of  $\text{SiO}_2$  concentrations and generally with most of the aforementioned oxides. Exceptions include most prominently the mafic dike, SMA-65, which is taken to be representative of the local dike population. SMA-37 exhibits a distinctive pattern in diagrams with CaO,

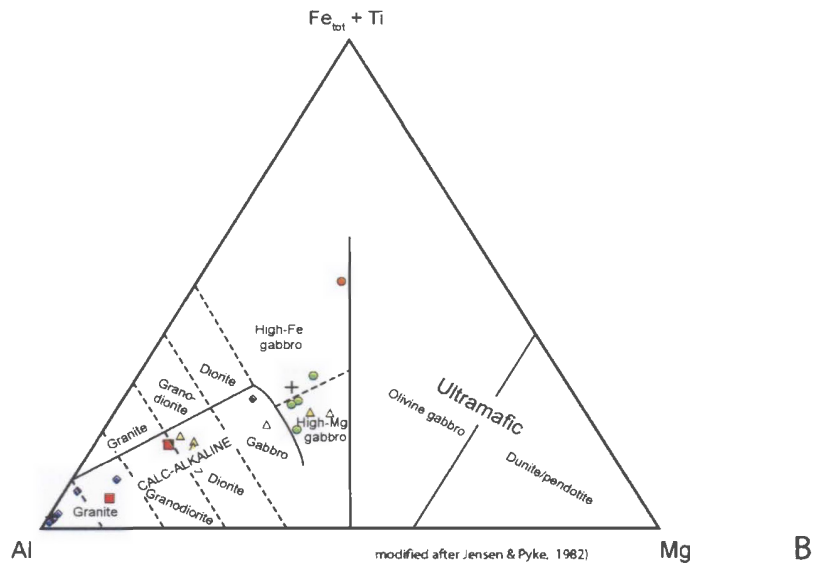
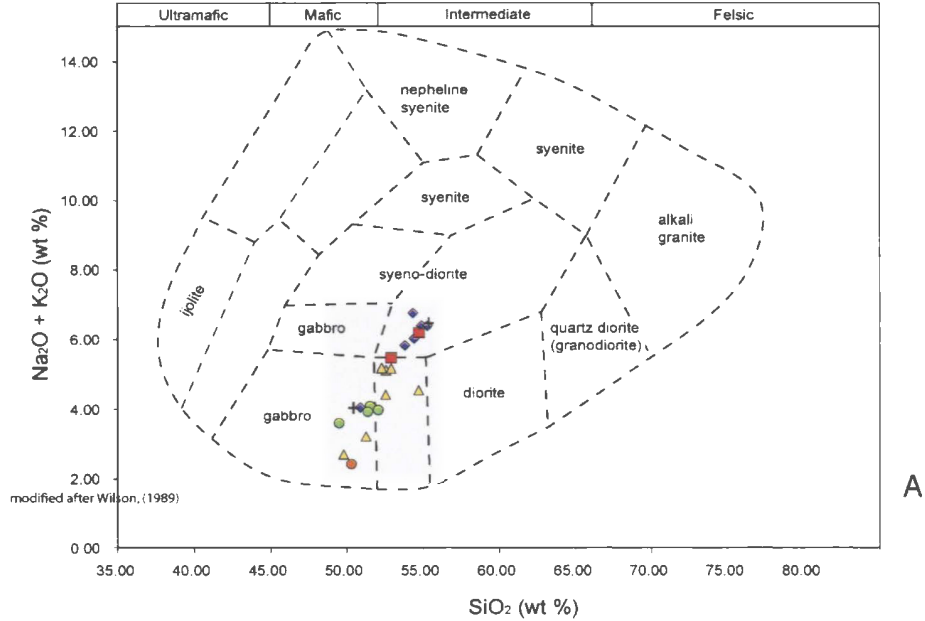


Figure 10.5 Igneous nomenclature for SMA samples. A) This TAS diagram indicates that most mafic samples have a gabbroic (or noritic) composition, while anorthosite samples plot in the syeno-diorite field. This diagram is not designed for anorthositic rocks, but demonstrates consistency with other nomenclature diagrams; B) This diagram of ionic Fe+Ti vs Al vs Mg indicates that most SMA samples are Mg-rich gabbro, while anorthosite samples plot as granite because this diagram does not accommodate anorthosite compositions.

reflecting elevated CPX and anorthite abundances, and SMA-61B and SMA-71 plot inconsistently with their petrographical classification.

Total alkali silica diagrams demonstrate that the SMA is sub-alkaline and mafic samples plot as gabbro whereas more felsic samples follow a trend with increasing SiO<sub>2</sub> and alkalis continuing into the syeno-diorite field. These diagrams indicate that the petrographical nomenclature used to differentiate samples is consistent, aside from a few outliers and that fractional crystallization likely formed the range of lithologies present in the map area.

Jensen plots accurately represent the full compositional range of SMA rocks and indicate that most mafic samples to fall into gabbroic fields and felsic samples to fall into the granitic spectrum of lithologies.

These samples contain relatively low abundances of most trace elements rendering most trace element diagrams unusable. Several trace elements that readily substitute into major minerals in these samples were used effectively to illustrate the overall differentiation of the sample suite in the SMA.

## **Chapter 11: Steel Mountain Anorthosite mineral geochemistry**

Twenty-one samples were analysed by microprobe techniques described above. Major phases investigated during this study include plagioclase, pyroxene, garnet, amphibole, biotite, Fe-Cu-Ni sulfides and Fe-Ti oxides.

The main goal of microprobe analysis was to characterize the composition of the minerals from the field area within the Steel Mountain Anorthosite, including solid solution and exsolution lamellae in oxides. Secondly, because of the extensive recrystallization textures documented in Chapter 9, microprobe data were used to determine if recrystallization changed mineral composition, particularly in plagioclase and pyroxene. Some plagioclase exhibits a pink- to lilac colouring, which is readily apparent in outcrop and transmitted light microscopy. Microprobe analyses were conducted on plagioclase in the hopes of determining whether detectable trace elements cause this colour. Finally, in the Sheep Brook area, it appears that there was potential for the presence of discrete platinum group metals, so microprobe and MLA analyses were employed to detect and analyse for these minerals.

Data in this chapter are presented using the same sample nomenclature that was developed in previous chapters. A full list of microprobe analyses are presented in Appendix 4, including detection limits and accuracy and precision calculations in a manner similar to RCLIS microprobe data. Likewise, data are filtered in a similar manner to RCLIS microprobe data.

### **11.1 Plagioclase**

Sixteen plagioclase-bearing samples from the SMA were analysed, comprising three anorthosite samples, two gabbronorite samples, three leucogabbronorite samples, three leuconorite samples, three norite plus melanorite samples and two massive oxide samples. Plagioclase analyses measured SiO<sub>2</sub>, Al<sub>2</sub>O<sub>3</sub>, CaO, Na<sub>2</sub>O, K<sub>2</sub>O, FeO, BaO, and in

some samples, Sr; Rb was not measured. Plagioclase was analysed to characterize its overall composition and to determine if there are compositional differences between the lithologies determined through petrography, to determine the degree of core-rim zoning or other small-scale zonation patterns, to determine the effect(s) recrystallization had on plagioclase compositions, and finally, to assess if the pink colouration described above has a measurable chemical cause.

The crystal morphologies in these samples are such that it is difficult to determine what is “core” and what is “rim”, because most crystals do not preserve a primary texture, thus most analyses are from the centre region of crystals, where the least amount of recrystallization occurs. When rims were analysed, it was often where the plagioclase was in contact with a different phase, making the distinction of what constitutes a rim less ambiguous. In some tables below, inclusions and blebs are listed separately. To clarify, the term inclusion is used in the petrographical sense in that they appear to be primary plagioclase crystals enclosed in primary minerals such as orthopyroxene or Fe-Ti oxides. Blebs describe unusual rounded zones within otherwise homogenous plagioclase crystals that displayed strong colour contrasts in backscatter electron images. In some examples, these “blebs” are distributed along apparently crystallographically controlled planes, but in other locations, they are randomly distributed. It is possible that these represent exsolved orthoclase, because they are all enriched in potassium and sometimes in Mn or Fe or Ba.

Plagioclase hosted in anorthosite averages An 45 with a standard deviation of 6.6 for 16 analyses from three samples. Gabbronorite plagioclase averages An 47 with a standard deviation of 14.0 for 13 analyses from two sample. Leucogabbronorite plagioclase averages An 45 with a standard deviation of 14.1 for 23 analyses from three samples. Leuconorite analyses average An 54 with a standard deviation of 18.4 for 15 analyses from three samples, whereas norite analyses average An 53 with a standard deviation of 13.6 for 21 analyses from three samples. The variation in these data is because cores,

rims and other types of locations within plagioclase crystals are included. Table 11.1 is a summary of the above data, and Table 11.2 is a more detailed presentation of the different types of location analyses. Figure 11.1 is a diagram that summarizes the composition of all SMA plagioclase analyses. The bulk of analyses plot near the andesine-labradorite compositional boundary, with only minor orthoclase deviations. Several data points fall quite far outside the normal compositional range, which are discussed below. There does not appear to be any systematic spatial distribution pattern in plagioclase compositions in the map area of the SMA (Figure 11.2), suggesting that little differentiation occurred during crystallization.

<b>Litho</b>	<b>AVG An</b>	<b>An StDev</b>	<b>n</b>
anorthosite	45.32	6.63	16
gabbronorite	47.24	14.00	13
leucogabbronorite	45.31	14.14	23
leuconorite	54.87	18.36	15
norite	53.30	13.55	21

Table 11.1 Average and standard deviation of plagioclase composition from SMA lithologies. All different crystal location types are included in this table.

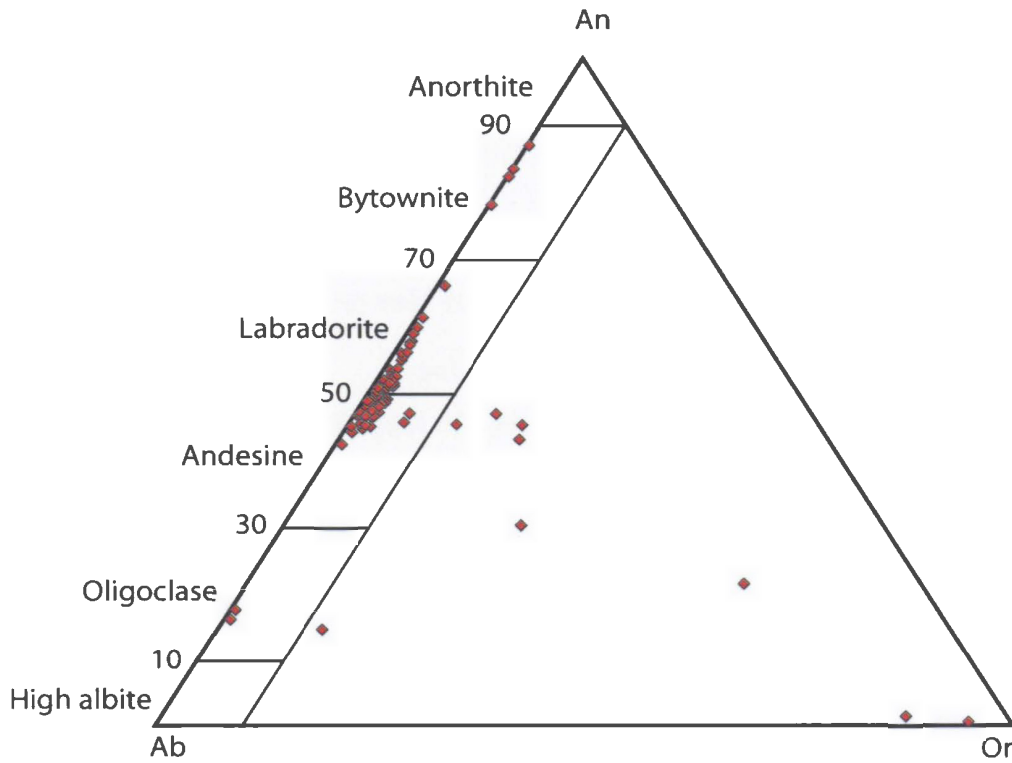


Figure 11.1 An-Ab-Or diagram of microprobe data for SMA samples. Only minor compositional variation between different lithologies occurs, thus analyses were not subdivided in this figure. Analyses that plot close to the Or corner represent exsolution lamellae or blebs hosted by normal plagioclase. Samples near the Ab corner represent recrystallized rims, whereas anorthositic analyses also represent recrystallized rims.

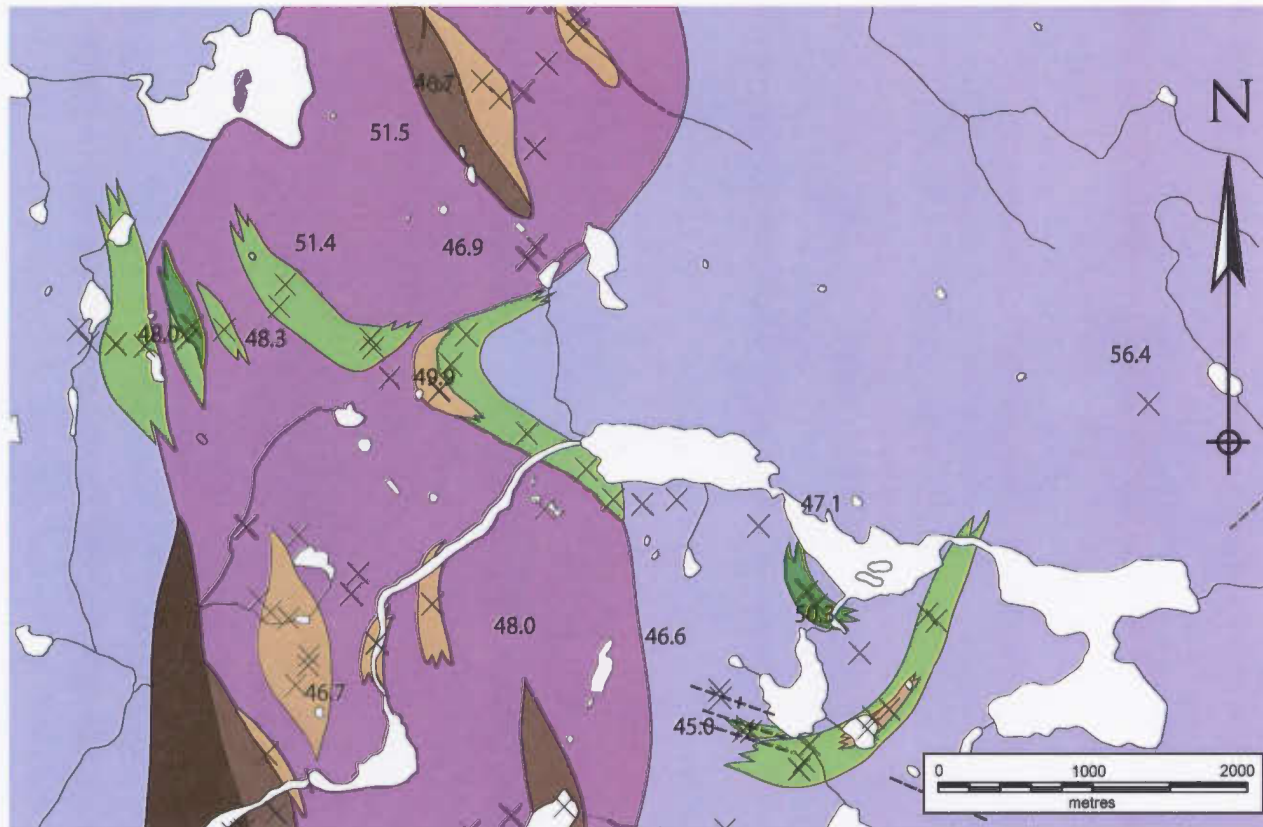


Figure 11.2 Inferred bedrock map of the west-central portion of the Steel Mountain Anorthosite. The map area comprises a series of gradational, N-S elongate lenses or zones of variable mineralogy. These lenses are discontinuous and patchy within mapped areas. Plagioclase composition does not appear to change systematically between different lithological units, suggesting little differentiation of the magma in this region. Scale bar in bottom right is in metres. Refer to Figure 8.1 for a legend of SMA lithologies.

<b>Crystal location</b>	<b>AN</b>	<b>GBN</b>	<b>LGBN</b>	<b>LNOR</b>	<b>NOR</b>
Core avg	47.78	51.88	48.78	49.66	48.47
Core stdev	0.99	4.34	2.32	2.42	2.93
n	9	9	13	9	11
Rim avg	46.61	56.63	52.34	59.92	52.61
Rim stdev	n/a	0.78	0.94	1.27	0.22
n	1	2	3	3	3
Bleb avg	36.46	n/a	1.15	n/a	n/a
Bleb stdev	13.28	n/a	0.61	n/a	n/a
n	3	0	2	0	0
Recrystallized avg	46.94	17.00	51.23	65.46	60.20
Recrystallized stdev	0.35	1.02	0.28	44.79	21.16
n	3	2	4	2	7
Inclusion avg	n/a	n/a	46.90	n/a	n/a
Inclusion stdev	n/a	n/a	0.22	n/a	n/a
n	0	0	2	0	0

Table 11.2 Summary of the different crystal location types in each lithology. Aside from core analyses, most other types do not have more than a few analyses, some which are quite variable, highlighting the heterogeneities of plagioclase at a microscopic scale. AN= anorthosite; GBN= gabbro-norite; LGBN= leucogabbro-norite; LNOR= leuconorite; NOR= norite

According to these analyses, the different lithologies do not exhibit statistically different core compositions. Rim compositions are more variable, owing to the varied rim morphologies and less consistent analytical techniques for determining what constitutes a rim. Despite this, rim compositions appear to be weakly more Ca-rich. Bleb analyses are limited and these vary considerably between samples. Blebs in anorthosite range from An 21 to An 45, whereas in leucogabbro-norite, two blebs exhibit extremely potassium-rich compositions. It is likely that these blebs are exsolution of orthoclase (antiperthite) or possible alteration products where K-rich fluids resulted in local recrystallization. Figure 11.3 is an example of bleb morphology, illustrating the possible crystallographic control on the location of these features. Aside from higher potassium contents in blebs, some analyses reveal slight Fe enrichments compared to background. However, this pattern is not consistent and may not be relevant to the relatively brighter colour of the blebs (*i.e.* greater average atomic mass).

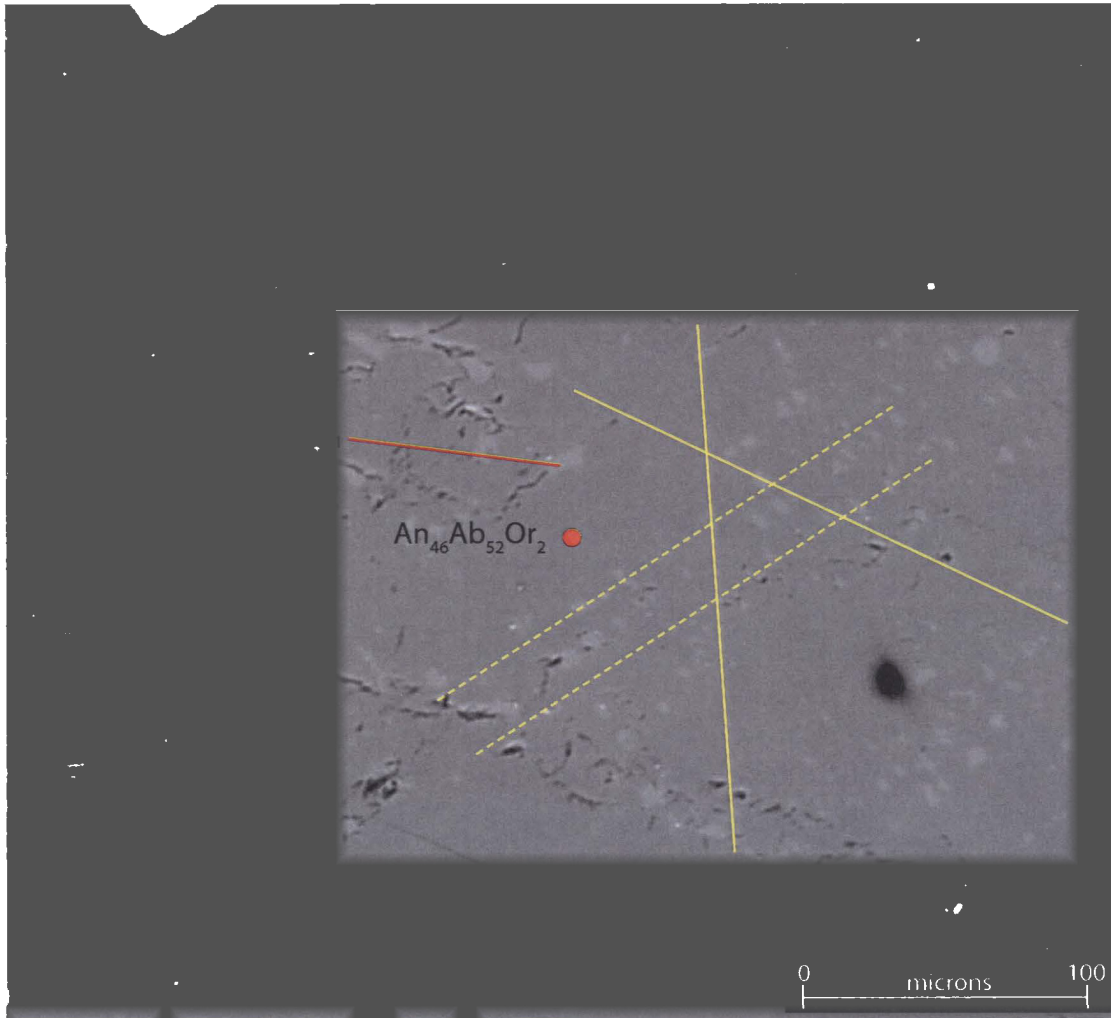
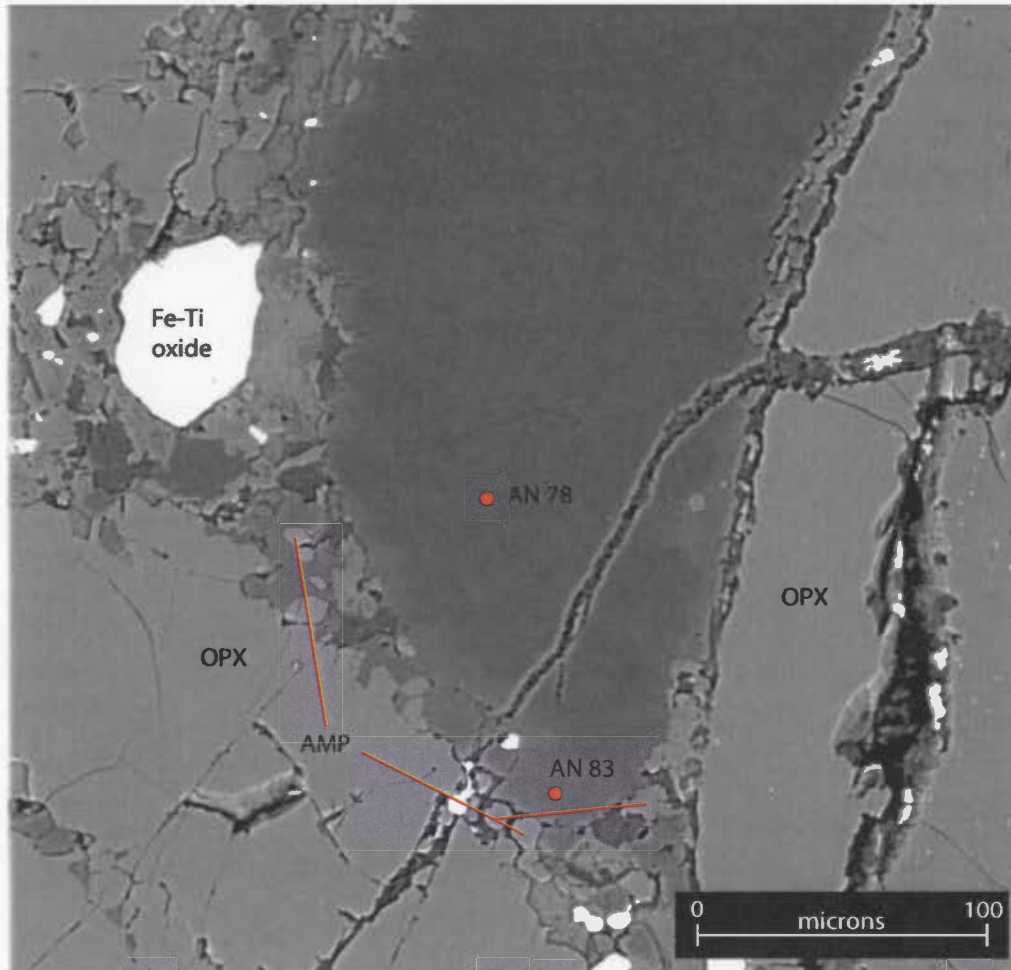


Figure 11.3 Backscatter electron image of SMA-24. An example of “blebs” in plagioclase. These blebs exhibit a linear distribution that is defined by the dashed lines. Solid lines mark a second orientation of blebs is not present in this image. This geometric pattern suggests that bleb distribution is crystallographically controlled. Many blebs exhibit high K contents, suggesting that these are antiperthite exsolution blebs. Note scale bar in lower right corner.

Recrystallized plagioclase, described in Chapter 9, was analysed to determine if recrystallization affected plagioclase composition. Often, recrystallization in plagioclase results in more albitic compositions (e.g. Rosenberg and Stünitz, 2003), but in the samples, the effects of recrystallization are inconsistent. In several examples, recrystallized plagioclase is more Ca-rich, but there is no obvious explanation for this change. In other examples, where plagioclase exhibits granoblastic textures, the core and rim compositions are relatively similar, and do not differ much from the average composition of whatever rock type it is from; any zonation present is generally expressed as Ca-rich rims and Na-rich cores. Figure 11.4 is an example of plagioclase rim-core zonation. In this example, from a norite sample, both core and rim are significantly more Ca-rich than the norite average.

Microprobe analysis of pink- to lilac-coloured plagioclase analysed to determine if trace element concentrations could be detected and linked to colouration. Figure 11.5 is a diagram of An content vs total trace metals,  $\text{Fe}_2\text{O}_3 + \text{TiO}_2 + \text{BaO}$  that was constructed using analyses from both pink plagioclase or white plagioclase. This diagram indicates that pink plagioclase contains slightly more trace metals than white plagioclase. Despite this, the total amount of trace metals is quite low and at low detection limits the degree of instrument precision decreases, therefore the data must be considered in this light. Perhaps analyses using LAM-ICP-MS, which has much greater detection limits for trace metals would be more appropriate for quantifying the degree of correlation between trace metals and plagioclase colour. This suggests that colour may be a useful tool for characterizing this portion of the SMA in terms of metasomatism or recrystallization, but further work is required in assessing the quantities of metals in these plagioclase analyses.



**Figure 11.4** Backscatter electron image from sample SMA-57. An inclusion of recrystallized plagioclase surrounded by weakly recrystallized orthopyroxene. The contact between plagioclase and OPX is marked by granular amphibole, OPX and relatively more Ca-rich plagioclase compared to plagioclase core compositions. Note scale bar in lower right corner.

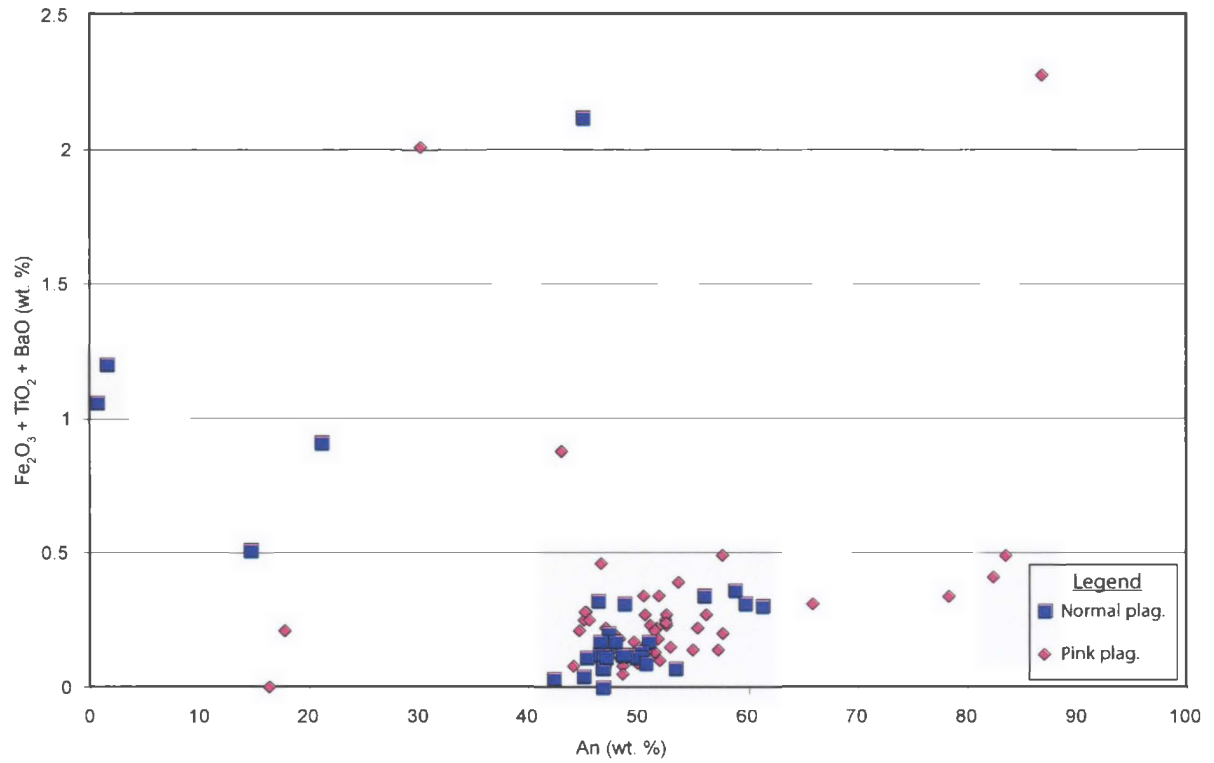


Figure 11.5 This diagram presents microprobe data from plagioclase that is classified by plagioclase colour in thin section and hand sample. Pink plagioclase exhibits slightly higher trace metal contents relative to “normal” white plagioclase. Pink plagioclase also appears to have slightly higher An contents.

## 11.2 Pyroxene

Eight pyroxene-bearing samples were analysed, comprising two anorthosite, ten gabbro-norite, ten leucogabbro-norite, five leuconorite and 29 norite analyses. Pyroxene was analysed for SiO<sub>2</sub>, TiO<sub>2</sub>, Al<sub>2</sub>O<sub>3</sub>, Cr<sub>2</sub>O<sub>3</sub>, Fe<sub>2</sub>O<sub>3(calc)</sub>, FeO<sub>(calc)</sub>, MnO, MgO, and CaO; NiO was not measured. Pyroxene was analysed to characterize the overall composition, to determine if there was any relationship between composition and location or host lithology and to determine the effect of recrystallization on trace metal distribution.

Ten analyses of clinopyroxene were conducted from various lithologies. These analyses demonstrate the magnesian composition of SMA clinopyroxene, which fall in the diopside field in Figure 11.6. Forty-six analyses from orthopyroxene reflect a similar trend compared to clinopyroxene, exhibiting a relatively magnesian composition, plotting in the middle of the enstatite field. Table 11.3 is a summary of SMA pyroxene analyses, which demonstrate the low compositional variation in both orthopyroxene and clinopyroxene. The lack of spatial variation of composition in pyroxene is similar to that of plagioclase, which also exhibits little to no spatial variation of composition.

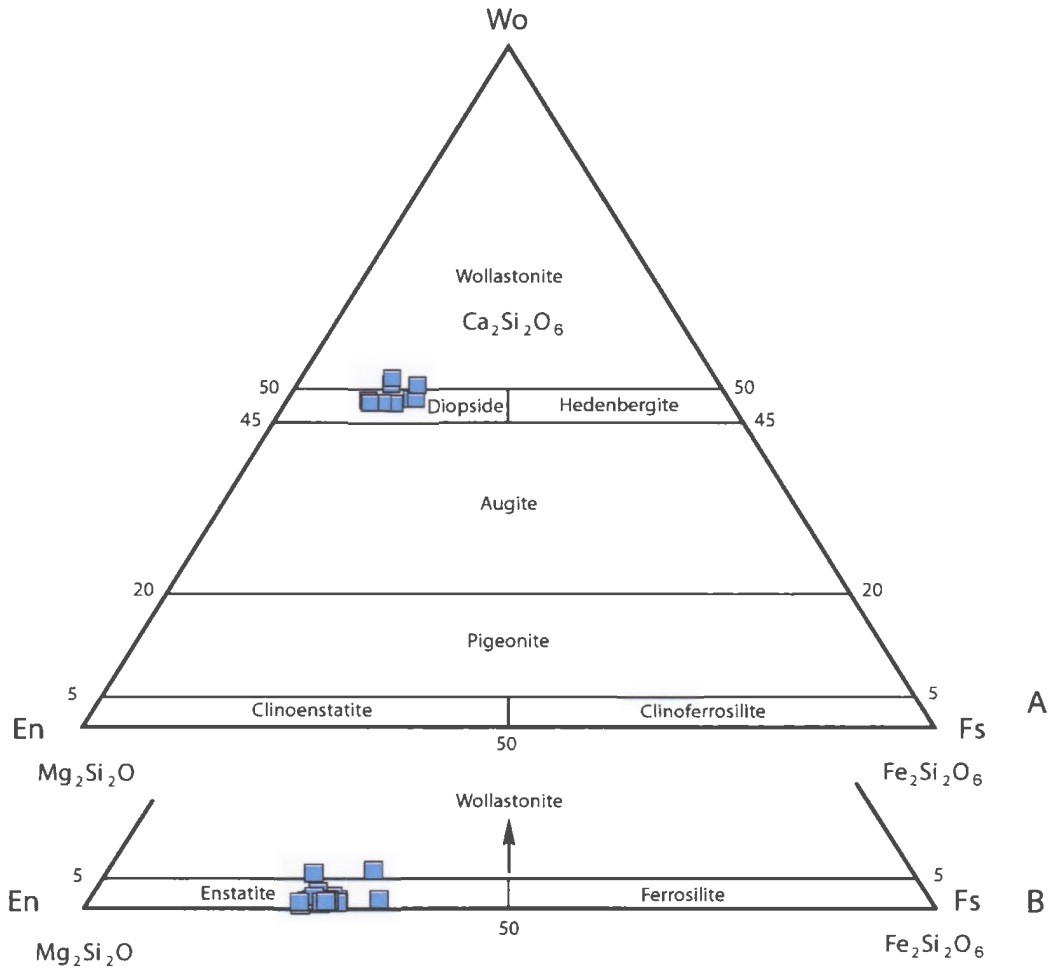


Figure 11.6 Microprobe data from SMA pyroxene is presented in ternary Wo-En-Fs compositional space after Morimoto, (1988). Clinopyroxene data (a) is tightly constrained to the diopside field. Orthopyroxene data (b), comprises nearly 4 times as many analyses, are nearly equally constrained in the enstatite field. The consistency of these analyses holds for recrystallized pyroxene as well as primary pyroxene in altered samples.

<b>CPX (n=10)</b>	<b>Wo</b>	<b>En</b>	<b>Fs</b>
Avg	49.15	39.04	11.80
StDev	1.34	2.41	2.16
<b>OPX (n=46)</b>	<b>Wo</b>	<b>En</b>	<b>Fs</b>
Average	0.96	71.75	27.30
StDev	0.92	1.86	1.55

Table 11.3 Summary of microprobe data from SMA clinopyroxene and orthopyroxene end-member compositions. The compositional for both phases exhibits very low variability.

A detailed traverse in sample RIC-57 across a large orthopyroxene crystal that exhibited weakly kinked cleavage and undulose extinction textures was completed to determine the effect of recrystallization on trace element distribution. Figure 11.7 illustrates the patterns of  $\text{TiO}_2$ ,  $\text{Cr}_2\text{O}_3$  and  $\text{MnO}$  across the crystal, from rim to rim. It appears that Cr and Ti behave similarly, whereas Mn exhibits the reverse pattern, although  $\text{Cr}_2\text{O}_3$  has a relatively sinuous trend rather than a simple rim-core-rim variation pattern. There appears to be weak MnO enrichment in the recrystallized rims, but the pattern in  $\text{TiO}_2$  and  $\text{Cr}_2\text{O}_3$  is inconclusive. Plotting the major elements  $\text{Fe}_2\text{O}_3$  and  $\text{Al}_2\text{O}_3$  (Figure 11.8) reveals only a weak pattern whereby they increase from low rim concentrations to higher core concentrations.  $\text{Fe}^{3+}$  was used instead of  $\text{Fe}^{2+}$  because it occupies the same crystallographic site as  $\text{Al}^{3+}$ , thus exchange should be possible between. It was postulated that  $\text{TiO}_2$  and  $\text{FeO}$  would decrease at the rims, because rutile inclusions, which are ubiquitous in OPX throughout the sample set, are absent from the recrystallized rims, and pleochroism and birefringence are significantly lower in the rims as well, which is often an indication of lower Fe and Ti.  $\text{Fe}^{3+}$  does show a decrease at the rims, but  $\text{TiO}_2$  is inconclusive, suggesting that if any changes occurred to OPX during recrystallization, it was only a slight loss of  $\text{Fe}_2\text{O}_3$  and  $\text{Al}_2\text{O}_3$  and a gain in  $\text{MnO}$  at the rims of the crystal.

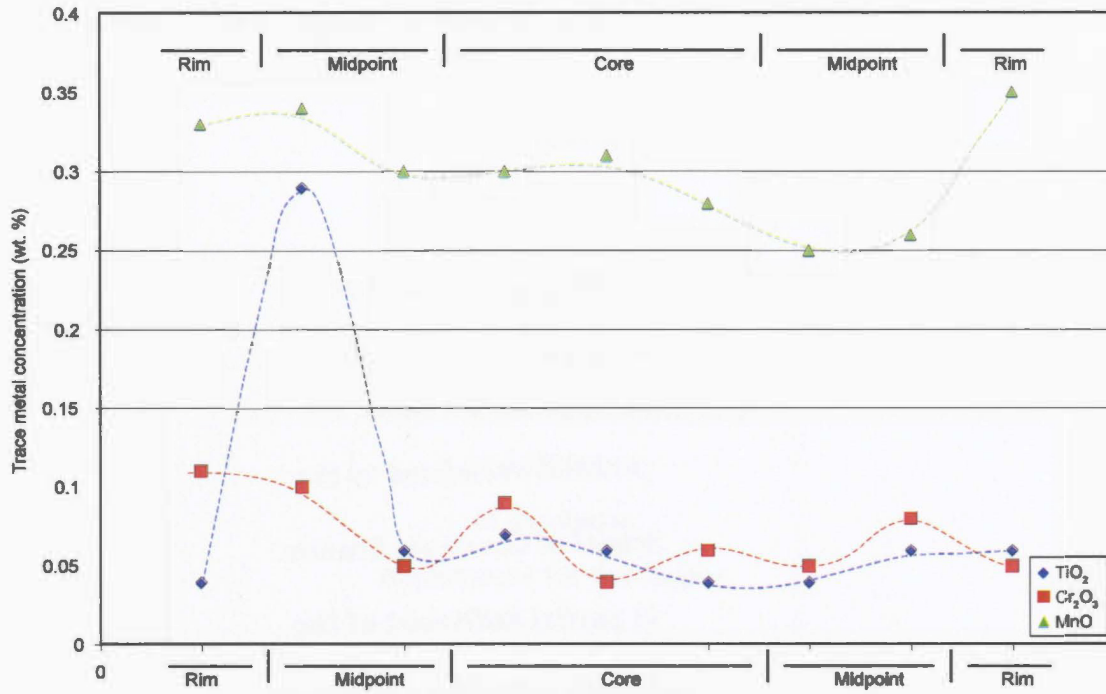


Figure 11.7 Microprobe data from sample RIC-57. A traverse across a large orthopyroxene crystal revealed that only MnO exhibits any systematic pattern across this crystal. TiO<sub>2</sub> and Cr<sub>2</sub>O<sub>3</sub> do not exhibit any consistent pattern.

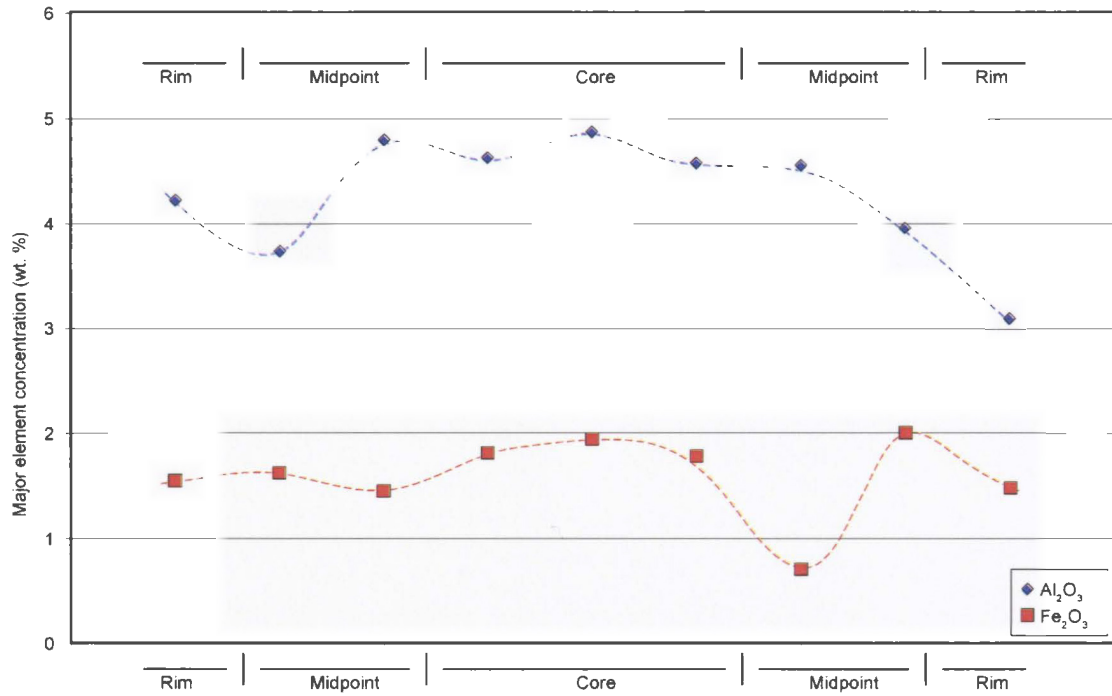


Figure 11.8 Microprobe data from sample RIC-57. Major element data from a traverse across orthopyroxene indicate that Al<sub>2</sub>O<sub>3</sub> and Fe<sub>2</sub>O<sub>3</sub> increase weakly in the core of the grain, slightly more pronounced in Al, suggesting that some loss of these elements may have occurred during recrystallization.

### 11.3 Garnet

Three garnet-bearing samples from the SMA map area were analysed, comprising eight analyses from a gabbro-norite, ten analyses from a leuconorite and three analyses from a norite. Garnet analyses measured SiO<sub>2</sub>, TiO<sub>2</sub>, Al<sub>2</sub>O<sub>3</sub>, Cr<sub>2</sub>O<sub>3</sub>, FeO, MnO, MgO and CaO; all Fe was assumed to be 2<sup>+</sup> and NiO was not analysed. The purpose of garnet analysis was to characterize their composition and to determine if there was compositional zoning, particularly because in microscope investigation, garnet appeared quite smooth and homogenous. In addition, the reaction rims surrounding garnet were analysed to determine mineralogy, because they were too fine to determine by microscope. As described in Chapter 9, some garnet occurs as reaction rims between pyroxene and plagioclase, while others form between Fe-Ti oxides and plagioclase ± pyroxene. In this section, analyses are sometimes grouped according to what phases they are adjacent to in order to determine what effect the host phases had on composition, and sometimes they are grouped by sample, to compare compositions between different locations. End-members were calculated by normalizing the cations for each major end-member. For example, almandine was calculated by:

$$(100 * \text{Fe}) / (\text{Fe} + \text{Mg} + \text{Ca} + \text{Mn}) = \text{percentage of almandine}$$

Garnets analysed from the SMA exhibit a composition intermediate between almandine and pyrope, which reflects the Mg-Fe dominated bulk compositions these garnets formed in, particularly given that they are spatially associated with Mg-rich pyroxene and Fe-rich oxides. Table 11.4 is a summary of garnet compositions. Most samples exhibit very little compositional variation, but between samples, there are minor differences and patterns.

Figure 11.9 is a plot of all four major end-members. From the diagram it is clear that there is an inverse relationship between Mg+Fe with Ca, such that when pyrope and almandine are elevated, grossular is depressed. This relationship is most apparent in analyses from a large garnet in a prominent reaction rim between orthopyroxene and Fe-Ti oxides from SMA-18. In SMA-33, which is a less detailed traverse from the rim to the

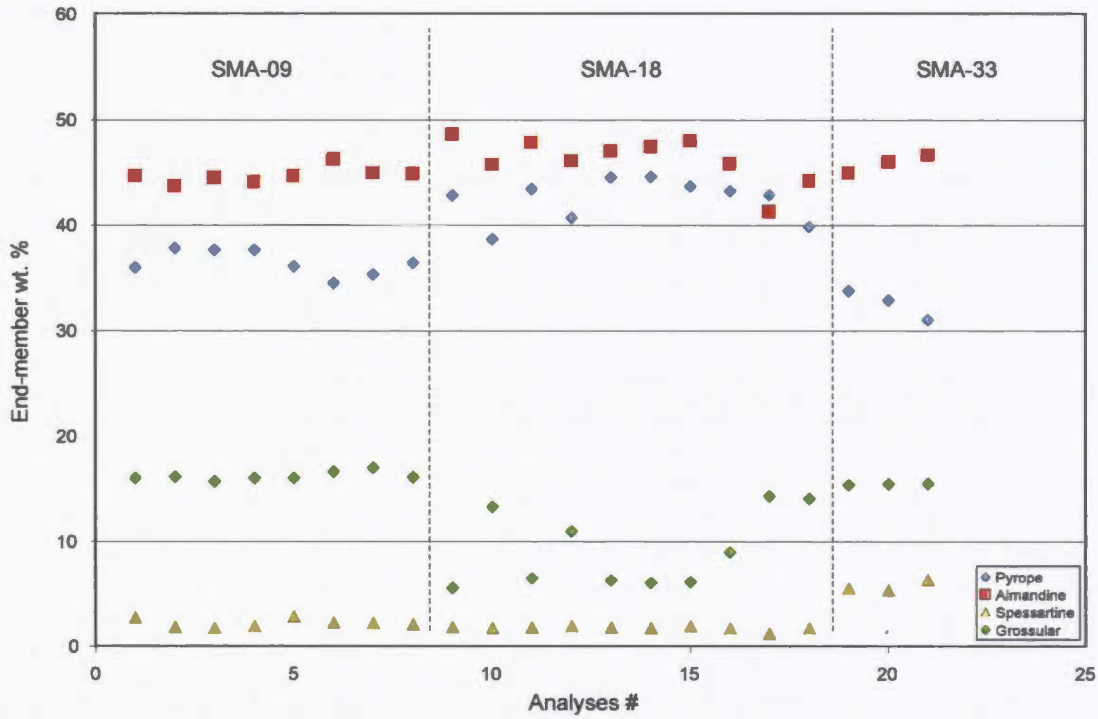


Figure 11.9 Microprobe data from all SMA garnet analyses are plotted according to major end-members. Each sample is divided by a vertical dashed line. In SMA-18, grossular is low when pyrope and almandine are elevated. However, in SMA-33, this relationship does not hold, with pyrope decreasing with increasing almandine and spessartine.

core of a garnet that formed between plagioclase and OPX, almandine and spessartine increase as pyrope decreases. The reason for compositional differences between these two garnets is unknown, but given their different host phases, it is possible that parent minerals play a role in garnet composition.

Traverses across garnet exhibit local systematic compositional variation, such as in SMA-09, where a traverse across a rounded, optically homogenous garnet revealed zoning in Mn, but not in other end-members. Figure 11.10 is a diagram of garnet end-members that illustrates this trend. In this diagram Mn is multiplied by 10 to reduce the range in composition, so that it is easier to compare the end-members side-by-side.

<b>Sample</b>	<b>Pyrope</b>	<b>Almandine</b>	<b>Spessartine</b>	<b>Grossular</b>	<b>n</b>
09 Average	36.46	44.74	2.20	16.23	8
09 StDev	1.20	0.74	0.39	0.40	8
18 Average	42.47	46.23	1.75	9.24	10
18 StDev	2.00	2.17	0.19	3.63	10
33 Average	32.58	45.91	5.74	15.46	3
33 StDev	1.42	0.89	2.36	0.04	3

Table 11.4 This table summarizes the composition of garnet from the mapped area of the SMA. End-members were calculated by normalizing the respective cation for each end-member. SMA-18 exhibits the greatest degree of variability, which is apparent in Figure 11.9.

Reaction rims surrounding garnet exhibit complex symplectic- to vermicular coronas. These rims were analysed to determine the mineralogy of intergrown phases because they were too fine to determine optically. Figure 11.11 illustrates two representative backscatter images of garnet reaction rims in SMA-33. These images feature the same intergrown phases, with slightly different textures for comparison. Figure 11.11b is shown in false colour to highlight the different phases in the corona, because they do not exhibit a great deal of contrast in grey-scale images. These garnets grew at the contact between plagioclase and orthopyroxene and were subsequently consumed during retrograde (greenschist ?) metamorphism. These rims, from garnet outwards comprise intergrown epidote, amphibole and plagioclase, then a discontinuous rim of nearly pure

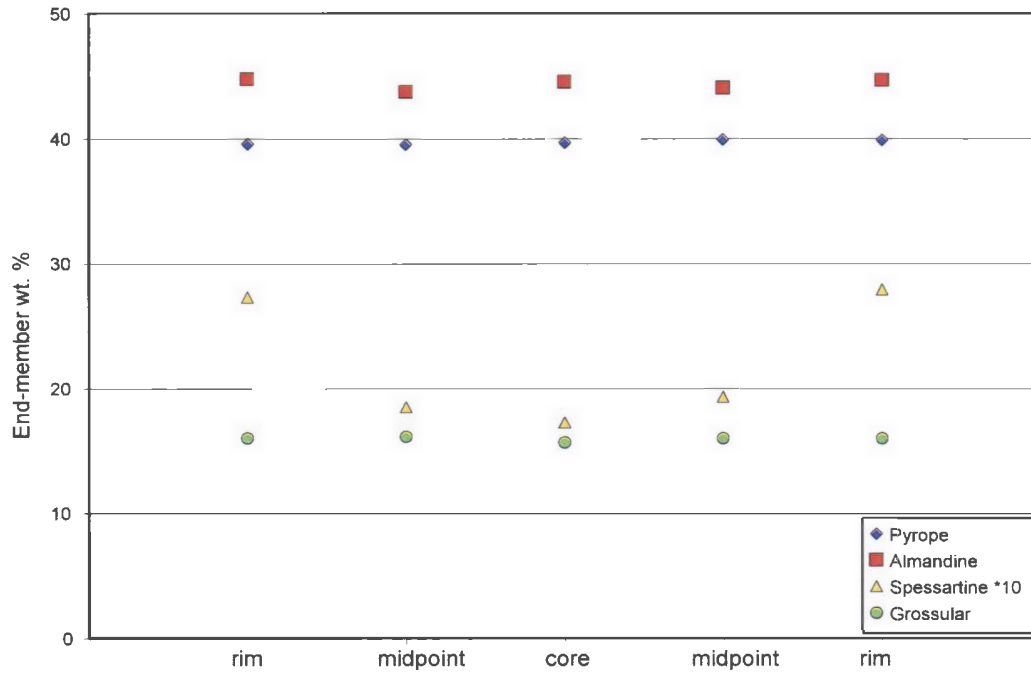


Figure 11.10 Microprobe data of garnet from sample SMA-09. Data from a traverse across a round, homogenous garnet reveals strong Mn zoning, but Mg, Fe and Ca remain relatively constant. In this figure Mn is multiplied by 10 to make side-by-side comparison easier.

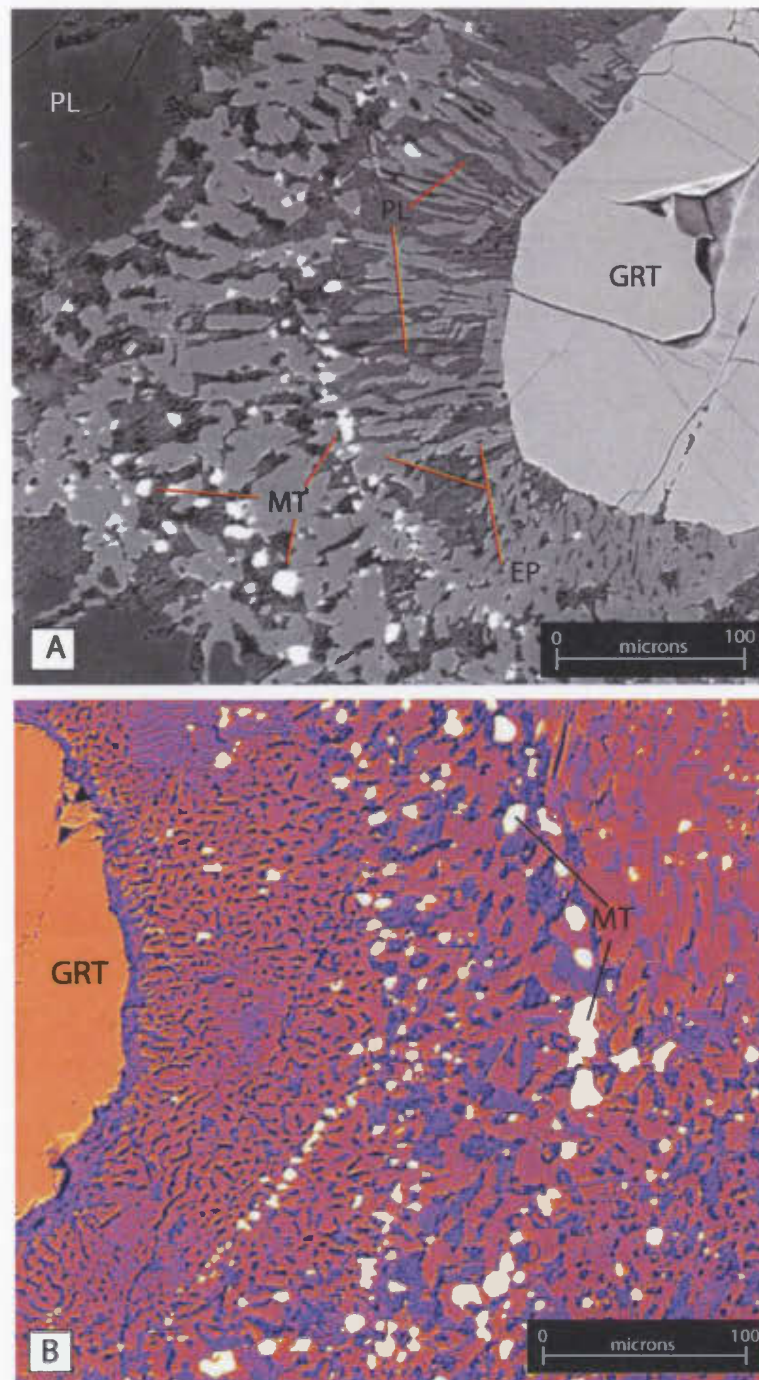
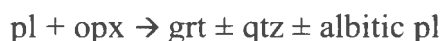


Figure 11.11 Backscatter electron images of garnet reaction rims in SMA-33. (a) This image highlights the decomposition of garnet (GRT) to a vermicular intergrowth of plagioclase (PL), epidote (EP) and amphibole. It is possible that pyroxene was also present but has reacted away ( $\text{pyx} + \text{pl} \rightarrow \text{amp?}$ ). The reaction appears to have occurred in two stages, based on the double-shelled structure of the reaction rim. Discontinuous white grains are magnetite (MT). (b) A similar image, but false-coloured to highlight the symplectitic texture of the reaction consuming garnet. In most samples, the outer shell is coarser-grained, but compositions are similar. Minerals are labeled as in (a). Scale bar (bottom right) is in microns.

magnetite grains, a second, sometimes coarser-grained rim of intergrown plagioclase, amphibole and epidote a second rim of magnetite of similar composition and then the host phases (plagioclase or OPX in this case). From these analyses it is possible to determine the overall petrogenetic sequence in these samples for the formation and destruction of garnet. Qualitatively, an approximate step-wise summary of garnet reactions is:

1. Igneous crystallization of plagioclase and orthopyroxene

2. Garnet grows by the reaction:



3. A second event of metamorphism, likely lower P, T (based on assemblages)



From the double coronal structure, it appears that the reaction occurred twice, or had a complex multistage process, because the two shells are mineralogically identical and chemically quite similar.

#### **11.4 Amphibole and other secondary phases**

Six amphibole-bearing samples were analysed, comprising one norite, two gabbronorite, eight leuconorite, eight leucogabbronorite, two massive oxide and one mafic dike analyses. Amphibole analyses measured SiO<sub>2</sub>, TiO<sub>2</sub>, Al<sub>2</sub>O<sub>3</sub>, Cr<sub>2</sub>O<sub>3</sub>, FeO, MnO, MgO, CaO, Na<sub>2</sub>O, K<sub>2</sub>O and NiO; Cl, F and H<sub>2</sub>O were calculated off-line assuming 2 OH and 24 O. The primary goal of amphibole and other secondary phase analyses was to characterize their overall composition and reaction rims.

In total 24 analyses of amphibole were completed, which exhibit an average Mg# of 0.50, with a standard deviation of 0.14. Similar to Chapter 5, with RCLIS amphiboles, a diagram after the methods of Hawthorne, (1981) was used to classify these analyses. Figure 11.12 plots Si cations versus calculated Mg# ( $\text{Mg}/(\text{Mg} + \text{FeO} + \text{Fe}_2\text{O}_3)$ ). According

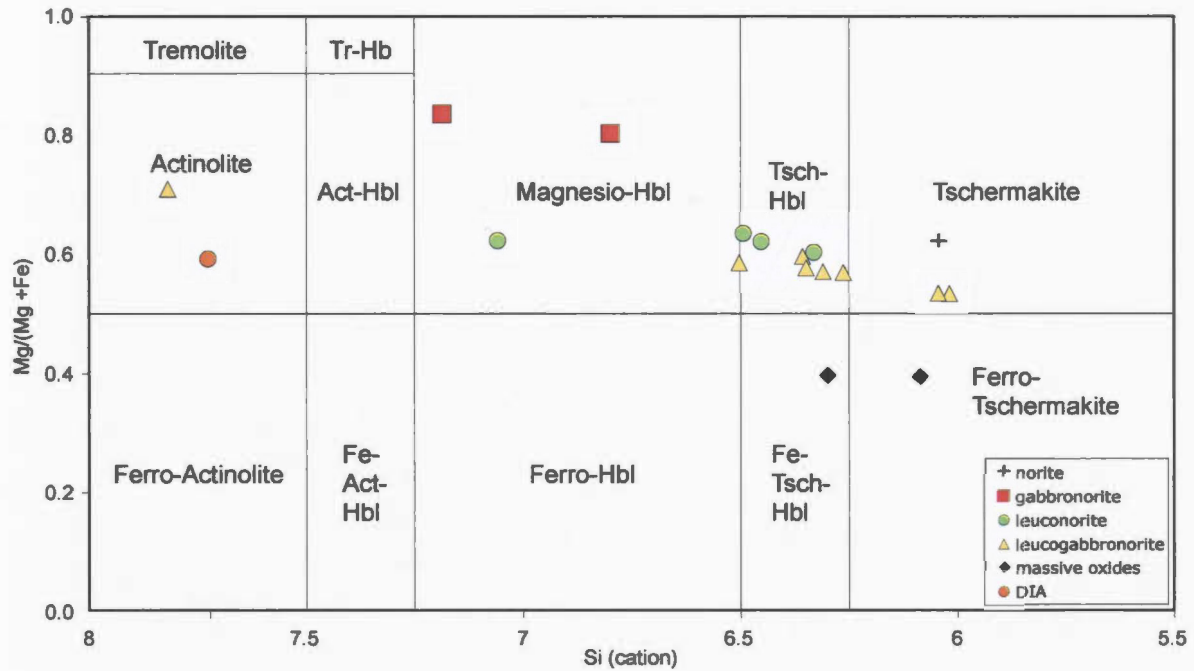


Figure 11.12 Microprobe analyses of SMA amphibole are classified in a method after Hawthorne (1981), by plotting Si cations vs Mg#. All samples except massive oxide analyses have a magnesian composition, reflecting the Mg-rich composition of the reactants that formed the amphibole. Only leuconorite and leucogabbronrite analyses exhibit similarities, particularly those plotting in the tschermakite-hornblende field (modified after Hawthorne, 1981).

to this diagram, all analyses except those from the massive oxides exhibit a magnesian composition. Massive oxide analyses lie within the ferro-tschermakite-hornblende to ferro-tschermakite fields. The majority of remaining samples plot within the tschermakite-hornblende field, and the rest plot broadly towards the greater Si cation end of the diagram, with variable Mg numbers. The elevated Mg nature of amphibole is probably a reflection of the Mg-rich reactants, which are typically enstatite, as indicated above. Gabbro-norite amphibole analyses exhibit the highest Mg numbers, and it is notable that the two highest Mg numbers in pyroxene analyses come from the same gabbro-norite sample (SMA-37).

Epidote group minerals were also analysed in SMA samples, using the same set of elements as amphibole. Epidote group analyses indicate that in general, where epidote grows at the expense of plagioclase (saussuritization), the surrounding plagioclase is somewhat depleted in Ca, resulting in more albitic plagioclase compositions. Most epidote analyses were measured qualitatively (EDS methods), thus they are not presented in this section. Figure 11.13 is a ternary diagram that plots analyses of zoisite, epidote and piemontite, which are the Al, Fe and Mn epidote group end-members respectively. These minerals have the general formula  $X_2Y_3Z_3(O, OH, F)_{13}$ , where Z is Si + Be, and O is assumed to be 12. This diagram was constructed by normalizing the end-members  $Al^{3+}$ ,  $Fe^{3+}$  and  $Mn^{3+}$ , which are the elements in the Y site that effect the overall composition, because  $Ca_2Al_2$  is constant in all epidote group minerals (aside from Allanite, not considered here). Essentially, these calculations determine what the relative proportion the third cation in the Y site is (where Al makes the first two cations). From this diagram it is apparent that the epidote minerals analysed in the SMA map area fall along the tie-line between the Al and Fe end-members (zoisite and epidote) and do not contain a significant proportion of piemontite, the Mn end-member.

Biotite and chlorite were also analysed using the same set of elements as amphibole but also included  $Na_2O$ ,  $K_2O$  and  $NiO$ . Similar to amphibole and epidote, F, Cl and OH were

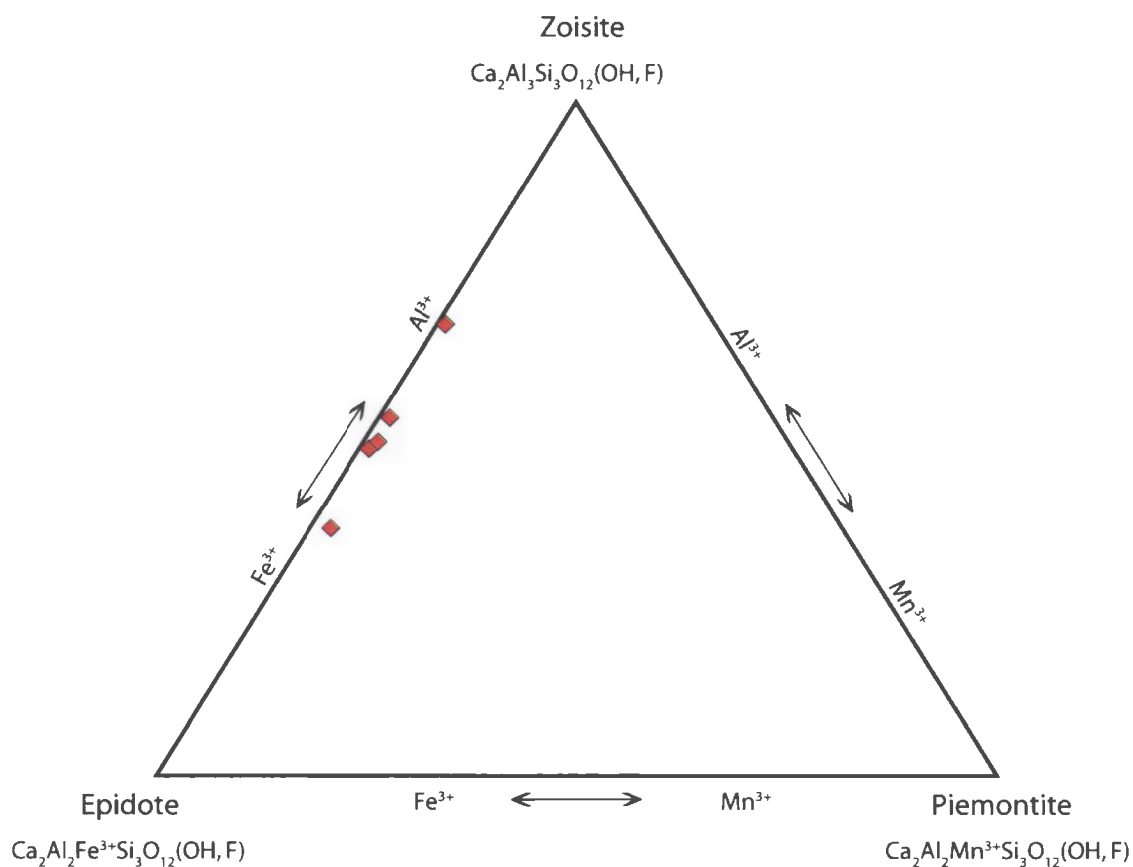


Figure 11.13 This ternary diagram of epidote end-members was created after the methods of Ercit, (2002) by normalizing  $\text{Fe}^{3+}$ ,  $\text{Al}^{3+}$  and  $\text{Mn}^{3+}$  microprobe data as described in the text. Arrows indicate possible solid solution exchange between different end-members. These data indicate SMA analyses are intermediate between epidote and zoisite.

calculated off-line. Eight analyses of biotite exhibit an average Mg# of 0.48 with a standard deviation of 0.07. There is little notable variation in biotite composition except in two analyses from SMA-Q2, a sample of massive oxide from the Bishop South quarry. These biotite analyses are from a reaction rim between coarse-grained plagioclase and massive Fe-Ti oxides (Figure 11.14). The reaction rim is very complex and appears to have formed in several events. Biotite from this reaction rim contains very little K<sub>2</sub>O and Na<sub>2</sub>O compared to the rest of the samples. They also contain very little TiO<sub>2</sub>, which is unusual, considering that they formed at the contact between plagioclase and Fe-Ti oxides. Refer to the figure caption for a complete description of the reaction rim.

The morphology of the reaction rim in Figure 11.14 is common throughout SMA samples where plagioclase is in contact with massive oxides, suggesting that the reaction products are partially a function of reactants. In SMA samples, the reaction rims between Fe-Ti oxides and pyroxene commonly contain garnet, and do not exhibit the complexity of the reaction rim in Figure 11.14. The presence of these phases around oxides also suggests that at least some modification of the oxide phases occurred following final crystallization. However, as described below, deformation and compositional modification have not occurred since initial oxide crystallization.

### **11.5 Sulfides and platinum group minerals**

Five sulfide-bearing samples were analysed from the SMA, of which four were massive sulfide samples and one, SMA-65, is from a mafic dike. Three of these samples were analysed at the electron microprobe laboratory at Dalhousie University to determine the composition of platinum group element bearing phases. The sulfide analyses measured S, Fe, Co, Ni, Cu and Zn, and PGM analyses measured Fe, Ni, Cu, S, Te, Sb, As, Pb, Co, Se, Sn, Cd, Au, Ag, Pt, Zn, Pd and Bi. The goal of sulfide analysis was to characterize the composition of the major sulfides such as pyrrhotite, pyrite, chalcopyrite and pentlandite, as well as to determine the composition of several unknown phases. Zoning in pyrite was suspected after reflected light examination, and microprobe imaging and analyses were

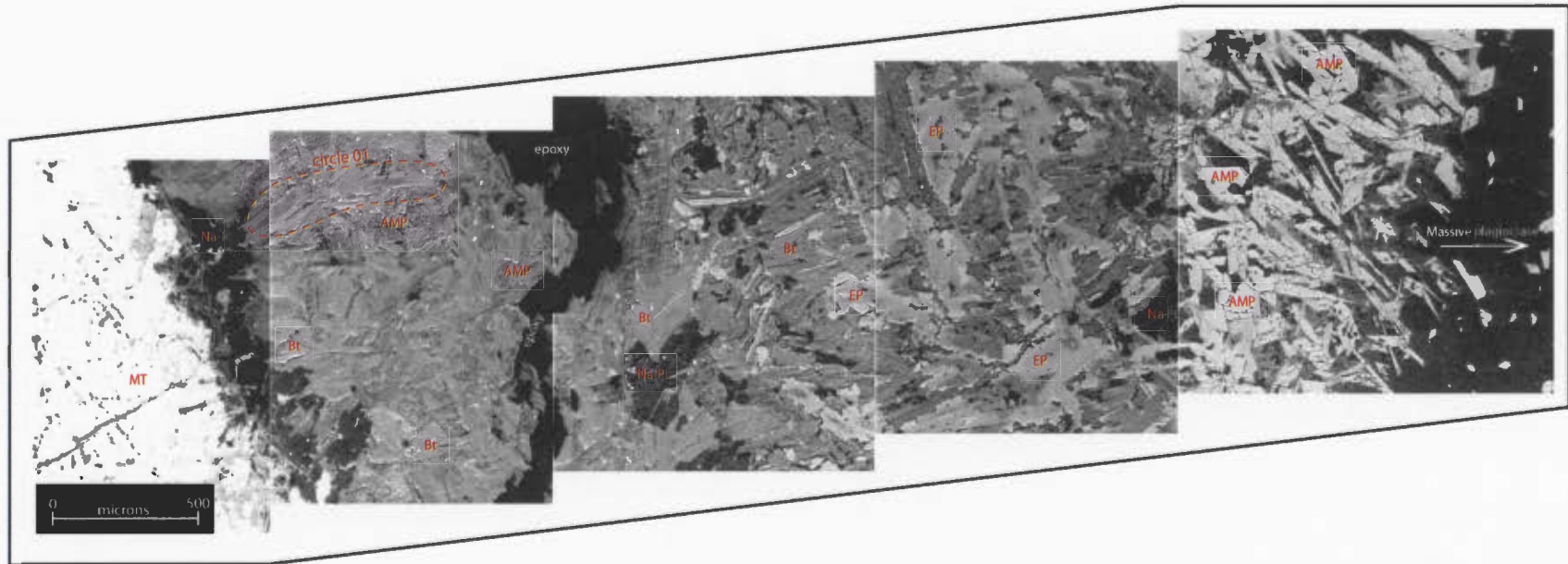


Figure 11.14 This figure is a mosaic of five backscatter electron images traversing a reaction rim between Fe-Ti oxides (left side) and massive plagioclase (right side). A crack is filled with epoxy (noted) left of centre. There is some brightness variation from image to image, which results from slight exposure differences during imaging. These differences do not reflect actual compositional differences. From massive oxides to the right is intergrown bladed amphibole and sodic plagioclase to intergrown coarse-grained biotite, some which displays Fe-rich rims (dashed circle 1). Right of the epoxy is more coarse-grained biotite with interstitial sodic plagioclase and local epidote replacing biotite, which changes gradually to splotchy epidote, locally with strong zonation intergrown with amphibole and biotite. Epidote textures suggest it may be pseudomorphing interstitial plagioclase and that it is consuming biotite and amphibole. Finally euhedral- to subhedral blades of amphibole are intergrown with plagioclase, which becomes more calcic towards the massive plagioclase.

used to confirm this. The goal of PGM analyses was to determine the composition of PGM grains and to determine the composition of the host phases of these minerals.

### 11.5.1 Sulfides

A total of 10 chalcopyrite analyses were completed, all from samples from the Sheep Brook area. These analyses have a consistent composition, with only trace amounts of Ni and Zn (0.03 and 0.10 weight percent, respectively). No cubanite was noted in the chalcopyrite.

Pentlandite was not noted in petrography, and was not discovered during microprobe analyses either. This initially seemed unusual, given that some samples from the Sheep Brook area contain over one weight percent Ni. However, as described below, Ni is abundant in solid solution in other sulfide phases.

Seven pyrrhotites were analysed from Sheep Brook massive sulfides. Pyrrhotite analyses have a consistent composition, although the amount of Fe is low and the amount of S is relatively high. Pyrrhotite contains abundant Ni and lesser quantities of Zn and Cu. Table 11.5 is a summary of pyrrhotite compositional data, including trace elements. It appears from Figure 11.15 that there is no relationship between low Fe and elevated trace element contents, because some samples with low Fe also have low Ni.

<b>Sample type</b>	<b>S</b>	<b>Fe</b>	<b>Ni</b>	<b>Cu</b>	<b>Zn</b>
Average	39.91	58.66	1.35	0.06	0.29
StDev	0.60	0.87	0.15	0.07	0.61

Table 11.5 A summary of SMA pyrrhotite data. Sulfur is generally closer to 36 wt. % and Fe closer to 63 wt. %, but in these samples S is high and Fe low. Ni and Zn total nearly 2 wt. % trace elements.

Most pyrrhotite analyses are from massive pyrrhotite rather than discrete blebs such as in the RCLIS, thus no rim-core traverses were conducted. Backscatter images do not exhibit

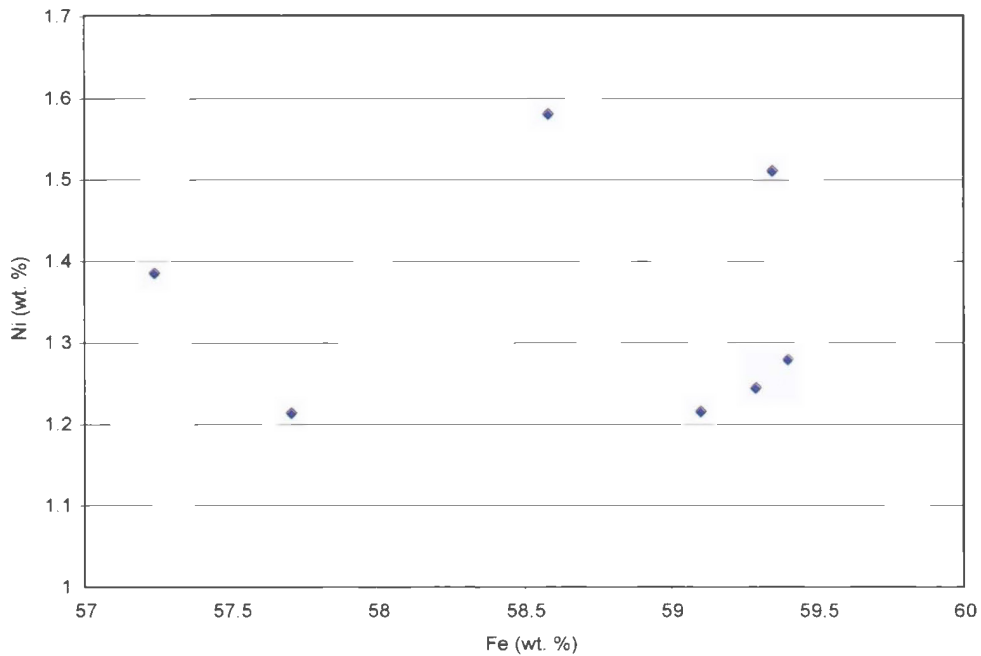


Figure 11.15 Ni vs Fe in pyrrhotite diagram derived from microprobe data. This diagram demonstrates that Ni substituting for Fe in pyrrhotite is not responsible for the low Fe contents in pyrrhotite. A linear trend with a negative slope would be expected if this were the case (i.e. lower Fe and higher Ni contents).

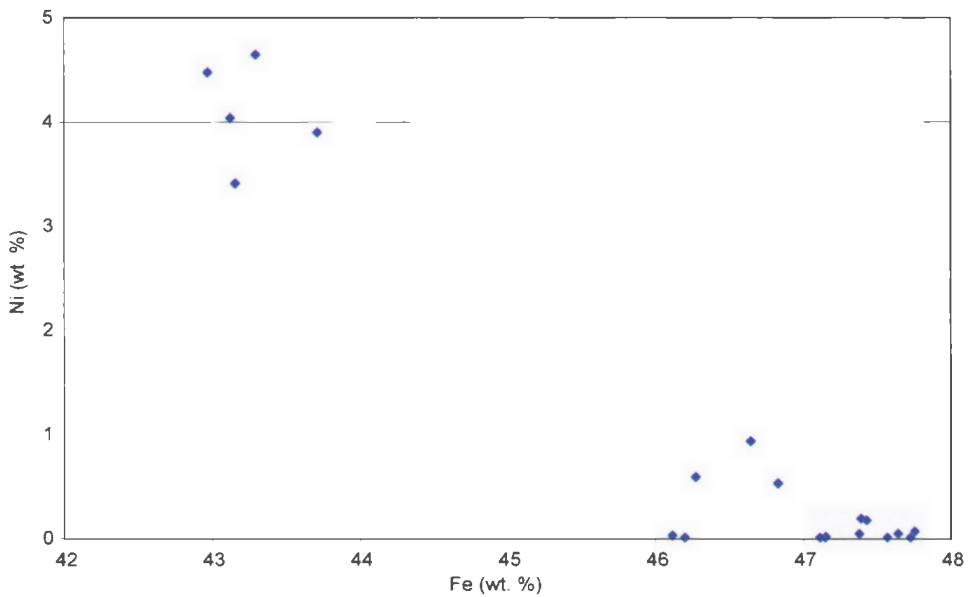


Figure 11.16 Ni in pyrite vs Fe in pyrite diagram derived from microprobe data. This diagram indicates that there is a positive correlation between low Fe and high Ni in pyrite, suggesting that Ni substitutes for Fe. High Ni analyses in this diagram correlate to the Ni-rich bands in Figure 11.17.

any evidence for compositional zoning in a lamellar morphology, which supports the hypothesis that the lamellae are deformation induced and not exsolution lamellae. Flame lamellae within pyrrhotite are abundant, particularly at the intersection of pressure lamellae. Analysis indicates that these are pyrite, not pentlandite, a pyrrhotite polytype, or troilite.

Twenty pyrite analyses were derived from three samples, including one mafic dike with the remainder from massive sulfides in the Sheep Brook area. Most pyrite conforms to normal pyrite stoichiometry, but there is a small group of samples with strongly elevated Ni – up to 4.7 weight percent Ni. Figure 11.16 demonstrates that unlike pyrrhotite, elevated Ni is related to a decrease in Fe, suggesting that Ni replaces Fe. The elevated Ni analyses are from a selection of pyrite cubes within a pyrrhotite host. As described above, some cubes of pyrite appear to have weak concentric zoning in reflected light, which was confirmed by backscatter images. In these images (Figure 11.17), concentric rings or bands are present within the cubes. These bands contain high Ni and are where low-Fe, high-Ni analyses in Figure 11.16 are from. These bands of elevated Ni in pyrite are parallel to the edges of the pyrite crystals, suggesting they are crystallographically controlled.

Sheep Brook massive sulfide whole rock assays report up to 1.6 weight percent Ni, but little to no pentlandite was observed in optical or backscatter observations. Secondly, euhedral to subhedral pyrite cubes exhibit bands of enriched Ni. The sulfides exhibit evidence of extreme deformation in reflected light, as do the silicates in backscatter electron images (Figure 11.18). Deformation appears to be syn- to late alteration in the Sheep Brook region, which comprises mainly silicification and amphibolitization. It may be that during deformation, pre-existing pentlandite was destroyed, or consumed in a reaction that coincided with pyrite growth. Pyrite textures indicate that they are late, with local Ni banding, which is compatible with Ni becoming available after initial sulfide crystallization. Therefore, the high Ni in whole rock assay could be a combination of

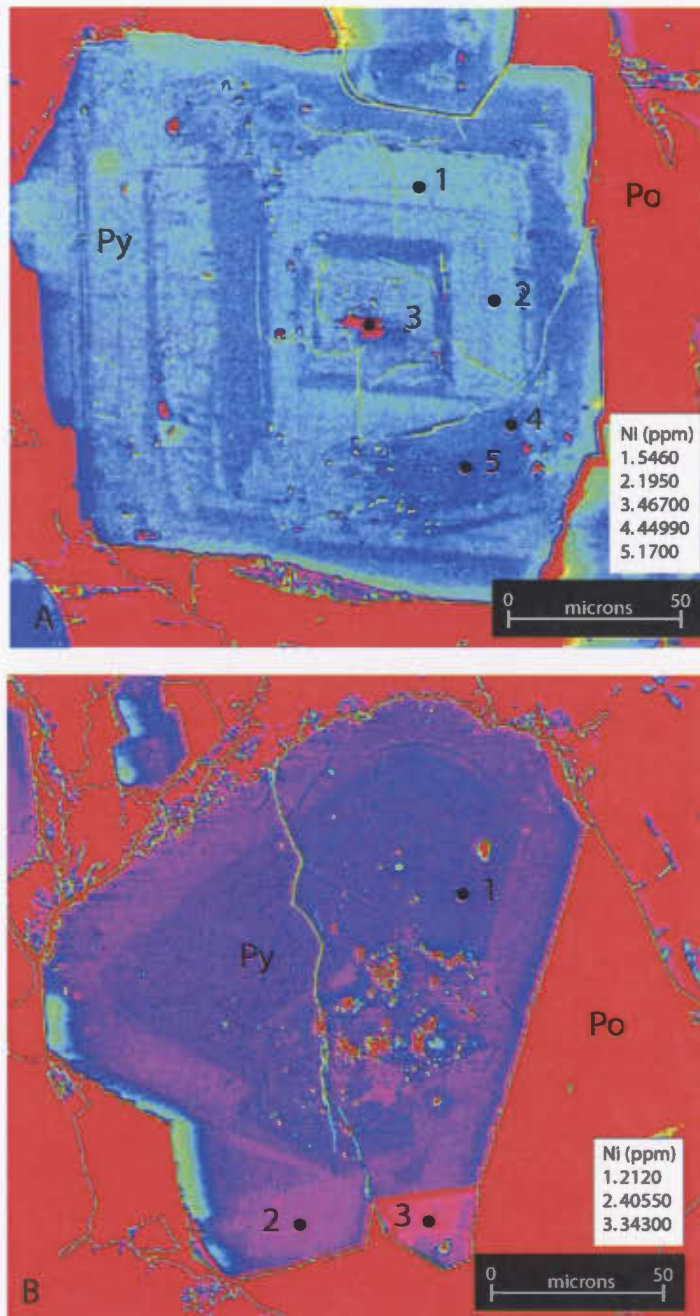


Figure 11.17 False coloured backscatter images of zoned pyrite in SMA-40-1C. Colour has been added to accentuate the contrast between Ni-rich and Ni-poor zones. Colour brightness does not necessarily correspond to greater Ni, just contrasting composition. (a) Most of this cube exhibits high Ni (cyan colour), but distinctive bands (blue) within the cube have extremely elevated Ni, up to almost 5 wt %. The core is intermixed pentlandite and Ni-rich pyrite. Some high Ni zones appear to truncate lower Ni zones, but others appear to be conformable. (b) The slightly different colour scheme does not represent different Ni concentrations, just relative brightness, which is related to the original image. Ni rich bands are magenta-to red (point 3), while lower Ni values are in the core (purple).

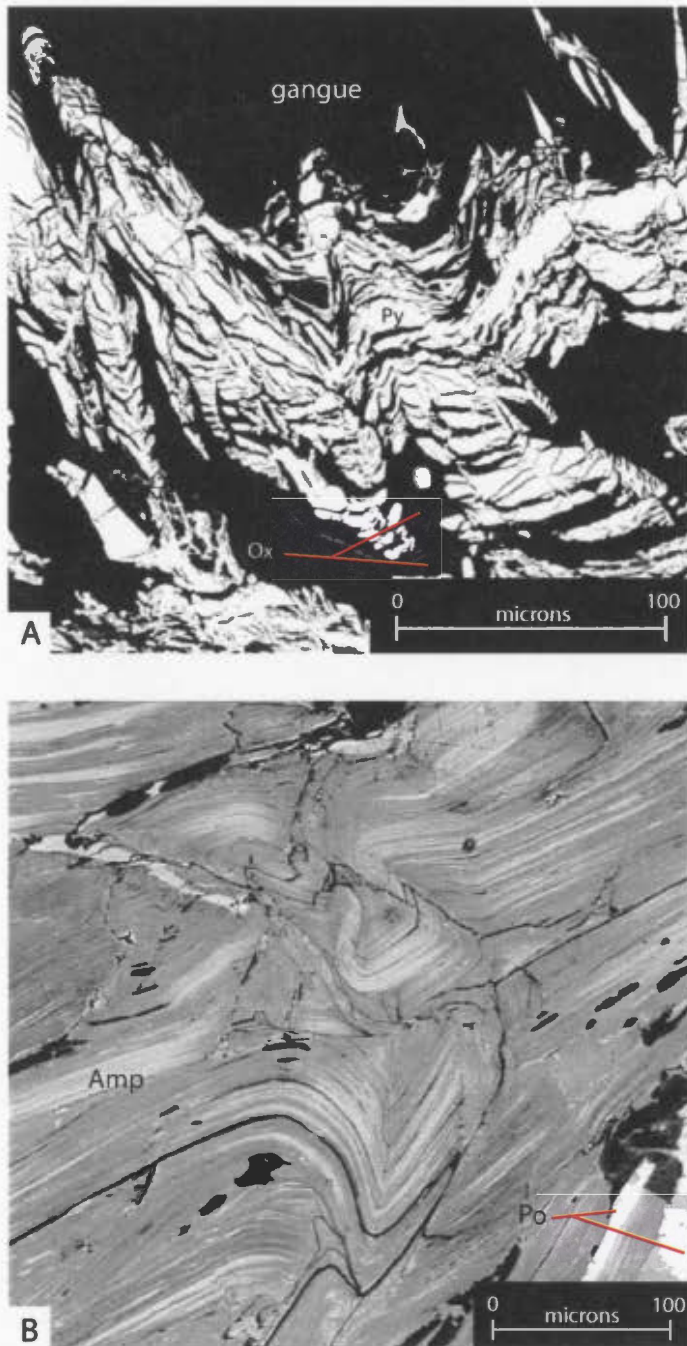


Figure 11.18 Backscatter electron images of Sheep Brook samples. (a) Pyrite veinlets hosted by silicate and carbonate gangue are tightly folded and brittlely deformed. Faint bands of oxides are also visible (Ox). (b) Fibrous amphibole in this image is strongly deformed by folding and microfaulting. Thin bands of pyrrhotite (Po) are visible in the lower right corner. Both of these images are from samples where pyrrhotite exhibits pressure lamellae, visible in reflected light, but not in BSE images. These images therefore support the hypothesis that lamellae in pyrrhotite are deformation induced and not exsolution of different pyrrhotite polytypes or troilite. Note scale bar in lower right corners.

elevated Ni in pyrrhotite, which averages 1.34 wt. %, and strongly elevated Ni in pyrite, which locally comprises 30% of the samples.

Accessory sulfides comprise sphalerite, arsenopyrite and galena. Sphalerite occurs as irregular blebs and veinlets within pyrrhotite, as described above. Sphalerite was the only accessory phase analysed from the Sheep Brook samples. It exhibits Zn concentrations of 60.62 weight percent, with a standard deviation of 0.99, sulfur concentrations of 33.68 weight percent and a standard deviation of 0.08 and Fe concentrations averaging 6.91 weight percent, with a standard deviation of 0.37.

### **11.5.2 Platinum group minerals**

Platinum group minerals (PGM) were identified in three out of four polished thin sections from the Sheep Brook area, which have whole rock ICP/MS fire assay results of up to 1.6 g/t Pt+Pd+Au. The techniques used to locate these PGM are described in Chapter 1. In total, 11 analyses were made of nine different discrete PGM. Several other PGM were identified near analysed PGM, but these were only analysed using EDS because they were too small to acquire accurate analyses.

Analyses and imaging revealed that the discrete PGMs are very small, generally <10 microns in diameter, making accurate and precise data acquisition difficult. In particular, because the electron beam is approximately 1µm in diameter, and the “sphere of influence”, wherein other atoms may be influenced by the beam, is greater than 5 µm, some analyses report up to tens of weight percent of elements not in the phase being analysed (*i.e.* from the host phase). Therefore, certain assumptions must be made about the data before it can be properly presented.

The assumptions are made to screen good quality analyses from those that exhibit contamination by other elements. A select group of phases have totals near 100% and little to no Fe, S, Ni and Cu – all elements that are not part of the PGM’s, but most

analyses contain some quantity of these elements. Table 11.6 lists the analyses that required only minimum correction – those analyses are considered "good". These data have been normalized to exclude S, Fe, Cu and Ni, which total < 4 wt. % in these samples. Although one analysis recorded Bi > 1%, it was screened out because of its relatively low concentration and inconsistent distribution throughout other analyses. Dividing the weight percent of each element by the atomic mass and then summing minerals that are commonly associated together in PGM's derived the empirical formulas in Table 11.6. The value for each group was factored to give the (nearly) integer subscripts in the empirical formula.

Sample	Te	Pt	Au	Pd	Total
COL-SMA-40-1A_PGM01	52.972	43.277	2.431	0.670	99.350
COL-SMA-40-1A_PGM2	53.380	43.429	2.700	0.101	99.610
COL-SMA-40-1A_PGM3	51.805	43.491	2.677	0.578	98.551
Empirical Formula					
COL-SMA-40-1A_PGM01	(Pt,Pd,Au) <sub>4</sub> (Te) <sub>6.91</sub>				
COL-SMA-40-1A_PGM2	(Pt,Pd,Au) <sub>4</sub> (Te) <sub>7.05</sub>				
COL-SMA-40-1A_PGM3	(Pt,Pd,Au) <sub>4</sub> (Te) <sub>6.71</sub>				

Table 11.6 Platinum telluride minerals from SMA-40-1A. These data contained less than 4 wt. % "contamination elements" Fe, S, Cu and Ni. Normalizing out the contamination that was present was the only processing of these data. Elements other than Fe, S, Cu and Ni that are <0.5 wt. % are excluded from this table, but were preserved during normalizing calculations. Raw data and processed data are listed in Appendix 4.

Cabri, (2002), lists only three Pt-Te minerals recognized by the Commission on new Minerals and Mineral Names (CNMMN) and International Mineralogical Association. These are Maslovite, Moncheite and Vincintite, the latter is written with a (?) mark, indicating some uncertainty in the nomenclature. The composition and stoichiometry of these phases are listed below in Table 11.7. The minerals in Table 11.6 bear little resemblance to those in Table 11.7, suggesting that the SMA-40-1A phase may be a new mineral. Figure 11.19 is an example of this phase, which has an elongate, needle- or plate-like habit.

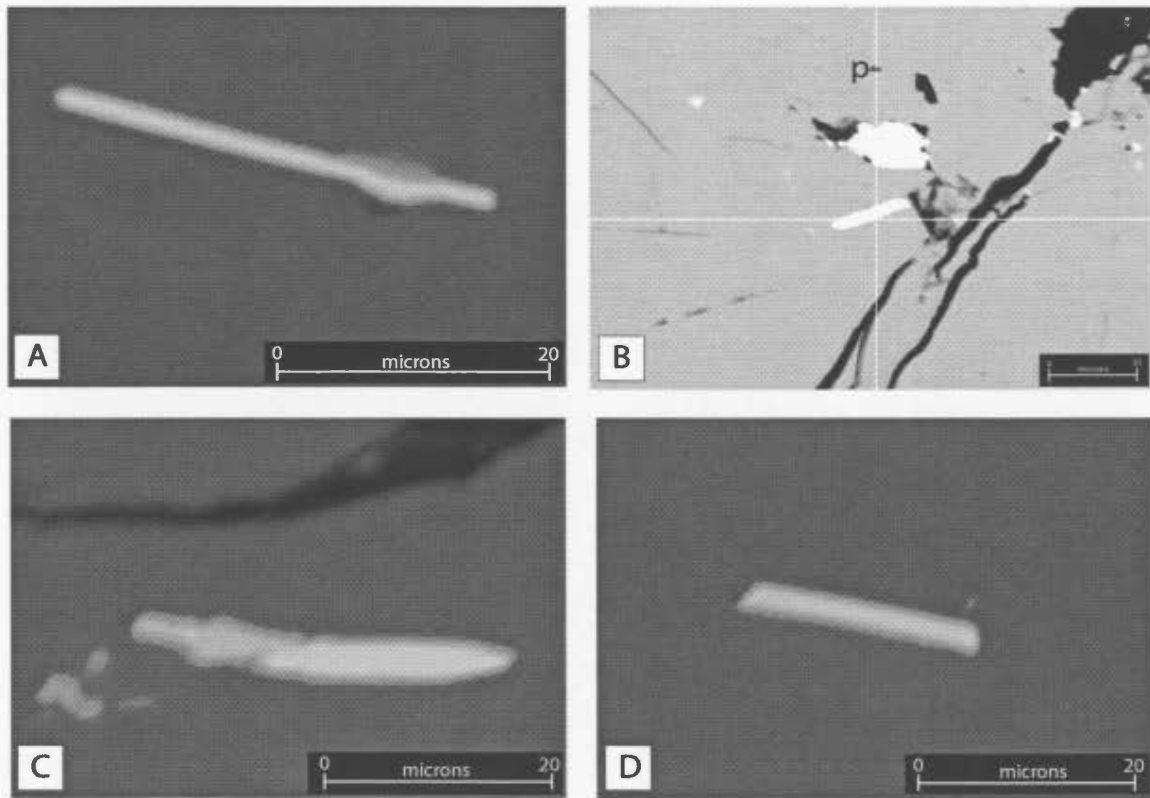


Figure 11.19 Backscatter electron images of a Pt-Te mineral located in SMA-40-1A. A, C and D were imaged on the MAF-IIC SEM-MLA, whereas B was imaged on the Dalhousie University EMPA. All grains have the same composition and relatively the same size and crystal habit. All grains are hosted by compositionally unzoned pyrrhotite, although deformation is notable in reflected light. In B, the angular subrounded bright spot (p) above the PGM (elongated bright spot) is Pb polishing paste from sample preparation. The analysis for this PGM contains zero Pb, indicating the paste has had no effect on the analyses. Note scale bar in lower right of each image.

<b>Mineral</b>	<b>Maslovite</b>	<b>Moncheite</b>	<b>Vincentite</b>
Formula	PtBiTe	(Pt,Pd)(Bi,Te) <sub>2</sub>	(Pt,Pd) <sub>3</sub> (As,Sb,Te)
Empirical Formula	PtBiTe	Pt <sub>0.75</sub> Pd <sub>0.25</sub> Bi <sub>1.5</sub> Te <sub>0.5</sub>	Pt <sub>2.6</sub> Pd <sub>0.4</sub> As <sub>0.5</sub> Sb <sub>0.3</sub> Te <sub>0.3</sub>
Ideal Composition (weight percent)	<b>Pt</b> 36.39 <b>Bi</b> 39.31 <b>Te</b> 24.00 - -	<b>Pt</b> 31.21 <b>Pd</b> 5.68 <b>Bi</b> 22.29 <b>Te</b> 40.83 -	<b>Pt</b> 16.71 <b>Pd</b> 59.25 <b>As</b> 8.02 <b>Sb</b> 7.82 <b>Te</b> 8.20

Table 11.7 Minerals listed in Cabri, (2002) that are defined by the Commission on New Minerals and Mineral Names (CNMMN) and International Mineralogical Association as the only recognized Pt-Te bearing minerals. None of the analyses in Table 11.6 resembles these minerals, suggesting that if analyses are correct, and they appear to be, then they may be a new mineral.

The remaining analyses comprise nine PGM. These analyses have undergone some normalizing and other correction calculations due to a greater content of “contaminant elements”. The two types of corrections are first to subtract the S, Fe Cu and Ni from these analyses, as per above, but in these analyses the impurities were up to 20 wt %. Secondly, as in the above, the other elements, Te, Sb, As, Pb, Co, Se, Sn, Cd, Au, Ag, Pt, Zn, Pd and Bi were normalized to 100%. Next, elements totaling <1 weight percent were ignored, which left 3-5 elements, which comprise the mineral. These calculations appear to be justified for some analyses but in others the corrections do not appear to generate useable data.

A second group of PGMs, comprising two analyses, exhibits a different composition from the Pt-Te group. These two analyses contain primarily Pd, Sb and Ag. One of these analyses is close to 100% total without subtracting S, Fe, Cu and Ni, suggesting that it represents a real composition but the other analysis exhibits a different proportion of Pd and Sb, suggesting that if the corrections are valid, some exchange between Pd and Sb may occur. The least corrected analysis is similar to a mineral named only IMA2004-020 ([www.webmineral.com](http://www.webmineral.com)) (*i.e.* is has no common name) except that the SMA sample

contains less Sb and more Ag. Table 11.8 is a comparison between the two SMA analyses and IMA2004-020.

Mineral	Pd	Sb	Ag
IMA2004-020	46.18	53.82	-
SMA-40-1A-PGM2	54.44	34.46	9.65
SMA-40-1B-PGM4	48.59	42.64	7.32
Empirical Formula			
IMA2004-020	Pd <sub>4</sub> Sb <sub>3</sub>		
SMA-40-1A-PGM2	n/a		
SMA-40-1B-PGM4	n/a		

Table 11.8 A second group of two analyses of SMA PGMs is dominated by Pd and Sb. SMA-40-1B-PGM4 is quite similar to IMA2004-020, an officially recognized Pd-Sb mineral, except that it contains Ag.

A final group of three PGM analyses are dominated by Pt and As, with lesser amounts of Sb, Au and Pd. Using the methods above for grouping elements and calculating empirical formulas from the microprobe analyses, it appears that one of the three analyses corresponds to sperrylite, PtAs<sub>2</sub> (Cabri, 2002). A second analysis corresponds to a different, unknown, Pt-As phase, but the correction factors appear to have distorted the composition of the final analysis too much to use. Table 11.9 summarizes the data from the analyses described above and compares them to true sperrylite.

Mineral	As	Sb	Au	Pt	Pd	Total
Sperrylite	43.44	-	-	56.56	-	100
SMA-1B_C04_PGM01	39.84	5.89	3.10	45.12	4.78	98.74
SMA-40-1B-C04_PGM5	49.19	1.15	2.70	41.94	3.77	98.73
Empirical Formulas						
Sperrylite	PtAs <sub>2</sub>					
SMA-1B_C04_PGM01	(Pt,Pd,Au)(As,Sb) <sub>1.99</sub>					
SMA-40-1B-C04_PGM5	(Pt,Pd,Au) <sub>5.04</sub> (As,Sb) <sub>2</sub>					

Table 11.9 A final group of PGM from the Sheep Brook area. Analysis SMA-1B\_C04\_PGM01 appears to be sperrylite, but the second analyses does not correspond to any officially described PGM.

The very small grain size of the SMA PGM makes it impossible to put too much weight on so few analyses. To discuss whether or not some of the above analyses represent truly new mineral species or just distorted or incorrect analyses of known minerals would require a greater number of samples.

## 11.6 Oxides

Fourteen oxide-bearing samples were analysed from the SMA, of which two were from the Bishop South quarry and comprised massive oxides, one was from the Sheep Brook area, and the rest were from the main map area. In all, three massive oxide samples were analysed and the rest comprised discrete blebs or lenses of oxides at a thin section scale. Oxide analyses measured SiO<sub>2</sub>, TiO<sub>2</sub>, Al<sub>2</sub>O<sub>3</sub>, Cr<sub>2</sub>O<sub>3</sub>, FeO (Fe<sub>2</sub>O<sub>3</sub> calculated), V<sub>2</sub>O<sub>3</sub>, MnO, MgO and NiO. All oxide analyses were processed off-line by microprobe software to determine the proportion of end-members and cations, which was confirmed manually. These calculations and assignment of Fe charges were based on detailed imaging and petrography so that various species, such as ilmenite and ulvöspinel were not misclassified because of differences in Fe<sup>2+</sup> and Fe<sup>3+</sup>, which is a serious difficulty in analyzing texturally and optically similar oxide species. The problem of Fe<sup>2+</sup> and Fe<sup>3+</sup> was nowhere more evident than in the oxide analyses presented below. The mineralogical and crystallographic attributes of the oxides described below are described in Chapter 5 and are not discussed in more detail unless required in this section.

The purpose of analyzing oxides in the SMA was first to characterize the composition of the oxides and their exsolution lamellae, because of the known solid solution in most of the oxides analysed. Secondly, analyses were intended to determine if the composition of the massive oxides at the Bishop South (and presumably Bishop North) were detectably different from the oxide occurrences within the main map area. Finally, oxides were analysed to determine if there was any compositional difference between different textures of oxides, such as massive or blebby oxides from those occupying fractures within silicates. For this section, samples are grouped as either spinel (e.g. magnetite and

hercynite) or ilmenite (ilmenite, hematite etc.) and sub classified by rock type where necessary.

### 11.6.1 Ilmenite Series

Ten ilmenite-bearing samples were analysed, comprising 53 analyses, including five from the Bishop South quarry, four anorthosite, 12 leucogabbronite, 14 leuconorite, two mafic dike and 16 norite analyses. Ilmenite composition is variable, mainly because of hematite solid solution, and minor variation in Mg and Fe<sup>3+</sup> contents. Table 11.10 is a summary of calculated end-members including hematite. The greatest uncertainty in these analyses lies with the actual hematite content, because many of the analyses are derived from points where it is impossible to avoid microscopic exsolution lamellae within ilmenite. These lamellae are usually hematite ( $\pm$  Ti) solid solution (Figure 11.20), which means that an analysis may actually record part hematite and part ilmenite, skewing the ilmenite composition to a more Fe-rich composition.

Type	Ilmenite	Geikielite	Pyrophanite	Hematite
Massive AVG	85.193	8.870	1.558	4.379
Massive STDEV	4.088	3.671	0.199	2.203
AN AVG	54.608	0.092	1.218	44.082
AN STDEV	31.844	0.086	1.074	32.621
LGBN AVG	49.204	0.134	1.331	49.331
LGBN STDEV	38.886	0.211	1.346	40.055
LNOR AVG	72.532	2.833	2.110	22.525
LNOR STDEV	21.267	3.617	1.797	22.934
MD AVG	86.088	0.203	7.339	6.371
MD STDEV	2.546	0.107	0.421	2.017
NOR AVG	69.736	0.429	3.058	26.778
NOR STDEV	28.178	0.255	2.197	29.926

Table 11.10 A summary of SMA ilmenite end-member analyses. Massive represents only Bishop South quarry analyses, AN is anorthosite, LGBN is leucogabbronite, LNOR is leuconorite, MD is mafic dike and NOR is norite. Hematite is the second most abundant end-member, but this not truly representative of the ilmenite composition, as described above. Geikielite, the Mg end-member exhibits the next most abundant variation.

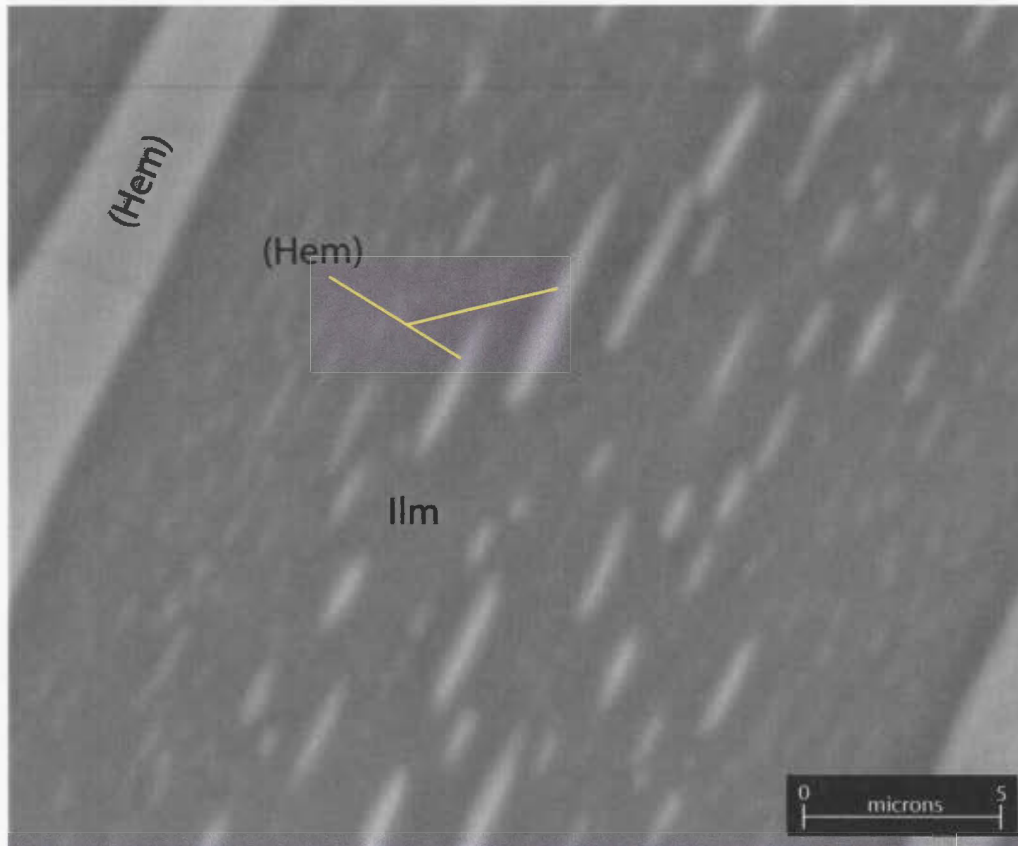


Figure 11.20 A backscatter image from SMA-18 of ultra-fine hematite (Hem) lamellae exsolving from ilmenite (Ilm) reveals that lamellae persist at sub-micron scales, making it difficult to acquire a perfectly accurate ilmenite analysis. Note the depletion halos around each lamellae, which appear to result from Fe diffusion in ilmenite. Care was taken to measure analyses at sites of minimal lamellae density, but it is impossible to completely avoid them. Moreover, low lamellae zones may have experienced sub-solidus Ti or Fe mobility during lamellae formation making them unrepresentative of primary composition. Image is magnified >9500x

To determine whether there is a compositional difference between different rock types or locations, several bivariate plots were created, which plot different oxides versus  $\text{TiO}_2$ . In these diagrams each rock type was grouped the same as previous chapters.

Figure 11.21a,  $\text{TiO}_2$  vs  $\text{FeO}$ , exhibits a positive correlation. There is a cluster of data near the top right of this diagram that represents the pure ilmenite analyses, and those points that fall towards the  $\text{TiO}_2$ - $\text{FeO}$  poor portion of the trend represent analyses with a greater degree of hematite in solid solution. These data points plot lower in  $\text{TiO}_2$  and  $\text{FeO}$  because pure hematite,  $\text{Fe}_2\text{O}_3$ , contains no  $\text{TiO}_2$  and only  $\text{Fe}^{3+}$ . Thus, this diagram demonstrates the mixing line between  $\text{TiO}_2$  and  $\text{FeO}$ . The quarry samples and some other massive oxides (e.g. SMA-18) exhibit the greatest number of samples at the ilmenite end of the mixing line, whereas the points further down the line are either measured from exsolution lamellae, discussed below, or from impure ilmenite.

Figure 11.21b, Ti vs V, exhibits little- to no correlation in any sample group. However, in terms of the pure ilmenite analyses, massive oxide samples from the quarry exhibit the lowest V contents. There appears to be three distinct groups of samples in this diagram: those exhibiting low Ti and high V, low Ti and low V, and the largest group, with relatively high Ti contents (almost pure ilmenite) and low to moderate V contents. All massive oxide analyses are in the final group, while anorthosite hosted oxides are in the second group; otherwise, there is no composition pattern for rock types. There are no petrologically obvious reasons for this trend, but it likely reflects a particular characteristic of how V is partitioned into the different oxides. Perhaps there is some degree of substitution of V with other  $3^+$  cations (Ti and  $\text{Fe}^{3+}$ ).

Figure 11.21c, Ti vs Mg, exhibits a strong pattern whereby nearly all analyses are Mg-poor except the analyses from quarry massive oxides and two SMA-18 analyses of massive oxides. Perhaps the elevated MgO in quarry ilmenite reflects the large volume of mafic (Mg-rich) minerals (e.g. enstatite) associated with the oxide deposits compared

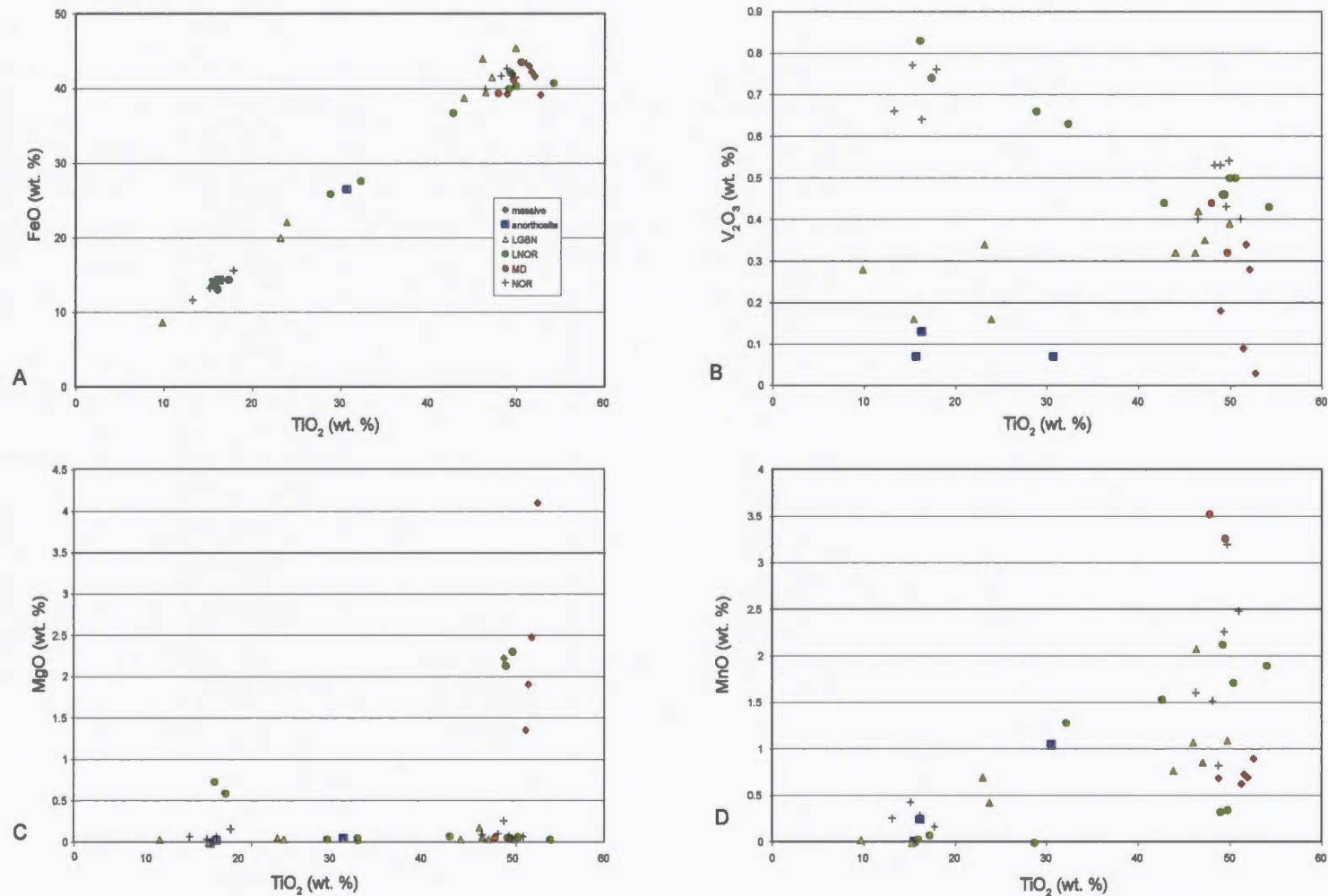


Figure 11.21 Bivariate plots comparing  $\text{TiO}_2$  to minor oxides substituting in ilmenite. The legend in A is the same for all figures. These cations (V, Mn and Mg) substitute for  $\text{Fe}^{2+}$  and  $\text{Ti}^{3+}$  in the ilmenite crystal. It is possible to differentiate between the massive oxides from the Bishop South quarry and other silicate-hosted oxides in some plots. In (A), massive oxide analyses are more Ti and Fe rich; (B) massive oxides analyses are V-poor compared to other analyses, although there is no strong pattern in the non-massive samples; (C) massive oxides from Bishop South quarry samples and some SMA-18 samples are distinctly more Mg-rich; this is the most pronounced trend amongst ilmenite samples; (D) there are no strong trends in Ti vs Mn, although massive oxides analyses do cluster more tightly than do other analyses.

with the more anorthositic samples. It is interesting to note that oxides from relatively Mg-rich areas in the main map area (e.g. SMA-33, 31) do not exhibit this trend. As will be demonstrated below, spinel analyses also exhibit elevated MgO contents, which probably reflect a generally more Mg-rich environment during primary crystallization.

Figure 11.21d, Ti vs Mn exhibits a weak positive correlation between  $\text{TiO}_2$  and MnO. However, similar to Figure 11.21b, the most Ti-rich analyses have a broader compositional range in MnO for a relatively fixed amount of  $\text{TiO}_2$ . Massive oxides analyses from quarry samples also exhibit less MnO than other analyses.

This pattern and others may be a reflection of the cooling history of ilmenite. During ilmenite cooling, impurities such as  $\text{Fe}^{3+}$  are exsolved, resulting in hematite lamellae, which is somewhat similar to how perthite textures develop in feldspar. Therefore, the analyses with less impurities (i.e. V, Mg, Mn) and high Ti may reflect oxides that had a relatively slow cooling history, with ample time to “clean-up” through exsolution of these impurities.

In one massive oxide sample from the Bishop South quarry, coarse-grained corundum crystals hosted by massive magnetite were discovered during microprobe analyses. These crystals were noted during petrographical study, but assumed to be plagioclase crystals because they resembled adjacent plagioclase crystals. Corundum,  $\alpha\text{-Al}_2\text{O}_3$ , exhibits the hematite structure, and is uncommon in this type of deposit, and may form when the magma is saturated in  $\text{Al}_2\text{O}_3$ . It is unknown how both hercynite and corundum can be stable at the same time, but it likely reflects a change in oxygen fugacity during crystallization of the massive oxide ores.

### 11.6.2 Spinel Series

Ten spinel-bearing samples were analysed from the SMA, comprising two leucogabbronorite, 13 leuconorite, one mafic dike, five norite, and 13 massive oxides

from the Bishop South quarry. The goal of spinel analyses was to characterize the compositional range within different rock types and to characterize the composition of the different exsolution phases and textures.

The majority of spinel compositions are either magnetite or titaniferous magnetite (ulvöspinel) and hercynite, which exhibits a pleonastic composition, *i.e.* contains a variable degree of Mg-spinel in solid solution. The chromite end-member is uncommon, indicating that spinel crystallized in a Cr-poor environment. It is possible to summarize the degree of magnetite-ulvöspinel solid solution by normalizing to Ti, because in these oxides there is only significant exchange between Ti and Fe, with little Cr present. In other words, the Ti# of magnetite is an index of ulvöspinel solid solution. Similarly, hercynite can be normalized to Mg, because there is solid solution only with Mg and Fe. Table 11.11 is a summary of the Ti# and Mg# for magnetite and spinel respectively. For the Ti#, both Fe<sup>2+</sup> and Fe<sup>3+</sup> are summed, because ulvöspinel, an inverse spinel like magnetite, forms with Ti<sup>4+</sup> and Fe<sup>2+</sup> randomly filling the octahedral sites and Fe<sup>3+</sup> filling the tetrahedral sites in the magnetite crystal, a phenomena which is also referred to as valency disorder (Waychunas, 1991).

	<b>Magnetite (Ti#)</b>	<b>Hercynite (Mg#)</b>
AVG	0.023	0.448
STDEDV	0.056	0.071

Table 11.11 A summary of spinel data is presented by the degree of solid solution in the two main phases, magnetite and hercynite. The Ti# is used for magnetite to describe the degree of mixing between magnetite and ulvöspinel, whereas the Mg# is used to describe the degree of mixing between hercynite and spinel.

From Table 11.11 it is apparent that magnetite is relatively pure, with only a few analyses containing appreciable amounts of ulvöspinel in solid solution. This is confirmed by Figure 11.22a. Conversely, hercynite contains an appreciable content of spinel in solid solution, exhibiting an average Mg# of nearly 0.5. Again, this relationship is supported graphically by Figure 11.22f, which presents the ratio of Al<sub>2</sub>O<sub>3</sub> vs Mg#; the latter

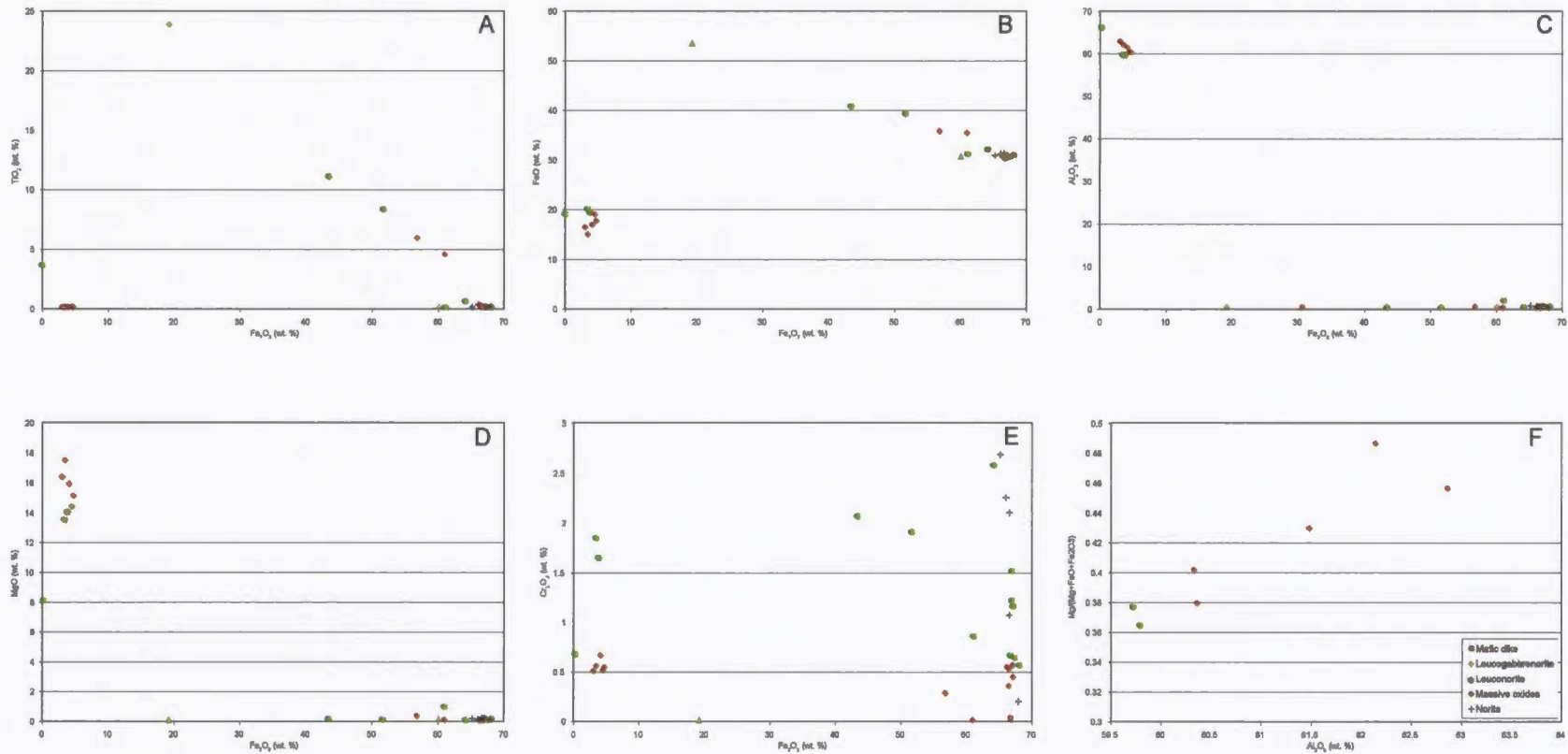


Figure 11.22 Bivariate diagrams plotting both  $\text{Fe}_2\text{O}_3$  and  $\text{Al}_2\text{O}_3$  are used to discriminate between different spinel species. The global legend is located in the bottom right corner of (f). (a) Fe vs Ti is plotted to reveal the degree of magnetite-ulvospinel solid solution; (b)  $\text{Fe}_2\text{O}_3$  vs FeO is used to discriminate between magnetite and hercynite, because both contain one mole of FeO, but Hc does not contain  $\text{Fe}_2\text{O}_3$ . The smaller population in the low FeO and  $\text{Fe}_2\text{O}_3$  regions is hercynite; (c)  $\text{Fe}_2\text{O}_3$  vs  $\text{Al}_2\text{O}_3$  is also useful for discriminating between magnetite and hercynite. Magnetite samples fall along the  $\text{Fe}_2\text{O}_3$  line, while hercynite samples cluster in the high Al, low Fe portion of the graph; (d)  $\text{Fe}_2\text{O}_3$  vs MgO is used to discriminate between magnetite and spinel because magnetite contains no MgO and spinel no Fe. Spinel analyses therefore plot in the top left, with high MgO and magnetite is spread along the  $\text{Fe}_2\text{O}_3$  line; (e)  $\text{Fe}_2\text{O}_3$  vs  $\text{Cr}_2\text{O}_3$  is plotted to reveal chromite solid solution in magnetite. This diagram is one of the few diagrams to separate the 2-3 SMA-18 analyses that commonly plot with quarry analyses on other diagrams; (f)  $\text{Al}_2\text{O}_3$  vs Mg# plots only hercynite samples and is created to illustrate the degree of solid solution between hercynite and spinel. This diagram demonstrates the presence of continuous solid solution between these phases and that the greater amount of Al in hercynite, the less Mg there is.

diagram is a graphical method for presenting the spinel content in hercynite, because both have  $\text{Al}_2\text{O}_3$  in common and simply exchange  $\text{Fe}^{2+}$  and  $\text{Mg}^{2+}$ . The relatively high Mg content in hercynite is mirrored in ilmenite compositions, described above.

The extensive solid solution in the spinel series can be distinguished by plotting different cations against  $\text{Fe}_2\text{O}_3$ , or  $\text{Al}_2\text{O}_3$ , depending on the type of spinel in question. Figure 11.22a is a plot of  $\text{Fe}_2\text{O}_3$  vs  $\text{TiO}_2$ , which is used to illustrate the degree of ulvöspinel solid solution in magnetite. This diagram exhibits a tight cluster of analyses near 65 wt. %  $\text{Fe}_2\text{O}_3$ , the approximate amount contained in pure magnetite, with a negatively sloping linear trend away from this cluster, indicating that with decreasing  $\text{Fe}_2\text{O}_3$ ,  $\text{TiO}_2$  increases. There is also a cluster of analyses between 2-5 wt. %  $\text{Fe}_2\text{O}_3$ , which are the hercynite analyses, which contain only sparse  $\text{Fe}^{2+}$ .

Figure 11.22b,  $\text{Fe}_2\text{O}_3$  vs  $\text{FeO}$ , also discriminates magnetite from hercynite, because hercynite contains only sparse  $\text{Fe}_2\text{O}_3$  compared to magnetite. A cluster of samples with minimal  $\text{Fe}_2\text{O}_3$  and 15-20 wt. %  $\text{FeO}$  corresponds to hercynite, whereas magnetite forms a separate cluster at the high  $\text{Fe}_2\text{O}_3$  end of the graph, sloping towards higher  $\text{FeO}$ . This trend may result from the presence of  $\text{Ti}^{4+}$  in ulvöspinel solid solution. Furthermore, Figure 11.22c,  $\text{Fe}_2\text{O}_3$  vs  $\text{Al}_2\text{O}_3$  also distinguishes magnetite from hercynite and spinel ( $\text{Al}_2\text{O}_3$ -bearing spinel). Hercynite analyses are at the top of the  $\text{Al}_2\text{O}_3$  axis, with very low  $\text{Fe}_2\text{O}_3$ , whereas magnetite exhibits a variable  $\text{Fe}_2\text{O}_3$  content, but with virtually no  $\text{Al}_2\text{O}_3$ . In addition, Figure 11.22d,  $\text{Fe}_2\text{O}_3$  vs  $\text{MgO}$ , demonstrates the content of spinel ( $\text{MgAl}_2\text{O}_4$ ) solid solution in magnetite. Here, magnetite exhibits a similar trend as in 11.22c, but a second population of analyses with low  $\text{Fe}_2\text{O}_3$  and high  $\text{MgO}$  represents spinel solid solution. This diagram indicates that magnetite does not contain the spinel solid solution, because if spinel were present in magnetite, the cluster of  $\text{MgO}$ -rich analyses would contain more  $\text{Fe}_2\text{O}_3$ . Figure 11.22e,  $\text{Fe}_2\text{O}_3$  vs  $\text{Cr}_2\text{O}_3$  demonstrates the presence of chromite. There are three distinct populations in this diagram. The first is magnetite, which exhibits a broad range of Cr. In this group, massive oxides from the Bishop South

quarry exhibit some of the lowest Cr contents, along with the magnetite analysis from SMA-65, the mafic dike. The other two populations both exhibit low  $\text{Fe}_2\text{O}_3$  and correspond to hercynitic analyses. One group comprises mainly hercynite from the quarry analyses and the final population is somewhat more elevated in Cr, but still hosted by hercynite. These analyses are from SMA-18 and correspond to the same two samples that are commonly compositionally similar to quarry analyses. Finally, Figure 11.22f,  $\text{Fe}_2\text{O}_3$  vs Mg# is a method of describing the degree of hercynite-spinel solid solution and was described above.

Figure 11.23 is a ternary diagram that summarizes the degree of solid solution from all spinel and ilmenite microprobe analyses. This diagram identifies the various solid solution fields within  $\text{TiO}_2\text{-FeO-}1/2\text{Fe}_2\text{O}_3$  compositional space. It is apparent from this diagram that solid solution is extensive in these data, particularly in ilmenite analyses. The ilmenite analyses occupy a broad cluster near the ilmenite end of the ilmenite-hematite tie lines. The analyses fall in the lower portion of the solid solution field of ferrobrookite + pseudobrookite solid solution and ilmenite + hematite solid solution (Fbr-Psb + Ilm-Hem). Ilmenite samples begin to plot within the narrow field of ilmenite + hematite solid solution as they approach the hematite corner. Magnetite analyses, as indicated above, exhibit relatively less solid solution, clustering near the magnetite portion of the  $\text{FeO-}1/2\text{Fe}_2\text{O}_3$  tie line. Some analyses project towards the ulvöspinel end, reflecting solid solution present in some analyses. Although not presented in this research, the ilmenite and co-existing magnetite analyses can be connected along constant temperature tie-lines as well, indicating the temperature and composition that exsolution occurred.

### 11.6.3 Exsolution lamellae

Exsolution lamellae in ilmenite and spinel are texturally and compositionally complex. The general morphology of the exsolution lamellae has already been described, thus this

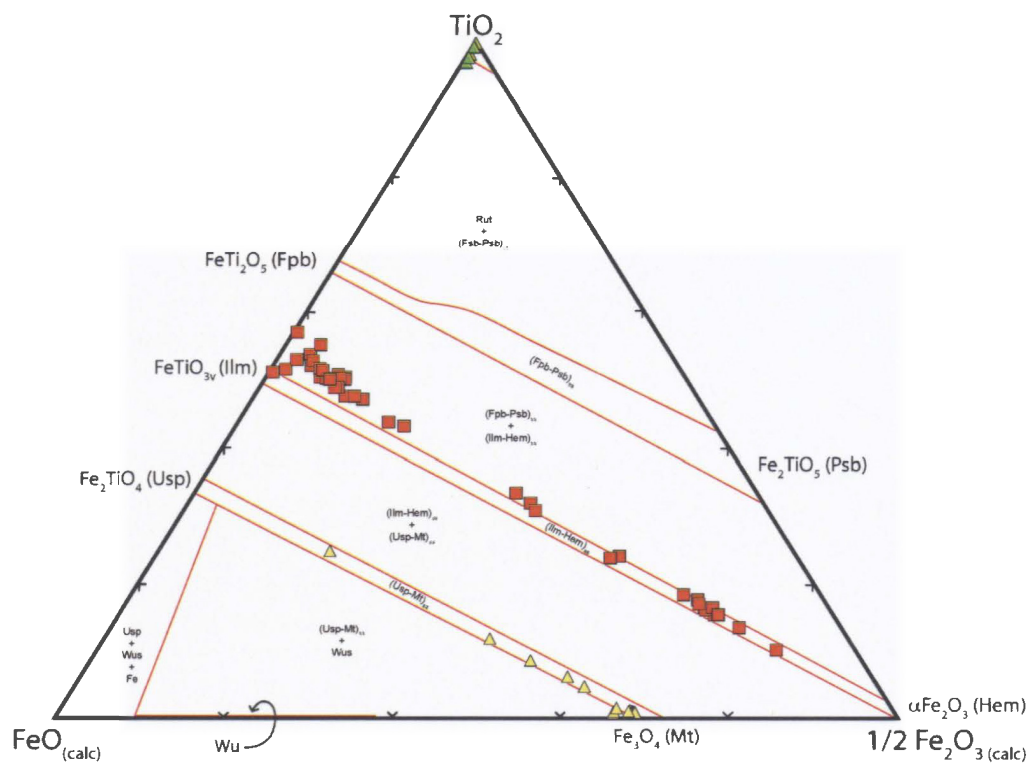


Figure 11.23 A ternary diagram of  $\text{TiO}_2$ - $\text{FeO}$ - $1/2\text{Fe}_2\text{O}_3$  for all microprobe data of Fe-Ti oxides in the SMA. This diagram demonstrates the degree of solid solution within ilmenite and spinel analyses. The lines joining ilmenite (Ilm) and hematite (Hem) represent a mixing line between ilmenite and hematite, which occurs as solid solution. The same is true for the lines joining ulvöspinel (Usp) and magnetite (Mt). The solid red bar along the  $\text{FeO}$ - $1/2\text{Fe}_2\text{O}_3$  edge of the triangle from ~90 wt. % FeO to ~62 wt. % FeO represents the compositional range of wüstite (Wu). Solid solution is denoted in each field by a mineral pair. Tick lines are in 20 wt. % increments. The cluster of data at the Mt field represents approximately 20 analyses. Refer to the text for explanation.

section describes the lamellae composition and presents some textural relationships in more detail.

Exsolution lamellae in the SMA can be grouped into two major populations: those with an ilmenite host, which comprise mainly hematite exsolution lamellae, and the others hosted by magnetite, comprising ilmenite, hercynite and spinel. The exsolution lamellae in these samples forms from a combination of cooling and oxidation, and is called oxidation exsolution. The fine textures in these oxides form only at high temperatures, during cooling, and not during deformation or alteration, although modification of the textures occurs during alteration and is described below.

Figure 11.24 is a compilation of different examples of hematite and magnetite exsolution from ilmenite. The textures formed in ilmenite are relatively consistent throughout the SMA map area, but compositions of the lamellae vary somewhat.

Figure 11.24a, from SMA-18, is an overview of typical the ilmenite-magnetite association, although in this sample, ilmenite is more abundant than magnetite (white). Ilmenite is dark grey in this image with abundant hematite exsolution lamellae (grey). Some ilmenite grains are distinctly darker, which appears to be related to the variable amount of Fe in solid solution (the darker ilmenite is relatively Fe poor). A large magnetite grain is present in the bottom centre of the image, and is host to E-W trending exsolution lamellae of hercynite, a common feature of magnetite.

Figure 11.24b illustrates the very fine textures of ilmenite and hematite lamellae common in SMA oxides. In this image, from SMA-24, the oxides comprise only ilmenite and hematite, with geikielite and pyrophanite comprising < 2 wt. %. The fact that hematite exsolution lamellae still contain appreciable quantities of ilmenite may actually be a reflection of the difficulty of locating points completely free of ultrafine lamellae within hematite, as illustrated in this image. The same may be true for ilmenite *i.e.* both ilmenite

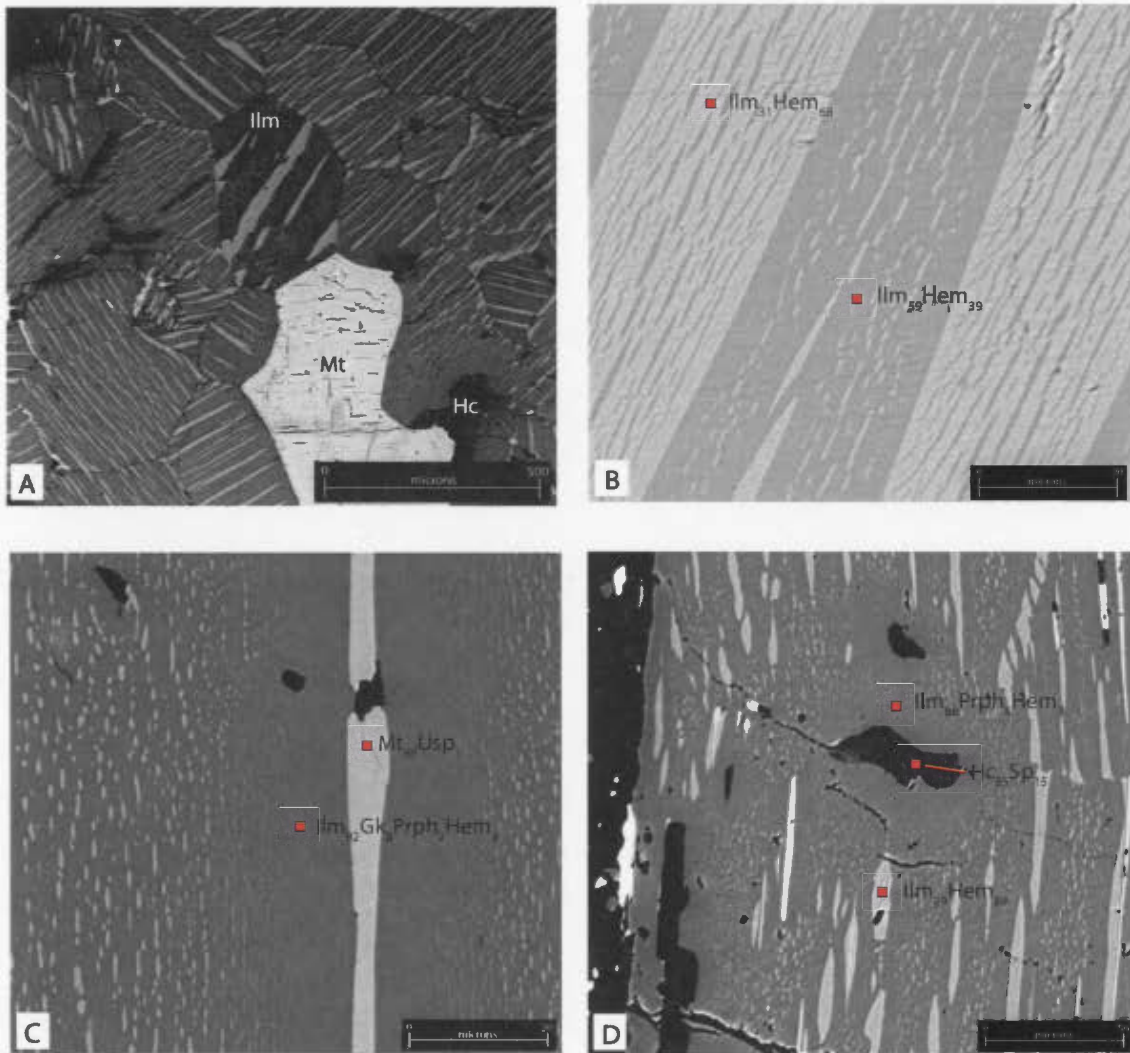


**Figure 11.24** Backscatter electron images from SMA ilmenite. This figure is an overview of the common ilmenite-hematite ( $\pm$ magnetite) exsolution textures and associated compositions. Compositions are listed in B-D in terms of end-members. Ilm= ilmenite; Gk= geikielite; Prph= pyrophanite; Hem=hematite; Mt= magnetite; Usp= ulvöspinel. From these backscatter electron images it is apparent that during and following exsolution, element diffusion occurred such that most coarse lamellae are surrounded by depletion halos. The proposed mode of formation is relatively homogenous exsolution of fine lamellae and over time diffusion of these lamellae into coarse lamellae. Note in A, in the magnetite grain (bottom centre), the discontinuous horizontal black lines are pleonaste and in D that ilmenite solid solution proximal to pleonaste (Mg-hercynite), contains no Gk component, suggesting that Mg diffused preferentially into Hc rather than remaining in ilmenite solid solution. A full explanation of textures is given in the text. Scale bars are in microns in lower right corners.

and hematite compositions may be closer to pure end-members, but microprobe resolution is not fine enough to measure points free of lamellae of the other species. The composition of the dark grey lamellae within hematite (light grey lamellae) is unknown because of the very small size. However, based on the relative brightness of these lamellae compared to ilmenite, it is possible they are also ilmenite.

Figure 11.24c, from BS-01, is an example of magnetite exsolution lamellae within ilmenite (dark grey), which again illustrates the difficulties of microprobe analyses of a specific phase, because of the density of finer lamellae. In this image, similar to Figure 11.20, the lamellae appear to continue decreasing in size to well below the micron scale. The black irregular blebs in this image are hercynite. In this image the exsolution lamellae are magnetite, but the effect of “contaminating” ilmenite analyses is the same as in Figure 11.20. Normally, hematite is the exsolution lamellae in ilmenite and not magnetite.

Figure 11.24d, from SMA-33, is the final example of hematite exsolution in ilmenite. Hercynite, the black grain in the centre of the image, is surrounded by only fine-grained hematite lamellae. The ilmenite adjacent to the hercynite is virtually Mg-free, whereas hercynite contains the Mg end-member spinel in solid solution, suggesting that perhaps Mg diffused from ilmenite into hercynite.

Figure 11.25 presents four backscatter images of spinel exsolution lamellae, which exhibit textures quite distinct from ilmenite-hosted lamellae. These textures are controlled partly by the crystallographic structure of the host phase, therefore, because magnetite and ilmenite are crystallographically different (inverse cubic and rhombohedral respectively), their respective lamellae exhibit different textures.

Figure 11.25a is a typical example of magnetite from the massive oxides in the Bishop South quarry. In this image, two morphologies of ilmenite exsolution lamellae are visible.

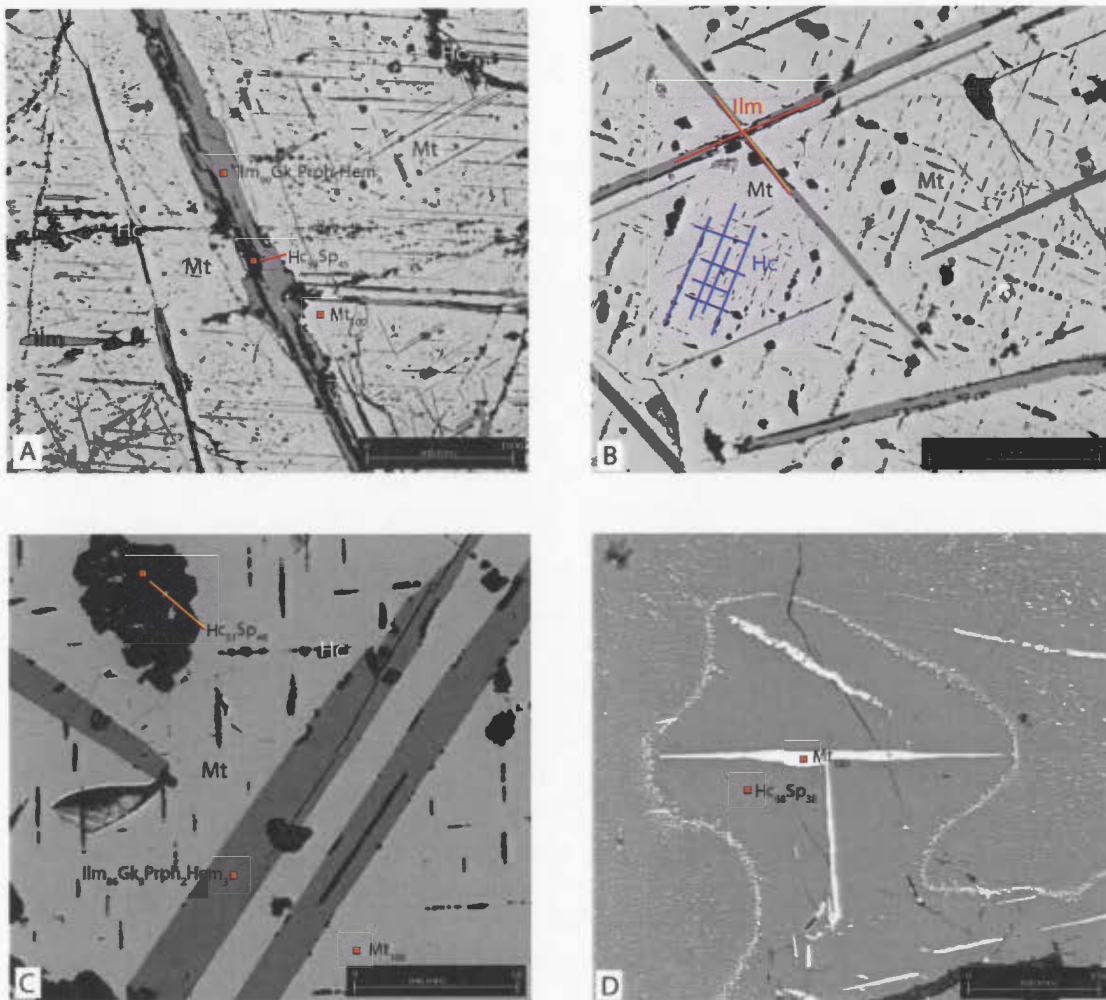


Figure 11.25 Backscatter electron images of exsolution textures in spinel. (a) An overview of typical massive quarry magnetite, which hosts appreciable hercynite (Hc) and ilmenite (Ilm) exsolution. Most exsolution is trellis-like, but in the centre a wide sandwich-type lamellae cuts magnetite. Hercynite is the last phase to form, cutting all other phases; (b) a zoom from a similarly textured area highlighting the hercynite and ilmenite exsolution lamellae, which exploit different crystallographic planes. Again, hercynite is the last phase to exsolve; (c) wide exsolution lamellae of ilmenite cut nearly pure magnetite, but are cut by hercynite, which locally forms irregular clusters; (d) an unusual exsolution texture in hercynite (pleonaste) whereby magnetite exsolution at the edges of the image is ultrafine-grained and evenly distributed, but appears to diffuse or migrate into coarse, crystallographically controlled lamellae in the middle of the image. The central hercynite contains virtually no magnetite, indicating a very efficient diffusion mechanism. Compositions are given where applicable as end-members. A and B were imaged at the MAF-IIC SEM lab while C and D were imaged on the MUN microprobe. Scale bars are in the lower right corners.

First, fine-grained trellis lamellae occur in orthogonal sets that appear to have exsolved first. The other type of ilmenite lamellae is coarse-grained and called sandwich-type lamellae (e.g. Haggerty, 1991), which cuts approximately diagonally down the centre of the image. This lamellae appears to have formed second. Hercynite forms a second set of orthogonal exsolution lamellae in magnetite that cross-cuts both sets of ilmenite lamellae, indicating it was the final generation of exsolution lamellae. Locally, very fine cubes of hercynite appear to aggregate together, forming larger irregular masses. Compared to SMA-18, hercynite in the quarry samples is more spinel-rich, often comprising nearly 50:50 hercynite to spinel (*i.e.* pleonaste).

Figure 11.25b is a more detailed image of the type of exsolution described above, and it is clear in this image that hercynite crystallized after ilmenite trellis lamellae.

Figure 11.25c is a final example of ilmenite and hercynite exsolution lamellae in magnetite. The composition of hercynite in this texture is relatively consistent from different locations, but between samples, is somewhat variable. In this strongly magnified image, many of the hercynite lamellae actually occur as parallel chains of cubic crystals, most likely because they nucleated along the same crystallographic plane.

Figure 11.25d presents an unusual texture only observed in Bishop South samples, and not noted in a literature review on spinel textures. In this image, magnetite occurs as a very fine, evenly distributed cloud within hercynite. At the centre of the image, homogenous hercynite hosts an orthogonal set of coarse-grained magnetite lamellae surrounded by a depletion halo that appears to approximately mirror the shape of these coarse lamellae. This texture suggests that the coarse lamellae crystallized after the cloud of fine magnetite formed. A mechanism to explain this texture is unknown, but it may have resulted from some type of diffusion whereby the cloudy magnetite diffused inwards to form the coarse lamellae. Magnetite exsolution from hercynite in SMA-18 occurs as irregular lenses.

#### **11.6.4 Oxide alteration**

Alteration of Fe-Ti oxides occurs locally, and is characterized by the destruction of primary oxides and growth of secondary, oxidized phases. In the SMA, alteration appears to have resulted from the infiltration of oxidizing fluids, which changed ilmenite into hematite and rutile, leaving the coarse hematite lamellae relatively unchanged. Figure 11.26 is an example of such alteration, whereby ilmenite on the left side of the image is altered to a combination of Fe-poor ilmenite, hematite, and rutile. Secondary amphibole locally overgrows the oxides, suggesting that alteration was widespread and not restricted to just oxide phases. The fine-scale textures and intergrowths prevent accurate analyses of these phases, thus, no compositions are presented on this figure, aside from the overall name of the phase.

#### **11.7 Summary**

Twenty-one samples from the SMA were analysed by electron microprobe to answer a wide range of questions related to the composition of silicates, oxides, sulfides and platinum group minerals. In total, 254 analyses are presented in this chapter for plagioclase, pyroxene, garnet, amphibole, biotite, chlorite, epidote, chalcopyrite, pyrrhotite, pyrite, sphalerite, ilmenite, spinel and three platinum group minerals.

Plagioclase exhibits relatively homogenous compositions throughout the different rocks types and does not exhibit any major spatial variation in composition. Anorthosite analyses average An 45, gabbro-norite An 47, leucogabbro-norite An 45, leuconorite An 55 and norite averages An 53. Although noritic samples exhibit higher An contents, the standard deviation in these and other lithologies is far greater than the average differences. There is considerable variation in core and rim analyses in plagioclase, but the changes are not systematic: some recrystallized rims are more calcic than the cores while in other samples the rims are more albitic.

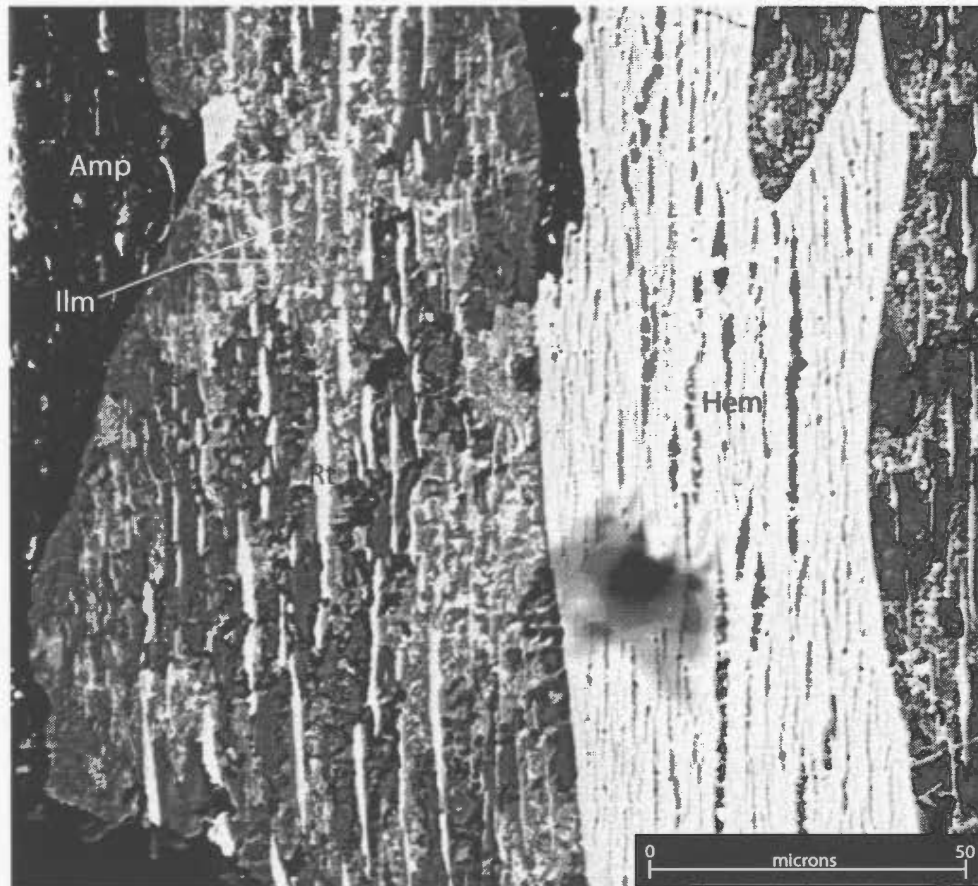


Figure 11.26 Backscatter electron image from SMA-15. Alteration of oxides in the SMA map area is characterized by oxidation of ilmenite to rutile and hematite. In this image, pre-existing hematite appears to be unaffected, remaining with a texture similar to pre-alteration. Locally, amphibole overgrows oxides, indicating that alteration may also have resulted in growth of secondary silicates. The diffuse black spot near the bottom of the wide hematite lamellae is a spot of contamination or poor carbon coating. Scale bar is in lower right corner.

A comparison between white, normal plagioclase and pink plagioclase indicates that coloured plagioclase contains slightly more trace metals than normal plagioclase. However, to convincingly determine if these trace elements are truly elevated in coloured plagioclase, LAM-ICP-MS analyses would be required.

Pyroxene compositions are quite consistent between different samples, and exhibit a magnesian composition in both clinopyroxene (diopside) and orthopyroxene (enstatite). The effects of recrystallization on pyroxene appears to be minor changes in  $\text{Al}_2\text{O}_3$ ,  $\text{Fe}_2\text{O}_3$  and MnO.

Garnet compositions are intermediate between almandine and pyrope with lesser grossular and only minimal spessartine. Zoning in garnet is locally present and is expressed by MnO enriched rims, and variable changes in major end-member compositions.

Most amphibole in the SMA has a magnesian composition, except for those oxides that form proximal to Fe-Ti oxides, which exhibit a more Fe dominated composition. The most abundant amphibole species is tschermakite-hornblende, whereas oxide-related amphibole is ferro-tschermakite-hornblende. Epidote compositions are intermediate between zoisite and epidote, reflecting the Fe-Al dominated bulk composition that epidote formed from.

Chalcopyrite from the Sheep Brook area exhibits typical compositions, with trace amounts of Zn and Ni. Pyrrhotite analyses indicate that lamellae observed in microscopic examination are related to deformation, because lamellae are not observed in backscatter images, which would occur if the lamellae were compositionally different. Pyrrhotite is strongly enriched in Ni, averaging 1.35 wt. % in seven analyses. Pyrite composition is also strongly enriched in Ni. Enrichment in pyrite occurs as concentric Ni-rich bands within subhedral to euhedral cubes that appear to have crystallized late in the

petrogenesis of Sheep Brook sulfides. It is possible that the elevated Ni in whole rock assayed results from Ni in solid solution in pyrrhotite and pyrite, because pentlandite is not present in Sheep Brook samples.

Platinum group minerals comprise sperrylite, PtAs<sub>2</sub> and three other un-named phases comprising two Pt-Te phases and one Pd-Sb-Ag phase. It is not possible to determine if these analyses represent new phases or if their very small size has affected the analyses. To properly assess whether these represent new phases will require further work with coarser-grained samples and a larger population of analyses as well as higher precision analysis, such as the LAM-ICP-MS. These analyses are the first characterization of PGM in insular Newfoundland, although not the first documentation of PGE's in assay.

Oxide minerals display many complex textures and chemical relationships. Ilmenite analyses contain variable quantities of hematite in solid solution, and lesser amounts of geikielite and pyrophanite, the Mg and Mn end-members respectively. Hematite is the most common type of exsolution lamellae in ilmenite, and textures are consistent with formation by oxidation exsolution processes. Analyses indicates samples of massive oxides from the Bishop South quarry and several analyses from SMA-18, also massive oxides, are distinctly elevated in Mg compared to the rest of the analyses. It is unknown if this chemical trait is useful as an exploration vector for large accumulations of massive oxides. It is probably easier to discover massive oxide occurrences using geophysical exploration techniques than using mineral chemistry as an exploration vector.

Spinel analyses demonstrate the magnetite is the most common spinel species and that it has a nearly pure composition, with only local occurrences of ulvöspinel in solid solution. Exsolution lamellae of Mg-hercynite, called pleonaste is common in massive oxides from the bishop South quarry, but less common in other locations. Magnetite also contains trellis and sandwich-type exsolution lamellae of ilmenite. It appears that trellis ilmenite formed first, then sandwich lamellae and all are cross-cut by pleonaste lamellae.

Diffusion appears to have played a large role in the formation of exsolution lamellae textures in spinel and ilmenite, which is evidenced by the common depletion halos surrounding exsolution lamellae. Alteration of oxides forms a second generation of relatively more oxidized oxide species, although some primary species appear to be unaffected by this alteration, particularly hematite.

## Chapter 12: Steel Mountain Anorthosite Sulfur Isotopes

Eight sulfide samples were collected for sulfur isotope analyses, comprising four samples from the main map area (disseminated blebs in various lithologies), three from massive sulfides at Sheep Brook and one from interstitial sulfides hosted in massive Fe-Ti oxides at the Bishop South quarry. The procedures for the collection and processing of these samples is described in detail in Chapter 1 and raw data are listed in Appendix 5.

The goal of sulfur isotope analyses was to characterize the isotopic composition of sulfides in the SMA, including those from mineralized areas such as the Bishop quarries and the Sheep Brook area. A brief overview of sulfur systematics was provided in Chapter 6 and is not elaborated in this chapter.

### 12.1 $\delta^{34}\text{S}$ isotope results

$\delta^{34}\text{S}$  isotope ratios from the main map area, which are hosted by leuconorite, norite and leucogabbronorite lithologies range from +7.3 ‰ to +2.8 ‰, averaging +4.0 ‰ with a standard deviation of 2.2 ‰, mainly because of the large positive value of SMA-100 (7.3 ‰). Massive and semi-massive (RIC-38) sulfides from the Sheep Brook area range from +1.2 ‰ to +2.0 ‰; the two massive sulfide samples, from the same lens of sulfides, but one from pyrrhotite and the other from pyrite are not statistically distinguishable, indicating that sulfur for both phases originate from the same  $\delta^{34}\text{S}$  reservoir. One massive oxide-hosted sulfide, from SMA-Q1, exhibits a  $\delta^{34}\text{S}$  value of -2.4 ‰, the only negative  $\delta^{34}\text{S}$  value in the SMA. The massive oxide is interesting, because it is located barely 1 km away from the Sheep Brook samples, but differs by over 3.0 ‰.

<b>Sample</b>	<b>Lithology</b>	<b><math>\Delta^{34}\text{S}</math> VCDT</b>	<b>Mineralogy</b>
SMA-100	leuconorite	7.3	Py
SMA-33	norite	2.8	Py
SMA-38C	altered GBN	2.0	Po+Py+Ccp
SMA-71	leuconorite	3.3	Py
SMA-95.1	GBN	2.8	Py
SMA-40B	MASU	1.2	Po
SMA-40B	MASU	1.2	Py
SMA-Q1	MO	-2.4	Po+Py

Table 12.1 A summary of SMA  $\delta^{34}\text{S}$  ratios. Most SMA sulfides comprise pyrite and lesser pyrrhotite. GBN= gabbro-norite; MASU= massive sulfide; MO= massive oxide

Figure 12.1 is a graphical presentation of SMA  $\delta^{34}\text{S}$  values, while Figure 12.2 is a comparison of SMA values to various igneous, sedimentary and marine sulfur reservoirs. From Figure 12.2 it is apparent that most samples fall within the  $\delta^{34}\text{S}$  range of mantle  $\delta^{34}\text{S}$ , which exhibits values of  $0 \pm 3$  ‰, except for SMA-100. The reason for the relatively positive (heavy)  $\delta^{34}\text{S}$  in SMA-100 is unknown, but it is possible that there is a larger contribution of granitic-like sulfur in this sample; granitic  $\delta^{34}\text{S}$  ranges from -10 ‰ to +15‰, which as Rollinson (1993) and references therein point out, is unusual, because average continental crust  $\delta^{34}\text{S}$  is +7 ‰.

### SMA $\delta^{34}\text{S}$ Sulfides

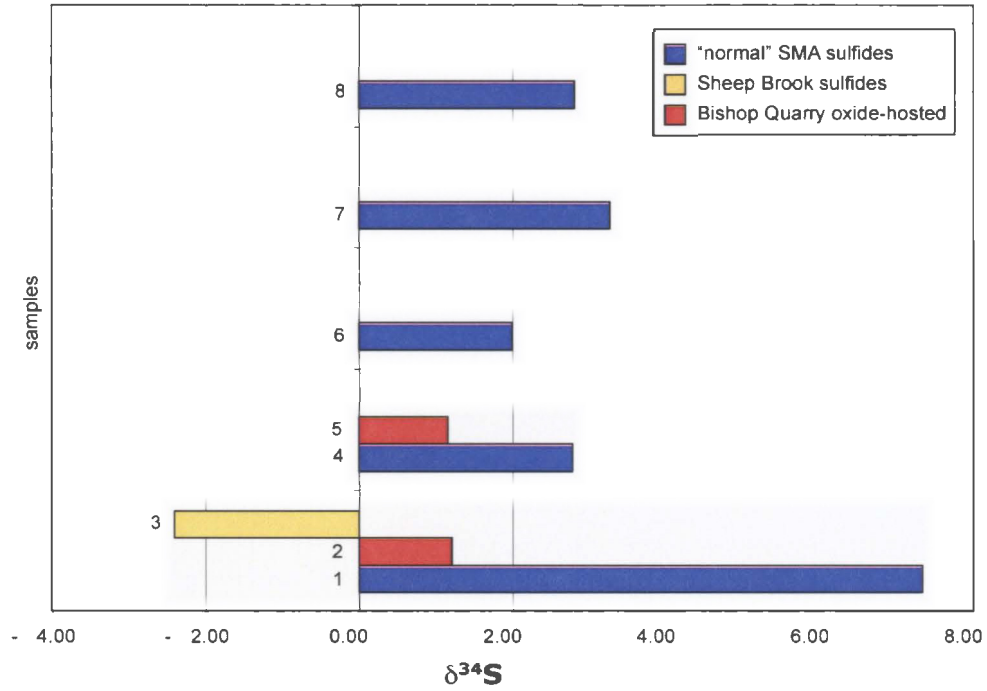


Figure 12.1 A diagram of SMA  $\delta^{34}\text{S}$  ratios, including samples hosted by massive oxides (Bishop South) massive sulfides (Sheep Brook) and disseminated sulfides from the main map area leucornorites and leucogabbronorites. Refer to the text for explanations for the large differences in  $\delta^{34}\text{S}$  values of the Bishop South sample, and SMA-100 (bottom bar).

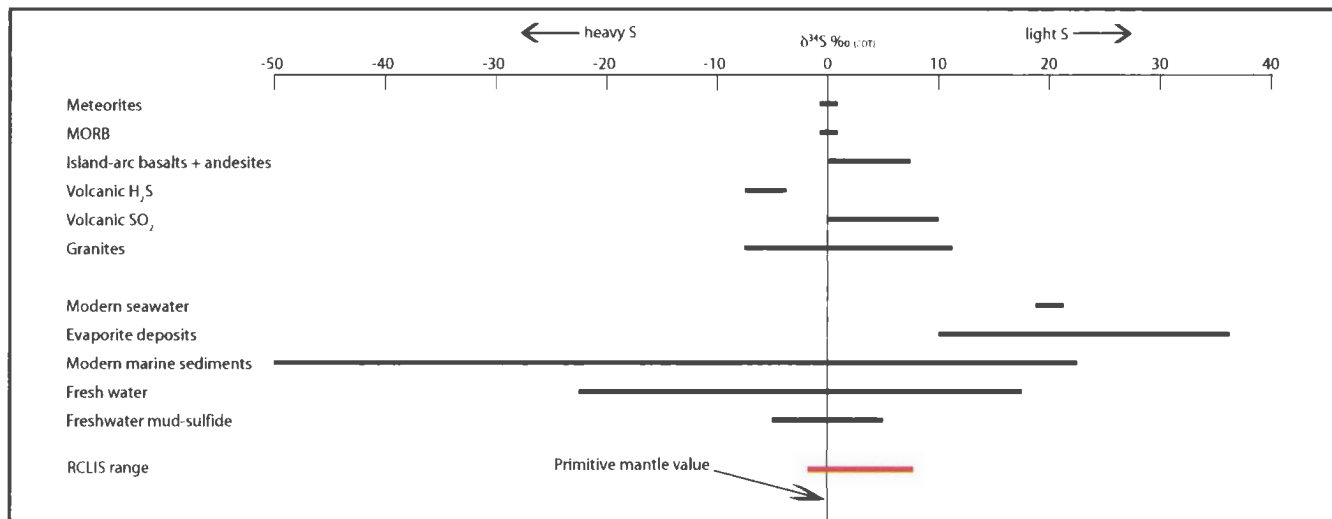


Figure 12.2 A compilation diagram of  $\delta^{34}\text{S}$  sulfur ranges from various igneous sources (top) and sedimentary or water reservoirs (bottom). The various ranges are compiled in Rollinson (1993). SMA samples are presented at the bottom of the diagram for comparative purposes. SMA samples fall within the range of mantle  $\delta^{34}\text{S}$ , which is the most likely reservoir that anorthositic rocks would fall into. It is possible that SMA-100 exhibits a more granitic signature, which can explain the more positive  $\delta^{34}\text{S}$  value.

## **Chapter 13: Discussion and Conclusions**

### **13.1 Overview**

The goals of Steel Mountain Anorthosite research were threefold. First, magnetite, particularly that from the Bishop South and Bishop North quarries was investigated to determine whether it formed through orthomagmatic or metasomatic processes. Secondly, two PGE anomalies were characterized and finally, purple- to lilac coloured plagioclase was investigated with the electron microprobe to determine if there are geochemical causes of the colouration.

### **13.2 Orthomagmatic vs metasomatic oxides**

Field mapping and petrography indicate that there are two texturally distinct populations of magnetite in the SMA. The main form of magnetite is semi-massive to massive, foliation parallel lenses with variable dimensions, ranging from a few centimeters long to the Bishop deposits, which comprise several large lenses (or dike-like bodies) totaling nearly 1 Mt.

Supporting evidence for an orthomagmatic origin include microtextures and mineral chemistry. The majority of the oxides in the study area exhibit delicate exsolution textures that form at high temperatures, typically greater than 600 °C, during cooling of magma. In contrast, oxides from the Indian Head iron oxide deposits, possibly part of the Steel Mountain Anorthosite, were recrystallized and altered at high temperatures. These latter oxides exhibit recrystallized granoblastic textures with compositional segregation of magnetite and ilmenite, which form discrete, homogenous subhedral crystals.

A common geochemical feature of the massive- to semi-massive oxides lenses is the solid solution of other oxide species (e.g. hercynite in magnetite or hematite in ilmenite). This is another typical trait of primary oxides but is uncommon in altered or

recrystallized oxides, which commonly are compositionally segregated during deformation-induced recrystallization.

In comparison, a more diagnostic texture of a metasomatic (or alteration-related) origin is the presence of volumetrically minor secondary oxides. These oxides mainly comprise magnetite, or less commonly ilmenite and occur as fracture fillings or small aggregates proximal to altered zones and locally as reaction rims around garnets. These oxides are compositionally homogenous within individual fracture systems or reaction rims. In addition, these oxides do not usually exhibit exsolution textures. Given that these oxides are located in fractures, often associated with alteration phases, it is easier to accept that they are the products of alteration or metasomatism.

The evidence from this study suggests that the majority of oxides observed in the SMA formed by primary, orthomagmatic processes. That these oxides are commonly hosted in foliation parallel lenses does not reduce the likelihood that they are primary, but suggests instead that they may have been emplaced late in the crystallization process.

### **13.3 PGE Occurrences**

The SMA is host to several small PGE mineralization occurrences. At Sheep Brook, PGE's are spatially associated with massive sulfides and hosted by a mafic dike. Although samples of massive sulfides were known to contain anomalous Pd and Pt, a systematic assessment of these samples was only completed in this study. Scanning electron microscope and electron microprobe analyses indicate that the PGE's occur as discrete mineral phases rather than in sulfide solid solution. Although sperrylite, PtAs<sub>2</sub>, was identified, the other phases appear be new species. The Sheep Brook dike is oriented parallel- to subparallel to a prominent structural fabric in this area, which should be a vector for further exploration. Thus, mapping of structure and the distribution of mafic dikes, particularly where it appears that structure controls the orientation of the dikes might prove fruitful in exploration for PGE's in this region.

### 13.4 Plagioclase colouration

It is apparent from petrographical observations that recrystallization commonly destroys the purple- to lilac colouration in plagioclase, suggesting that whichever elements are responsible for the colour, they are mobile during minor recrystallization. An extensive evaluation of SMA plagioclase mineral chemistry was conducted and it was found that aside from a few samples with elevated Fe, Ti or Mn values, most geochemical variation was undetectable by standard EMPA techniques. To properly investigate the compositional differences between “normal” plagioclase and purple or lilac plagioclase, more sensitive instrumentation such as a multi-collector LAM-ICP-MS would be warranted.

### 13.5 Conclusions

Most magnetite in the SMA formed through orthomagmatic processes, particularly massive- to semi-massive lenses and the Bishop North and South deposits. Minor amounts of magnetite appear to have formed through secondary processes, but are volumetrically insignificant. Furthermore, it appears that secondary magnetite would have formed too late in the petrogenesis to achieve any significant volume.

For the first time, discrete platinum group minerals have been identified in the Steel Mountain Anorthosite. Several of these minerals may be new but further work is required. Future exploration should focus along the strike distribution of mafic magmatism on this area; shearing fabrics may be more obvious than dikes and could be used as an exploration vector.

Coloured plagioclase may be the result of elevated Fe, Ti or Mn, but the microprobe sensitivity is too low to detect statistically significant concentrations of these elements.

## **Chapter 14: Taylor Brook Gabbro Suite field geology**

### **14.1 Introduction**

Taylor Brook Gabbro Suite is a heterogeneous mafic intrusion. This statement is supported by the weakly consistent orientation of fabrics, and variable textures between different outcrops: few outcrops, even those nearby each other exhibit much resemblance to each other. In general, the gabbro ranges from medium-grained equigranular, to coarse-grained, or porphyritic in texture, and exhibits local zones of cumulate textures. It is characterized by variable gabbroic to ferrogabbroic composition based on the local abundance of oxides; overall, the TBGS has approximately 1-2% oxides. Small zones of pyroxenite and olivine gabbro occur in the TBGS, although they are more frequent in the northern TBGS and the TBGP. Pyroxenite, which is often altered to fibrous amphibole and chlorite, is usually spatially associated with melagabbro and it is possible it represents less differentiated components of the TBGS. Figure 14.1 is a geological map of the TBGS and the surrounding country rock the bedrock (Colman-Sadd and Crisby-Whittle, 2004). The units and features of this map are described below.

### **14.2 Field Geology**

#### **14.2.1 Igneous layering**

Layering is present locally and generally dips shallowly into the center of the intrusion (Figure 14.2). This is not always consistent, and in some locations layering dips north where it would have been expected to dip east or west. For example, the west-central area of the intrusion, where one would expect layers to dip away from the contact (i.e. dip west), layers actually dip east-northeast. Where layers are present, they are defined by changes in grain size and/or relative modal mineral abundances. Cyclical graded layers like those described in the RCLIS do not exist in the TBGS. Layer composition varies from melagabbro to leucogabbro, although normal gabbro is the dominant composition. Ferrogabbro layers are also locally present and contain up to 15% magnetite  $\pm$  ilmenite, which may decrease in abundance upwards from the base of individual layers (Figure

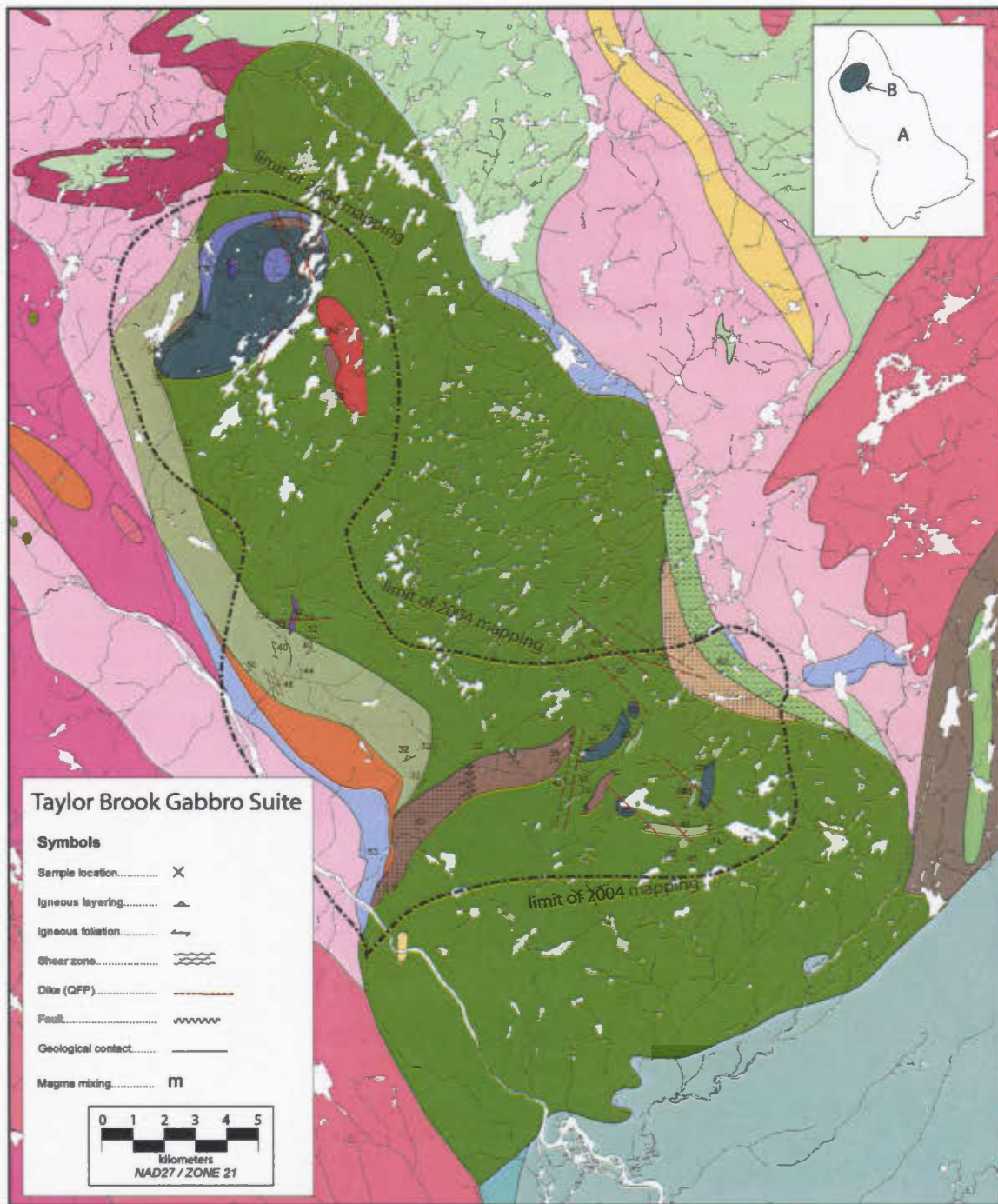


Figure 14.1 A geological map of the TBGS and surrounding country rock. A detailed description of each unit is provided in Chapter 14. Inset in top right corner denotes the TBGS (A) and TBGP (B). Symbol legend and scale are located in the lower left corner and the lithological units are on the preceding page. Country rock geology is modified after Colman-Sadd & Crisby-Whittle, 2004.

## Geology of the Taylor Brook Gabbro Suite

### Taylor Brook Gabbro Suite

	Pyroxene amphibole gabbro ( $\pm$ leuco)
	Amphibole leucogabbro
	Amphibole gabbro ( $\pm$ biotite and carbonate alteration)
	Leucogabbronorite
	Oxide gabbro, oxide gabbronorite ( $\geq$ 10% Fe-Ti oxides)
	Anorthosite
	Leucogabbro
	Troctolite
	Clinopyroxenite
	Tonalite
	Quartz-feldspar porphyry (QFP) dike (make line type)
	Xenolith-bearing

### Long Range Gneiss Complex

	Unsubdivided orthogneiss (may include some paragneiss)
	Leucocratic granitoids (Main River Pluton)
	Unsubdivided orthogneiss (may include some paragneiss)
	Unsubdivided paragneiss (carbonate marble)
	Unsubdivided paragneiss
	Unsubdivided orthogneiss (may include some paragneiss)
	Siliclastic quartzite
	Plutonic felsic
	Siliclastic non-marine conglomerate
	Siliclastic marine sandstone
	Plutonic mafic

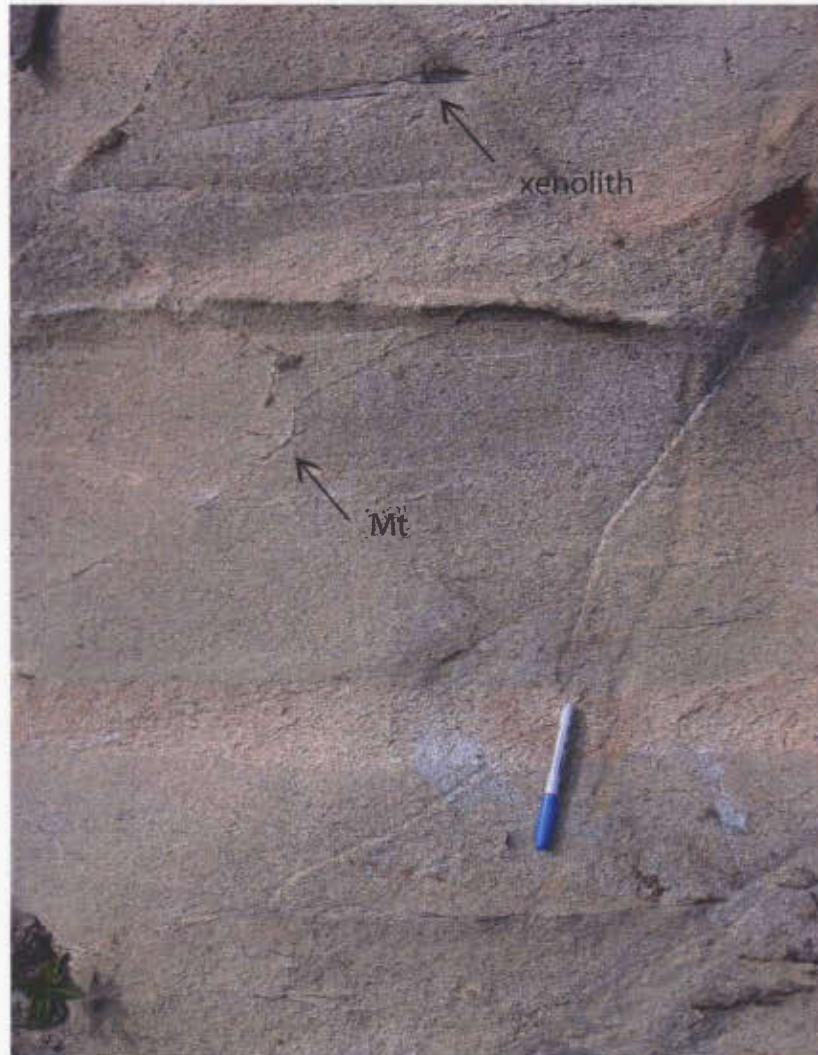


Figure 14.2 Magmatic layering in TBC-53, near the centre of the TBGS, is wispy and diffuse. This texture is similar for many locations, where layering is commonly difficult to identify. Layering in this image is cut by thin, post-layering veinlets of magnetite. Many outcrops exhibit post-layering features such as oxide veinlets, or other signs of textural modification. Near the top of this image, a thin, elongate xenolith is present. This location is >2.5 km from a contact in the east or west. Note marker for scale.

14.3). Many layers have a recrystallized or deformed appearance, and it is possible that weak deformation during emplacement or cooling modified original textures somewhat.

Rarely, blocks or fragments of igneous rock, likely autoliths from within the TBGS, have disrupted layers. Apparently, these blocks dropped from above, and dragged and distorted layers as they passed through (Figure 14.4). Another peculiarity includes one location in the central southern portion of the TBGS, where a large outcrop (TBC-31) displays weak mafic layering that ends abruptly in ragged, irregular vestiges. Layering appears to continue past the abrupt ending of the mafic component in the same attitude but with a felsic composition. There is a thin reaction rim along the contact of the layered mafic rock where it is in contact with the layered gabbro of the TBGS proper (Figure 14.5). The processes that could lead to these textures are unexplained, but it may be that this is a large block of the TBGS, or a large raft of country rock, that has dropped from elsewhere, and is now partially digested. It may also represent *in situ* layering that was altered by a metasomatic front that has changed the composition of the rocks. This outcrop was too smooth to sample. These examples and others demonstrate the variable and dynamic nature of the TBGS.

### **14.2.2 Contact relationships**

All contacts between the TBGS and host rock, except for the thrust southern margin, are with Grenville orthogneiss, paragneiss and metacarbonate/calc-silicate, although there is a minimal amount of marble and calc-silicate in the east (Owen and Erdmer, 1986). Paleozoic conglomerates of the Deer Lake Basin unconformably overlie the southern margin of the TBGS after being thrust westward overtop of the TBGS during late Devonian to early Carboniferous times (Hyde, 1982; 1988). The southern unconformable contact and the northeastern contact were not part of this study, but a transect across the central TBGS was completed, as well as several other transects across internal igneous contacts.



Figure 14.3 TBGS layering locally comprises oxide-rich cumulate textures, such in TBC-55. The dark material in the layers is poikilitic orthopyroxene, clinopyroxene, magnetite and ilmenite. The pen magnet, oriented ~ parallel to layering, is hanging by its magnetic end from this steep outcrop, indicating the abundance of magnetic minerals. The red arrow (top right) indicates the dip direction of the layers, east, towards the centre of the intrusion.



Figure 14.4 Layering in the TBGS can be quite chaotic, such as in this outcrop at TBC-24. The approximate trend of layering is defined by the dashed blue line. Layering commonly exhibits a weakly foliated texture, such as in this image. In addition, layers in this image are disrupted or cross-cut by several features. First, a black arrow (MD?) marks a fine-grained mafic selvage, which is probably a mafic dike that was injected while the magma was still hot and possibly not completely crystallized. Secondly, as outlined in a red dashed line, a coarse-grained leucocratic pod of rock appears to be dropping into the lower layers (top is towards the bottom of the image). It is also possible that this represents a diapir of felsic rock intruding into the mafic layers. It may also preserve a metasomatic front that is replacing the mafic layers. Several other coarse-grained pods are also visible in this image. The inconsistent fabrics and textures such as at this outcrop raise more questions than they answer in the TBGS.



Figure 14.5 These images, from TBC-31, are a further indication of the complex features in the TBGS. (a) melacratic rocks on the right side of this image end in a ragged contact with leucocratic igneous rocks. The melacratic rocks are fine-grained and exhibit weak layering that appears to continue into the leucocratic rocks, but the nature of layering is not consistent between the two rock types. Whether this rock is metamorphic (amphibolite xenolith?) or igneous (mafic dike) in nature is ambiguous. This outcrop is cut by a discontinuous and splaying mafic dike (MD). A yellow arrow points to the same dike, which is featured in Figure 14.9. A red arrow denotes where the dike cuts layering, and also highlights a wide leucosome surrounding a “layer” of rocks intermediate in colour between the right melacratic rocks and the leucocratic rocks on the left. (b) a zoom of the reaction rim that occurs at the contact between these contrasting lithologies. The melacratic rocks are cut by at least 3 generations of veining. Note the local pods of plagioclase phenocrysts in the leucocratic layer (P).

The eastern contact is poorly defined due to thick vegetation and till. It is characterized by the presence of country rock xenoliths more than one kilometer from the contact; even 750 meters from the contact, large xenoliths are present. In addition, east of the contact proper, pods of gabbro  $>5 \text{ m}^2$  intrude calcisilicate and marble. Although the majority of the xenoliths are relatively small ( $< 50 \text{ cm}^2$ ) and the gabbroic rocks are relatively massive, it is possible that the original intrusive contact was locally sheeted, leading to this progressive decrease of xenoliths inwards. Before cooling, the sheeted nature could have been obscured by wholesale digestion of stoped blocks, leaving only the observed remnant xenoliths. Along the western margin, the contact is less ambiguous because there is a lower frequency of xenoliths within the TBGS. In one location (TBC-01), however, approximately 300 meters from the contact, a strongly deformed, boudinaged and completely dismembered mafic dike was observed within the country rock paragneiss (Figure 14.6). This dike has extensive reaction rims, and if it is derived from the TBGS, helps to constrain timing of emplacement and deformation. If it was derived from the TBGS, it suggests that post emplacement deformation occurred at a ductile level, and at temperatures hot enough to allow subsequent alteration forming the reaction rims. If this dike is Grenville in age, however, since it is remarkably fresh, it begs the question of the age of other dikes within the TBGS and the TBGS itself.

### 14.2.3 Xenoliths

Xenoliths occur widely distributed in the southern TBGS and generally reflect composition and textures observed in surrounding country rock (*i.e.* gneiss). These xenoliths, as indicated above, are present for approximately one kilometer inside the TBGS, and were observed in various states of alteration or metamorphism. Xenoliths exhibit partial melt textures consistent with being partially consumed by the magma rather than a primary metamorphic texture (Figure 14.7a). For example, veins of magma sometimes intruded parallel to gneissic fabric of the xenoliths, and often a thin leucosome rim is preserved (Figure 14.7b). In addition, xenoliths are locally deformed because of



Figure 14.6 In TBC-01, which is located ~300 m from the TBGS-country rock contact, a mafic dike is strongly disaggregated within Grenville paragneiss. Selvages of this dike exhibit thick reaction rims (inset). Within 200m of this outcrop undeformed dikes are hosted by calc-silicates, also Grenville in age. If this dike was derived from the TBGS, it suggests that the TBGS was present during Grenville metamorphism. If it is not from the TBGS it suggests there are more generations of dikes in this area than previously indicated.



Figure 14.7 Xenoliths occur in many textures and compositions in the TBGS. (a) The xenolith in TBC-16 comprises paragneiss, with a fine dusting of pink garnets. It is being consumed by the TBGS and is surrounded by dendritic veins and fracture fillings of apparent melt material; (b) this paragneiss xenolith from TBC-11 is surrounded by a thin reaction rim and appears to be surrounded by similar veins of felsic melt material. Partial melt textures within the xenolith appear to be pre-assimilation, but may have been further melted upon incorporation into the TBCS.

weakening due to partial melting. In some locations, xenoliths comprise 15 to 25% of the rock.

Another feature noted in the TBGS is the presence of pegmatite pipes, or pegmatite zones that have a variable spatial association with xenoliths. These pipes or zones range in size from less than 10 cm up to ~50 cm in diameter and are locally associated with dendritic and irregular veins that extend for several metres into the gabbro. The pipes appear to have metasomatized the surrounding rocks, as evidenced by locally distinct textures and mineralogy. Rocks surrounding these pipes contain a relatively greater abundance of plagioclase, which is generally more euhedral to subhedral and megacrystic or porphyritic than rocks away from the influence of the pipes. In several locations, the cores of pipes located over 500 meters from the external contact contain well preserved xenoliths (Figure 14.8), sometimes over one meter in length. Neither sulfide nor oxide mineralization was found to be associated with these features, and in general, they were devoid of mafic minerals. These pipes are different from pipes observed in the TBGP, as described below.

#### **14.2.4 Mafic dikes**

At least three texturally distinct forms of dikes were observed in the southern TBGS; locally four phases of dikes may exist. Mafic dikes in the TBGS are ubiquitous, and at least one generation of mafic dike is present in many of the outcrops studied. The oldest generation of mafic dike has textures that suggest it was emplaced before the TBGS had completely crystallized. Evidence for this is the highly discontinuous, boudinaged or stretched nature of the dikes relative to the enclosing gabbro, irregular and embayed or cusped contacts, a lack of chilled margins, partial melting and metamorphic/metasomatic reaction of the margins, and general appearance of recrystallization (Figure 14.9a). These dikes cut primary textures of the TBGS, such as magmatic layering, but are cut by all other veining or alteration. The second less common phase of mafic dike has plagioclase-phyric cores, and chilled margins. These dikes do not commonly exceed 50 cm in

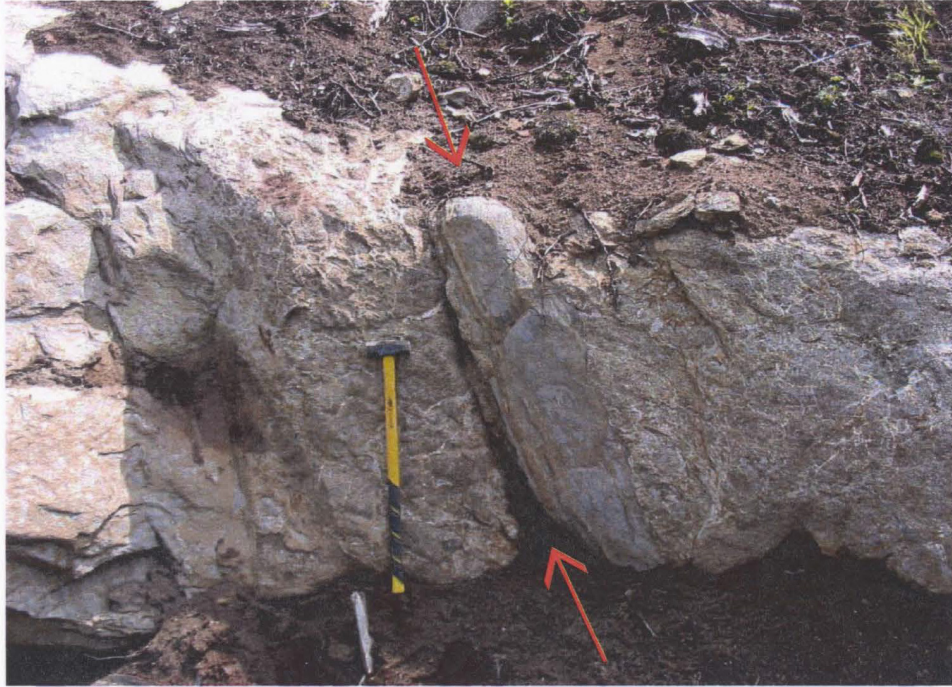


Figure 14.8 This large xenolith in TBC-21 is over 1 km from the western margin of the TBGS. Red arrows indicate the orientation of this xenolith, which is spatially associated with a zone of dendritic felsic material, which is several meters wide in this image. The morphology of this area and others suggest that xenoliths are locally transported upwards by pipe-like bodies in the TBGS. There is ample textural evidence in this image and others for large volumes of fluid interacting with the surrounding rocks.

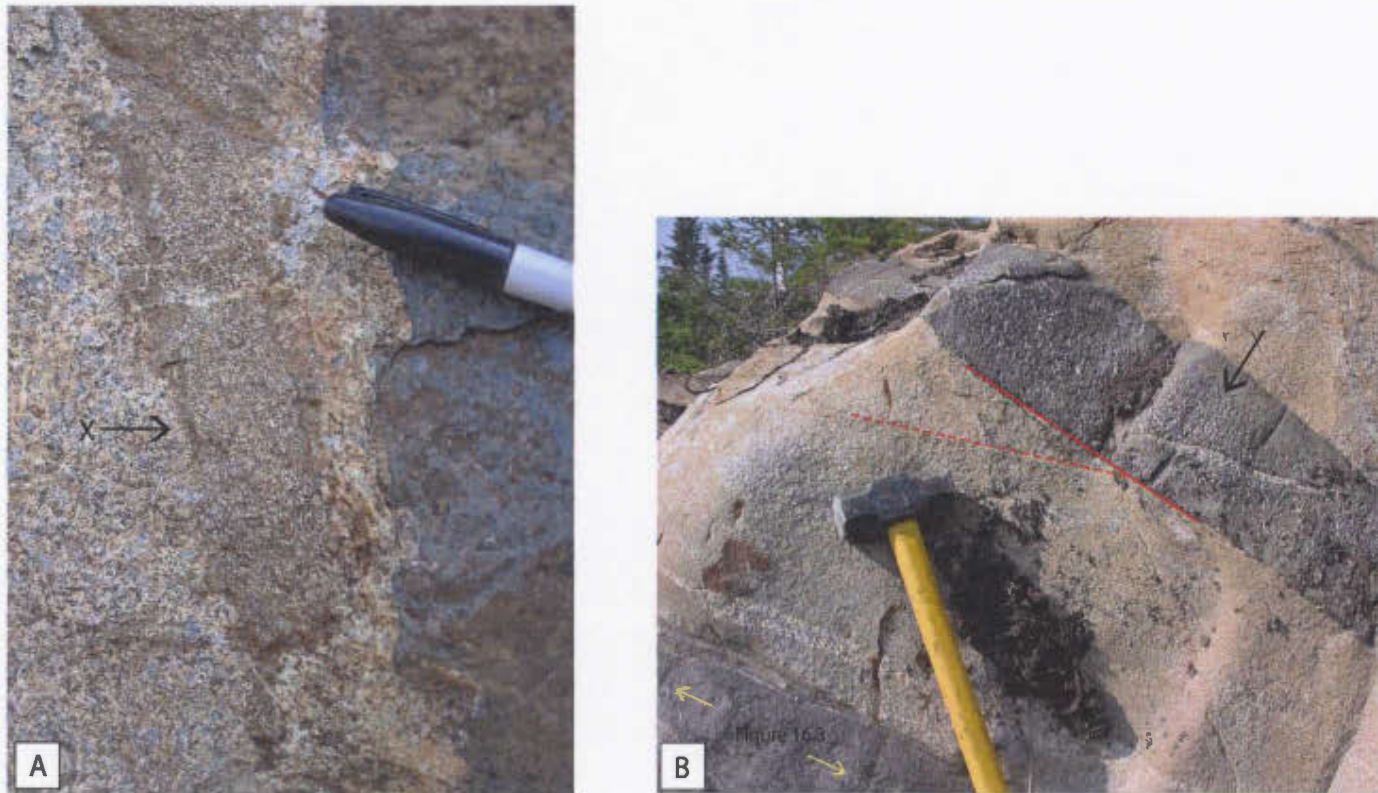


Figure 14.9 Mafic dikes in the TBGS come in all shapes and sizes. Pictured above are two examples from TBC-17 and 30 respectively. (a) A zoom of the contact of a large (~2 m wide) mafic dike near the western margin of the TBGS. The cusped texture of this contact and lack of strongly chilled margin suggests it was emplaced while the TBGS was also relatively hot. Arrow (X) denotes a small xenolith with reaction rim; (b) this narrow dike, also pictured in Figure 14.5, has chill margins and a plagioclase-rich core (black arrow). This dike clearly truncates local layering (red lines). Dikes with this morphology were observed in several other locations in the main mass of the TBGS. The yellow arrows indicate the fabric in the melacratic rocks in the lower left corner - it is these rocks that were pictured in Figure 14.5. The fabric in those rocks is conformable with the leucocratic rocks that host the dike. Note that the dike in this image is the same as the splayed one in Figure 14.5, suggesting that these dikes may change orientation or shape rapidly.

thickness (Figure 14.9b). Less commonly, these dikes were observed to be assimilated or strongly deformed. These dikes locally cut the first generation of dikes. The final mafic dike morphology in the southern TBGS is the least common, and was observed at only three outcrops, but is distinct enough to separate from the other types. At approximately two meters wide, these dikes are considerably wider than the other two generations. They lack chilled margins, but locally have irregular or cusped margins, suggesting very high temperature emplacement. These dikes have a massive texture, and locally contain finely disseminated sulfides. There are no cross-cutting relationships with other dikes, but texturally, they appear to have undergone the least amount of modification, suggesting they are the youngest.

In addition to mafic dikes, several locations in the TBGS contain quartz-feldspar porphyry dikes (QFP dikes). The contacts are rarely visible, but in one outcrop, a true thickness of approximately two meters was determined. The contacts, where observed, were straight, and appeared unmodified, although the contacts were observed in only one location, and this may not be representative of each QFP dike occurrence. In addition to QFP dikes, several small outcrops of a more potassic, biotite-bearing igneous rock that contained only quartz phenocrysts were noted in several widely spaced locations. Here it was not possible to determine the geometry of the bodies, hence no genetic classification can be assigned.

A final aspect of the southern Taylor Brook Gabbro Suite is the presence of magma mixing textures, which were noted in several widely spaced outcrops in the southern TBGS. Despite their occurrence over a wide area, the textures are quite similar for all locations. These outcrops exhibit the mixing or immiscibility between a mafic magma and felsic magma, possibly leucomonzonite, of the TBGS (Figure 14.10). It is not possible, from the limited exposure, to determine which phase intruded into the other, but injection of mafic magma into the felsic phase is more likely, based on field relationships. When observed in the field, only one contact was ever noted, thus a source for the mafic



Figure 14.10 Magma mingling textures in the TBGS are widespread. These images, from TBC-26 and 36 respectively are ~2 km apart, but are remarkably similar. In both images, mafic magma appears to be immiscible in a coarse-grained leucocratic magma. As discussed in the text, these mixing textures do not appear to be the marginal expression of large dikes, but rather they represent mafic bodies of unknown shape or size.

magma cannot be determined (*i.e.*, if these were dike-TBGS contacts, only one side of the dike was ever observed). It is possible that these textures are the edge of mafic dikes, but in some locations, there was a large amount of mafic magma, and a dike geometry is not supported. Furthermore, in one location, the mixing is associated with a significant amount of thin, wispy or dendritic pegmatite textures. It is possible this texture is related to local pulses of fresh magma, although the widespread nature of these textures suggests a more localized, yet consistent process.

#### **14.2.5 Sulfide mineralization**

Along the western margin, within 500 meters of the contact with country rocks, a sulfide-bearing fracture system hosted by melagabbro to pyroxenite was discovered. This fracture system hosts 2-3% sulfide including pyrite, pyrrhotite, chalcopyrite and magnetite. Based on the presence of fracturing, brittle jointing and brecciation this system appears to be relatively late.

### **14.3 Taylor Brook Gabbro Pegmatite**

The Taylor Brook Gabbro Pegmatite (TBGP) is compositionally, texturally, and morphologically different from the rest of the TBGS. Field observations indicate that the TBGP has a more mafic composition overall, and is characterized by more abundant pyroxene compared to TBGS. More significantly, however, are the textural differences between the pegmatitic zone (TBGP) in the north and the rest of the TBGS. The northern portion of the TBGS was classified as a pegmatitic gabbro and mapped as a separate map unit by Owen (1986). Mapping for this project confirmed that this unit should remain a separate map unit.

The TBGP is generally coarse (~10- to 25 mm) to medium-grained (~2-10 mm), and locally contains megacrystic zones (>25 mm). On an outcrop scale, grains are

equigranular, or bimodally equigranular (*i.e.* the pyroxenes are coarse-grained, whereas the plagioclase is medium-grained). In most instances, grains are subhedral to anhedral and cumulate textures are rare. Small (<15 cm) patches of pegmatitic material are common, as are larger, sometimes circular shaped pods, which may be pegmatite pipes (Figure 14.11). Where these pods occur, mafic minerals are common either as crystals or as fragments, unlike the main mass of the TBGS, where pegmatite pipes do not contain mafic minerals.

Although layering is rare in the TBGP, weak layering, defined by grain size variation or modal layering is seen locally. A variation of the layering observed in several outcrops consists of patchy to subplanar zones of pegmatoidal textures bounded by normal textured gabbro, or coarse-grained gabbro. Locally, cumulate textures are developed, but these are not widespread, and have locally been modified by alteration or metasomatism, resulting in the destruction of primary textures and mineralogy.

In the TBGP, mafic dikes are common, but do not exhibit the textural varieties observed in the TBGS. It is possible that this is a reflection of the lack of good quality outcrop in the TBGP. Generally, the dikes do not exceed 50 cm in width, dip vertically to subvertically, and have a diabasic texture in most outcrops. Compared to the TBGS, these dikes are not strongly disrupted or deformed, do not contain plagioclase-phyric cores, and are not strongly altered. It was not possible to determine if these dikes have preserved chilled margins due to thick lichen cover. Some of these dikes contain rare blebs of pyrite with magmatic textures. Where outcrop was better, it was possible to observe parallel dikes over spacings of 50 to 150 meters that all had roughly the same strike and dip, implying these dikes were emplaced under similar conditions and/or timing.

Xenoliths in the TBGP are much less common than in the TBGS. This may be due to the greater distance of the TBGP from the country rocks, as this is an internal unit. In the TBGP, xenoliths are commonly fine-grained gabbro, which may be derived from the



Figure 14.11 Pegmatite pipes in the TBGP are different from those in the main mass because they do not contain xenolith material. Instead, as noted in TBC-83, pegmatites contain coarse-grained pyroxene crystals that have been subsequently retrogressed to greenschist minerals. In A there are fragmental felsic pieces within the mafic phase. Although less common than in the TBGS, pegmatite pipes were observed in several locations in the TBGP.

TBGS, if there is a temporal difference between the main mass of the TBGS and the TBGP, or they could have been more locally derived. In the absence of geochemical data of xenoliths, it is not possible to choose between these alternatives. In one location, xenoliths were observed as a “train”, of large rafts along strike for approximately 1 km. These xenoliths are quite unusual in terms of size (the largest was  $\sim 6 \text{ m}^2$ ), textures, composition, and location within the TBGS. The xenoliths display well-defined layering, which although diffuse or patchy on a small scale is defined mainly by compositional variation (Figure 14.12a). The xenoliths also contain porphyroblast kinematic indicators, implying that the xenoliths had undergone some degree of deformation prior to incorporation. Most striking are the layers of magnetite, which occur up to 25 cm thick in several of the xenoliths (Figure 14.12b). The mineral assemblage does not appear to be primary, and has a fibrous to massive texture when examined with a hand lens. Petrography is described in a later chapter. In some locations, the xenoliths resemble mafic gneiss, whereas in others they appear to be magmatic in origin. The rafts of xenoliths occur less than one kilometer from the contact with country rock, which is mafic gneiss, but textures and mineral assemblages are quite different from those in the country rocks. Furthermore, these rafts occur parallel to an internal igneous contact, which may define the boundary between the TBGS and TBGP. More work, particularly geochemical and petrographical, is required to understand these rocks. There are several speculative explanations for the origin of these unusual xenoliths. It is possible that these represent country rock from deeper levels in the crust, brought to the surface during emplacement of the pluton. Another explanation is that these rocks represent a deformed basal or marginal facies of the TBGS that has been entrained in the melt during emplacement of the TBGP. Given that some of the xenoliths resemble igneous rocks while others have gneissic textures, a combination of both hypotheses may prove most accurate.



Figure 14.12 Along the boundary between the TBGP and TBGS, from TBC-119 (pictured) to TBC-122 there is a train of large inclusions of ambiguous affinity. These xenoliths contain abundant magnetite layers that are parallel to layering within the inclusions, and locally exhibit kinematic indicators that suggests that they were deformed prior to emplacement in their current location. At the edge of the inclusions, the layers of silicates and oxides discontinuously ductily deformed (denoted by red lines in inset, A and left side of B).

#### **14.4 Late intrusive phases**

The final point of interest in the TBGS is the occurrence of a relatively large alkali feldspar granite intrusion near the eastern TBGS-TBGP contact. The intrusion occurs over a strike length of approximately 2.5 kilometers, and has a sill-like morphology. Mineralogy and textures are consistent throughout the unit. Where the sill-TBGS contact was observed, the sill does not appear to have caused any contact metamorphism of the TBGS, suggesting it may have been emplaced while ambient temperatures were still hot. In one location, a mafic dike constrains the relative timing of emplacement of the alkali feldspar granite. The dike has a thickness of approximately 30 cm, and has sharp contacts with the TBGS, but where it cuts the sill, it is partially digested, dismembered and altered. The fragments of mafic dike in the sill are restricted to a plane that is approximately parallel to the strike of the dike in the gabbro, implying that that dike intruded the sill, but the sill was not completely crystallized, and thus partially reacted with the dike. This unit was not recognized by Owen (1986), likely because it is exposed along a relatively recently developed logging road. This intrusion and several other felsic intrusions within the TBGS, and evidence for magma mixing textures imply bimodal magmatism during late stage crystallization, and implies that at least some of the mafic dikes cutting the TBGS are relatively young.

#### **14.5 Summary**

Overall, the Taylor Brook Gabbro Suite is heterogeneous on all scales, from outcrop-scale textures, to the scale of the separate pegmatitic gabbro unit in the north and the alkali sill south of the TBGP. The heterogeneities of the TBGS and TBGP include texture, composition, alteration styles, xenolith composition and morphology, and presence of late felsic intrusions. Layering in the TBGS is has a roughly concentric geometry, and dips shallowly to moderately into the core of the pluton, although variations in expected geometry are common. Although previous U-Pb zircon dating indicates an age of  $\sim 430.5 \pm 2.5$  Ma (Heaman *et al.*, 2002), the amount of deformation, and other types of textural modification, variable alteration zonation, different

generations of dikes, suggest that material previously dated might not have been representative of the entire TBGS. Due to time constraints and logistics of this research, geochronology cannot be undertaken, and further analysis is required to fully constrain the temporal evolution of the TBGS.

Very low concentrations of sulfide mineralization in outcrop or float samples reduces the prospectivity of this intrusion. Although several large regions of this intrusion remain unmapped at a moderate to high resolution, many of these are in the middle of the intrusion, where sulfide mineralization is not expected to develop. Before complete abandonment of exploration in this intrusion, further mapping of the margins could be undertaken.

## Chapter 15: Taylor Brook Gabbro Suite Petrography

### 15.1 Introduction

The Taylor Brook Gabbro Suite (TBGS) is a large, heterogeneous gabbroic intrusion that comprises mainly amphibole gabbro and pyroxene amphibole gabbro. The northwest corner of the intrusion is markedly different in composition and texture and comprises a late pulse termed the Taylor Brook Gabbro Pegmatite (TBGP).

Rock names are based on visual estimations of modal abundances and then the three most abundant silicate phases in each thin section were normalized to 100%, and plotted on ternary diagrams developed by Streckeisen (1976). Where there are contradictions between calculated and observed rock nomenclature, petrographical observations are favoured because of the assumptions associated with normalized plotting. However, in altered samples, more weight is placed on calculated rock names, and the names applied do not necessarily reflect a protolith name, but the actual mineralogy. For example, an altered gabbroic rock is most often classified as a pyroxene amphibole gabbro, which reflects the presence of secondary amphibole, as well as primary pyroxene. Normalized data and lithologies are listed for all samples in Appendix 2.

In total, 50 polished thin sections were examined from the TBGS area: one marble country rock sample from the western contact, 19 from the TBGS, 22 from the TBGP, seven mafic dikes and one late felsic intrusion within the northern TBGS.

The heterogeneity of the Taylor Brook Gabbro prevents intrusion-scale grouping of textures, thus, each area of the intrusion is described separately, followed by a description of the mafic dikes, which are more similar in texture and mineralogy.

## 15.2 Taylor Brook Gabbro Suite mineralogy and petrography

The main mass of the Taylor Brook gabbro comprises predominantly leuco pyroxene amphibole gabbro and pyroxene amphibole gabbro and lesser leuco-amphibole gabbro and amphibole gabbro (Figure 15.1). Minor lithologies include leucogabbronorite and pyroxenite. Although there is a relative variation in modal mineralogy, the textures of these lithologies are more similar than they are different, thus all main mass TBGS mineral textures are described below according to mineralogy.

Leuco pyroxene amphibole gabbro and pyroxene amphibole gabbro are most abundant lithology in the main mass, comprising normalized plagioclase contents of 65.2 % (SD= 9.3), 14.6% clinopyroxene (SD= 9.5), 7.4% orthopyroxene (SD= 7.6) and 12.8% amphibole (SD= 8.9). Minor amounts of quartz, olivine, Fe-Ti oxides and alteration minerals such as biotite and chlorite are present in some samples.

Leuco-amphibole gabbro and amphibole gabbro comprise most of the remaining TBGS samples. These lithologies comprise an average of 65.8% plagioclase (SD= 13.2), 1.9% clinopyroxene (SD= 1.9), zero orthopyroxene, 32.4% amphibole (SD= 13.3). Minor amounts of quartz, Fe-Ti oxides and secondary alteration products such as biotite and chlorite are present in variable proportions.

Mafic dikes consistently exhibit an amphibole gabbro mineralogy comprising an average of 46.4% plagioclase (SD= 10.6), 52% amphibole (SD= 8.7) and lesser amounts of pyroxene, biotite and Fe-Ti oxides. Most mafic dikes also contain several percent of moderately corroded or embayed plagioclase megacrysts that were excluded from these totals prior to normalization calculations.

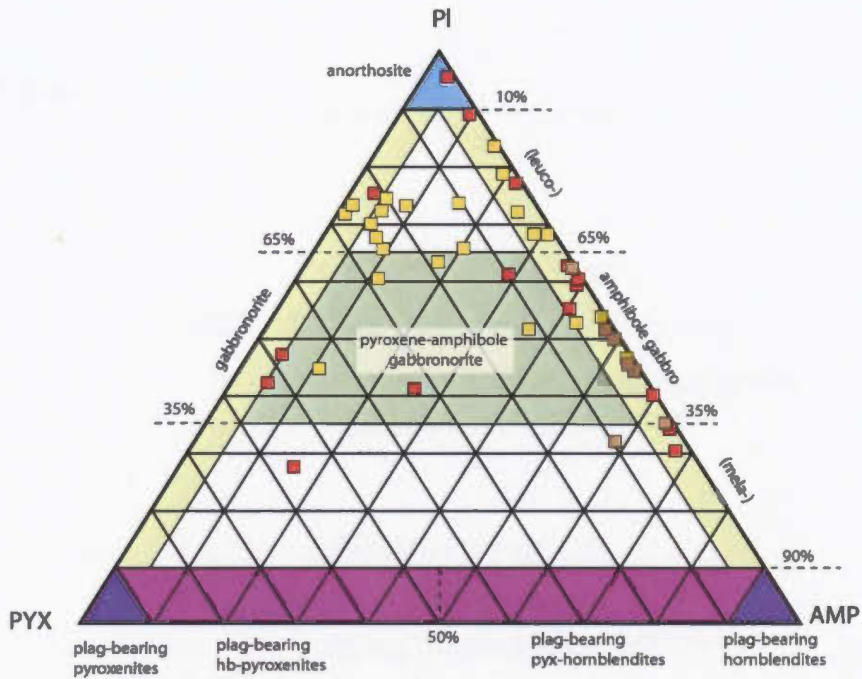


Figure 15.1a TBGS normalized mineralogy. Red squares represent TBGP samples, yellow squares are TBGS and brown are mafic dikes. Amphibole bearing samples are generally indicative of a greater degree of alteration whereas pyroxene-bearing samples are relatively fresher. The mineralogy of mafic dikes is similar regardless of location.

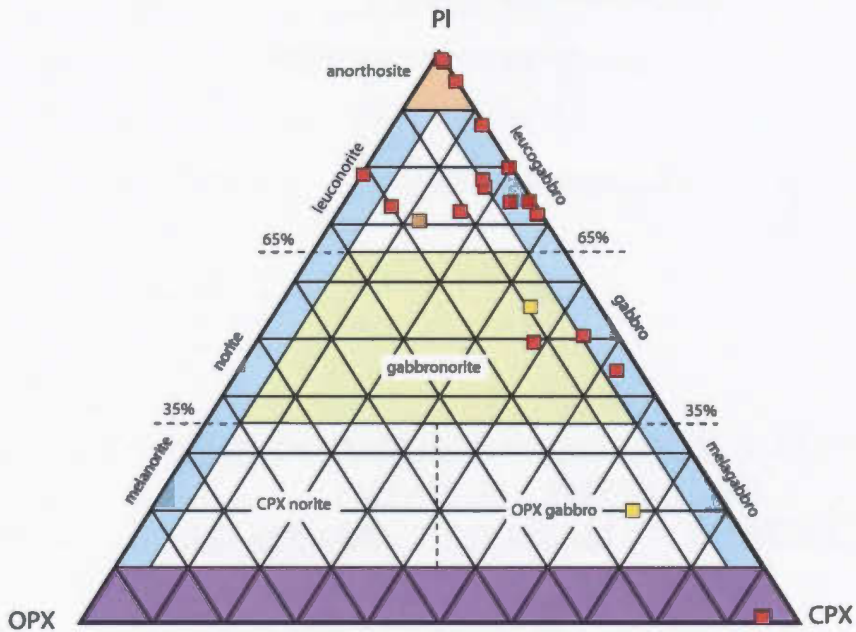


Figure 15.1b TBGS normalized mineralogy for samples with minimal amphibole. This diagram indicates that most samples exhibit a gabbroic rather than noritic mineralogy. Sample colouring is as above.

### **15.2.1 Taylor Brook Gabbro Suite plagioclase**

Plagioclase in the TBGS exhibits a wide range of textures. Overall, it occurs as medium- to coarse-grained, irregular crystals, although locally elongate or stubby laths occur. The most common plagioclase texture is irregular coarse-grained crystals with strong to moderate undulose extinction, which is locally concentrically zoned. This plagioclase is normally spatially associated with finer-grained plagioclase (Figure 15.2a), in which undulose extinction is absent to weak, and is assumed to have formed by recrystallization of the larger crystals. In many examples of concentrically zoned extinction, a core zone is defined by irregular, diffuse boundaries with different extinction properties than rims, suggesting that remnant, corroded cores are preserved and that some initial modification of plagioclase during crystallization occurred (Figure 15.2b). The other common plagioclase texture is large, irregular- to lath-like crystals that are spatially associated with poikilitic clinopyroxene. Samples that contain these textures, in association with other phases such as Fe-Ti oxides are the only samples to demonstrate definitive cumulate textures. There does not appear to be any consistency in the spatial distribution of cumulate textures in samples, therefore it is difficult to correlate the spatial distribution between different samples with similar cumulate textures.

The majority of samples do not exhibit preferred orientation of plagioclase or any other phase, and deformation and recrystallization textures are restricted to undulose extinction, deformation lamellae, warped twinning, subgrain rotation and grain size reduction. Sericite alteration is ubiquitous, and is often concentrated in the cores of medium- to coarse-grained crystals rather than finer, recrystallized grains.

### **15.2.2 Taylor Brook Gabbro Suite pyroxene**

Pyroxene in the TBGS occurs in a continuum of textures from granular to poikilitic. Generally, clinopyroxene and orthopyroxene exhibit similar textures, thus they are described together. Pyroxene occurs as medium- to coarse-grained, anhedral to subhedral

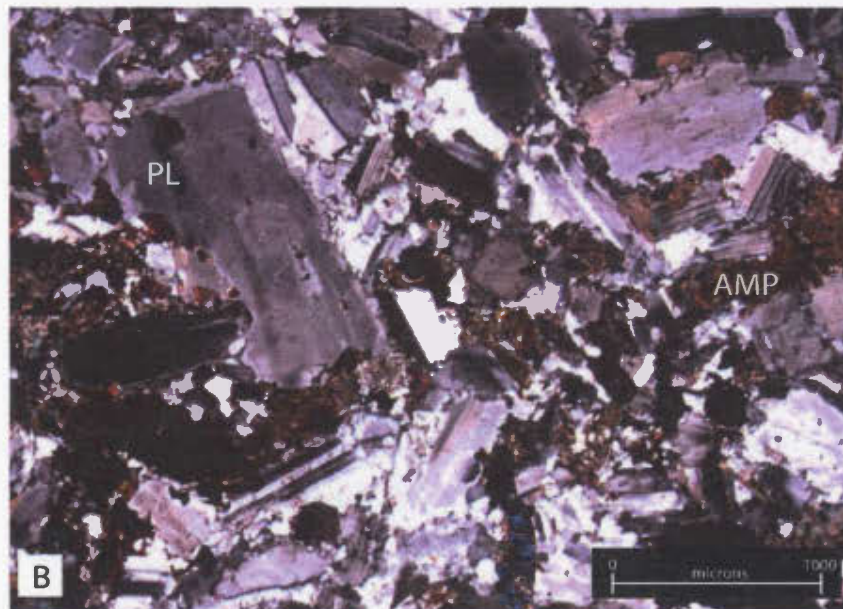
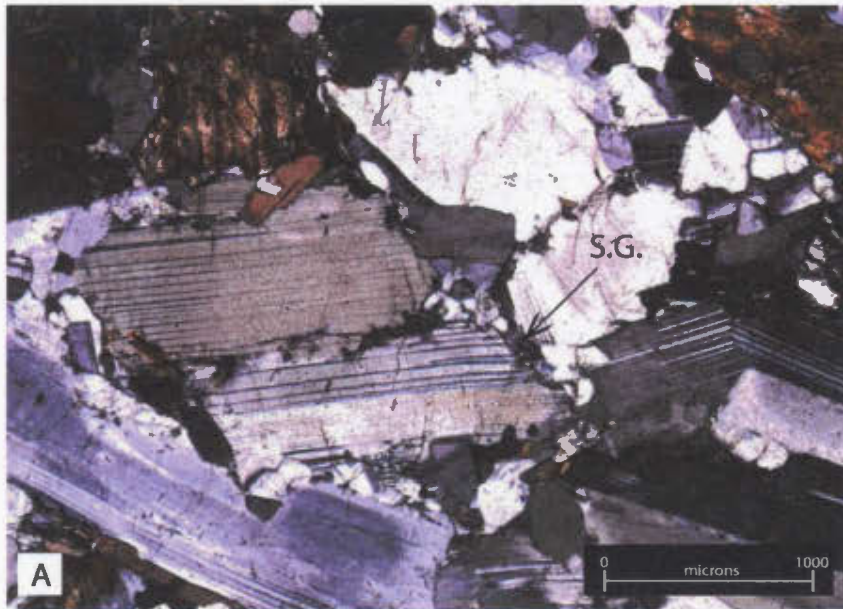


Figure 15.2 Transmitted, cross-polarized light photomicrograph from the TBGS. A) Coarse-grained plagioclase is commonly surrounded by rims of recrystallized subgrains (SG). The location of the subgrains in this image suggest that the four crystals in the centre of the image were probably one large crystal that was progressively recrystallized along the grain boundaries now present; B) Many phenocrysts in the TBGS, such as the large lath in the top left corner, exhibit concentric zonation and undulose extinction. Some phenocrysts exhibit cores with embayed grain boundaries, indicating that some modification of crystal morphology occurred during the crystallization of the magma. Note the scale bar in the lower right corner of both figures.

crystals that locally exhibit twinning. The most common texture of pyroxene is medium- to fine-grained, interstitial to granular crystals that locally define a weak fabric, possibly a modified igneous lamination (Figure 15.3a). Granular pyroxene is locally associated with plagioclase with a similar morphology. In TBC-91, pyroxene, amphibole (after pyroxene?) and plagioclase all approach a granoblastic texture (Figure 15.3b). This sample displays compositional layering, and it is thought that it represents a marginal facies of the TBGS that has been recrystallized. In pyroxene-rich samples, the most common pyroxene texture is coarse-grained granular aggregates with local interstitial plagioclase.

The second common pyroxene texture is poikilitic and subpoikilitic crystals or aggregates. These crystals are generally more coarse-grained than the above textures and commonly occur in more coarse-grained samples, often spatially associated with plagioclase (Figure 15.4). The pyroxene oikocrysts may contain inclusions of plagioclase or Fe-Ti oxides. Alteration of this texture by amphibole and biotite is ubiquitous. Amphibole, usually a combination of hornblende and actinolite, replace pyroxene as rims of variable thickness, along cleavage planes, fractures and as wholesale replacement. Pyroxene is also replaced, less commonly, by coarse-grained aggregates or small sheaves of biotite.

### **15.2.3 Taylor Brook Gabbro Suite amphibole**

Amphibole is abundant most TBGS samples, occurring as irregular, fine- to medium-grained fibrous to granular crystals. Amphibole is nearly exclusively a secondary phase that forms at the expense of pyroxene. The two main morphologies of amphibole are first as a partial to complete replacement of granular pyroxene described above (Figure 15.3a), and secondly as rims or hornblende and actinolite that progressively replace clinopyroxene and orthopyroxene (Figure 15.3b). In the most strongly altered samples, pyroxene is nearly completely replaced. Amphibole is sometimes spatially associated with Fe-Ti oxides and biotite. Where amphibole is spatially associated with Fe-Ti oxides

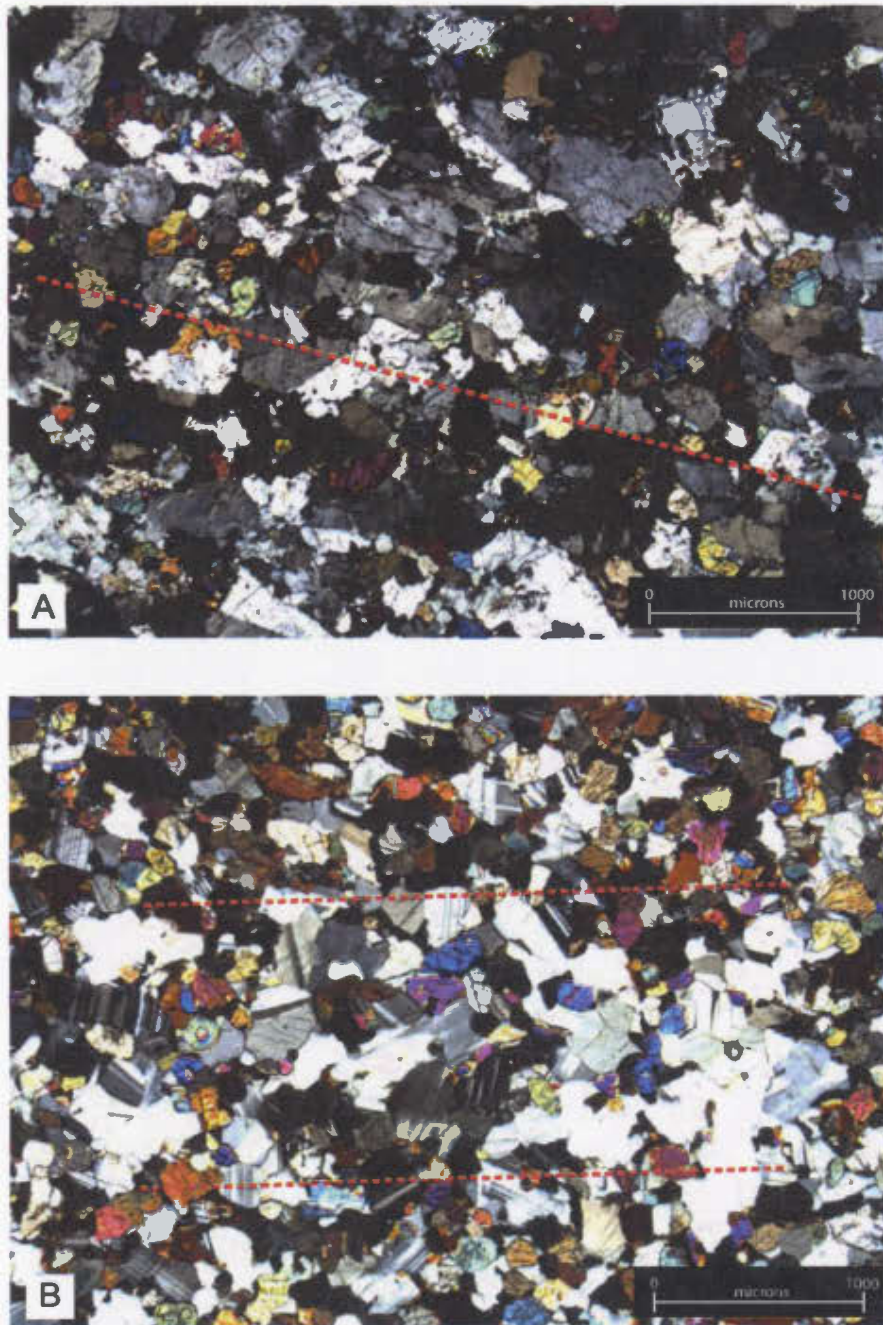


Figure 15.3 Transmitted, cross-polarized light photomicrograph from the TBGS. A) Fine- to medium-grained, granular or interstitial anhedral pyroxene or amphibole after pyroxene from TBC-06 locally define a weak fabric, noted in this image by a dashed red line; B) In TBC-91 a metamorphic fabric that is defined by compositional variation and grain size is present. This sample, from the margin of the intrusion, exhibits the only true metamorphic layering in the sample suite. The dashed lines in this image approximately bound a coarser-grained, plag-rich layer (centre) that is not as apparent in the image. Note the scale bar in the bottom right corners.

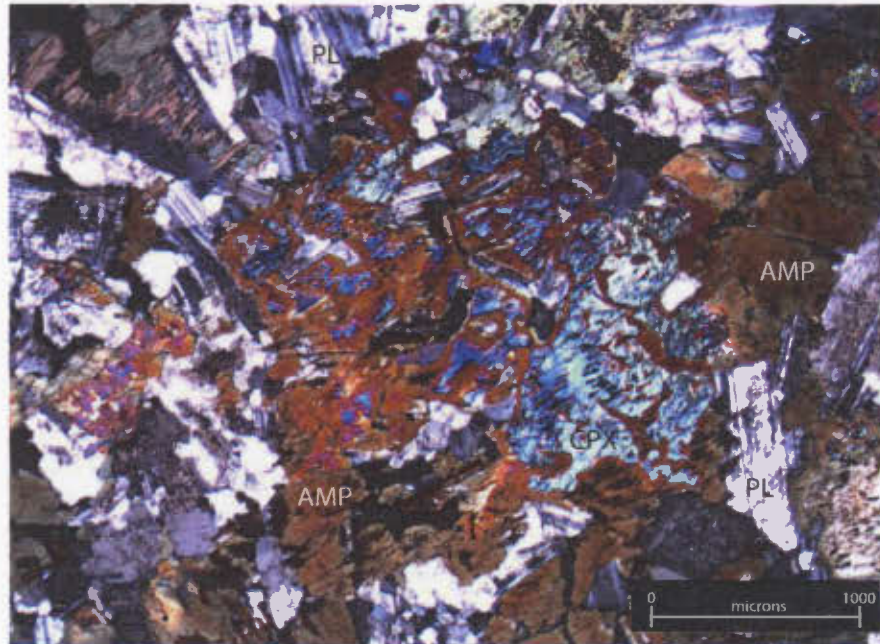


Figure 15.4 Transmitted, cross-polarized light photomicrograph from the TGBS. In this image, from TBC-34, poikilitic clinopyroxene (CPX) is partially pseudomorphed by amphibole (AMP). Amphibole replacement occurs as rims of hornblende and bladed actinolite, the latter, which locally appears to consume the hornblende rims . Originally, this oikocryst contained inclusions of plagioclase and Fe-Ti oxides, but replacement has partially or totally destroyed them. In the top right corner, green amphibole is partially replaced by biotite (pink). Note the scale bar in the bottom right corner.

(Figure 15.5), it commonly occurs as a thin, smooth rim surrounding the oxides and locally accumulates to become interstitial to surrounding plagioclase or pyroxene. It is ambiguous whether or not this texture is a metamorphic product or a late magmatic product; amphibole does not exhibit optical continuity, which might be expected if it was a primary growth texture. The secondary nature of amphibole suggests that its abundance is controlled primarily by the protolith mineralogy, pyroxene in particular.

#### **15.2.4 Taylor Brook Gabbro Suite accessory phases**

Accessory phases in the TBGS include olivine, quartz, biotite, muscovite, chlorite, epidote and sericite. Olivine is rare in TBGS samples, occurring as fine- to medium-grained, altered, subrounded crystals, often spatially associated with clinopyroxene and plagioclase. Quartz occurs in some samples as late, interstitial accumulations, generally forming an insignificant proportion of the sample. Locally, it is intergrown with fibrous amphibole replacing pyroxene. Biotite is relatively common in samples that contain appreciable quantities of amphibole and in some pyroxene-bearing samples. Locally, biotite exhibits primary textures, such as occupying interstitial space adjacent to pyroxene or plagioclase. However, biotite is nearly always a secondary replacement phase, commonly replacing pyroxene directly, along cleavage or fracture planes, but more commonly, it replaces amphibole, which usually has itself replaced pyroxene (Figure 15.6). Thus, biotite represents a progression in alteration of TBGS samples. It is common for Fe-Ti oxides to be surrounded by clusters of fresh looking brown-green biotite, but it is unknown what reactions contribute to the juxtaposition of these two phases. Biotite is locally intergrown with chlorite and muscovite, although both also occur independent of biotite. Muscovite occurs locally in association with plagioclase and relatively unaltered pyroxene and sometimes epidote. Sericite is ubiquitous in TBGS samples occurring as the primary alteration phase replacing plagioclase. Sericite often occurs in the core of coarse-grained plagioclase preferential to the rims, as fracture fillings and wholesale replacement.

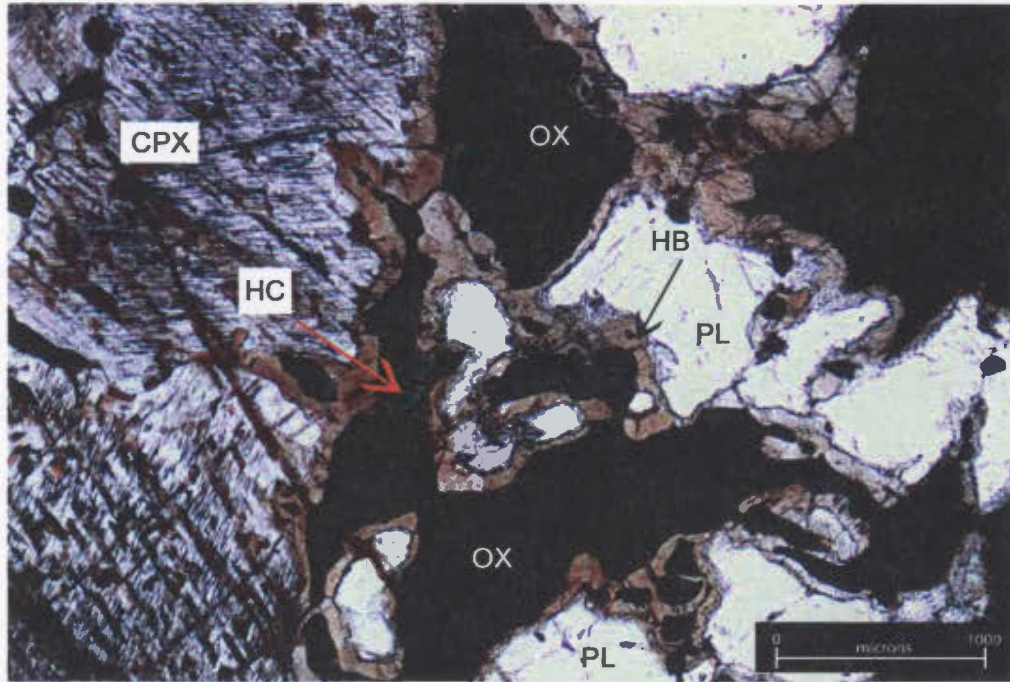


Figure 15.5 Transmitted, normal light photomicrograph from the TBGS. Fe-Ti oxides (magnetite and ilmenite) (OX) in TBC-107 are rimmed by brown hornblende (HB) and minor hercynite (HC). Although hornblende occurs as a smooth rim, it is not optically continuous, and locally appears to be consuming clinopyroxene (CPX) and the oxides. It is ambiguous whether this texture is primary magmatic, metamorphic or a combination of the two processes. Amphibole is also present along cleavage planes and fractures in CPX, suggesting at least some of it exists as a secondary phase. The white phase is plagioclase (PL) and green is hercynite (HC). Note the scale bar in bottom right.

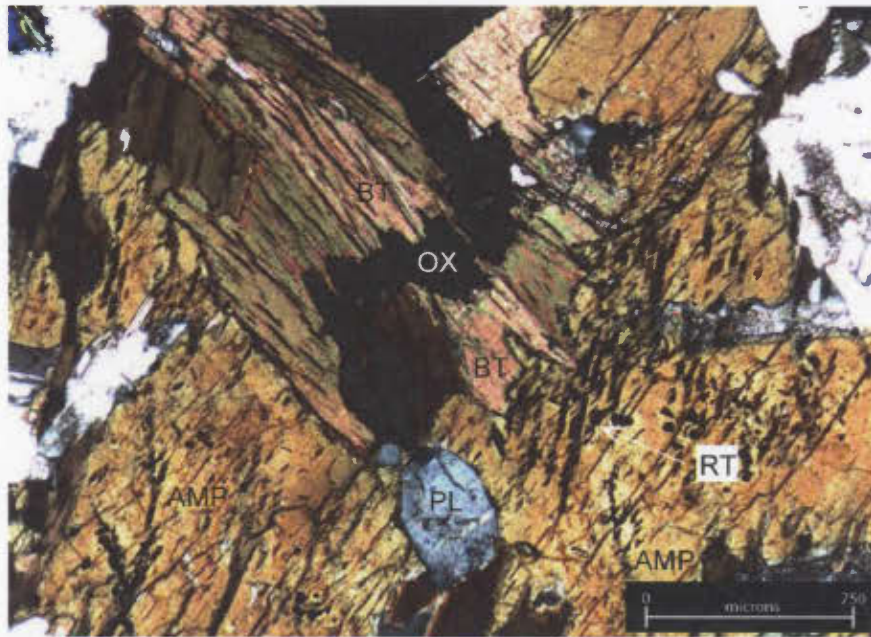


Figure 15.6 Transmitted, normal light photomicrograph from the TBGS. Biotite commonly replaces secondary amphibole in the TBGS and TBGP. In this image, from TBC-34, coarse-grained biotite (BT) consumes amphibole, which is a pseudomorph after poikilitic clinopyroxene. Inclusions of plagioclase and some grain boundaries at the edges of this image are preserved from the poikilitic texture. Biotite replacement does not appear to consume the Fe-Ti oxides (OX) or the fine inclusions of rutile (RT), which are preserved from CPX. Note the scale bar in the lower right corner.

In several samples, inclusions of country rock are present, comprising mainly quartz and biotite, but also magnetite and clinopyroxene. Quartz in particular occurs as fine-grained, granoblastic clusters with interstitial magnetite.

Sulfides are rare in TBGS samples, usually occurring as fine- to medium-grained interstitial blebs comprising primarily pyrite and lesser amounts of chalcopyrite and pyrrhotite, although in the TBGP pyrrhotite is more abundant than pyrite. Sulfides are commonly altered, which is normally as hematite rims or a generally dusty, oxidized appearance; pyrrhotite is the most prone to alteration, while chalcopyrite remains the freshest.

### **15.3 Taylor Brook Gabbro Pegmatite mineralogy and petrography**

The Taylor Brook gabbro pegmatite, located in the northern portion of the TBGS comprises predominantly amphibole gabbro, including samples with both leuco- and melagabbro mineralogy. The TBGP also contains lesser quantities of anorthosite, gabbronorite and pyroxene amphibole gabbro (Figure 15.1). The TBGP is divisible from the TBGS by bulk composition, mineralogy and textures. Overall, the TBGP exhibits a greater degree of alteration, which is reflected by the relatively high amount of amphibole observed in samples.

Normalized calculations of amphibole gabbro mineralogy, including leuco-amphibole gabbro and mela-amphibole gabbro, indicate that it comprises 52.9% plagioclase (SD= 16.3), 1.1% combined clinopyroxene and orthopyroxene (SD= 1.9) and 46.0% amphibole (SD=15.9). Accessory phases include olivine, Fe-Ti oxides, hercynite, quartz, and alteration phases such as epidote, sericite, biotite and chlorite. There are not enough samples of other lithologies to present meaningful mineralogical calculations.

### **15.3.1 Taylor Brook Gabbro Pegmatite plagioclase**

Plagioclase in the northern pegmatitic unit is somewhat texturally distinct from most main mass samples. Plagioclase is medium- to coarse-grained and irregular or anhedral; locally, plagioclase forms elongate laths, usually spatially associated with poikilitic clinopyroxene. On average, plagioclase in the TBGP is more coarse-grained than TBGS plagioclase. It is common for plagioclase to exhibit core and mantle textures. Locally, it appears that mantles of finer-grained plagioclase have developed granoblastic textures, although granoblastic textures also occur independently of core and mantle textures (e.g. TBC-91). The main difference between plagioclase in the TBGP and that of the main mass is the mineralogical association: in the majority of samples from the TBGP, plagioclase is interstitial to mafic phases such as clinopyroxene or mafic alteration phases, whereas in the main mass, mafic phases are interstitial to plagioclase.

### **15.3.2 Taylor Brook Gabbro Pegmatite amphibole**

Amphibole is the second most abundant phase in the TBGP and its textures suggest that it forms as a secondary alteration phase after pyroxene. Amphibole occurs in several species, most commonly actinolite and hornblende. It ranges from fine-grained uralite in many samples to coarse-grained sheaves of actinolite or variable thickness replacement rims of hornblende. Actinolite in particular is often intergrown with muscovite and chlorite, as elongated fibrous replacements of pyroxene. Although not of the amphibole group chlorite and epidote are described here because of their intimate association with amphibole in these samples (Figure 15.7). The reactions that control amphibole replacement of pyroxene appear to consume plagioclase where it is in contact with pyroxene such that actinolite blades penetrate into plagioclase crystals. Hornblende occurs as rims around clinopyroxene and orthopyroxene. Locally, this texture appears to be primary, possibly having formed during initial cooling of the magma. In these examples, the grain boundaries with clinopyroxene are smooth, and hornblende fills the interstices between plagioclase smoothly, similarly to poikilitic pyroxene. However, in

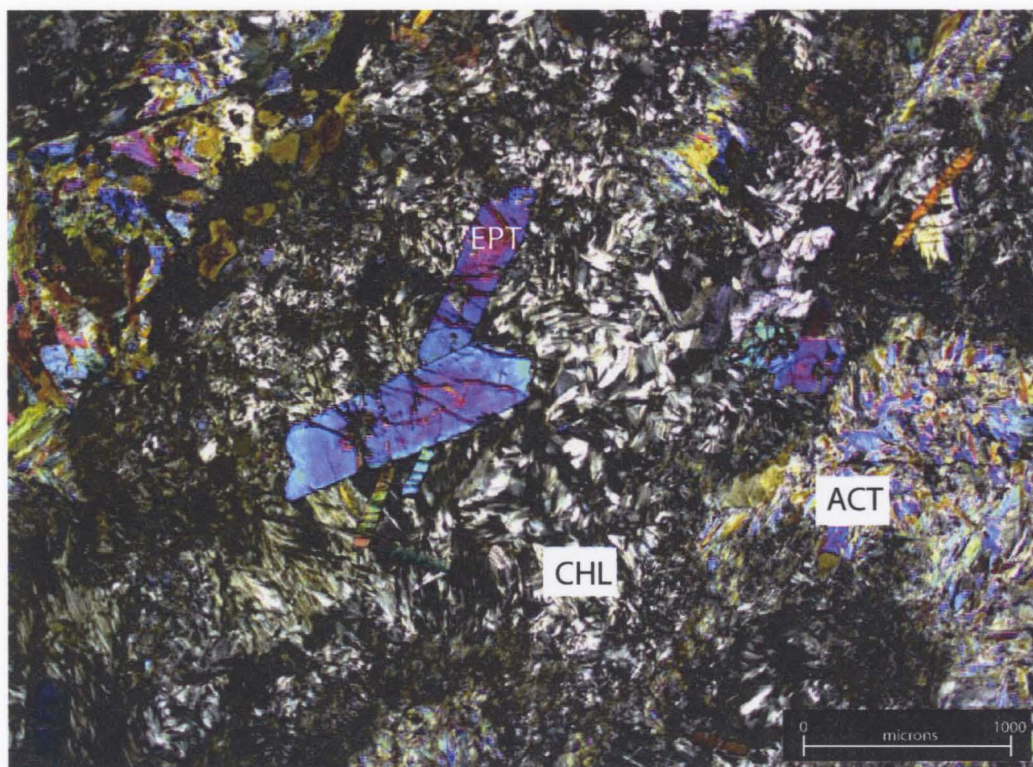


Figure 15.7 Transmitted, cross-polarized light photomicrograph from the TBGS. Prismatic epidote (EPT) overgrows sheaves of chlorite (CHL) and actinolite (ACT), which have replaced clinopyroxene in TBC-88.2. Epidote exhibits weak zoning throughout the TBGS but the specific cause of zoning is unknown in the absence of microprobe analysis. Note the scale bar in lower right corner.

most cases, these rims are clearly destructive, exhibiting embayed contact into pyroxene and exploiting fractures and cleavage planes to grow into the cores of host pyroxene crystals. Hornblende rims are commonly overgrown by blades of actinolite, chlorite and epidote and epidote may occur as coarse-grained prismatic crystals overgrowing actinolite and chlorite, suggesting it forms late in the paragenesis (Figure 15.6).

### **15.3.3 Taylor Brook Gabbro Pegmatite pyroxene**

Although uncommon in many TBGP samples, pyroxene is locally abundant, particularly in less altered samples, and textures in many samples suggest that prior to alteration, it was far more common. Pyroxene occurs in two main textures. First, it occurs as fine- to coarse-grained granular crystals or interstitial to plagioclase. This texture is commonly pseudomorphed by hornblende or actinolite, although in several pyroxene amphibole gabbros it remains relatively unaltered. Secondly, pyroxene occurs as coarse-grained poikilitic crystals, which are nearly always partially to completely replaced by a progressive series of amphibole replacement reactions described above. It is not well understood why pyroxene alteration is more intense in the TBGP relative to the TBGS, but this is an obvious difference between the two units.

### **15.3.4 Taylor Brook Gabbro Pegmatite accessory phases**

The main accessory phases in the TBGP are Fe-Ti oxides, which locally comprise up to 15% of a sample, olivine and chlorite, epidote, muscovite, quartz and sulfides, which were described above.

Fe-Ti oxides include magnetite, ilmenite and hercynite. These oxides generally occur as fine- to medium-grained interstitial accumulations. They exhibit smoothly curving grain boundaries with adjacent phases and appear to have a primary texture. The primary, interstitial texture suggests that little deformation has occurred in samples that exhibit these oxide textures. Locally, magnetite is host to fine trellis or sandwich exsolution

lamellae of ilmenite, but in general, both ilmenite and magnetite occur as discrete phases, though often in the same interstitial bleb. Hercynite occurs in only a few samples when oxide concentrations are relatively high, such as in TBC-107, where it is spatially associated with magnetite and occurs as anhedral blebs or an exsolution product.

Olivine is present in only a few samples, and occurs as medium- to coarse-grained subrounded crystals that are commonly spatially associated with coarse-grained clinopyroxene. Locally, they form medium-grained chains that define a weak igneous fabric. Most olivine is moderately altered to serpentine and iddingsite and may be cut by thin veinlets of magnetite.

#### **15.4 Taylor Brook Gabbro Suite petrographical summary**

Textures observed in the Taylor Brook Gabbro Suite are complex and inconsistent from location to location, making it difficult to describe the petrogenetic sequence. However, it is possible to make some generalized conclusions about the crystallization history.

The overall lack of deformation fabrics observed throughout the TBGS, despite the appearance of metamorphic fabrics in outcrop suggests that layering that was noted in the field has a magmatic origin. However, several locations exhibit brittle and medium-temperature deformation textures suggesting that at least some post-crystallization or late-crystallization textural modification has occurred. Magmatic layering, where developed, is controlled primarily by changes in modal mineralogy and not crystal size or crystal sorting. Cumulate textures are uncommon, but may have been more widespread prior to pervasive alteration in the TBGS and TBGP.

The presence of undulose extinction and/or concentric zonation, relict, corroded and sericitized cores in plagioclase combined with multiple stages of (metasomatic?) alteration and amphibolitization of mafic minerals suggests that during the latter stages of crystallization or during cooling, large volumes of fluids interacted with the rocks. This

hypothesis is supported by the widespread development of cross-cutting pegmatitic pipes and late veins in many locations.

In general, the more altered compositions and more pervasive replacement textures in the TBGP suggest that perhaps this unit or zone in the TBGS was emplaced late along with late magmatic fluids, which could have circulated during cooling resulting in hydrous alteration. The presence of locally preserved poikilitic pyroxene and intercumulus Fe-Ti oxides suggests that prior to alteration, cumulate textures were well developed. Furthermore, some of the low-grade metamorphism or alteration is likely a result of Paleozoic deformation.

## Chapter 16: Taylor Brook Gabbro Suite rock lithogeochemistry

### 16.1 Introduction

Fifty samples from the TBGS were analysed by XRF methods outlined above, including three duplicate samples that were used to calculate precision (Appendix 3). All major oxides were analysed ( $\text{SiO}_2$ ,  $\text{Al}_2\text{O}_3$ ,  $\text{MgO}$ ,  $\text{CaO}$ ,  $\text{Fe}_2\text{O}_3$  (Fe total),  $\text{Na}_2\text{O}$ ,  $\text{K}_2\text{O}$ ,  $\text{TiO}_2$ ,  $\text{P}_2\text{O}_5$ ,  $\text{MnO}$ ). Additionally, the trace elements (<1%,) S, Cl, Sc, V, Cr, Ni, Cu, Zn, Ga, As, Rb, Sr, Zr, Y, Nb, Ba, Ce, Pb, Th and U were analysed. Precious metals (Pt, Pd and Au) were analysed by fire assay ICP-MS methods. LOI is not reported in these analyses, but major oxides are normalized to 100% anhydrous for all diagrams. Iron is presented as  $\text{FeO}$ , which is calculated from  $\text{Fe}_2\text{O}_3$ .

This chapter presents data in several sections. Major element data are presented first followed by trace element data. Throughout the rest of the thesis, TBGS samples are subdivided into the main mass Taylor Brook Gabbro Suite (TBGS) and the Taylor Brook Gabbro Pegmatite (TBGP), mafic dikes, one granitic sample and one country rock sample. Most plots illustrate a weak distinction between the TBGP and TBGS samples, justifying this separation. In some diagrams, outlying samples are not plotted, but are mentioned in the text. Outlying samples include the country rock and granite. Many TBGS and TBGP samples are characterized by hydration reactions such as amphibole replacing pyroxene, or biotite replacing pyroxene and amphibole and some samples exhibit evidence of fluid interaction. This requires that the data be used cautiously and the possibility of element mobility cannot be ignored. That said, the trends and distinctions found on oxide plots that are more susceptible to alteration effects are repeated on immobile element plots, suggesting that there has not been a great deal of element mobility.

## 16.2 Bivariate plots

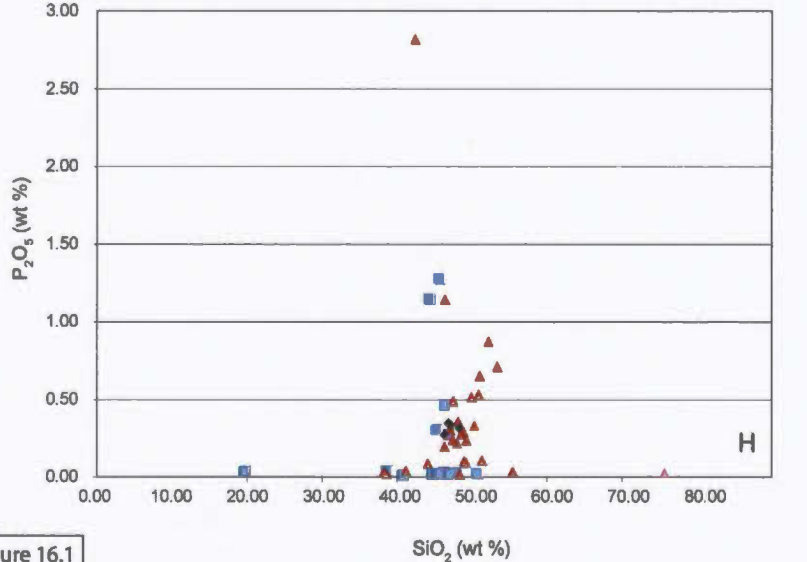
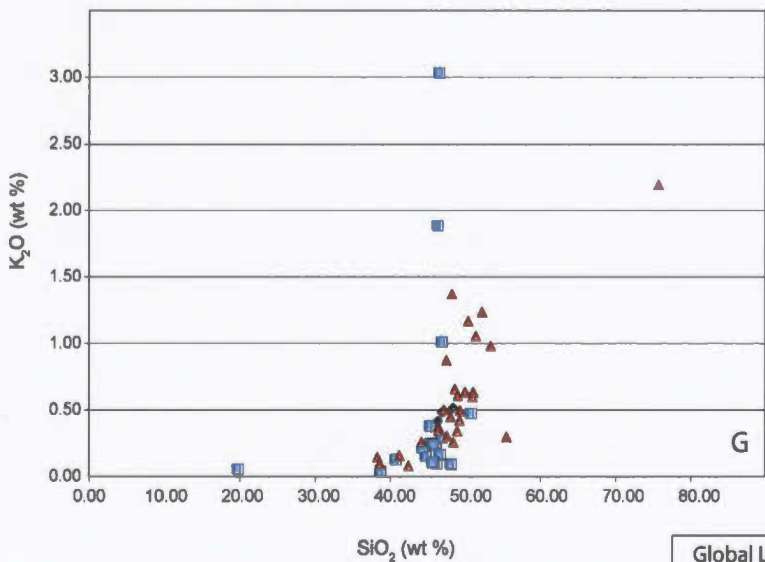
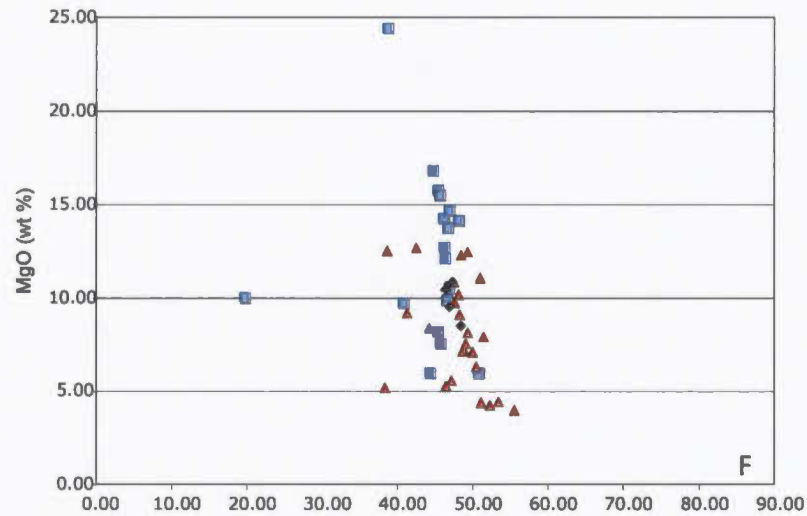
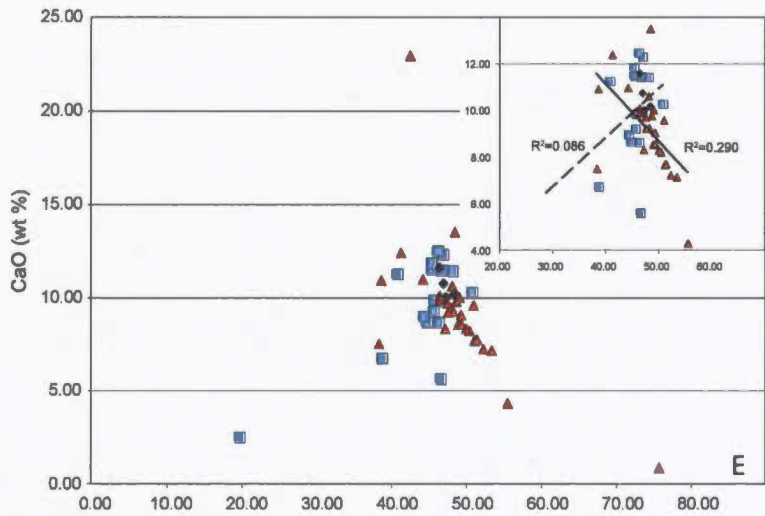
### 16.2.1 Harker diagrams

Harker diagrams are used to compare the major oxides ( $\text{TiO}_2$ ,  $\text{Al}_2\text{O}_3$ ,  $\text{Fe}_2\text{O}_3$ ,  $\text{Na}_2\text{O}$ ,  $\text{CaO}$ ,  $\text{MgO}$ ,  $\text{K}_2\text{O}$ ,  $\text{P}_2\text{O}_5$ ) with  $\text{SiO}_2$  and identify large-scale geochemical trends. In these plots, oxides are normalized to 100%, ignoring trace elements, which generally total less than 1% combined and are thus insignificant.

$\text{SiO}_2$  vs  $\text{TiO}_2$  (Figure 16.1a) has a weakly defined vertical trend that indicates the TBGS is slightly more  $\text{SiO}_2$ -rich relative to the TBGP. The TBGS samples show a weak trend of increasing  $\text{TiO}_2$  with decreasing  $\text{SiO}_2$  that is not present in TBGP samples. There are several outliers in the data set of which two result from variation in  $\text{TiO}_2$  whereas one results from  $\text{SiO}_2$  variation and is thus consistently outlying on all Harker diagrams; TBC-119c is very poor in  $\text{SiO}_2$ , but TBC-107 (TBGS) and TBC-118 (marginal TBGP) are considerably enriched in  $\text{TiO}_2$ . A plot of FeO versus  $\text{TiO}_2$  (inset) exhibits a much stronger correlation between Fe and Ti in the TBGS compared to the TBGP ( $R^2=0.687$  and 0.189 respectively). In particular, the aforementioned samples (TBC-118 and 107) do not fall on the main trend line, but do show relatively strong correlations between Fe and Ti, whereas TBC-119c shows a weak correlation.

$\text{SiO}_2$  vs  $\text{Al}_2\text{O}_3$  (Figure 16.1b) has a broad circular pattern with a very weak positive trend in the TBGS. Aside from TBC-119c, which is strongly enriched in  $\text{Al}_2\text{O}_3$ , the TBGP is more tightly constrained indicating a relatively constant proportion of  $\text{SiO}_2$  vs  $\text{Al}_2\text{O}_3$  in the TBGS samples. Petrographical study of the samples does not reveal an obvious cause for the lack of correlation between  $\text{SiO}_2$  and  $\text{Al}_2\text{O}_3$ . It may be that this, along with other diagrams, are circumstantial evidence for a lack of differentiation in the TBGS.

$\text{SiO}_2$  vs FeO (Figure 16.1c) defines a broad negative correlation for both the TBGP and TBGS. The TBGS samples exhibit an overall relative enrichment in FeO compared to the TBGP. The most likely explanation for the larger FeO content in the TBGS is a greater



Global Legend for Figure 16.1

- ▲ TBGS
- ◆ Mafic dikes
- TBGP
- ▲ Granite

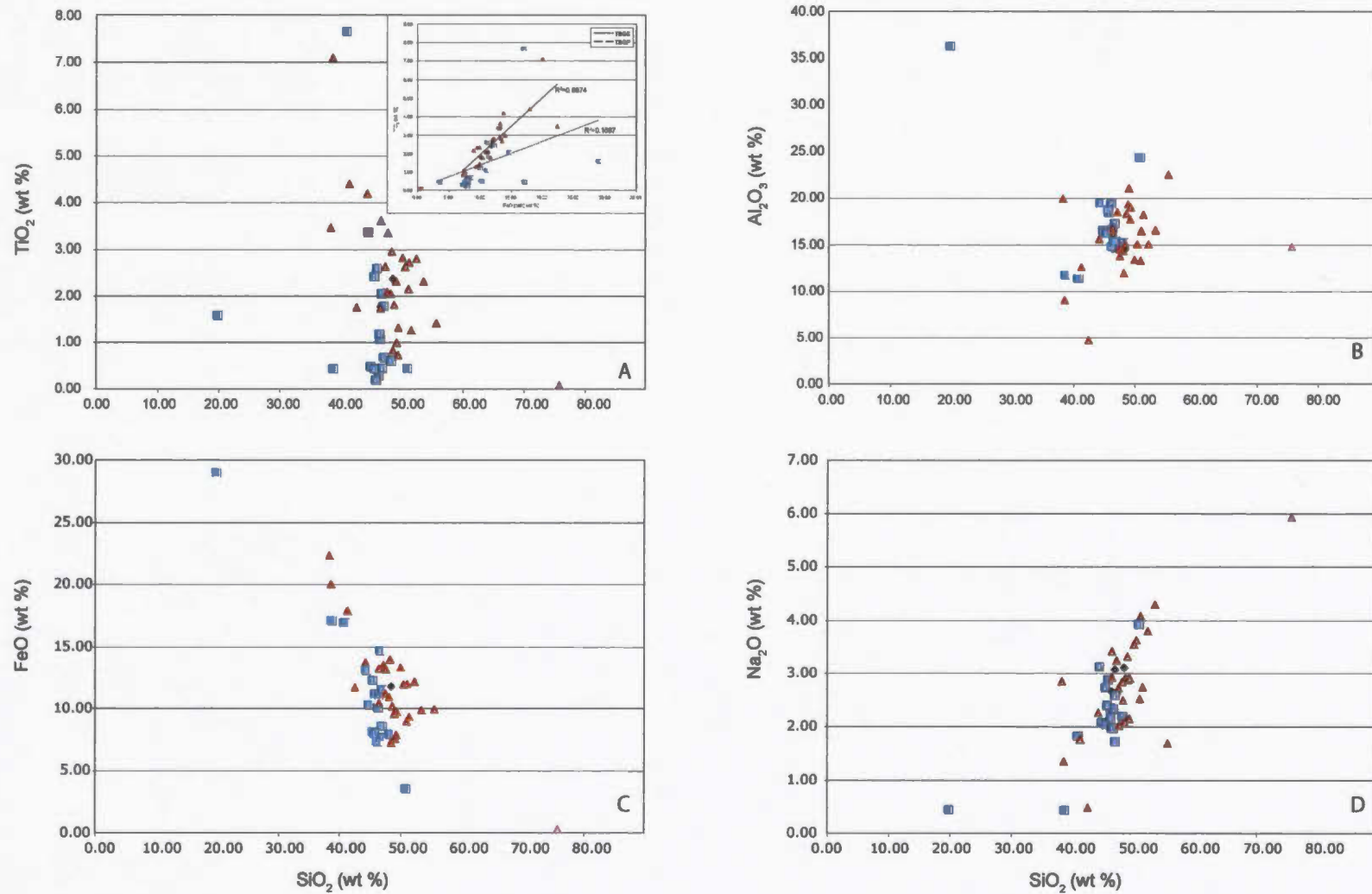


Figure 16.1 Harker diagrams for TBGS whole rock data. Descriptions for each diagram including the insets in (a) and (e), are given in the text. A global legend for all Chapter 16 figures is presented at the bottom of the preceding page. All data is in weight percent and Fe<sub>2</sub>O<sub>3</sub> is total Fe. Country rock samples are not plotted in this or any other diagrams in this chapter.

abundance of magnetite and ilmenite, which are locally abundant in the TBGS and were noted as a primary phase in most TBGS thin sections. Sulfide concentrations are very low and therefore would not contribute noticeably to the overall FeO abundance. A small subgroup of samples, (TBC-107, 83, 68.1, 55 and 64.1) are distinctly FeO-rich and SiO<sub>2</sub>-poor, but there is no apparent spatial or petrographical correlation between them.

SiO<sub>2</sub> vs Na<sub>2</sub>O (Figure 16.1d) displays a positive correlation and TBGS samples exhibit elevated Na concentrations relative to TBGP samples. Although not analysed by electron microprobe, a likely explanation for this trend is more albitic plagioclase in the TBGS. Several samples plot relatively lower than the main group of samples and petrography indicates that these samples are relatively plagioclase-poor.

SiO<sub>2</sub> vs CaO (Figure 16.1e) exhibits a broad, clustered pattern, but there are weak trends in both the TBGS and the TBGP. Several outliers (TBC-119c and 069) in the TBGS and TBGP cause a relative distortion of the spatial distribution of the rest of the samples, but by removing them from the plot, the trends in TBGS and TBGP samples become clearer. TBC-119c has very low CaO concentrations, whereas TBC-69 abundant CaO, which is a function of the mineralogy; this sample is >90% clinopyroxene, which likely has a relatively Ca-rich composition. A revised plot (inset) defines a weak negative correlation in the TBGS trend ( $R^2=0.290$ ), whereas the TBGP exhibits a vertical trend with two small clusters and no SiO<sub>2</sub>-CaO correlation ( $R^2=0.086$ ). The trend in TBGP samples suggests that fractionation has been insignificant, but the weak correlation in TBGS samples indicates minor fractionation may have occurred.

SiO<sub>2</sub> vs MgO (Figure 16.1f) exhibits a relatively well constrained linear pattern with a vertical trend. Despite the outlier of TBC-119c, and the well defined trend, there is only minimal correlation between MgO and SiO<sub>2</sub>. TBGS samples contain relatively less MgO and  $R^2=0.164$ , and the TBGP samples have a slightly negatively sloping trend and  $R^2=0.231$ . These data are further evidence of a lack of fractional crystallization in the

TBGS. Had that process occurred, a negatively sloping trend with strong correlation between MgO and SiO<sub>2</sub> would be expected.

SiO<sub>2</sub> vs K<sub>2</sub>O (Figure 16.1g) exhibits a vertical trend with a poor correlation. TBGS samples have relatively more K<sub>2</sub>O compared to TBGP samples, which cluster near zero on the y-axis. There are several TBGP samples with significantly elevated K<sub>2</sub>O, but there is no obvious mineralogical explanation for this trend. TBGS samples have a slightly positive slope whereby increasing K<sub>2</sub>O is better correlated with increasing SiO<sub>2</sub> ( $R^2=0.342$ ). This correlation may reflect the presence of orthoclase, which is noted in several samples.

SiO<sub>2</sub> vs P<sub>2</sub>O<sub>5</sub> (Figure 16.1h) displays a similar trend to the K<sub>2</sub>O pattern and lacks a strong correlation. Many TBGP samples are near zero on the y-axis, with a small group that is relatively more elevated in P<sub>2</sub>O<sub>5</sub>. TBGS samples have a slight positive correlation, suggesting some fractionation with late enrichment in P<sub>2</sub>O<sub>5</sub>. There is no clear mineralogical explanation for these trends, because apatite was not observed in thin sections. TBC-069 contains almost 3% P<sub>2</sub>O<sub>5</sub> but comprises >90% CPX, which is not commonly associated with apatite.

### 16.3 General compositional nomenclature

Figure 16.2a demonstrates the sub-alkaline nature of the TBGS samples. Although some samples fall in the alkaline field of the diagram, the major cluster is in the sub-alkaline field. The granitic sample is quite different because it has considerably more SiO<sub>2</sub> and alkalis than other samples, although it still falls in the sub-alkaline field. This diagram highlights the compositional differences between the TBGS and TBGP. As a whole, the TBGS contains greater amounts of SiO<sub>2</sub> and generally greater total alkalis.

AFM diagrams are a plot of Na<sub>2</sub>O+<sub>2</sub>O vs FeO vs MgO and are useful for characterizing the relative tholeiitic or calc-alkaline nature of a suite of samples (Irvine and Baragar,

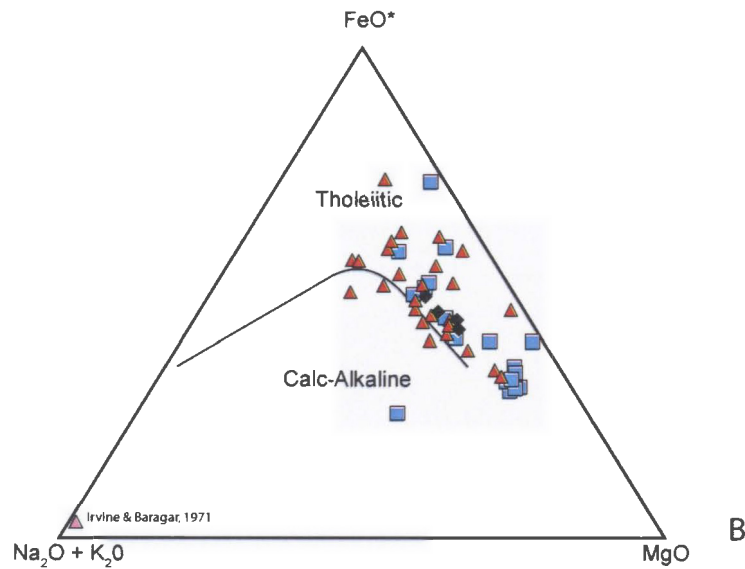
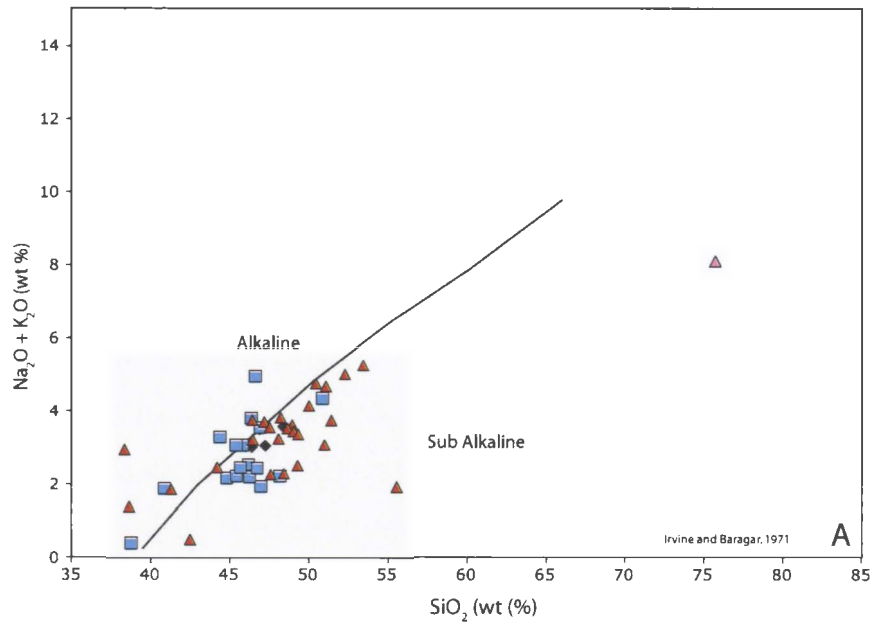


Figure 16.2 Total alkali silica diagrams (TAS) are used to demonstrate geochemical evolution of the TBGS samples and describe the general composition of the intrusion. A) this diagram indicates that most TBGS samples exhibit a sub-alkaline composition. This diagram also illustrates the relatively more felsic composition of the TBGS compared to the TBGP; B) This diagram also indicates that the TBGP samples are more mafic than the main mass (TBGS). Overall, the TBGS sample suite displays an evolutionary trend from relatively more Mg-rich in the TBGP to more Fe-rich in the main mass.

1971). Like all ternary diagrams, there are problems related to the relative proportion of oxides that are actually represented on the diagram, which is commonly < 50% of the total weight percent oxides (Rollinson, 1993). The process of normalizing a sample to 100% using less than 50% of the oxides can cause a misrepresentation of the data.

Most samples (Figure 16.2b) have a tholeiitic composition, but overall the data are characterized by more primitive, MgO-rich samples in the TBGP that grade into the more evolved, FeO-rich TBGS samples. However, there is considerable overlap in the sample compositions. Mafic dikes in this sample set are intermediate to the TBGS and TBGP samples. The granitic sample plots in the alkali corner because it contains very little MgO or FeO. One major outlier, TBC-119c, consistently falls outside the normal range of TBGS samples in other diagrams because of its low SiO<sub>2</sub> content.

#### **16.4 Igneous nomenclature**

TAS diagrams, described in previous chapters, require that samples are not altered, a criteria that is met by most TBGS samples, although there are several samples that have clearly been altered by fluids. However, these samples appear to plot with unaltered samples that have similar textures. The diagrams below are designed for a specific compositional range, therefore, certain samples are not included. The country rock marble sample is removed for the obvious reason that it is not an igneous rock, and TBC-119c is not included because of its low silica content. The granitic sample is included on these diagrams because it falls within the compositional range.

Figure 16.3a (after Wilson, 1989) indicates that both the TBGS and TBGP have gabbroic compositions, although some samples are more mafic and lie outside the assigned fields. The TBGS samples exhibit a more evolved composition than the TBGP samples and some approach the diorite field, while most TBGP samples, which are generally more mafic, approach the lower corner of the gabbro field. Although not included, a different

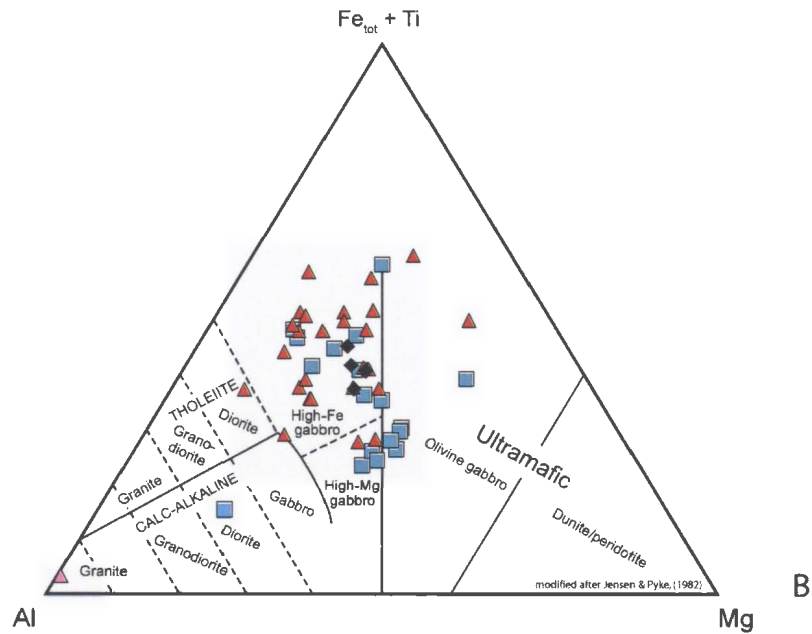
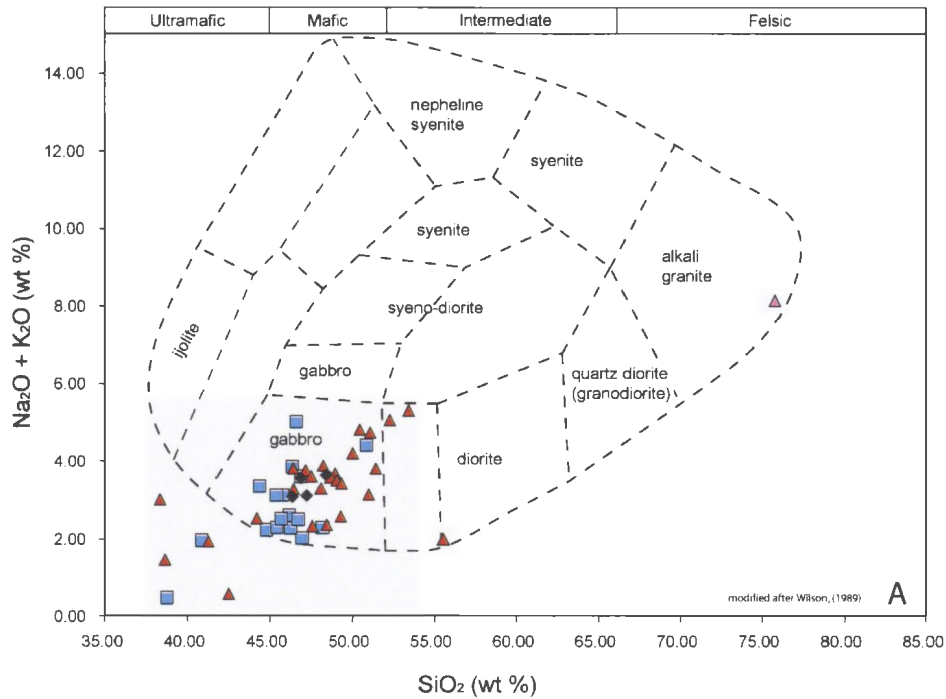


Figure 16.3 Igneous nomenclature of the TBGS. A) This TAS diagram, modified from Wilson (1989) to present plutonic rather than volcanic nomenclature indicates that most samples have a gabbroic composition. Similar to Figure 16.2, the trend from more primitive gabbro of the TBGP compared to the main mass is present; B) this diagram indicates that the majority of TBGS samples have an Fe-rich gabbro composition, while a small population of TBGP samples are Mg-rich, plotting in the olivine gabbro to Mg-rich gabbro fields.

diagram after LeMaitre (1989) indicates that the samples that fall outside the gabbro field plotting in the picrobasalt or foidite fields in a volcanic nomenclature.

Plotting the cations ( $\text{Fe}^{2+} + \text{Ti}^{4+}$ ) vs  $\text{Al}^{3+}$  vs  $\text{Mg}^{2+}$  (Figure 16.3b) is a different method for assigning rock names to a sample suite rather than using TAS diagrams. Such a diagram is called a Jensen plot, after Jensen and Pyke (1982). This diagram is probably more representative of the samples than TAS diagrams because the sum of elements it represents is greater (*i.e.*  $\text{Na}_2\text{O} + \text{K}_2\text{O} = \sim 3$  wt. % compared to  $\text{Fe} + \text{Ti} + \text{Al} + \text{Mg}$  cations =  $\sim 40$  wt/ %). However, problems related to normalizing data to 100% are still present. This diagram indicates that the majority of TBGS samples and approximately 50% of TBGP samples have a high-Fe gabbro composition, whereas most other TBGP samples fall near the olivine gabbro–high-Fe gabbro dividing lines, due to the relative enrichment in MgO of these samples. The granitic sample plots in the lowermost granitic field, owing to its great amount of  $\text{Al}^{3+}$  from plagioclase. Mafic dikes also fall within the high-Fe gabbro field.

## 16.5 Tectono-magmatic discrimination

Immobile element diagrams are useful for characterizing many different geochemical processes or illustrating different geochemical classification schemes because they are thought to be relatively immobile during hydrothermal alteration and metamorphism. Immobile element diagrams normally do not include cumulate rocks because the cumulus minerals may dilute the relative concentrations of the immobile elements (Rollinson, 1993). Field and petrographical data do not indicate an abundance of cumulate textures, so most samples are plotted. Several diagrams are used to discriminate between the potentially different tectono-magmatic environments reflected by the TBGS magmas. Although these diagrams are designed for volcanic rocks, they are commonly applied to plutonic rocks.

Zr/Y vs Zr diagrams discriminate between different types of basalt (Pearce and Norry, 1979). In Figure 16.4, TBGS and TBGP samples plot in two broad clouds that do not fall convincingly into one particular field. In general, TBGS samples contain more Zr compared to TBGP samples, and most TBGS samples have a greater Zr/Y ratio. Although the within-plate basalt field contains more samples than other fields, followed closely by the MORB field, the broad sample distribution and lack of consistent pattern render this diagram inconclusive.

To avoid the affects of elevated Ti, which the  $\text{TiO}_2$  Harker diagram indicates to be common, a different approach is employed. Plotting  $(2 \times \text{Nb})$  vs  $(\text{Zr}/4)$  vs Y (Figure 16.5) (Meschende, 1986) is a method of differentiating different types of MORB. This diagram demonstrates that most TBGS samples are within-plate tholeiite basalts to E-type MORB, which are sometimes called P-type MORB or plume related MORB because of their enrichment in incompatible elements (Rollinson, 1993). Field D, which is N-type MORB and volcanic arc rocks, contains most TBGP samples, but they fall along the Zr/4 vs Y tie-line, indicating a lack of, or minimal amount of Nb. Rollinson (1993) cautions against interpreting samples with  $<10$  ppm Nb that were analysed by XRF, as these samples are, because XRF methods do not produce accurate results below 10 ppm. There is overlap in the fields of this diagram such that only E-type MORB and within-plate alkali basalts can be identified unambiguously. Therefore, this diagram, aside from a handful of samples that fall in the E-type MORB field is inconclusive.

A less ambiguous diagram, Zr/Y vs Ti/Y (Figure 16.6), can be used to differentiate between plate margin basalts and within-plate basalts. Several samples were excluded from this diagram because they did not fit within the plotting space. These samples were all relatively enriched in Ti, because of the presence of cumulus ilmenite, causing them to fall too far to the right on the Ti/Y axis. This diagram indicates that nearly all samples have a within-plate composition.

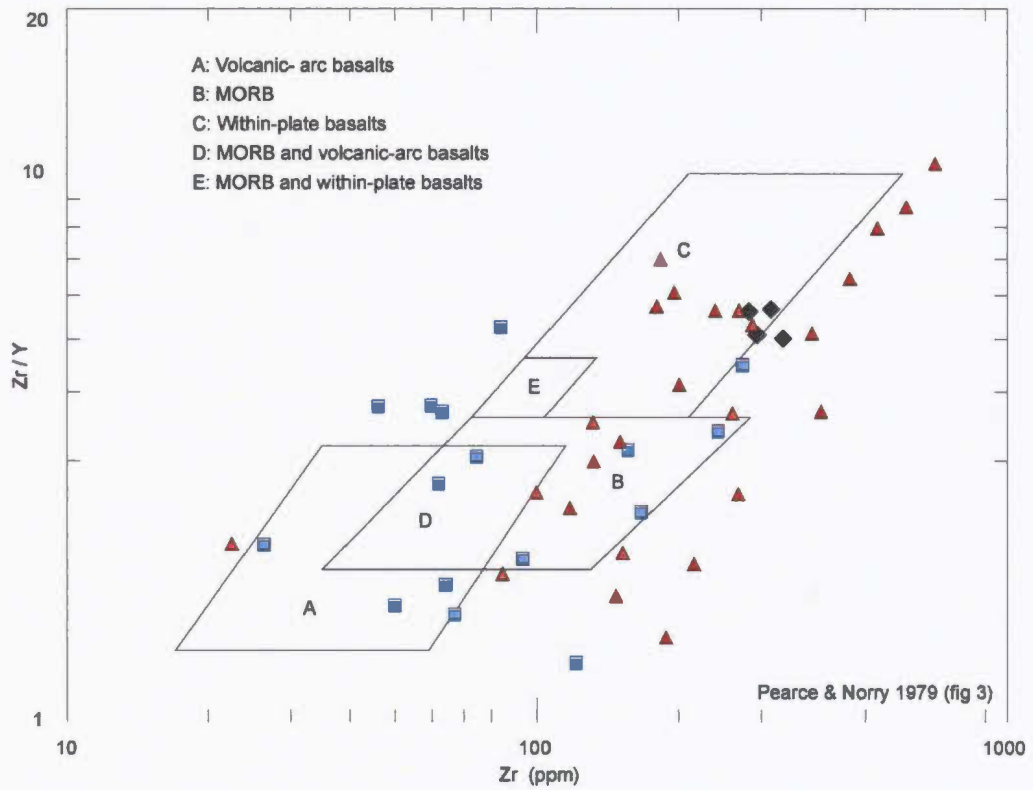


Figure 16.4 Tectono-magmatic discrimination diagram of TBGS samples (not including country rock samples). TBGS and TBGP samples plot as two weakly distinct clouds, with TBGP samples containing less Zr than TBGS samples. This diagram does not yield any conclusive results, therefore, refer to Figure 16.5 and 16.6. Symbols are as per previous diagrams.

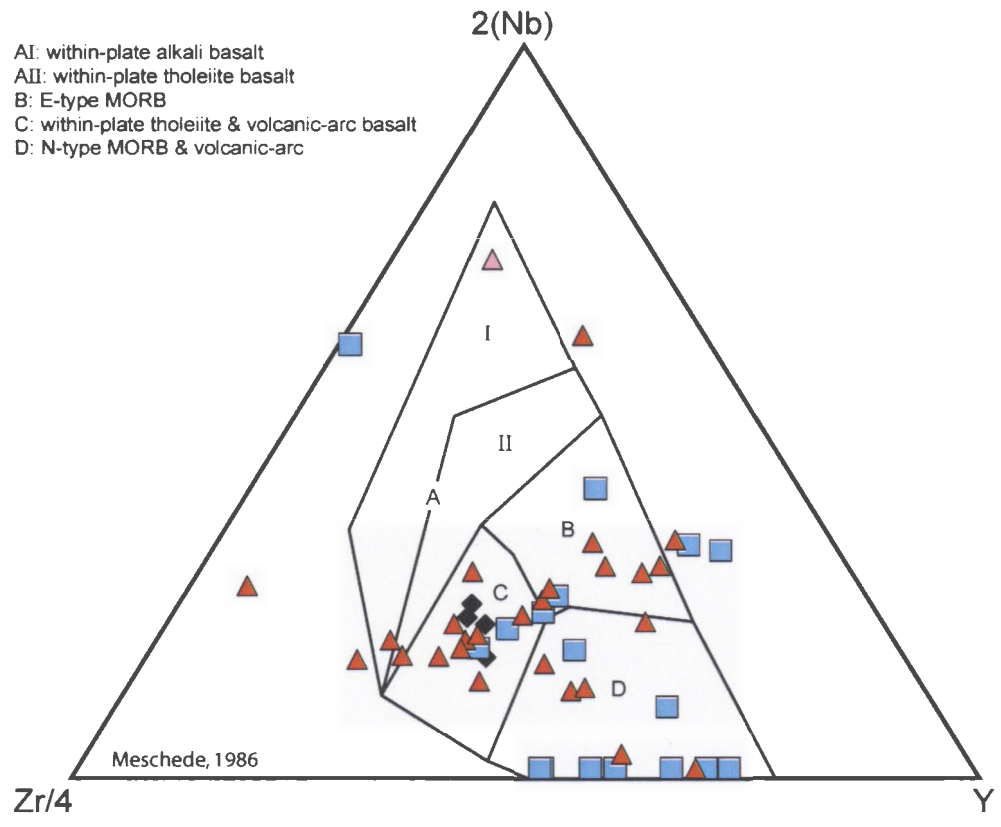


Figure 16.5 This tectono-magmatic discrimination diagram of TBGS samples is used to differentiate between different types of MORB. It indicates that most TBGS samples plot within the C and B fields, while TBGP samples are more concentrated in the D field, but are present in many of the fields. For reasons discussed in the text, this diagram is not a reliable method for discriminating between TBGS samples.

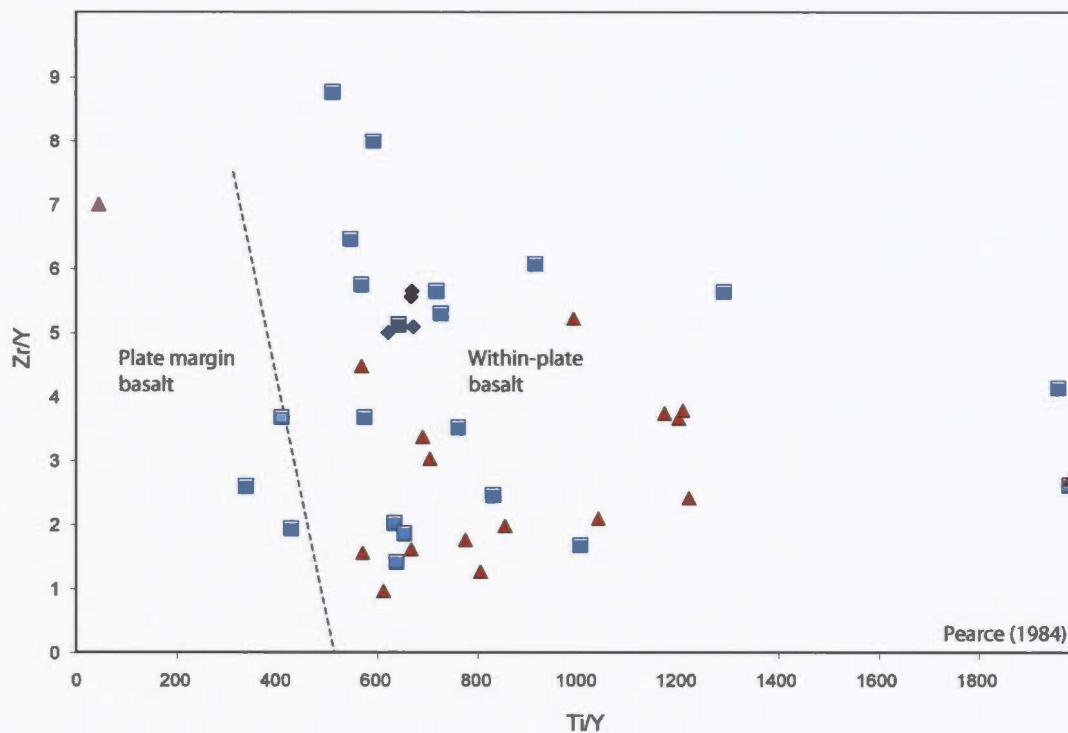


Figure 16.6 This tectono-magmatic discrimination diagram indicates that TBGS samples are conclusively within-plate basalts. The granitic sample plots quite differently in this diagram, clearly within the plate-margin basalt field, near the limit of this diagram.

## 16.6 Summary

The Taylor Brook Gabbro Suite demonstrates only minor evidence of fractional crystallization or differentiation between the TBGS and TBGP units. Overall, the TBGS is more enriched in  $\text{TiO}_2$ , and alkalis, but less enriched in  $\text{FeO}$ ,  $\text{MgO}$  and  $\text{Al}_2\text{O}_3$ . These trends suggest that the TBGS is relatively more fractionated than the TBGP. These patterns are generally consistent with mineralogy in the TBGS and TBGP, the latter which generally contains more pyroxene and the only samples with olivine. Generally, oxides are more common in the main mass of the TBGS compared to the TBGP. Within the main mass (TBGS) there does not appear to be any systematic distribution of geochemically similar rocks, thus, it is possible that differentiation occurred in localized zones, creating the heterogeneous patterns observed. The TBGP exhibits a relatively more constrained composition, and it is mapped as a small circular body in the northwest of the TBGS, suggesting it might have been emplaced in a single pulse of magma that cooled relatively quickly, thus not allowing time for fractionation. Although it has a more primitive composition, this may be a reflection of the differentiation processes prior to emplacement. Alternatively, it may be that this portion of the TBGS did not experience the same degree of low-grade metamorphism or alteration and the main mass had a similar composition prior to metamorphism.

The TBGS has an overall sub-alkaline composition and an AFM diagram indicates it has a tholeiitic composition. Several different diagrams confirm the high-Fe ( $\pm\text{Ti}$ ) gabbroic composition of the TBGS (Figure 16.3) and demonstrate the relatively more primitive composition of the TBGP. Mafic dikes also exhibit a ferrogabbro composition, and in general, plot approximately half way between the composition of the TBGS and TBGP.

Tectono-magmatic diagrams were only partially successful in defining a consistent tectono-magmatic environment of emplacement of the TBGS. Several diagrams define only weak trends ( $\text{Zr/Y}$  vs  $\text{Zr}$  and  $\text{Nb-Zr-Y}$ ). Although there are overlapping fields in the  $\text{Nb-Zr-Y}$  ternary diagram, many samples fall into the within-plate tholeiitic field. A plot

of Zr/Y vs Ti/Y is in agreement with the former diagram in that the vast majority of samples fall into a within-plate environment. Overall, the TBGS can be said to have been emplaced a within-plate tectono-magmatic environment, and several diagrams provide supporting evidence for its tholeiitic composition.

## Chapter 17: Taylor Brook Gabbro Suite Sulfur Isotopes

Six sulfide-bearing samples were used to determine the  $\delta^{34}\text{S}$  values for the Taylor Brook Gabbro Suite. Sample processing methods are described in Chapter 1. Five samples were from the TBGP and one from the TBGS, near the boundary with the TBGP.  $\delta^{34}\text{S}$  values are reported in Appendix 5.

The goal of  $\delta^{34}\text{S}$  analyses in the TBGS was to characterize the  $\delta^{34}\text{S}$  values, which can be used to characterize the source of S and determine if multiple S reservoirs are represented in these rocks, which would be expected if contamination had occurred.

### 17.1 $\delta^{34}\text{S}$ Isotope results

TBGS samples range from +2.2 ‰ to +4.8 ‰ and are presented in Figure 17.1. Table 17.1 presents the  $\delta^{34}\text{S}$  ratios and mineralogy of the sulfide separates. There is no statistical difference between TBGS and TBGP  $\delta^{34}\text{S}$  values, suggesting that they originate from the same source. Most samples comprise a mixture of pyrite and pyrrhotite, but given the similarity of the  $\delta^{34}\text{S}$  values, there does not appear to be any compositional differences between the phases. Overall, these samples exhibit  $\delta^{34}\text{S}$  values similar to that of granite- to island-arc basalts + andesite (Figure 17.2). This compositional range is compatible with the TBGS samples, because the intrusion was emplaced into bedrock comprising predominantly granitic or felsic rocks, thus, the TBGS magma may have assimilated enough sulfur from these rocks to influence the S composition. Some of the samples fall within a mantle or MORB  $\delta^{34}\text{S}$  range of  $0 \pm 3$  ‰, which may also be a reasonable explanation for TBCS isotopic compositions.

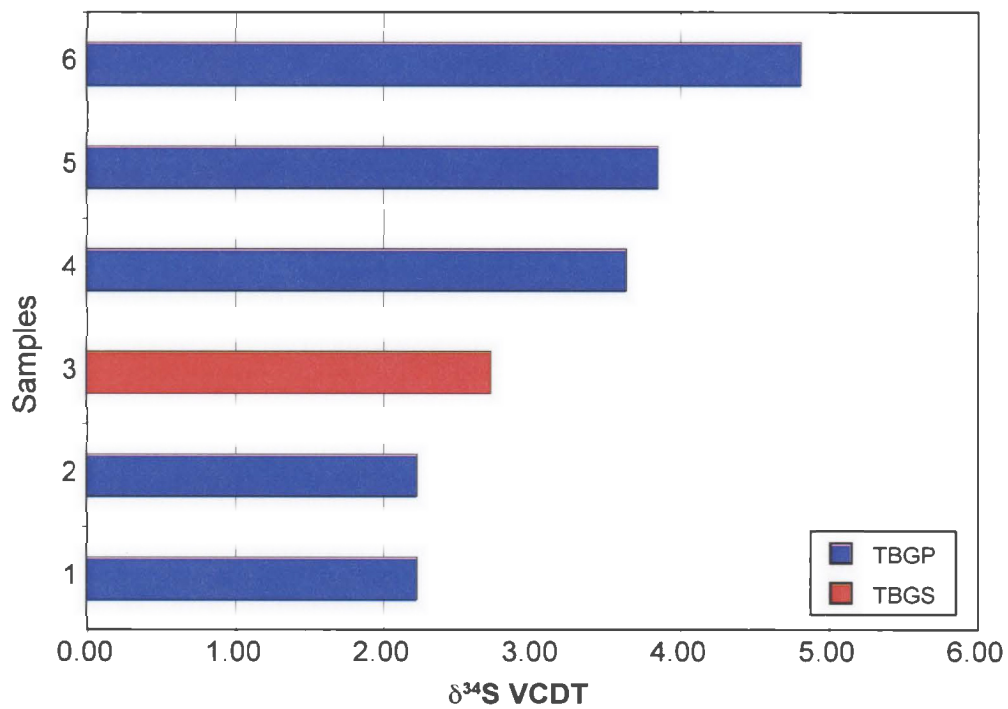


Figure 17.1 A summary of TBGS and TBGS  $\delta^{34}\text{S}$  (‰) ratios. All samples exhibit positive  $\delta^{34}\text{S}$  ratios that plot within with the range of mantle sulfur to granitic sulfur. Values suggest that the TBGS and TBGP sulfur originated from the same source.

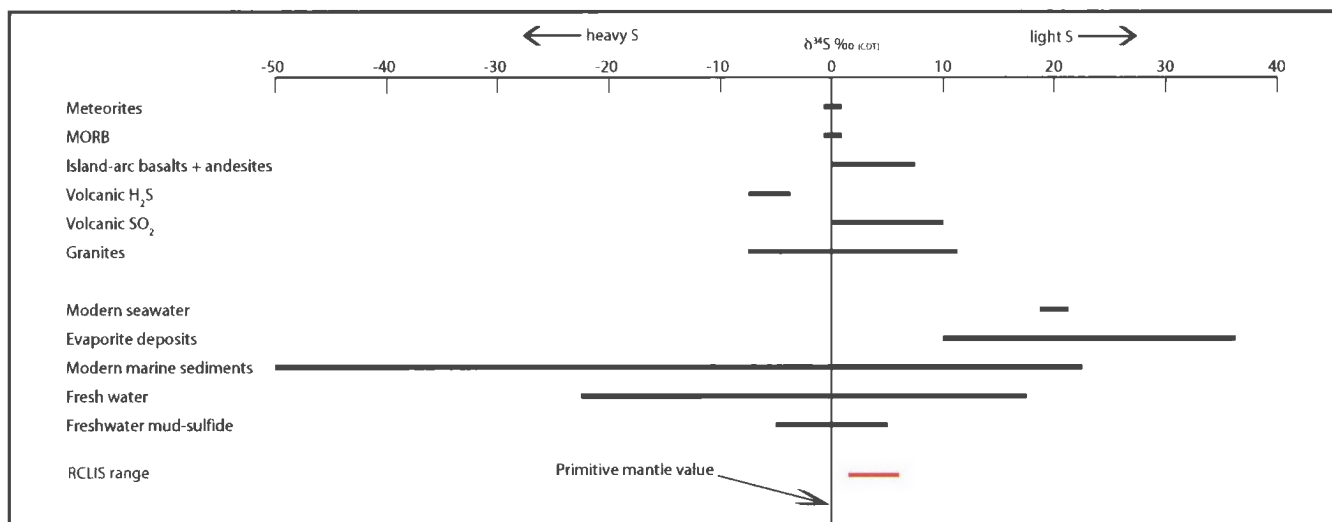


Figure 17.2 A compilation diagram of  $\delta^{34}\text{S}$  sulfur ranges from various igneous sources (top) and sedimentary or water reservoirs (bottom). The various ranges are compiled in Rollinson (1993). TBGS samples are presented at the bottom of the diagram for comparative purposes. TBGS samples fall within the range of granitic- to island-arc basalts + andesites  $\delta^{34}\text{S}$ . It is likely that these samples represent a mixture of granitic and IAB sulfur values, because the intrusion was emplaced into predominantly granitic basement rocks, but has a gabbroic (basaltic) composition itself.

<b>Standard ID</b>	<b>Unit</b>	<b><math>\delta^{34}\text{S}</math> VCDT</b>	<b>Mineralogy</b>
TBC-107	TBGP	2.2	Py
TBC-085	TBGP	2.2	Po+Py
TBC-119B	TBGP	2.7	Po+Py
TBS-105	TBGP	3.6	Py
TBC-069	TBGS	3.8	Po+Py
TBC-100	TBGP	4.8	Py

Table 17.1 A summary of TBGS  $\delta^{34}\text{S}$  ratios. All but TBGS-069 are from the TBGP area. Samples comprise mainly pyrite and lesser pyrrhotite, but mineralogy does not appear to affect the  $\delta^{34}\text{S}$  composition.

Overall, these  $\delta^{34}\text{S}$  values suggest that no large volume of light, sedimentary sulfur was assimilated, unlike the case for Ni-Cu sulfide-bearing mafic rocks (e.g. Duluth, Voisey's Bay) (Naldrett, 2004). These data are further evidence against the potential of this intrusion to host significant volumes of Ni-Cu sulfides. However, these data should be considered in light of a lack of country rock sulfur analysis: it is assumed that the assimilated country rock sulfur would have a light composition, but it may be the case that the country rock sulfur is heavy. The lack of sulfide-bearing country rock samples may make this a moot point, however.

## Chapter 18: Discussion and Conclusions

### 18.1 Overview

The Taylor Brook Gabbro Suite (TBGS) was originally selected as a target for mapping because of its potential to host Ni-Cu-PGE mineralization. Mapping and geochemical analyses failed to demonstrate any anomalous base metal mineralization or even potential (olivine-rich) host rocks in the suite. What follows is an explanation of some of the textural features of this intrusion and possible explanations for a lack of even weakly anomalous mineralization in an apparently prospective intrusion.

### 18.2 Field relationships

Mapping demonstrated an abundance of xenoliths throughout the TBGS and although they were more concentrated along the contacts, xenoliths were not uncommon almost 1000 m from the contacts. These xenoliths range from those that were quite obviously derived from the surrounding country rock (i.e. metapelites) to more ambiguous affinities such as the large block in Figure 14.4. The abundance of xenoliths is often cited as a positive criterion for base metal mineralization in mafic intrusions, particularly if the xenoliths contain sulfur. This does not appear to be the case in the TBGS, although it is unclear why. Of the xenoliths examined, however, none contained any sulfides, thus, contamination may not have introduced any extra sulfur. An abundance of xenoliths, pegmatitic pipes and stockwork veining are suggestive of upper level processes in a magma chamber and might be expected if the TBGS was only shallowly eroded. Conversely, magma mixing textures might be expected at deeper levels, possibly nearer to the base of an intrusion. The inconsistent layering suggests that there may have been several pulses of magma but contacts are not exposed, likely due to the heavy overburden. Alternatively, the different orientations may have resulted if the TBGS was intruded into a tectonically active region and layering became distorted syn- to post emplacement.

These inconsistencies make it difficult to relate different units to each other in the field and preclude exploration for laterally continuous, traceable units with the potential to host base metals.

### **18.3 Geochemical considerations**

Although Rose (1998) describes soil and lake sediment anomalies in the TBGS, it is likely that these originate from a combination of Ni from silicates (e.g. olivine and pyroxene) and small zones of sulfide mineralization such as those at TBC-49. During this study, which covered a much larger area of mapping and included a larger quantity of samples, the maximum concentration of Ni in a whole rock assay was 308 ppm. This sample contains abundant S, suggesting that a lack of sulfur is not a factor in a lack of Ni mineralization. If this intrusion was more fertile (i.e. higher potential for Ni mineralization), it would be expected that ultramafic rocks and in particular, olivine-bearing rocks would contain more Ni.

### **18.4 Conclusions**

Mapping, geochemical analyses, petrography and sulfur isotope analyses of the TBGS have demonstrated that there is little obvious potential for Ni-Cu-PGE mineralization. A combination of factors, such as low total Ni in lithochemical assays, inconsistent rock units and orientation of magmatic layering all support a lack of exploration potential. If, as suggested above, the TBGS is only shallowly eroded, there may be potential for mineralization at depth, but exploring for this would not be feasible.

## References

- Arnold, R.G., 1971. Evidence for liquid immiscibility in the System FeS-S. *Economic Geology and the Bulletin of the Society of Economic Geologists*, **66** No. 8: 1121-1130.
- Attendorn, H.G. and Bowen, R.N.C. 1997. *Radioactive and Stable Isotope Geology*. Chapman & Hall: 385 – 389.
- Arth, J.G., 1976. Behaviour of trace elements during magmatic processes – a summary of theoretical models and their applications. *Journal of Research, USGS*, **4**: 41-47.
- Barbour, D.M., 1998. Report of Geological mapping, prospecting and Diamond Drilling on the Valentine Lake Project, Central Newfoundland covering AND Charter Long Term Mineral Leasehold Lands and R.L. 227 and R.L. 229 Fee Simple Mining Grants. NTS 12A/06 and 12A/07. (GSB File 012A/0831)
- Baird, D.M., 1954. The magnetite and gypsum deposits of the Sheep Brook-Lookout Brook area. *Contributions to the Economic Geology of Western Newfoundland*, Geological Survey of Canada Bulletin **27**: 20– 40.
- Barrett, A.M. and Shebib & Associates, 1994. An evaluation of the potential of the Steel Mountain magnetite deposits as specialty industrial minerals: A report submitted as part of the work requirements for the renewal of Exploration License number 4393, GSB File 012B/08/04 27
- Barrett, A.M., 1999. An evaluation of the Steel Mountain magnetite deposits product potential: A report submitted as part of the work requirements for renewal of the Quarry Materials Exploration License. GSB File 012B/08/0426
- Bradley, P., 1995. First year assessment report, License No.'s 4502, 4493, 4498, 4503, 4504, Cabot Exploration Ltd., Flat Bay Brook Option, NST12B/8. Unpublished Report, Cabot Exploration Ltd. 1-14.
- Brem, A.G., Davis, D.W., McNicoll, V.J., Lin, S., and van Stall, C.R., 2005. Geochronological studies in the Long Range Mountains of southwestern Newfoundland. GAC-MAC-CSPG-CSSS Joint Meeting, Halifax Nova Scotia, Abstracts (Volume 30), ISBN 1-897095-05-8
- Brem, A.G., Lin, S. and van Stall, C.R., 2002. Humber Zone-Dunnage Zone relationships and the Long Range Fault, south of Grand Lake, western Newfoundland: Preliminary results. *Current Research, Newfoundland Department of Mines and Energy Geological Survey*, **Report 02-1**:135-144.

- Brem, A.G., Lin, S. and van Stall, C.R., 2003. Structural relationships south of Grand Lake, Newfoundland. Current Research, Newfoundland Department of Mines and Energy Geological Survey, **Report 03-1**: 1-13.
- Brownlow, A.H. 1996. Geochemistry (2<sup>nd</sup> Ed). Prentice-Hall 580 p
- Campbell, I.H. and Naldrett, A.J., 1979. The influence of silicate : sulfide ratios on the geochemistry of magmatic sulfides. *Economic Geology*, **74**: 1503-1506.
- Carpenter, R.H. and Desborough, G.A., 1964. Range in solid solution and structure of naturally occurring troilite and pyrrhotite. *American Mineralogist*, **49**: 1350-1365.
- Cawood, P.A., Dunning, G.R., Lux, D., and van Gool, J.A.M., 1994. Timing of peak metamorphism and deformation along the Appalachian margin of Laurentia in Newfoundland: Silurian, not Ordovician. *Geology*, **22**: 399-402.
- Cawood, P.A., van Gool, J.A.M., and Dunning, G.R., 1996. Geological development of eastern Humber and western Dunnage zones: Corner Brook – Glover Island region, Newfoundland. *Canadian Journal of Earth Sciences*, **33**: 182-198.
- Colman-Sadd, S.P. & Crisby-Whittle, L.J.V., 2004. Partial Bedrock Geology Dataset for the Island of Newfoundland, Open File NFLD/2616 Version 5.0.
- Colman-Sadd, S.P., 1987. Snowshoe Pond, Newfoundland. Map 87-087. Government of Newfoundland and Labrador, Department of Mines and Energy, Mineral Development Division, Open File 012A/07/0438; GSB# 012A/07/0438.
- Coplen, T.B., Hoppie, J.A., Böhlke, J.K., Peiser, H.S., Rieder, S.E., Krouse, H.R., Rosman, K.J.R., Ding, T., Vocke, R.D., Révész, K.M., Lamberty, A., Taylor, P. and Bièvre, P. De, 2002. Compilation of Minimum and Maximum Isotope Ratios of Selected Elements in Naturally Occurring Terrestrial Materials and Reagents. Water-Resources Investigations Report 01-4222, U.S. Department of the Interior and U.S. Geological Survey.
- Cox, K.G., Bell, J.D. and Pankhurst, R.J., 1979. *The Interpretation of Igneous Rocks*. George, Allen & Unwin, London.
- Currie, K.L. and van Berkel, J.T., 1992. Notes to accompany a geological map of the southern Long Range, southwestern Newfoundland. Geological Survey of Canada **Paper 91-10**: 1-10.
- Currie, K.L. and van Berkel, J.T. 1992 b: Geology, Southern Long Range Mountains, Newfoundland. Map 1815A. Scale: 1:100 000. In Notes to accompany a geological

map of the Southern Long Range, southwestern Newfoundland. Geological Survey of Canada, Paper **91-10**: 15p. GS# NFLD/2553.

- Currie, K.L. and Piasecki, M.A.J., 1989. Kinematic model for southwestern Newfoundland based upon Silurian sinistral shearing. *Geology*, **17**: 938-941.
- Currie, K.L., van Breemen, O., Hunt, P.A., and van Berkel, J.T., 1992. Age of high-grade gneisses south of Grand Lake, Newfoundland. *Atlantic Geology*, **28**: 153-161.
- Currie, K.L., 1987. A preliminary account of the geology of Harry's River map area, southern Long Range of Newfoundland. Current Research, Part A, Geological Survey of Canada, Paper **87-1A**: 653-662.
- Czamanske, G.K., Kunilov, V.E., Zienter, M.L., Cabri, L.J., Likhachev, A.P., Calk, L.C. and Oscarson, R.L., 1992. A proton-microprobe study of magmatic sulfide ores from the Noril'sk-Talnakh district, Siberia. *Canadian Mineralogist*, **30**: 249-287.
- Davenport, P.H., 1989. Gold and associated elements in lake sediment from regional surveys in the Sandy Lake Map Area (12H); Geological Survey Branch, Dept. of Mines and Energy, Government of Newfoundland and Labrador, Open File 12H/1012
- Deer, W.A, Howie, R.A. and Zussman, J., 1992. An introduction to the Rock Forming Minerals. Addison Wesley Longman Limited, Edinburgh Gate, England 696p
- Dunham, A.C. and Wilkinson, F.C.F., 1985. Sulphide droplets and the Unit 11/12 chromite band, Rhum: a mineralogical study. *Geological Magazine*, **122**: 539-548.
- Erdmer, P., 1986. Geology of the Long Range Inlier in Sandy Lake map area, western Newfoundland; *in* Current Research, Part B, Geological Survey of Canada, Paper **86-1B**, 19-27.
- Ercit, T.S., 2002. The mess that is "Allanite". *Canadian Mineralogist*, **40**: 1411-1419.
- Faithfull, J.W., 1985. The Lower Eastern Layered Series of Rhum. *Geological Magazine*, **122**: 459-468.
- Fitzpatrick, D., Butler, R. Jr. and Churchill, R., 2000. First and second year supplementary report on geology, line cutting, geophysics & trenching conducted on map staked licenses 6339M, 6943M, 69991M & 6993M, Taylor Brook Property, White Bay, north central Newfoundland, NTS Sheet 12H/11 (File 012H/11/1588)
- Harris, A. and Rose, M., 1997. Twin Ponds: Reconnaissance Geological and Geochemical Surveys, Licensees 5342M & 5674M NTS 12H/11

- Harris, A., 1998. Burin Minerals Limited, Twin Ponds Project: Geological and reconnaissance geochemical surveys. Licenses 5342M, 5674M & 5764M; NTS 12H/11. GS# 012H/11/1442
- Harris, A., 1998. Burin Minerals Limited, Twin Ponds Project: Geological and reconnaissance geochemical surveys. Licenses 5342M & 5764M; NTS 12H/11. GS# 012H/11/1596
- Hawthorne, F.C., 1981. Crystal chemistry of the amphiboles. *Reviews in Mineralogy*, **9A**: 1-102.
- Heaman, L.M., Erdmer, P, and Owen, J.V., 2002. U-Pb geochronologic constraints on the crustal evolution of the Long Range Inlier, Newfoundland. *Canadian Journal of Earth Sciences*, **39**: 845-865,
- Hoffman, E.L. and Dunn, B., 2002. Sample preparation and bulk analytical methods for PGE. *The Geology, Geochemistry, Mineralogy and Mineral Beneficiation of Platinum Group Elements*, *Edited by* L.J. Cabri, CIM Special Volume **54**: 1-11.
- Hunter, R.H., 1996. Textural Development in Cumulate Rocks. *In Layered Intrusions. Edited by* R.G. Cawthorn, Elsevier Science
- Hull, G., 2003. Flat Bay Brook property – Au & Ni-Cu-PGM's. Unpublished report prepared by the Matty Mitchell Prospectors Resource Room
- Hyde, R.S. 1982. Geology of the Carboniferous Deer Lake Basin. Map 82-007 (coloured). Scale: 1:100 000. Government of Newfoundland and Labrador, Department of Mines and Energy, Mineral Development Division. GS# NFLD/1849
- Hyde, R.S, Miller, H.G., Hiscott, R.N., and Wright, J.A., 1988. Basin architecture and thermal maturation in the strike-slip Deer Lake basin, Carboniferous of Newfoundland. *Basin Research*: **1**: 85-105.
- Irvine, T.N., and Baragar, W.R.A., 1971. A guide to the chemical classification of the common volcanic rocks. *Canadian Journal of Earth Sciences*, **8**: 523-548.
- Jensen, L.S. and Pyke, D.R., 1982. Komatiites in the Ontario portion of the Abitibi belt. *In*: Arndt, N.T. and Nisbet, E.G. (eds), *Komatiites*. George Allen and Unwin, London: 147-157.
- Kean, B.F., 1977. Geology of the Victoria Lake Map Area, Nfld; Report 77-4, Newfoundland Department of Mines and Energy, Mineral Development Division

- Kean, B.F., 1977. Victoria Lake, Windsor-Buchans, Newfoundland. Map 77-006. *In* Geology of the Victoria Lake map area (12A/6), Newfoundland. Government of Newfoundland and Labrador, Department of Mines and Energy, Mineral Development Division, Report 77-04, 14 pages, enclosure (map). GS# 012A/06/0198
- Kerr, A. and Leitch, A.M., 2005. Self-destructive sulfide segregation systems and the formation of high-grade magmatic ore deposits. *Economic Geology*, **100**: 311-332.
- Kissin, S.A., 1974. Phase relations in a portion of the Fe-S system. Doctoral dissertation, University of Toronto. Diss. Abst. Int., **37**, No. 12: p6033
- Lafrance, B., John, B.E., and Scoates, J.S., 1996. Syn-emplacement recrystallization and deformation microstructures in the Poe Mountain anorthosite, Wyoming. *Contributions to Mineralogy and Petrology*, **122**: 431-440.
- LeMaitre, R.W., Bateman, P., Dudek, A., Keller, J., Lameyer, LeBas M.J., Sabine, P.A., Schmid, R., Sorensen, H., Streckeinsen, A., Woolley, A.R., and Zanettin, B., 1989. A classification of igneous rocks and glossary of terms. Blackwell, Oxford.
- Li, C., Lightfoot, P.C., Amelin, Y and Naldrett, A.J., 2000. Contrasting petrological and geochemical relationships in the Voisey's Bay and Mushuau intrusions, Labrador Canada: implications for ore genesis. *Economic Geology*, **95**: 771-800.
- Lindsley, D.H., 1991. Experimental studies of oxide minerals. *Reviews in Mineralogy*, **25** 61-106. Mineralogical Society of America, Washington, DC, *Ed.* Lindsley, D.H.
- Longerich, H.P., 1995. Analysis of pressed pellets of geological samples using wavelength-dispersive X-ray fluorescence spectrometry; *X-Ray Spectrometry*, **24**: 123-136.
- McLelland and Whitney, 1977. The origin of garnet in the anorthosite charnockite suite of the Adirondacks; *Contributions to Mineralogy and Petrology*, **60**: 61-181.
- Macintosh, J., and French, V.A., 1995. Burgeo Highway Property: Licenses 4529 and 4531 first year assessment report on geology, prospecting and geochemistry: Parts of NTS 12B/08, 12B/09 and 12A/12. For New Island Minerals Limited, File NFLD 2617
- McDonough, W.F., and Sun, S.S., 1995. The composition of the Earth. *Chemical Geology*, **120**, no. 3-4: 223-253.

- Meschede, M., 1986. A method of discriminating between different types of mid-ocean ridge basalts and continental tholeiites with the Nb–Zr–Y diagram. *Chemical Geology*, **56**, no. 3-4: 207-218
- Morimoto, N., 1988. Nomenclature of pyroxenes. *Mineralogical Magazine*, **52**: 535-550.
- Naldrett, A.J., 2004. *Magmatic Sulfide Deposits: Geology, Geochemistry and Exploration*. Springer 727p.
- Nielson, H. 1979. *Lectures in Isotope Geology*. Ed. Jager E. and Hunziker J.C. Springer-Verlag. NY: 283-312.
- Nuri, A., 1980. Geological reconnaissance of a portion of the AND Grant west central Newfoundland. NTS 12A/3, A/5, A/6, A/7 includes Reid Lots 227 and 229. Victoria Lake Project. (File 12A(290))
- Owen, J.V., 1991. Geology of the Long Range Inlier, Newfoundland. Geological Survey of Canada: Bulletin 395.
- Owen, J.V. and Currie, K.L., 1991. The Disappointment Hill complex: Proterozoic granulites in southwestern Newfoundland. *Transactions of the Royal Society of Edinburgh: Earth Sciences*, **82**: 55-63.
- Owen, J.V., and Erdmer, P., 1986. Precambrian and Paleozoic metamorphism in the Long Range Inlier, western Newfoundland; in *Current Research, Part B*, Geological Survey of Canada, Paper **86-1B**: 29-38.
- Owen, J.V., and Erdmer, 1989. Metamorphic geology and regional geothermobarometry of Grenvillian massif: the Long Range Inlier, Newfoundland. *Precambrian Research*, **43**: 79-100.
- Pearce, J.A. and Norry, M.J., 1979. Petrogenetic implications of Ti, Zr, Y and Nb variations in volcanic rocks. *Contributions to Mineralogy and Petrology*, **69**: 33-47.
- Pearce, J.A., Harris, N.B. and Tindle, A.G., 1984. Trace Element Discrimination Diagrams for the Tectonic Interpretation of Granitic Rocks. *Journal of Petrology*, **25**, no. 4: 956-983.
- Pilgrim, L., and Regular, K., 1998. Third year assessment report, License 4525, Cabot Exploration Ltd., Flat Bay Brook Option, NST12B/8. Unpublished Report Cabot Exploration Ltd., 10pp
- Pollard, D.D., Muller, O.H. and Dockstader, D.R., 1975. The form and growth of fingered sheet intrusions. *Geological Society of America Bulletin*, **86**: 351-363.

- Riley, G.C., 1957. Red Indian Lake (west half), Newfoundland; Geological Survey of Canada, Map 8-1957, with descriptive notes
- Rollinson, H.R., 1993. Using geochemical data: evaluation, presentation, interpretation. Longman Scientific and Technical, New York, 353 p.
- Rose, M.J., 1998. The Economic Potential of the Taylor Brook Gabbro. Unpublished BSc Honours thesis, Memorial University of Newfoundland.
- Rosenberg, C.L., and Stünitz, H., 2003. Deformation and recrystallization of plagioclase along a temperature gradient: an example from the Bergell tonalite. *Journal of Structural Geology*, **25**: 389-408.
- Rudashevsky, N.S., Garuti, G., Andersen, J.C.Ø., Kretser, Y.L., Rudashevsky, V.N. and Zaccarini, F., 2002. Separation of accessory minerals from rocks and ores by hydroseparation (HS) technology: method and application to CHR-2 chromitite, Niquelândia, Brazil. *Trans. Institution Mining and Metallurgy (Section B: Applied. Earth Sci.)*, **111**: B87-B94.
- Sack, R.O. and Ghiorso, M.S., 1991. Chromian spinel as petrogenetic indicators: thermodynamic and petrological applications. *American Mineralogist*, **76**: 397-416.
- Strauss, H. 1997. The isotopic composition of sulphur through time. *Palaeogeography, Palaeoclimatology, Palaeoecology*, **132**: 97-118.
- Streckeisen, A., 1976. To each plutonic rock its proper name; *Earth Science Reviews*, **12**: 1-33
- Tait, S.R., 1985. Fluid dynamic and geochemical evolution of cyclic unit 10, Rhum Eastern Layered Series. *Geological Magazine*, **122**: 469-484.
- Taylor, R.W., 1964. Phase equilibria in the system FeO-Fe<sub>2</sub>O<sub>3</sub>-TiO<sub>2</sub> at 1300 °C. *American Mineralogist*, **49**: 1016-1030.
- Thurlow, J G, Barbour, D M, Desnoyers, D W, Burton, G B, MacNeil, J, Salib, P, Reed, L, and Balch, S J., 1987. Assessment report on geological, geochemical, geophysical, trenching and diamond drilling exploration for 1986 submission for the Anglo Newfoundland Development Company Limited charter, Reid lots 227-229, 231-235 and 247, crown lease lots A-B, E and R and fee simple grants volume 1 folios 61-62 and 110 and volume 2 folios 23 and 29 in the Buchans, Great Burnt Lake, Valentine Lake, Mary March, Victoria Lake and Bobbys Pond areas, Newfoundland, 8 reports. Noranda Exploration Company Limited, Canacord

- Incorporated, and Canacord Resources Incorporated Unpublished report, 2422 pages. [GSB# NFLD/1737].
- Van Berkel, J.T., 1987. Geology of the Dashwoods Pond, St. Fintan's and Main Gut map areas, southwest Newfoundland. Current Research, Part A, Geological Survey of Canada, Paper : 399-408.
- Van Berkel, J.T., Johnston, H.P., and Currie, K.L., 1986. A preliminary report on the geology of the southern Long Range, southwest Newfoundland; *in* Current Research, Part B, Geological Survey of Canada, Paper **86-1B**: 157-170.
- Waldron, J.W.F., Anderson, S.D., Cawood, P.A., Goodwin, L.B., Hall, J., Jamieson, R.A., Palmer, S.E., Stockmal, G.S. and Williams, P.F., 1998. Evolution of the Appalachian Laurentian Margin: Lithoprobe results in western Newfoundland. Canadian Journal of Earth Science, **35**: 1271-1287.
- Waychunas, G.A., 1991. Crystal chemistry of oxides and oxyhydroxides. Reviews in Mineralogy, **25**: 11-68. Mineralogical Society of America, Washington, DC, *Ed.* Lindsley, D.H.
- White, D.R., and Green, V., 1995. Report of work to November 1995, Little Barachois Brook Property, NTS 12B/08. GSB File 012B/08/0428
- Whitney, P.R. and McLelland, J.M., 1972. Origin of Coronas in Metagabbros of the Adirondack Mtns., NY. Contributions to Mineralogy and Petrology, **39**: 81-98.
- Williams, H., 1970. Red Indian Lake (east half), Newfoundland; Geological Survey of Canada, Map 1196 A, with descriptive notes.
- Williams, H, Colman-Sadd, S.P., and Swindon, H.S., 1988. Tectonic-stratigraphic subdivisions of central Newfoundland. Current Research, Part B, Geological Survey of Canada, Paper **88-1B**: 91-98.
- Williams, H., 1979. Appalachian Orogen in Canada. Canadian Journal of Earth Science, **16**: 792-807.
- Wilson, M., 1989. Igneous Petrogenesis. Unwin Hyman, London
- Winter, J.D., 2001. An introduction to Igneous and Metamorphic Petrology. Prentice Hall, NJ. 697p

Appendix 1.1: Red Cross Lake Intrusive Suite sample locations  
 All locations are in NAD 27, Zone 21

<b>Sample</b>	<b>UTM East</b>	<b>UTM North</b>	<b>Sample</b>	<b>UTM East</b>	<b>UTM North</b>
<b>RIC01</b>	497999	5360096	<b>RIC49</b>	502602	5360842
<b>RIC02</b>	498010	5359947	<b>RIC50</b>	499870	5360670
<b>RIC03</b>	498165	5359794	<b>RIC51</b>	499230	5360402
<b>RIC04</b>	498326	5359667	<b>RIC52</b>	499771	5360382
<b>RIC05</b>	498655	5359602	<b>RIC53</b>	499960	5360410
<b>RIC06</b>	498835	5359573	<b>RIC54</b>	500103	5360428
<b>RIC07</b>	499026	5359612	<b>RIC55</b>	499929	5361743
<b>RIC08</b>	499334	5359867	<b>RIC56</b>	499878	5361709
<b>RIC09</b>	500203	5360065	<b>RIC57</b>	499521	5362606
<b>RIC10</b>	497240	5362275	<b>RIC58</b>	499552	5362751
<b>RIC11</b>	497539	5362010	<b>RIC59</b>	498960	5363471
<b>RIC12</b>	497532	5361852	<b>RIC60</b>	498116	5364041
<b>RIC13</b>	497502	5361599	<b>RIC61</b>	499184	5363028
<b>RIC14</b>	497665	5361496	<b>RIC62</b>	499206	5362715
<b>RIC15</b>	497974	5360985	<b>RIC63</b>	499801	5362153
<b>RIC16</b>	498047	5360950	<b>RIC64</b>	502782	5360584
<b>RIC17</b>	498150	5360703	<b>RIC65</b>	502812	5360555
<b>RIC18</b>	497933	5360421	<b>RIC66</b>	502571	5360841
<b>RIC19</b>	498016	5360179	<b>RIC67</b>	502694	5360704
<b>RIC20</b>	498445	5360083	<b>RIC68</b>	502964	5360533
<b>RIC21</b>	498307	5360099	<b>RIC69</b>	503090	5360518
<b>RIC22</b>	498712	5360178	<b>RIC70</b>	503185	5360047
<b>RIC23</b>	499105	5360114	<b>RIC71</b>	503134	5360109
<b>RIC24</b>	497891	5358465	<b>RIC72</b>	503115	5360241
<b>RIC25</b>	497986	5358644	<b>RIC73</b>	503147	5360335
<b>RIC26</b>	497985	5358695	<b>RIC74</b>	503161	5360373
<b>RIC27</b>	498045	5359174	<b>RIC75</b>	503125	5360470
<b>RIC28</b>	498045	5359406	<b>RIC76</b>	501320	5360601
<b>RIC29</b>	498349	5360286	<b>RIC77</b>	502740	5363276
<b>RIC30</b>	498807	5360598	<b>RIC78</b>	474027	5350499
<b>RIC31</b>	499387	5360703			
<b>RIC32</b>	499450	5360762			
<b>RIC33</b>	502723	5360619			
<b>RIC34</b>	505589	5360780			
<b>RIC35</b>	505637	5360819			
<b>RIC36</b>	505482	5360723			
<b>RIC37</b>	505278	5360739			
<b>RIC38</b>	505167	5360826			
<b>RIC39</b>	504782	5360980			
<b>RIC40</b>	504710	5361062			
<b>RIC41</b>	504657	5361042			
<b>RIC42</b>	504604	5361025			
<b>RIC43</b>	504013	5360920			
<b>RIC44</b>	503789	5360791			
<b>RIC45</b>	503534	5360848			
<b>RIC46</b>	503449	5360855			
<b>RIC47</b>	503266	5360791			
<b>RIC48</b>	503090	5360610			

Appendix 1.2: Steel Mountain Anorthosite sample locations  
 All locations are in NAD 27, Zone 21

<b>Sample</b>	<b>UTM East</b>	<b>UTM North</b>	<b>Sample</b>	<b>UTM East</b>	<b>UTM North</b>
<b>SMA01</b>	406525	5359686	<b>SMA49</b>	405593	5359278
<b>SMA02</b>	406397	5359978	<b>SMA50</b>	405623	5359367
<b>SMA03</b>	406120	5360410	<b>SMA51</b>	405354	5359535
<b>SMA04</b>	406050	5360278	<b>SMA52</b>	405175	5359253
<b>SMA05</b>	406000	5360169	<b>SMA53</b>	n/a	n/a
<b>SMA06</b>	405770	5360222	<b>SMA54</b>	405310	5359172
<b>SMA07</b>	405697	5360353	<b>SMA55</b>	406135	5358235
<b>SMA08</b>	405684	5360389	<b>SMA56</b>	406325	5358305
<b>SMA09</b>	405267	5360532	<b>SMA57</b>	406568	5358343
<b>SMA10</b>	n/a	n/a	<b>SMA58</b>	406954	5358204
<b>SMA11</b>	405016	5360433	<b>SMA59</b>	407297	5358241
<b>SMA12</b>	404870	5360446	<b>SMA60</b>	407292	5358133
<b>SMA13</b>	404851	5360392	<b>SMA61</b>	407259	5358070
<b>SMA14</b>	404554	5360482	<b>SMA62</b>	n/a	n/a
<b>SMA15</b>	404430	5360487	<b>SMA63</b>	407215	5357793
<b>SMA16</b>	404382	5360547	<b>SMA64</b>	407427	5357761
<b>SMA17</b>	404686	5360474	<b>SMA65</b>	407478	5357639
<b>SMA18</b>	405996	5360162	<b>SMA66</b>	407542	5357561
<b>SMA19</b>	405707	5359063	<b>SMA67</b>	407564	5357635
<b>SMA20</b>	406402	5360742	<b>SMA68</b>	407492	5357793
<b>SMA21</b>	406434	5360793	<b>SMA69</b>	407634	5358506
<b>SMA22</b>	406431	5361223	<b>SMA70</b>	407656	5358540
<b>SMA23</b>	406625	5361813	<b>SMA71</b>	407683	5358616
<b>SMA24</b>	406369	5361902	<b>SMA72</b>	407946	5358683
<b>SMA25</b>	406453	5361866	<b>SMA73</b>	407970	5358732
<b>SMA26</b>	406631	5361738	<b>SMA74</b>	408045	5358771
<b>SMA27</b>	406486	5361597	<b>SMA75</b>	407575	5359090
<b>SMA28</b>	406379	5361470	<b>SMA76</b>	408120	5359020
<b>SMA29</b>	406274	5361446	<b>SMA77</b>	408077	5359048
<b>SMA30</b>	406194	5361518	<b>SMA78</b>	407768	5358880
<b>SMA31</b>	406015	5361501	<b>SMA79</b>	407415	5358673
<b>SMA32</b>	405252	5358321	<b>SMA80</b>	407380	5358674
<b>SMA33</b>	405252	5358321	<b>SMA81</b>	407278	5358819
<b>SMA34</b>	405252	5358321	<b>SMA82</b>	407272	5358852
<b>SMA35</b>	409815	5359800	<b>SMA83</b>	407530	5359149
<b>SMA36</b>	410076	5359652	<b>SMA84</b>	407292	5359360
<b>SMA37</b>	410214	5360291	<b>SMA85</b>	n/a	n/a
<b>SMA38</b>	400155	5361827	<b>SMA86</b>	406780	5359533
<b>SMA39</b>	401440	5361767	<b>SMA87</b>	406648	5359554
<b>SMA40</b>	396567	5361201	<b>SMA88</b>	406336	5359510
<b>SMA41</b>	405110	5358247	<b>SMA89</b>	405962	5359233
<b>SMA42</b>	405097	5358237	<b>SMA90</b>	405708	5359064
<b>SMA43</b>	405057	5358230			
<b>SMA44</b>	404982	5358181			
<b>SMA45</b>	405210	5358579			
<b>SMA46</b>	405343	5358878			
<b>SMA47</b>	405398	5358967			
<b>SMA48</b>	405403	5359007			

Appendix 1.3: Taylor Brook Gabbro Suite sample locations

All locations are in NAD 27, Zone 21

Sample	UTM East	UTM North	Sample	UTM East	UTM North
TBC01	488111	5493487	TBC46	493727	5495266
TBC02	488082	5493617	TBC47	493771	5495222
TBC03	488023	5494906	TBC48	493804	5494901
TBC04	488469	5495263	TBC49	493555	5494871
TBC05	489665	5495545	TBC50	493155	5494642
TBC06	492579	5495972	TBC51	492432	5494737
TBC07	494437	5497507	TBC52	491946	5494989
TBC08	494394	5497657	TBC53	491411	5495437
TBC09	494318	5497645	TBC54	491034	5495435
TBC10	493990	5497595	TBC55	490663	5495379
TBC11	493871	5497596	TBC56	490459	5495421
TBC12	493830	5497582	TBC57	489838	5495546
TBC12B	493847	5497583	TBC58	489038	5495560
TBC13	493815	5497544	TBC59	488229	5493802
TBC13B	493848	5497536	TBC60	488483	5493932
TBC13C	493858	5497468	TBC61	n/a	n/a
TBC14	493715	5497596	TBC62	488746	5494258
TBC15	493743	5497567	TBC63	488720	5494268
TBC16	493629	5497594	TBC64	488604	5494310
TBC17	493559	5497535	TBC65	488527	5494318
TBC18	493528	5497483	TBC66	488056	5494369
TBC19	493427	5497337	TBC67	486610	5498194
TBC20	493487	5497390	TBC68	486641	5498100
TBC21	493263	5497209	TBC69	486653	5498020
TBC22	493192	5497181	TBC70	486662	5497833
TBC23	493057	5497067	TBC71	486682	5497606
TBC24	492969	5496922	TBC72	486679	5497448
TBC25	492854	5496774	TBC73	486626	5497231
TBC26	492545	5496439	TBC74	486554	5497075
TBC27	492398	5496289	TBC75	486436	5496971
TBC28	492141	5495977	TBC76	486387	5496919
TBC29	492064	5495698	TBC77	486334	5496861
TBC30	491829	5495490	TBC78	486254	5496749
TBC31	491522	5495477	TBC79	486094	5496550
TBC32	493119	5494346	TBC80	486578	5503407
TBC33	493481	5493993	TBC81	486460	5503503
TBC34	493671	5494007	TBC82	486381	5503560
TBC35	494551	5493998	TBC83	486402	5503673
TBC36	494398	5493922	TBC84	486218	5503902
TBC37	494281	5493984	TBC85	486192	5504046
TBC38	494258	5494027	TBC86	486061	5503981
TBC39	494120	5494033	TBC87	485812	5503916
TBC40	n/a	n/a	TBC88	485565	5503866
TBC41	492832	5493796	TBC89	485255	5503843
TBC42	493157	5494100	TBC90	485018	5503781
TBC43	493273	5494318	TBC91	484392	5503722
TBC44	493350	5494327	TBC92	485152	5504262

Appendix 1.3: Taylor Brook Gabbro Suite sample locations  
 All locations are in NAD 27, Zone 21

<b>TBC45</b>	493402	5494346	<b>TBC93</b>	485414	5504264
<b>Sample</b>	<b>UTM East</b>	<b>UTM North</b>			
<b>TBC94</b>	486015	5504257			
<b>TBC95</b>	486460	5504508			
<b>TBC96</b>	486236	5504223			
<b>TBC97</b>	486081	5504241			
<b>TBC98</b>	485933	5504303			
<b>TBC99</b>	485763	5504306			
<b>TBC100</b>	485599	5504343			
<b>TBC101</b>	485469	5504354			
<b>TBC102</b>	485405	5504327			
<b>TBC103</b>	n/a	n/a			
<b>TBC104</b>	484606	5500996			
<b>TBC105</b>	486666	5504827			
<b>TBC106</b>	486468	5504915			
<b>TBC107</b>	486424	5505085			
<b>TBC108</b>	486578	5505158			
<b>TBC109</b>	486708	5505053			
<b>TBC110</b>	486937	5504573			
<b>TBC111</b>	487165	5503655			
<b>TBC112</b>	487264	5503458			
<b>TBC113</b>	n/a	n/a			
<b>TBC114</b>	487515	5502126			
<b>TBC115</b>	487802	5501980			
<b>TBC115B</b>	487802	5501980			
<b>TBC116</b>	487160	5503756			
<b>TBC117</b>	484742	5503562			
<b>TBC118</b>	484649	5503329			
<b>TBC119</b>	484450	5503063			
<b>TBC120</b>	484442	5502937			
<b>TBC121</b>	484266	5502711			
<b>TBC122</b>	484147	5502630			
<b>TBC123</b>	488713	5495514			
<b>TBC124</b>	488570	5495314			

## Appendix 2.1: Red Cross Lake Intrusive Suite nomenclature and mineralogy

RIC	Series	Normative name	Silicates % (normalized/ set to 100% silicates where applicable)
RIC-01	Lower	melatroctolite	Ol 85% + Pl 13% + Cpx 2%
RIC-02	Lower	dunite	Ol 85% + Opx 9% + Pl 5%
RIC-03	Lower	leucotroctolite	Pl 80% + Ol 20%
RIC-04	Lower	leucotroctolite	Pl 72% + Ol 25% + trace Opx
RIC-06	Lower	troctolite	Pl 65% + Ol 30% + Cpx 4% ± amp+ sulfide+oxides 1%
RIC-08	Lower	olivine gabbro	Pl 50% + Cpx 35% + Ol 5% + (serp+chl+act) 5%
RIC-09	xeno	xenolith	
RIC-10	CR	xenolith	
RIC-12	Upper	pyroxene amphibole gabbronorite	Pl 50% + (Hb + Act) 25% + Cpx 20% + Bt 5% ± Opx
RIC-14	Upper	leucogabbro	Pl 80% + Hb 10% + Cpx 7% + Bt 1% + Mt+Ilm 2%
RIC-15	Lower	leucogabbro	Pl 65% +( Bt + brown grunge) 5% + (Cpx + Amp) 25% + oxides (5%)
RIC-17	Upper	EPTGB	Pl 40%+ ept 15% + (amp +grunge) 40% + (Pyx + cal) 5%
RIC-18R	Lower	leucogabbronorite	Pl 65% + Cpx 10% + Opx 10% + Bt 5% + Ol 2% oxides+grunge 8%
RIC-20	Lower	olivine gabbro	Pl 60% + Ol 20% + Cpx 20%
RIC-21	Lower	melatroctolite	Ol 80% + Pl 15% + Cpx 5%
RIC-22	Lower	leucogabbro	Pl 70% + Ol 20% + Cpx 10% + trace amp
RIC-23A	xeno	xenolith	
RIC-23B	Upper	leucogabbro	Pl 75% + Cpx10% + Opx 2% + Ol 5% + Bt 3% + Amp <5%
RIC-23C	Upper	pyroxene amphibole gabbronorite	n/a
RIC-24	n/a		
RIC-25	CR	xenolith	n/a
RIC27	Lower	pyroxene amphibole gabbronorite	Pl 50% + Srp 10% + Cpx 15% + (Act+musc +Chl) 20% + Hb 5%
RIC-30A	Lower	leucotroctolite	Pl 70% + Ol 25% + Cpx 5%
RIC-30B	Lower	leucotroctolite (layer in leucogabbro)	Pl 70% + Cpx 20% + Ol 10%
RIC-32	Upper	pyroxene amphibole gabbronorite	Pl 30% + Cpx 30% + Act 15% + Hb 10% + Opx 10% + Bt 5%
RIC-38A	xeno	xenolith	n/a
RIC-38B	Upper	pyroxene amphibole gabbronorite	Pl 50% + Amp 40% + Bt 5% + (Qtz + ept+ oxides) 5%
RIC-42	Upper	pyroxene amphibole gabbronorite	Pl 40% + Cpx 10% + Act 35% + Bt 5% + Qtz 10% + trace OPX
RIC-44	Upper	pyroxene amphibole gabbronorite	Pl 55% + Cpx 10% + Act 15% + Hb 10% + Bt 5% + Qtz 5% + Opx (tr)
RIC-46	Lower	pyroxene amphibole gabbronorite	Pl 50% + Cpx 5% + Opx 5% +Hb 15% Act 15% + Bt 5% + Ol (tr)
RIC-48	Lower	pyroxene amphibole gabbronorite	Pl 40% + Cpx 10% + Opx 5% + Hb 15% + Act 20% + Bt 8% + oxides 2%

Appendix 2.1: Red Cross Lake Intrusive Suite nomenclature and mineralogy

Sample	Series	Normative name	Silicates % (normalized/est. to 100% silicates where applicable)
RIC-50	Upper	leucogabbro	Pl 65% + Cpx 5% + Opx 5% + Bt 10% + Hb 10% + Act 5%
RIC-51.1C	xeno	olivine gabbro	Pl 45% + Cpx 20% + Opx 10% + Ol 10% + Bt 5% ± graphite/grunge 5%
RIC-51.2C	xeno	olivine gabbro	Pl 40% + Cpx 15% + Ol 20% + Bt 10% + Amp 15%
RIC-51A	Upper	leucogabbro	Pl 65% + Cpx 10% + Opx 2% + Act 10% + Hb 3% + Bt 5% ± Or ± Mc ± Ol
RIC-51B	Upper	amphibole gabbro	Pl 40% + Amp 10% + Qtz 5% + Bt 35% + Act/meta pyx 10%
RIC-52A	Upper	pyroxene amphibole gabbronorite	Pl 35% + Cpx 5% + Opx 40% + Ol (tr) + Amp 15% + Bt 5%
RIC-53	xeno	pyroxene amphibole gabbronorite	n/a
RIC-54	Upper	pyroxene amphibole gabbronorite	Pl 60% + Cpx 10% + Hb 25% + Bt 2% + Opx 3% ± Or ± Mc
RIC-56	Upper	leucogabbro	Pl 65% + Cpx 13% + Bt 10% + Amp 5% + Qtz 5% ± Opx
RIC-57	xeno	xenolith	
RIC-61	CR	xenolith	
RIC-62	CR	xenolith	
RIC-63	Upper	pyroxene amphibole gabbronorite	Pl 35% + Amp 12% + Cpx 30% + Opx 5% + Bt 10% + Ol 8%
RIC-65	Lower	serpentinite	Srp 55% + Cal 15% + (Amp + grunge) 18% + Opx 10% + Ol 2% (relict)
RIC-67	Upper	leucogabbro	Pl 60% + Cpx 5% + Bt 15% + Hb 5% + Act 15%
RIC-68A	Lower	serpentinite	Tic + Chl + Srp + Cal + Act + Bt ± Cpx
RIC-68B	Lower	mafic dike	Cal + grunge
RIC-69	Lower	serpentinite	(Srp + Chl) 45% + Cpx 25% + Opx 5% + Cal 25% + (Amp ± Ol) tr
RIC-71	xeno	xenolith	n/a
RIC-74	Upper	amphibole gabbro	Pl 50% + Cpx 5% + Hb 15% + Act 25% + Bt 5% + Ep
RIC-76	Upper	pyroxene amphibole gabbronorite	Pl 45% + Amp 30% + Bt 10% + Cpx 15%
RIC-76B	xeno	xenolith	n/a
RIC-78A	VL	pyroxene amphibole gabbronorite	
RIC-78B	VL	pyroxene amphibole gabbronorite	

**Abbreviations**

EPTGB epidote gabbro

VL Victoria Lake Intrusion

CR Country rock - may or may not be a xenolith

Appendix 2.2: Steel Mountain Anorthosite nomenclature and mineralogy

Sample	Normative name	Silicates + oxides % (normalized/set to 100% silicates where applicable)
SMA-05	leuconorite	100% Pl
SMA-09	leucogabbronorite	70% Pl + 20% Opx + 8% Cpx + 2% Mt + Ilm
SMA-12	gabbronorite	60% Pl + 25% Amp + 10% Chl + 5% ser + <1% accessory silicates+oxides
SMA-15	anorthosite	98% Pl + 2% OPX ; trace Bt ± rutile inclusions
SMA-18	massive oxide (avg. field mineralogy is leuconorite)	PTS is MO + 20% Opx + 5% Cpx + 5% Gnt + 1% Pl
SMA-20A	anorthosite	>99% Pl + trace ept ± Or ± oxides
SMA-20B	melanorite	80% OPX + 20% Pl
SMA-24	anorthosite	95% Pl + 2% Chl+Ept + 3% Mt+Ilm+po (±marcasite)
SMA-26	leuconorite	95% Pl (± Mc) + 4% Cpx + 1% Opx
SMA-31	melanorite (avg. field mineralogy is norite)	70% Opx + 20% Pl (± Mc) + 5% Cpx + 2% Amp + 1% Rt + 2% Mt+Ilm; trace py
SMA-33	norite	50% Pl + 40% Opx + 5% uralite/Amp + 5% (Cpx + Gnt + Mt + Ilm + Chl)
SMA-37	gabbronorite	60% Pl + 20% Opx 10% Cpx + 10% Amp
SMA-38c	leuconorite	60% sericite/calcite/grunge + 20% chlorite + 10% qtz + 8-10% (py+ccp) + 2% Amp
SMA-40A	Sheep Brook	70% Po + 25% Py + 4% Ccp + trace Pn + trace (mt+ hem)
SMA-42	gabbronorite (avg. field mineralogy is melanorite)	50% Pl/ser/cal + 45% chl+act+Bt ±cal + 5% relict pyx + oxides
SMA-48	leuconorite	70% Pl + 22% Opx + 3% Cpx + 3% Bt + 2% oxides (Mt + Ilm + Hc)
SMA-57	norite	50% Pl + 40% Opx + 5% uralite/Amp + 5% (Cpx + Gnt + Mt + Ilm + Chl)
SMA-61A	leuconorite	65% Pl + 15% ept + 10% act + 5% Mt + 4% chl + 1% unknown brown opaque (Fe carbonate?)
SMA-61B	leucogabbronorite	65% Pl + 30% act + 2% chl + 2% Mt + <1% Bt+Ept+Rt
SMA-65	anorthosite	55% Act + 30% Ept + 10% Pl + 2% (relict) Cpx + 2% (Mt+Ilm+Hem) + 1% (Py+Ccp)
SMA-71	leucogabbronorite	>99% Plagioclase
SMA-73	leuconorite (avg. field mineralogy is gabbronorite)	70% Pl + 25% Opx + 3% Hb+Act + 2% Bt + trace Rt/Spn
SMA-76	leucogabbronorite	70% Pl (+ minor Mc + 15% Act+Hb + 10% Bt + 4% chl + 1% Mt + Ilm + Hem + trace Ept
SMA-87	anorthosite (avg. field mineralogy)	65% Green (act+chl+ept) + 35% white (Pl+ser)
SMA-90A	leuconorite	60% Plagioclase (incl. 25% ser) + 20% meta pyx + 15% act+chl + 4% (Mt+Ilm+Hem) + 1% (Bt + Ept)
SMA-90B	norite	65% Pl + 20% Opx + 10% Cpx + 2% Amp + 3% Bt+Rt+Mt-Ilm + <1% Gnt
SMA-Q1	massive oxides	no silicates
SMA-Q2	semimassive oxide	50% Mt + 32% Pl + 8% Ilm + 3% Amp (act?) + 2% Bt + 2% Ept + 1% Chl + trace hercynite

\*In some cases, the PTS was not representative of the outcrop or surrounding rocks and here both the field name and normative PTS name are listed

Appendix 2.3: Taylor Brook Gabbro Suite nomenclature and mineralogy

Sample	Zone	Normative name	Modal Mineralogy
TBC-002A	CR	marble	98% cal + 1% Cpx + 1 % Trem
TBC-002B	MD	amphibole gabbro	60% pl + 35% amp + 2% Bt + 1% Po + 1% graphite + 1% Qtz ± Ol
TBC-006B	TBGS	leuco gabbro	65% pl + 25% Cpx + 2% Ol + 3% Qtz + 5% Fe-Ti ox
TBC-011B	TBGS	leuco PAG	65% pl + 20% Cpx + 5% Bt + 3% Opx + 2% Fe-Ti ox (+ 2% xeno) ± Sulfide
TBC-016A	TBGS	leuco PAG	65% pl + 18% Opx + 6% Cpx + 5% Amp + 2% Qtz + 2% Bt + 2% Fe-Ti ox ± Sulfide
TBC-021A	TBGS	PAG	60% pl + 15% Opx + 10% Cpx + 10% Amp + 1% Qtz + 1% Bt + 3% Fe-Ti ox
TBC-021B	MD	amphibole gabbro	45% pl 50% Amp + 2% Fe-Ti ox + 2% Uralite + 1% Cpx+Sulfide
TBC-024A	MD	amphibole gabbro	50% pl + 45% Amp + 1% Sulfide + 2% Bt + 2% Fe-Ti ox
TBC-024B	TBGS	leuco PAG	65% pl + 4% Bt + 5% Amp + 10% Opx + 15% Cpx + 1% Fe-Ti ox ± Sulfide
TBC-026B.1	TBGS	leuco amphibole gabbro	80% pl + 10% Hb + 5% Bt + 3% Qtz + 2% Fe-Ti ox
TBC-026B.2	TBGS	amphibole gabbro	50% pl + 42% Amp + 3% Bt + 1% Sulfide + 1% Qtz + 3% Fe-Ti ox
TBC-030A	TBGS	leuco gabbro	70% pl + 24% Cpx + 5% Fe-Ti ox + 1% Bt ± Opx
TBC-030B	MD	mela PAG	30% pl + 55% Amp + 10% Cpx + 3% Qtz + 2% Fe-Ti ox
TBC-032	TBGS	leuco amphibole gabbro	65% pl + 25% Amp + 1% Cpx + 3% Bt + 1% Chl + 5% Fe-Ti ox
TBC-034	TBGS	PAG	50% pl + 30% Amp + 10% Cpx + 2% Opx + 5% Bt + 3% Fe-Ti ox ± Sulfide
TBC-039	TBGS	leuco PAG	70% pl + 5% Amp + 10% Bt + 10% Cpx + 5% Fe-Ti ox
TBC-047	TBGS	amphibole gabbro	40% pl + 10% Cal + 10% Bt + 5% Amp + 5% Fe-Ti ox + 30% grunge
TBC-048A	TBGS	leuco PAG	25% pl + 10% Qtz + 5% Cpx + 8% Fe-Ti ox + 2% Amp + 50% grunge
TBC-048B	TBGS	leuco PAG	70% pl + 5% Qtz + 19% Opx + 5% Amp + 1% Fe-Ti ox
TBC-048C	TBGS	leuco amphibole gabbro	65% pl + 3% Cpx + 2% Bt + 8% Qtz + 2% Fe-Ti ox + 20% grunge

Appendix 2.3: Taylor Brook Gabbro Suite nomenclature and mineralogy

Sample	Zone	Normative name	Modal Mineralogy
TBC-049	TBGS	leuco amphibole gabbro	65% pl + 3% cpx + 4% Bt + 8% amp + 3% Sulfide + 2 % Fe-Ti ox + 15% grunge
TBC-055	TBGS	PAG	40% pl + 35% cpx + 5% opx + 7% amp + 3% Bt + 10% Fe-Ti ox
TBC-056	TBGS	PAG	60% pl + 15% amp + 13% cpx + 5% opx + 2% Bt + 5% Fe-Ti ox
TBC-060	TBGS	leuco PAG	65% pl + 15% Cpx + 5% opx + 2% Bt + 3% amp + 10% Fe-Ti ox
TBC-064.1	MD	amphibole gabbro	50% pl + 49% amp + 1% Fe-Ti ox ± Sulfide
TBC-068.2	TBGS	leuco PAG	65% pl + 20% amp + 14% cpx + 1% Fe-Ti ox
TBC-069	TBGS	pyroxenite	92% cpx + 5% opx + 2% Sulfide + 1% Fe-Ti ox
TBC-070	TBGS	leuco amphibole gabbro	75% pl + 5% Fe-Ti ox + 2% cpx + 18% amp/grunge
TBC-083	TBGP	mela amphibole gabbro	30% pl + 15% chl + 2% opx + 1% cpx + 2% ept + 50% act ± Sulfide, Fe-Ti ox
TBC-085	TBGP	amphibole gabbro	60% pl + 8% hb + 2% ept + 25% act + 5% chl ± cpx, opx Fe-Ti ox
TBC-088.1	TBGP	PAG	60% pl + 10% cpx + 2% ept + 3% Hb + 3% Chl + 22% act
TBC-088.2	TBGP	amphibole gabbro	40% pl + 15% chl + 5% Hb + 2% ept + 38% Act ± Fe-Ti ox, Sulfide
TBC-089	TBGP	gabbronorite	40% pl + 47% cpx + 5% Ol + 5% Hb + 3% opx ± Fe-Ti ox, Sulfide
TBC-090F	TBGP	amphibole gabbro	60% pl + 25% act + 5% ept + 5% Hb + 5% Chl
TBC-090M	MD	amphibole gabbro	35% pl + 58% Act + 5% Hb + 2% Chl
TBC-091	TBGP	PAG	40% pl + 25% Hb + 25 % Cpx + 7% Opx + 3% Fe-Ti ox
TBC-092	TBGP	leuco amphibole gabbro	90% pl + 5% act + 4% Chl + 1% Hb
TBC-095.1	TBGP	anorthosite	95% pl + 3% act + 1% Cpx + 1% ept
TBC-095.2	MD	amphibole gabbro	45% pl + 55% Hb ± trace Sulfide, Fe-Ti ox
TBC-100	TBGP	troctolite	50% pl + 42% Ol + 4% Cpx + 4% amp ± Fe-Ti ox, Sulfide
TBC-104	TBGP	amphibole gabbro	60% pl + 20% chl + 15% act + 4% Hb + 1% Cpx ± trace Her
TBC-105	TBGP	amphibole gabbro	55% pl + 30% act + 10% Hb + 5% Cpx
TBC-107	TBGP	gabbronorite	40% pl + 15% Fe-Ti ox + 10% Opx + 4% Hb + 31% Cpx ± Her
TBC-111	TBGP	granite	60% pl + 40% qtz
TBC-113	TBGP	mela PAG	15% pl + 50% Cpx + 15% Hb + 10% Opx + 10% Fe-Ti ox

Appendix 2.3: Taylor Brook Gabbro Suite nomenclature and mineralogy

Sample	Zone	Normative name	Modal Mineralogy
TBC-117	TBGP	leuco amphibole gabbro	75% pl + 1% Hb + 4% Fe-Ti ox + 20% Act + trace ept, Sulfide
TBC-118	TBGP	leuco gabbronorite	70% pl + 3% Hb + 7% Fe-Ti ox + 15% Cpx + 5% opx
TBC-119A	TBGP	n/a	n/a
TBC-119B	TBGP	mela amphibole gabbro	35% pl + 25% Hb + 40% Act
TBC-119C	TBGP	n/a	n/a
TBC-124	TBGS	amphibole gabbro	50% pl + 40% Hb + 5% Cpx + 5% Fe-Ti ox

\* because of the heterogeneity of samples from mapping, only samples with a PTS is listed here

**Abbreviations**

TBGS= Taylor Brook Gabbro Suite (main mass)

TBGP= Taylor Brook Gabbro Pegmatite (northern unit)

CR= country rock

MD= mafic dike

PAG= pyroxene amphibole gabbro



Detaction Limit	0.01	0.01	0.02	0.01	<0.01	26	45	<0.01	<0.01	11	<0.01	7	8	<0.01	0.01	5	4	<0.1	<0.1	<1	2	4	18	1	2	1	2	1	29	47	5	4	5	Total - (S+P+K+Ca)
SMA-05	5.08	1.89	26.55	52.98	0.07	199	864	0.67	8.72	<11	0.29	27	33	0.04	2.19	22	8	<0.1	1	2	8	18	<18	2	940	2	6	<1	331	<47	<5	<4	<5	98.69
SMA-09	4.42	3.90	24.33	51.02	0.04	282	0	0.62	7.78	<11	0.43	58	131	0.06	4.84	98	33	<0.1	1	14	13	17	<18	1	820	1	<2	<1	282	<47	<5	<4	<5	97.60
SMA-12	4.14	5.78	24.04	54.21	0.02	280	134	0.41	7.13	<11	0.17	22	121	0.04	3.21	28	12	<0.1	1	8	12	16	<18	1	841	<1	<2	<1	244	<47	<5	<4	<5	99.33
SMA-15	5.11	0.21	27.97	52.96	0.03	176	60	0.83	9.26	<11	0.12	9	10	0.01	0.59	7	7	<0.1	1	2	<2	17	<18	1	1021	<1	<2	<1	368	<47	<5	<4	<5	97.25
SMA-18	0.23	5.74	7.72	10.93	0.02	396	164	0.08	0.89	14	12.61	2500	7419	0.20	58.62	726	50	<0.1	3	8	467	95	21	2	37	<1	65	4	33	<47	15	7	<5	98.23
SMA-20A	5.36	0.08	28.18	54.20	0.03	117	105	0.94	8.91	<11	0.10	<7	<8	0.00	0.45	<5	6	<0.1	1	2	<2	17	<18	2	988	<1	<2	<1	434	<47	<5	<4	<5	98.42
SMA-24	5.47	0.04	28.51	54.04	0.02	161	49	0.82	8.82	<11	0.09	<7	<8	0.00	0.39	36	27	<0.1	1	<1	<2	17	<18	3	992	<1	<2	<1	372	<47	<5	<4	<5	98.37
SMA-26	4.52	4.83	24.14	53.02	0.02	135	0	0.70	8.16	<11	0.24	44	141	0.07	4.73	51	7	<0.1	<0.1	<1	19	15	<18	3	759	3	2	<1	298	<47	<5	<4	<5	100.59
SMA-31	3.20	11.12	18.57	49.19	0.02	189	63	0.41	5.86	14	0.40	113	512	0.14	10.44	157	11	1	2	<1	40	13	<18	<1	495	3	5	<1	189	<47	<5	<4	<5	99.54
SMA-33	3.47	9.58	18.78	49.84	0.03	111	290	0.48	6.58	13	0.30	64	218	0.10	7.53	85	6	<0.1	1	<1	28	16	<18	2	656	2	3	<1	206	<47	<5	<4	<5	98.87
SMA-37	2.56	10.71	17.67	49.75	0.01	139	40	0.18	11.58	30	0.43	149	100	0.12	6.85	79	42	1	1	<1	17	16	<18	<1	534	6	8	<1	79	<47	<5	<4	<5	99.98
SMA-38C	1.85	6.04	16.76	43.37	0.02	23489	159	0.68	0.79	<11	0.12	22	30	0.12	20.23	621	1510	59	184	11	725	16	77	2	280	1	3	<1	201	<47	88	<4	<5	92.70
SMA-40	0.06	0.00	0.13	0.74	0.00	385223	0	0.00	0.02	<11	<0.01	<7	<8	0.00	48.60	15311	6661	489	1210	3	362	<4	88	<1	<2	<1	<2	<1	<29	<47	370	<4	<5	90.35
SMA-42	3.41	10.81	19.43	50.85	0.02	218	86	0.50	6.30	15	0.24	56	133	0.09	6.02	70	7	<0.1	2	<1	23	16	<18	2	766	1	<2	<1	220	<47	<5	<4	<5	97.83
SMA-48	4.53	4.93	24.30	52.26	0.03	115	297	0.58	8.09	<11	0.24	38	170	0.06	4.46	61	5	<0.1	2	<1	17	17	<18	2	805	1	<2	<1	275	<47	<5	<4	<5	99.68
SMA-57	3.45	9.65	19.26	49.78	0.02	106	50	0.55	6.35	21	0.37	89	330	0.12	9.00	113	8	<0.1	1	<1	38	14	<18	1	561	3	4	<1	245	<47	<5	<4	<5	99.71
SMA-61A	5.64	0.44	28.46	54.46	0.03	102	70	1.14	8.20	<11	0.40	35	80	0.01	1.52	14	8	<0.1	1	<1	4	18	<18	2	1032	<1	<2	<1	480	<47	<5	<4	<5	100.49
SMA-61B	3.56	7.17	21.09	49.37	0.02	115	169	0.41	7.01	16	0.87	176	564	0.07	7.34	65	10	<0.1	1	<1	28	19	<18	<1	849	<1	<2	<1	236	<47	<5	<4	<5	97.14
SMA-65	2.18	8.11	10.63	47.82	0.22	335	300	0.18	9.98	47	1.66	393	160	0.18	14.09	69	217	10	11	3	54	20	<18	3	384	32	143	10	53	<47	11	<4	<5	95.26
SMA-71	5.48	0.02	28.32	54.85	0.02	129	88	0.92	8.85	<11	0.09	<7	<8	0.00	0.43	8	8	<0.1	0	3	<2	18	<18	2	1025	<1	<2	<1	402	62	<4	<5	<5	99.16
SMA-73	3.47	10.23	18.90	50.69	0.03	167	579	0.48	6.33	16	0.35	75	231	0.11	7.98	81	5	<0.1	1	<1	35	17	<18	2	651	3	<2	<1	201	<47	6	<4	<5	98.77
SMA-76	3.81	8.25	19.64	49.50	0.03	304	528	0.38	6.45	13	0.40	81	386	0.07	5.68	69	9	<0.1	<0.1	<1	19	19	<18	2	781	2	13	<1	166	<47	<5	<4	<5	94.45
SMA-87	2.73	12.40	17.08	47.69	0.02	253	125	0.29	5.29	16	0.23	58	314	0.11	7.23	78	11	<0.1	<0.1	<1	27	16	<18	2	846	1	<2	<1	160	46	<5	<4	<5	93.24
SMA-90A	5.16	1.87	26.10	52.66	0.12	86	128	0.81	7.85	<11	0.19	13	13	0.02	1.44	13	5	<0.1	<0.1	<1	2	19	<18	3	980	<1	<2	<1	361	<47	<5	<4	<5	96.39
SMA-90B	4.51	3.44	24.22	51.37	0.15	162	131	0.79	8.12	<11	0.43	53	132	0.05	4.12	47	7	<0.1	1	<1	13	18	<18	2	832	3	27	<1	350	<47	<5	<4	<5	97.38
SMA-Q1	0.19	1.54	8.55	3.69	0.01	37312	170	0.00	0.72	<11	11.74	2474	1867	0.21	66.23	1868	607	2	3	<1	1562	87	<18	<1	4	<1	21	1	<29	54	28	<4	<5	97.47



### Appendix 3.4 Example Calculation for normative sulfides

This appendix demonstrates with an example calculation, how the normative sulfides were calculated in Chapter 3

**Step 1:** Determine the weight percent of each element in each sulfide phase

Divide molecular weight of element by atomic mass of mineral

<b>Atomic mass of sulfides</b>	
Chalcopyrite	183.523
Pentlandite	773.375
Pyrrhotite	82.3265

<b>Atomic mass of elements</b>	
Cu	63.546
Fe	55.845
Ni	58.6934
S	32.066
O	15.999

Therefore, the weight percent Cu in chalcopyrite is:  
 $= 63.546 / 183.523$   
wt.% Cu = 0.346

Continue calculations until weight percent for each phase is complete

**Step 2:** Calculate the amount of chalcopyrite from whole rock geochemistry

Divide the weight percent Cu in whole rock assay by the weight percent Cu in chalcopyrite

For example, in RIC-01 there is 0.035% Cu and there is 0.346% Cu in chalcopyrite

**RIC-01**

0.035 wt% Cu

**CCP**

0.346 wt. % Cu

Therefore, the weight percent chalcopyrite in RIC-01 is:  
 $= 0.035 / 0.346$   
wt% ccp = 0.101

**Step 3:** Correct for Ni in olivine

Average the Ni content in olivine from electron microprobe analyses for each sample

For example, in RIC-01 there were 23 olivine analyses, which average 1765 ppm (0.1735 %)  
There is an average of 85% olivine in these samples

#### Appendix 3.4 Example Calculation for normative sulfides

There is 0.1635 wt.% Ni in whole rock geochemistry analysis

The correction factor for Ni in olivine is calculated by subtracting the product of multiplying the estimated percent olivine by the average weight percent Ni in olivine from the weight percent Ni in whole rock assay.

Therefore, the Ni correction factor in RIC-01 is:  
= 0.1635 - (0.85 x 0.1765)  
Correction factor = 0.0136

This means that after accounting for Ni in olivine, there is 136 ppm attributable to Ni in sulfide

**Step 4:** Calculate amount of pentlandite from whole rock geochemistry as per chalcopyrite. Use the corrected Ni from Step 3

**RIC-01**  
0.0136 wt. % Ni  
**PN**  
0.379 wt. % Ni

Therefore, the weight percent pentlandite in RIC-01 is:  
= 0.0136/0.379  
wt.% Pn = 0.036

**Step 5:** Calculate amount of pyrrhotite from whole rock geochemistry

Subtract the weight percent S from whole rock assay from the weight percent S in chalcopyrite multiplied by the calculated percent chalcopyrite. Repeat for S in pentlandite. Finally, divide the weight percent S in pyrrhotite

**RIC-01**  
**wt.% ccp**     **wt.% S in ccp**  
0.101         0.349  
**wt.% pn**     **wt.% S in pn**  
0.036         0.332  
**wt.% S in po**  
0.389  
**wt.% S in whole rock**  
0.541

= (wt.% S in whole rock - (wt.% S in ccp x calculated ccp) - (wt.% S in pn x calculated pn))/(wt.% S in po)

Therefore, the weight percent pyrrhotite in RIC-01 is:  
=(0.561 - (0.349\*0.101)-(0.332 x 0.036))/(0.389)  
wt.% Po = 0.553

## Appendix 4.1 Red Cross Lake Intrusive Suite olivine mineral chemistry

Label	Location	Series	Fe	Fe	Mg#	SiO <sub>2</sub>	Cr <sub>2</sub> O <sub>3</sub>	FeO	MnO	MgO	NiO	Sum Ox%
RIC-01_c01_ol01	core	Lower	12.6	87.4	79.5	39.420	0.010	12.180	0.220	47.330	0.160	99.320
RIC-01_c01_ol10	rim	Lower	12.8	87.2	79.2	39.930	0.040	12.490	0.240	47.630	0.190	100.510
RIC-01_c01_ol11	MP	Lower	13.1	86.9	78.7	39.050	0.000	12.660	0.230	46.910	0.140	99.000
RIC-01_c01_ol12	core	Lower	13.1	86.9	78.8	39.640	0.000	12.580	0.210	46.870	0.180	99.470
RIC-01_c01_ol3	rim	Lower	12	88	80.4	39.560	0.010	11.640	0.250	47.690	0.140	99.300
RIC-01_c01_ol6	MP	Lower	12.9	87.1	79.2	39.680	0.010	12.350	0.180	47.010	0.170	99.400
RIC-01_c01_ol7	core	Lower	12.9	87.1	79.1	39.980	0.000	12.430	0.190	46.960	0.200	99.770
RIC-01_c01_ol8	MP	Lower	12.7	87.3	79.5	40.010	0.020	12.240	0.220	47.350	0.180	100.030
RIC-01_c01_ol9	rim	Lower	12.6	87.4	79.5	39.740	0.010	12.180	0.210	47.210	0.160	99.500
RIC-01_c03_ol2	rim	Lower	13.3	86.7	78.5	39.530	0.000	12.750	0.210	46.660	0.190	99.350
RIC-01_c03_ol4	MP	Lower	12.7	87.3	79.4	39.430	0.000	12.280	0.300	47.280	0.130	99.420
RIC-01_c03_ol5	core	Lower	13.3	86.7	78.5	40.070	0.030	12.860	0.220	46.940	0.170	100.280
RIC-01_c03_ol6	rim	Lower	13.5	86.5	78.2	39.770	0.000	13.020	0.240	46.600	0.120	99.750
RIC-01_c05_ol2	rim	Lower	12.2	87.8	80.2	40.150	0.000	11.780	0.200	47.580	0.170	99.890
RIC-01_c05_ol3	MP	Lower	12.4	87.6	79.8	40.030	0.020	12.010	0.220	47.580	0.190	100.050
RIC-01_c05_ol4	core	Lower	12.3	87.7	79.9	40.040	0.010	11.930	0.220	47.530	0.180	99.920
RIC-01_c05_ol5	MP	Lower	12.3	87.7	79.9	39.890	0.000	11.950	0.200	47.600	0.160	99.800
RIC-01_c05_ol6	rim	Lower	12.2	87.8	80.2	39.910	0.020	11.710	0.190	47.420	0.180	99.440
RIC-01_c06_ol2	rim	Lower	13.3	86.7	78.6	39.030	0.020	12.720	0.290	46.640	0.220	98.920
RIC-01_c06_ol3	MP	Lower	13.7	86.3	78	38.940	0.010	13.090	0.200	46.350	0.210	98.800
RIC-01_c06_ol4	core	Lower	13.4	86.6	78.4	39.180	0.010	12.790	0.240	46.490	0.200	98.910
RIC-01_c06_ol5	MP	Lower	13.6	86.4	78	39.600	0.000	13.090	0.230	46.490	0.240	99.650
RIC-01_c06_ol6	rim	Lower	13.4	86.6	78.4	39.360	0.040	12.750	0.270	46.350	0.180	98.950
RIC-02_c02_ol2	rim	Lower	15.2	84.8	75.8	38.970	0.020	14.310	0.240	44.710	0.210	98.450
RIC-02_c02_ol3	MP	Lower	15.4	84.6	75.5	39.220	0.010	14.460	0.230	44.550	0.190	98.650
RIC-02_c02_ol4	core	Lower	15.3	84.7	75.6	39.250	0.020	14.450	0.250	44.720	0.210	98.890
RIC-02_c02_ol5	MP	Lower	15.3	84.7	75.7	39.370	0.020	14.360	0.270	44.640	0.200	98.850
RIC-02_c02_ol6	rim	Lower	15.2	84.8	75.8	39.420	0.010	14.350	0.240	44.890	0.190	99.110
RIC-02_c03_ol2	rim	Lower	14.8	85.2	76.4	39.750	0.020	14.000	0.260	45.330	0.190	99.550
RIC-02_c03_ol3	MP	Lower	14.7	85.3	76.5	39.490	0.010	14.030	0.220	45.620	0.210	99.580
RIC-02_c03_ol4	core	Lower	15.3	84.7	75.7	39.540	0.030	14.490	0.240	45.140	0.170	99.620
RIC-02_c03_ol5	MP	Lower	15.3	84.7	75.7	39.270	0.000	14.450	0.260	44.910	0.190	99.080
RIC-02_c03_ol6	rim	Lower	15.7	84.3	75.1	39.480	0.010	14.910	0.250	44.880	0.170	99.700
RIC-02_c04.5_ol3	rim	Lower	15.3	84.7	75.7	39.360	0.000	14.320	0.280	44.580	0.210	98.740
RIC-02_c04.5_ol4	MP	Lower	15.4	84.6	75.5	38.980	0.020	14.620	0.260	45.100	0.210	99.200
RIC-02_c04.5_ol5	core	Lower	15.2	84.8	75.7	39.010	0.010	14.470	0.230	45.130	0.180	99.040
RIC-02_c04.5_ol6	MP	Lower	15.4	84.6	75.5	38.650	0.010	14.530	0.240	44.840	0.220	98.490
RIC-02_c04.5_ol7	rim	Lower	15.5	84.5	75.4	38.720	0.030	14.540	0.250	44.570	0.200	98.320
RIC-02_c04_ol2	rim	Lower	15.1	84.9	75.9	39.710	0.030	14.450	0.260	45.420	0.170	100.030
RIC-02_c04_ol3	MP	Lower	15.1	84.9	75.9	39.200	0.000	14.370	0.270	45.330	0.180	99.340
RIC-02_c04_ol4	core	Lower	15.3	84.7	75.6	39.440	0.010	14.450	0.270	44.800	0.160	99.130
RIC-02_c04_ol5	MP	Lower	15.4	84.6	75.5	39.300	0.020	14.560	0.220	44.980	0.190	99.270
RIC-02_c04_ol6	rim	Lower	15	85	76	39.750	0.020	14.330	0.250	45.440	0.170	99.960
RIC-02_c05_ol3	rim	Lower	13.8	86.2	77.8	39.550	0.040	13.150	0.240	46.010	0.170	99.160
RIC-02_c05_ol4	MP	Lower	14.2	85.8	77.2	38.660	0.000	13.550	0.260	45.810	0.180	98.460
RIC-02_c05_ol5	core	Lower	14.3	85.7	77.1	39.310	0.020	13.610	0.290	45.900	0.200	99.340

## Appendix 4.1 Red Cross Lake Intrusive Suite olivine mineral chemistry

Label	Location	Series	Fa	Fe	Mg#	SiO <sub>2</sub>	Cr <sub>2</sub> O <sub>3</sub>	FeO	MnO	MgO	NiO	Sum Ox%
RIC-02_c05_ol6	MP	Lower	14.4	85.6	77	39.280	0.000	13.550	0.250	45.350	0.160	98.600
RIC-02_c05_ol7	rim	Lower	14.4	85.6	76.9	39.160	0.040	13.640	0.200	45.450	0.140	98.630
RIC-03_c01_ol2	rim	Lower	16.8	83.2	73.6	38.230	0.000	15.890	0.250	44.200	0.080	98.670
RIC-03_c01_ol3	MP	Lower	16.8	83.2	73.5	38.790	0.000	15.930	0.290	44.140	0.100	99.250
RIC-03_c01_ol4	core	Lower	16.8	83.2	73.5	38.750	0.010	15.900	0.280	44.210	0.100	99.250
RIC-03_c01_ol5	core	Lower	16.8	83.2	73.6	38.720	0.000	15.920	0.270	44.360	0.080	99.350
RIC-03_c01_ol6	MP	Lower	16.7	83.3	73.7	38.550	0.000	15.900	0.270	44.530	0.070	99.310
RIC-03_c01_ol7	rim	Lower	17	83	73.2	38.060	0.010	16.160	0.300	44.240	0.110	98.890
RIC-03_c02_ol8	rim	Lower	16.5	83.5	73.9	39.190	0.000	15.730	0.260	44.650	0.070	99.910
RIC-03_c02_ol9	MP	Lower	16.8	83.2	73.6	39.100	0.200	15.880	0.260	44.240	0.080	99.760
RIC-03_c02_ol10	core	Lower	16.8	83.2	73.6	38.600	0.010	15.700	0.270	43.750	0.090	98.430
RIC-03_c02_ol11	core	Lower	16.9	83.1	73.4	38.830	0.010	15.800	0.230	43.650	0.080	98.600
RIC-03_c02_ol12	MP	Lower	16.8	83.2	73.6	38.590	0.010	15.470	0.230	43.100	0.090	97.490
RIC-03_c02_ol13	rim	Lower	16.6	83.4	73.8	39.090	0.000	15.710	0.220	44.210	0.110	99.330
RIC-03_c02_ol2	rim	Lower	16.3	83.7	74.2	39.080	0.000	15.490	0.240	44.510	0.120	99.420
RIC-03_c02_ol3	MP	Lower	16.4	83.6	74	38.710	0.000	15.470	0.250	44.090	0.090	98.620
RIC-03_c02_ol4	core	Lower	16.8	83.2	73.5	38.600	0.010	15.800	0.250	43.920	0.080	98.660
RIC-03_c02_ol5	core	Lower	16.8	83.2	73.6	38.920	0.040	15.710	0.280	43.730	0.080	98.760
RIC-03_c02_ol6	MP	Lower	16.5	83.5	74	38.760	0.000	15.530	0.260	44.180	0.090	98.820
RIC-03_c03_ol2	rim	Lower	17	83	73.2	39.120	0.010	16.180	0.230	44.240	0.080	99.850
RIC-03_c03_ol3	MP	Lower	17.1	82.9	73.1	38.920	0.000	16.290	0.260	44.280	0.110	99.860
RIC-03_c03_ol4	core	Lower	17.1	82.9	73.2	38.770	0.010	16.230	0.280	44.280	0.100	99.650
RIC-03_c03_ol5	MP	Lower	17	83	73.2	38.780	0.000	16.200	0.290	44.300	0.090	99.660
RIC-03_c03_ol6	rim	Lower	17.1	82.9	73.2	38.940	0.010	16.230	0.210	44.290	0.100	99.780
RIC-03_c04_ol2	rim	Lower	17.6	82.4	72.5	39.110	0.000	16.460	0.280	43.380	0.110	99.340
RIC-03_c04_ol3	MP	Lower	16.7	83.3	73.6	39.050	0.010	15.840	0.250	44.230	0.110	99.490
RIC-03_c04_ol4	core	Lower	16.9	83.1	73.4	38.840	0.000	16.110	0.250	44.370	0.120	99.680
RIC-03_c04_ol5	core	Lower	16.8	83.2	73.5	39.270	0.000	15.870	0.250	44.000	0.100	99.500
RIC-03_c04_ol6	MP	Lower	17.2	82.8	73	38.680	0.010	16.080	0.290	43.570	0.090	98.710
RIC-03_c04_ol7	rim	Lower	17.3	82.7	72.9	38.860	0.040	16.260	0.270	43.690	0.090	99.210
RIC-04_c01_OL2	rim	Lower	16.5	83.5	73.9	38.150	0.030	15.570	0.260	44.090	0.110	98.220
RIC-04_c01_OL3	MP	Lower	16.9	83.1	73.4	38.220	0.000	15.880	0.250	43.740	0.120	98.200
RIC-04_c01_OL4	core	Lower	16.8	83.2	73.6	38.340	0.000	15.850	0.210	44.080	0.120	98.590
RIC-04_c01_OL5	MP	Lower	16.7	83.3	73.7	38.280	0.000	15.760	0.270	44.250	0.150	98.710
RIC-04_c01_OL6	rim	Lower	16.5	83.5	73.9	38.280	0.000	15.630	0.260	44.270	0.130	98.560
RIC-04_c02_OL2	rim	Lower	16.8	83.2	73.6	37.630	0.020	15.840	0.230	44.060	0.150	97.930
RIC-04_c02_OL3	MP	Lower	16.6	83.4	73.8	38.030	0.000	15.620	0.210	43.910	0.130	97.890
RIC-04_c02_OL4	core	Lower	16.6	83.4	73.8	38.190	0.010	15.620	0.230	43.980	0.110	98.130
RIC-04_c02_OL5	MP	Lower	16.8	83.2	73.5	37.940	0.000	15.700	0.230	43.540	0.110	97.520
RIC-04_c02_OL6	rim	Lower	16.7	83.3	73.6	37.990	0.020	15.800	0.270	44.120	0.120	98.320
RIC-04_c04_OL2	rim	Lower	16.5	83.5	74	38.640	0.000	15.460	0.240	44.050	0.120	98.520
RIC-04_c04_OL3	MP	Lower	16.3	83.7	74.3	37.690	0.020	15.360	0.230	44.350	0.140	97.790
RIC-04_c04_OL4	core	Lower	16.2	83.8	74.4	38.230	0.010	15.330	0.270	44.520	0.090	98.460
RIC-04_c04_OL5	MP	Lower	16.2	83.8	74.4	37.960	0.020	15.340	0.270	44.640	0.140	98.360
RIC-04_c04_OL6	rim	Lower	16.7	83.3	73.7	38.110	0.010	15.720	0.240	44.140	0.100	98.320

## Appendix 4.1 Red Cross Lake Intrusive Suite olivine mineral chemistry

Label	Location	Series	Fe	Fe	Mg#	SiO <sub>2</sub>	Cr <sub>2</sub> O <sub>3</sub>	FeO	MnO	MgO	NiO	Sum Ox%
RIC-04_c05_OL5	core	Lower	16.6	83.4	73.8	37.650	0.010	15.690	0.240	44.110	0.120	97.810
RIC-04_c05_OL6	MP	Lower	17.1	82.9	73.1	38.210	0.010	16.050	0.250	43.700	0.150	98.390
RIC-04_c05_OL7	rim	Lower	17.2	82.8	73	38.300	0.000	16.240	0.220	43.840	0.130	98.740
RIC-04_c06_OL2	rim	Lower	16.6	83.4	73.8	38.170	0.000	15.460	0.210	43.650	0.090	97.580
RIC-04_c06_OL3	MP	Lower	16.8	83.2	73.5	38.500	0.030	15.890	0.240	44.140	0.120	98.920
RIC-04_c06_OL4	core	Lower	17	83	73.2	38.330	0.000	15.880	0.240	43.400	0.110	97.950
RIC-04_c06_OL5	MP	Lower	17.1	82.9	73.1	37.820	0.000	16.080	0.240	43.720	0.100	97.970
RIC-04_c06_OL6	rim	Lower	17.4	82.6	72.7	38.250	0.010	16.350	0.250	43.640	0.130	98.630
RIC-06_c01_ol2	MP	Lower	17.8	82.2	72.2	37.490	0.000	16.760	0.310	43.420	0.180	98.160
RIC-06_c01_ol3	core	Lower	18	82	71.9	37.550	0.000	16.800	0.290	42.940	0.170	97.750
RIC-06_c01_ol4	MP	Lower	18.2	81.8	71.6	37.590	0.010	17.050	0.330	42.970	0.160	98.110
RIC-06_c01_ol5	rim	Lower	18.3	81.7	71.5	37.880	0.000	17.070	0.290	42.810	0.120	98.180
RIC-06_c02_ol1	rim	Lower	18.5	81.5	71.2	37.880	0.040	17.350	0.320	42.910	0.160	98.670
RIC-06_c02_ol2	MP	Lower	18.4	81.6	71.3	37.690	0.010	17.210	0.300	42.760	0.190	98.160
RIC-06_c02_ol3	MP	Lower	18.2	81.8	71.6	37.440	0.000	17.150	0.310	43.200	0.170	98.260
RIC-06_c02_ol4	core	Lower	18.2	81.8	71.6	37.930	0.010	17.100	0.320	43.030	0.190	98.580
RIC-06_c02_ol5	MP	Lower	18.3	81.7	71.5	37.750	0.010	17.110	0.320	42.980	0.180	98.340
RIC-06_c02_ol6	MP	Lower	18.3	81.7	71.5	37.710	0.020	17.110	0.280	42.840	0.190	98.140
RIC-06_c02_ol7	rim	Lower	18.4	81.6	71.4	37.570	0.010	17.310	0.300	43.130	0.120	98.440
RIC-06_c03_ol2	rim	Lower	18.2	81.8	71.7	38.360	0.020	16.980	0.320	42.920	0.180	98.780
RIC-06_c03_ol3	MP	Lower	18.3	81.7	71.5	37.880	0.000	17.140	0.300	42.900	0.170	98.390
RIC-06_c03_ol4	core	Lower	18.5	81.5	71.3	38.140	0.140	17.270	0.280	42.830	0.170	98.830
RIC-06_c03_ol5	MP	Lower	18.3	81.7	71.4	37.640	0.020	17.170	0.340	42.900	0.140	98.200
RIC-06_c04_ol2	rim	Lower	18.5	81.5	71.1	37.550	0.000	17.340	0.290	42.760	0.110	98.040
RIC-06_c04_ol3	MP	Lower	18.5	81.5	71.3	37.440	0.000	17.170	0.320	42.560	0.160	97.640
RIC-06_c04_ol4	core	Lower	18.1	81.9	71.7	37.230	0.000	17.030	0.270	43.150	0.160	97.830
RIC-06_c04_ol5	core	Lower	18.4	81.6	71.4	36.600	0.010	17.050	0.300	42.520	0.180	96.650
RIC-06_c04_ol6	MP	Lower	18	82	71.8	37.310	0.010	16.920	0.320	43.180	0.160	97.900
RIC-06_c04_ol7	rim	Lower	17.6	82.4	72.4	37.460	0.000	16.520	0.280	43.360	0.170	97.810
RIC-18_c01_OL3	MP	Lower	46.4	53.6	39.3	34.160	0.000	39.080	0.680	25.320	0.050	99.280
RIC-18_c01_OL4	core	Lower	46.7	53.3	39	34.360	0.000	39.110	0.730	25.040	0.070	99.300
RIC-18_c01_OL5	MP	Lower	46.3	53.7	39.4	34.110	0.010	39.220	0.660	25.500	0.000	99.510
RIC-18_c01_OL6	rim	Lower	46.5	53.5	39.2	34.380	0.000	39.020	0.650	25.190	0.070	99.310
RIC-18_c02_OL2	rim	Lower	47.4	52.6	38.4	34.260	0.000	39.860	0.780	24.800	0.050	99.750
RIC-18_c02_OL3	MP	Lower	46.4	53.6	39.3	34.660	0.020	39.250	0.740	25.430	0.060	100.150
RIC-18_c02_OL4	core	Lower	46.5	53.5	39.3	34.540	0.000	39.350	0.710	25.440	0.040	100.090
RIC-18_c02_OL5	MP	Lower	46.3	53.7	39.4	34.430	0.000	39.070	0.740	25.450	0.060	99.760
RIC-18_c02_OL6	rim	Lower	46.3	53.7	39.4	34.440	0.020	39.020	0.700	25.420	0.030	99.630
RIC-18_c02_OL8	rim	Lower	34.9	65.1	51.2	52.370	0.010	21.880	0.640	22.920	0.010	97.840
RIC-18_c04_OL4	core	Lower	39.2	60.8	46.5	51.690	0.000	24.290	0.660	21.100	0.010	97.740
RIC-18_c04_OL5	MP	Lower	40.2	59.8	45.5	51.320	0.020	24.850	0.720	20.740	0.020	97.670
RIC-18_c04_OL6	rim	Lower	40	60	45.7	51.300	0.000	24.800	0.670	20.900	0.020	97.700
RIC-18_c04_OL7	rim	Lower	46.1	53.9	39.6	34.680	0.000	39.160	0.690	25.660	0.040	100.240
RIC-18_c04_OL8	MP	Lower	46.7	53.3	39.1	34.390	0.000	39.470	0.680	25.310	0.070	99.920
RIC-18_c04_OL9	core	Lower	46.8	53.2	39	34.430	0.000	39.360	0.690	25.140	0.020	99.650

Appendix 4.1 Red Cross Lake Intrusive Suite olivine mineral chemistry

Sample	Location	Series	Fe	Fe	Mg#	SiO <sub>2</sub>	Cr <sub>2</sub> O <sub>3</sub>	FeO	MnO	NiO	NiO	Sum Ox%
RIC-18_c04_OL11	rim	Lower	45.4	54.6	40.3	34.690	0.000	38.590	0.800	26.000	0.040	100.120
RIC-21.1_c01_ol2	rim	Lower	18.2	81.8	71.6	37.180	0.000	17.030	0.260	42.990	0.060	97.520
RIC-21.1_c01_ol3	MP	Lower	18.5	81.5	71.3	37.510	0.040	17.150	0.280	42.520	0.040	97.530
RIC-21.1_c01_ol4	core	Lower	18.2	81.8	71.6	37.250	0.000	17.130	0.270	43.090	0.030	97.770
RIC-21.1_c01_ol5	MP	Lower	18	82	71.8	37.580	0.020	16.930	0.280	43.170	0.060	98.020
RIC-21.1_c01_ol6	rim	Lower	18.5	81.5	71.2	36.980	0.000	17.260	0.260	42.690	0.040	97.230
RIC-21.1_c02_ol2	rim	Lower	18.4	81.6	71.4	37.220	0.000	17.080	0.280	42.620	0.070	97.280
RIC-21.1_c02_ol3	MP	Lower	18.2	81.8	71.6	37.480	0.000	17.080	0.250	43.080	0.050	97.930
RIC-21.1_c02_ol4	core	Lower	18.1	81.9	71.8	37.500	0.010	16.980	0.250	43.190	0.050	97.970
RIC-21.1_c02_ol5	MP	Lower	18.3	81.7	71.5	37.840	0.010	17.220	0.250	43.190	0.090	98.600
RIC-21.1_c02_ol6	rim	Lower	18.5	81.5	71.1	37.840	0.010	17.360	0.270	42.790	0.020	98.290
RIC-21.1_c03_ol2	rim	Lower	18.6	81.4	71.1	37.940	0.000	17.390	0.310	42.850	0.040	98.520
RIC-21.1_c03_ol3	core	Lower	18.2	81.8	71.6	38.030	0.000	17.160	0.280	43.200	0.040	98.710
RIC-21.1_c03_ol4	MP	Lower	18.1	81.9	71.8	37.820	0.010	16.970	0.250	43.110	0.060	98.220
RIC-21.1_c03_ol5	rim	Lower	17.6	82.4	72.4	38.140	0.020	16.660	0.300	43.750	0.050	98.910
RIC-21.1_c04_ol2	core	Lower	18.5	81.5	71.2	37.230	0.010	17.410	0.230	43.080	0.050	98.020
RIC-21.1_c04_ol3	core	Lower	18.7	81.3	70.9	37.860	0.020	17.670	0.260	43.040	0.050	98.910
RIC-21.1_c04_ol4	rim	Lower	20	80	69.2	37.480	0.010	18.740	0.300	42.040	0.090	98.650
RIC-21.1_c04_ol5	MP	Lower	19	81	70.6	37.630	0.010	17.810	0.290	42.690	0.040	98.460
RIC-21.1_c04_ol6	core	Lower	18.6	81.4	71.1	37.440	0.000	17.560	0.270	43.160	0.080	98.500
RIC-21.1_c04_ol7	MP	Lower	19	81	70.5	37.510	0.010	17.750	0.280	42.390	0.050	97.990
RIC-21.1_c04_ol8	rim	Lower	19.2	80.8	70.3	37.310	0.030	17.900	0.320	42.350	0.050	97.950
RIC-21.1_c05_ol5	MP	Lower	19.9	80.1	69.3	36.910	0.030	18.650	0.250	42.040	0.050	97.940
RIC-21.1_c05_ol6	rim	Lower	19.9	80.1	69.3	37.710	0.010	18.640	0.300	42.130	0.070	98.850
RIC-21.1_c06_ol2	rim	Lower	17.8	82.2	72.1	37.490	0.000	17.010	0.290	43.930	0.050	98.770
RIC-21.1_c07_ol3	core	Lower	18.9	81.1	70.6	37.270	0.010	17.900	0.260	42.970	0.060	98.480
RIC-22_c01_OL2	rim	Lower	19.5	80.5	69.8	37.620	0.020	18.210	0.300	42.050	0.100	98.300
RIC-22_c01_OL3	MP	Lower	19.3	80.7	70.1	37.500	0.010	18.070	0.300	42.430	0.100	98.410
RIC-22_c01_OL5	MP	Lower	19.4	80.6	69.9	37.930	0.010	18.150	0.300	42.210	0.090	98.690
RIC-22_c01_OL6	rim	Lower	19.6	80.4	69.7	37.840	0.000	18.250	0.340	41.910	0.140	98.480
RIC-22_c03_OL2	rim	Lower	20.3	79.7	68.8	36.950	0.010	18.910	0.310	41.680	0.110	97.980
RIC-22_c03_OL3	MP	Lower	20.2	79.8	68.9	37.010	0.000	18.640	0.350	41.380	0.110	97.480
RIC-22_c03_OL4	core	Lower	19.8	80.2	69.4	37.720	0.010	18.450	0.300	41.930	0.100	98.500
RIC-22_c03_OL5	MP	Lower	19.8	80.2	69.4	37.680	0.000	18.440	0.310	41.830	0.110	98.370
RIC-22_c03_OL6	rim	Lower	20	80	69.2	37.490	0.000	18.650	0.280	41.990	0.080	98.490
RIC-22_c04_OL2	rim	Lower	19.2	80.8	70.3	38.170	0.000	18.130	0.340	42.840	0.130	99.620
RIC-22_c04_OL3	MP	Lower	19.3	80.7	70.2	38.240	0.010	18.190	0.350	42.800	0.120	99.710
RIC-22_c04_OL4	core	Lower	19.9	80.1	69.4	38.430	0.010	18.640	0.300	42.180	0.110	99.670
RIC-22_c04_OL5	MP	Lower	20	80	69.1	38.330	0.020	18.800	0.270	42.070	0.110	99.600
RIC-22_c04_OL6	rim	Lower	19.9	80.1	69.3	37.780	0.000	18.600	0.330	42.000	0.140	98.850
RIC-22_c05_OL2	rim	Lower	19.5	80.5	69.9	37.800	0.000	18.160	0.280	42.130	0.110	98.490
RIC-22_c05_OL3	MP	Lower	20.2	79.8	68.9	37.900	0.020	18.880	0.300	41.850	0.110	99.050
RIC-23B_c05_OL2	rim	Xenolith	90	10	5.85	29.990	0.000	63.790	2.090	3.960	0.010	99.850
RIC-23B_c05_OL3	MP	Xenolith	89.3	10.7	6.31	29.840	0.010	62.960	2.110	4.240	0.000	99.160

## Appendix 4.1 Red Cross Lake Intrusive Suite olivine mineral chemistry

Label	Location	Series	Fe	Fe	Mg#	SiO <sub>2</sub>	Cr <sub>2</sub> O <sub>3</sub>	FeO	MnO	MgO	NiO	Sum Ox%
RIC-23B_c05_OL4	core	Xenolith	89.2	10.8	6.34	29.900	0.000	63.130	2.080	4.270	0.010	99.400
RIC-23B_c05_OL6	rim	Xenolith	89.8	10.2	6	30.140	0.010	63.310	2.120	4.040	0.020	99.630
RIC-24_c04_OL2	rim	Lower	48.9	51.1	36.9	32.980	0.000	40.820	0.820	23.900	0.040	98.570
RIC-24_c04_OL3	MP	Lower	50	50	35.9	33.290	0.000	41.740	0.790	23.420	0.030	99.270
RIC-24_c04_OL4	core	Lower	49	51	36.9	33.240	0.000	41.050	0.770	23.970	0.010	99.040
RIC-24_c04_OL6	rim	Lower	49.8	50.2	36.1	33.930	0.000	41.600	0.740	23.490	0.030	99.790
RIC-24_c05_OL2	rim	Lower	52.2	47.8	33.9	33.910	0.000	43.260	0.780	22.230	0.020	100.200
RIC-24_c05_OL4	core	Lower	51.1	48.9	34.9	33.930	0.000	42.800	0.800	22.970	0.000	100.510
RIC-24_c05_OL5	MP	Lower	50.7	49.3	35.3	34.080	0.000	41.910	0.790	22.830	0.020	99.640
RIC-24_c05_OL6	rim	Lower	47.5	52.5	38.3	34.330	0.010	39.910	0.800	24.780	0.050	99.870
RIC-30B_c01_OL2	rim	Lower	21.3	78.7	67.4	38.160	0.000	19.650	0.300	40.700	0.100	98.910
RIC-30B_c01_OL3	MP	Lower	20.4	79.6	68.6	38.010	0.000	19.000	0.330	41.520	0.110	98.970
RIC-30B_c01_OL4	core	Lower	20.2	79.8	68.9	38.660	0.020	18.810	0.330	41.750	0.090	99.660
RIC-30B_c01_OL5	MP	Lower	20.4	79.6	68.6	38.350	0.020	19.000	0.300	41.530	0.090	99.290
RIC-30B_c01_OL6	rim	Lower	20.5	79.5	68.6	38.520	0.000	18.890	0.290	41.220	0.150	99.060
RIC-30B_c02_OL2	rim	Lower	20.3	79.7	68.8	38.620	0.000	18.910	0.330	41.630	0.120	99.610
RIC-30B_c02_OL3	MP	Lower	20.5	79.5	68.5	38.300	0.010	19.120	0.350	41.580	0.120	99.470
RIC-30B_c02_OL4	core	Lower	20.4	79.6	68.7	38.280	0.000	19.030	0.330	41.690	0.120	99.440
RIC-30B_c02_OL5	MP	Lower	20.6	79.4	68.4	38.240	0.000	19.090	0.340	41.350	0.100	99.120
RIC-30B_c03_OL2	rim	Lower	20.9	79.1	68	38.980	0.000	19.560	0.290	41.580	0.110	100.520
RIC-30B_c03_OL5	MP	Lower	20.6	79.4	68.3	38.690	0.010	19.100	0.320	41.240	0.140	99.490
RIC-30B_c03_OL6	rim	Lower	20.7	79.3	68.2	38.310	0.000	19.080	0.320	40.970	0.140	98.810
RIC-30B_c05_OL3	MP	Lower	21.1	78.9	67.8	38.470	0.000	19.410	0.330	40.790	0.120	99.130
RIC-30B_c05_OL4	core	Lower	20.8	79.2	68.1	38.550	0.000	19.350	0.300	41.310	0.140	99.650
RIC-30B_c05_OL5	MP	Lower	21.2	78.8	67.6	38.420	0.030	19.640	0.350	41.030	0.140	99.600
RIC-51.2c_c02_OL2	rim	Xenolith	69.4	30.6	19.8	30.800	0.010	53.570	0.930	13.220	0.050	98.570
RIC-51.2c_c02_OL4	rim	Xenolith	69.4	30.6	19.8	30.760	0.000	53.650	0.940	13.280	0.020	98.650
RIC-51.2c_c04_OL2	rim	Xenolith	67.9	32.1	20.9	32.330	0.000	52.880	0.890	14.010	0.040	100.170
RIC-51.2c_c04_OL3	core	Xenolith	67.8	32.2	21	31.860	0.010	52.690	0.850	14.010	0.050	99.480
RIC-51c.1_c01_ol3	rim	Xenolith	59.5	40.5	27.6	32.930	0.000	47.280	0.880	18.030	0.080	99.200
RIC-51c.1_c01_ol4	MP	Xenolith	58.5	41.5	28.4	32.650	0.000	47.040	0.860	18.700	0.060	99.310
RIC-51c.1_c01_ol5	core	Xenolith	58.8	41.2	28.2	32.580	0.000	47.250	0.860	18.560	0.080	99.340
RIC-51c.1_c01_ol6	MP	Xenolith	57.9	42.1	28.9	32.560	0.000	46.680	0.820	19.020	0.060	99.140
RIC-51c.1_c01_ol7	rim	Xenolith	58.4	41.6	28.6	32.740	0.010	46.720	0.850	18.700	0.090	99.100
RIC-51c.1_c02_ol2	rim	Xenolith	60	40	27.3	32.050	0.010	48.230	0.870	18.080	0.090	99.330
RIC-51c.1_c02_ol3	MP	Xenolith	61.7	38.3	25.8	32.180	0.000	48.640	0.900	16.950	0.080	98.750
RIC-51c.1_c02_ol4	core	Xenolith	60.2	39.8	27.1	31.860	0.000	48.560	0.820	18.020	0.080	99.340
RIC-51c.1_c02_ol5	MP	Xenolith	60.7	39.3	26.7	32.130	0.010	48.520	0.880	17.650	0.060	99.260
RIC-51c.1_c02_ol6	rim	Xenolith	61.2	38.8	26.2	32.090	0.010	48.780	0.950	17.360	0.080	99.270
RIC-51c.1_c03_ol2	rim	Xenolith	61.2	38.8	26.3	32.400	0.020	48.130	1.000	17.150	0.080	98.780
RIC-51c.1_c03_ol3	rim	Xenolith	60.6	39.4	26.7	32.100	0.000	47.790	0.920	17.430	0.080	98.320
RIC-51c.1_c03_ol4	core	Xenolith	61.2	38.8	26.2	32.300	0.000	48.440	0.800	17.220	0.070	98.830
RIC-51c.1_c03_ol5	rim	Xenolith	61.9	38.1	25.7	32.020	0.000	48.810	0.930	16.870	0.080	98.700

Appendix 4.1 Red Cross Lake Intrusive Suite olivine mineral chemistry

Label	Location	Series	PA	Fe	Mg#	SiO <sub>2</sub>	Cr <sub>2</sub> O <sub>3</sub>	FeO	MnO	MgO	NiO	Sum Ox%
RIC-51c.1_c04_ol2	rim	Xenolith	60.1	39.9	27.1	32.770	0.000	47.870	0.870	17.840	0.070	99.420
RIC-51c.1_c04_ol3	MP	Xenolith	58.8	41.2	28.2	32.820	0.010	46.630	0.960	18.320	0.070	98.810
RIC-51c.1_c04_ol4	core	Xenolith	58.8	41.2	28.3	33.000	0.000	47.150	0.850	18.570	0.090	99.670
RIC-51c.1_c04_ol5	rim	Xenolith	59.5	40.5	27.6	32.690	0.010	47.470	0.900	18.120	0.090	99.280
RIC-52_c02_OL3	MP	Upper	52.7	47.3	33.4	33.980	0.010	43.340	0.710	21.780	0.010	99.830
RIC-52_c02_OL4	core	Upper	52.2	47.8	33.9	34.280	0.000	42.850	0.770	22.010	0.030	99.930
RIC-52_c02_OL5	MP	Upper	57.3	42.7	29.5	33.650	0.000	43.910	0.400	18.360	0.020	96.350
RIC-52_c02_OL6	rim	Upper	38	62	47.8	52.120	0.000	23.730	0.570	21.730	0.010	98.160
RIC-52_c03_OL2	rim	Upper	54.4	45.6	32	33.900	0.000	44.590	0.620	20.940	0.000	100.060
RIC-52_c05_OL2	rim	Upper	58.5	41.5	28.5	33.470	0.000	46.560	0.820	18.520	0.020	99.400
RIC-52_c05_OL3	MP	Upper	56.8	43.2	29.9	33.230	0.000	45.820	0.690	19.580	0.040	99.360
RIC-52_c05_OL4	core	Upper	56.2	43.8	30.4	33.120	0.000	45.130	0.650	19.750	0.000	98.660
RIC-52_c05_OL5	MP	Upper	56.1	43.9	30.6	33.550	0.000	45.370	0.680	19.960	0.010	99.580
RIC-52_c05_OL6	core	Upper	56.3	43.7	30.3	33.250	0.000	45.510	0.690	19.790	0.010	99.260
RIC-63_c03_ol2	rim	Upper	31.8	68.2	54.6	36.390	0.000	28.370	0.480	34.170	0.120	99.540
RIC-63_c03_ol3	MP	Upper	30.9	69.1	55.7	36.050	0.010	27.720	0.480	34.860	0.140	99.260
RIC-63_c03_ol4	core	Upper	31.1	68.9	55.4	36.170	0.000	27.970	0.470	34.720	0.120	99.450
RIC-63_c03_ol5	MP	Upper	31.1	68.9	55.5	35.810	0.000	27.840	0.510	34.660	0.080	98.890
RIC-63_c03_ol6	rim	Upper	31.4	68.6	55.1	36.490	0.020	28.120	0.480	34.540	0.090	99.730
RIC-63_c03_ol7	rim	Upper	32.1	67.9	54.3	35.850	0.000	28.520	0.450	33.860	0.110	98.800
RIC-63_c03_ol8	MP	Upper	32.5	67.5	53.9	36.160	0.000	28.820	0.480	33.650	0.120	99.230
RIC-63_c03_ol9	core	Upper	32.9	67.1	53.4	35.820	0.010	29.250	0.470	33.490	0.130	99.160
RIC-63_c03_ol10	MP	Upper	33.1	66.9	53.2	35.830	0.000	29.360	0.450	33.310	0.120	99.070
RIC-63_c03_ol11	rim	Upper	32.8	67.2	53.5	35.710	0.010	29.250	0.510	33.610	0.130	99.220
RIC-63_c05_ol2	rim	Upper	31.7	68.3	54.7	36.190	0.000	28.170	0.460	34.060	0.090	98.970
RIC-63_c05_ol3	MP	Upper	31.4	68.6	55	35.470	0.000	28.130	0.430	34.410	0.100	98.550

## Appendix 4.2 Red Cross Lake Intrusive Suite pyroxene mineral chemistry

		SiO <sub>2</sub>	TiO <sub>2</sub>	Al <sub>2</sub> O <sub>3</sub>	Cr <sub>2</sub> O <sub>3</sub>	FeO (C)	FeO (O)	MnO	MgO	CaO	Sum Oxide			
RIC-06_c02_PYX2	Lower	0.31	80.31	19.38	54.1	0.02	1.75	0.03	0.6	12.48	0.29	29.03	0.16	98.46
RIC-18_c02_cpx2	Lower	45.08	41.82	13.10	51.91	0.5	2.28	0	0	7.9	0.25	14.15	21.22	98.21
RIC-18_c02_cpx3	Lower	44.27	42.26	13.47	51.42	0.52	1.98	0.01	0	8.24	0.34	14.5	21.13	98.15
RIC-18_c02_cpx4	Lower	7.10	56.17	36.73	52.76	0.14	0.71	0	0	22.89	0.79	19.64	3.45	100.39
RIC-18_c03_cpx2	Lower	46.58	44.14	9.29	51.85	0.44	1.76	0.35	0	5.7	0.28	15.2	22.31	97.91
RIC-18_c03_cpx4	Lower	6.58	65.11	28.31	53.98	0.22	0.65	0.12	0.31	18.1	0.79	23.36	3.29	100.84
RIC-18_c05_opx2	Lower	4.36	76.45	19.19	53.73	0.3	2.24	0.7	0	12.19	0.43	27.25	2.16	99.01
RIC-18_c05_opx3	Lower	3.96	77.95	18.09	53.92	0.28	2.13	0.57	0.39	11.63	0.43	28.12	1.99	99.46
RIC-18_c05_opx4	Lower	3.28	73.63	23.09	54.05	0.17	1.47	0.42	0	14.83	0.5	26.53	1.65	99.62
RIC-23B_c01_pyx2	Xeno	3.20	39.99	56.81	50.18	0.19	0.45	0.03	0.07	33.37	1.43	13.18	1.47	100.36
RIC-23B_c02_pyx2	Xeno	3.02	26.67	70.31	48.46	0.17	0.34	0.03	0.34	39.68	1.65	8.44	1.33	100.45
RIC-23B_c02_pyx3	Xeno	2.79	30.78	66.43	48.99	0.19	0.56	0.02	0.44	37.99	1.54	9.88	1.25	100.86
RIC-23B_c02_pyx4	Xeno	2.96	30.91	66.13	48.28	0.19	0.52	0.01	1.22	37.22	1.59	9.76	1.3	100.09
RIC-23B_c02_pyx5	Xeno	0.90	35.20	63.90	48.97	0	0.7	0	0.39	36.51	1.41	11.28	0.4	99.66
RIC-23B_c02_pyx6	Xeno	2.88	33.16	63.97	48.01	0.19	0.64	0.01	1.69	35.86	1.51	10.43	1.26	99.59
RIC-23B_c02_pyx7	Xeno	2.20	33.25	64.56	47.26	0.14	0.68	0	3.08	35.57	1.52	10.28	0.94	99.48
RIC-23B_c04_pyx2	Xeno	1.29	26.29	72.42	47.73	0.08	0.37	0.02	1.07	39.88	2.05	8.12	0.55	99.87
RIC-23B_c05_pyx3	Xeno	2.33	26.72	70.95	47.74	0.12	0.54	0	1.31	39.3	1.77	8.3	1.01	100.1
RIC-23C_c01_pyx2	Upper	45.18	36.59	18.23	51.48	0.36	1.36	0.04	0	11.12	0.34	12.53	21.52	98.74
RIC-24_c04_pyx2	Lower	1.20	63.11	35.69	52.27	0.01	0.37	0.02	1.32	22.05	0.71	21.88	0.58	99.21
RIC-24_c05_pyx2	Lower	0.68	64.04	35.29	33.2	0.05	0.35	0	38.84	13.85	0.47	14.11	0.21	101.08
RIC-27_c03_pyx2	Lower	27.68	59.76	12.56	48.86	0.05	11.27	0.02	0	7	0.15	18.68	12.04	98.06
RIC-30B_c02_pyx3	Lower	44.85	46.58	8.57	50.49	0.93	3.87	0.88	0	5.1	0.18	15.55	20.83	97.84
RIC-30B_c02_pyx4	Lower	43.05	46.92	10.04	50.89	1.04	4.46	0.7	0	6.03	0.22	15.82	20.19	99.37
RIC-30B_c05_pyx2	Lower	47.81	44.31	7.89	50.29	1.08	3.61	0.53	0	4.73	0.15	14.92	22.4	97.72
RIC-32_c01_pyx2	Upper	39.21	37.16	23.63	46.88	7.7	1.41	0.12	0	14.06	0.46	12.41	18.21	101.27
RIC-32_c01_pyx3	Upper	45.23	38.55	16.22	52.42	0.28	1.37	0.1	0	9.71	0.29	12.95	21.13	98.24
RIC-32_c01_pyx4	Upper	46.07	37.49	16.44	52.42	0.18	0.99	0.08	0	10.14	0.35	12.98	22.18	99.33
RIC-32_c01_pyx5	Upper	45.15	37.50	17.35	51.98	0.34	1.29	0.05	0	10.58	0.35	12.83	21.49	98.9
RIC-32_c03_pyx2	Upper	45.84	37.70	16.47	51.79	0.33	1.57	0.08	0	9.96	0.3	12.8	21.65	98.49
RIC-51.1C_c03_pyx2	Xeno	36.03	36.35	27.62	50.74	0.43	1.56	0.07	0	16.72	0.49	12.35	17.02	99.38
RIC-51.1C_c04_pyx2	Xeno	4.53	49.93	45.53	50.03	0.03	0.51	0.04	2.23	26.93	0.7	16.57	2.09	99.15
RIC-51.1C_c04_pyx3	Xeno	2.79	49.84	47.37	50.45	0.13	0.92	0.02	0.98	28.29	0.7	16.7	1.3	99.5
RIC-51A_c03_pyx4	Upper	3.09	54.03	42.88	51.16	0.13	0.73	0	0.92	25.97	0.72	18.36	1.46	99.44
RIC-51A_c05_pyx3	Upper	45.47	36.73	17.81	50.94	0.3	1.27	0.02	0.07	10.83	0.36	12.53	21.58	97.9
RIC-51A_c05_pyx4	Upper	3.24	57.15	39.62	50.63	0.21	0.86	0	2.26	23.76	0.74	19.23	1.52	99.19
RIC-52_c02_pyx2	Upper	0.47	61.72	37.81	53.25	0	0.81	0	0.21	23.86	0.57	21.85	0.23	100.77
RIC-52_c04_pyx2	Upper	48.34	38.44	13.22	49.58	0.42	2.15	0.24	1.77	7.83	0.42	12.78	22.35	97.54
RIC-52_c04_pyx3	Upper	46.48	38.22	15.30	50.56	0.36	2.19	0.31	0.59	9.24	0.38	12.95	21.91	98.49
RIC-52_c04_pyx4	Upper	1.86	56.03	42.11	51.02	0.13	0.63	0.02	1.09	25.38	0.85	18.95	0.87	98.94
RIC-56_c04_pyx3	Upper	56.11	5.96	37.94	100.22	0.02	0.04	0	0	0.22	0.01	0.02	0.25	100.79
RIC-67_c02_pyx2	Upper	46.51	39.40	14.09	52.04	0.23	0.89	0.04	0	8.72	0.31	13.68	22.46	98.36
RIC-67_c02_pyx3	Upper	46.06	39.04	14.90	51.94	0.2	1.22	0.3	0	9.2	0.26	13.52	22.19	98.82
RIC-76B_c01_pyx2	Upper	3.22	58.83	37.95	53.64	0.04	2.08	0.03	0	21.77	0.76	18.93	1.44	98.7

## Appendix 4.3 Red Cross Lake Intrusive Suite feldspar mineral chemistry

Location	Series	An	Ab	Or	Di	Pl	Al	Ca	Na	K	Sum	Other	Count
RIC-03_c01_fsp2	core	Lower	76.528	23.161	0.311	48.8	-	33.17	0.14	15.7	2.63	0.05	100.48
RIC-03_c01_fsp3	rim	Lower	75.473	24.496	0.031	48.48	-	32.78	0.4	15.51	2.78	0.01	99.95
RIC-03_c01_fsp4	core	Lower	75.759	24.1	0.141	49.3	-	32.24	0.21	15.59	2.74	0.02	100.1
RIC-03_c02_fsp2	core	Lower	82.01	17.943	0.047	47.34	-	34.26	0.1	16.87	2.04	0.01	100.62
RIC-03_c02_fsp3	rim	Lower	76.613	23.287	0.1	48.21	-	33.14	0.24	15.76	2.65	0.02	100.02
RIC-03_c03_fsp2	core	Lower	77.725	22.058	0.218	48.39	-	33.33	0.16	16.12	2.53	0.04	100.57
RIC-03_c04_fsp2	core	Lower	75.03	24.632	0.338	49.02	-	32.9	0.02	15.31	2.78	0.06	100.08
RIC-03_c04_fsp3	rim	Lower	76.622	23.154	0.224	48.77	-	32.7	0.08	15.79	2.64	0.04	100.03
RIC-03_c01_fsp2	core	Lower	76.528	23.161	0.311	48.8	-	33.17	0.14	15.7	2.63	0.05	100.48
RIC-03_c04_fsp4	core	Lower	76.025	23.818	0.157	48.37	-	32.68	0.09	15.58	2.7	0.03	99.44
RIC-04_c01_FSP2	core	Lower	76.075	23.78	0.145	49.48	-	32.86	0.14	15.32	2.65	0.02	100.47
RIC-04_c02_FSP2	core	Lower	76.324	20.811	2.866	46.96	-	33.24	0.13	15.35	2.31	0.48	98.47
RIC-04_c03_FSP3	core	Lower	76.886	23.022	0.092	47.89	-	32.61	0.24	15.31	2.53	0.02	98.59
RIC-04_c04_FSP2	core	Lower	75.686	24.309	0.005	48.25	-	33.11	0.14	15.31	2.72	0	99.53
RIC-04_c05_FSP2	core	Lower	76.115	23.757	0.128	48.62	-	32.8	0.14	15.38	2.65	0.02	99.6
RIC-06_c01_fsp1	rim	Lower	66.597	33.235	0.168	49.5	-	31.71	0.28	13.71	3.78	0.03	99.01
RIC-06_c01_fsp2	core	Lower	79	20.877	0.123	46.92	-	33.57	0.09	16.01	2.34	0.02	98.96
RIC-06_c02_fsp2	rim	Lower	68.43	31.532	0.038	49.94	-	31.53	0.19	13.7	3.49	0.01	98.86
RIC-06_c03_fsp2	core	Lower	75.75	24.046	0.205	47.81	-	33.1	0.05	15.24	2.67	0.03	98.9
RIC-06_c04_fsp2	rim	Lower	66.629	33.312	0.059	49	-	31.27	0.14	13.63	3.76	0.01	97.81
RIC-18_c01_fsp5	incl in Bt	Lower	69.887	29.996	0.117	51.15	-	31.1	0.15	14.5	3.44	0.02	100.36
RIC-18_c01_fsp6	rim	Lower	50.146	49.806	0.049	56.18	-	28.44	0.11	10.38	5.7	0.01	100.82
RIC-18_c01_fsp7	rim	Lower	67.501	32.419	0.08	51.37	-	31.42	0.14	13.99	3.71	0.01	100.65
RIC-18_c02_fsp2	rim	Lower	45.966	53.692	0.342	56.83	-	27.95	0.16	9.57	6.18	0.06	100.74
RIC-18_c02_fsp3	core	Lower	71.723	27.99	0.287	50.45	-	32.4	0.02	14.58	3.14	0.05	100.65
RIC-18_c02_fsp4	rim	Lower	59.651	40.151	0.198	53.79	-	30.47	0.14	12.35	4.59	0.03	101.38
RIC-18_c03_fsp2	n/a	Lower	74.151	25.562	0.286	50.35	-	32.98	0.1	15.07	2.87	0.05	101.43
RIC-18_c03_fsp3	n/a	Lower	52.146	47.416	0.438	55.19	-	29.34	0.09	10.94	5.5	0.08	101.14
RIC-18_c03_fsp4	n/a	Lower	72.679	26.974	0.346	50.19	-	32.63	0.08	14.91	3.06	0.06	100.93
RIC-18_c03_fsp5	n/a	Lower	54.491	44.874	0.635	55.54	-	29.7	0.11	11.35	5.16	0.11	101.97
RIC-18_c03_fsp6	n/a	Lower	46.942	52.587	0.471	56.66	-	28.32	0.09	9.81	6.07	0.08	101.04
RIC-18_c04_fsp2	rim	Lower	52.163	47.431	0.406	55.48	-	29.26	0.16	11.14	5.6	0.07	101.71
RIC-18_c04_fsp3	rim	Lower	70.084	29.915	0.001	50.96	-	31.69	0.13	14.29	3.37	0	100.44
RIC-18_c04_fsp4	core	Lower	47.728	52.069	0.204	56.99	-	28.09	0.09	9.99	6.02	0.04	101.21
RIC-18_c04_fsp5	rim	Lower	60.528	39.196	0.276	53.8	-	30.49	0.12	12.48	4.46	0.05	101.39
RIC-18_c04_fsp6	core	Lower	45.74	54.074	0.186	57.37	-	27.91	0.09	9.69	6.33	0.03	101.43
RIC-18_c05_fsp2	incl in Opx	Lower	72.139	27.776	0.085	50.31	-	32.56	0.06	14.98	3.19	0.01	101.11
RIC-18_c05_fsp3	incl in Opx	Lower	70.227	29.623	0.15	51.17	-	31.92	0.01	14.53	3.39	0.03	101.03
RIC-18_c05_fsp4	incl in Opx	Lower	67.048	32.86	0.092	52.07	-	31.61	0.19	13.68	3.71	0.02	101.28
RIC-18_c05_fsp5	rim	Lower	54.036	45.694	0.269	54.92	-	29.32	0.03	11.15	5.21	0.05	100.67
RIC-21.1_c01_fsp4	core	Lower	77.014	22.691	0.295	47.64	-	32.71	0.08	15.58	2.54	0.05	98.6
RIC-21.1_c04_fsp3	core	Lower	65.904	33.708	0.388	50.19	-	31.48	0	13.5	3.81	0.07	99.05
RIC-21.1_c05_fsp2	core	Lower	74.431	25.399	0.17	47.37	-	32.61	0.14	14.98	2.83	0.03	97.95
RIC-21.1_c07_fsp2	core	Lower	76.791	22.949	0.259	46.71	-	33.16	0.1	15.76	2.6	0.04	98.37
RIC-22_c01_fsp2	core	Lower	70.162	29.597	0.242	51.1	-	32.36	0.24	14.53	3.39	0.04	101.67
RIC-22_c01_fsp3	rim	Lower	67.224	32.473	0.302	51.22	-	31.94	0.23	14.2	3.79	0.05	101.43
RIC-22_c01_fsp4	rim	Lower	67.201	32.623	0.177	50.44	-	31.58	0.24	13.5	3.62	0.03	99.41
RIC-22_c03_fsp3	rim	Lower	85.092	14.902	0.005	47.34	-	34.76	0.23	17.12	1.66	0	101.12
RIC-22_c03_fsp4	rim	Lower	68.952	30.937	0.111	50.98	-	32.29	0.36	14.37	3.56	0.02	101.58
RIC-22_c03_fsp5	n/a	Lower	69.778	30.061	0.16	51.32	-	31.95	0.32	14.17	3.37	0.03	101.15
RIC-22_c04_fsp2	rim	Lower	65.368	34.529	0.103	52.73	-	31.12	0.12	13.4	3.91	0.02	101.29
RIC-22_c04_fsp3	rim	Lower	65.349	34.44	0.211	52.62	-	31.42	0.04	13.4	3.9	0.04	101.41
RIC-22_c05_fsp2	rim	Lower	67.601	32.145	0.255	51.24	-	31.85	0.46	13.95	3.67	0.04	101.21

## Appendix 4.3 Red Cross Lake Intrusive Suite feldspar mineral chemistry

Label	Location	Series	An	Ab	Or	SiO <sub>2</sub>	TiO <sub>2</sub>	Al <sub>2</sub> O <sub>3</sub>	Fe <sub>2</sub> O <sub>3</sub>	CaO	Na <sub>2</sub> O	K <sub>2</sub> O	Sum Ox%
RIC-22_c05_fsp3	rim	Lower	67.581	32.269	0.15	50.85	-	31.85	0.43	13.95	3.68	0.03	100.8
RIC-23B_c02_fsp2	core	Upper	47.284	51.561	1.155	55.74	0	28.02	0	9.4	5.66	0.19	99.01
RIC-23B_c02_fsp3	core	Upper	45.513	53.331	1.156	55.49	0	27.93	0	9.12	5.91	0.19	98.65
RIC-23B_c04_fsp2	core	Upper	43.31	55.514	1.177	56.3	0	27.28	0	8.73	6.18	0.2	98.69
RIC-23B_c05_fsp2	core	Upper	44.22	54.514	1.266	55.39	0	27.71	0	8.8	6	0.21	98.12
RIC-23B_c05_fsp3	rim	Upper	50.941	48.321	0.738	54.05	0	28.21	0	10.04	5.26	0.12	97.68
RIC-23B_c05_fsp4	core	Upper	49.118	50.189	0.693	55.23	0	28.82	0	9.85	5.56	0.12	99.58
RIC-23B_c06_fsp2	core	Upper	45.171	54.144	0.686	56.36	0	27.78	0	9.12	6.04	0.12	99.42
RIC-23B_c06_fsp3	core	Upper	61.527	38.078	0.395	51.66	0	30.2	0	12.22	4.18	0.07	98.33
RIC-23C_c01_fsp2	core	Upper	61.664	37.817	0.519	51	0	30.8	0	12.26	4.16	0.09	98.31
RIC-23C_c01_fsp3	rim	Upper	62.151	37.201	0.648	50.52	0	30.44	0	12.63	4.18	0.11	97.89
RIC-23C_c02_fsp2	n/a	Upper	49.117	50.135	0.748	53.61	0	27.3	0	9.68	5.46	0.12	96.17
RIC-23C_c02_fsp3	n/a	Upper	48.875	50.515	0.609	54.29	0	28.48	0	9.96	5.69	0.1	98.53
RIC-23C_c02_fsp4	n/a	Upper	57.27	42.192	0.538	53.2	0	30.23	0	11.75	4.78	0.09	100.05
RIC-23C_c02_fsp5	n/a	Upper	45.698	53.72	0.582	57.02	0	28.36	0	9.26	6.01	0.1	100.76
RIC-23C_c02_fsp6	n/a	Upper	39.498	59.202	1.3	57.49	0	26.63	0	7.95	6.59	0.22	98.88
RIC-23C_c02_fsp7	core	Upper	62.107	36.921	0.972	51.83	0	30.59	0	12.58	4.13	0.17	99.31
RIC-23C_c02_fsp8	core	Upper	45.09	53.338	1.573	56.71	0	28.04	0	9.11	5.96	0.27	100.09
RIC-27_c02_fsp2	rim	Lower	71.491	28.503	0.006	50.14	-	33.72	0.01	14.67	3.23	0	101.78
RIC-27_c02_fsp3	core	Lower	77.087	22.858	0.055	47.15	-	32.93	0.14	15.41	2.53	0.01	98.17
RIC-27_c03_fsp2	core	Lower	83.172	16.827	0.001	46.64	-	34.52	0.06	16.78	1.88	0	99.88
RIC-27_c03_fsp3	core	Lower	79.316	20.478	0.207	46.83	-	33.82	0.1	16.06	2.29	0.04	99.15
RIC-27_c03_fsp4	core	Lower	77.812	22.093	0.095	46.33	-	31.85	0	15.45	2.42	0.02	96.06
RIC-27_c01_fsp2	n/a	Upper	42.017	56.81	1.173	58.17	-	26.72	0.01	8.51	6.36	0.2	99.98
RIC-27_c03_fsp2	n/a	Upper	45.801	53.955	0.244	54.61	-	27.37	0.07	9.34	6.08	0.04	97.52
RIC-30B-c01_fsp2	rim	Lower	70.156	29.826	0.018	51.37	-	32.21	0.1	14.37	3.38	0	101.43
RIC-30B-c01_fsp3	core	Lower	71.85	27.909	0.241	50.46	-	32.13	0.18	14.63	3.14	0.04	100.58
RIC-30B-c02_fsp2	core	Lower	66.106	33.748	0.145	51.16	-	31.19	0.06	13.74	3.88	0.03	100.04
RIC-30B-c02_fsp3	core	Lower	64.673	35.327	0.001	51.83	-	31.08	0.07	13.4	4.04	0	100.42
RIC-30B-c03_fsp2	core	Lower	72.058	27.676	0.266	49.77	-	32.3	0.23	14.79	3.14	0.05	100.27
RIC-30B-c05_fsp2	rim	Lower	66.647	33.219	0.134	51.66	-	31.59	0.23	13.75	3.79	0.02	101.04
RIC-30B-c05_fsp3	core	Lower	69.07	30.599	0.331	50.24	-	32.07	0.14	14.59	3.57	0.06	100.66
RIC-32_c01_fsp2	core	Upper	44.188	55.613	0.199	60.48	-	29.81	0.11	9.76	6.79	0.04	106.98
RIC-32_c03_fsp2	core	Upper	50.363	49.217	0.419	54.64	-	28.29	0.07	10.15	5.48	0.07	98.7
RIC-32_c03_fsp3	core	Upper	62.063	37.78	0.157	51.69	-	30.53	0.09	12.56	4.23	0.03	99.13
RIC-51.2c_c02_fsp2	core	Xenoliths	51.972	47.635	0.393	53.78	0.01	28.59	0.33	10.59	5.37	0.07	98.75
RIC-51A_c01_fsp2	core	Xenoliths	46.408	52.409	1.183	55.46	0.03	27.25	0	9.45	5.9	0.2	98.29
RIC-51A_c01_fsp3	core	Xenoliths	44.966	53.995	1.04	56.25	0.01	27.39	0.01	9.15	6.07	0.18	99.04
RIC-51A_c01_fsp4	core	Xenoliths	30.262	68.316	1.422	59.25	0.01	24.72	0.06	6.23	7.78	0.25	98.3
RIC-51A_c01_fsp5	core	Xenoliths	30.606	68.867	0.527	60.64	0	25.55	0.01	6.46	8.03	0.09	100.78
RIC-51A_c02_fsp2	rim	Xenoliths	27.537	71.965	0.498	60.44	0	24.33	0.06	5.72	8.26	0.09	98.9
RIC-51A_c02_fsp3	rim	Xenoliths	45.263	54.377	0.361	55.72	0.04	27.39	0.05	9.19	6.1	0.06	98.55
RIC-51A_c04_fsp2	rim	Xenoliths	52.235	47.588	0.177	53.33	0.05	28.45	0.11	10.7	5.39	0.03	98.06
RIC-51A_c04_fsp3	core	Xenoliths	74.762	25.221	0.017	48.69	0	32.69	0.26	14.89	2.78	0	99.31
RIC-51A_c05_fsp2	rim	Xenoliths	39.279	60.34	0.381	58.54	0.01	26.29	0.09	8.07	6.85	0.07	99.92
RIC-51A_c05_fsp3	rim	Xenoliths	49.343	50.264	0.392	55.26	0.02	28.32	0.12	9.96	5.61	0.07	99.36
RIC-51c.1_c01_fsp2	core	Xenoliths	80.365	19.634	0.001	47.45	-	33.69	0.32	16.26	2.2	0	99.91
RIC-51c.1_c01_fsp3	core	Xenoliths	51.256	48.673	0.071	55.53	-	28.68	0.9	10.54	5.53	0.01	101.19
RIC-51c.1_c01_fsp4	Incl in OI	Xenoliths	46.141	53.714	0.144	56.82	-	28.3	0.38	9.75	6.27	0.03	101.55
RIC-51c.1_c01_fsp5	rim	Xenoliths	44.233	55.703	0.064	56.7	-	27.85	0.09	9.29	6.46	0.01	100.4
RIC-51c.1_c01_fsp7	rim	Xenoliths	44.928	54.932	0.14	57.14	-	27.78	0.04	9.44	6.38	0.02	100.8

			Al	Si	Di	Fe2	TiO2	Al2O3	Fe2O3	CaO	Na2O	K2O	Sum Owt%
RIC-51c.1_c02_fsp2	rim	Xenoliths	46.613	53.291	0.096	56.79	-	28.07	0.17	9.89	6.25	0.02	101.2
RIC-51c.1_c02_fsp3	core	Xenoliths	46.609	53.316	0.075	57.2	-	27.91	0	9.74	6.16	0.01	101.03
RIC-51c.1_c02_fsp4	rim	Xenoliths	46.289	53.539	0.172	56.96	-	28.48	0.07	9.64	6.16	0.03	101.34
RIC-51c.1_c02_fsp5	core	Xenoliths	42.329	57.632	0.038	57.94	-	27.52	0.05	8.67	6.53	0.01	100.72
RIC-51c.1_c03_fsp2	rim	Xenoliths	43.699	56.163	0.137	57.57	-	27.86	0.02	9.28	6.59	0.02	101.34
RIC-51c.1_c03_fsp3	core	Xenoliths	42.746	57.167	0.087	57.84	-	27.53	0.03	8.86	6.55	0.02	100.81
RIC-51c.1_c03_fsp4	rim	Xenoliths	45.278	54.646	0.076	57.44	-	27.58	0	9.27	6.18	0.01	100.49
RIC-51c.1_c03_fsp5	Incl in OI	Xenoliths	46.806	52.894	0.3	57.12	-	27.77	0.87	9.54	5.96	0.05	101.31
RIC-51c.1_c04_fsp2	rim	Xenoliths	46.799	53.078	0.123	56.95	-	27.75	0.49	9.72	6.09	0.02	101.01
RIC-51c.1_c04_fsp3	core	Xenoliths	46.175	53.784	0.041	56.37	-	27.86	0.39	9.85	6.34	0.01	100.8
RIC-51c.1_c04_fsp4	rim	Xenoliths	46.857	52.993	0.15	56.59	-	28.45	0.54	9.98	6.24	0.03	101.82
RIC-51c.1_c04_fsp5	core	Xenoliths	44.17	55.649	0.181	57.08	-	27.61	0.04	9.18	6.39	0.03	100.34
RIC-52_c02_fsp2	core	Upper	56.369	43.47	0.161	54.07	0.05	30.17	0.09	11.53	4.91	0.03	100.84
RIC-52_c02_fsp3	core	Upper	75.23	24.703	0.068	49.2	0	33.81	0.1	15.53	2.82	0.01	101.48
RIC-52_c02_fsp5	core	Upper	84.787	15.15	0.063	47	0	34.75	0.18	17.19	1.7	0.01	100.83
RIC-52_c03_fsp2	core	Upper	71.301	28.094	0.605	50.32	0.03	32.28	0.52	14.53	3.16	0.1	100.94
RIC-52_c03_fsp3	core	Upper	72.19	27.775	0.034	50.35	0.02	32.65	0.08	14.67	3.12	0.01	100.9
RIC-52_c03_fsp4	core	Upper	55.833	43.988	0.179	53.43	0.02	29.31	0.37	11.37	4.95	0.03	99.49
RIC-52_c03_fsp5	core	Upper	68.537	31.254	0.209	50.74	0.01	32.1	0.1	14.2	3.58	0.04	100.75
RIC-52_c04_fsp2	core	Upper	57.05	42.542	0.408	54.07	0.04	30.07	0.02	11.99	4.94	0.07	101.21
RIC-52_c04_fsp3	core	Upper	67.069	32.527	0.404	52.38	0.02	31.92	0.11	13.83	3.71	0.07	102.03
RIC-52_c05_fsp2	core	Upper	20.544	79.221	0.235	64.26	0	23.84	0.04	4.33	9.22	0.04	101.74
RIC-52_c05_fsp3	core	Upper	65.559	34.018	0.423	51.94	0.03	31.82	0.11	13.61	3.9	0.07	101.49
RIC-56_c02_fsp2	core	Upper	40.458	58.553	0.989	57.87	0.01	27.51	0.15	8.36	6.69	0.17	100.77
RIC-56_c02_fsp3	core	Upper	55.958	43.261	0.781	53.19	0.01	30.15	0.08	11.55	4.93	0.14	100.05
RIC-56_c03_fsp2	core	Upper	56.294	43.133	0.573	52.05	0.04	29.53	0.04	11.58	4.9	0.1	98.24
RIC-56_c03_fsp3	core	Upper	39.89	58.567	1.543	56.53	0.06	26.92	0.11	8.35	6.78	0.27	99.01
RIC-56_c03_fsp4	core	Upper	40.825	58.444	0.731	57.44	0	27.79	0.23	8.55	6.76	0.13	100.89
RIC-56_c04_fsp2	core	Upper	52.593	41.791	5.616	54.87	0.03	29.27	0.1	10.62	4.66	0.95	100.49
RIC-56_c04_fsp3	core	Upper	49.172	49.914	0.914	55.75	0.02	28.66	0.06	10	5.61	0.16	100.26
RIC-63_c01_fsp2	core	Upper	51.624	48.276	0.101	54.14	-	29.08	0.18	10.5	5.43	0.02	99.35
RIC-63_c01_fsp3	core	Upper	45.628	54.34	0.032	55.69	-	27.98	0.12	9.39	6.18	0.01	99.36
RIC-63_c02_fsp2	rim	Upper	47.854	52.145	0.001	55.78	-	28.91	0.09	9.8	5.9	0	100.48
RIC-63_c03_fsp2	core	Upper	45.916	54.067	0.016	55.4	-	28.08	0.13	9.24	6.01	0	98.87
RIC-63_c03_fsp3	rim	Upper	45.709	54.232	0.059	55.54	-	27.82	0.04	9.22	6.04	0.01	98.67
RIC-63_c03_fsp4	core	Upper	58.783	41.216	0.001	51.99	-	30.05	0.04	11.86	4.6	0	98.53
RIC-63_c03_fsp5	core	Upper	54.409	45.449	0.142	53.75	-	29.54	0.08	11.16	5.15	0.02	99.7
RIC-63_c03_fsp6	core	Upper	60.977	38.9	0.123	51.78	-	30.34	0	12.22	4.31	0.02	98.68
RIC-63_c05_fsp2	core	Upper	66.14	33.797	0.063	50.08	-	31.31	0.06	13.48	3.81	0.01	98.74
RIC-63_c05_fsp3	core	Upper	65.01	34.838	0.152	50.82	-	31.37	0.04	13.29	3.94	0.03	99.48
RIC-63_c05_fsp4	rim	Upper	46.058	53.808	0.134	55.4	-	27.89	0.16	9.28	5.99	0.02	98.76
RIC-63_c05_fsp5	core	Upper	62.605	37.353	0.042	50.86	-	30.99	0.04	12.77	4.21	0.01	98.88
RIC-63_c05_fsp6	rim	Upper	48.036	51.943	0.021	54.51	-	28.39	0.06	9.88	5.9	0	98.75
RIC-67_c01_fsp2	core	Upper	39.552	59.796	0.651	59.66	0.04	27.16	0.06	8.15	6.81	0.11	101.98
RIC-67_c01_fsp3	rim	Upper	40.838	58.428	0.734	59.17	0.03	26.99	0.13	8.32	6.58	0.13	101.35
RIC-67_c01_fsp5	core	Upper	60.675	39.109	0.216	54.85	0.02	30.75	0.1	12.22	4.35	0.04	102.33
RIC-67_c02_fsp2	core	Upper	49.615	49.401	0.985	56.27	0.03	28.47	0.08	9.94	5.47	0.17	100.44
RIC-67_c02_fsp3	core	Upper	63.272	36.272	0.455	53.3	0.01	30.62	0.03	12.54	3.97	0.08	100.55
RIC-67_c02_fsp4	core	Upper	56.165	43.563	0.272	54.45	0	29.42	0.09	11.45	4.91	0.05	100.37
RIC-67_c02_fsp5	core	Upper	39.804	59.996	0.2	59.51	0	26.71	0.07	8.04	6.7	0.03	101.07
RIC-67_c02_fsp7	core	Upper	57.894	41.56	0.546	53.71	0.03	29.74	0.04	11.86	4.7	0.09	100.17
RIC-67_c03_fsp2	core	Upper	41.165	57.707	1.128	59.11	0.01	27.12	0.12	8.41	6.52	0.19	101.48
RIC-67_c04_fsp2	core	Upper	63.127	36.111	0.762	52.98	0.06	30.5	0.08	12.65	4	0.13	100.4
RIC-67_c04_fsp3	core	Upper	40.961	58.183	0.856	58.87	0.02	27.01	0.01	8.19	6.43	0.14	100.68

Appendix 4.3 Red Cross Lake Intrusive Suite feldspar mineral chemistry

Label	Location	Series	An	Ab	Or	SiO2	TiO2	Al2O3	Fe2O3	CaO	Na2O	K2O	Sum Ox%
RIC-74_c02_fsp2	core	Upper	64.983	34.797	0.22	52.11	0.01	30.36	0.04	13.12	3.88	0.04	99.56
RIC-74_c02_fsp3	core	Upper	62.95	36.969	0.081	52.57	0	30.66	0.02	12.73	4.13	0.01	100.12
RIC-74_c03_fsp2	core	Upper	59.981	39.865	0.155	53.99	0.01	30.11	0	12.26	4.5	0.03	100.89
RIC-74_c03_fsp3	core	Upper	47.016	52.691	0.293	57.71	0.03	28.21	0.04	9.46	5.86	0.05	101.36
RIC-76B_c02_fsp2	core	Upper	60.805	39.072	0.123	54.06	0	30.5	0.09	12.32	4.38	0.02	101.37
RIC-76B_c02_fsp3	rim	Upper	61.449	38.269	0.282	54.41	0.04	30.59	0.19	12.55	4.32	0.05	102.14
RIC-76B_c02_fsp4	core	Upper	46.911	52.659	0.43	56.46	0.02	27.14	1.63	9.01	5.59	0.07	99.91
RIC-76B_c03_fsp2	rim	Upper	49.807	50.002	0.191	57.37	0.03	28.79	0.15	10.04	5.57	0.03	101.97
RIC-76B_c03_fsp3	core	Upper	54.313	43.087	2.6	55.14	0	29.34	0.17	10.7	4.69	0.43	100.47
RIC-76B_c03_fsp4	rim	Upper	50.663	49.285	0.052	56.91	0	28.88	0.09	10.17	5.47	0.01	101.53
RIC-76B_c03_fsp5	rim	Upper	53.269	40.882	5.849	54.78	0.01	30.62	0.2	10.3	4.37	0.95	101.21

		SiO <sub>2</sub>	TiO <sub>2</sub>	Al <sub>2</sub> O <sub>3</sub>	FeO	MnO	MgO	CaO	Na <sub>2</sub> O	K <sub>2</sub> O	H <sub>2</sub> O	Sum Ox%			
RIC-01 c04 spn4	Lower	66.31	29.66	4.03	0.00	0.02	57.29	0.04	0.1	0	33.61	2.01	8.44	0.04	101.56
RIC-02 c02 spn4	Lower	70.63	26.00	1.37	0.00	0.51	55.53	0.04	0.99	0	35.15	0.67	7.82	0.08	100.79
RIC-18_c02_ox1	Lower	93.27	4.87	1.86	0.00	0.03	53.82	0.05	0.02	0	44.18	0.87	1.29	0	100.25
RIC-18_c04_ox2	Lower	96.23	1.91	1.86	0.00	0	52.9	0.06	0	0	45.47	0.87	0.51	0	99.81
RIC-18_c04_ox3	Lower	96.64	1.53	1.83	0.00	0	53.1	0.04	0	0	45.4	0.85	0.4	0	99.8
RIC-21.1 c04_ox2	Lower	74.39	24.21	1.40	0.00	0.22	55.78	0.06	0.38	0	37.31	0.69	6.82	0.01	101.27
RIC-22 c04_ox2	Lower	85.49	10.11	1.95	2.45	0.03	51.99	0.05	0.2	2.61	40.98	0.92	2.72	0.03	99.53
RIC-23C_c01_ilm2	Upper	96.03	0.47	3.10	0.41	0	52.95	0.02	0.03	0.43	45.91	1.46	0.13	0	100.94
RIC-23C_c03_ilm2	Upper	95.21	0.11	2.66	2.02	0.02	51.52	0.04	0	2.12	45.04	1.24	0.03	0	100.01
RIC-24_c01_ilm2	Lower	96.16	1.67	2.17	0.00	0	53.25	0.01	0.07	0	45.82	1.02	0.45	0.02	100.63
RIC-24_c01_ilm3	Lower	96.11	1.71	2.18	0.00	0	53.21	0	0.02	0	45.64	1.02	0.45	0.03	100.37
RIC-24_c03_ilm2	Lower	96.67	1.18	2.15	0.00	0	53.58	0.04	0.05	0	45.83	1.01	0.31	0	100.82
RIC-27_c01_ilm2	Lower	93.74	3.08	3.18	0.00	0.04	53.67	0.03	0.04	0	44.1	1.48	0.81	0.01	100.19
RIC-27_c01_ilm2	Lower	93.71	3.16	3.13	0.00	0.02	54.45	0.05	0.07	0	45.08	1.49	0.85	0.04	102.05
RIC-27_c01_ilm3	Lower	93.58	3.21	3.21	0.00	0	53.7	0.04	0.05	0	44.17	1.49	0.85	0.04	100.35
RIC-27_c01_ilm3	Lower	94.68	2.55	2.77	0.00	0.01	54.21	0.05	0.06	0	44.24	1.28	0.67	0.03	100.55
RIC-27_c04_ilm2	Lower	94.15	3.54	2.31	0.00	0.02	53.07	0.79	0.11	0	43.62	1.06	0.92	0.05	99.65
RIC-27_c04_ilm2	Lower	94.18	3.51	2.31	0.00	0.01	53.82	0.04	0.11	0	43.95	1.06	0.92	0.02	99.94
RIC-32_c01_ilm3	Upper	96.30	1.16	2.54	0.00	0.06	53.47	0.04	0.02	0	45.68	1.19	0.31	0	100.78
RIC-32_c03_ilm2	Upper	96.96	1.03	2.02	0.00	0.1	53.78	0.1	0.04	0	46.17	0.95	0.27	0.04	101.44
RIC-32_c04_ilm2	Upper	96.68	0.90	2.42	0.00	0.08	53.38	0.05	0.02	0	46.33	1.15	0.24	0	101.24
RIC-32_c04_ilm3	Upper	96.86	0.72	2.42	0.00	0.04	52.78	0.06	0.06	0	45.54	1.12	0.19	0.02	99.81
RIC-51.1C_c01_ilm2	Xenolith	95.23	2.31	1.53	0.93	0	52.02	0.07	0.06	0.98	44.93	0.71	0.61	0.03	99.42
RIC-51.1C_c02_ilm2	Xenolith	95.70	2.43	1.46	0.41	0.02	52.29	0.08	0.02	0.43	45.19	0.68	0.64	0.02	99.37
RIC-51A_c01_ilm2	Upper	96.91	0.77	2.32	0.00	0	53.18	0.04	0.06	0	45.38	1.07	0.2	0	99.93
RIC-51A_c03_ilm2	Upper	95.64	2.61	1.75	0.00	0.05	53.12	0.04	0.07	0	44.92	0.81	0.69	0	99.7
RIC-51A_c03_ilm3	Upper	95.58	2.62	1.80	0.00	0	52.88	0.04	0	0	44.98	0.83	0.69	0	99.43
RIC-51c.1_c01_ox2	Xenolith	94.73	2.46	1.51	1.31	0.05	52.12	0.05	0.07	1.38	45.03	0.71	0.65	0.01	100.05
RIC-51c.1_c01_ox3	Xenolith	95.48	1.47	2.09	0.96	0.01	52.02	0.02	0.1	1.01	45.09	0.97	0.39	0.03	99.63
RIC-51c.1_c01_ox4	Xenolith	92.99	2.70	2.37	1.95	0.07	51.78	0.02	0.08	2.06	44.24	1.11	0.72	0	100.08
RIC-51c.1_c02_ox2	Xenolith	90.81	5.01	3.29	0.89	1.01	50.76	0.89	0.08	0.94	42.92	1.53	1.33	0.01	99.48
RIC-51c.1_c02_ox3	Xenolith	96.45	0.39	3.16	0.00	0.04	52.79	0.03	0.12	0	45.17	1.46	0.1	0	99.72
RIC-51c.1_c02_ox4	Xenolith	92.31	2.25	2.32	3.11	0.01	48.36	0.7	3.03	3.1	41.42	1.03	0.57	0.03	98.26
RIC-51c.1_c03_ox3	Xenolith	96.36	1.03	2.48	0.14	0.01	51.89	0.34	1.38	0.14	45.01	1.14	0.27	0.03	100.22
RIC-51c.1_c03_ox5	Xenolith	96.75	1.24	2.02	0.00	0.02	52.76	0.02	0.16	0	45.77	0.94	0.33	0.01	100.01
RIC-51c.1_c03_ox6	Xenolith	94.38	2.68	1.63	1.30	0.02	52.22	0.02	0.16	1.38	44.9	0.77	0.71	0.03	100.2
RIC-51c.1_c04_ox2	Xenolith	96.87	0.89	2.24	0.00	0	52.51	0.03	0.13	0	45.04	1.03	0.23	0.05	99.02
RIC-56_c01_ilm2	Upper	95.96	0.66	3.38	0.00	0	53.07	0.05	0	0	44.93	1.56	0.17	0.03	99.82
RIC-56_c02_ilm2	Upper	96.15	0.55	3.30	0.00	0.05	52.76	0.04	0	0	45.3	1.53	0.15	0	99.83
RIC-63_c04_ilm1	Upper	90.90	7.43	1.67	0.00	0.44	54.11	0.06	0	0	44.16	0.8	2.03	0.03	101.62
RIC-63_c04_ilm2	Upper	89.93	8.42	1.65	0.00	0.43	54.19	0.03	0.07	0	43.76	0.79	2.3	0.02	101.59
RIC-63_c05_ilm2	Upper	94.27	5.13	0.60	0.00	0.04	53.9	0.01	0.05	0	42.31	0.27	1.29	0.02	97.89
RIC-67_C02_ilm2	Upper	96.43	1.47	2.10	0.00	0	54.66	0.03	0.13	0	45.97	0.99	0.39	0.01	102.19
RIC-69_c03_ilm2	Lower	84.26	11.83	3.27	0.64	0	54.87	0.04	0.12	0.71	41.83	1.6	3.29	0.01	102.49
RIC-69_c04_ilm2	Lower	86.20	11.05	1.80	0.96	0.03	54.22	0.05	0.13	1.05	42.43	0.87	3.05	0.03	101.86
RIC-74_c02_ilm2	Upper	96.23	0.72	3.05	0.00	0.04	54.06	0.05	0	0	46.31	1.45	0.19	0.01	102.12
RIC-74_c03_ilm2	Upper	95.93	0.72	3.35	0.00	0.01	53.78	0.04	0	0	46.11	1.59	0.19	0	101.73
RIC-76B_c01_ilm2	Upper	93.77	0.72	2.27	3.25	0.09	51.49	0.06	0.05	3.46	44.98	1.08	0.19	0	101.4
RIC-76B_c03_ilm2	Upper	95.39	0.72	2.79	1.11	0.03	53.02	0.04	0.08	1.18	46	1.33	0.19	0.02	101.9

Appendix 4.5 Red Cross Lake Intrusive Sulte spinel mineral chemistry

Label	Series	SiO <sub>2</sub>	TiO <sub>2</sub>	Al <sub>2</sub> O <sub>3</sub>	Cr <sub>2</sub> O <sub>3</sub>	Fe <sub>2</sub> O <sub>3</sub> (c)	FeO	MnO	MgO	NiO	Sum Ox%
RIC-01_c03_spn2	Lower	0.08	0.86	26.12	36.61	4.7	19.63	0.3	10.96	0.09	99.35
RIC-02_c02_spn2	Lower	0.4	1.14	26.92	34.69	3.69	20.01	0.31	11.02	0.09	98.27
RIC-02_c02_spn3	Lower	0.19	1.08	27.82	34.46	3.19	20.93	0.3	10.33	0.08	98.38
RIC-02_c03_spn2	Lower	0.17	1.61	26.95	33.15	4.54	19.77	0.3	11.12	0.11	97.72
RIC-02_c05_spn2	Lower	0.47	0.98	31.39	31.11	2.98	20.74	0.28	11.2	0.08	99.23
RIC-04_c02_spn2	Lower	0.32	1.81	18.98	33.14	10.18	28.48	0.36	4.89	0.1	98.26
RIC-04_c02_spn2.1	Lower	0.27	1.88	18.88	33.38	9.84	28.49	0.32	4.85	0.08	97.99
RIC-18_c05_spn2	Lower	0	3.38	21.14	38.32	0.72	28.44	0.46	5.87	0.04	98.37
RIC-22_c02_ox2	Lower	0.02	0.87	22.32	26.52	14.87	29.66	0.39	3.6	0.09	98.34

## Appendix 4.6 Red Cross Lake Intrusive Suite pyrrhotite mineral chemistry

	Phase	Series	W%(S)	W%(Fe)	W%(Co)	W%(Ni)	W%(Cu)	W%(Zn)	W% Total
RIC-01_c03_01po1	po	Lower	36.804	63.516	0.000	0.024	0.016	0.045	100.40
RIC-01_c03_01po2	po	Lower	36.704	64.008	0.008	0.006	0.011	0.026	100.76
RIC-01_c03_02pn4	po	Lower	36.980	63.522	0.005	0.043	0.000	0.016	100.57
RIC-01_c04_04po2	po	Lower	36.872	63.941	0.000	0.029	0.041	0.078	100.96
RIC-01_c04_04po4	po	Lower	36.324	63.693	0.011	0.022	0.030	0.000	100.08
RIC-01_c06_04po2	po	Lower	36.524	63.949	0.000	0.029	0.000	0.000	100.50
RIC-01_c06_04po3	po	Lower	36.155	63.300	0.000	0.037	0.000	0.041	99.53
RIC-01_c06_04po4	po	Lower	36.229	63.223	0.000	0.008	0.025	0.047	99.53
RIC-01_c06_04po5	po	Lower	36.115	64.053	0.004	0.042	0.055	0.026	100.29
RIC-01_c06_po7	po	Lower	36.192	63.332	0.000	0.030	0.018	0.000	99.57
RIC-01c01_po	po	Lower	36.133	63.148	0.024	0.016	0.052	0.031	99.40
RIC-02_c03_po3	po	Lower	36.399	63.160	0.004	0.013	0.039	0.014	99.63
RIC-02_c03_po6	po	Lower	36.087	62.970	0.008	0.028	0.149	0.049	99.29
RIC-02_c03_po7	po	Lower	36.141	62.900	0.000	0.012	0.106	0.067	99.22
RIC-02_c03_py2	po	Lower	36.252	63.237	0.000	0.053	0.055	0.000	99.60
RIC-02_c04_p2	po	Lower	36.006	57.235	0.126	6.054	0.172	0.022	99.61
RIC-02_c04_p4	po	Lower	36.205	63.159	0.000	0.021	0.087	0.039	99.51
RIC-02_c04_py2	po	Lower	36.082	62.985	0.000	0.029	0.004	0.047	99.15
RIC-03_c02_po2	po	Lower	36.005	63.048	0.016	0.033	0.078	0.000	99.18
RIC-03_c02_po3	po	Lower	36.492	62.767	0.000	0.004	0.063	0.000	99.33
RIC-03_c02_po4	po	Lower	36.218	63.151	0.000	0.012	0.034	0.000	99.42
RIC-06_c01_po3	po	Lower	39.580	58.304	0.068	0.738	0.097	0.033	98.82
RIC-06_c03_po3	po	Lower	39.488	57.890	0.006	0.507	1.096	0.000	98.99
RIC-06_c03_po5	po	Lower	36.327	63.543	0.023	0.067	0.107	0.000	100.07
RIC-21.1_c01_po2	po	Lower	36.609	63.516	0.006	0.021	0.062	0.010	100.22
RIC-21.1_c01_po3	po	Lower	38.628	61.195	0.006	0.033	0.000	0.021	99.88
RIC-21.1_c02_po2	po	Lower	38.503	61.196	0.000	0.042	0.160	0.020	99.92
RIC-21.1_c02_po3	po	Lower	36.792	63.286	0.006	0.029	0.046	0.067	100.23
RIC-21.1_c05_po2	po	Lower	36.097	64.226	0.000	0.000	0.000	0.061	100.38
RIC-21.1_c05_po3	po	Lower	36.601	62.728	0.000	0.035	0.166	0.000	99.53
RIC-21.1_c05_po4	po	Lower	38.781	61.159	0.000	0.043	0.065	0.019	100.07
RIC-21.1_c05_po5	po	Lower	38.587	61.751	0.007	0.063	0.006	0.050	100.46
RIC-21.1_c05_po6	po	Lower	36.447	63.829	0.018	0.013	0.085	0.067	100.46
RIC-21.1_c05_po7	po	Lower	36.651	63.841	0.000	0.033	0.076	0.000	100.60
RIC-21.1_c07_po10	po	Lower	36.749	63.490	0.000	0.028	0.000	0.002	100.27
RIC-21.1_c07_po11	po	Lower	36.630	63.475	0.000	0.004	0.069	0.000	100.18
RIC-21.1_c07_po12	po	Lower	38.379	61.450	0.003	0.062	0.118	0.000	100.01
RIC-21.1_c07_po2	po	Lower	38.414	61.555	0.011	0.013	0.034	0.000	100.03
RIC-21.1_c07_po4	po	Lower	38.766	61.409	0.000	0.066	0.054	0.025	100.32
RIC-21.1_c07_po5	po	Lower	38.529	61.388	0.000	0.032	0.000	0.000	99.95
RIC-21.1_c07_po6	po	Lower	38.626	61.572	0.033	0.028	0.016	0.062	100.34

Appendix 4.6 Red Cross Lake Intrusive Suite pyrrhotite mineral chemistry

Lab#	Phase	Series	W%(S)	W%(Fe)	W%(Co)	W%(Ni)	W%(Cu)	W%(Zn)	W% Total
RIC-21.1_c07_po8	po	Lower	36.119	63.509	0.020	0.022	0.065	0.000	99.74
RIC-21.1_c07_po9	po	Lower	38.528	61.216	0.000	0.030	0.004	0.025	99.80
RIC-22_box1_po2	po	Lower	37.113	63.773	0.000	0.000	0.007	0.075	100.97
RIC-22_box1_po3	po	Lower	36.534	63.879	0.000	0.009	0.049	0.000	100.47
RIC-22_box1_po4	po	Lower	36.681	63.724	0.000	0.000	0.098	0.000	100.50
RIC-22_box1_po5	po	Lower	36.761	64.451	0.000	0.062	0.042	0.020	101.34
RIC-22_box1_po6	po	Lower	36.538	63.780	0.000	0.118	0.084	0.016	100.54
RIC-22_c01_po2	po	Lower	36.351	63.605	0.000	0.000	0.000	0.000	99.96
RIC-22_c01_po3	po	Lower	36.602	64.138	0.000	0.013	0.035	0.155	100.94
RIC-22_c01_po4	po	Lower	36.480	64.184	0.000	0.039	0.000	0.000	100.70
RIC-22_c01_po5	po	Lower	36.571	63.972	0.000	0.044	0.049	0.016	100.65
RIC-22_c02_po6	po	Lower	36.347	64.377	0.000	0.065	0.085	0.000	100.87
RIC-22_c02_po7	po	Lower	36.650	64.183	0.000	0.000	0.098	0.000	100.93
RIC-22_c02_po8	po	Lower	36.774	63.673	0.000	0.028	0.021	0.032	100.53
RIC-23B_c03_ccp1	po	Upper	38.573	63.447	0.000	0.064	0.151	0.016	102.25
RIC-24_c03_po2	po	Lower	39.174	61.480	0.000	0.396	0.106	0.060	101.22
RIC-30B_c02_pn3	po	Lower	35.854	63.261	0.000	0.042	0.162	0.080	99.40
RIC-30B_c02_po2	po	Lower	35.763	63.205	0.000	0.002	0.035	0.060	99.06
RIC-30B_c04_p2	po	Lower	35.767	61.578	0.000	0.232	0.000	0.000	97.58
RIC-30B_c04_p3	po	Lower	35.545	63.089	0.000	0.077	0.035	0.036	98.78
RIC-30B_c04_pn2	po	Lower	35.803	62.825	0.000	0.088	0.056	0.020	98.79
RIC-32_c01_ccp2	po	Upper	39.055	59.642	0.000	0.472	0.150	0.000	99.32
RIC-32_c01_po1	po	Upper	38.830	58.588	0.000	0.662	0.248	0.028	98.36
RIC-32_c04_po4	po	Upper	39.412	58.761	0.000	0.743	0.000	0.036	98.95
RIC-51.1C_c01_pn4	po	Xenolith	39.239	59.097	0.000	0.463	0.265	0.035	99.10
RIC-51.1C_c01_po2	po	Xenolith	38.940	59.388	0.000	0.339	0.041	0.128	98.84
RIC-51.1C_c01_po3	po	Xenolith	38.738	59.825	0.000	0.251	0.116	0.112	99.04
RIC-51.1C_c01_po4	po	Xenolith	37.927	59.398	0.000	0.219	0.082	0.051	97.68
RIC-51.1C_c03_po2	po	Xenolith	38.351	59.604	0.000	0.384	0.000	0.000	98.34
RIC-51.1C_c03_po3	po	Xenolith	40.099	57.048	0.000	0.362	0.114	0.053	97.68
RIC-52_c01_ccp2	po	Upper	38.151	62.377	0.000	0.242	0.061	0.095	100.93
RIC-52_c03_pn2	po	Upper	39.879	61.692	0.000	0.181	0.000	0.000	101.75
RIC-52_c03_pn3	po	Upper	39.111	62.201	0.000	0.431	0.101	0.073	101.92
RIC-52_c03_po2	po	Upper	39.315	62.253	0.000	0.402	0.121	0.080	102.17
RIC-52_c03_po3	po	Upper	39.168	62.281	0.000	0.437	0.155	0.076	102.12
RIC-52_c03_po4	po	Upper	39.218	61.130	0.000	0.411	0.081	0.110	100.95
RIC-67_c02_po2	po	Upper	39.532	59.417	0.000	0.251	0.244	0.112	99.56
RIC-67_c04_po2	po	Upper	39.098	60.749	0.000	0.404	0.137	0.016	100.40

Appendix 4.6 Red Cross Lake Intrusive Suite pyrrhotite mineral chemistry

Label	Phase	Series	W%(S)	W%(Fe)	W%(Co)	W%(Ni)	W%(Cu)	W%(Zn)	W% Total
RIC-69_c01_po2	po	Lower	36.792	64.136	0.000	0.076	0.047	0.085	101.14
RIC-69_c01_po3	po	Lower	36.734	63.396	0.000	0.000	0.130	0.095	100.36
RIC-69_c01_po4	po	Lower	36.582	63.690	0.000	0.011	0.000	0.053	100.34
RIC-69_c02_po2	po	Lower	36.700	63.806	0.000	0.277	0.084	0.032	100.90
RIC-69_c02_po3	po	Upper	36.709	63.754	0.000	0.000	0.093	0.042	100.60
RIC-74_C01_ccp2	po	Upper	39.700	60.245	0.000	0.425	0.184	0.086	100.64
RIC-74_C01_po2	po	Upper	39.762	60.158	0.000	0.588	0.132	0.000	100.64
RIC-74_C02_po2	po	Upper	39.584	59.991	0.000	0.655	0.060	0.049	100.34

## Appendix 4.7 Red Cross Lake Intrusive Suite pentlandite mineral chemistry

Label	Series	Phase	W%(S)	W%(Fe)	W%(Co)	W%(Ni)	W%(Cu)	W%(Zn)	W% Total
RIC-01_c03_01pn3	Lower	pn	33.591	36.674	1.285	29.503	0.154	0.067	101.27
RIC-01_c03_01po3	Lower	pn	33.211	36.579	1.305	28.363	0.103	0.020	99.58
RIC-01_c04_04pn7	Lower	pn	33.769	37.327	0.710	29.142	0.000	0.057	101.00
RIC-01_c06_04pn2	Lower	pn	33.339	35.260	0.961	30.386	0.138	0.043	100.13
RIC-01_c06_pn4	Lower	pn	33.826	37.917	0.768	29.006	0.040	0.059	101.62
RIC-01_c06_pn5	Lower	pn	33.552	37.523	0.857	28.561	0.059	0.065	100.62
RIC-01c01_ccp01	Lower	pn	33.253	39.176	1.177	26.616	0.037	0.013	100.27
RIC-01c01_pn02	Lower	pn	33.668	39.354	1.037	26.354	0.004	0.025	100.44
RIC-02_c01_pn2	Lower	pn	37.648	38.887	0.685	20.801	0.373	0.043	98.44
RIC-02_c01_pn3	Lower	pn	40.546	41.405	0.873	13.747	1.247	0.000	97.82
RIC-02_c03_pn2	Lower	pn	33.031	35.927	0.732	30.284	0.171	0.000	100.15
RIC-02_c04_pn2	Lower	pn	33.381	35.243	0.097	26.741	4.716	0.031	100.21
RIC-02_c04_pn4	Lower	pn	33.203	36.845	0.741	29.129	0.235	0.000	100.15
RIC-03_c02_pn2	Lower	pn	33.455	36.218	1.692	28.043	2.430	0.061	101.90
RIC-03_c02_pn3	Lower	pn	32.983	35.678	1.808	28.693	0.240	0.000	99.40
RIC-04_c02_pn2	Lower	pn	41.184	25.689	1.863	29.772	0.022	0.035	98.56
RIC-04_c02_pn2.1	Lower	pn	34.460	36.163	1.766	27.764	0.000	0.000	100.15
RIC-04_c03_pn1	Lower	pn	34.977	39.665	1.360	23.197	0.131	0.049	99.38
RIC-04_c03_pn2	Lower	pn	33.438	33.362	1.521	27.933	4.505	0.049	100.81
RIC-04_c06_pn1.1	Lower	pn	33.399	36.889	1.496	28.373	0.211	0.000	100.37
RIC-06_c01_pn2	Lower	pn	42.167	29.895	1.098	25.315	0.866	0.024	99.37
RIC-06_c01_pn3	Lower	pn	41.773	30.282	1.053	24.444	0.120	0.044	97.72
RIC-06_c03_pn2	Lower	pn	41.474	30.578	1.118	24.090	0.217	0.029	97.51
RIC-06_c03_pn4	Lower	pn	42.994	33.462	1.051	21.539	0.175	0.028	99.25
RIC-06_c03_pn5	Lower	pn	33.674	34.851	0.843	30.184	0.125	0.000	99.68
RIC-06_c03_pn6	Lower	pn	33.295	34.303	0.909	29.465	3.697	0.000	101.67
RIC-21.1_c01_ccp2	Lower	pn	32.946	35.084	0.875	30.969	0.048	0.075	100.00
RIC-21.1_c01_pn2	Lower	pn	33.923	32.639	1.913	32.704	0.076	0.025	101.28
RIC-21.1_c07_pn2	Lower	pn	41.458	31.455	1.757	21.267	2.207	0.087	98.23
RIC-21.1_c07_pn4	Lower	pn	36.830	30.838	0.284	12.650	18.411	0.027	99.04
RIC-22_box1_pn2	Lower	pn	32.889	36.051	1.048	28.261	0.001	0.031	98.28
RIC-22_c01_pn1	Lower	pn	32.925	37.428	1.109	26.861	0.007	0.071	98.40
RIC-22_c02_pn2	Lower	pn	33.553	39.187	0.753	26.454	0.102	0.027	100.08
RIC-22_c02_pn3	Lower	pn	33.481	36.986	0.000	25.852	4.497	0.040	100.86

Appendix 4.7 Red Cross Lake Intrusive Suite pentlandite mineral chemistry

Label	Series	Phase	W%(S)	W%(Fe)	W%(Co)	W%(Ni)	W%(Cu)	W%(Zn)	W% Total
RIC-51.1C_c03_ccp2	Xenolith	pn	33.258	28.516	4.281	31.795	0.080	0.121	98.05
RIC-69_c01_pn2	Lower	pn	32.885	36.275	0.000	30.227	0.001	0.166	99.55
RIC-69_c01_pn3	Lower	pn	35.569	52.765	0.000	11.386	0.142	0.028	99.89
RIC-69_c02_pn2	Lower	pn	33.407	35.570	0.936	29.107	0.001	0.047	99.07
RIC-69_c02_pn3	Lower	pn	32.946	36.104	0.904	28.864	0.039	0.071	98.93

## Appendix 4.8 Red Cross Lake Intrusive Suite chalcopyrite mineral chemistry

Label	Series	Phase	W%(S)	W%(Fe)	W%(Co)	W%(Ni)	W%(Cu)	W%(Zn)	W% Total
RIC-01_c04_04ccp2	Lower	ccp	34.225	30.295	0.006	0.029	33.703	0.100	98.36
RIC-01_c04_04ccp4	Lower	ccp	34.787	30.243	0.009	0.033	34.306	0.000	99.38
RIC-01_c06_ccp7	Lower	ccp	34.001	31.405	0.000	0.937	32.242	0.007	98.59
RIC-03_c02_ccp2	Lower	ccp	34.527	30.295	0.000	0.029	34.130	0.084	99.06
RIC-06_c01_ccp1	Lower	ccp	34.780	30.161	0.000	0.122	33.835	0.071	98.97
RIC-06_c03_ccp2	Lower	ccp	35.045	30.631	0.000	0.032	34.417	0.077	100.20
RIC-06_c03_po4	Lower	ccp	35.993	32.257	0.058	7.448	23.514	0.042	99.31
RIC-21.1_c05_ccp2	Lower	ccp	34.694	30.523	0.000	0.180	34.114	0.109	99.62
RIC-21.1_c05_ccp3	Lower	ccp	34.865	31.438	0.000	0.038	34.412	0.046	100.80
RIC-21.1_c07_ccp3	Lower	ccp	34.581	30.622	0.014	0.033	33.954	0.087	99.29
RIC-30B_c04_ccp2	Lower	ccp	33.770	30.168	0.000	0.000	34.486	0.210	98.63
RIC-52_c03_ccp2	Upper	ccp	35.210	31.595	0.000	0.019	35.038	0.098	101.96
RIC-67_c04_ccp2	Upper	ccp	33.984	30.578	0.000	0.037	35.750	0.122	100.47
RIC-69_c01_ccp2	Lower	ccp	35.219	40.712	0.000	0.031	23.478	0.191	99.63
RIC-69_c01_ccp3	Lower	ccp	34.859	30.116	0.000	0.000	34.534	0.000	99.51
RIC-76B_C04_ccp2	Upper	ccp	34.485	29.760	0.000	0.000	35.832	0.000	100.08

Appendix 4.9 Red Cross Lake Intrusive Suite pyrite and millerite mineral chemistry

Label	Series	Phase	W%(S)	W%(Fe)	W%(Co)	W%(Ni)	W%(Cu)	W%(Zn)	W% Total
RIC-04_c05_pn2	Lower	Mi	28.000	2.125	0.008	71.307	0.146	0.026	101.61
RIC-21.1_c03_po2	Lower	py	52.628	43.540	0.118	0.531	0.752	0.000	97.57
RIC-76B_C04_po2	Upper	py	53.318	43.290	0.000	3.976	0.269	0.069	100.92
RIC-76B_C04_po3	Upper	py	53.330	45.180	0.000	2.436	0.121	0.016	101.08

Mi = millerite  
 py = pyrite

	P	Type	Location	Al	Si	Ca	Na	K	Fe	Mg	CaO	SiO <sub>2</sub>	Na <sub>2</sub> O	K <sub>2</sub> O	Sum Oxide
SMA-09_c01_fsp2	pink	leucogabbronorite	core	47.016	50.943	2.04	56.09	28.86	0.16	10.64	-	0	5.42	0.36	101.53
SMA-09_c02_fsp3	pink	leucogabbronorite	core	49.422	48.901	1.673	56.22	28.84	0.11	10.49	-	0	5.86	0.3	101.83
SMA-09_c02_fsp5.1	pink	leucogabbronorite	core	47.141	51.625	1.234	53.83	27.8	0.22	10.25	-	0	5.17	0.21	97.49
SMA-09_c02_fsp6.1	pink	leucogabbronorite	core	47.901	50.55	1.454	54.06	28.91	0.22	10.66	-	0.05	5.58	0.26	99.75
SMA-09_c03_fsp2	pink	leucogabbronorite	core	45.936	52.424	1.585	54.81	27.71	0.22	10.68	-	0.03	5.17	0.27	98.9
SMA-09_c03_fsp5	pink	leucogabbronorite	core	46.821	51	2.123	54.55	28.46	0.13	10.37	-	0.03	5.26	0.36	99.16
SMA-09_c03_fsp1.1	pink	leucogabbronorite	rim	45.026	53.588	1.333	54.44	28.58	0.36	11.1	-	0.03	5.15	0.23	99.9
SMA-09_c02_fsp2.1	pink	leucogabbronorite	rxn core	47.39	51.032	1.474	55.4	28.78	0.17	10.57	-	0.06	5.42	0.26	100.65
SMA-09_c03_fsp4.2	pink	leucogabbronorite	rxn core	46.576	51.425	1.905	55.82	28.98	0.15	11.07	-	0.06	5.54	0.34	101.95
SMA-09_c02_fsp1.1	pink	leucogabbronorite	rxn rim	45.849	52.508	1.639	55.52	29	0.23	10.88	-	0	5.25	0.29	101.16
SMA-09_c02_fsp3.2	pink	leucogabbronorite	rxn rim	46.54	51.796	1.528	55.59	28.87	0.26	10.6	-	0.08	5.26	0.26	100.92
SMA-09_c03_fsp3	pink	leucogabbronorite	rxn rim	47.134	51.458	1.408	53.46	28.06	0.13	10.45	-	0	5.29	0.24	97.64
SMA-12_c01_fsp1	pink	gabbronorite	core	49.744	48.223	2.033	55.61	27.99	0.18	9.89	-	0	5.64	0.35	99.65
SMA-12_c01_fsp1	pink	gabbronorite	core	50.482	48.901	0.617	57.07	28.52	0.11	10.47	-	0	5.97	0.11	102.26
SMA-12_c01_fsp1.1	pink	gabbronorite	core	51.626	47.653	0.67	55.91	28.62	0.14	10.16	-	0.03	6.08	0.12	101.06
SMA-12_c02_fsp1	pink	gabbronorite	core	50.911	47.71	1.236	54.49	27.66	0.12	10	-	0.08	5.9	0.22	98.47
SMA-12_c02_fsp2	pink	gabbronorite	core	48.602	49.094	2.292	56.24	29.22	0.11	10.47	-	0.01	5.73	0.41	102.18
SMA-12_c01_fsp2	pink	gabbronorite	rxn/rxlz	83.56	16.277	0.163	63.31	22.23	0	3.43	-	0	9.74	0.03	98.74
SMA-12_c01_fsp2	pink	gabbronorite	rxn/rxlz	82.126	17.713	0.012	63.28	22.75	0.13	3.67	-	0.08	9.41	0	99.34
SMA-15_c01_fsp1	white	anorthosite	bleb	20.084	21.173	57.214	58.04	22.69	0.03	4.48	-	0.88	2.35	10.17	98.65
SMA-15_c01_fsp2	white	anorthosite	core	48.875	48.931	2.194	54.66	27.95	0.12	9.97	-	0	5.5	0.38	98.58
SMA-15_c02_fsp1	white	anorthosite	core	50.536	47.111	2.316	56.62	27.89	0.12	9.92	-	0.02	5.88	0.41	100.87
SMA-18_c01_fsp1.1	pink	leuconorite	core	49.499	49.858	0.642	55.89	28.02	0.09	10.12	0	0	5.55	0.11	99.79
SMA-18_c01_fsp2	pink	leuconorite	rxn core	17.516	82.301	0.074	48.75	33.43	0.35	16.65	0	0.06	1.96	0.01	101.22
SMA-20A_c01_fsp1	white	anorthosite	core	51.722	46.373	1.79	55.24	27.81	0.26	9.57	0	0.06	5.9	0.31	99.15
SMA-20A_c02_fsp2	white	anorthosite	core	52.225	47.254	0.471	56.73	28.35	0.12	9.73	0	0.03	5.94	0.08	100.98
SMA-20A_c02_fsp2.1	white	anorthosite	core	50.911	48.579	0.464	55.25	28.04	0.09	9.91	0	0.03	5.74	0.08	99.14
SMA-20A_c01_fsp3	white	anorthosite	core	34.47	44.988	20.001	53.95	25.88	1.81	9.39	0	0.31	3.98	3.51	98.82
SMA-20A_c01_fsp2	white	anorthosite	rxn/rxlz	51.221	47.309	1.42	55.6	27.51	0.17	9.62	0	0.03	5.75	0.24	98.92
SMA-20A_c02_fsp1	white	anorthosite	rxn/rxlz	46.956	46.893	5.969	56.2	27.94	0.05	9.54	0.04	0.05	5.28	1.02	100.1
SMA-24_c02_fsp1	pink	anorthosite	bleb	42.228	45.227	12.232	55.9	27.41	0.1	9.32	-	0.18	4.81	2.12	99.83
SMA-24_c03_fsp3	pink	anorthosite	bleb	35.961	42.972	20.717	56.35	26.63	0.51	8.74	-	0.19	4.04	3.54	100.18
SMA-24_c01_fsp1	pink	anorthosite	core	49.15	48.513	2.329	55.53	28.14	0.08	9.95	-	0	5.57	0.4	99.68
SMA-24_c02_fsp2	pink	anorthosite	core	49.617	48.518	1.865	54.85	27.45	0.05	10.03	-	0	5.67	0.32	98.37
SMA-24_c03_fsp2	pink	anorthosite	core	49.717	48.288	1.995	55.96	27.92	0.11	9.97	-	0	5.67	0.35	99.98
SMA-24_c03_fsp4	pink	anorthosite	core	51.676	46.432	1.831	56.24	27.71	0.12	9.66	-	0.03	5.94	0.32	100.02
SMA-24_c01_fsp2	pink	anorthosite	rxn rim	36.662	46.61	16.188	55.96	26.96	0.16	9.53	-	0.3	4.14	2.78	99.83
SMA-31_c01_fsp1	pink	norite	core	48.053	50.42	1.283	57.1	27.69	0.28	10.25	0.05	0.06	5.4	0.22	101.06
SMA-31_c02_fsp1.1	pink	norite	core	48.1	50.663	1.236	56.74	28.31	0.16	10.23	0	0	5.37	0.21	101.03
SMA-31_c03_fsp2	pink	norite	core	47.436	51.725	0.794	56.33	28.74	0.15	10.85	0	0.03	5.5	0.14	101.74
SMA-31_c03_fsp4	pink	norite	core	49.401	49.558	0.947	57.82	28.42	0.17	10.09	0.04	0	5.56	0.16	102.26
SMA-31_c03_fsp1	pink	norite	rim	46.098	52.87	1.032	54.99	28.53	0.15	10.86	0	0	5.23	0.18	99.95
SMA-31_c03_fsp3	pink	norite	rim	46.446	52.505	1.049	55.99	28.48	0.27	10.75	0	0	5.26	0.18	100.94
SMA-31_c04_fsp2	pink	norite	rim	45.9	52.467	1.533	55.82	29.45	0.24	10.95	0.04	0	5.3	0.27	102.07
SMA-31_c02_fsp2	pink	norite	rxn rim	33.335	65.894	0.654	52.49	30.87	0.24	13.53	0	0.07	3.78	0.11	101.1
SMA-33_c01_fsp1	pink	norite	core	52.532	45.029	2.381	56.7	27.43	0.22	9.31	0	0.03	6	0.41	100.11
SMA-33_c01_fsp2	pink	norite	core	55.149	44.072	0.684	56.29	26.65	0.08	9	0.03	0	6.22	0.12	98.39
SMA-33_c02_fsp2	pink	norite	core	47.874	50.645	1.48	55.11	28.65	0.13	10.45	0	0	5.46	0.26	100.06
SMA-33_c02_fsp3	pink	norite	core	50.899	46.975	1.799	55.8	27.93	0.22	9.65	0.12	0	5.78	0.31	99.8
SMA-33_c01_fsp3	pink	norite	rxn/rxlz	42.069	30.12	27.236	53.17	28.62	1.68	5.45	0.03	0.23	4.21	4.14	97.64
SMA-37_c01_fsp2	pink	gabbronorite	core	43.895	54.877	1.109	53.99	29.33	0.07	11.66	-	0.07	5.15	0.2	100.46
SMA-37_c02_fsp2	pink	gabbronorite	core	43.545	55.298	1.056	53.9	29.86	0.16	11.48	-	0.06	4.99	0.18	100.63
SMA-37_c02_fsp4	pink	gabbronorite	core	41.37	57.614	0.869	53.43	29.68	0.12	11.86	-	0.08	4.71	0.15	100.03

## Appendix 4.10 Steel Mountain Anorthosite feldspar mineral chemistry

SMA-37_c03_fsp1	pink	gabbronorite	core	41.606	57.548	0.818	52.54	29.71	0.47	11.95	-	0.02	4.77	0.14	99.6
SMA-37_c01_fsp1	pink	gabbronorite	rim	41.84	57.181	0.979	53.95	30.2	0.14	11.84	-	0	4.79	0.17	101.09
SMA-37_c02_fsp3	pink	gabbronorite	rim	42.739	56.075	1.186	53.85	29.76	0.27	11.75	-	0	4.95	0.21	100.79
SMA-57_c01_fsp01	pink	norite	core	51.858	47.622	0.504	56.79	27.5	0.18	10.12	-	0.01	6.09	0.09	100.77
SMA-57_c03_fsp3	pink	norite	core	47.495	51.886	0.619	55.4	28.86	0.1	10.92	-	0	5.52	0.11	100.92
SMA-57_c05_fsp4	pink	norite	core	53.598	44.616	1.67	57.65	27.35	0.14	9.19	-	0.07	6.1	0.29	100.79
SMA-57_c03_fsp2	pink	norite	rxn core	21.639	78.221	0.128	49.6	33.73	0.33	16.29	-	0.01	2.49	0.02	102.47
SMA-57_c03_fsp1.2	pink	norite	rxn rim	16.471	83.402	0.047	47.27	34.56	0.44	17.2	-	0.05	1.88	0.01	101.4
SMA-57_c01_fsp02	pink	norite	rxn/rxiz	52.321	46.603	1.063	55.93	27.54	0.1	9.63	-	0.01	5.97	0.18	99.36
SMA-57_c02_fsp2	pink	norite	rxn/rxiz	12.889	86.752	0.158	46.32	32.01	2.18	16.53	-	0.1	1.36	0.03	98.53
SMA-57_c05_fsp2	pink	norite	rxn/rxiz	48.236	45.505	6.038	56.41	28.34	0.12	10.02	-	0.13	5.87	1.12	102.01
SMA-57_c05_fsp2.2	pink	norite	rxn/rxiz	52.954	45.101	1.722	56.75	26.97	0.15	9.28	-	0.13	6.02	0.3	99.59
SMA-61A_box1_fsp1	white	leuconorite	core	54.81	45.024	0.165	56.22	27.4	0.04	9.35	-	0	6.29	0.03	99.32
SMA-61A_box1_fsp2	white	leuconorite	rxn/rxiz	73.36	14.69	11.88	60.92	25.71	0.47	2.94	-	0.04	8.11	2	100.2
SMA-61A_c02_fsp2	white	leuconorite	rxn/rxiz	0.623	99.376	0.001	38.24	29.14	6.99	24.17	-	0	0.08	0	98.62
SMA-71_c01_fsp1	white	leucogabbronorite	bleb	4.255	0.724	93.14	65.52	19.02	0.03	0.15	0	1.03	0.47	15.66	101.88
SMA-71_c02_fsp3	white	leucogabbronorite	bleb	11.009	1.583	85.33	64.53	19.41	0.07	0.32	0	1.13	1.21	14.26	100.93
SMA-71_c01_fsp2	white	leucogabbronorite	core	50.122	47.908	1.883	57.2	27.83	0.12	9.96	0	0.05	5.76	0.33	101.24
SMA-71_c02_fsp1	white	leucogabbronorite	core	53.471	45.334	1.064	57.88	28.03	0.09	9.47	0.03	0.02	6.17	0.19	101.87
SMA-71_c02_fsp2	white	leucogabbronorite	core	51.451	46.512	2.037	57.35	27.75	0.12	9.55	0	0	5.84	0.35	100.97
SMA-73_c01_fsp1	white	leuconorite	core	48.561	50.956	0.417	55.61	28.86	0.13	10.68	0	0.04	5.63	0.07	101.02
SMA-73_c01_fsp2	white	leuconorite	core	52.007	46.793	1.118	56.24	26.98	0.08	9.38	0	0.04	5.76	0.19	98.67
SMA-73_c02_fsp2	white	leuconorite	core	49.366	49.828	0.628	55.56	28.33	0.06	10.23	0.03	0.05	5.6	0.11	99.98
SMA-73_c02_fsp2	white	leuconorite	core	49.06	50.284	0.499	56.27	28.24	0.12	10.32	0.05	0.01	5.57	0.09	100.66
SMA-73_c03_fsp2	white	leuconorite	core	49.262	50.175	0.562	54.95	28.18	0.11	10.21	0	0	5.54	0.1	99.08
SMA-73_c03_fsp2	white	leuconorite	core	48.718	50.705	0.473	56.4	28.74	0.08	10.59	0.04	0.01	5.62	0.08	101.56
SMA-73_c03_fsp3	white	leuconorite	core	45.944	53.347	0.519	55.28	28.46	0.04	10.75	0.05	0.03	5.12	0.09	99.81
SMA-73_c02_fsp3	white	leuconorite	rxn rim	39.666	59.705	0.473	53.17	29.91	0.22	11.99	0	0.09	4.4	0.08	99.86
SMA-73_c02_fsp3	white	leuconorite	rxn rim	38.304	61.273	0.422	53.25	30.44	0.3	12.82	0	0	4.43	0.07	101.31
SMA-73_c02_fsp3	white	leuconorite	rxn rim	40.657	58.769	0.516	54.17	30.01	0.33	12.11	0	0.03	4.63	0.09	101.38
SMA-76_c01_fsp3	white	leucogabbronorite	core	53.008	46.795	0.197	55.49	27.86	0	9.83	-	0	6.16	0.03	99.38
SMA-76_c02_fsp1	white	leucogabbronorite	core	52.823	46.842	0.334	54.24	27.72	0.07	9.91	-	0	6.18	0.06	98.18
SMA-76_c03_fsp1	white	leucogabbronorite	core	53.208	46.554	0.206	56.18	27.84	0.15	9.84	-	0.02	6.21	0.04	100.28
SMA-76_c03_fsp2	white	leucogabbronorite	core	51.056	48.745	0.198	53.7	27.73	0.31	10.1	-	0	5.85	0.03	97.72
SMA-76_c01_fsp1	white	leucogabbronorite	Incl	52.865	46.749	0.385	55.9	27.43	0.07	9.71	-	0	6.07	0.07	99.25
SMA-76_c01_fsp2	white	leucogabbronorite	Incl	52.648	47.056	0.296	55.62	27.79	0.11	9.64	-	0	5.96	0.05	99.18
SMA-Q2_fsp1		massive oxide	core	57.227	42.371	0.377	56.82	27.52	0.02	8.8	-	0.01	6.56	0.07	99.8
SMA-Q2_fsp2		massive oxide	core	43.472	55.964	0.563	54.08	29.46	0.34	11.75	-	0	5.05	0.1	100.78

Label	Location	Litho	Type	Mg#	Wo(Ca)	En(Mg)	Fs(Fe <sup>2+</sup> )	SiO <sub>2</sub>	TiO <sub>2</sub>	Al <sub>2</sub> O <sub>3</sub>	Cr <sub>2</sub> O <sub>3</sub>	Fe <sub>2</sub> O <sub>3</sub> (c)	FeO(c)	MnO	MgO	CaO	Sum OX%
SMA-09_c01_pyx2	matrix	leucogabbro	CPX	0.59	48.66	36.91	14.43	48.86	1.38	8.11	0.14	0.00	8.37	0.17	12.01	22.03	101.07
SMA-09_c01_pyx3	matrix	leucogabbro	OPX	0.56	0.73	70.79	28.48	50.47	0.06	5.00	0.07	1.88	17.11	0.30	23.87	0.34	99.10
SMA-09_c02_fsp2	rim	leucogabbro	OPX	0.57	0.99	73.12	25.89	52.03	0.09	4.44	0.07	3.08	16.04	0.32	25.42	0.48	101.96
SMA-09_c02_pyx3	rim	leucogabbro	OPX	0.57	0.92	71.32	27.75	50.97	0.33	4.41	0.10	1.74	16.92	0.29	24.39	0.44	99.58
SMA-09_c02_pyx4	incl	leucogabbro	CPX	0.59	48.56	37.10	14.34	47.75	1.32	7.23	0.18	0.00	8.32	0.17	12.08	21.99	99.04
SMA-09_c03_pyx1	matrix	leucogabbro	OPX	0.55	0.93	70.18	28.90	51.17	0.05	4.73	0.05	1.68	17.60	0.33	23.98	0.44	100.03
SMA-09_c03_pyx2	matrix	leucogabbro	OPX	0.56	1.51	70.41	28.08	50.94	0.07	4.55	0.05	1.74	17.03	0.33	23.96	0.71	99.38
SMA-09_c03_pyx3	rim	leucogabbro	OPX	0.57	0.78	71.21	28.01	51.41	0.06	3.92	0.07	1.65	17.16	0.29	24.47	0.37	99.39
SMA-09_c03_pyx4	rim	leucogabbro	OPX	0.58	0.75	71.28	27.97	52.08	0.09	3.53	0.00	0.91	17.35	0.30	24.81	0.36	99.44
SMA-09_c03_pyx5	incl	leucogabbro	CPX	0.60	48.59	37.44	13.97	48.56	1.04	6.55	0.15	0.00	7.97	0.14	11.98	21.62	98.00
SMA-15_c01_pyx1	matrix	anorthosite	OPX	0.52	5.14	63.82	31.04	50.82	0.12	4.02	0.06	0.86	18.75	0.46	21.63	2.42	99.14
SMA-15_c01_pyx2	rim	anorthosite	OPX	0.50	1.00	65.23	33.77	50.60	0.08	3.14	0.00	1.69	20.30	0.46	22.00	0.47	98.74
SMA-18_c01_pyx1	matrix	leuconorite	OPX	0.56	0.39	72.49	27.13	50.77	0.13	5.15	0.03	3.10	16.43	0.25	24.63	0.18	100.66
SMA-18_c01_pyx2	rim	leuconorite	OPX	0.56	0.17	74.96	24.87	51.25	0.03	4.39	0.00	3.22	15.19	0.22	25.69	0.08	100.08
SMA-18_c01_pyx3	matrix	leuconorite	OPX	0.57	0.37	72.74	26.88	50.23	0.05	4.95	0.03	2.67	16.08	0.27	24.42	0.17	98.88
SMA-18_c01_pyx4	rim	leuconorite	OPX	0.60	0.63	74.75	24.62	51.20	0.05	5.27	0.01	2.15	15.02	0.23	25.60	0.30	99.83
SMA-31_c01_pyx1	matrix	norite	OPX	0.56	0.87	72.44	26.69	50.50	0.07	4.84	0.10	3.20	16.05	0.33	24.43	0.41	99.93
SMA-31_c03_pyx1	matrix	norite	OPX	0.57	0.88	71.88	27.24	50.30	0.07	5.70	0.14	2.19	16.32	0.31	24.15	0.41	99.59
SMA-31_c03_pyx2	matrix	norite	OPX	0.58	4.80	71.06	24.14	50.67	0.14	5.12	0.11	2.91	14.58	0.31	24.08	2.26	100.18
SMA-31_c03_pyx3	matrix	norite	OPX	0.58	2.13	71.89	25.99	50.54	0.11	5.16	0.13	2.11	15.65	0.28	24.30	1.00	99.27
SMA-31_c03_pyx4	matrix	norite	OPX	0.58	0.74	73.23	26.03	50.77	0.10	5.24	0.13	2.50	15.75	0.28	24.86	0.35	99.99
SMA-31_c04_pyx1	core	norite	OPX	0.57	0.72	73.84	25.44	49.26	0.10	6.10	0.11	3.56	14.93	0.30	24.31	0.33	99.01
SMA-31_c04_pyx2	rim	norite	OPX	0.57	0.74	73.68	25.58	50.77	0.10	3.81	0.09	3.67	15.47	0.32	25.00	0.35	99.58
SMA-31_c04_pyx3	matrix	norite	OPX	0.57	0.73	72.38	26.89	50.70	0.07	5.59	0.14	2.18	16.23	0.33	24.51	0.34	100.09
SMA-31_c04_pyx4	matrix	norite	OPX	0.57	0.74	71.59	27.67	50.65	0.05	5.64	0.13	1.57	16.68	0.32	24.21	0.35	99.61
SMA-31_c04_pyx5	rim	norite	OPX	0.57	0.93	71.55	27.52	51.08	0.09	4.55	0.10	1.99	16.74	0.35	24.41	0.44	99.75
SMA-33_c02_pyx2	core	norite	OPX	0.57	0.70	71.83	27.47	51.06	0.09	4.70	0.09	1.85	16.69	0.39	24.48	0.33	99.69
SMA-33_c02_pyx3	core	norite	CPX	0.65	47.97	39.79	12.24	48.10	0.96	6.80	0.16	0.00	7.10	0.19	12.94	21.70	97.95
SMA-33_c02_pyx4	core	norite	CPX	0.66	50.82	38.79	10.40	48.30	0.94	6.02	0.09	0.62	6.07	0.19	12.71	23.17	98.11
SMA-33_c02_pyx5	rim	norite	CPX	0.63	51.66	38.25	10.09	47.75	1.08	6.91	0.16	1.35	5.84	0.22	12.41	23.32	99.03
SMA-37_c01_pyx1	core	gabbro	OPX	0.59	0.72	71.22	28.06	53.00	0.51	2.33	0.02	0.00	17.78	0.32	25.33	0.36	99.65
SMA-37_c01_pyx2	MP	gabbro	OPX	0.59	0.80	71.86	27.34	52.30	0.18	1.87	0.02	0.69	17.05	0.32	25.15	0.39	97.97
SMA-37_c01_pyx3	rim	gabbro	OPX	0.58	0.86	71.46	27.68	52.98	0.15	1.73	0.02	0.85	17.48	0.34	25.32	0.43	99.30
SMA-37_c01_pyx4	relict	gabbro	OPX	0.57	0.84	72.29	26.87	51.86	0.06	1.27	0.02	2.47	16.57	0.41	25.01	0.41	98.08
SMA-37_c01_pyx6	relict	gabbro	CPX	0.73	48.48	42.59	8.94	51.95	0.16	1.48	0.03	0.00	5.54	0.15	14.81	23.45	97.55
SMA-37_c02_pyx1	matrix	gabbro	OPX	0.60	0.75	72.23	27.03	52.54	0.54	2.69	0.00	0.00	16.96	0.26	25.44	0.37	98.78
SMA-37_c02_pyx2	rim	gabbro	CPX	0.68	48.08	41.11	10.80	51.68	0.21	1.95	0.00	0.05	6.67	0.22	14.25	23.18	98.21
SMA-37_c03_pyx1	MP	gabbro	OPX	0.59	0.81	73.05	26.15	52.83	0.07	2.53	0.03	1.17	16.45	0.31	25.79	0.40	99.57
SMA-37_c03_pyx2	rim	gabbro	OPX	0.59	1.40	72.66	25.94	52.40	0.09	2.20	0.01	1.38	16.19	0.33	25.44	0.68	98.72
SMA-37_c03_pyx4	matrix	gabbro	CPX	0.72	48.11	42.64	9.25	52.55	0.10	1.17	0.01	0.00	5.80	0.17	14.99	23.53	98.32
SMA-57_c02_pyx1	rim	norite	OPX	0.58	0.57	72.31	27.12	51.72	0.04	4.23	0.11	1.55	16.69	0.33	24.97	0.27	99.91
SMA-57_c02_pyx11	matrix	norite	OPX	0.57	0.79	71.72	27.49	50.70	0.07	5.08	0.16	1.51	16.58	0.36	24.27	0.37	99.10
SMA-57_c02_pyx2	MP	norite	OPX	0.58	0.48	72.52	27.01	51.71	0.29	3.74	0.10	1.62	16.68	0.34	25.13	0.23	99.83
SMA-57_c02_pyx3	MP	norite	OPX	0.57	0.50	71.90	27.60	50.87	0.06	4.80	0.05	1.45	16.72	0.30	24.44	0.23	98.92
SMA-57_c02_pyx4	core	norite	OPX	0.57	0.46	72.45	27.09	51.00	0.07	4.63	0.09	1.81	16.46	0.30	24.69	0.22	99.26
SMA-57_c02_pyx5	core	norite	OPX	0.57	0.60	72.26	27.14	50.92	0.06	4.88	0.04	1.94	16.46	0.31	24.88	0.28	99.47
SMA-57_c02_pyx6	core	norite	OPX	0.57	0.72	72.10	27.18	51.07	0.04	4.58	0.06	1.78	16.53	0.28	24.61	0.34	99.28
SMA-57_c02_pyx7	MP	norite	OPX	0.57	0.56	70.44	29.01	51.63	0.04	4.56	0.05	0.71	17.85	0.25	24.31	0.27	99.68
SMA-57_c02_pyx8	MP	norite	OPX	0.57	0.65	72.33	27.02	51.12	0.06	3.96	0.08	2.00	16.46	0.26	24.72	0.31	98.98
SMA-57_c02_pyx9	rim	norite	OPX	0.57	0.70	71.68	27.62	52.04	0.06	3.10	0.05	1.48	17.10	0.35	24.90	0.34	99.41
SMA-57_c03_pyx2	matrix	norite	OPX	0.57	0.62	72.21	27.17	50.49	0.06	5.71	0.07	1.87	16.33	0.32	24.35	0.29	99.49
SMA-57_c03_pyx3	matrix	norite	OPX	0.57	0.88	71.76	27.35	50.49	0.07	5.89	0.10	1.62	16.46	0.26	24.23	0.42	99.53
SMA-57_c03_pyx4	matrix	norite	OPX	0.57	0.69	72.11	27.20	50.30	0.17	5.55	0.07	1.91	16.31	0.32	24.27	0.32	99.22
SMA-57_c03_pyx5	matrix	norite	OPX	0.57	0.70	72.01	27.29	50.79	0.07	5.64	0.13	1.81	16.51	0.32	24.44	0.33	100.05
SMA-57_c05_pyx2	matrix	norite	CPX	0.60	50.63	35.82	13.55	47.35	1.03	7.78	0.20	0.00	7.61	0.16	11.28	22.19	97.60
SMA-73_c01_pyx1	core	leuconorite	OPX	0.53	0.58	70.21	29.21	50.03	0.06	3.13	0.04	3.35	17.38	0.37	23.44	0.27	98.08

Appendix 4.12 Steel Mountain Anorthosite garnet mineral chemistry

				CaO	FeO	MgO	MnO	Al <sub>2</sub> O <sub>3</sub>	TiO <sub>2</sub>	Cr <sub>2</sub> O <sub>3</sub>	Sum Oxide							
SMA-09_co2_gnt3	leucogabbronite	rim	pl-pyx	36.01	44.73	2.73	16.06	39.57	0	21.88	0.15	0	21.11	1.27	9.54	6.09		99.62
SMA-09_co2_ant4	leucogabbronite	MP	pl-pyx	37.85	43.76	1.85	16.18	39.56	0.05	22.02	0.12	0	20.01	0.84	9.71	5.9		98.21
SMA-09_co2_ant5	leucogabbronite	core	pl-pyx	37.66	44.52	1.73	15.74	39.67	0.08	21.88	0.12	0	20.48	0.79	9.72	5.78		98.52
SMA-09_co2_ant6	leucogabbronite	MP	pl-pyx	37.70	44.11	1.93	16.07	39.92	0.05	22.02	0.06	0	20.39	0.88	9.78	5.87		98.98
SMA-09_co2_ant7	leucogabbronite	rim	pl-pyx	36.12	44.69	2.79	16.05	39.89	0	22.01	0.12	0	20.73	1.28	9.4	5.94		99.37
SMA-09_co3_ant1.1	leucogabbronite	core	pl-pyx	34.54	46.27	2.26	16.65	39.88	0	22.77	0.1	0	21.8	1.05	9.13	6.23		100.96
SMA-09_co3_ant2	leucogabbronite	core	pl-pyx	35.37	45.00	2.20	17.02	39.32	0.03	22.06	0.13	0	20.62	0.99	9.09	6.23		98.47
SMA-09_co3_ant3	leucogabbronite	core	pl-pyx	36.44	44.87	2.09	16.12	39.71	0	22.17	0.16	0	20.77	0.95	9.47	6		99.23
SMA-18_c01_ant2	leuconorite	rim	Fe-Tl	42.84	48.62	1.85	5.58	39.58	0	23.02	0.17	0.23	23.01	0.86	11.38	2.48		100.72
SMA-18_c01_ant3	leuconorite	MP	Fe-Tl	38.72	45.78	1.76	13.33	39.33	0	22.1	0.13	0	21.35	0.81	10.13	5		98.86
SMA-18_c01_ant4	leuconorite	MP	Fe-Tl	43.44	47.91	1.81	6.52	39.85	0	22.51	0.11	0	22.62	0.84	11.51	2.52		99.96
SMA-18_c01_ant5	leuconorite	core	Fe-Tl	40.72	46.14	1.91	10.98	39.71	0	22.23	0.08	0	21.59	0.88	10.69	4.1		99.3
SMA-18_c01_ant6	leuconorite	MP	Fe-Tl	44.55	47.04	1.81	6.31	40.13	0	22.46	0.1	0	22.22	0.84	11.81	2.43		100
SMA-18_c01_ant7	leuconorite	MP	Fe-Tl	44.62	47.43	1.77	6.08	39.62	0	22.84	0.03	0	22.24	0.82	11.74	2.26		99.55
SMA-18_c01_ant8	leuconorite	rim	Fe-Tl	43.71	48.01	1.92	6.16	39.78	0	22.39	0.07	0	22.37	0.88	11.43	2.31		99.23
SMA-18_c03_ant1	leuconorite	rim	Fe-Tl	43.26	45.82	1.72	9.02	39.7	0	22.5	0.06	0	21.34	0.79	11.31	3.35		99.05
SMA-18_c03_ant2	leuconorite	core	Fe-Tl	42.90	41.31	1.24	14.35	40.1	0	22.38	0.07	0	19.6	0.58	11.42	5.39		99.54
SMA-18_c03_ant3	leuconorite	rim	Fe-Tl	39.89	44.26	1.72	14.11	39.41	0	22.58	0.01	0	20.58	0.79	10.41	5.13		98.91
SMA-33_c02_ant1	norite	core	pl-pyx	33.80	44.97	5.49	15.41	39.31	0.03	22.22	0.11	0	21.04	2.54	8.88	5.75		99.88
SMA-33_c02_ant2	norite	MP	pl-pyx	32.90	46.03	5.35	15.47	39.53	0.05	22.14	0.08	0	21.24	2.44	8.52	5.66		99.65
SMA-33_c02_ant3	norite	rim	pl-pyx	31.02	46.74	6.37	15.50	39.08	0.05	22.12	0.12	0	21.45	2.89	7.99	5.68		99.37

Label	Type	Ilmenite	Gaikielita	Pyrophanite	Hematite	SiO <sub>2</sub>	TiO <sub>2</sub>	Al <sub>2</sub> O <sub>3</sub>	Cr <sub>2</sub> O <sub>3</sub>	Fe <sub>2</sub> O <sub>3</sub> (c)	FeO(c)	V <sub>2</sub> O <sub>5</sub>	MnO	MgO	NiO	Sum Ox%
BS-01_c01_ox5	massive oxides	86.47	9.13	1.50	2.90	0.00	52.03	0.04	0.09	3.10	41.55	0.28	0.71	2.47	0.03	100.40
BS-01_c02_ox2	massive oxides	89.81	5.05	1.36	3.78	0.00	51.34	0.04	0.01	4.03	43.06	0.09	0.64	1.36	0.04	100.61
BS-01_c02_ox4	massive oxides	87.72	7.08	1.56	3.65	0.00	51.65	0.04	0.06	3.91	42.27	0.34	0.74	1.91	0.02	100.93
BS-01_c03_ox1	massive oxides	81.99	8.26	1.48	8.27	0.03	48.86	0.04	0.00	8.81	39.26	0.18	0.70	2.22	0.05	100.14
BS-01_c03_ox4.1	massive oxides	79.98	14.84	1.89	3.29	0.01	52.68	0.01	0.05	3.59	39.18	0.03	0.91	4.08	0.00	100.54
SMA-09_c03_ox1	leucogabbronite	0.32	0.09	0.04	99.55	0.04	0.42	0.39	1.97	104.37	0.15	0.19	0.02	0.02	0.22	107.80
SMA-09_c03_ox1.1	leucogabbronite	0.39	0.00	0.09	99.52	0.04	0.39	0.41	1.50	98.21	0.17	0.28	0.04	0.00	0.20	101.24
SMA-09_c03_ox2	leucogabbronite	44.81	0.17	1.61	53.42	0.01	23.11	0.16	0.52	52.95	19.98	0.34	0.71	0.04	0.01	97.85
SMA-09_c03_ox3	leucogabbronite	83.32	0.28	4.45	11.95	0.04	46.42	0.10	0.15	12.99	39.50	0.42	2.08	0.08	0.04	101.42
SMA-18_c02_ox2	leuconorite	28.92	2.92	0.12	68.05	0.01	16.07	0.14	0.56	68.44	13.09	0.83	0.05	0.74	0.00	99.92
SMA-18_c02_ox3	leuconorite	83.45	8.47	0.75	7.33	0.02	49.85	0.04	0.14	7.88	40.36	0.50	0.36	2.30	0.03	101.47
SMA-18_c02_ox3	leuconorite	83.45	8.47	0.75	7.33	0.02	49.85	0.04	0.14	7.88	40.36	0.50	0.36	2.30	0.03	101.47
SMA-18_c02_ox4	leuconorite	31.61	2.33	0.21	65.86	0.00	17.31	0.17	0.50	66.65	14.39	0.74	0.09	0.60	0.02	100.47
SMA-18_c02_ox5	leuconorite	82.99	7.89	0.71	8.41	0.02	49.08	0.06	0.09	9.01	40.00	0.46	0.34	2.13	0.02	101.22
SMA-18_c02_ox5	leuconorite	82.99	7.89	0.71	8.41	0.02	49.08	0.06	0.09	9.01	40.00	0.46	0.34	2.13	0.02	101.22
SMA-24_c01_ox1	anorthosite	30.12	0.00	0.07	69.81	0.02	15.66	0.04	0.33	72.31	14.04	0.07	0.03	0.00	0.03	102.53
SMA-24_c01_ox2	anorthosite	98.12	0.04	1.84	0.00	0.02	98.25	0.04	0.35	0.00	1.90	0.22	0.04	0.00	0.00	100.81
SMA-24_c03_ox1	anorthosite	58.66	0.18	2.38	38.79	0.06	30.69	0.04	0.00	38.95	26.51	0.07	1.06	0.04	0.00	97.42
SMA-24_c03_ox2	anorthosite	31.53	0.15	0.58	67.73	0.02	16.27	0.13	0.02	68.33	14.31	0.13	0.26	0.04	0.01	99.52
SMA-31_c01_ox1	norite	87.92	0.43	3.26	8.39	0.04	48.24	0.00	0.32	8.84	41.66	0.53	1.52	0.11	0.03	101.30
SMA-31_c01_ox1	norite	87.92	0.43	3.26	8.39	0.04	48.24	0.00	0.32	8.84	41.66	0.53	1.52	0.11	0.03	101.30
SMA-31_c03_ox1	norite	34.69	0.67	0.41	64.24	0.00	17.88	0.76	1.17	64.07	15.57	0.76	0.18	0.17	0.03	100.58
SMA-31_c03_ox2	norite	89.18	1.02	1.76	8.04	0.03	48.88	0.04	0.24	8.54	42.62	0.53	0.83	0.27	0.05	102.03
SMA-31_c03_ox2	norite	89.18	1.02	1.76	8.04	0.03	48.88	0.04	0.24	8.54	42.62	0.53	0.83	0.27	0.05	102.03
SMA-33_c02_ox10	norite	25.65	0.31	0.61	73.42	0.12	13.26	0.18	0.67	73.81	11.60	0.66	0.27	0.08	0.05	100.70
SMA-33_c02_ox10	norite	25.65	0.31	0.61	73.42	0.12	13.26	0.18	0.67	73.81	11.60	0.66	0.27	0.08	0.05	100.70
SMA-33_c02_ox11	norite	87.57	0.23	6.82	5.38	0.02	49.81	0.02	0.07	5.66	41.47	0.54	3.19	0.06	0.01	100.86
SMA-33_c02_ox11	norite	87.57	0.23	6.82	5.38	0.02	49.81	0.02	0.07	5.66	41.47	0.54	3.19	0.06	0.01	100.86
SMA-33_c02_ox5	norite	28.95	0.19	0.98	69.89	0.04	15.25	0.14	0.74	70.77	13.19	0.77	0.44	0.05	0.05	101.45
SMA-33_c02_ox5	norite	28.95	0.19	0.98	69.89	0.04	15.25	0.14	0.74	70.77	13.19	0.77	0.44	0.05	0.05	101.45
SMA-57_c02_ox2	norite	92.57	0.30	5.37	1.76	0.07	51.08	0.05	0.12	1.83	43.33	0.40	2.48	0.08	0.03	99.47
SMA-57_c05_ox2	norite	32.27	0.29	0.69	66.75	0.05	16.29	0.07	1.23	65.52	14.25	0.64	0.30	0.07	0.03	98.45
SMA-57_c05_ox3	norite	85.31	0.38	3.49	10.82	0.00	46.42	0.02	0.38	11.25	39.93	0.40	1.61	0.10	0.00	100.12
SMA-65_c02_ox1	MD	84.29	0.28	7.64	7.80	0.02	47.85	0.06	0.02	8.09	39.36	0.44	3.52	0.07	0.00	99.43
SMA-65_c04_ox2	MD	87.89	0.13	7.04	4.94	0.01	49.58	0.03	0.00	5.15	41.21	0.32	3.26	0.03	0.03	99.63
SMA-71_c01_ox1	leucogabbronite	88.22	0.00	1.88	9.90	0.01	47.12	0.03	0.00	10.34	41.48	0.35	0.87	0.00	0.02	100.23
SMA-71_c01_ox2	leucogabbronite	96.86	0.73	2.41	0.00	3.87	46.08	2.53	0.01	0.00	43.99	0.32	1.08	0.19	0.02	98.09
SMA-71_c01_ox3	leucogabbronite	96.44	0.00	2.37	1.19	1.49	49.82	1.25	0.00	1.25	45.46	0.39	1.10	0.00	0.00	100.76
SMA-71_c02_ox2	leucogabbronite	47.13	0.00	0.95	51.92	0.97	23.86	0.16	0.00	54.17	22.12	0.16	0.44	0.00	0.04	101.93
SMA-71_c02_ox2.1	leucogabbronite	81.60	0.00	1.66	16.73	0.03	43.97	0.04	0.00	17.67	38.77	0.32	0.78	0.00	0.02	101.60
SMA-73_c03_ox2	leuconorite	88.82	0.28	4.58	6.39	0.03	49.30	0.05	0.21	6.73	42.09	0.46	2.13	0.07	0.01	101.07
SMA-73_c03_ox3	leuconorite	95.28	0.23	4.50	0.00	0.06	54.16	1.57	0.28	0.00	40.76	0.43	1.90	0.05	0.03	99.25
SMA-73_c03_ox4	leuconorite	59.57	0.00	0.03	40.39	0.04	28.80	0.35	1.50	39.03	25.90	0.66	0.01	0.00	0.04	96.32
SMA-73_c03_ox5	leuconorite	60.68	0.17	2.87	36.28	0.02	32.26	0.07	1.14	36.73	27.63	0.63	1.29	0.04	0.02	99.83
SMA-73_c03_ox5	leuconorite	77.74	0.33	3.30	18.63	0.04	42.75	0.00	0.75	19.57	36.75	0.44	1.54	0.09	0.03	101.95
SMA-73_c04_ox4	leuconorite	90.46	0.30	3.63	5.62	0.05	50.48	0.03	0.30	6.02	43.56	0.50	1.72	0.08	0.01	102.74
SMA-73_c04_ox5	leuconorite	60.68	0.17	2.87	36.28	0.02	32.26	0.07	1.14	36.73	27.63	0.63	1.29	0.04	0.02	99.83
SMA-76_c03_ox1.1	leucogabbronite	0.00	0.08	0.39	99.53	0.03	0.01	0.12	5.55	94.54	0.00	0.31	0.17	0.02	0.05	100.80
SMA-76_c03_ox2	leucogabbronite	31.63	0.03	0.02	68.32	0.03	15.37	0.06	1.98	66.39	13.83	0.16	0.01	0.01	0.00	97.83
SMA-76_c03_ox3	leucogabbronite	19.72	0.22	0.10	79.96	0.00	9.79	0.07	2.08	77.80	8.63	0.28	0.04	0.05	0.04	98.80

Appendix 4.14 Steel Mountain Anorthosite spinel mineral chemistry

	Phase	Type	SiO <sub>2</sub>	TiO <sub>2</sub>	Al <sub>2</sub> O <sub>3</sub>	Cr <sub>2</sub> O <sub>3</sub>	FeO	MgO	Y <sub>2</sub> O <sub>3</sub>	MnO	CaO	Na <sub>2</sub> O	Sum Ox%
BS-01_c01_ox1	Hc	massive oxides	0.02	0.03	60.36	0.52	4.49	19.06	0.12	0.14	14.41	0.09	99.24
BS-01_c01_ox2	Mt	massive oxides	0.07	0.22	0.42	0.36	66.5	30.8	0.38	0.02	0.15	0.07	99
BS-01_c01_ox4	Mt	massive oxides	0	0.18	0.34	0.53	66.55	30.61	0.55	0.02	0.16	0.1	99.04
BS-01_c01_ox6	Hc	massive oxides	0.2	0.16	62.14	0.56	3.46	15.02	0.08	0.09	17.52	0.08	99.31
BS-01_c02_ox1	Mt	massive oxides	0	0.08	0.33	0.45	67.14	30.53	0.16	0.01	0.14	0.07	98.91
BS-01_c02_ox3	Hc	massive oxides	0.01	0.02	62.86	0.51	3.03	16.49	0	0.14	16.4	0.09	99.56
BS-01_c02_ox3	Hc	massive oxides	0.01	0.02	62.86	0.51	3.03	16.49	0	0.14	16.4	0.09	99.56
BS-01_c02_ox5	Mt	massive oxides	0.04	0.35	0.32	0.55	66.22	30.96	0.45	0.03	0.1	0.05	99.08
BS-01_c02_ox7	Hc	massive oxides	0.02	0.01	60.33	0.55	4.72	17.81	0.05	0.13	15.14	0.05	98.81
BS-01_c02_ox8	Hc	massive oxides	0.02	0	61.48	0.67	4.11	17	0.09	0.11	15.92	0.09	99.47
BS-01_c02_ox9	Mt	massive oxides	0.02	0.05	0.28	0.57	67.08	30.71	0.5	0.04	0.12	0.07	99.47
BS-01_c03_ox2	Mt	massive oxides	0.03	5.96	0.22	0.29	56.79	35.86	0.07	0.07	0.36	0.09	99.73
BS-01_c03_ox5	Mt	massive oxides	0	4.59	0.02	0	61	35.49	0.08	0.02	0.11	0.05	101.35
SMA-18_c01_ox1	Mt	leuconorite	0	0.03	0.26	0.65	67.39	30.73	0.21	0.02	0.06	0.13	99.47
SMA-18_c01_ox2	Mt	leuconorite	0	0.03	0.3	0.57	68.08	31.06	0.31	0	0.08	0.12	100.54
SMA-18_c01_ox3.2	Hc	leuconorite	0.06	3.67	66.21	0.68	0	19.1	0.16	0.05	8.12	0.18	98.23
SMA-18_c01_ox4	Mt	leuconorite	1.4	0.14	2.14	0.86	61.11	31.24	0.23	0.04	0.98	0.12	98.25
SMA-18_c02_ox1	Mt	leuconorite	0.05	0.03	0.2	1.52	66.96	31.04	0.38	0.03	0.11	0.1	100.43
SMA-18_c03_ox1	Hc	leuconorite	0.04	0.02	59.72	1.65	3.81	19.38	0	0.09	14.04	0.19	98.96
SMA-18_c03_ox2	Hc	leuconorite	0	0	59.79	1.85	3.42	20.16	0.05	0.09	13.54	0.19	99.11
SMA-18_c03_ox3	Mt	leuconorite	0	0.09	0.3	1.22	66.96	30.86	0.46	0	0.18	0.12	100.19
SMA-18_c03_ox4.1	Mt	leuconorite	0.01	0.03	0.27	1.16	67.14	30.84	0.48	0.03	0.13	0.15	100.23
SMA-33_c02_ox1	Mt	norite	0.05	0	0.05	1.07	66.56	30.54	0.05	0.03	0	0.05	98.4
SMA-33_c02_ox12	Mt	norite	0.04	0.08	0.17	2.1	66.58	31.33	0.5	0.05	0.03	0.11	100.99
SMA-33_c02_ox13	Mt	norite	0.07	0.06	0.04	0.2	67.98	30.93	0.12	0.02	0	0.09	99.52
SMA-33_c02_ox2	Mt	norite	0.03	0.02	0.31	2.68	65.23	30.88	0.46	0.03	0.04	0.17	99.87
SMA-33_c02_ox8	Mt	norite	0	0.2	0.03	2.25	66.07	31.17	0.36	0.04	0.01	0.09	100.22
SMA-61A_c01_ox2	Mt	leuconorite	0	0.08	0.08	0.67	66.71	30.41	0.1	0.06	0	0.1	98.21
SMA-65_c02_ox2	Mt	MD	0.05	0.03	0.07	0.02	66.74	30.66	0.99	0.03	0	0.04	98.62
SMA-71_c02_ox2	Mt	leucogabbronorite	0.97	23.86	0.16	0	19.21	53.58	0.16	0.44	0	0.04	98.43
SMA-73_c03_ox2	Mt	leuconorite	0.21	0.65	0.13	2.58	64.15	32.16	0.75	0.01	0	0.02	100.65
SMA-73_c03_ox3	Mt	leuconorite	0.03	11.12	0.09	2.07	43.38	40.87	0.82	0.13	0	0	98.52
SMA-73_c03_ox6	Mt	leuconorite	0.04	8.36	0.05	1.91	51.65	39.34	0.66	0.2	0.03	0.04	102.28
SMA-76_c03_ox1	Mt	leucogabbronorite	0.04	0	0.26	8.46	60.04	30.81	0.22	0.42	0.05	0.06	100.35

## Appendix 4.15 Steel Mountain Anorthosite pyrrhotite mineral chemistry

Label	Phase	W%(S)	W%(Fe)	W%(Co)	W%(Ni)	W%(Cu)	W%(Zn)	W % Total
SMA-40-1B_po1	po	38.82	57.24	0	1.39	0.00	0.08	97.53
SMA-40-1B_SU1.2	po	39.61	57.71	0	1.21	0.21	1.68	100.42
SMA-40-1B_SU1.1	po	39.64	59.10	0	1.22	0.01	0.12	100.09
SMA-40-1B_C05_po1	po	40.17	59.29	0	1.25	0.05	0.00	100.75
SMA-40-1B_c02_po2	po	40.22	59.35	0	1.51	0.06	0.04	101.17
SMA-40-1B_c02_po1	po	40.67	58.58	0	1.58	0.06	0.03	100.92
SMA-40-1C_c03_SU1	po	40.24	59.40	0	1.28	0.00	0.07	100.99

Appendix 4.16 Steel Mountain Anorthosite pyrite mineral chemistry

Label	Phase	W%(S)	W%(Fe)	W%(Co)	W%(Ni)	W%(Cu)	W%(Zn)	W % Total
SMA-65_c04_SU2	py	53.93	46.12	0.00	0.05	0.05	0.11	100.26
SMA-40-1C_c04_py1.1	py	54.33	47.15	0.00	0.01	0.10	0.05	101.65
SMA-40-1C_c03_SU3	py	54.44	47.57	0.00	0.00	0.14	0.00	102.15
SMA-40-1C_c02_SU2	py	54.13	47.15	0.00	0.00	0.00	0.08	101.35
SMA-40-1C_c02_SU1	py	54.54	47.73	0.00	0.00	0.04	0.00	102.31
SMA-40-1C_c01_SU2	py	54.53	46.20	0.75	0.00	0.00	0.00	101.47
SMA-40-1B_py2	py	54.25	47.76	0.00	0.09	0.10	0.02	102.21
SMA-40-1B_py1	py	54.57	47.64	0.00	0.06	0.06	0.05	102.39
SMA-40-1B_L04_SU3	py	54.44	47.39	0.00	0.21	0.08	0.03	102.15
SMA-40-1B_L04_SU2	py	54.02	43.12	0.00	4.06	0.12	0.02	101.33
SMA-40-1B_L04_SU1	py	55.39	43.16	0.00	3.43	0.09	0.00	102.07
SMA-40-1B_C05_SU1	py	54.00	46.65	0.00	0.95	0.05	0.01	101.67
SMA-40-1B_c04_py4	py	54.85	47.43	0.00	0.20	0.03	0.00	102.50
SMA-40-1B_c04_py3	py	54.05	42.97	0.00	4.50	0.02	0.08	101.62
SMA-40-1B_c04_py1	py	54.44	46.83	0.00	0.55	0.00	0.03	101.84
SMA-40-1B_c04_pn1	py	54.15	43.30	0.00	4.67	0.00	0.14	102.26
SMA-40-1B_c03_py1	py	54.67	47.12	0.00	0.00	0.04	0.00	101.83
SMA-40-1B_c02_py4	py	54.23	47.38	0.00	0.06	0.04	0.00	101.71
SMA-40-1B_c02_py3	py	54.23	46.27	0.00	0.61	0.12	0.05	101.27
SMA-40-1B_c02_py1	py	54.11	43.71	0.00	3.92	0.01	0.00	101.75

Appendix 4.17 Steel Mountain Anorthosite chalcopyrite mineral chemistry

Label	Phase	W%(S)	W%(Fe)	W%(Co)	W%(Ni)	W%(Cu)	W%(Zn)	W % Total
SMA-40-1B_c03_SU4	ccp	35.21	31.03	0.00	0.06	34.04	0.00	100.34
SMA-40-1C_c04_ccp1	ccp	35.00	30.94	0.00	0.03	34.61	0.23	100.81
SMA-40-1C_c04_SU1	ccp	35.19	30.58	0.00	0.06	34.50	0.15	100.47
SMA-40-1C_c03_ccp1	ccp	35.34	30.52	0.00	0.01	34.33	0.10	100.30
SMA-40-1C_c01_SU1	ccp	35.37	30.95	0.00	0.00	34.20	0.00	100.53
SMA-40-1C_c04_SU1.2	ccp	35.42	30.76	0.00	0.04	34.29	0.05	100.56
SMA-40-1C_c04_ccp2	ccp	35.55	31.13	0.00	0.02	34.25	0.18	101.13
SMA-40-1C_c04_SU1.4	ccp	35.82	30.77	0.00	0.00	34.37	0.12	101.07
SMA-65_c01_ccp1	ccp	34.87	30.48	0.00	0.00	34.67	0.10	100.11
SMA-65_c04_SU1	ccp	34.91	30.59	0.00	0.00	34.45	0.07	100.02

Appendix 4.18 Steel Mountain Anorthosite sphalerite mineral chemistry

Label	Phase	W%(S)	W%(Fe)	W%(Ni)	W%(Co)	W%(Cu)	W%(Zn)	W % Total
SMA-40-1B_c04_SU1	sph	33.53	6.50	0.00	0.00	0.00	62.42	102.46
SMA-40-1B_c03_SU2	sph	33.67	6.84	0.00	0.00	0.00	60.21	100.72
SMA-40-1B_c03_SU2	sph	33.68	6.85	0.00	0.00	0.00	60.22	100.75
SMA-40-1B_c03_SU3	sph	33.71	6.58	0.00	0.00	0.00	60.59	100.88
SMA-40-1B_C05_SU3	sph	33.76	7.39	0.18	0.00	0.00	60.81	102.14
SMA-40-1C_c03_SU2	sph	33.74	7.30	0.01	0.00	0.00	59.48	100.53

Appendix 4.19 Steel Mountain Anorthosite unprocessed PGE mineral chemistry

Sample	Fe	Ni	Cu	S	Te	As	Sb	Pb	Co	Se	Sn	Cd	Au	Ag	Pt	Zn	Pd	Bi	Total
COL-SMA-40-1D_PGM3	1.47	0.00	2.24	0.12	50.75	0.00	0.00	0.20	0.02	0.06	0.00	0.00	2.62	0.12	42.61	0.00	0.57	1.05	101.82
COL-SMA-40-1A_PGM2	0.97	0.11	0.02	0.95	25.70	0.00	0.00	0.29	0.00	0.05	0.00	0.00	3.09	0.62	29.33	0.00	1.16	0.08	62.37
COL-SMA-40-1A_PGM3	0.90	0.03	0.00	0.34	25.58	0.02	0.00	0.22	0.00	0.00	0.00	0.00	3.36	0.49	29.13	0.00	0.89	0.15	61.11
COL-SMA-40-1A_PGM2	1.76	0.00	0.02	33.66	7.41	0.00	0.00	0.00	0.03	0.06	0.00	0.00	1.08	0.00	11.75	0.15	0.18	0.06	56.17
COL-SMA-40-1B-C04_PGM5	15.37	0.27	17.87	18.50	0.05	23.98	0.56	0.31	0.79	0.00	0.00	0.00	1.31	0.25	20.44	0.00	1.84	0.00	101.53
COL-SMA-1B_C04_PGM01	7.18	0.26	9.54	9.81	0.00	34.10	5.04	0.45	0.50	0.00	0.01	0.00	2.65	0.62	38.63	0.04	4.10	0.00	112.94
COL-SMA-40-1B-C04_PGM3	20.01	0.35	22.49	24.05	0.00	17.85	0.32	0.00	0.77	0.00	0.00	0.00	0.83	0.26	13.21	0.04	1.78	0.00	101.96
COL-SMA-40-1B-C04_PGM4	1.70	0.37	3.36	1.22	0.00	0.77	32.43	0.26	0.05	0.00	0.00	0.00	0.00	9.09	0.34	0.00	51.24	0.00	100.81
COL-SMA-40-1B-C04_PGM6	14.45	0.05	20.79	18.10	0.00	0.43	24.18	0.05	0.02	0.03	0.00	0.00	0.12	3.65	0.09	0.00	21.22	0.00	103.18

Appendix 4.20 Steel Mountain Anorthosite normalized PGE mineral chemistry

Sample	Point ID	Te	Pt	Au	Pd	Total
SMA-40-1A	COL-SMA-40-1A_PGM01	52.97	43.28	2.43	0.67	99.35
SMA-40-1A	COL-SMA-40-1A_PGM2	53.38	43.43	2.70	0.10	99.61
SMA-40-1A	COL-SMA-40-1A_PGM3	51.80	43.49	2.68	0.58	98.55
SMA-40-1B	COL-SMA-40-1B-C04_PGM6	42.60	48.62	5.13	1.92	98.27
SMA-40-1B	COL-SMA-40-1B-C04_PGM5	42.74	48.69	5.62	1.48	98.53
SMA-40-1B	COL-SMA-1B_C04_PGM01	36.09	57.15	5.24	0.85	99.32

Sample	Point ID	Sb	Pd	Ag	Total
SMA-40-1A	COL-SMA-40-1A_PGM2	34.46	54.44	9.65	98.55
SMA-40-1B	COL-SMA-40-1B-C04_PGM4	48.59	42.64	7.33	98.55

Sample	Point ID	Pt	As	Sb	Au	Pd	Total
SMA-40-1B	COL-SMA-40-1B-C04_PGM3	41.94	49.19	1.15	2.70	3.77	98.73
SMA-40-1D	COL-SMA-40-1D_PGM2	45.12	39.84	5.89	3.10	4.78	98.74
SMA-40-1D	COL-SMA-40-1D_PGM3	38.58	52.12	0.92	2.42	5.20	99.23

Appendix 4.21 Electron microprobe accuracy and precision

Accuracy	Sulfides	Pyroxene	Oxides	Olivine	Feldspar
Fe	1.008			1.004	
S	0.999				
Cu	1.008				
Ni	1.000				
Co	1.002				
Zn	1.003				
Mg		0.996	0.997	0.999	
Si		0.999		0.996	1.008
Al			1.000		0.997
Mn			0.997		
Ti			0.998		
Cr			1.001		
Ca					1.002
K					0.995
Na					1.001

Precision	Sulfides	Pyroxene	Oxides	Olivine	Feldspar
Fe	1.170			0.762	
S	1.074				
Cu	2.886				
Ni	1.651				
Co	0.781				
Zn	0.717				
Mg		1.245	1.072	0.533	
Si		0.898		0.517	2.517
Al			1.372		1.084
Mn			0.580		
Ti			0.912		
Cr			1.227		
Ca					0.720
K					2.018
Na					3.870

Accuracy is determined by calculating the average of the known composition divided by the measured composition for the standards. A value of 1.000 indicates 100% accuracy. Precision is determined by calculating the relative standard deviation of the actual measured standards. The lower the value, the more precise the analysis.

Each phase has a list of calculated values, which comprises the elements from each standard that was used during analyses. For example, in pyroxene, Mg and Si were measured from the MUN STD JTHY pyroxene standard whereas other elements would have been measured from other standards that contained the required elements such as olivine or an oxide standard in the case of pyroxene. Furthermore, several elements appear multiple times. This occurs because different standards were used to calculate the particular element for each phase i.e. the Fe standard for sulfides and olivine are different.

Appendix 4.22 Electron microprobe elemental standards

Standards	Sulfides	n	Pyroxene	n	Oxides	n	Olivine	n	Feldspar	n
Fe	MUN STD Carnet_pyr239	6					MUN STD FASY	5		
S	MUN STD Carnet_pyr239	6								
Cu	MUN STD CCPY	6								
Ni	MUN STD NiS	6								
Co	MUN STD CoS	3								
Zn	MUN STD ZnS	6								
Mg			MUN STD JTHY	6	MUN STD OXBU	5	MUN STD SWOL	5		
Si			MUN STD JTHY	6			MUN STD SWOL	5	MUN STD Orthoclase	7
Al					MUN STD OXBU	5			MUN STD An95	6
Mn					MUN STD MnTi ox	5				
Ti					MUN STD MnTi ox	5				
Cr					MUN STD OXBU	5				
Ca									MUN STD An95	6
K									MUN STD Orthoclase	7
Na									MUN STD Albite ox	6

This table lists the different standards used during analyses. Thus, Fe in sulfides was measured using MUN STD Carnet\_pyr239 whereas Fe in olivine was measured using MUN STD FASY. "n" denotes the number of standards used to calculate the accuracy and precision.

Appendix 5 Sulfur isotopes, all intrusions

Sample	$\delta^{34}\text{S}$ VCDT	phase
RIC-02	- 0.32	po+pn
RIC-06	- 0.58	po+pn
RIC-15	1.51	po
RIC-21	- 1.79	po+pn
RIC-22	1.36	po+pn
RIC-51A	1.47	po
RIC-53	3.85	po+py
RIC-65	2.60	po+py
RIC-78A	5.98	po+py
RIC-78B	4.92	po+py
SMA-100	7.33	py
SMA-33	2.78	py
SMA-38C	1.99	po+py+ccp
SMA-71	3.26	py
SMA-95.1	2.80	py
SMA-40B	1.20	po
SMA-40B	1.16	po+py
SMA-Q1	- 2.41	po+py
TBC-100	4.81	py
TBC-107	2.22	py
TBC-119B	2.72	po+py
TBC-69	3.85	po+py
TBC-85	2.22	po+py
TBS-105	3.63	py

**Abbreviations**

po = pyrrhotite

py = pyrite

ccp = chalcopyrite

3A PPTA



